LHeC

The Large Hadron-Electron Collider at the HL-LHC

LHeC and FCC-he Study Group

The Large Hadron-Electron Collider at the HL-LHC

LHeC and FCC-he Study Group

Abstract

The Large Hadron electron Collider (LHeC) is designed to move the field of deep inelastic scattering (DIS) to the energy and intensity frontier of particle physics. Exploiting energy recovery technology, it collides a novel, intense electron beam with a proton or ion beam from the High Luminosity–Large Hadron Collider (HL-LHC). The accelerator and interaction region are designed for concurrent electron-proton and proton-proton operation. This report represents an update of the Conceptual Design Report (CDR) of the LHeC, published in 2012. It comprises new results on parton structure of the proton and heavier nuclei, QCD dynamics, electroweak and top-quark physics. It is shown how the LHeC will open a new chapter of nuclear particle physics in extending the accessible kinematic range in lepton-nucleus scattering by several orders of magnitude. Due to enhanced luminosity, large energy and the cleanliness of the hadronic final states, the LHeC has a strong Higgs physics programme and its own discovery potential for new physics. Building on the 2012 CDR, the report represents a detailed updated design of the energy recovery electron linac (ERL) including new lattice, magnet, superconducting radio frequency technology and further components. Challenges of energy recovery are described and the lower energy, high current, 3-turn ERL facility, PERLE at Orsay, is presented which uses the LHeC characteristics serving as a development facility for the design and operation of the LHeC. An updated detector design is presented corresponding to the acceptance, resolution and calibration goals which arise from the Higgs and parton density function physics programmes. The paper also presents novel results on the Future Circular Collider in electron-hadron mode, FCC-eh, which utilises the same ERL technology to further extend the reach of DIS to even higher centre-of-mass energies.

LHeC Study Group

P. Agostini[1], H. Aksakal[2], H. Alan[3], S. Alekhin[4,5], P. P. Allport[6], N. Andari[7], K. D. J. Andre[8,9],
D. Angal-Kalinin[10,11], S. Antusch[12], L. Aperio Bella[13], L. Apolinario[14], R. Apsimon[15,11], A. Apyan[16],
G. Arduini[9], V. Ari[17], A. Armbruster[9], N. Armesto[1], B. Auchmann[9], K. Aulenbacher[18,19],
G. Azuelos[20], S. Backovic[21], I. Bailey[15,11], S. Bailey[22], F. Balli[7], S. Behera[23], O. Behnke[24],
I. Ben-Zvi[25], M. Benedikt[9], J. Bernauer[26,27], S. Bertolucci[9,28], S. S. Biswal[29], J. Blümlein[24],
A. Bogacz[30], M. Bonvini[31], M. Boonekamp[32], F. Bordry[9], G. R. Boroun[33], L. Bottura[9], S. Bousson[7],
A. O. Bouzas[34], C. Bracco[9], J. Bracinik[6], D. Britzger[37], S. J. Brodsky[36], C. Bruni[7], O. Brüning[9],
H. Burkhardt[9], O. Cakir[17], R. Calaga[9], A. Caldwell[37], A. Calıskan[38], S. Camarda[9],
N. C. Catalan-Lasheras[9], K. Cassou[39], J. Cepila[40], V. Cetinkaya[41], V. Chetvertkova[9], B. Cole[42],
B. Coleppa[43], A. Cooper-Sarkar[22], E. Cormier[44], A. S. Cornell[45], R. Corsini[9], E. Cruz-Alaniz[8],
J. Currie[46], D. Curtin[47], M. D'Onofrio[8], J. Dainton[15], E. Daly[30], A. Das[48], S. P. Das[49], L. Dassa[9],
J. de Blas[46], L. Delle Rose[50], H. Denizli[51], K. S. Deshpande[52], D. Douglas[30], L. Duarte[53],
K. Dupraz[39,54], S. Dutta[55], A. V. Efremov[56], R. Eichhorn[57], K. J. Eskola[3], E. G. Ferreiro[1],
O. Fischer[58], O. Flores-Sánchez[59], S. Forte[60,61], A. Gaddi[9], J. Gao[62], T. Gehrmann[63],
A. Gehrmann-De Ridder[63,64], F. Gerigk[9], A. Gilbert[65], F. Giuli[66], A. Glazov[24], N. Glover[46],
R. M. Godbole[67], B. Goddard[9], V. Gonçalves[68], G. A. Gonzalez-Sprinberg[53], A. Goyal[69], J. Grames[30],
E. Granados[9], A. Grassellino[70], Y. O. Gunaydin[2], Y. C. Guo[71], V. Guzey[72], C. Gwenlan[22],
A. Hammad[12], C. C. Han[73,74], L. Harland-Lang[22], F. Haug[9], F. Hautmann[22], D. Hayden[75],
J. Hessler[37], I. Helenius[3], J. Henry[30], J. Hernandez-Sanchez[59], H. Hesari[76], T. J. Hobbs[77], N. Hod[78],
G. H. Hoffstaetter[57], B. Holzer[9], C. G. Honorato[59], B. Hounsell[8,11,39], N. Hu[39], F. Hug[18,19],
A. Huss[9,46], A. Hutton[30], R. Islam[23,79], S. Iwamoto[80], S. Jana[58], M. Jansova[81], E. Jensen[9], T. Jones[8],
J. M. Jowett[9], W. Kaabi[39], M. Kado[31], D. A. Kalinin[10,11], H. Karadeniz[82], S. Kawaguchi[83], U. Kaya[84],
R. A. Khalek[85], H. Khanpour[76,86], A. Kilic[87], M. Klein[8], U. Klein[8], S. Kluth[37], M. Köksal[88],
F. Kocak[87], M. Korostelev[22], P. Kostka[8], M. Krelina[89], J. Kretzschmar[8], S. Kuday[90], G. Kulipanov[91],
M. Kumar[92], M. Kuze[83], T. Lappi[3], F. Larios[34], A. Latina[9], P. Laycock[25], G. Lei[93], E. Levitchev[91],
S. Levonian[24], A. Levy[94], R. Li[95,96], X. Li[62], H. Liang[62], V. Litvinenko[25,26], M. Liu[71], T. Liu[97],
W. Liu[98], Y. Liu[99], S. Liuti[100], E. Lobodzinska[24], D. Longuevergne[39], X. Luo[101], W. Ma[62],
M. Machado[102], S. Mandal[103], H. Mäntysaari[3,104], F. Marhauser[30], C. Marquet[105], A. Martens[39],
R. Martin[9], S. Marzani[106,107], J. McFayden[9], P. Mcintosh[10], B. Mellado[92], F. Meot[57], A. Milanese[9],
J. G. Milhano[14], B. Militsyn[10,11], M. Mitra[108], S. Moch[24], M. Mohammadi Najafabadi[76], S. Mondal[104],
S. Moretti[109], T. Morgan[46], A. Morreale[26], P. Nadolsky[77], F. Navarra[110], Z. Nergiz[111], P. Newman[6],
J. Niehues[46], E. W. Nissen[9], M. Nowakowski[112], N. Okada[113], G. Olivier[39], F. Olness[77], G. Olry[39],
J. A. Osborne[9], A. Ozansoy[17], R. Pan[95,96], B. Parker[25], M. Patra[114], H. Paukkunen[3], Y. Peinaud[39],
D. Pellegrini[9], G. Perez-Segurana[15,11], D. Perini[9], L. Perrot[39], N. Pietralla[115], E. Pilicer[87], B. Pire[105],
J. Pires[14], R. Placakyte[116], M. Poelker[30], R. Polifka[117], A. Polini[118], P. Poulose[23], G. Pownall[22],
Y. A. Pupkov[91], F. S. Queiroz[119], K. Rabbertz[120], V. Radescu[121], R. Rahaman[122], S. K. Rai[108],
N. Raicevic[123], P. Ratoff[15,11], A. Rashed[124], D. Raut[125], S. Raychaudhuri[114], J. Repond[126],
A. H. Rezaeian[127,128], R. Rimmer[30], L. Rinolfi[9], J. Rojo[85], A. Rosado[59], X. Ruan[92], S. Russenschuck[9],
M. Sahin[129], C. A. Salgado[1], O. A. Sampayo[130], K. Satendra[23], N. Satyanarayan[131], B. Schenke[25],
K. Schirm[9], H. Schopper[9], M. Schott[19], D. Schulte[9], C. Schwanenberger[24], T. Sekine[83], A. Senol[51],
A. Seryi[30], S. Setiniyaz[15,11], L. Shang[132], X. Shen[95,96], N. Shipman[9], N. Sinha[133], W. Slominski[134],
S. Smith[10,11], C. Solans[9], M. Song[135], H. Spiesberger[19], J. Stanyard[9], A. Starostenko[91], A. Stasto[136],
A. Stocchi[39], M. Strikman[136], M. J. Stuart[9], S. Sultansoy[84], H. Sun[101], M. Sutton[137],
L. Szymanowski[138], I. Tapan[87], D. Tapia-Takaki[139], M. Tanaka[83], Y. Tang[140], A. T. Tasci[141],
A. T. Ten-Kate[9], P. Thonet[9], R. Tomas-Garcia[9], D. Tommasini[9], D. Trbojevic[25,57], M. Trott[142],
I. Tsurin[8], A. Tudora[9], I. Turk Cakir[82], K. Tywoniuk[143], C. Vallerand[39], A. Valloni[9], D. Verney[39],
E. Vilella[8], D. Walker[46], S. Wallon[39], B. Wang[95,96], K. Wang[95,96], K. Wang[144], X. Wang[101],
Z. S. Wang[145], H. Wei[146], C. Welsch[8,11], G. Willering[9], P. H. Williams[10,11], D. Wollmann[9],
C. Xiaohao[13], T. Xu[147], C. E. Yaguna[148], Y. Yamaguchi[83], Y. Yamazaki[149], H. Yang[150], A. Yilmaz[82],
P. Yock[151], C. X. Yue[71], S. G. Zadeh[152], O. Zenaiev[9], C. Zhang[153], J. Zhang[154], R. Zhang[62],
Z. Zhang[39], G. Zhu[95,96], S. Zhu[132], F. Zimmermann[9], F. Zomer[39], J. Zurita[155,156] and P. Zurita[35]

[1] Universidade de Santiago de Compostela (USC), Santiago de Compostela, Spain
[2] Kahramanmaras Sutcu Imam University, Kahramanmaras, Turkey
[3] University of Jyväskylä, Jyväskylä, Finland
[4] Universität Hamburg, Hamburg, Germany
[5] Institute of High Energy Physics (IHEP), Protvino, Russia
[6] University of Birmingham, Birmingham, United Kingdom
[7] Université Paris-Saclay, Saint-Aubin, France
[8] University of Liverpool, Liverpool, United Kingdom
[9] European Organization for Nuclear Research (CERN), Genève, Switzerland
[10] Science and Technology Facilities Council (STFC) - Daresbury Laboratory, Daresbury, United Kingdom
[11] Cockcroft Institue of Accelerator Science and Technology, Daresbury, United Kingdom
[12] Universität Basel, Basel, Switzerland
[13] Chinese Academy of Sciences - Institute of High Energy Physics (IHEP), Beijing, China
[14] Laboratorio de Instrumentacao e Fisica Experimental de Particulas (LIP), Lisbon, Portugal
[15] University of Lancaster, Lancaster, United Kingdom
[16] A. Alikhanian National Laboratory (AANL), Yerevan, Armenia
[17] Ankara University, Ankara, Turkey
[18] Johannes Gutenberg University Mainz (JGU) - PRISMA Cluster of Excellence, Mainz, Germany
[19] Johannes Gutenberg-Universität Mainz (JGU), Mainz, Germany
[20] Université de Montréal, Montreal, Candada
[21] University of Montenegro, Podgorica, Montenegro
[22] University of Oxford, Oxford, United Kingdom
[23] Department of Physics, Indian Institute of Technology, Guwahati, Assam, India
[24] Deutsches Elektronen-Synchrotron (DESY), Hamburg, Germany
[25] Brookhaven National Laboratory (BNL), Upton, USA
[26] Stony Brook University, Stony Brook, USA
[27] BNL Research Center, RIKEN, Upton, NY, USA
[28] Università di Bologna, Bologna, Italy
[29] Ravenshaw University, Cuttack, India
[30] Thomas Jefferson National Accelerator Facility (Jefferson Lab), Newport News, USA
[31] Istituto Nazionale di Fisica Nucleare (INFN) - Sezione di Roma, Rome, Italy
[32] Commissariat à l'Energie Atomique (CEA) - Institut de Recherche sur les Lois Fondamentales de l'Univers (IRFU), Gif-sur-Yvette, France
[33] Razi University, Kermanshah, Iran
[34] Centro de Investigación y Estudios Avanzados (CINVESTAV), San Pedro, Mexico
[35] Universität Regensburg, Regensburg, Germany
[36] SLAC National Accelerator Laboratory, Menlo Park, USA
[37] Max-Planck-Institut für Physik, Munich, Germany
[38] Gumushane University, Gumushane, Turkey
[39] Université Paris-Saclay, CNRS/IN2P3, IJCLab, Orsay, France
[40] Faculty of Nuclear Sciences and Physical Engineering, Czech Technical University in Prague, Prague, Czech Republic
[41] Kutahya Dumlupinar University, Kutahya, Turkey
[42] Columbia University, New York, USA
[43] Indian Institute of Technology (IIT), Gandhinagar, India
[44] Centre Lasers Intenses et Applications (CELIA), Bordeaux, France
[45] University of Johannesburg (UJ), Johannesburg, South Africa
[46] Institute for Particle Physics Phenomenology, Durham University, Durham, United Kingdom
[47] University of Toronto, Toronto, Canada
[48] Osaka University, Osaka, Japan
[49] Universidad de los Andes, Santiago, Columbia
[50] Istituto Nazionale di Fisica Nucleare (INFN) - Sezione di Firenze, Firenze, Italy
[51] Bolu Abant Izzet Baysal University, Bolu, Turkey
[52] University of Maryland, College Park, USA
[53] Universidad de la Republica - Instituto de Fisica Facultad de Ciencias (IFFC), Montevideo, Uruguay

[54] Université Paris-Sud, Orsay, France
[55] Sri Guru Tegh Badadur Khalsa College, Delhi, India
[56] Joint Institute for Nuclear Research (JINR), Dubna, Russia
[57] Cornell University, Ithaca, USA
[58] Max-Planck-Institut für Kernphysik, Heidelberg, Germany
[59] Benemerita Universidad Autonoma de Puebla (BUAP), Puebla, Mexico
[60] Università degli Studi di Milano, Milano, Italy
[61] Istituto Nazionale di Fisica Nucleare (INFN) - Sezione di Milano, Milano, Italy
[62] University of Science and Technology of China (USTC), Hefei, China
[63] Department of Physics, Universität Zürich, Zurich, Switzerland
[64] Institute for Theoretical Physics, ETH, Zurich, Switzerland
[65] Northwestern University, Evanston, USA
[66] University of Rome Tor Vergata and INFN, Sezione di Roma 2, Rome, Italy
[67] Indian Institute of Science (IISc), Bangalore, India
[68] Universidade Federal de Pelotas (UFPel), Pelotas, Brazil
[69] University of Delhi, Delhi, India
[70] Fermi National Accelerator Laboratory (FNAL), Batavia, USA
[71] Liaoning Normal University (LNNU), Dalian, China
[72] Petersburg Nuclear Physics Institute (PNPI), Petersburg, Russia
[73] University of Tokyo, Tokyo, Japan
[74] Kavli Institute for the Physics and Mathematics of the Universe (KIPMU), Kashiwa, Japan
[75] Michigan State University, East Lansing, USA
[76] Institute for Research in Fundamental Sciences (IPM), Tehran, Iran
[77] Southern Methodist University, Dallas, USA
[78] Weizmann Institute of Science, Rehovot, Israel
[79] Department of Physics, Mathabhanga College, Cooch Behar, West Bengal, India
[80] Università degli Studi di Padova, Padua, Italy
[81] Université de Strasbourg, Strasbourg, France
[82] Giresun University, Giresun, Turkey
[83] Tokyo Institute of Technology, Tokyo, Japan
[84] TOBB University of Economic and Technology (TOBB ETU), Ankara, Turkey
[85] Vrije University, Amsterdam, Netherlands
[86] University of Science and Technology of Mazandaran, Behshahr, Iran
[87] Uludag University, Bursa, Turkey
[88] Sivas Cumhuriyet University, Sivas, Turkey
[89] Universidad Tecnica Federico Santa Maria, Valparaiso, Chile
[90] Istanbul Aydin University, Istanbul, Turkey
[91] Siberian Branch of Russian Academy of Science - Budker Institute of Nuclear Physics (BINP), Novosibirsk, Russia
[92] University of the Witwatersrand, Johannesburg, South Africa
[93] Tsinghua University, Beijing, China
[94] Tel-Aviv University, Tel Aviv, Israel
[95] Zhejiang Institute of Modern Physics (ZIMP), Hangzhou, China
[96] Zhejiang University (ZJU), Hangzhou, China
[97] Xiamen University (XMU), Xiamen, China
[98] University College London, London, United Kingdom
[99] Henan Institute of Science and Technology (HIST), Xinxiang, China
[100] University of Virginia, Charlottesville, USA
[101] Dalian University of Technology (DLUT), Dalian, China
[102] Universidade Federal do Rio Grande do Sul (UFRGS), Porto Alegre, Brazil
[103] Institut de Física Corpuscular – CSIC/Universitat de València, Paterna (Valencia), Spain
[104] University of Helsinki, Helsinki, Finland
[105] CPHT, CNRS, Ecole Polytechnique, I. P. Paris, France
[106] University Genova, Genova, Italy
[107] Istituto Nazionale di Fisica Nucleare (INFN) - Sezione di Genova, Genova, Italy
[108] Harish-Chandra Research Institute (HRI), Allahabad, India

109 University of Southampton, Southampton, United Kingdom
110 Universidade de Sao Paulo (USP), Sao, Paolo
111 Nigde Omer Halisdemir University, Nigde, Turkey
112 Universidad de los Andes, Carrera, Colombia
113 The University of Alabama, Tuscaloosa, USA
114 Tata Institute of Fundamental Research (TIFR), Mumbai, India
115 Technische Universität Darmstadt, Darmstadt, Germany
116 Homeday GmbH Berlin, Berlin, Germany
117 Charles University, Praque, Czech Republic
118 Istituto Nazionale di Fisica Nucleare (INFN) - Sezione di Bologna, Bologna, Italy
119 Univ. Federal do Rio Grande do Norte, Natal, Brazil
120 Karlsruher Institut für Technologie (KIT), Karlsruhe, Germany
121 IBM Deutschland RnD, GmbH, Urbar, Germany
122 Indian Institute of Science Education and Research (IISER), Kolkata, India
123 Univ. of Montenegro, Podgorica, YUOGSLAVIA
124 Shippensburg University of Pennsylvania, Shippensburg, Pennsylvania, USA
125 University of Delaware, Newark, USA
126 Argonne National Laboratory, Argonne, USA
127 Oracle, San Fransisco, USA
128 Applied AI Center of Excellence, San Francisco, USA
129 Usak University, Usak, Turkey
130 National University of Mar del Plata, Mar del Plata, Argentina
131 Oklahoma State University (OSU), Stillwater, USA
132 Peking University (PKU), Beijing, China
133 Institute of Mathematical Sciences (IMSc), Chennai, India
134 Jagiellonian University, Cracow, Poland
135 Anhui University (AHU), Hefei, China
136 Pennsylvania State University (PSU), University Park, USA
137 University of Sussex, Sussex, United Kingdom
138 Narodowe Centrum Badań Jądrowych (NCBJ), Warsaw, Poland
139 Kansas State University, Manhattan, USA
140 Korea Institute for Advanced Study (KIAS), Cheongryangri-dong, Korea
141 Kastamonu University, Kastamonu, Turkey
142 Københavns, Universitet - Niels Bohr Institutet (NBI), Copenhagen
143 University of Bergen, Bergen, Norway
144 Wuhan University of Technology, Wuhan, China
145 Asia Pacific Center for Theoretical Physics (APCTP), Pohang, Korea
146 University of California (UC), Riverside, USA
147 Hebrew University of Jerusalem - Racah Inst. of Physics, Jerusalem, Israel
148 Universidad Pedagogica y Tecnologica de Colombia, Tunja, Colombia
149 Kobe University, Kobe, Japan
150 Lawrence Berkeley National Laboratory (LBNL), Berkeley, USA
151 Fellow Royal Astronomical Society of New Zealand (FRASNZ), Auckland, New Zealand
152 Universität Rostock, Rostock, Germany
153 National Center for Theoretical Sciences (NCTS), Hsinchu, Taiwan
154 Nankai University (NKU), Tianjin, China
155 Karlsruher Institut für Technologie (KIT) - Institut für Theoretische Teilchenphysik (TTP), Karlsruhe, Germany
156 Karlsruher Institut für Technologie (KIT) - Institut für Kernphysik (IKP), Karlsruhe, Germany

Preface

This paper represents the updated design study of the Large Hadron-electron Collider, the LHeC, a TeV energy scale electron-hadron (eh) collider which may come into operation during the third decade of the lifetime of the Large Hadron Collider (LHC) at CERN. It is an account, accompanied by numerous papers in the literature, for many years of study and development, guided by an International Advisory Committee (IAC) which was charged by the CERN Directorate to advise on the directions of energy frontier electron-hadron physics at CERN. End of 2019 the IAC summarised its observations and recommendations in a brief report to the Director General of CERN, which is here reproduced as an Appendix.

The paper outlines a unique, far reaching physics programme on deep inelastic scattering (DIS), a design concept for a new generation collider detector, together with a novel configuration of the intense, high energy electron beam. This study builds on the previous, detailed LHeC Conceptual Design Report (CDR), which was published eight years ago [1]. It surpasses the initial study in essential characteristics: i) the depth of the physics programme, owing to the insight obtained mainly with the LHC, and ii) the luminosity prospect, for enabling a novel Higgs facility to be built and the prospects to search for and discover new physics to be strengthened. It builds on recent and forthcoming progress of modern technology, due to major advances especially of the superconducting RF technology and as well new detector techniques.

Unlike in 2012, there has now a decision been taken to configure the LHeC as an electron linac-proton or nucleus ring configuration, which leaves the ring-ring option [1, 2] as a backup. In ep, the high instantaneous luminosity of about $10^{34}\,\mathrm{cm}^{-2}\mathrm{s}^{-1}$ may be achieved with the electron accelerator built as an energy recovery linac (ERL) and because the brightness of the LHC exceeds early expectations by far, not least through the upgrade of the LHC to its high luminosity version, the HL-LHC [3, 4]. For ePb collisions, the corresponding per nucleon instantaneous luminosity would be about $10^{33}\,\mathrm{cm}^{-2}\mathrm{s}^{-1}$. The LHeC is designed to be compatible with concurrent operation with the LHC. It thus represents a unique opportunity to advance particle physics by building on the singular investments which CERN and its global partners have made into the LHC facility.

Since the 2012 document, significant experience with multi-turn ERL design, construction, and operation has been gained with the Cornell-BNL ERL Test Accelerator (CBETA), which has accelerated and energy recovered beam in all of its 4 turns [5, 6]. Extending much beyond the CDR, a configuration has newly been designed for a low energy ERL facility, termed PERLE [7], which is moving ahead to be built at Orsay by an international collaboration. The major parameters of PERLE have been taken from the LHeC, such as the 3-turn configuration, source, the 802 MHz frequency and cavity-cryomodule technology, in order to make PERLE a suitable facility for the development of LHeC ERL technology and the accumulation of operating ex-

perience prior to and later in parallel with the LHeC. In addition, the PERLE facility has a striking low energy physics programme, industrial applications and will be an enabler for ERL technology as the first facility to operate in the 10 MW power regime.

While the 2012 CDR focussed the physics discussion on the genuine physics of deep inelastic scattering leading much beyond HERA, a new focus arose through the challenges and opportunities posed by the HL-LHC. It is demonstrated that DIS at the LHeC can play a crucial role in sustaining and enriching the LHC programme, a consequence of the results obtained at the LHC, i.e. the discovery of the Higgs boson, the non-observation of supersymmetry (SUSY) or other non Standard Model (SM) exotic particles and, not least, the unexpected realisation of the huge potential of the LHC for discovery through precision measurements in the strong and electroweak sectors. Thus, it was felt time to summarise the recent seven years of LHeC development, also in support of the current discussions on the future of particle physics, especially at the energy frontier. Both for the LHeC [8–10] and PERLE [11], documents were submitted for consideration to the European Strategy for Particle Physics Update.

The LHeC is a once in our lifetime opportunity for substantial progress in particle physics. It comprises, with a linac shorter than the pioneering two-mile linac at SLAC, a most ambitious and exciting physics programme, the introduction of novel accelerator technology and the complete exploitation of the unique values of and spendings into the LHC. It requires probably less courage than that of Pief Panofsky and colleagues half a century ago. Finally, not least, one may realise that the power LHeC needed without the energy recovery technique is beyond 1 GW while the electron beam is dumped at injection energy. It therefore is a significant step towards green accelerator technology, a major general desire and requirement of our times. This paper aims at substantiating these statements in the various chapters following.

Oliver Brüning (CERN) and Max Klein (University of Liverpool)

Contents

Chapter 1

Introduction

1.1 The Context

1.1.1 Particle Physics - at the Frontier of Fundamental Science

Despite its striking success, the Standard Model (SM) has been recognised to have major deficiencies. These may be summarised in various ways. Some major questions can be condensed as follows:

- **Higgs boson** Is the electroweak scale stabilised by new particles, interactions, symmetries? Is the Higgs boson discovered in 2012 the SM Higgs boson, what is its potential? Do more Higgs bosons exist as predicted, for example, in super-symmetric theories?

- **Elementary Particles** The SM has 61 identified particles: 12 leptons, 36 quarks and anti-quarks, 12 mediators, 1 Higgs boson. Are these too many or too few? Do right-handed neutrinos exist? Why are there three families? What makes leptons and quarks different? Do leptoquarks exist, is there a deeper substructure?

- **Strong Interactions** What is the true parton dynamics and structure inside the proton, inside other hadrons and inside nuclei – at different levels of resolution? How is confinement explained and how do partons hadronise? How can the many body dynamics of the Quark Gluon Plasma (QGP) state be described in terms of the elementary fields of Quantum Chromodynamics? What is the meaning of the AdS/CFT relation and of supersymmetry in strong interactions? Do axions, odderons, instantons exist?

- **GUT** Is there a genuine, grand unification of the interactions at high scales, would this include gravitation? What is the correct value of the strong coupling constant, is lattice theory correct in this respect? Is the proton stable?

- **Neutrinos** Do Majorana or/and sterile neutrinos exist, is there CP violation in the neutrino sector?

- **Dark Matter** Is dark matter constituted of elementary particles or has it another origin? Do hidden or dark sectors of nature exist and would they be accessible to accelerator experiments?

These and other open problems are known, and they have been persistent questions to Particle Physics. They are intimately related and any future strategic programme should not be confined

to only one or a few of these. The field of particle physics is far from being understood, despite the phenomenological success of the $SU_L(2) \times U(1) \times SU_c(3)$ gauge field theory termed the Standard Model. Certain attempts to declare its end are in contradiction not only to the experience from a series of past revolutions in science but indeed contrary to the incomplete status of particle physics as sketched above. The question is not why to end particle physics but how to proceed. The answer is not hidden in philosophy but requires new, better, affordable experiments. Indeed the situation is special as expressed by Guido Altarelli a few years ago: *It is now less unconceivable that no new physics will show up at the LHC... We expected complexity and instead we have found a maximum of simplicity. The possibility that the Standard model holds well beyond the electroweak scale must now be seriously considered [12]*. This is reminiscent of the time before 1969, prior to anything like a Standard Model, when gauge theory was just for theorists, while a series of new accelerators, such as the 2 mile electron linac at Stanford or the SPS at CERN, were planned which resulted in a complete change of the paradigm of particle physics.

Ingenious theoretical hypotheses, such as on the existence of extra dimensions, on SUSY, of unparticles or the embedding in higher gauge groups, like E8, are a strong motivation to develop high energy physics rigorously further. In this endeavour, a substantial increase of precision, the conservation of diversity of projects and the extension of kinematic coverage are a necessity, likely turning out to be of fundamental importance. The strategic question in this context, therefore, is not just which new collider should be built next, as one often hears, but how we may challenge the current and incomplete knowledge best. A realistic step to progress comprises a new e^+e^- collider, built perhaps in Asia, and complementing the LHC with an electron energy recovery linac to synchronously operate ep with pp at the LHC, the topic of this paper.

One may call these machines first technology generation colliders as their technology has been proven to principally work [13]. Beyond these times, there is a long-term future reaching to the year 2050 and much beyond, of a second, further generation of hadron, lepton and electron-hadron colliders. CERN has recently published a design study of a future circular hh, eh and e^+e^- collider (FCC) complex [14–16], which would provide a corresponding base. For electron-hadron scattering this opens a new horizon with the FCC-eh, an about 3 TeV centre-of-mass system (cms) energy collider which in this paper is also considered, mostly for comparison with the LHeC. A prospect similar to FCC is also being developed in China [17, 18].

A new collider for CERN at the level of $\mathcal{O}(10^{10})$ CHF cost should have the potential to change the paradigm of particle physics with direct, high energy discoveries in the 10 TeV mass range. This may only be achieved with the FCC-hh including an eh experiment. The FCC-hh/eh complex does access physics to several hundred TeV, assisted by a qualitatively new level of QCD/DIS. A prime, very fundamental goal of the FCC-pp is the clarification of the Higgs vacuum potential which can not be achieved in e^+e^-. This collider therefore has an overriding justification beyond the unknown prospects of finding new physics nowadays termed "exotics". It accesses rare Higgs boson decays, high scales and, when combined with ep, it measures the SM Higgs couplings to below percent precision. There is a huge, fundamental program on electroweak and strong interactions, flavour and heavy ions for FCC-hh to be explored. This represents CERN's unique opportunity to build on the ongoing LHC program, for many decades ahead. The size of the FCC-hh requires this to be established as a global enterprise. The HL-LHC and the LHeC can be understood as very important steps towards this major new facility, both in terms of physics and technology. The present report outlines a road towards realising a next generation, energy frontier electron-hadron collider as part of this program, which would maximally exploit and support the LHC.

1.1.2 Deep Inelastic Scattering and HERA

The field of deep inelastic lepton-hadron scattering (DIS) [19] was born with the discovery [20,21] of partons [22,23] about 50 years ago. It readily contributed fundamental insights, for example on the development of QCD with the confirmation of fractional quark charges and of asymptotic freedom or with the spectacular finding that the weak isospin charge of the right-handed electron was zero [24] which established the Glashow-Weinberg-Salam "Model of Leptons" [25] as the base of the united electroweak theory. The quest to reach higher energies in accelerator based particle physics led to generations of colliders, with HERA [26] as the so far only electron-proton one.

HERA collided electrons (and positrons) of $E_e = 27.6\,\text{GeV}$ energy off protons of $E_p = 920\,\text{GeV}$ energy achieving a centre-of-mass energy, $\sqrt{s} = 2\sqrt{E_e E_p}$, of about $0.3\,\text{TeV}$. It therefore extended the kinematic range covered by fixed target experiments by two orders of magnitude in Bjorken x and in four-momentum transfer squared, Q^2, with its limit $Q^2_{max} = s$. HERA was built in less than a decade, and it operated for 16 years. Together with the Tevatron and LEP, HERA was pivotal to the development of the Standard Model.

HERA had a unique collider physics programme and success [27]. It established QCD as the correct description of proton substructure and parton dynamics down to $10^{-19}\,\text{m}$. It demonstrated electroweak theory to hold in the newly accessed range, especially with the measurement of neutral and charged current ep scattering cross sections beyond $Q^2 \sim M^2_{W,Z}$ and with the proof of electroweak interference at high scales through the measurement of the interference structure functions $F_2^{\gamma Z}$ and $xF_3^{\gamma Z}$. The HERA collider has provided the core base of the physics of parton distributions, not only in determining the gluon, valence, light and heavy sea quark momentum distributions in a much extended range, but as well in supporting the foundation of the theory of unintegrated, diffractive, photon, neutron PDFs through a series of corresponding measurements. It discovered the rise of the parton distributions towards small momentum fractions, x, supporting early QCD expectations on the asymptotic behaviour of the structure functions [28]. Like the TeVatron and LEP/SLC colliders which explored the Fermi scale of a few hundred GeV energy, determined by the vacuum expectation value of the Higgs field, $v = 1/\sqrt{\sqrt{2}G_F} = 2M_W/g \simeq 246\,\text{GeV}$, HERA showed too that there was no supersymmetric or other exotic particle with reasonable couplings existing at the Fermi energy scale.

HERA established electron-proton scattering as an integral part of modern high energy particle physics. It demonstrated the richness of DIS physics, and the feasibility of constructing and operating energy frontier ep colliders. What did we learn to take into a next, higher energy ep collider design? Perhaps there arose three lessons about:

- *the need for higher energy*, for three reasons: i) to make charged currents a real, precision part of ep physics, for instance for the complete unfolding of the flavour composition of the sea and valence quarks, ii) to produce heavier mass particles (Higgs, top, exotics) with favourable cross sections, and iii) to discover or disproof the existence of gluon saturation for which one needs to measure at lower $x \propto Q^2/s$, i.e. higher s than HERA had available;

- *the need for much higher luminosity*: the first almost ten years of HERA provided just a hundred pb^{-1}. As a consequence, HERA could not accurately access the high x region, and it was inefficient and short of statistics in resolving puzzling event fluctuations;

- *the complexity of the interaction region* when a bent electron beam caused synchrotron radiation while the opposite proton beam generated quite some halo background through beam-gas and beam-wall proton-ion interactions.

Based on these and further lessons a first LHeC paper was published in 2006 [29]. The LHeC design was then intensely worked on, and a comprehensive CDR appeared in 2012 [1]. This has now been pursued much further still recognising that the LHC is the only existing base to realise a TeV energy scale electron-hadron collider in the accessible future. It offers highly energetic, intense hadron beams, a long time perspective and a unique infrastructure and expertise, i.e. everything required for an energy frontier DIS physics and innovative accelerator programme.

1.2 The Paper

1.2.1 The LHeC Physics Programme

This paper presents a design concept of the LHeC, using a $50\,\text{GeV}$ energy electron beam to be scattered off the LHC hadron beams (proton and ion) in concurrent operation[1]. Its main characteristics are presented in **Chapter 2**. The instantaneous luminosity is designed to be $10^{34}\,\text{cm}^{-2}\text{s}^{-1}$ exceeding that of HERA, which achieved a few times $10^{31}\,\text{cm}^{-2}\text{s}^{-1}$, by a factor of several hundreds. The kinematic range nominally is extended by a factor of about 15, but in fact by a larger amount because of the hugely increased luminosity which is available for exploring the maximum Q^2 and large $x \leq 1$ regions, which were major deficiencies at HERA. The coverage of the Q^2, x plane by previous and future DIS experiments is illustrated in Fig. 1.1.

The LHeC would provide a major extension of the DIS kinematic range as is required for the physics programme at the energy frontier. For the LHC, the ep/A detector would be a new major experiment. A number of major themes would be explored with significant discovery potential. These are presented in quite some detail in seven chapters of this paper dedicated to physics:

- Based on the unique hadron beams of the LHC and employing a point-like probe, the LHeC would represent the world's cleanest, high resolution microscope for exploring the substructure of and dynamics inside matter, which may be termed the Hubble telescope for the smallest dimensions. The first chapter on physics, **Chapter 3**, is devoted to the measurement of parton distributions with the LHeC, and it also presents the potential to resolve proton structure in 3D.

- **Chapter 4** is devoted to the deep exploration of QCD. A key deliverable of the LHeC is the clarification of the parton interaction dynamics at small Bjorken x, in the new regime of very high parton densities but small coupling which HERA discovered but was unable to clarify for its energy was limited. It is first shown that the LHeC can measure α_s to per mille accuracy followed by various studies to illustrate the unique potential of the LHeC to pin down the dynamics at small x. The chapter also covers the seminal potential for diffractive DIS to be developed. It concludes with brief presentations on theoretical developments on pQCD and of novel physics on the light cone.

- The maximum Q^2 exceeds the Z, W boson mass values (squared) by two orders of magnitude. The LHeC, supported by variations of beam parameters and high luminosity, thus

---

[1]The CDR in 2012 used a $60\,\text{GeV}$ beam energy. Recent considerations of cost, effort and synchrotron radiation effects led to preference of a small reduction of the energy. Various physics studies presented here still use $60\,\text{GeV}$. While for BSM, top and Higgs physics the high energy is indeed important, the basic conclusions remain valid if eventually the energy was indeed chosen somewhat smaller than previously considered. This is further discussed below. A decision on the energy would come with the approval obviously.
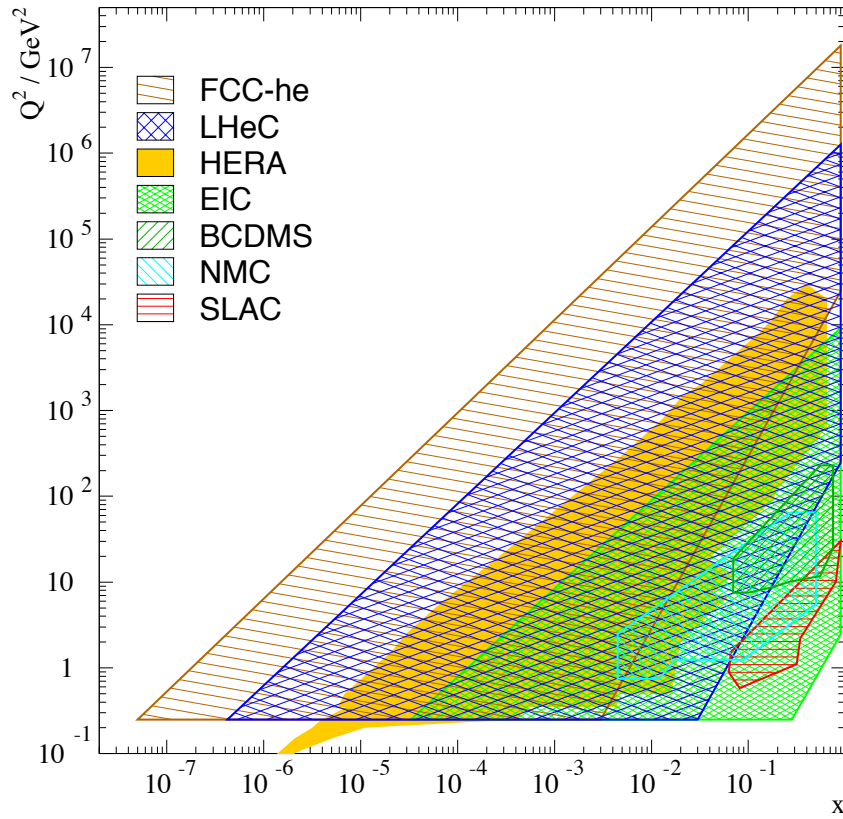
Figure 1.1: Coverage of the kinematic plane in deep inelastic lepton-proton scattering by some initial fixed target experiments, with electrons (SLAC) and muons (NMS, BCDMS), and by the *ep* colliders: the EIC (green), HERA (yellow), the LHeC (blue) and the FCC-eh (brown). The low Q^2 region for the colliders is here limited to about $0.2\,\mathrm{GeV}^2$, which is covered by the central detectors, roughly and perhaps using low electron beam data. Electron taggers may extend this to even lower Q^2. The high Q^2 limit at fixed x is given by the line of inelasticity $y = 1$. Approximate limitations of acceptance at medium x, low Q^2 are illustrated using polar angle limits of $\eta = -\ln\tan\theta/2$ of 4, 5, 6 for the EIC, LHeC, and FCC-eh, respectively. These lines are given by $x = \exp\eta \cdot \sqrt{Q^2}/(2E_p)$, and can be moved to larger x when E_p is lowered below the nominal values.

.

offers a unique potential to test the electroweak SM in the spacelike region with unprecedented precision. The high *ep* cms energy leads to the copious production of top quarks, of about $2 \cdot 10^6$ single top and $5 \cdot 10^4$ $t\bar{t}$ events. Top production could not be observed at HERA but will thus become a central theme of precision and discovery physics with the LHeC. In particular, the top momentum fraction, top couplings to the photon, the W boson and possible flavour changing neutral currents (FCNC) interactions can be studied in a uniquely clean environment (**Chapter 5**).

- The LHeC extends the kinematic range in lepton-nucleus scattering by nearly four orders of magnitude. It thus will transform nuclear particle physics completely, by resolving the hitherto hidden parton dynamics and substructure in nuclei and clarifying the QCD base for the collective dynamics observed in QGP phenomena (**Chapter 6**).

- The clean DIS final state in neutral and charged current scattering and the high integrated

luminosity enable a high precision Higgs physics programme with the LHeC. The Higgs production cross section is comparable to the one of Higgs-strahlung at e^+e^-. This opens unexpected extra potential to independently test the Higgs sector of the SM, with high precision insight especially into the $H - WW/ZZ$ and $H - bb/cc$ couplings (**Chapter 7**).

- As a new, unique, luminous TeV scale collider, the LHeC has an outstanding opportunity to discover new physics, such as in the exotic Higgs, dark matter, heavy neutrino and QCD areas (**Chapter 8**).

- With concurrent ep and pp operation, the LHeC would transform the LHC into a 3-beam, twin collider of greatly improved potential which is sketched in **Chapter 9**. Through ultra-precise strong and electroweak measurements, the ep experiment would make the HL-LHC complex a much more powerful search and measurement laboratory than current expectations, based on pp only, do entail. The joint pp/ep LHC facility together with a novel e^+e^- collider will make a major step in the study of the SM Higgs Boson, leading far beyond the HL-LHC. Putting pp and ep results together, as is illustrated for PDFs, will lead to new insight, especially when compared with its single pp and ep components.

The development of particle physics, the future of CERN, the exploitation of the singular LHC investments, the culture of accelerator art, all make the LHeC a unique project of great interest. It is challenging in terms of technology, affordable given budget constraints and it may still be realised in the two decades of currently projected LHC lifetime.

1.2.2   The Accelerator

The LHeC provides an intense, high energy electron beam to collide with the LHC. It represents the highest energy application of energy recovery linac (ERL) technology which is increasingly recognised as one of the major pilot technologies for the development of particle physics because it utilises and stimulates superconducting RF technology progress, and it increases intensity while keeping the power consumption low.

The LHeC instantaneous luminosity is determined through the integrated luminosity goal of $\mathcal{O}(1)\,\text{ab}^{-1}$ caused by various physics reasons. The electron beam energy is chosen to achieve TeV cms collision energy and enable competitive searches and precision Higgs boson measurements. A cost-physics-energy evaluation is presented here which points to choosing $E_e \simeq 50\,\text{GeV}$ as a new default value, which was $60\,\text{GeV}$ before [1]. The wall-plug power has been constrained to $100\,\text{MW}$. Two super-conducting linacs of about $900\,\text{m}$ length, which are placed opposite to each other, accelerate the passing electrons by $8.3\,\text{GeV}$ each. This leads to a final electron beam energy of about $50\,\text{GeV}$ in a 3-turn racetrack energy recovery linac configuration.

For measuring at very low Q^2 and for determining the longitudinal structure function F_L, see below, the electron beam energy may be reduced to a minimum of about $10\,\text{GeV}$. For maximising the acceptance at large Bjorken x, the proton beam energy, E_p, may be reduced to $1\,\text{TeV}$. This determines a minimum cms energy of $200\,\text{GeV}$, below HERA's $319\,\text{GeV}$. If the ERL may be combined in the further future with the double energy HE-LHC [30], the proton beam energy E_p could reach $14\,\text{TeV}$ and $\sqrt{s}$ be increased to $1.7\,\text{TeV}$. This is extended to $3.5\,\text{TeV}$ for the FCC-eh with a $50\,\text{TeV}$ proton energy beam. We thus have the unique, exciting prospect for future DIS ep scattering at CERN with an energy range from below HERA to the few TeV region, at hugely increased luminosity and based on much more sophisticated experimental techniques than had been available at HERA times.

A spectacular extension of the kinematic range will be expected for deep inelastic lepton-nucleus scattering which was not pursued at DESY. Currently, highest energy lN data are due to fixed target muon-nucleus experiments, such as NMC and COMPASS, with a maximum $\sqrt{s}$ of about 20 GeV which permits a maximum Q^2 of 400 GeV^2. This will be extended with the EIC at Brookhaven to about 10^4 GeV^2. The corresponding numbers for ePb scattering at LHeC (FCC-eh) are $\sqrt{s} \simeq 0.74$ (2.2) TeV and $Q^2_{max} = 0.54$ (4.6) 10^6 GeV^2. The kinematic range in eA scattering will thus be extended through the LHeC (FCC-eh) by three (four) orders of magnitude as compared to the current status. This will thoroughly alter the understanding of parton and collective dynamics inside nuclei.

The ERL beam configuration is located inside the LHC ring but outside its tunnel, which minimises any interference with the main hadron beam infrastructure. The electron accelerator may thus be built independently, to a considerable extent, of the status of operation of the proton machine. The length of the ERL has configuration to be a fraction $1/n$ of the LHC circumference as is required for the e and p matching of bunch patterns. Here the return arcs count as two single half rings. The chosen electron beam energy of 50 GeV leads, for $n = 5$, to a circumference U of 5.4 km for the electron racetrack [2]. A 3-pass ERL configuration had been adopted also for the FCC-eh albeit maintaining the original 60 GeV as default which had a 9 km circumference.

For the LHC, the ERL would be tangential to IP2. According to current plans, IP2 is given to the ALICE detector with a program extending to LS4, the first long shutdown following the three year pause of the LHC operation for upgrading the luminosity performance and detectors. There are plans for a new heavy ion detector to move into IP2. The LS4 shutdown is currently scheduled to begin in 2031 with certain likelihood of being postponed to 2032 or later as recent events seem to move LS3 forward and extend its duration to three years.

For FCC-eh the preferred position is interaction point L, for geological reasons mainly, and the time of operation fully depending on the progress with FCC-hh, beginning at the earliest in the late 40ies if CERN went for the hadron collider directly after the LHC.

The LHeC operation is transparent to the LHC collider experiments owing to the low lepton bunch charge and resulting small beam-beam tune shift experienced by the protons. The LHeC is thus designed to run simultaneously with pp (or pA or AA) collisions with a dedicated final operation of a few years.

The paper presents in considerable detail the design of the LHeC (**Chapter 10**), i.e. the optics and lattice, components, magnets, as well as designs of the linac and interaction region besides special topics such as the prospects for electron-ion scattering, positron-proton operation and a novel study of beam-beam interaction effects. With the more ambitious luminosity goal, with a new lattice adapted to 50 GeV, with progress on the IR design, a novel analysis of the civil engineering works and, especially, the production and successful test [31] of the first SC cavity at the newly chosen default frequency of 801.58 MHz, this report considerably extends beyond the initial CDR. This holds especially since several LHeC institutes have recently embarked on the development of the ERL technology with a low energy facility, PERLE, to be built at IJC Laboratory at Orsay.

---

[2] The circumference may eventually be chosen to be 6.8 km, the length of the SPS, which would relax certain parameters and ease an energy upgrade.

1.2.3 PERLE

Large progress has been made in the development of superconducting, high gradient cavities with quality factors, Q_0, beyond 10^{10}. This will enable the exploitation of ERLs in high-energy physics colliders, with the LHeC as a prime example, while considerations are also brought forward for future e^+e^- colliders [32] and for proton beam cooling with an ERL tangential to eRHIC. The status and challenges of energy recovery linacs are summarised in **Chapter 11**. This chapter also presents the design, status and prospects for the ERL development facility PERLE. The major parameters of PERLE have been taken from the LHeC, such as the 3-turn configuration, source, frequency and cavity-cryomodule technology, in order to make PERLE a suitable facility for the development of LHeC ERL technology and the accumulation of operating experience prior to and later in parallel with the LHeC.

An international collaboration has been established to build PERLE at Orsay. With the design goals of 500 MeV electron energy, obtained in three passes through two cryo-modules and of 20 mA, corresponding to 500 nC charge at 40 MHz bunch frequency, PERLE is set to become the first ERL facility to operate at 10 MW power. Following its CDR [7] and a paper submitted to the European strategy [11], work is directed to build a first dressed cavity and to release a TDR by 2021/22. Besides its value for accelerator and ERL technology, PERLE is also of importance for pursuing a low energy physics programme, see [7], and for several possible industrial applications. It also serves as a local hub for the education of accelerator physicists at a place, previously called Linear Accelerator Laboratory (LAL), which has long been at the forefront of accelerator design and operation.

There are a number of related ERL projects as are characterised in Chapter 11. The realisation of the ERL for the LHeC at CERN represents a unique opportunity not only for physics and technology but as well for a next and the current generation of accelerator physicists, engineers and technicians to realise an ambitious collider project while the plans for very expensive next machines may take shape. Similarly, this holds for a new generation of detector experts, as the design of the upgrade of the general purpose detectors (GPDs) at the LHC is reaching completion, with the question increasingly posed about opportunities for new collider detector construction to not loose the expertise nor the infrastructure for building trackers, calorimeters and alike. The LHeC offers the opportunity for a novel 4π particle physics detector design, construction and operation. As a linac-ring collider, it may serve one detector of a size smaller than CMS and larger than H1 or ZEUS.

1.2.4 The Detector

Chapter 12 on the detector relies to a large extent on the very detailed write-up on the kinematics, design considerations, and realisation of a detector for the LHeC presented in the CDR [1]. In the previous report one finds detailed studies not only on the central detector and its magnets, a central solenoid for momentum measurements and an extended dipole for ensuring head-on ep collisions, but as well on the forward (p and n) and backward (e and γ) tagging devices. The work on the detector as presented here was focussed on an optimisation of the performance and on the scaling of the design towards higher proton beam energies. It presents a new, consistent design and summaries of the essential characteristics in support of many physics analyses that this paper entails.

The most demanding performance requirements arise from the ep Higgs measurement programme, especially the large acceptance and high precision desirable for heavy flavour tagging

and the requirement to resolve the hadronic final state. This has been influenced by both the rapidity acceptance extensions and the technology progress of the HL-LHC detector upgrades. A key example, also discussed, is the HV-CMOS Silicon technology, for which the LHeC is an ideal application due to the much limited radiation level as compared to pp.

Therefore we have now completed two studies of design: previously, of a rather conventional detector with limited cost and, here, of a more ambitious device. Both of these designs appear feasible. This regards also the installation. The paper presents a brief description of the installation of the LHeC detector at IP2 with the result that it may proceed within two years, including the dismantling of the there residing detector. This calls for modularity and pre-mounting of detector elements on the surface, as was done for CMS too. It will be for the LHeC detector Collaboration, to be established with and for the approval of the project, to eventually design the detector according to its understanding and technical capabilities.

1.3 Outline

The paper is organised as follows. For a brief overview, Chapter 2 summarises the LHeC characteristics. Chapter 3 presents the physics of the LHeC seen as a microscope for measuring PDFs and exploring the 3D structure of the proton. Chapter 4 contains further means to explore QCD, especially low x dynamics, together with two sections on QCD theory developments. Chapter 5 describes the electroweak and top physics potential of the LHeC. Chapter 6 presents the seminal nuclear particle physics potential of the LHeC, through luminous electron-ion scattering exploring an unexplored kinematic territory. Chapter 7 presents a detailed analysis of the opportunity for precision SM Higgs boson physics with charged and neutral current ep scattering. Chapter 8 is a description of the salient opportunities to discover physics beyond the Standard Model with the LHeC, including non-SM Higgs physics, right-handed neutrinos, physics of the dark sector, heavy resonances and exotic substructure phenomena. Chapter 9 describes the interplay of ep and pp physics, i.e. the necessity to have the LHeC for fully exploiting the potential of the LHC facility, e.g. through the large increase of electroweak precision measurements, the considerable extension of search ranges and the joint ep and pp Higgs physics potential. Chapter 10 presents the update of the design on the electron accelerator with many novel results such as on the lattice and interaction region, updated parameters for ep and eA scattering, new specifications of components, updates on the electron source,... The chapter also presents the encouraging results of the first LHeC 802 MHz cavity. Chapter 11 is devoted, first, to the status and challenges of energy recovery based accelerators and, second, to the description of the PERLE facility between its CDR and a forthcoming TDR. Chapter 12 describes the update of the detector studies towards an optimum configuration in terms of acceptance and performance. Chapter 13 presents a summary of the paper including a time line for realising the LHeC to operate with the LHC. An Appendix presents the statement of the International Advisory Committee on its evaluation of the project together with recommendations about how to proceed. It also contains an account for the membership in the LHeC organisation, i.e. the Coordination Group and finally the list of Physics Working Group convenors.

Chapter 2

LHeC Configuration and Parameters

2.1 Introduction

The Conceptual Design Report (CDR) of the LHeC was published in 2012 [1]. The CDR default configuration uses a 60 GeV energy electron beam derived from a racetrack, three-turn, intense energy recovery linac (ERL) achieving a cms energy of $\sqrt{s} = 1.3\,\mathrm{TeV}$, where $s = 4E_p E_e$ is determined by the electron and proton beam energies, E_e and E_p. In 2012, the Higgs boson, H, was discovered which has become a central topic of current and future high energy physics. The Higgs production cross section in charged current (CC) deep inelastic scattering (DIS) at the LHeC is roughly 100 fb. The Large Hadron Collider has so far not led to the discovery of any exotic phenomenon. This forces searches to be pursued, in pp but as well in ep, with the highest achievable precision in order to access a maximum range of phase space and possibly rare channels. The DIS cross section at large x roughly behaves like $(1 - x)^3/Q^4$, demanding very high luminosities for exploiting the unknown regions of Bjorken x near 1 and very high Q^2, the negative four-momentum transfer squared between the electron and the proton. For the current update of the design of the LHeC this has set a luminosity goal about an order of magnitude higher than the $10^{33}\,\mathrm{cm}^{-2}\mathrm{s}^{-1}$ which had been adopted for the CDR. There arises the potential, as described subsequently in this paper, to transform the LHC into a high precision electroweak, Higgs and top quark physics facility.

The ep Higgs production cross section rises approximately with E_e. New physics may be related to the heaviest known elementary particle, the top quark, the ep production cross section of which rises more strongly than linearly with E_e in the LHeC kinematic range as that is not very far from the $t\bar{t}$ threshold. Searches for heavy neutrinos, SUSY particles, etc. are the more promising the higher the energy is. The region of deep inelastic scattering and pQCD requires that Q^2 be larger than $M_p^2 \simeq 1\,\mathrm{GeV}^2$. Access with DIS to very low Bjorken x requires high energies because of $x = Q^2/s$, for inelasticity $y = 1$. In DIS, one needs $Q^2 > M_p^2 \simeq 1\,\mathrm{GeV}^2$. Physics therefore requires a maximally large energy. However, cost and effort set realistic limits such that twice the HERA electron beam energy, of about 27 GeV, appeared as a reasonable and affordable target value.

In the CDR [1] the default electron energy was chosen to be 60 GeV. This can be achieved with an ERL circumference of 1/3 of that of the LHC. Recently, the cost was estimated in quite some detail [33], comparing also with other accelerator projects. Aiming at a cost optimisation and providing an option for a staged installation, the cost estimate lead to defining a new default configuration of $E_e = 50\,\mathrm{GeV}$ with the option of starting in an initial phase with a beam energy

of $E_e = 30\,\text{GeV}$ and a a circumference of $5.4\,\text{km}$ which is 1/5 of the LHC length. Lowering E_e is also advantageous for mastering the synchrotron radiation challenges in the interaction region. Naturally, the decision on E_e is not taken now. This paper comprises studies with different energy configurations, mainly $E_e = 50$ and $60\,\text{GeV}$, which are close in their centre-of-mass energy values of 1.2 and 1.3 TeV, respectively.

Up to beam energies of about $60\,\text{GeV}$, the ERL cost is dominated by the cost for the superconducting RF of the linacs. Up to this energy the ERL cost scales approximately linearly with the beam energy. Above this energy the return arcs represent the main contribution to the cost and to the ERL cost scaling is no longer linear. Given the non-linear dependence of the cost on E_e, for energies larger than about $60\,\text{GeV}$, significantly larger electron beam energy values may only be justified by overriding arguments, such as, for example, the existence of leptoquarks [1]. Higher values of $\sqrt{s}$ are also provided with enlarged proton beam energies by the High Energy LHC ($E_p = 13.5\,\text{TeV}$) [30] and the FCC-hh [16] with E_p between 20 and possibly $75\,\text{TeV}$, depending on the dipole magnet technology.

2.2 Cost Estimate, Default Configuration and Staging

In 2018 a detailed cost estimate was carried out [33] following the guidance and practice of CERN accelerator studies. The assumptions were also compared with the DESY XFEL cost. The result was that for the $60\,\text{GeV}$ configuration about half of the total cost was due to the two SC linacs. The cost of the arcs decreases more strongly than linearly with decreasing energy, about $\propto E^4$ for synchrotron radiation losses and $\propto E^3$ when emittance dilution is required to be avoided [34]. It was therefore considered to set a new default of $50\,\text{GeV}$ with a circumference of 1/5 of that of the LHC, see Sect. 2.3, compared to 1/3 for $60\,\text{GeV}$. Furthermore, an initial phase at $30\,\text{GeV}$ was considered, within the 1/5 configuration but with only partially equipped linacs. The HERA electron beam energy was $27\,\text{GeV}$. The main results, taken from [33] are reproduced in Tab. 2.1.

The choice of a default of $50\,\text{GeV}$ at 1/5 of the LHC circumference results, as displayed, in a total cost of $1,075\,\text{MCHF}$ for the initial $30\,\text{GeV}$ configuration and an additional, upgrade cost to $50\,\text{GeV}$ of $296\,\text{MCHF}$. If one restricted the LHeC to a non-upgradeable $30\,\text{GeV}$ only configuration one would, still in a triple racetrack configuration, come to roughly a $1\,\text{km}$ long structure with two linacs of about $500\,\text{m}$ length, probably in a single linac tunnel configuration. The cost of this version of the LHeC is roughly $800\,\text{MCHF}$, i.e. about half the $60\,\text{GeV}$ estimated cost. However, this would essentially reduce the LHeC to a QCD and electroweak machine, still very powerful but accepting substantial losses in its Higgs, top and BSM programme.

A detailed study was made on the cost of the civil engineering, which is also discussed subsequently. This concerned a comparison of the 1/3 vs the 1/5 LHC circumference versions, and the FCC-eh. The result is illustrated in Fig. 2.1. It shows that the CE cost for the 1/5 version is about a quarter of the total cost. The reduction from 1/3 to 1/5 economises about $100\,\text{MCHF}$.

Choices of the final energy will be made later. They depend not only on a budget but also on the future development of particle physics at large. For example, it may turn out that, for some years

---

[1] If these existed with a mass of say $M = 1.5\,\text{TeV}$ this would require, at the LHC with $E_p = 7\,\text{TeV}$, to choose E_e to be larger than $90\,\text{GeV}$, and to pay for it. Leptoquarks would be produced by ep fusion and appear as resonances, much like the Z boson in e^+e^- and would therefore fix E_e (given certain E_p which at the FCC exceeds $7\,\text{TeV}$). The genuine DIS kinematics, however, is spacelike, the exchanged four-momentum squared $q^2 = -Q^2$ being negative, which implies that the choice of the energies is less constrained than in an e^+e^- collider aiming at the study of the Z or H bosons.

Component	CDR 2012 (60 GeV)	Stage 1 (30 GeV)	Default (50 GeV)
SRF System	805	402	670
SRF R+D and Prototyping	31	31	31
Injector	40	40	40
Arc Magnets and Vacuum	215	103	103
SC IR Magnets	105	105	105
Source and Dump System	5	5	5
Cryogenic Infrastructure	100	41	69
General Infrastructure and Installation	69	58	58
Civil Engineering	386	289	289
Total Cost	1756	1075	1371

Table 2.1: Summary of cost estimates, in MCHF, from [33]. The 60 GeV configuration is built with a 9 km triple racetrack configuration as was considered in the CDR [1]. It is taken as the default configuration for FCC-eh, with an additional CE cost of 40 MCHF due to the larger depth on point L (FCC) as compared to IP2 (LHC). Both the 30 and the 50 GeV assume a 5.4 km configuration, i.e. the 30 GeV is assumed to be a first stage of LHeC upgradeable to 50 GeV ERL. Whenever a choice was to be made on estimates, in [33] the conservative number was chosen.

into the future, the community may not find the $\mathcal{O}(10)$ GCHF required to build any of the e^+e^- colliders currently considered. Then the only way to improve on the Higgs measurements beyond HL-LHC substantially is the high energy $(50-60\,\text{GeV})$, high luminosity $(\int L = 1\,\text{ab}^{-1})$ LHeC. Obviously, physics and cost are intimately related. Based on such considerations, but also taking into account technical constraints as resulting from the amount of synchrotron radiation losses in the interaction region and the arcs, we have chosen 50 GeV in a 1/5 of U(LHC) configuration as the new default. This economises about 400 MCHF as compared to the CDR configuration.

If the LHeC ERL were built, it may later be transferred, with some reconfiguration and upgrades, to the FCC to serve as the FCC-eh. The FCC-eh has its own location, L, for the ERL which requires a new accelerator tunnel. It has been decided to keep the 60 GeV configuration for the FCC, as described in the recently published CDR of the FCC [16]. The LHeC ERL configuration may also be used as a top-up injector for the Z and possibly WW phase of the FCC-e should the FCC-ee indeed precede the FCC-hh/eh phase.

2.3 Configuration Parameters

A possible transition from the 60 GeV to the 50 GeV configuration of the LHeC was already envisaged in 2018, as considered in the paper submitted to the European Strategy [9]. The machine layout shown in that paper is reproduced in Fig. 2.2. It is a rough sketch illustrating the reduction from a 60 GeV to a 50 GeV configuration, which results not only in a reduction of capital costs, as discussed above, but also of effort.

The ERL configuration has been recently revisited [34] considering its dependence on the electron beam energy. Applying a dimension scaling which preserves the emittance dilution, the results have been obtained as are summarised in Tab. 2.2. The 1/5 configuration is chosen as the new LHeC default while the CDR on the LHeC from 2012 and the recent CDR on FCC-eh have used the 1/3 configuration. The energy and configuration may be decided as physics, cost and effort dictate, once a decision is taken.
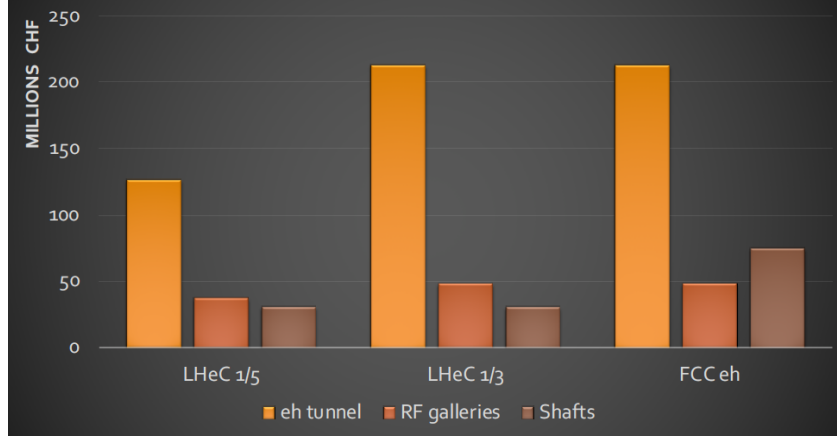
Figure 2.1: Cost estimate for the civil engineering work for the tunnel, rf galleries and shafts for the LHeC at 1/5 of the LHC circumference (left), at 1/3 (middle) and the FCC-eh (right). The unit costs and percentages are consistent with FCC and CLIC unit prices. The estimate is considered reliable to 30 %. The cost estimates include: Site investigations: 2 %, Preliminary design, tender documents and project changes: 12 % and the Contractors profit: 3 %. Surface site work is not included, which for LHeC exists with IP2.

Parameter	Unit	LHeC option			
		1/3 LHC	1/4 LHC	1/5 LHC	1/6 LHC
Circumference	m	9000	6750	5332	4500
Arc radius	m · 2π	1058	737	536	427
Linac length	m · 2	1025	909	829	758
Spreader and recombiner length	m · 4	76	76	76	76
Electron energy	GeV	61.1	54.2	49.1	45.2

Table 2.2: Scaling of the electron beam energy, linac and further accelerator element dimensions with the choice of the total circumference in units $1/n$ of the LHC circumference. For comparison, the CERN SPS has a circumference of 6.9 km, only somewhat larger than 1/4 of that of the LHC.

2.4 Luminosity

The luminosity L for the LHeC in its linac-ring configuration is determined as

$$L = \frac{N_e N_p n_p f_{rev} \gamma_p}{4\pi \epsilon_p \beta^*} \cdot \prod_{i=1}^{3} H_i,$$

(2.1)

where $N_{e(p)}$ is the number of electrons (protons) per bunch, n_p the number of proton bunches in the LHC, f_{rev} the revolution frequency in the LHC [the bunch spacing in a batch is given by Δ, equal to 25 ns for protons in the LHC] and γ_p the relativistic factor E_p/M_p of the proton beam. Further, ϵ_p denotes the normalised proton transverse beam emittance and β^* the proton beta function at the IP, assumed to be equal in x and y. The luminosity is moderated by the hourglass factor, $H_1 = H_{geo} \simeq 0.9$, the pinch or beam-beam correction factor, $H_2 = H_{b-b} \simeq 1.3$, and the filling factor $H_3 = H_{coll} \simeq 0.8$, should an ion clearing gap in the electron beam be required. This justifies taking the product of these factors. As the product is close to unity, the factors are not listed for simplicity in the subsequent tables.
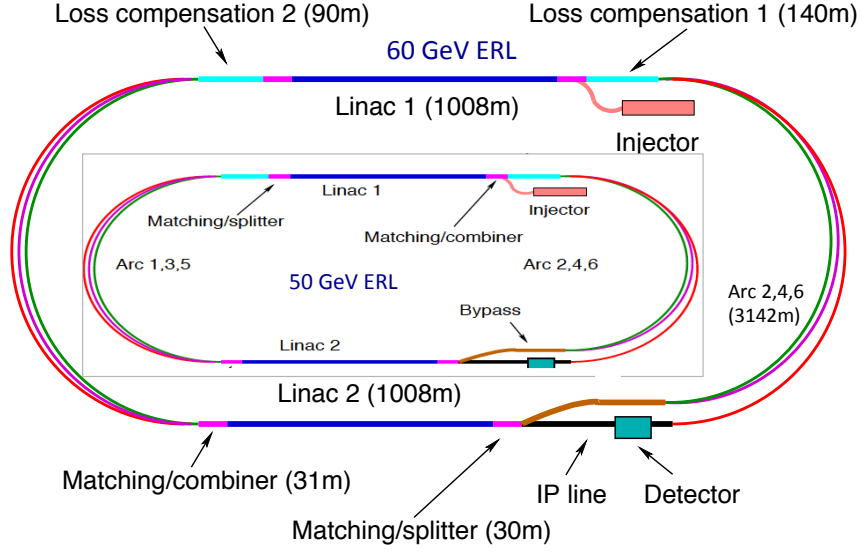
Figure 2.2: Schematic view of the three-turn LHeC configuration with two oppositely positioned electron linacs and three arcs housed in the same tunnel. Two configurations are shown: Outer: Default $E_e = 60\,\mathrm{GeV}$ with linacs of about $1\,\mathrm{km}$ length and $1\,\mathrm{km}$ arc radius leading to an ERL circumference of about $9\,\mathrm{km}$, or $1/3$ of the LHC length. Inner: Sketch for $E_e = 50\,\mathrm{GeV}$ with linacs of about $0.8\,\mathrm{km}$ length and $0.55\,\mathrm{km}$ arc radius leading to an ERL circumference of $5.4\,\mathrm{km}$, or $1/5$ of the LHC length, which is smaller than the size of the SPS. The $1/5$ circumference configuration is flexible: it entails the possibility to stage the project as funds of physics dictate by using only partially equipped linacs, and it also permits upgrading to somewhat higher energies if one admits increased synchrotron power losses and operates at higher gradients.

The electron beam current is given as

$$I_e = e N_e f \,, \tag{2.2}$$

where f is the bunch frequency $1/\Delta$. The current for the LHeC is limited by the charge delivery of the source. In the new default design we have $I_e = 20\,\mathrm{mA}$ which results from a charge of $500\,\mathrm{pC}$ for the bunch frequency of $40\,\mathrm{MHz}$. It is one of the tasks of the PERLE facility to investigate the stability of the 3-turn ERL configuration in view of the challenge for each cavity to hold the sixfold current due to the simultaneous acceleration and deceleration of bunches at three different beam energies each.

2.4.1 Electron-Proton Collisions

The design parameters of the luminosity were recently provided in a note describing the FCC-eh configuration [35], including the LHeC. Tab. 2.3 represents an update comprising in addition the initial 30 GeV configuration and the lower energy version of the FCC-hh based on the LHC magnets[2]. For the LHeC, as noted above, we assume $E_e = 50\,\mathrm{GeV}$ while for FCC-eh we retain 60 GeV. Since the source limits the electron current, the peak luminosity may be taken not to

---

[2] The low energy FCC-pp collider, as of today, uses a 6 T LHC magnet in a 100 km tunnel. If, sometime in the coming decades, high field magnets become available based on HTS technology, then a 20 TeV proton beam energy may even be achievable in the LHC tunnel. To this extent the low energy FCC considered here and an HTS based HE-LHC would be comparable options in terms of their energy reach.

depend on E_e. Studies of the interaction region design, presented in this paper, show that one may be confident of reaching a β^* of $10\,\mathrm{cm}$ but it will be a challenge to reach even smaller values. Similarly, it will be quite a challenge to operate with a current much beyond $20\,\mathrm{mA}$. That has nevertheless been considered [36] for a possible dedicated LHeC operation mode for a few years following the pp operation program.

Parameter	Unit	LHeC				FCC-eh	
		CDR	Run 5	Run 6	Dedicated	E_p=20 TeV	E_p=50 TeV
E_e	GeV	60	30	50	50	60	60
N_p	10^{11}	1.7	2.2	2.2	2.2	1	1
ϵ_p	μm	3.7	2.5	2.5	2.5	2.2	2.2
I_e	mA	6.4	15	20	50	20	20
N_e	10^9	1	2.3	3.1	7.8	3.1	3.1
β^*	cm	10	10	7	7	12	15
Luminosity	$10^{33}\,\mathrm{cm}^{-2}\mathrm{s}^{-1}$	1	5	9	23	8	15

Table 2.3: Summary of luminosity parameter values for the LHeC and FCC-eh. Left: CDR from 2012; Middle: LHeC in three stages, an initial run, possibly during Run 5 of the LHC, the $50\,\mathrm{GeV}$ operation during Run 6, both concurrently with the LHC, and a final, dedicated, stand-alone ep phase; Right: FCC-eh with a 20 and a $50\,\mathrm{TeV}$ proton beam, in synchronous operation.

The peak luminosity values exceed those at HERA by 2–3 orders of magnitude. The operation of HERA in its first, extended running period, 1992-2000, provided an integrated luminosity of about $0.1\,\mathrm{fb}^{-1}$ for the collider experiments H1 and ZEUS. This may now be expected to be taken in a day of initial LHeC operation.

2.4.2   Electron-Ion Collisions

The design parameters and luminosity were also provided recently [35] for collisions of electrons and lead nuclei (fully stripped $^{208}\mathrm{Pb}^{82+}$ ions). Tab. 2.4 is an update of the numbers presented there for consistency with the Run 6 LHeC configuration in Tab. 2.3 and with the addition of parameters corresponding to the $E_p = 20\,\mathrm{TeV}$ FCC-hh configuration. Further discussion of this operating mode and motivations for the parameter choices in this table are provided in Section 10.3.

One can expect the average luminosity during fills to be about 50% of the peak in Tab. 2.4 and we assume an overall operational efficiency of 50%. Then, a year of eA operation, possibly composed by combining shorter periods of operation, would have the potential to provide an integrated data set of about 5 (25) fb^{-1} for the LHeC (FCC-eh), respectively. This exceeds the HERA electron-proton luminosity value by about tenfold for the LHeC and much more at FCC-eh while the fixed target nuclear DIS experiment kinematics is extended by 3–4 orders of magnitude. These energy frontier electron-ion configurations therefore have the unique potential to radically modify our present view of nuclear structure and parton dynamics. This is discussed in Chapter 4.

Parameter	Unit	LHeC	FCC-eh (E_p=20 TeV)	FCC-eh (E_p=50 TeV)
Ion energy E_{Pb}	PeV	0.574	1.64	4.1
Ion energy/nucleon E_{Pb}/A	TeV	2.76	7.88	19.7
Electron beam energy E_e	GeV	50	60	60
Electron-nucleon CMS $\sqrt{s_{eN}}$	TeV	0.74	1.4	2.2
Bunch spacing	ns	50	100	100
Number of bunches		1200	2072	2072
Ions per bunch	10^8	1.8	1.8	1.8
Normalised emittance ϵ_n	μm	1.5	1.5	1.5
Electrons per bunch	10^9	6.2	6.2	6.2
Electron current	mA	20	20	20
IP beta function β_A^*	cm	10	10	15
e-N Luminosity	$10^{32}\mathrm{cm}^{-2}\mathrm{s}^{-1}$	7	14	35

Table 2.4: Baseline parameters of future electron-ion collider configurations based on the electron ERL, in concurrent *eA* and *AA* operation mode with the LHC and the two versions of a future hadron collider at CERN. Following established convention in this field, the luminosity quoted, at the start of a fill, is the *electron-nucleon* luminosity which is a factor *A* larger than the usual (i.e. electron-nucleus) luminosity.

2.5 Linac Parameters

The brief summary of the main LHeC characteristics here concludes with a table of the main ERL parameters for the new default electron energy of 50 GeV, Tab. 2.5, which are discussed in detail in Chapter 8.

Parameter	Unit	Value
Frequency	MHz	801.58
Bunch charge	pC	499
Bunch spacing	ns	24.95
Electron current	mA	20
Injector energy	MeV	500
Gradient	MV/m	19.73
Cavity length, active	m	0.918
Cavity length, flange-to-flange	m	1.5
Cavities per cryomodule		4
Length of cryomodule	m	7
Acceleration per cryomodule	MeV	72.45
Total number of cryomodules		112
Acceleration energy per pass	GeV	8.1

Table 2.5: Basic LHeC ERL characteristics for the default configuration using two such linacs located opposite to each other in a racetrack of 5.4 km length. Each linac is passed three times for acceleration and three times for deceleration.

2.6 Operation Schedule

The LHeC parameters are determined to be compatible with a parasitic operation with the nominal HL-LHC proton-proton operation. This implies limiting the electron bunch current to

sufficiently small values so that the proton beam-beam parameter remains small enough to be negligible for the proton beam dynamics.

Assuming a ten year construction period for the LHeC after approval of the project and a required installation window of two years for the LHeC detector, the earliest realistic operation period for the LHeC coincides with the LHC Run 5 period in 2032 and with a detector installation during LS4 which is currently scheduled during 2030 and would need to be extended by one year to 2031. The baseline HL-LHC operation mode assumes 160 days of proton operation, 20 days of ion operation and 20 days of machine development time for the Run 4 period, amounting to a total of 200 operation days per year. After the Run 4 period the HL-LHC does not consider ion operation at present and assumes 190 days for proton operation. The HL-LHC project assumes an overall machine efficiency of 54 % (e.g. fraction of scheduled operation time spent in physics production) and we assume that the ERL does not contribute to significant additional downtime for the operation. Assuming an initial 15 mA of electron beam current, a β^* of 10 cm and HL-LHC proton beam parameters, the LHeC reaches a peak luminosity of $0.5 \cdot 10^{34}\,\mathrm{cm^{-2}s^{-1}}$. Assuming further a proton beam lifetime of 16.7 hours, a proton fill length of 11.7 hours and an average proton beam turnaround time of 4 hours, the LHeC can reach in this configuration an annual integrated luminosity of $20\,\mathrm{fb^{-1}}$.

For the evaluation of the physics potential it is important to note that the Run 5 initial ep operation period may accumulate about $50\,\mathrm{fb^{-1}}$ of integrated luminosity. This is the hundredfold value which H1 (or ZEUS) took over a HERA lifetime of 15 years. As one may expect, for details see Chapter 3, such a huge DIS luminosity is ample for pursuing basically the complete QCD programme. In particular, the LHeC would deliver on time for the HL-LHC precision analyses the external, precise PDFs and with just a fraction of the $50\,\mathrm{fb^{-1}}$ the secrets of low x parton dynamics would unfold. Higher ep luminosity is necessary for ultimate precision and for the top, BSM and the Higgs programme of the LHeC to be of competitive value.

For the Run 6 period of the HL-LHC, the last of the HL-LHC operation periods, we assume that the number of machine development sessions for the LHC can be suppressed, providing an increase in the operation time for physics production from 190 days to 200 days per year. Furthermore, we assume that the electron beam parameters can be slightly further pushed. Assuming a β^* reduced to 7 cm, an electron beam current of up to 25 mA and still nominal HL-LHC proton beam parameters, the LHeC reaches a peak performance of $1.2 \cdot 10^{34}\,\mathrm{cm^{-2}s^{-1}}$ and an annual integrated luminosity of $50\,\mathrm{fb^{-1}}$. This would add up to an integrated luminosity of a few hundred $\mathrm{fb^{-1}}$, a strong base for top, BSM and Higgs physics at the LHeC.

Beyond the HL-LHC exploitation period, the electron beam parameters could be further pushed in dedicated ep operation, when the requirement of a parasitic operation to the HL-LHC proton-proton operation may no longer be imposed. The proton beam lifetime without proton-proton collisions would be significantly larger than in the HL-LHC configuration. In the following we assume a proton beam lifetime of 100 hours and a proton beam efficiency of 60 % without proton-proton beam collisions. The electron beam current in this configuration would only be limited by the electron beam dynamics and the SRF beam current limit. Assuming that electron beam currents of up to 50 mA, the LHeC would reach a peak luminosity of $2.4 \cdot 10^{34}\,\mathrm{cm^{-2}s^{-1}}$ and an annual integrated luminosity of up to $180\,\mathrm{fb^{-1}}$. Table 2.6 summarises the LHeC configurations over these three periods of operation.

Depending on the years available for a dedicated final operation (or through an extension of the pp LHC run, currently not planned but interesting for collecting 4 instead of $3\,\mathrm{ab^{-1}}$ to, for example, observe di-Higgs production at the LHC), a total luminosity of $1\,\mathrm{ab^{-1}}$ could be available for the LHeC. This would double the precision of Higgs couplings measured in ep as compared to

Parameter	Unit	Run 5 Period	Run 6 Period	Dedicated
Brightness $N_p/(\gamma\epsilon_p)$	$10^{17}\mathrm{m}^{-1}$	2.2/2.5	2.2/2.5	2.2/2.5
Electron beam current	mA	15	25	50?
Proton β^*	m	0.1	0.7	0.7
Peak luminosity	$10^{34}\,\mathrm{cm}^{-2}\mathrm{s}^{-1}$	0.5	1.2	2.4
Proton beam lifetime	h	16.7	16.7	100
Fill duration	h	11.7	11.7	21
Turnaround time	h	4	4	3
Overall efficiency	%	54	54	60
Physics time / year	days	160	180	185
Annual integrated lumi.	fb^{-1}	20	50	180

Table 2.6: The LHeC performance levels during different operation modes.

the default HL-LHC run period with *ep* added as described. It would also significantly enlarge the potential to observe or/and quantify rare and new physics phenomena. Obviously such considerations are subject to the grand developments at CERN. A period with most interesting physics and on-site operation activity could be particularly welcome for narrowing a possible large time gap between the LHC and its grand successor, the FCC-hh. One may, however, be interested in ending LHC on time. It thus is important for the LHeC project to recognise its particular value as an asset of the HL-LHC, and on its own, with even less than the ultimate luminosity, albeit values which had been dreamt of at HERA.

Chapter 3

Parton Distributions - Resolving the Substructure of the Proton

3.1   Introduction

Since the discovery of quarks in the famous $ep \rightarrow eX$ scattering experiment at Stanford [20,21], the deep inelastic scattering process has been established as the most reliable method to resolve the substructure of protons, which was immediately recognised, not least by Feynman [19]. Since that time, a series of electron, muon and neutrino DIS experiments validated the Quark-Parton Model and promoted the development of Quantum Chromodynamics. A new quality of this physics was realised with HERA, the first electron-proton collider built, which extended the kinematic range in momentum transfer squared to $Q^2_{max} = s \simeq 10^5 \, \mathrm{GeV}^2$, for $s = 4E_e E_p$. Seen from today's perspective, largely influenced by the LHC, it is necessary to advance to a further level in these investigations, with higher energy and much increased luminosity than HERA could achieve. This is a major motivation for building the LHeC, with an extension of the Q^2 and $1/x$ range by more than an order of magnitude and an increase of the luminosity by a factor of almost a thousand. QCD may breakdown, be embedded in a higher gauge symmetry, or unconfined colour might be observed; These phenomena raise a number a series of fundamental questions of the QCD theory [37] and highlight the importance of a precision DIS programme with the LHeC.

The subsequent chapter is mainly devoted to the exploration of the seminal potential of the LHeC to resolve the substructure of the proton in an unprecedented range, with the first ever complete and coherent measurement of the full set of parton distribution functions (PDFs) in one experiment. The precise determination of PDFs, consistently to high orders pQCD, is crucial for the interpretation of LHC physics, i.e. its precision electroweak and Higgs measurements as well as the exploration of the high mass region where new physics may occur when the HL-LHC operates. Extra constraints on PDFs arise also from pp scattering as is discussed in a later chapter. Conceptually, however, the LHeC provides the singular opportunity to completely separate the PDF determination from proton-proton physics. This approach is not only more precise for the PDFs, but it is theoretically more accurate and enables incisive tests of QCD, by confronting independent predictions with LHC (and later FCC) measurements, as well as providing an indispensable base for reliable interpretations of searches for new physics.

While the resolution of the longitudinal, collinear structure of the proton is key to the physics programme of the LHeC (and the LHC), the ep collider provides further fundamental insight

in the structure of the proton: semi-inclusive measurements of jets and vector mesons, and especially Deeply Virtual Compton Scattering, a process established at HERA, will shed light on also the transverse structure of the proton in a new kinematic range. This is presented at the end of the current chapter.

3.1.1 Partons in Deep Inelastic Scattering

Parton Distribution Functions $xf(x,Q^2)$ represent a probabilistic view on hadron substructure at a given distance, $1/\sqrt{Q^2}$. They depend on the parton type $f = (q_i, \ g)$, for quarks and gluons, and must be determined from experiment, most suitably DIS, as perturbative QCD is not prescribing the parton density at a given momentum fraction Bjorken x. PDFs are important also for they determine Drell-Yan, hadron-hadron scattering processes, supposedly universally through the QCD factorisation theorem [38] [1]. The PDF programme of the LHeC is of unprecedented reach for the following reasons:

- For the first time it will resolve the partonic structure of the proton (and nuclei) completely, i.e. determine the u_v, d_v, u, d, s, c, b, and gluon momentum distributions through neutral and charged current cross section as well as direct heavy quark PDF measurements, performed in a huge kinematic range of DIS, from $x = 10^{-6}$ to 0.9 and from Q^2 above 1 to $10^6 \, \mathrm{GeV}^2$. The LHeC explores the strange density and the momentum fraction carried by top quarks [40] which was impossible at HERA.

- Very high luminosity and unprecedented precision, owing to both new detector technology and the redundant evaluation of the event kinematics from the leptonic and hadronic final states, will lead to extremely high PDF precision.

- Because of the high LHeC energy, the weak probes (W, Z) dominate the interaction at larger Q^2 which permits the up and down sea and valence quark distributions to be resolved in the full range of x. Thus no additional data will be required [2]: that is, there is no influence from higher twists nor nuclear uncertainties or data inconsistencies, which are main sources of uncertainty of current so-called global PDF determinations.

While PDFs are nowadays often seen as merely a tool for interpreting LHC data, in fact what really is involved is a new understanding of strong interaction dynamics and the deeper resolution of substructure extending into hitherto uncovered phase space regions, in particular the small x region, by virtue of the very high energy s, and the very small spatial dimension $(1/\sqrt{Q^2})$ and the $x \to 1$ region, owing to the high luminosity and energy. The QPM is not tested well enough, despite decades of DIS and other experiments, and QCD is not developed fully either in these kinematic regimes.

Examples of issues of fundamental interest for the LHeC to resolve are: i) the long awaited resolution of the behaviour of u/d near the kinematic limit ($x \to 1$); ii) the flavour democracy of the light quark sea (is $d \simeq u \simeq s$?); iii) the existence of quark-level charge-symmetry [41]; iv) the behaviour of the ratio $\bar{d}/\bar{u}$ at small x; v) the turn-on and the values of heavy quark PDFs;

---

[1]In his referee report on the LHeC CDR, in 2012, Guido Altarelli noted on the factorisation theorem in QCD for hadron colliders that: "many people still advance doubts. Actually this question could be studied experimentally, in that the LHeC, with its improved precision, could put bounds on the allowed amount of possible factorisation violations (e.g. by measuring in DIS the gluon at large x and then comparing with jet production at large p_T in hadron colliders)." This question was addressed also in a previous LHeC paper [39].

[2]The LHeC may be operated at basically HERA energies and collect a fb^{-1} of luminosity for cross checks and maximising the high x, medium Q^2 acceptance, see Sect. 3.2.

vi) the value of the strong coupling constant and vii) the question of the dynamics, linear or non-linear, at small x where the gluon and quark densities rise.

Of special further interest is the gluon distribution, for the gluon self-interaction prescribes all visible mass, the gluon-gluon fusion process dominates Higgs production at hadron colliders (the LHC and the FCC) and because its large x behaviour, essentially unknown today, affects predictions of BSM cross sections at the LHC.

The LHeC may be understood as an extension of HERA to a considerable extent. It has the reach in $x \propto 1/s$ to resolve the question of new strong interaction dynamics at small x and it accesses high Q^2, much larger than $M^2_{W,Z}$, with huge luminosity to make accurate use of weak NC and CC cross sections in DIS PDF physics for the first time. QCD analyses of HERA data are still ongoing. For obvious reasons, there is no quantitative analysis of LHC related PDF physics possible without relying on the HERA data, and often on its QCD analyses. These are introduced briefly next. Albeit with certain assumptions and limited luminosity, HERA completely changed the field of PDF physics as compared to the times of solely fixed target data, see Ref. [42], and it opened the era of physics of high parton densities at small x.

3.1.2 Fit Methodology and HERA PDFs

The methodology of PDF determinations with HERA data has been developed over decades by the H1 and ZEUS Collaborations [27, 43, 44], in close contact with many theorists. It has been essentially adopted with suitable modifications for the LHeC PDF prospect study as is detailed subsequently.

HERAPDF fits use information from both $e^\pm p$ neutral current and charged current scattering from exclusively the ep collider experiments, H1 and ZEUS, up to high $Q^2 = 30\,000\,\mathrm{GeV}^2$ and down to about $x = 5 \cdot 10^{-5}$. The precision of the HERA combined data is below $1.5\,\%$ over the Q^2 range of $3 < Q^2 < 500\,\mathrm{GeV}^2$ and remains below 3% up to $Q^2 = 3000\,\mathrm{GeV}^2$. The precision for large $x > 0.5$ is rather poor due to limited luminosity and high-x acceptance limitations at medium Q^2.

The QCD analysis is performed at LO, NLO and NNLO within the *xFitter* framework [43, 45, 46], and the latest version is the HERAPDF2.0 family [44]. The DGLAP evolution of the PDFs, as well as the light-quark coefficient functions, are calculated using QCDNUM [47, 48]. The contributions of heavy quarks are calculated in the general-mass variable-flavour-number (GMVFN) scheme of Refs. [49, 50]. Experimental uncertainties are determined using the Hessian method imposing a $\chi^2 + 1$ criterion. This is usually impossible in global fits over rather incoherent data sets originating from different processes and experiments, but has been a major advantage of the solely HERA based QCD analyses.

In the HERAPDF analysis, as well as subsequently in the LHeC study, the starting scale is chosen to be $Q_0^2 = 1.9\,\mathrm{GeV}^2$ such that it is below the charm mass, m_c^2. The data is restricted to $Q^2_{min} \geq 3.5\,\mathrm{GeV}^2$ in order to stay in the DIS kinematic range. The forward hadron final state acceptance introduces a lower W cut which removes the region which otherwise is potentially sensitive to higher twist effects [51]. The strong coupling constant is set to $\alpha_S(M_Z) = 0.118$ [3]. All these assumptions are varied in the evaluation of model uncertainties on the resulting fit.

---

[3] The strong coupling constant cannot be reliably determined from inclusive HERA data alone. DIS results, including fixed target data, have provided values which tend to be lower [52] than the here chosen value, see for a discussion Ref. [53]. As is further presented in detail in Sect. 4.1 the LHeC reaches a sensitivity to α_s at the per mille level based on inclusive and jet data as well as their combination.

These variations will essentially have no significant effect with the LHeC as the sensitivity to the quark masses, for example, is hugely improved with respect to HERA, α_s known to 1–2 per mille, and the kinematic range of the data is much extended.

In HERAPDF fits, the quark distributions at the initial Q_0^2 are represented by the generic form

$$xq_i(x) = A_i x^{B_i}(1-x)^{C_i}P_i(x), \tag{3.1}$$

where i specifies the flavour of the quark distribution and $P_i(x) = (1 + D_i x + E_i x^2)$. The inclusive NC and CC cross sections determine four independent quark distributions, essentially the sums of the up and down quark and anti-quark densities. These may be decomposed into any four other distributions of up and down quarks with an ad-hoc assumption on the fraction of strange to anti-down quarks which has minimal numeric effect on the PDFs, apart from that on xs itself. The parameterised quark distributions, xq_i, are chosen to be the valence quark distributions (xu_v, xd_v) and the light anti-quark distributions ($x\bar{u}$, $x\bar{d}$). This has been adopted for the LHeC also.

The parameters A_{u_v} and A_{d_v} are fixed using the quark counting rule. The normalisation and slope parameters, A and B, of $\bar{u}$ and $\bar{d}$ are set equal such that $x\bar{u} = x\bar{d}$ at $x \to 0$, a crucial assumption which the LHeC can validate. The strange quark PDF $x\bar{s}$ is set as a fixed fraction $r_s = 0.67$ of $x\bar{d}$. This fraction is varied in the determination of model uncertainties. By default it is assumed that $xs = x\bar{s}$ and that u and d sea and anti-quarks have the same distributions also. These assumptions will be resolved by the LHeC and their uncertainties will essentially be eliminated, see Sect. 3.3.4. The D and E parameters are used only if required by the data, following a χ^2 saturation procedure [43]. This leads for HERAPDF2.0 to two non-zero parameters, E_{u_v} and $D_{\bar{u}}$.

The gluon distribution is parameterised differently

$$xg(x) = A_g x^{B_g}(1-x)^{C_g} - A_g' x^{B_g'}(1-x)^{C_g'}. \tag{3.2}$$

The normalisation parameter A_g is calculated using the momentum sum rule. Variations of the PDFs were also considered with $A_g' = 0$ which for earlier HERA data fits had been the default choice. The appearance of this second term may be understood as coming from a not-well constrained behaviour of $xg(x, Q^2)$ at small x. In fact, xg is resembling a valence-quark distribution at $Q^2 \simeq Q_0^2$. The much extended Q^2 range of the LHeC at a given small x and the access to much smaller x values than probed at HERA will quite certainly enable this behaviour to be clarified. Since also C_g' had been set to just a large value, there is negligible effect of that second term in Eq. (3.2) on the resulting PDF uncertainties. Consequently A_g' is set to zero in the LHeC study.

Alternative parameterisations are used in the evaluation of the parameterisation uncertainty. These variations include: introducing extra parameters D, E for each quark distribution; the removal of primed gluon parameters; and the relaxation of assumptions about the low-x sea. These fits provide alternative extracted PDFs with similar fit χ^2. The maximum deviation from the central PDF at each value of x is taken as an envelope and added in quadrature with the experimental and model uncertainties to give the total uncertainty. As for the model uncertainties, the extended range and improved precision of the LHeC data may well be expected to render such variations negligible.

The results of the HERA PDF analysis [44] are shown in Fig. 3.1 for the HERAPDF2.0NNLO PDF set, displaying experimental, model and parameterisation uncertainties separately. The structure of the proton is seen to depend on the resolution $\propto 1/\sqrt{Q^2}$, with which it is probed.
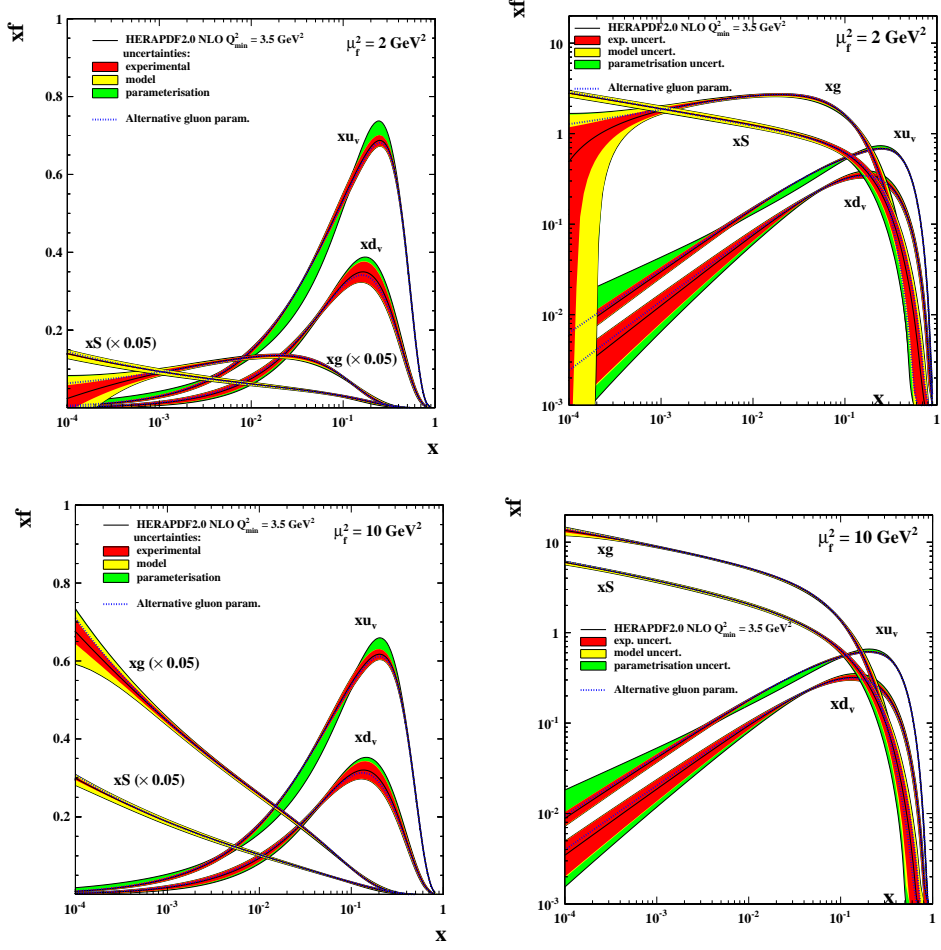
Figure 3.1: Parton distributions as determined by the QCD fit to the combined H1 and ZEUS data at $Q^2 = 1.9\,\mathrm{GeV}^2$ (top) and at $Q^2 = 10\,\mathrm{GeV}^2$ (bottom). The color coding represents the experimental, model and parameterisation uncertainties separately. Here $xS = 2x(\overline{u} + \overline{d})$ denotes the total sea quark density. Note that xg and xS are scaled by $1/20$ in the left side plots with a linear y scale.

At Q^2 of about $1 - 2\,\mathrm{GeV}^2$, corresponding to $0.2\,\mathrm{fm}$, the parton contents may be decomposed as is shown in Figure 3.1 top. The gluon distribution at $Q^2 \simeq 2\,\mathrm{GeV}^2$ has a valence like shape, i.e. at very low x the momentum is carried by sea quarks, see Fig. 3.1 (top). At medium $x \sim 0.05$ the gluon density dominates over all quark densities. At largest x, above 0.3, the proton structure is dominated by the up and down valence quarks. This picture evolves such that below $10^{-16}\,\mathrm{m}$, for $x \leq 0.1$, the gluon density dominates also over the sea quark density, see Figure 3.1 (bottom). The valence quark distributions are rather insensitive to the resolution which reflects their non-singlet transformation behaviour in QCD.

The HERAPDF set differs from other PDF sets in that: i) it represents a fit to a consistent data set with small correlated systematic uncertainties; ii) it uses data on solely a proton target such that no heavy target corrections are needed and the assumption of strong isospin invariance, $d_{\mathrm{proton}} = u_{\mathrm{neutron}}$, is not required; iii) a large x, Q^2 region is covered such that no regions where higher twist effects are important are included in the analysis.

The limitations of HERA PDFs are known as well: i) the data is limited in statistics such that the region $x > 0.5$ is poorly constrained; ii) the energy is limited such that the very low x region, below $x \simeq 10^{-4}$, is not or not reliably accessed; iii) limits of luminosity and energy

implied that the potential of the flavour resolution through weak interactions, in NC and CC, while remarkable, could not be utilised accurately and α_s not been determined alongside PDFs in solely inclusive fits; iv) while the strange quark density was not accessed by H1 and ZEUS, only initial measurements of xc and xb could be performed. The strong success with respect to the fixed target PDF situation *ante* HERA has yet been most remarkable. The thorough clarification of parton dynamics and the establishment of a precision PDF base for the LHC and later hadron colliders, however, make a next generation, high energy and luminosity ep collider a necessity.

The PDF potential of the LHeC is presented next. This study follows closely the first extended analysis, developed for the CDR and detailed subsequently in Ref. [54]. The main differences compared to that analysis result from the choice of the Linac-Ring LHeC configuration, with preferentially e^-p of high polarisation (and much less e^+p) combined with an order of magnitude enhanced luminosity and developments of the apparatus design.

3.2 Simulated LHeC Data

3.2.1 Inclusive Neutral and Charged Current Cross Sections

In order to estimate the uncertainties of PDFs from the LHeC, several sets of LHeC inclusive NC/CC DIS data with a full set of uncertainties have been simulated and are described in the following. The systematic uncertainties of the DIS cross sections have a number of sources, which can be classified as uncorrelated and correlated across bin boundaries. For the NC case, the uncorrelated sources, apart from event statistics, are a global efficiency uncertainty, due for example to tracking or electron identification errors, as well as uncertainties due to photo-production background, calorimeter noise and radiative corrections. The correlated uncertainties result from imperfect electromagnetic and hadronic energy scale and angle calibrations. In the classic ep kinematic reconstruction methods used here, the scattered electron energy E'_e and polar electron angle θ_e, complemented by the energy of the hadronic final state E_h, can be employed to determine Q^2 and x in a redundant way.

Briefly, Q^2 is best determined with the electron kinematics and x is calculated from $y = Q^2/sx$. At large y, the inelasticity is best measured using the electron energy, $y_e \simeq 1 - E'_e/E_e$. At low y, the relation $y_h = E_h \sin^2(\theta_h/2)/E_e$ can be used to provide a measurement of the inelasticity with the hadronic final state energy E_h and angle θ_h. This results in the uncertainty $\delta y_h/y_h \simeq \delta E_h/E_h$, which is determined by the E_h calibration uncertainty to good approximation.

There have been various refined methods proposed to determine the DIS kinematics, such as the double angle method [55], which is commonly used to calibrate the electromagnetic energy scale, or the so-called Σ method [56], which exhibits reduced sensitivity to QED radiative corrections, see a discussion in Ref. [57]. For the estimate of the cross section uncertainty the electron method (Q_e^2, y_e) is used at large y, while at low y we use Q_e^2, y_h, which is transparent and accurate to better than a factor of two. In much of the phase space, moreover, it is rather the uncorrelated efficiency or further specific errors than the kinematic correlations, which dominate the cross section measurement precision.

The assumptions used in the simulation of pseudodata are summarised in Tab. 3.1. The procedure was gauged with full H1 Monte Carlo simulations and the assumptions are corresponding to H1's achievements with an improvement by at most a factor of two. Using a numerical procedure developed in Ref. [58], the scale uncertainties are transformed to kinematics-dependent

correlated cross-section uncertainties caused by imperfect measurements of E'_e, θ_e and E_h. These

Source of uncertainty	Uncertainty
Scattered electron energy scale $\Delta E'_e/E'_e$	0.1 %
Scattered electron polar angle	0.1 mrad
Hadronic energy scale $\Delta E_h/E_h$	0.5 %
Radiative corrections	0.3 %
Photoproduction background (for $y > 0.5$)	1 %
Global efficiency error	0.5 %

Table 3.1: Assumptions used in the simulation of the NC cross sections on the size of uncertainties from various sources. The top three are uncertainties on the calibrations which are transported to provide correlated systematic cross section errors. The lower three values are uncertainties of the cross section caused by various sources.

data uncertainties were imposed for all data sets, NC and CC, as are subsequently listed and described.

The design of the LHeC assumes that it operates with the LHC in the high luminosity phase, following LS4 at the earliest. As detailed in Chapter 2, it is assumed there will be an initial phase, during which the LHeC may collect $50\,\text{fb}^{-1}$ of data. This may begin with a sample of $5\,\text{fb}^{-1}$. Such values are very high when compared with HERA, corresponding to the hundred(ten)-fold of luminosity which H1 collected in its lifetime of about 15 years. The total luminosity may come close to $1\,\text{ab}^{-1}$.

The bulk of the data is assumed to be taken with electrons, possibly at large negative helicity P_e, because this configuration maximises the number of Higgs bosons that one can produce at the LHeC: e^- couples to W^- which interacts primarily with an up-quark and the CC cross section is proportional to $(1 - P_e)$. However, for electroweak physics there is a strong interest to vary the polarisation and charge [4]. It was considered that the e^+p luminosity may reach $1\,\text{fb}^{-1}$ while the tenfold has been simulated for sensitivity studies. A dataset has also been produced with reduced proton beam energy as that enlarges the acceptance towards large x at smaller Q^2. The full list of simulated sets is provided in Tab. 3.2.

Parameter	Unit	Data set								
		D1	D2	D3	D4	D5	D6	D7	D8	D9
Proton beam energy	TeV	7	7	7	7	1	7	7	7	7
Lepton charge		-1	-1	-1	-1	-1	$+1$	$+1$	-1	-1
Longitudinal lepton polarisation		-0.8	-0.8	0	-0.8	0	0	0	$+0.8$	$+0.8$
Integrated luminosity	fb^{-1}	5	50	50	1000	1	1	10	10	50

Table 3.2: Summary of characteristic parameters of data sets used to simulate neutral and charged current $e^\pm$ cross section data, for a lepton beam energy of $E_e = 50\,\text{GeV}$. Sets D1-D4 are for $E_p = 7\,\text{TeV}$ and e^-p scattering, with varying assumptions on the integrated luminosity and the electron beam polarisation. The data set D1 corresponds to possibly the first year of LHeC data taking with the tenfold of luminosity which H1/ZEUS collected in their lifetime. Set D5 is a low Ep energy run, essential to extend the acceptance at large x and medium Q^2. D6 and D7 are sets for smaller amounts of positron data. Finally, D8 and D9 are for high energy e^-p scattering with positive helicity as is important for electroweak NC physics. These variations of data taking are subsequently studied for their effect on PDF determinations.

---

[4]With a linac source, the generation of an intense positron beam is very challenging and will not be able to compete with the electron intensity. This is discussed in the accelerator chapter.
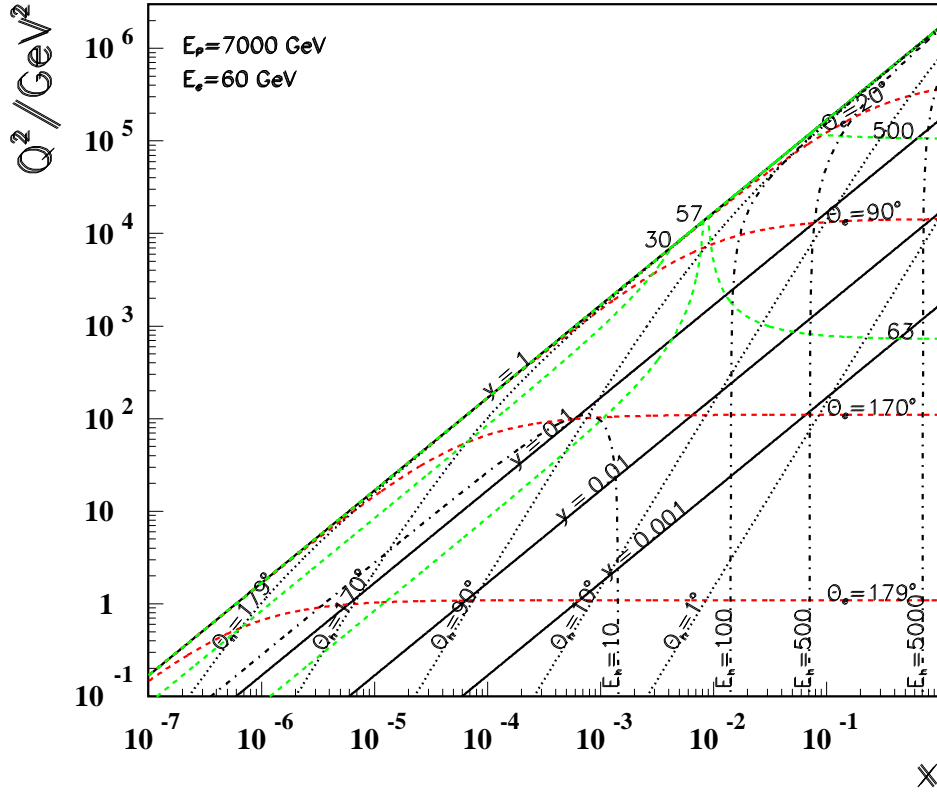
Figure 3.2: Kinematic plane covered with the maximum beam energies at the LHeC. Red dashed: Lines of constant scattered electron polar angle. Note that low Q^2 is measured with electrons scattered into the backward region, highest Q^2 is reached with Rutherford backscattering; Black dotted: lines of constant angle of the hadronic final state; Black solid: Lines of constant inelasticity $y = Q^2/sx$; Green dashed: Lines of constant scattered electron energy E'_e. Most of the central region is covered by what is termed the kinematic peak, where $E'_e \simeq E_e$. The small x region is accessed with small energies E'_e below E_e while the very forward, high Q^2 electrons carry TeV energies; Black dashed-dotted: lines of constant hadronic final state energy E_h. Note that the very forward, large x region sees very high hadronic energy deposits too.

The highest energies obviously give access to the smallest x at a given Q^2, and to the maximum Q^2 at fixed x. This is illustrated with the kinematic plane and iso-energy and iso-angle lines, see Fig. 3.2. It is instructive to see how the variation of the proton beam energy changes the kinematics considerably and enables additional coverage of various regions. This is clear from Fig. 3.3 which shows the kinematic plane choosing the approximate minimum energies the LHeC could operate with. There are striking changes one may note which are related to kinematics (c.f. Ref. [58]). For example, one can see that the line of $\theta_e = 179°$ now corresponds to $Q^2 \simeq 0.1\,\mathrm{GeV}^2$ which is due to lowering E_e as compared to $1\,\mathrm{GeV}^2$ in the maximum energy case, cf. Fig. 3.2. Similarly, comparing the two figures one finds that the lower Q^2, larger x region becomes more easily accessible with lower energies, in this case solely owing to the reduction of E_p from 7 to $1\,\mathrm{TeV}$. It is worthwhile to note that the LHeC, when operating at these low energies, would permit a complete repetition of the HERA programme, within a short period of special data taking.

The coverage of the kinematic plane is illustrated in the plot of the x, Q^2 bin centers of data
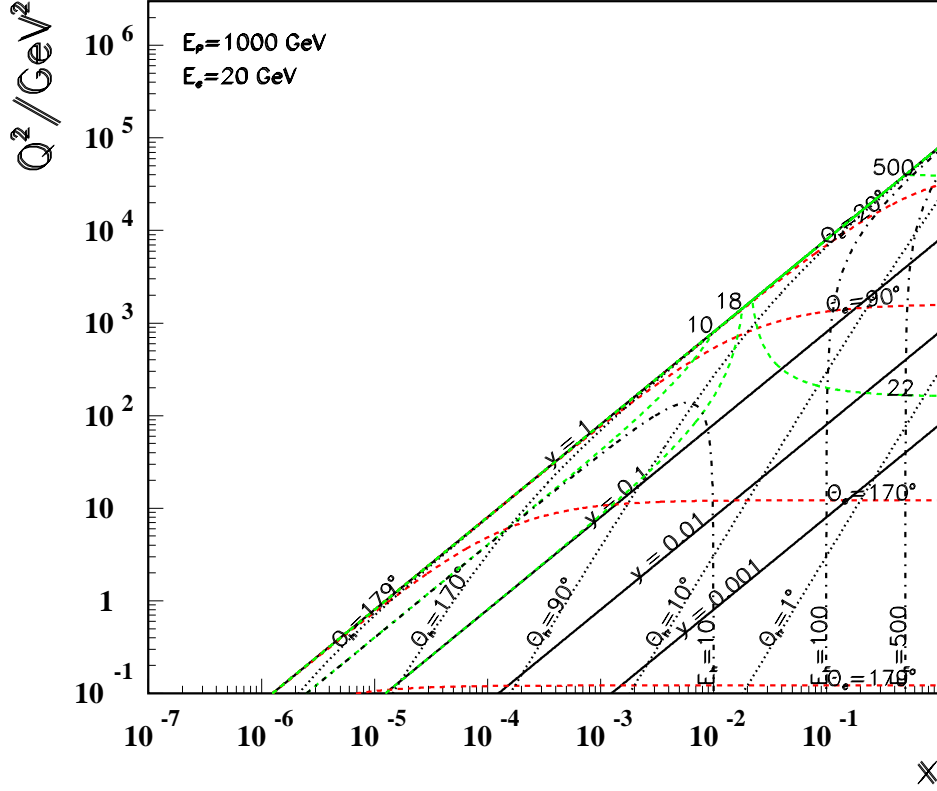
Figure 3.3: Kinematic plane covered with the minimum beam energies at LHeC. The meaning of the curves is the same as in the previous figure. This coverage is very similar to that by HERA as the energies are about the same.

points used in simulations, see Fig. 3.4 [59]. The full coverage at highest Bjorken-x, i.e. very close to $x = 1$, is enabled by the high luminosity of the LHeC. This was impossible to achieve for HERA as the NC/CC DIS cross sections decrease proportional to some power of $(1 - x)$ when x approaches 1, as has long been established with Regge counting [60–62].

It has been a prime goal, leading beyond previous PDF studies, to understand the importance of these varying data taking conditions for measuring PDFs with the LHeC. This holds especially for the question about what can be expected from an initial, lower luminosity LHeC operation period, which is of highest interest for the LHC analyses during the HL-LHC phase. Some special data sets of lowered electron energy have also been produced in order to evaluate the potential to measure F_L, see Sect. 4.2.3. These data sets have not been included in the bulk PDF analyses presented subsequently in this Chapter.

3.2.2 Heavy Quark Structure Functions

The LHeC is the ideal environment for a determination of the strange, charm and bottom density distributions which is necessary for a comprehensive unfolding of the parton contents and dynamics in protons and nuclei. The principal technique is charm tagging (in CC for xs, in NC for xc) and bottom tagging (in NC for xb). The beam spot of the LHeC has a transverse extension of about $(7\,\mu\mathrm{m})^2$. The inner Silicon detectors has a resolution of typically

41
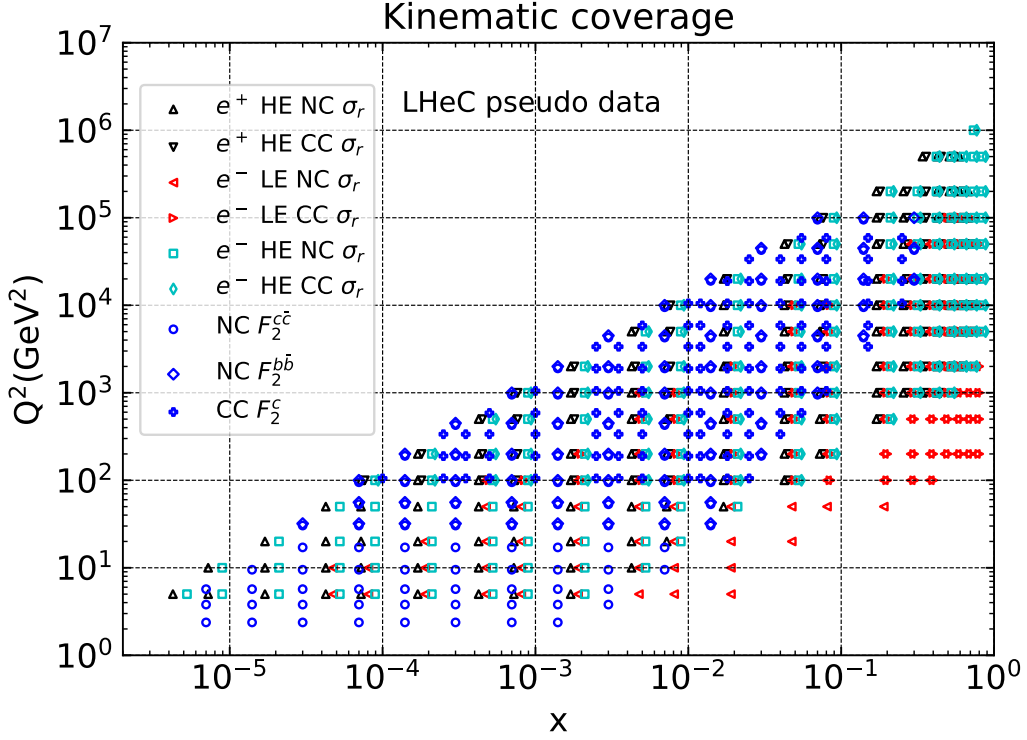
Figure 3.4: Illustration of the x, Q^2 values of simulated cross section and heavy quark density data used in LHeC studies. The red points illustrate the gain in acceptance towards large x at fixed Q^2 when E_p is lowered, see text.

10 microns to be compared with decay lengths of charm and beauty particles of hundreds of μm. The experimental challenges then are the beam pipe radius, coping at the LHeC with strong synchrotron radiation effects, and the forward tagging acceptance, similar to the HL-LHC challenges albeit much easier through the absence of pile-up in ep. Very sophisticated techniques are being developed at the LHC in order to identify bottom production through jets [63] which are not touched upon here.

A simulation was made of the possible measurements of the anti-strange density (Fig. 3.5) using impact parameter tagging in ep CC scattering, and of the charm and beauty structure functions using c and b tagging in NC (Figs. 3.6, 3.7). The results served as input for the PDF study subsequently presented.

Following experience on heavy flavour tagging at HERA and ATLAS, assumptions were made on the charm and beauty tagging efficiencies, to be 10 % and 60 %, respectively. The light-quark background in the charm analysis is assumed to be controllable to per cent level, while the charm background in the beauty tagging sample is assumed to be 10 %. The tagging efficiencies and background contaminations affect the statistical error which for the assumed 100 fb^{-1} is negligible, apart from edges of phase space as the figures illustrate for all three distribution.

An additional uncorrelated systematic error is assumed in the simulated strange and beauty quark measurements of 3 % while for charm a 2 % error is used. These errors determine the measurement uncertainties in almost the full kinematic range. At higher Q^2 and x, these increase, for example to 10, 5 and 7 % for xs, xc and xb, respectively, at $x \simeq 0.1$ and $Q^2 \simeq 10^5$ GeV^2. As
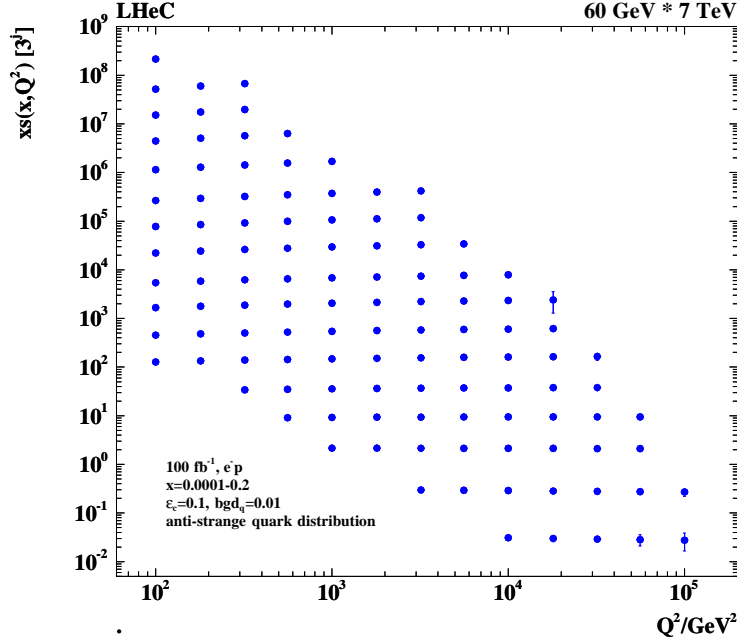
Figure 3.5: Simulation of the measurement of the (anti)-strange quark distribution, $x\bar{s}(x, Q^2)$, in charged current $e^- p$ scattering through the t-channel reaction $W^- \bar{s} \to c$. The data are plotted with full systematic and statistical errors added in quadrature, mostly non-visible. The covered x range extends from 10^{-4} (top left bin), determined by the CC trigger threshold conservatively assumed to be at $Q^2 = 100\,\text{GeV}^2$, to $x \simeq 0.2$ (bottom right) determined by the forward tagging acceptance limits, which could be further extended by lowering E_p.

is specified in the figures, the x and Q^2 ranges of these measurements extend over 3, 5 and 4 orders of magnitude for s, c and b. The coverage of very high Q^2 values, much beyond M_Z^2, permits to determine the c and b densities probed in γZ interference interactions for the first time. At HERA, xs was not directly accessible while pioneering measurements of xc and xb could be performed [64], albeit in a smaller range and less precise than shall be achieved with the LHeC. These measurements, as discussed below and in much detail in the 2012 LHeC CDR [1], are of vital importance for the development of QCD and for the interpretation of precision LHC data.

3.3 Parton Distributions from the LHeC

3.3.1 Procedure and Assumptions

In this section, PDF constraints from the simulation of LHeC inclusive NC and CC cross section measurements and heavy quark densities are investigated. The analysis closely follows the one for HERA as presented above.

The expectations on PDFs for the "LHeC inclusive" dataset, corresponding to the combination of datasets D4+D5+D6+D9, are presented, see Tab. 3.2. These datasets have the highest sensitivity to general aspects of PDF phenomenology. Since the data are recorded concurrently to the HL-LHC operation they will become available only after the end of the HL-LHC. Therefore, these PDFs will be valuable for re-analysis or re-interpretation of (HL-)LHC data, and for further future hadron colliders.

Figure 3.6: Simulation of the measurement of the charm quark distribution expressed as $F_2^c = e_c^2 x(c+\bar{c})$ in neutral current e^-p scattering. The data are plotted with full systematic and statistical errors added in quadrature, mostly invisible. The minimum x (left top bin) is at $7 \cdot 10^{-6}$, and the data extend to $x = 0.3$ (right bottom bin). The simulation uses a massless scheme and is only indicative near threshold albeit the uncertainties entering the QCD PDF analysis are estimated consistently.

In order that LHeC will be useful already during the lifetime of the HL-LHC, it is of high relevance that the LHeC can deliver PDFs of transformative precision already on a short timescale. Therefore, in the present study particular attention is paid to PDF constraints that can be extracted from the first $50\,\mathrm{fb}^{-1}$ of electron-proton data, which corresponds to the first three years of LHeC operation. The dataset is labelled D2 in Tab. 3.2 and also referred to as "LHeC 1st run" in the following.

Already the data recorded during the initial weeks of data taking will be highly valuable and impose new PDF constraints. This is because already the initial instantaneous luminosity will be comparably high, and the kinematic range is largely extended in comparison to the HERA data. These initial analyses will provide the starting point for the LHeC PDF programme. It may be recalled that the HERA I data period (1992-2000) provided just $0.1\,\mathrm{fb}^{-1}$ of data which was ample for discovering the rise of F_2 and of xg towards small x at low Q^2, and still today these data form the most important ingredient to the combined legacy HERA data [44]. The sets in Tab. 3.2 comprise D1, with $5\,\mathrm{fb}^{-1}$, still the tenfold of what H1 collected in 15 years, and D3, which resembles D2 but has the electron polarisation set to zero.

Additional dedicated studies of the impact of s, c, b data on the PDFs are then also presented, based on $10\,\mathrm{fb}^{-1}$ of e^-p simulated data. Further important PDF constraints that would be provided by measurements of F_L and jets are not considered in the present study. These remarks are significant in that they mean one has to be cautious when comparing the LHeC PDF potential with some global fits: F_L will resolve the low x non-linear parton interaction issue, see Sect. 4.2.3, and jets are important to pin down the gluon density behaviour at large x as well as providing a precision measurement of α_s, Sect. 4.1.
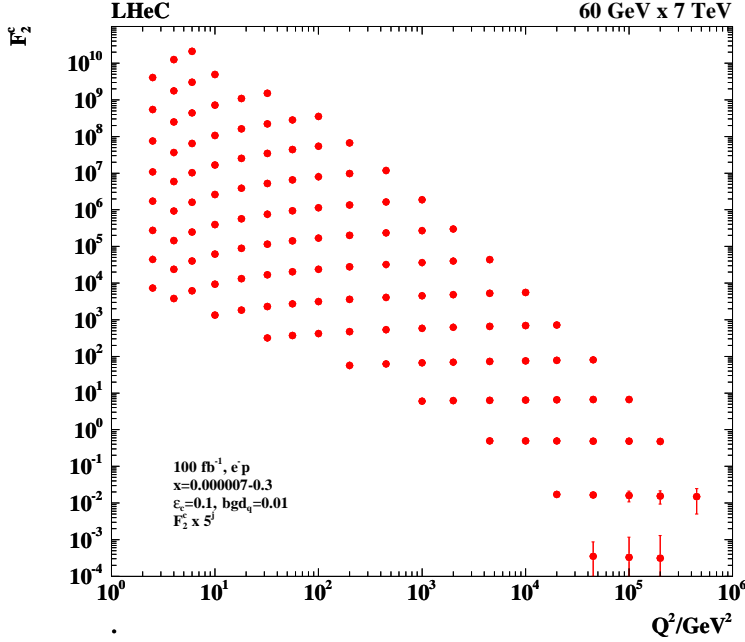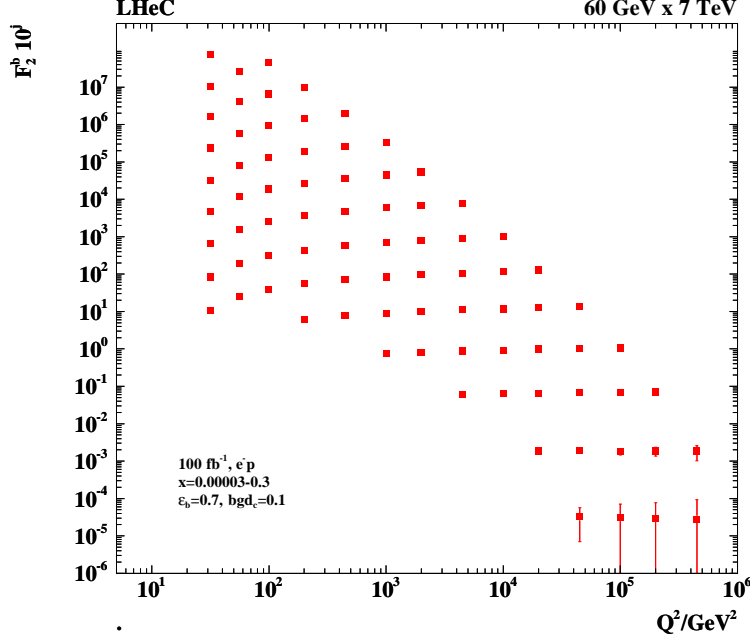
Figure 3.7: Simulation of the measurement of the bottom quark distribution expressed as $F_2^b = e_b^2 x(b + \bar{b})$ in neutral current $e^- p$ scattering. The data are plotted with full systematic and statistical errors added in quadrature, mostly invisible. The minimum x (left top bin) is at $3 \cdot 10^{-5}$, and the data extend to $x = 0.3$ (right bottom bin). The simulation uses a massless scheme and is only indicative near threshold albeit the uncertainties entering the QCD PDF analysis are estimated consistently.

To assess the importance of different operating conditions, the impact of datasets with: differing amounts of integrated luminosity (D1 vs. D4); positrons (D6 vs. D7); and with different polarisation states for the leptons (D3 vs. D8) are also considered.

In the following, PDF fits are presented, which make use of the simulated data and NLO QCD predictions. Fits in NNLO have been performed as a cross check. The analysis follows closely the HERAPDF procedure (c.f. Sect. 3.1.2 and Ref. [44]). The parametric functions in Eqs. (3.1) and (3.2) are used, and the parameterised PDFs are the valence distributions $x u_v$ and $x d_v$, the gluon distribution xg, and the $x\bar{U}$ and $x\bar{D}$ distributions, using $x\bar{U} = x\bar{u}$ and $x\bar{D} = x\bar{d} + x\bar{s}$. In total the following 14 parameters are set free for the nominal fits: B_g, C_g, D_g, B_{uv}, C_{uv}, E_{uv}, B_{dv}, C_{dv}, $A_{\bar{U}}$, $B_{\bar{U}}$, $C_{\bar{U}}$, $A_{\bar{D}}$, $B_{\bar{D}}$, $C_{\bar{D}}$. These fit parameters are similar to HERAPDF2.0, albeit to some extent more flexible due to the stronger constraints from the LHeC. Note, the B parameters for u_v and d_v, and the A and B parameters for $\bar{U}$ and $\bar{D}$ are fitted independently, such that the up and down valence and sea quark distributions are uncorrelated in the analysis, whereas for HERAPDF2.0 $x\bar{u} \to x\bar{d}$ as $x \to 0$ is imposed. The other main difference is that no negative gluon term has been included, i.e. $A_g' = 0$ but $D_g \neq 0$.

This ansatz is natural to the extent that the NC and CC inclusive cross sections determine the sums of up and down quark distributions, and their anti–quark distributions, as the four independent sets of PDFs, which may be transformed to the ones chosen if one assumes $u_v = U - \bar{U}$ and $d_v = D - \bar{D}$, i.e. the equality of anti– and sea–quark distributions of given flavour. For the majority of the QCD fits presented here, the strange quark distribution at Q_0^2 is assumed to be a constant fraction of $\bar{D}$, $x\bar{s} = f_s x\bar{D}$ with $f_s = 0.4$ as for HERAPDF, while this assumption is relaxed for the fits including simulated s, c, b data.

45

Note, that the prospects presented here are illustrations for a different era of PDF physics, which will be richer and deeper than one may be able to simulate now. For instance, without real data one cannot determine the actual parameterisation needed for the PDFs. In particular the low x kinematic region was so far unexplored and the simulated data relies on a simple extrapolation of current PDFs, and no reliable data or model is available that provides constraints on this region[5]. The LHeC data explores new corners of phase space with high precision, and therefore it will have a great potential, much larger than HERA had, to determine the parameterisation. As another example, with LHeC data one can directly derive relations for how the valence quarks are determined with a set of NC and CC cross section data in a redundant way, since the gluon distribution at small x can be determined from the Q^2 derivative of F_2 and from a measurement of F_L. The question of the optimal gluon parameterisation may then be settled by analysing these constraints and not by assuming some specific behaviour of a given fit.

Furthermore, the precise direct determinations of s, c and b densities with measurements of the impact parameter of their decays, will put the treatment of heavy flavours in PDF analyses on a new level. The need for the phenomenological introduction of the f_s factor will disappear and the debate on the value of fixed and variable heavy flavour schemes will be settled.

3.3.2 Valence Quarks

Since the first measurements of DIS physics, it had been proposed to identify partons with quarks and to consider the proton to consist of valence quarks together with "an indefinite number of $(q\bar{q})$ pairs" [65]. 50 years later there are still basic questions unanswered about the behaviour of valence quarks, such as the d_v/u_v ratio at large x, and PDF fits struggle to resolve the flavour composition and interaction dynamics of the sea. The LHeC is the most suited machine to resolve these challenges.

The precision that can be expected for the valence quark distributions from the LHeC is illustrated in Fig. 3.8, and compared to a variety of modern PDF sets. Today, the knowledge of the valence quark distributions, particularly at large x, is fairly limited as it can be derived from the Figure. This is due to the limited HERA luminosity, challenging systematics that rise $\propto 1/(1-x)$, and to nuclear correction uncertainties. At low x the valence quark distributions are very small compared to the sea quarks and cannot be separated easily from these.

The u valence quark distribution is much better known than the d valence, since it enters with a four-fold weight in F_2 due to the electric quark charge ratio squared. Nevertheless, a substantial improvement in d_v by the LHeC is also visible, because the relative weight of d_v to u_v is changing favourably towards the down quark due to the influence of weak NC and CC interactions at high Q^2 where the LHeC is providing very accurate data. The strong constraints to the highest x valence distributions are due to the very high integrated luminosity. Note, at the HL-LHC, albeit its high integrated luminosity, the highest x are there only accessible as convolutions with partons at lower x, and those can therefore not be well constrained.

Note that the "LHeC 1st run" PDF, displayed by the yellow band in Fig. 3.8, includes only electron, i.e. no positron, data. In fact, from the $e^{\pm}p$ cross section differences access to valence quarks at low x can be obtained. As has already been illustrated in the CDR from 2012 [1] the sum of $2u_v + d_v$ may be measured directly with the NC γZ interference structure function $xF_3^{\gamma Z}$

---

[5] It is expected that real LHeC data, and also the inclusion of further information such as F_L, will certainly lead to a quite different optimal parameterisation ansatz than was used in the present analysis. Though, it has been checked that with a more relaxed set of parameters, very similar results on the PDF uncertainties are obtained, which justifies the size of the prospected PDF uncertainties.

Figure 3.8: Valence quark distributions at $Q^2 = 1.9\,\mathrm{GeV}^2$ as a function of x, presented as the ratio to the CT18 [66] central values. The yellow band corresponds to the "LHeC 1st run" PDFs (D2), while the dark blue shows the final "LHeC inclusive" PDFs based on the data sets (D4+D5+D6+D9), as described in Sect. 3.3.1. For the purposes of illustrating the improvement to the uncertainties more clearly, the central values of the LHeC PDFs have been scaled to the CT18 PDF, which itself is displayed by the green band.

down to $x \simeq 10^{-4}$ with very good precision. Thus the LHeC will have a direct access to the valence quarks at small x. This also tests the assumption of the equality of sea- and anti-quark densities which if different would cause $xF_3^{\gamma Z}$ to rise towards small x.

As becomes evident in Fig. 3.8 there is a striking difference and even contradiction between the estimates of the uncertainties of the parton distributions between the various fit groups. This is due to different fit technologies but as well a result of different choices of data and assumptions on the d/u ratio. Such major uncertainties would be resolved by the LHeC.

The precise determinations of the valence quark distributions at large x have strong implications for physics at the HL-LHC, in particular for BSM searches. The precise determinations of the valence quarks will resolve the long standing mystery of the behaviour of the d/u ratio at large x, see Fig. 3.9. As exemplarily shown in Fig. 3.9, there are currently conflicting theoretical pictures for the central value of the d/u ratio, albeit the large uncertainty bands of the different PDF sets mainly overlap. As of today, the constraints from data are inconclusive statistically and also suffer from large uncertainties from the use of DIS data on nuclear targets, which therefore cause those large uncertainties.

3.3.3 Light Sea Quarks

Our knowledge today about the anti-quark distributions is fairly poor and uncertainties are very large at smaller values of x, and also at the highest x. In particular, at low x the size of the anti-quark PDFs are large and they contribute significantly to precision SM measurements at
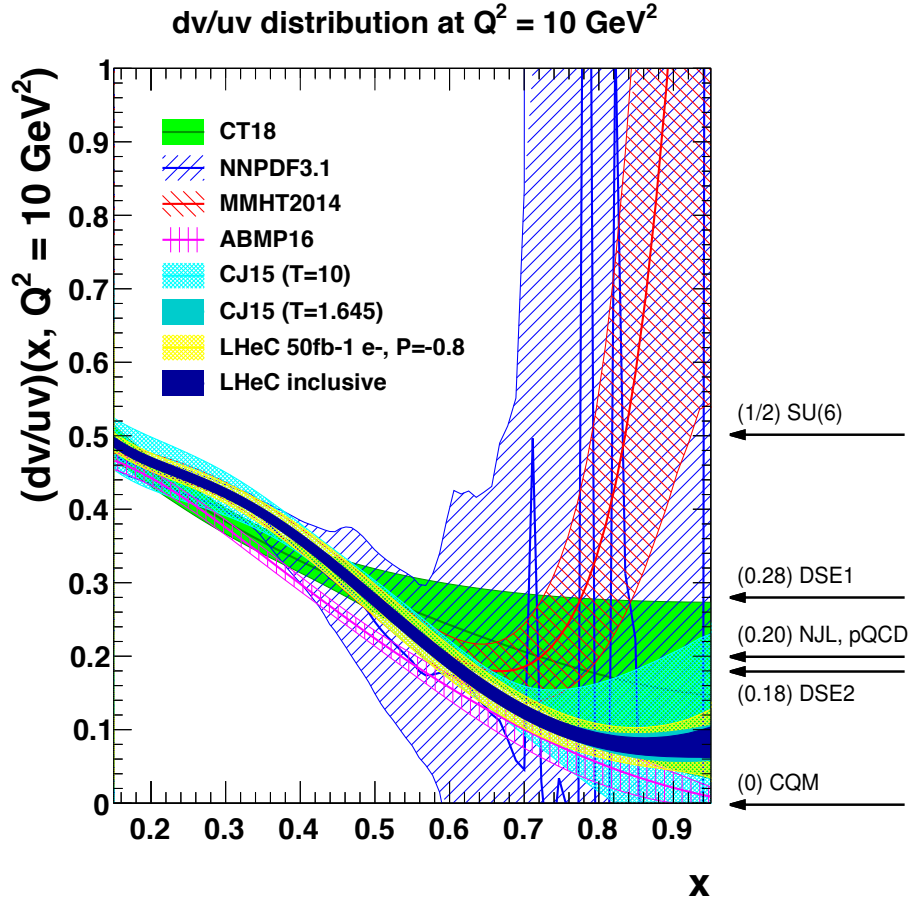
Figure 3.9: The d_v/u_v distribution at $Q^2 = 10 \, \text{GeV}^2$ as a function of x. The yellow band corresponds to the "LHeC 1st run" PDFs (D2), while the dark blue shows the final "LHeC inclusive" result. Both LHeC PDFs shown are scaled to the central value of CT18.

the HL-LHC. At high x, sea and valence need to be properly distinguished and accurately be measured for reliable BSM searches at high mass.

Our knowledge about the anti-quark PDFs will be changed completely with LHeC data. Precise constraints are obtained with inclusive NC/CC DIS data despite the relaxation of any assumptions in the fit ansatz that would force $\bar{u} \to \bar{d}$ as $x \to 0$, as it is present in other PDF determinations today. At smaller Q^2 in DIS one measures essentially $F_2 \propto 4\bar{U} + \bar{D}$. Thus, at HERA, with limited precision at high Q^2, one could not resolve the two parts, and neither will that be possible at any other lower energy ep collider which cannot reach small x. At the LHeC, in contrast, the CC DIS cross sections are measured very well down to x values even below 10^{-4}, and in addition there are strong weak current contributions to the NC cross section which probe the flavour composition differently than the photon exchange does. This enables this distinction of $\bar{U}$ and $\bar{D}$ at the LHeC.

The distributions of $\bar{U}$ and $\bar{D}$ for the PDFs from the 1st run and the "LHeC inclusive data" are shown in Figs. 3.10 and 3.11 for $Q^2 = 1.9 \, \text{GeV}^2$ and $Q^2 = 10^4 \, \text{GeV}^2$, respectively, and compared to present PDF analyses. One observes a striking increase in precision for both $\bar{U}$ and $\bar{D}$ which persists from low to high scales. The relative uncertainty is large at high $x \geq 0.5$. However, in that region the sea-quark contributions are already very tiny. In the high x region one recognises

the value of the full LHeC data sample fitted over the initial one while the uncertainties below $x \simeq 0.1$ of both the small and the full data sets are of comparable, very small size.
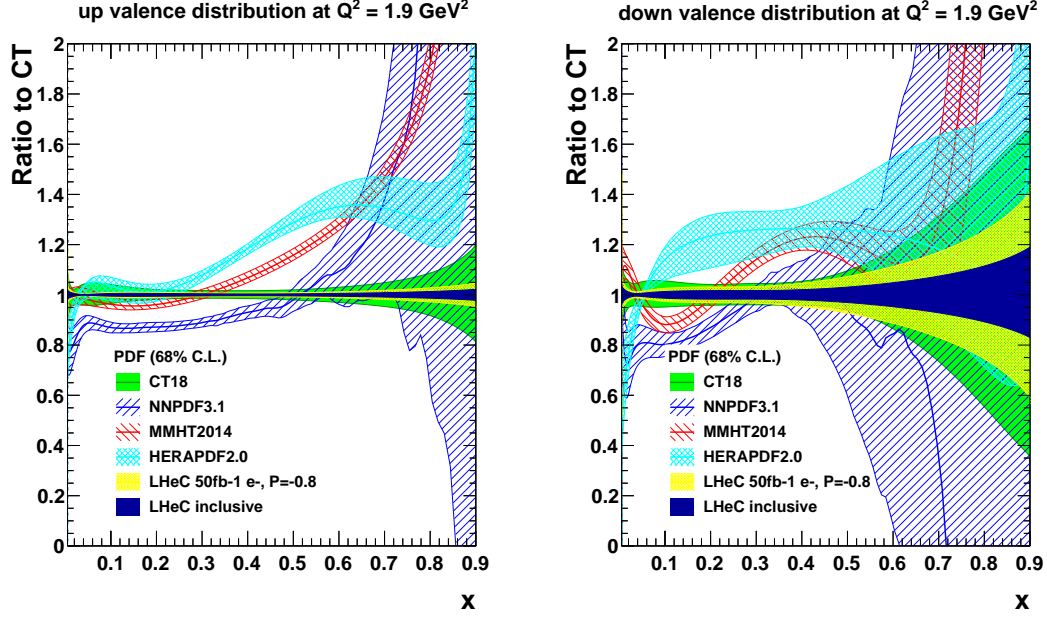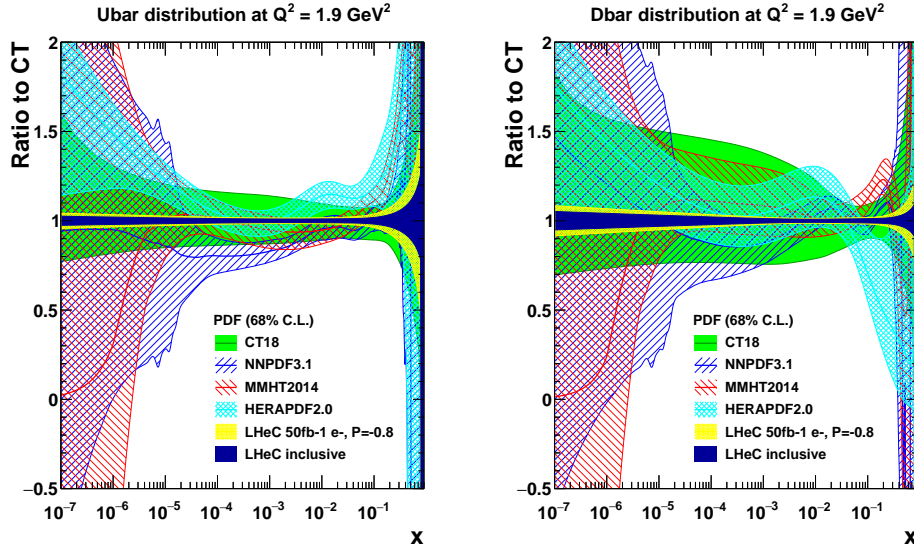

Figure 3.10: Sea quark distributions at $Q^2 = 1.9\,\text{GeV}^2$ as a function of x, presented as the ratio to the CT18 central values. The yellow band corresponds to the "LHeC 1st run" PDFs (D2), while the dark blue shows the final "LHeC inclusive" PDFs (D4+D5+D6+D9), as described in the text. Both LHeC PDFs shown are scaled to the central value of CT18.
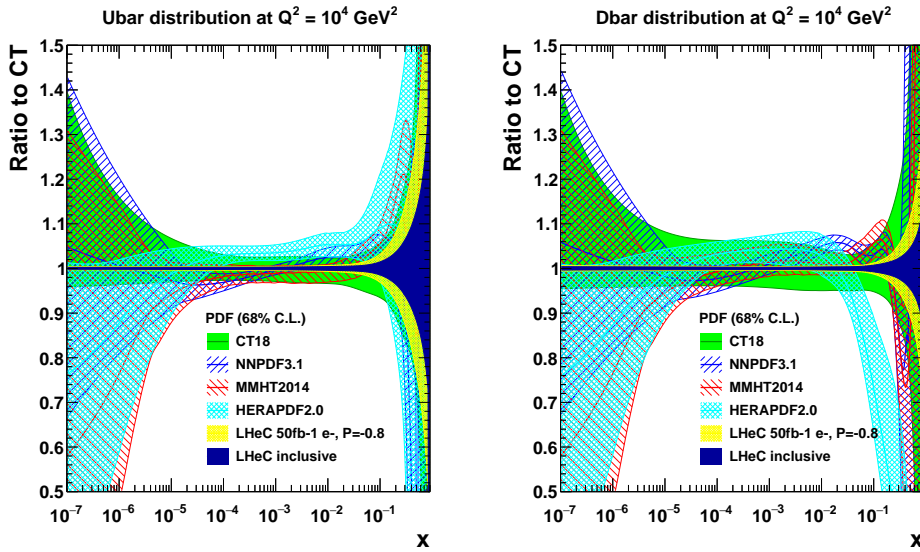
Figure 3.11: Sea quark distributions at $Q^2 = 10^4\,\text{GeV}^2$ as a function of x, presented as the ratio to the CT18 central values. The yellow band corresponds to the "LHeC 1st run" PDFs (D2), while the dark blue shows the final "LHeC inclusive" PDFs (D4+D5+D6+D9), as described in the text. Both LHeC PDFs shown are scaled to the central value of CT18.

3.3.4 Strange Quark

The determination of the strange PDF has generated significant controversy in the literature for more than a decade. Fixed-target neutrino DIS measurements [67–71] typically prefer a strange

PDF that is roughly half of the up and down sea distribution; $\kappa = (s + \bar{s})/(\bar{u} + \bar{d}) \sim 0.5$. The recent measurements from the LHC [72–75] and related studies [76,77] suggest a larger strange quark distribution, that may potentially even be larger than the up and down sea quarks. The x dependence of xs is essentially unknown, and it may differ from that of $x\bar{d}$, or $x(\bar{u} + \bar{d})$, by more than a normalisation factor. A recent paper ascribes the strange enhancement to a suppression of the anti-down distribution related to suspected parameterisation effects and the behaviour of the ratio d/u for $x \to 1$ [78]. Apparently, a direct measurement of $xs(x, Q^2)$ and the resolution of the complete light-quark structure of the proton is required, which is a fundamental goal of the LHeC.

The precise knowledge of the strange quark PDF is of high relevance, since it provides a significant contribution to *standard candle* measurements at the HL-LHC, such as W/Z production, and it imposes a significant uncertainty on the W mass measurements at the LHC. The question of light-sea flavour 'democracy' is of principle relevance for QCD and the parton model. For the first time, as has been presented in Sect. 3.2.2, $x\bar{s}(x, Q^2)$ can be accurately measured, namely through the charm tagging $Ws \to c$ reaction in CC e^-p scattering at the LHeC. The inclusion of the CC charm data in the PDF analysis will settle the question of how strange the strange quark distribution really is [6]. This prospect has been analysed within the LHeC fit framework here introduced and as well studied in detail in a profiling analysis using *xFitter*. Both analyses yield rather compatible results and are presented in the following.

In the standard LHeC fit studies, the parameterised PDFs are the four quark distributions xu_v, xd_v, $x\bar{U}$, $x\bar{D}$ and xg (constituting a 4+1 parameterisation), as the inclusive NC and CC data determine only the sums of the up and down quark and anti-quark distribution, as discussed previously. The strange quark PDF is then assumed to be a constant fraction of $x\bar{d}$.

With the strange quark data available, the LHeC PDF fit parameterisations can be extended to include $xs = x\bar{s}$, parameterised as $A_s x^{B_s}(1 - x)^{C_s}$ [7]. For the fits presented in the following, the $\bar{d}$ and $\bar{s}$ are treated now separately, and therefore a total of five quark distributions are parameterised (xu_v, xd_v, $x\bar{U}$, $x\bar{d}$, $x\bar{s}$) as well as g. This provides a 5+1 parameterisation, and the total number of free parameters of the PDF fit then becomes 17.

Results of the 5+1 PDF fits are shown in Fig. 3.12, where fits to inclusive NC/CC DIS data are displayed as reference (both for the 4+1 and 5+1 ansatz) and the fits where in addition strange density measurements and even further measurements of $F_2^{c,b}$ are considered. As expected, the uncertainties of the 5+1 fit to the inclusive DIS data, especially on the $\bar{d}$ and $\bar{s}$ distributions (c.f. Fig. 3.12), become substantially larger in comparison to the respective 4+1 fit, since the $\bar{d}$ and $\bar{s}$ distributions are treated now separately. This demonstrates that the inclusive DIS data alone does not have the flavour separating power to determine the individual distributions very precisely.

When including an LHeC measurement of the $\bar{s}$ quark density based on $10\,\mathrm{fb}^{-1}$ of e^-p data, the uncertainties on the $\bar{d}$ and $\bar{s}$ PDFs become significantly smaller. By chance, those uncertainties are then comparable to the 4+1 fit in which $x\bar{s}$ is linked to $x\bar{d}$ by a constant fraction.

The constraints from a measurement of charm quark production cross sections in charged current

---

[6]The provision of positron-proton data will enable very interesting tests of charge symmetry, i.e. permit to search for a difference between the strange and the anti-strange quark densities. This has not been studied in this paper.

[7] It is worth mentioning that the W, Z data [72] essentially determine only a moment of xs at $x \sim 0.02$, not the x dependence. Therefore, in analyses of HERA and ATLAS data such as Ref. [77], there is no determination attempted of the relevant parameter, B_s, which instead is set equal to $B_{\bar{d}}$. The kinematic dependence of xs is basically not determined by LHC data while the hint to the strange being unsuppressed has been persistent.

(a) $x\bar{d}$ quark distribution.

(b) $x\bar{s}$ quark distribution.
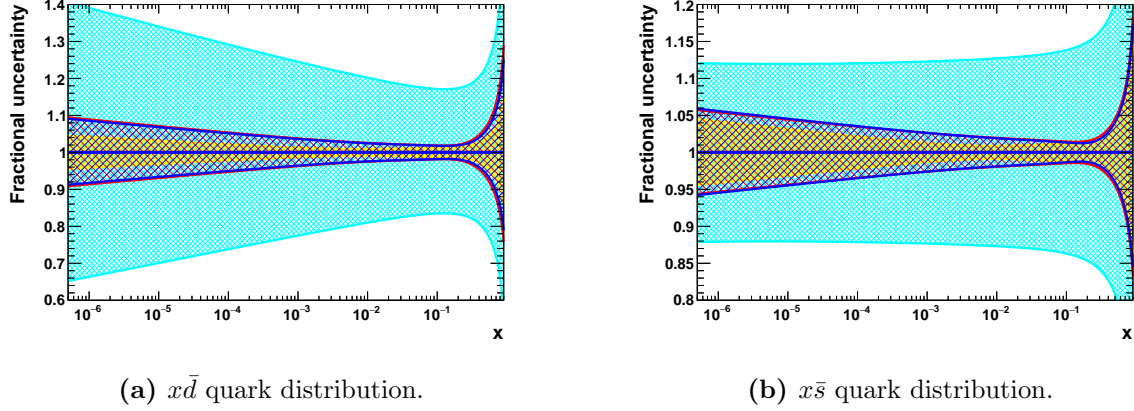
Figure 3.12: PDF uncertainties at $Q^2 = 1.9\,\text{GeV}^2$ as a function of x for the $\bar{d}$ and $\bar{s}$ distributions. The yellow band displays the uncertainties of the nominal "LHeC inclusive" PDF, which was obtained in a 4+1 PDF fit. From the same dataset, results of the more flexible 5+1 fit (see text) are displayed as a cyan band. The red band displays the results, when in addition an LHeC measurement of the $\bar{s}$ quark density is included. When even further including LHeC measurements of F_2^c and F_2^b, the PDF fits yields uncertainties as displayed by the blue band.

DIS have also been studied in a profiling analysis using *xFitter* [79]. The treatment of heavy quark production to higher orders in pQCD is discussed extensively in this paper. At leading-order QCD, the subprocess under consideration is $Ws \rightarrow c$, where the s represents an intrinsic strange quark. Fig. 3.13 displays the tight constraints obtained for the strange PDF when
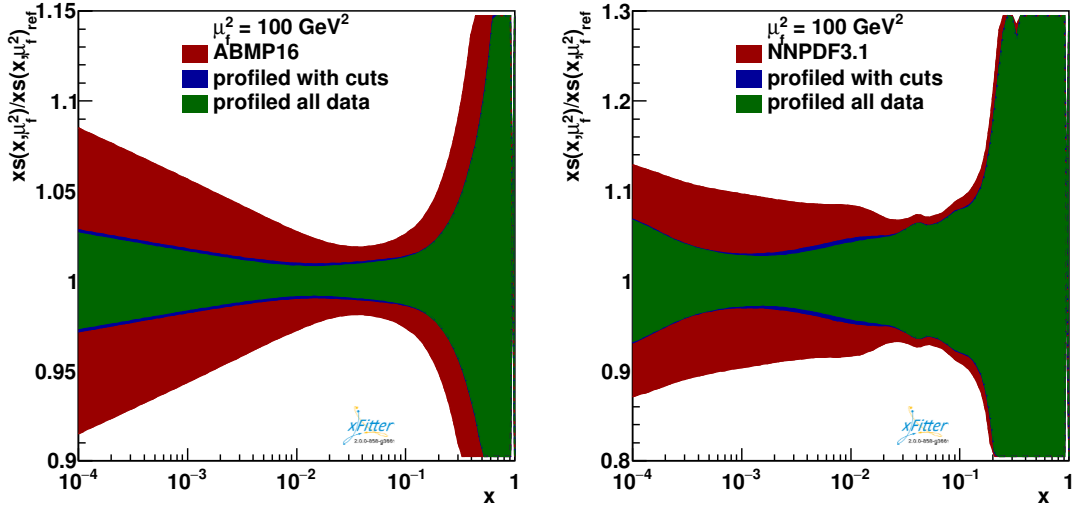
Figure 3.13: Constraints on the strange quark PDF xs using simulated data for charged-current production of charm quarks at the LHeC, from a profiling study [79] using the ABMP16 (left) and the NNPDF3.1 (right) PDF sets. The red band displays the nominal PDF uncertainties, and the green and blue bands the improved uncertainties due to the LHeC strange quark data.

using the LHeC pseudo-data for the CC charm production channel. The results of this profiling analysis, both when based on the ABM16 and the NNPDF3.1 PDF sets, and of the direct fit presented above, are very similar, reaching about $3 - 5\,\%$ precision for x below $\simeq 0.01$

In a variation of the study [79], a large reduction of uncertainties is already observed when restricting the input data to the kinematic range where the differences between the different

heavy flavour schemes (VFNS and FFNS) are not larger than the present PDF uncertainties. This further indicates that the PDF constraints are stable and independent of the particular heavy-flavour scheme.

It may thus be concluded that the LHeC, through high luminosity, energy and precise kinematic reconstruction, will be able to solve a long standing question about the role of the strange-quark density in the proton, and its integration into a consistent QCD treatment of parton dynamics.

3.3.5 Heavy Quarks

One of the unsolved mysteries of the Standard Model is the existence of three generations of quarks and leptons. The strongly interacting fermion sector contains altogether six quarks with masses differing by up to five orders of magnitude. This hierarchy of masses is on one hand a challenge to explain, on the other hand it offers a unique opportunity to explore dynamics at a variety of different scales and thus develop different facets of the strong interaction. While the light quarks at low scales are non-perturbative and couple strongly, the heavier quarks charm, bottom and top are separated from the soft sea by their masses and thus can serve as a suitable additional probe for the soft part of QCD.

There are a number of deep and unresolved questions that can be posed in the context of the proton structure: what is the individual contribution of the different quark flavours to the structure functions?; are heavy quarks like charm and bottom radiatively generated or is there also an intrinsic heavy quark component in the proton?; to what extent do the universality and factorisation theorems work in the presence of heavy quarks? It is therefore imperative to be able to perform precise measurements of each individual quark flavour and their contribution to the proton structure. The LHeC is the ideal place for these investigations because it resolves the complete composition of the proton flavour by flavour. In particular, as shown in Sect. 3.2.2, the LHeC provides data on F_2^c and F_2^b extending over nearly 5 and 6 orders of magnitude in x, Q^2, respectively. These are obtained through charm and beauty tagging with high precision in NC ep scattering. A thorough PDF analysis of the LHeC data thus can be based on the inclusive NC/CC cross sections and tagged s, c, b data. In addition, one may use DIS jets, here used for the α_s prospective study (Sect. 4.1) and low energy data, here analysed for resolving the low x dynamics with a precision measurement of F_L (Sect. 4.2.3). The current studies in this chapter therefore must be understood as indicative only as we have not performed a comprehensive analysis using all these data as yet [8].

The production of heavy quarks at HERA (charm and bottom) is an especially interesting process as the quark mass introduces a new scale ($m = m_{c,b}$) which was neither heavy or light (see e.g. reviews [80,81]). Actually, the treatment of heavy quark mass effects is essential in PDF fits which include data from fixed target to collider energies and thus require the computation of physical cross sections over a large range of perturbative scales μ^2. With these scales passing through (or close to) the thresholds for charm, bottom and, eventually, top, precise computations demand the incorporation of heavy quark mass effects close to threshold, $\mu^2 \sim m^2$, and the resummation of collinear logarithms $\ln(\mu^2/m^2)$ at scales far above the threshold, $\mu^2 \gg m^2$. The first problem can be dealt with through the use of massive matrix elements for the generation of heavy quark-antiquark pairs but keeping a fixed number of parton densities (fixed flavour number schemes, FFNS). On the other hand, the proper treatment of resummation is achieved through the use of variable flavour number schemes (VFNS) which consider an increasing number

---

[8]This is to be considered when one compares the precision of the inclusive PDF fits with so-called global analyses, for example regarding the behaviour of xg at large x.

of massless parton species, evolved through standard DGLAP, when the scale is increased above heavy quark mass thresholds. At present, calculations involving heavy quarks in DIS in different schemes (generalised mass VFNS) with different numbers of active flavours participating to DGLAP evolution are combined to derive an expression for the coefficient functions which is valid both close to threshold, and far above it. Such multi-scale problems are particularly difficult, and numerous techniques were developed to cope with this challenging problem [51, 82–90]. Additional complications, see e.g. Ref. [91], arise when the possibility of a non-perturbative origin of heavy quark distributions is allowed above the heavy quark mass threshold - intrinsic heavy flavour. The ABMP16 analysis [52] underlines that the available DIS data are compatible with solely an FFNS treatment assuming that the heavy quarks are generated in the final state.

(a) Gluon distribution ($\log_{10} x$ scale)

(b) Gluon distribution (linear x scale).
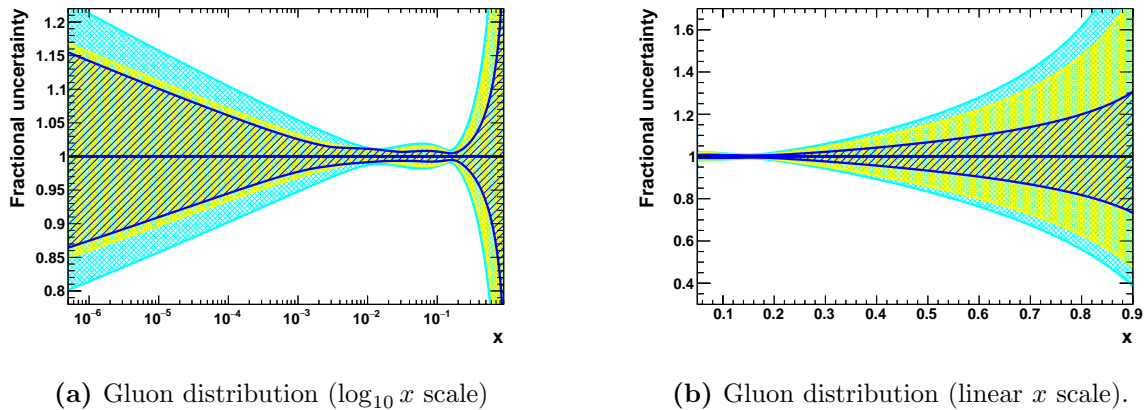
Figure 3.14: PDF uncertainties at $Q^2 = 1.9\,\mathrm{GeV}^2$ as a function of x to illustrate the constraints from additional heavy quark sensitive measurements at LHeC. Displayed is the gluon distribution on a logarithmic and linear scale. The yellow band illustrates the uncertainties of the nominal "LHeC inclusive" PDF, obtained in a 4+1 PDF fit. From the same dataset, results of the more flexible 5+1 fit (see text) are displayed as a cyan band. When further including LHeC measurements of F_2^c and F_2^b, the PDF fits yields uncertainties as displayed by the blue band.

At the LHeC, as illustrated in Figs. 3.6, 3.7, the large polar angle acceptance and the high centre-of-mass energy allow heavy quark physics to be investigated from below threshold to almost $10^6\,\mathrm{GeV}^2$. The extended reach in comparison to HERA is dramatic. This permits to comprehensively explore the *asymptotic* high energy limit where $m_{c,b}^2/Q^2 \to 0$, as well as the low energy *decoupling* region $m_{c,b}^2/Q^2 \sim 1$.

For the PDF determination the obviously direct impact of the tagged charm and bottom data will be on the determination of xc and xb, and the clarification of their appropriate theoretical treatment. In addition, however, there is a remarkable improvement achieved for the determination of the gluon density, see Fig. 3.14. The determination of xg will be discussed in much more detail in the following section.

These channels will also strongly improve the determination of the charm and bottom quark masses and bring these uncertainties down to about $\delta m_{c(b)} \simeq 3(10)\,\mathrm{MeV}$ [1] [9]. These accuracies are crucial for eliminating the corresponding model uncertainties in the PDF fit. Precision tagged charm and bottom data are also essential for the determination of the W-boson mass in pp, and the extraction of the Higgs $\to c\bar{c}$ and $b\bar{b}$ couplings in ep, as is discussed further below.

---

[9] Such precision demands the availability of calculations with higher orders in pQCD, and those computations are already ongoing [92–94]. Note than in PDF fits the heavy quark mass is an effective parameter that has to be related with the pole mass, see e.g. Ref. [95] and refs. therein.

3.3.6 The Gluon PDF

The LHeC, with hugely increased precision and extended kinematic range of DIS, i.e. the most appropriate process to explore $xg(x, Q^2)$, can pin down the gluon distribution much more accurately than it is known today. This primarily comes from the extension of range and precision in the measurement of $\partial F_2 / \partial \ln Q^2$, which at small x is a direct measure of xg. The precision determination of the quark distributions, discussed previously, also strongly constrains xg. Further sensitivity arises with the high-y part of the NC cross section which is controlled by the longitudinal structure function as is discussed in Sect. 4.2.3.

The result for the gluon distribution from the LHeC inclusive NC/CC data fits is presented in Fig. 3.15, and compared to several other PDF sets. On the left, the distribution is presented as a ratio to CT18, and is displayed on a log-x scale to highlight the small x region. On the right, the xg distribution is shown on a linear-x scale, accentuating the region of large x. The determination of xg will be radically improved with the LHeC NC and CC precision data, which provide constraints on $\partial F_2 / \partial \ln Q^2$ down to very low x values, $\geq 10^{-5}$, and large $x \leq 0.8$.
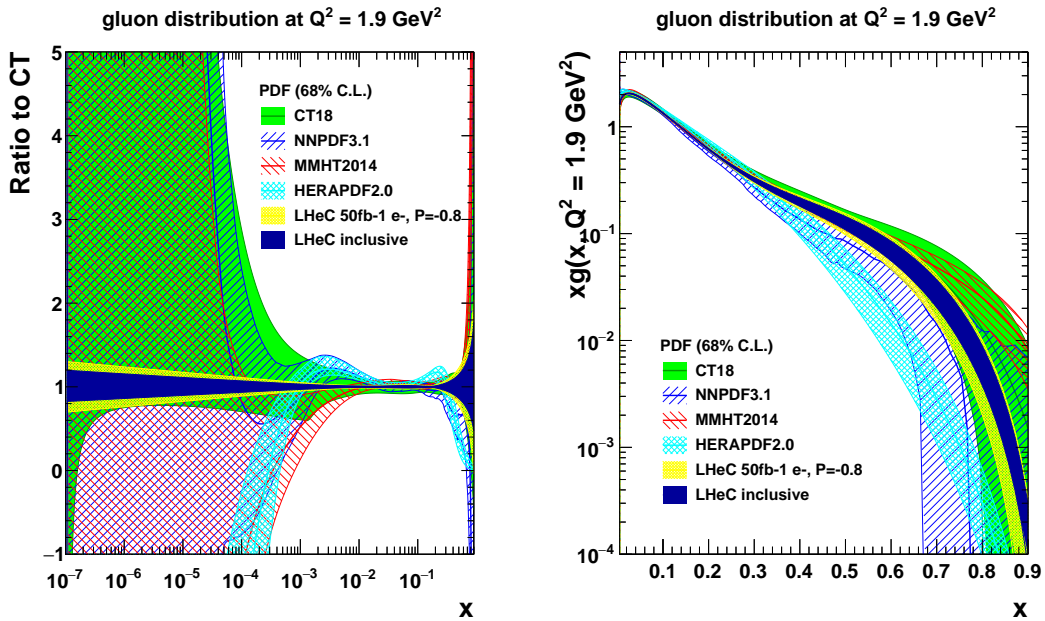
Figure 3.15: Gluon distribution at $Q^2 = 1.9 \, \text{GeV}^2$ as a function of x, highlighting (left) the low x and (right) the high x regions. The yellow band corresponds to the "LHeC 1st run" PDFs (D2), while the dark blue shows the "LHeC inclusive" PDFs (D4+D5+D6+D9), as described in the text. Both LHeC PDFs shown are scaled to the central value of CT18.

Below $x \simeq 5 \cdot 10^{-4}$, the HERA data have almost vanishing constraining power due to kinematic range limitations, as one needs a lever arm to determine the Q^2 derivative, and so the gluon is simply not determined at lower x. This can be seen in all modern PDF sets. With the LHeC, a precision of a few per cent at small x becomes possible down to nearly 10^{-5}. This should resolve the question of non-linear parton interactions at small x (cf. Sect. 4.2). It also has direct implications for the LHC (and even stronger for the FCC): with the extension of the rapidity range to about 4 at the HL-LHC by ATLAS and CMS, Higgs physics will become small x physics for which xg must be known very accurately since $gg \rightarrow H$ is the dominant production mechanism.

At large $x \geq 0.3$, the gluon distribution becomes very small and large variations appear in

its determination from several PDF groups, differing by orders of magnitude. That is related to uncertainties on jet measurements, theoretical uncertainties, and the fact that HERA did not have sufficient luminosity to cover the high x region where, moreover, the sensitivity to xg diminishes, since the valence quark evolution is insensitive to it. For the LHeC, the sensitivity at large x comes as part of the overall package: large luminosity allowing access to x values close to 1, fully constrained quark distributions and strong constraints at small x which feed through to large x via the momentum sum rule. The high precision illustrated will be crucial for BSM searches at high scales. It is also important for testing QCD factorisation and scale choices, as well as pinning down electroweak effects.

The analysis presented here has not made use of the additional information that can be provided at the LHeC in measurements of $F_2^{c,b}$ (see Sect. 3.3.5) or F_L. The large x situation can be expected to further improve by using LHeC jet data, providing further, direct constraints at large x which, however, have not yet been studied in comparable detail.

The LHeC is the ideal laboratory to resolve all unknowns of the gluon density, which is the origin for all visible mass in the universe, and one of the particular secrets of particle physics for the gluon cannot directly be observed but is confined inside hadrons. It is obvious that resolving this puzzle is an energy frontier DIS task and goal, including electron-ion scattering since the gluon inside heavy matter is known even much less. Therefore, the special importance of this part of high energy PDF physics is not primarily related to the smallness of uncertainties: it is about a consistent understanding and resolution of QCD at all regions of spatial and momentum dimensions which the LHeC will explore.

3.3.7 Luminosity and Beam Charge Dependence of LHeC PDFs

It is informative to study the transition of the PDF uncertainties from the "LHeC 1st run" PDFs, which exploits only a single electron-proton dataset, D2, through to the "LHeC final inclusive" PDFs, which makes use of the full datasets D4+D5+D6+D9 as listed in Tab. 3.2, i.e. including high luminosity data (D4), small sets of low energy $E_p = 1\,\mathrm{TeV}$ and positron data (D5 and D6) together with $10\,\mathrm{fb}^{-1}$ of opposite helicity data. Various intermediate PDF fits are performed using subsets of the data in order to quantify the influence of the beam parameters on the precision of the various PDFs. All fits use the same, standard 4+1 fit parameterisation and exclude the use of s, c, b data, the effect of which was evaluated before. The fits do neither include the low electron energy data sets generated for the F_L analysis, cf. Sect. 4.2.3, nor any jet ep data. The emphasis is on the development of the u_v, d_v, total sea and xg uncertainty.

A first study, Fig. 3.16, shows the influence of the integrated luminosity. This compares four cases, three with evolving luminosity, from 5 over 50 to $1000\,\mathrm{fb}^{-1}$. These assumptions, according to the luminosity scenarios presented elsewhere, correspond to year 1 (D1), the initial 3 years (D2) and to the maximum attainable integrated luminosity (D4). The fourth case is represented by what is denoted the LHeC inclusive fit. One observes a number of peculiarities. For example, the initial $5\,\mathrm{fb}^{-1}$ (yellow in Fig. 3.16), i.e. the tenfold of what H1 collected over its lifetime (albeit with different beam parameters), leads i) to an extension of the HERA range to low and higher x, ii) to high precision at small x, for example of the sea quark density of $5\,\%$ below $x = 10^{-5}$ or iii) of also $5\,\%$ for u_v at very high $x = 0.8$. With $50\,\mathrm{fb}^{-1}$ the down valence distribution is measured to within $20\,\%$ accuracy at $x = 0.8$, an improvement by about a factor of two as compared to the $5\,\mathrm{fb}^{-1}$ case, and a major improvement to what is currently known about xd_v at large x, compare with Fig. 3.8. The very high luminosity, here taken to be $1\,\mathrm{ab}^{-1}$, leads to a next level of high precision, for example of $2\,\%$ below $x = 10^{-5}$ for the total sea. The full data set

further improves, especially the xd_v and the gluon at high x. The valence quark improvement is mostly linked to the positron data while the gluon improvement is related to the extension of the lever arm towards small values of Q^2 as the reduction of E_p extends the acceptance at large x. The visible improvement through the final inclusive fit is probably related to the increased precision at high x for there exists a momentum sum rule correlation over the full x range. In comparison to the analogous HERA fit, it becomes clear, that the vast majority of the gain comes already from the first $5 - 50\,\text{fb}^{-1}$.

The second study presented here regards the impact on the PDF uncertainties when adding additionally positron data of different luminosity to a baseline fit on $50\,\text{fb}^{-1}$ of $e^- p$ data, the "LHeC 1st run" dataset. The results are illustrated in Fig. 3.17. It is observed, that the addition of positron data does bring benefits, which, however, are not striking in their effect on the here considered PDFs. A prominent improvement is obtained for the d-valence PDF, primarily due to the sensitivity gained via the CC cross section of the positron data. The benefit of the precise access to NC and CC weak interactions by the LHeC is clearer when one studies the cross sections and their impact on PDFs. This is illustrated in the subsequent section.

3.3.8 Weak Interactions Probing Proton Structure

It had long been considered to use the weak interactions to probe proton structure in deep inelastic scattering [96]. First important steps in this direction could be pursued with HERA, especially with the measurements of the polarisation and beam charge asymmetries in NC ep scattering by H1 and ZEUS [44]. This area of research will become a focus at the LHeC, because the Q^2 range extends by 2-3 orders of magnitude beyond the weak scale $Q^2 \simeq M_{W,Z}^2$, with hugely increased luminosity. In Sect. 5.1 below, the emphasis is on accessing the electroweak theory parameters at a new level of sensitivity. Here we illustrate the importance of using the Z and also W exchange for pinning down the parton contents of the proton. This has been implicit for the QCD fits presented above, it yet emerges clearly only when one considers cross sections directly, their asymmetries with respect to beam charge and polarisation, and certain kinematic limits.

Parity violation is accessed in NC DIS through a variation of the lepton beam helicity, P, as can be deduced from [96]

$$\frac{\sigma_{r,NC}^{\pm}(P_R) - \sigma_{r,NC}^{\pm}(P_L)}{P_R - P_L} = \mp \kappa_Z g_A^e F_2^{\gamma Z} - (\kappa_Z g_A^e)^2 \frac{Y_-}{Y_+} x F_3^Z \tag{3.3}$$

where $\sigma_{r,NC}$ denotes the double differential NC scattering cross section scaled by $Q^4 x/2\pi\alpha^2 Y_+$. Here κ_Z is of the order of Q^2/M_Z^2, $F_2^{\gamma Z} = 2x \sum Q_q g_V^q (q - \bar{q})$ and the NC vector couplings are determined as $g_V^f = I_{3,L}^f - 2Q_f \sin^2 \theta_W$, where Q_f is the electric charge and $I_{3,L}^f$ the left handed weak isospin charge of the fermion $f = e, q$, which also determines the axial vector couplings g_A^f, with $g_A^e = -1/2$. At LHeC (unlike FCC-he) the second term in Eq. 3.3 is suppressed with respect to the first one as it results from pure Z exchange and because the Y factor is small, $\propto y$ since $Y_{\mp} = (1 \mp (1-y)^2)$.

For the approximate value of the weak mixing angle $\sin^2 \theta_W = 1/4$ one obtains $g_V^e = 0$, $g_V^u = 1/6$ and $g_V^d = -1/3$. Consequently, one may write to good approximation

$$F_2^{\gamma Z}(x, Q^2) = 2x \sum_q Q_q g_V^q (q - \bar{q}) \simeq x \frac{2}{9} [U + \bar{U} + D + \bar{D}] \tag{3.4}$$
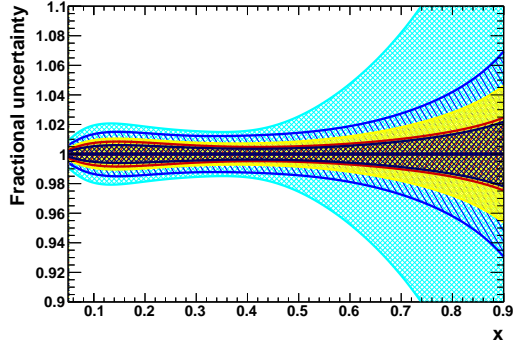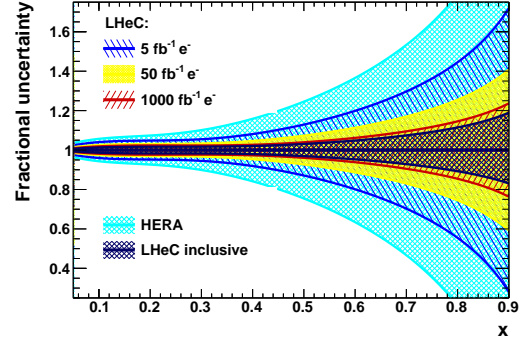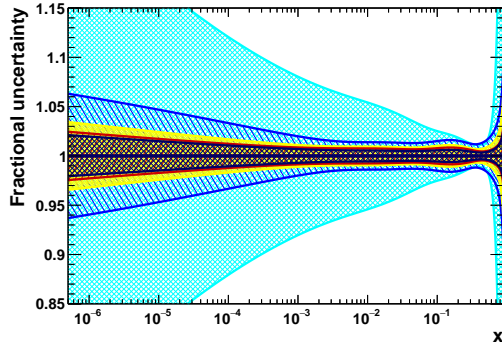
56

(a) u-valence distribution.

(b) d-valence distribution.

(c) Sea quark distribution ($\log_{10} x$ scale).
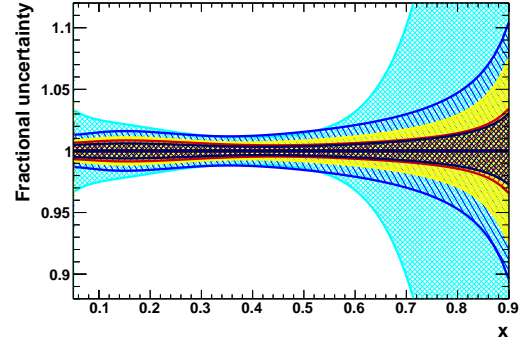
(d) Sea quark distribution (linear x scale).
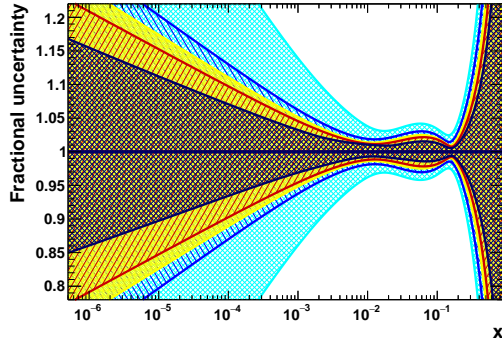
(e) Gluon distribution ($\log_{10} x$ scale).
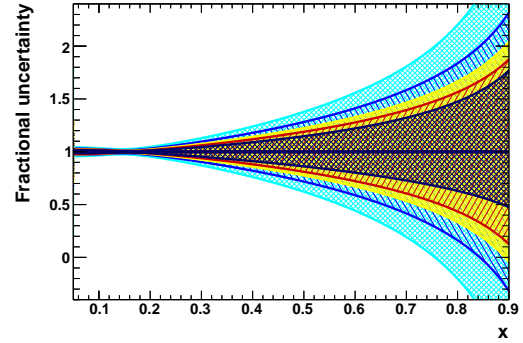
(f) Gluon distribution (linear x scale).

Figure 3.16: PDF distributions at $Q^2 = 1.9\,\text{GeV}^2$ as a function of x, illustrating the impact of different amounts of integrated luminosity. The blue, yellow and red bands correspond to LHeC PDFs using electron-only NC and CC inclusive measurements with 5, 50 and $1000\,\text{fb}^{-1}$ (datasets D1, D2 and D4), respectively. The yellow band is therefore equivalent to the "LHeC 1st run" PDF. For reference, the dark blue band shows the results of the final "LHeC inclusive" PDF. For comparison, the cyan band represents an identical PDF fit using HERA combined inclusive NC and CC data [44], restricted to solely the experimental uncertainties. Note that this, unlike the LHeC, extends everywhere beyond the narrow limits of the y scale of the plots.
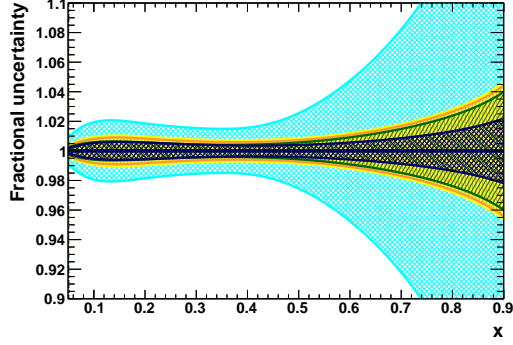
(a) *u*-valence distribution.
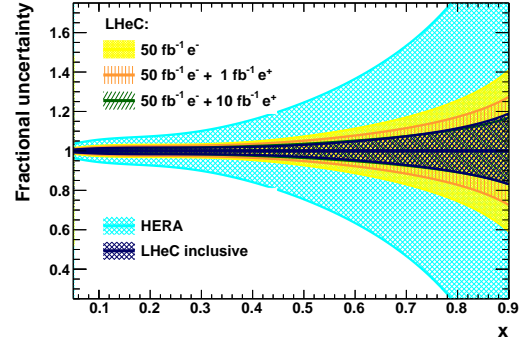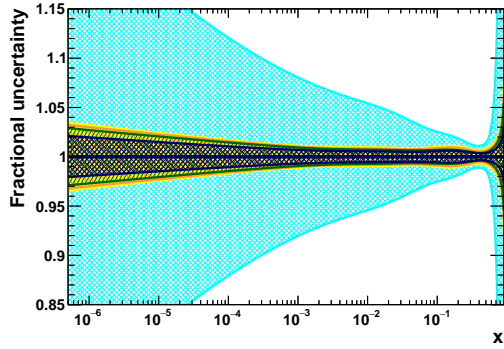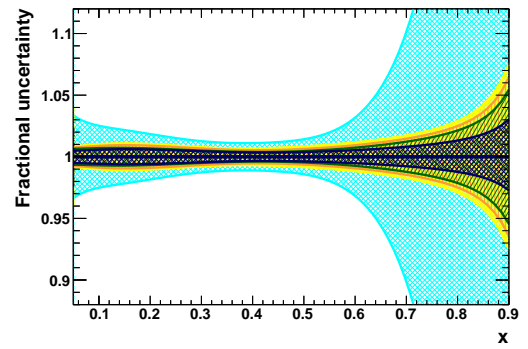
(b) *d*-valence distribution.

(c) Sea quark distribution ($\log_{10} x$ scale).

(d) Sea quark distribution (linear x scale).
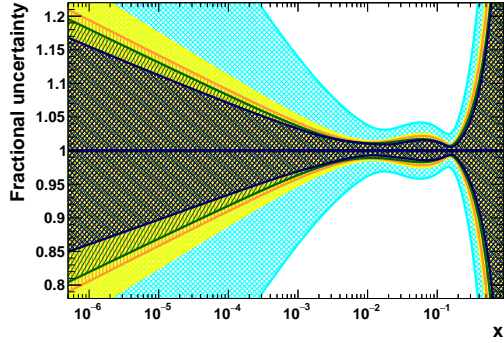
(e) Gluon distribution ($\log_{10} x$ scale).
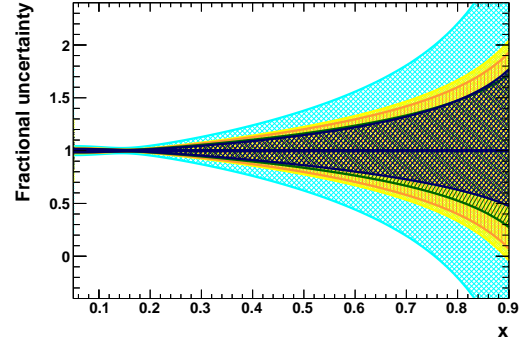
(f) Gluon distribution (linear x scale).

Figure 3.17: PDF distributions at $Q^2 = 1.9\,\mathrm{GeV}^2$ as a function of x, illustrating the impact of including positron data. The yellow ("LHeC 1st run") and dark blue ("LHeC final inclusive") and cyan bands (HERA data) are as in Fig. 3.16. The orange band corresponds to a fit with $1\,\mathrm{fb}^{-1}$ of inclusive NC and CC positron-proton data, in addition to $50\,\mathrm{fb}^{-1}$ of electron-proton data (D2+D6), while the green band is similar, but with $10\,\mathrm{fb}^{-1}$ of positron-proton data (D2+D7).

The beam helicity asymmetry therefore determines the total sea. A simulation is shown in Fig. 3.18 for integrated luminosities of $10\,\text{fb}^{-1}$ and helicities of $P = \pm 0.8$. Apparently, this
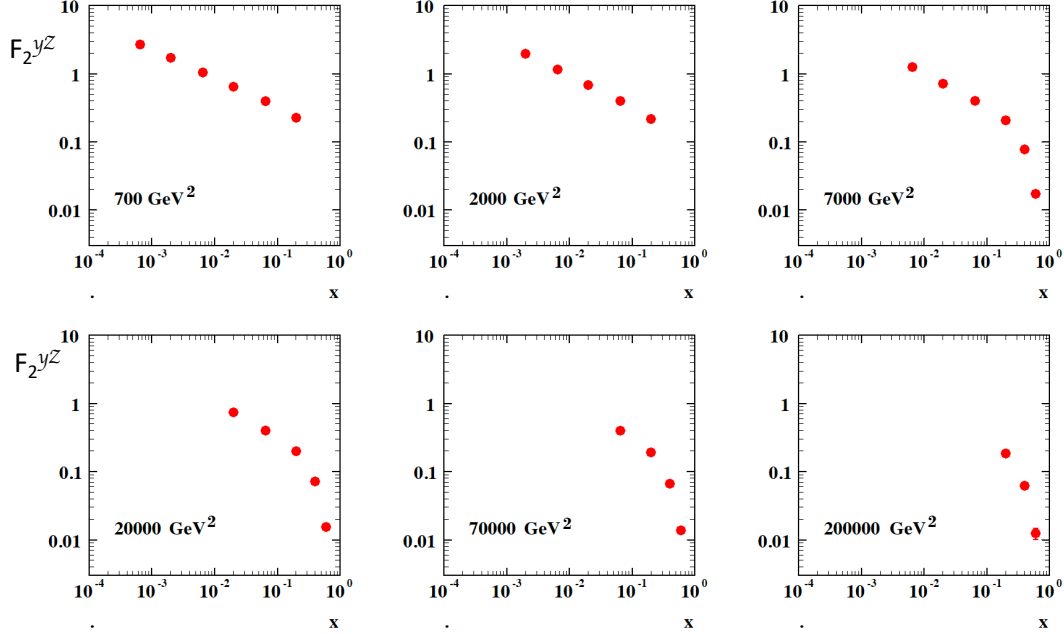
Figure 3.18: Prospective measurement of the photon-Z interference structure function $F_2^{\gamma Z}(x, Q^2)$ at the LHeC using polarised electron beams of helicity ± 0.8 and an integrated luminosity of $10\,\text{fb}^{-1}$ for each state. The uncertainties are only statistical.

asymmetry will provide a very precise measurement of the total sea. The combination of up and down quarks accessed with $F_2^{\gamma Z}$ (Eq. 3.4) is different from that provided by the known function

$$F_2(x, Q^2) = 2x \sum_q Q_q^2 (q - \bar{q}) = x \frac{1}{9}[4(U + \bar{U}) + D + \bar{D}] \tag{3.5}$$

because of the difference of the photon and Z boson couplings to quarks. Following Eq. 3.3, the beam polarisation asymmetry

$$A^{\pm} = \frac{\sigma_{NC}^{\pm}(P_R) - \sigma_{NC}^{\pm}(P_L)}{\sigma_{NC}^{\pm}(P_R) + \sigma_{NC}^{\pm}(P_L)} \simeq \mp (P_L - P_R)\kappa_Z g_A^e \frac{F_2^{\gamma Z}}{F_2}. \tag{3.6}$$

measures to a very good approximation the F_2 structure function ratio. The different composition of up and down quark contributions to $F_2^{\gamma Z}$ and F_2, see above, indicates that the weak neutral current interactions will assist to separate the up and down quark distributions which HERA had to link together by setting $B_d = B_u$.

Inserting $P_L = -P_R = -P$ and considering the large x limit, one observes that the asymmetry measures the d/u ratio of the valence quark distributions according to

$$A^{\pm} \simeq \pm \kappa_Z P \frac{1 + d_v/u_v}{4 + d_v/u_v}. \tag{3.7}$$

This quantity will be accessible with very high precision, as Fig. 3.18 illustrates, which is one reason, besides the CC cross sections, why the d/u ratio comes out to be so highly constrained by the LHeC (see Fig. 3.9).
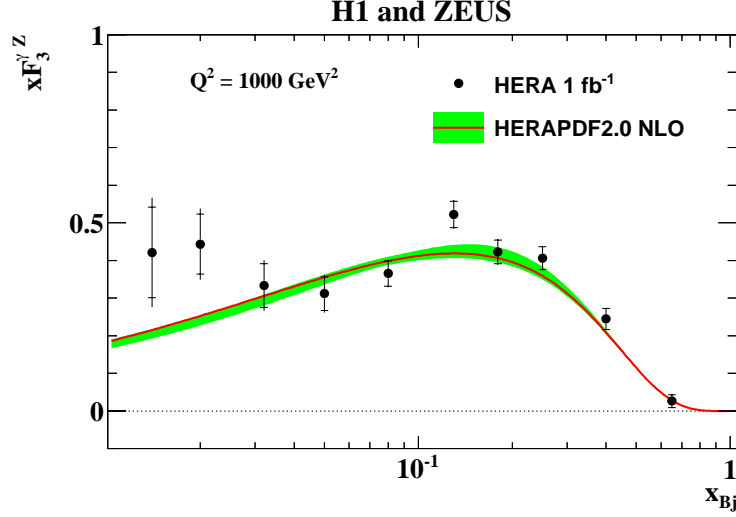
Figure 3.19: Combination of H1 and ZEUS measurement of the structure function $xF_3^{\gamma Z}(x, Q^2)$ as a function of x projected to a fixed Q^2 value of $2000\,\text{GeV}^2$, from [44]. The inner error bar represents the statistical uncertainty.

A further interesting quantity is the the lepton beam charge asymmetry, which is given as

$$\sigma_{r,NC}^{+}(P_1) - \sigma_{r,NC}^{-}(P_2) = \kappa_Z a_e [-(P_1 + P_2)F_2^{\gamma Z} - \frac{Y_-}{Y_+}(2xF_3^{\gamma Z} + \kappa_Z a_e (P_1 - P_2)xF_3^{Z})] \quad (3.8)$$

neglecting terms $\propto g_V^e$. For zero polarisation this provides directly a parity conserving measurement of the structure function

$$xF_3^{\gamma Z}(x, Q^2) = 2x \sum_q Q_q g_A^q (q - \bar{q}) = \frac{2}{3}x(U - \bar{U}) + \frac{1}{3}x(D - \bar{D}). \quad (3.9)$$

The appearance of this function in weak NC DIS resembles that of xW^3 in CC, or fixed target neutrino-nucleon, scattering. It enables one to resolve the flavour contents of the proton. The function $xF_3^{\gamma Z}$ was first measured by the BCDMS Collaboration in $\mu^{\pm}C$ scattering [97] at the SPS.

The HERA result is shown in Fig. 3.19. It covers the range from about $x = 0.05$ to $x = 0.6$ with typically $10\,\%$ statistical precision. Assuming that sea and anti-quark densities are equal, such as $u_s = \bar{u}$ or $d_s = \bar{d}$, $xF_3^{\gamma Z}$ is given as $x/3(2u_v + d_v)$. This function therefore accesses valence quarks down to small values of x where their densities become much smaller than that of the sea quarks. Since the Q^2 evolution of the non-singlet valence quark distributions is very weak, it has been customary to project the various charge asymmetry measurements to some lowish value of Q^2 and present the measurement as the x dependence of $xF_3^{\gamma Z}$.

If, however, there would be differences between the sea and anti-quarks, if $s \neq \bar{s}$, for example, one expected a rise of $xF_3^{\gamma Z}$ towards low x. This may be a cause for the undershoot of the QCD fit below the HERA data near to $x \simeq 0.01$, see Fig. 3.19, which yet are not precise enough. However, it is apparent that, besides providing constraints on the valence quark densities, this measurement indeed has the the potential to discover a new anti-symmetry in the quark sea.

Such a discovery would be enabled by the LHeC as is illustrated in Fig. 3.20 with an extension of the kinematic range by an order of magnitude towards small x and a much increased precision in the medium x region. The simulation is performed for 10 and for $1\,\text{fb}^{-1}$ of e^+p luminosity.

Obviously it would be very desirable to reach high values of integrated luminosity in positron-proton scattering too.
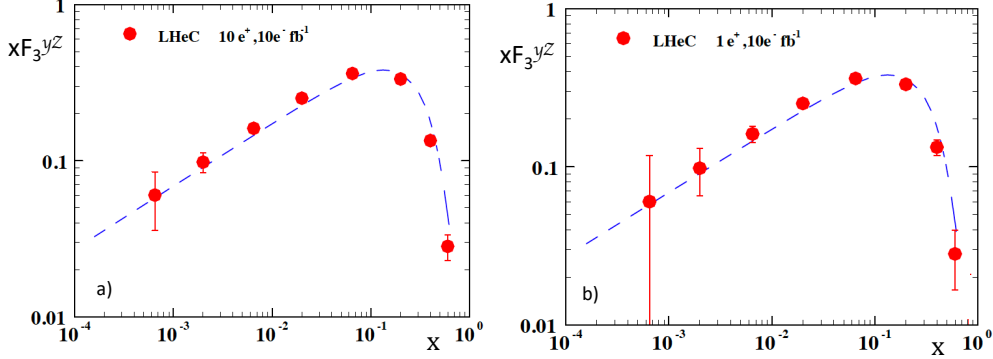
Figure 3.20: Prospective measurement of the photon-Z interference structure function $xF_3^{\gamma Z}(x, Q^2)$ at the LHeC projected to a fixed Q^2 value of $2000\,\text{GeV}^2$. The result corresponds to a cross section charge asymmetry for an unpolarised $e^- p$ beam with $10\,\text{fb}^{-1}$ luminosity combined with unpolarised $e^+ p$ beams of a) $10\,\text{fb}^{-1}$ (left) and b) $1\,\text{fb}^{-1}$ (right). The error bars represent the statistical uncertainty. The curve is drawn to guide the eye. It is possible that the measurement would discover a rise of $xF_3^{\gamma Z}$ towards low x should there exits so far unknown differences between sea and anti-quark densities, see text.

It is finally of interest to consider the role of precisely measured cross sections in CC scattering. The coupling of the W boson to quarks is flavour dependent resulting in the relations

$$\sigma_{r,CC}^+ = (1+P)[x\bar{U} + (1-y)^2 xD], \tag{3.10}$$

$$\sigma_{r,CC}^- = (1-P)[xU + (1-y)^2 x\bar{D}]. \tag{3.11}$$

Here $\sigma_{r,CC}$ is the double differential charged current DIS cross section scaled by a factor $2\pi x \cdot (M_W^2 + Q^2)^2/(G_F M_W^2)^2$ with the Fermi constant G_F and the W boson mass M_W. The positron beam at the LHeC is most likely unpolarised, $P = 0$. Maximum rate in $e^- p$ is achieved with large negative polarisation. In the valence-quark approximation, the $e^+ p$ CC cross section is proportional to $(1-y)^2 x d_v$ while $\sigma_{r,CC}^- \propto u_v$. This provides direct, independent measurements of d_v and u_v as had been illustrated already in the LHeC CDR [1].

Inclusive NC and CC DIS accesses four combinations of parton distributions, as is obvious from Eq. 3.10 for CC above and from the NC relation

$$\sigma_{r,NC}^\pm \simeq [c_u(U + \bar{U}) + c_d(D + \bar{D})] + \kappa_Z[d_u(U - \bar{U}) + d_d(D - \bar{D})]$$

$$\text{with } c_{u,d} = Q_{u,d}^2 + \kappa_Z(-g_V^e \mp P g_A^e)Q_{u,d}g_V^{u,d} \text{ and } d_{u,d} = \pm g_A^e g_A^{u,d} Q_{u,d}, \tag{3.12}$$

restricted to photon and γZ interference contributions. These four PDF combinations are complemented by the s, c, b measurements introduced before. The parton contents can therefore be completely resolved, which was impossible at HERA.

It is the high energy and high luminosity access to DIS, the high precision NC/CC and tagged heavy quark measurement programme, which makes the LHeC the uniquely suited environment to uncover the secrets of parton structure and dynamics. This will establish a new level with possible discoveries of strong interaction physics and also provide the necessary base for precision

electroweak and Higgs measurements at the LHC, for massively extending the range of BSM searches and reliably interpreting new physics signals in hadron-hadron scattering at the LHC.

3.3.9   Parton-Parton Luminosities

The energy frontier in accelerator particle physics is the LHC, with a cms energy of $\sqrt{s} = 2E_p \simeq 14\,\text{TeV}$, with the horizon of a future circular hadron collider, the FCC-hh, reaching energies up to $\sqrt{s} = 100\,\text{TeV}$. Proton-proton collider reactions are characterised by the Drell-Yan scattering [98]. To leading order, the double differential Drell-Yan scattering cross section [99] for the neutral current reaction $pp \to (\gamma, Z)X \to e^+e^- X$ and the charged current (CC) reaction $pp \to W^\pm X \to e\nu X$, can be written as

$$\frac{d^2\sigma}{dMdy} = \frac{4\pi\alpha^2(M)}{9} \cdot 2M \cdot P(M) \cdot \Phi(x_1, x_2, M^2) \quad [\text{nb}\,\text{GeV}^{-1}]. \tag{3.13}$$

Here M is the mass of the e^+e^- and $e^+\nu$ and $e^-\bar{\nu}$ systems for the NC and CC process, respectively, and y is the boson rapidity. The cross section implicitly depends on the Bjorken x values of the incoming quark q and its anti-quark $\bar{q}$, which are related to the rapidity y as

$$x_1 = \sqrt{\tau}e^y \quad x_2 = \sqrt{\tau}e^{-y} \quad \tau = \frac{M^2}{s}. \tag{3.14}$$

For the NC process, the cross section is a sum of a contribution from photon and Z exchange as well as an interference term. In the case of photon exchange, the propagator term $P(M)$ and the parton distribution term Φ are given by

$$P_\gamma(M) = \frac{1}{M^4} \qquad \Phi_\gamma = \sum_q Q_q^2 F_{q\bar{q}} \tag{3.15}$$

$$F_{q\bar{q}} = x_1 x_2 \cdot [q(x_1, M^2)\bar{q}(x_2, M^2) + \bar{q}(x_1, M^2)q(x_2, M^2)]. \tag{3.16}$$

Similar to DIS, the corresponding formulae for the γZ interference term read as

$$P_{\gamma Z} = \frac{\kappa_Z g_V^e (M^2 - M_Z^2)}{M^2[(M^2 - M_Z^2)^2 + (\Gamma_Z M_Z)^2]} \qquad \Phi_{\gamma Z} = \sum_q 2Q_q g_V^q F_{q\bar{q}} \tag{3.17}$$

The interference contribution is small being proportional to the vector coupling of the electron g_V^e. One also sees in Eq 3.17 that the interference cross section contribution changes sign from plus to minus as the mass increases and passes M_Z. The expressions of P and Φ for the pure Z exchange part are

$$P_Z = \frac{\kappa_Z^2(g_V^{e2} + g_A^{e2})}{(M^2 - M_Z^2)^2 + (\Gamma_Z M_Z)^2} \qquad \Phi_Z = \sum_q (g_V^{q2} + g_A^{q2})F_{q\bar{q}}. \tag{3.18}$$

For the CC cross section the propagator term is

$$P_W = \frac{\kappa_W^2}{(M^2 - M_W^2)^2 + (\Gamma_W M_W)^2} \tag{3.19}$$

and the charge dependent parton distribution forms are

$$\Phi_{W^+} = x_1 x_2 [V_{ud}^2(u_1\bar{d}_2 + u_2\bar{d}_1) + V_{cs}^2(c_1\bar{s}_2 + c_2\bar{s}_1) + V_{us}^2(u_1\bar{s}_2 + u_2\bar{s}_1) + V_{cd}^2(c_1\bar{d}_2 + c_2\bar{d}_1)] \tag{3.20}$$

$$\Phi_{W^-} = x_1 x_2 [V_{ud}^2(\overline{u}_1 d_2 + \overline{u}_2 d_1) + V_{cs}^2(\overline{c}_1 s_2 + \overline{c}_2 s_1) + V_{us}^2(\overline{u}_1 s_2 + \overline{u}_2 s_1) + V_{cd}^2(\overline{c}_1 d_2 + \overline{c}_2 d_1)], \quad (3.21)$$

with $\kappa_W = 1/(4\sin^2\Theta)$ and $q_i = q_i(x, M^2)$ and the CKM matrix elements V_{ij}. The expressions given here are valid in the QPM. At higher order pQCD, Drell-Yan scattering comprises also quark-gluon and gluon-gluon contributions. Certain production channels are sensitive to specific parton-parton reactions, Higgs production, for example, originating predominantly from gluon-gluon fusion. Based on the factorisation theorem [38] one therefore opened a further testing ground for PDFs, and much of the current PDF analyses is about constraining parton distributions by Drell-Yan scattering measurements and semi-inclusive production processes, such as top, jet and charm production, at the LHC. An account of this field is provided below, including a study as to how LHeC would add to the "global" PDF knowledge at the time of the HL-LHC.

There are drawbacks to the use of Drell-Yan and other hadron collider data for the PDF determination and advantages for *ep* scattering: i) DIS has the ability to prescribe the reaction type and the kinematics (x, Q^2) through the reconstruction of solely the leptonic vertex; ii) there are no colour reconnection and, for the lepton vertex, no hadronisation effects disturbing the theoretical description; iii) the most precise LHC data, on W and Z production, are located at a fixed equivalent $Q^2 = M_{W,Z}^2$ and represent a snapshot at a fixed scale which in DIS at the LHeC varies by more than 5 orders of magnitude [10].

There are further difficulties inherent to the use of LHC data for PDF determinations, such as hadronisation corrections and incompatibility of data. For example, the most recent CT18 [66] global PDF analysis had to arrange for a separate set (CT18A) because the standard fit would not respond well to the most precise ATLAS W, Z data taken at $7\,\mathrm{TeV}$ cms. The intent to include all data can only be realised with the introduction of so-called χ^2 tolerance criteria which fundamentally affect the meaning of the quoted PDF uncertainties.

Conceptually, the LHeC enables us to change this approach completely. Instead of trying to use all previous and current PDF sensitive data, to which nowadays one has no alternative, it replaces these by pure *ep* collider DIS data. Then one will bring order back into the PDF field: parton distributions, completely resolved, and from a single process, extending over nearly six orders of magnitude and calculated from NLO pQCD up to probably even N^{4}LO (see Sect. 4.4.1). These PDFs will be applicable for i) identifying new dynamics and symmetries; ii) testing factorisation; iii) confronting other PDF analsyses at that time; iv) performing high precision Higgs and electroweak analyses, and v) interpreting any peculiar HL-LHC signal for BSM using that independent PDF. higg It has been customary, which is obvious from Eqs. 3.15, 3.20 and 3.21, to express the usefulness of various PDF determinations and prospects for the LHC, and similarly the FCC, with four so-called parton luminosities which are defined as

$$L_{ab}(M_X) = \int dx_a dx_b \sum_q F_{ab}\, \delta(M_X^2 - sx_a x_b) \quad (3.22)$$

where F_{ab} for $(a,b) = (q\bar{q})$ is defined in Eq. 3.15 and (a,b) could also be (g,q), $(g,\bar{q})$ and (gg), without a sum over quarks in the latter case. The expectations for the quark and gluon related four parton luminosities are presented in Fig. 3.21. The LHeC provides very precise parton luminosity predictions in the complete range of M_X up to the high mass edge of the

---

[10]This is mitigated by measurements of Drell-Yan scattering at low masses, which are less precise, however. At high masses, $M = \sqrt{sx_1x_2} >> M_{W,Z}$, one soon reaches the region where new physics may occur, i.e. there arises the difficulty to separate unknown physics from the uncertainty of the quark and gluon densities at large x. High mass Drell Yan searches often are performed at the edge of the data statistics, i.e. they can not really be guided by data but miss a reliable guidance for the behaviour of the SM background around and beyond a (non-) resonant effect they would like to discover.
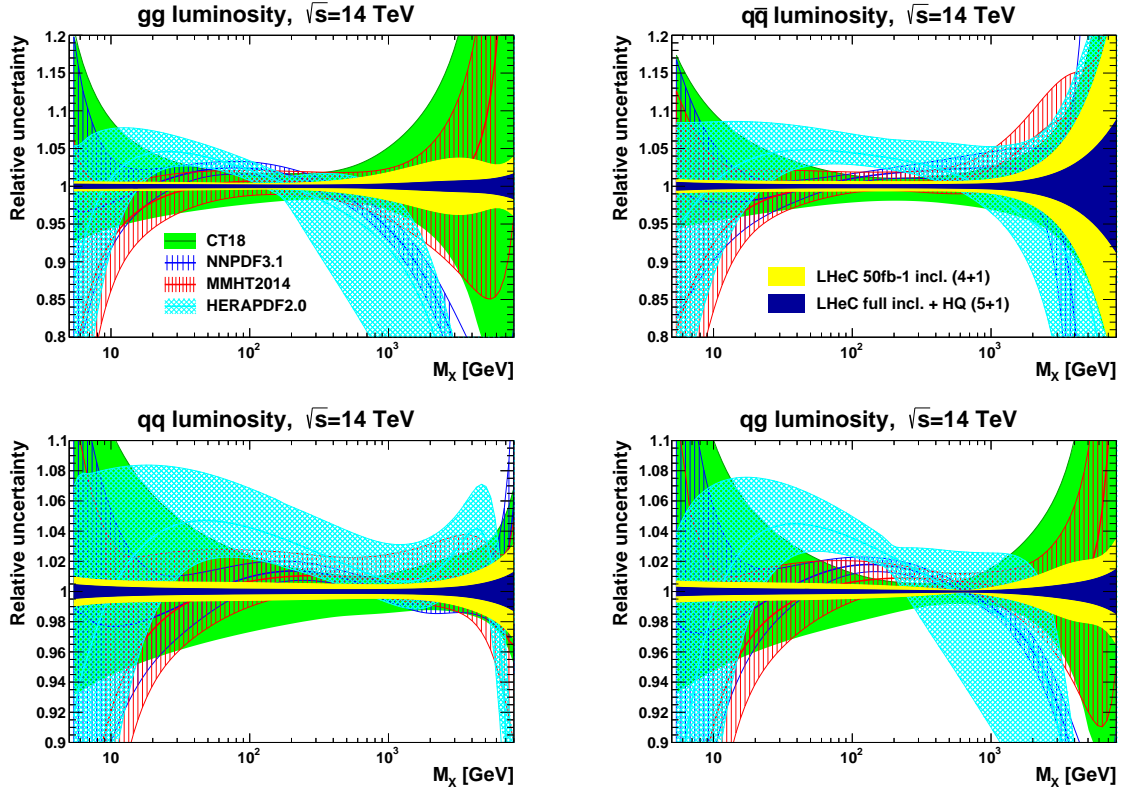
Figure 3.21: Uncertainty bands for parton luminosities as a function of the mass $M_X = \sqrt{sx_1x_2}$ for LHC energies. The yellow band corresponds to the "LHeC 1st run" PDFs (D2), while the dark blue shows a fit to the LHeC inclusive data sets (D4+D5+D6+D9) in Tab. 3.2 together with the simulated heavy flavour s, c, b data with a 5 quark distribution parameterisation as described in the text. Both LHeC PDFs shown are scaled to the central value of CT18.

search range at the LHC. This eliminates the currently sizeable PDF uncertainty of precision electroweak measurements at the LHC, as for example for the anticipated measurement of M_W to within 10^{-4} uncertainty, see below. One may also notice that the gluon-gluon luminosity (left top in Fig. 3.21) is at a per cent level for the Higgs mass $M_X = M_H \simeq 125\,\text{GeV}$. This is evaluated further in the chapter on Higgs physics with the LHeC.

3.4 The 3D Structure of the Proton

As is evident from the discussion in the previous Sections, the LHeC machine will be able to measure the collinear parton distribution functions with unprecedented accuracy in its extended range of x and Q^2. Thus, it will provide a new insight into the details of the one-dimensional structure of the proton and nuclei, including novel phenomena at low x. In addition to collinear dynamics, the LHeC opens a new window into proton and nuclear structure by allowing a precise investigation of the partonic structure in more than just the one dimension of the longitudinal momentum. Precision DIS thus gives access to multidimensional aspects of hadron structure. This can be achieved by accurately measuring processes with more exclusive final states like production of jets, semi-inclusive production of hadrons and exclusive processes, in particular the elastic diffractive production of vector mesons and deeply virtual Compton (DVCS) scattering that were explored in the 2012 LHeC CDR [1]. These processes have the potential to provide

information not only on the longitudinal distribution of partons in the proton or nucleus, but also on the dependence of the parton distribution on transverse momenta and momentum transfer. Therefore, future, high precision DIS machines like the LHeC or the Electron Ion Collider (EIC) in the US [100], open a unique window into the details of the 3D structure of hadrons. Note that the measurement of these processes requires a detector with large acceptance, $|\eta| < 4$, see e.g. [1, 101]. The current LHeC central detector design covers $|\eta| \lesssim 4.5$, see Chapter 12.

The most general quantity that can be defined in QCD, that would contain very detailed information about the partonic content of the hadron, is the Wigner distribution [102]. This function $W(x, \mathbf{k}, \mathbf{b})$ is a 1+4 dimensional function. One can think of it as the "mother" or "master" parton distribution, from which lower-dimensional distributions can be obtained. In the definition of the Wigner function, $\mathbf{k}$ is the transverse momentum of the parton and $\mathbf{b}$ is the 2-dimensional impact parameter, which can be defined as a Fourier conjugate to the momentum transfer of the process. The other, lower dimensional parton distributions can be obtained by integrating out different variables. Thus, transverse momentum dependent (TMD) parton distributions (or unintegrated parton distribution functions) $f_{\text{TMD}}(x, \mathbf{k})$ can be obtained by integrating out the impact parameter $\mathbf{b}$ in the Wigner function, while the generalised parton densities (GPD), $f_{\text{GPD}}(x, \mathbf{b})$, can be obtained from the Wigner function through the integration over the transverse momentum $\mathbf{k}$. In the regime of small x, or high energy, a suitable formalism is that of the dipole picture [103–108], where the fundamental quantity which contains the details of the partonic distribution is the dipole amplitude $N(x, \mathbf{r}, \mathbf{b})$. This object contains the dependence on the impact parameter $\mathbf{b}$ as well as another transverse size $\mathbf{r}$, the dipole size, which can be related to the transverse momentum of the parton $\mathbf{k}$ through a Fourier transform. The important feature of the dipole amplitude is that it should obey the unitarity limit $N \leq 1$. The dipole amplitude N within this formalism can be roughly interpreted as a Wigner function in the high energy limit, as it contains information about the spatial distribution of the partons in addition to the dependence on the longitudinal momentum fraction x.
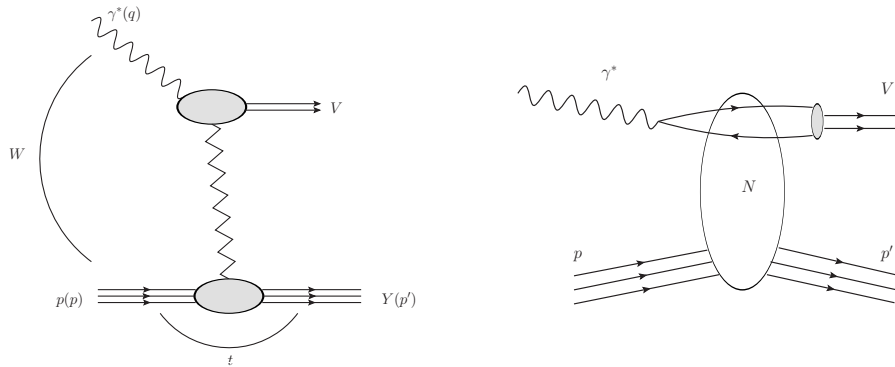
Figure 3.22: Left: diagram for the quasi-elastic production of the vector meson. Right: schematic illustration of the same process, quasi-elastic vector meson production, within the framework of the dipole picture. The initial virtual photon, fluctuates into a quark-antiquark pair which then scatters off the hadronic target and forms the vector meson. The details of the hadronic interaction of the dipole with the target are encoded in the dipole amplitude N.

Detailed simulations of elastic J/ψ vector meson production were performed for the LHeC kinematic region and beyond [1], using the formalism of the dipole picture. This particular process is shown in Fig. 3.22, left plot. The proton is scattered elastically with momentum transfer t, and the vector meson is produced, which is separated from the final state proton by a rapidity gap. Of particular importance is the measurement of the t slope of this process, since it can be related directly to the impact parameter distribution and is thus sensitive to the

transverse variation of the partonic density in the target. The first type of analysis like this, in the context of elastic scattering, was performed by Amaldi and Schubert [109], where it was demonstrated that the Fourier transform of the elastic cross section yields access to the impact parameter profile of the scattering amplitude. This method can be used in the context of vector meson scattering in DIS, where the transverse distribution of partons, in the perturbative regime, can be extracted through the appropriate Fourier transform [110]. The additional advantage of studying diffractive vector meson production is the fact that the partonic distributions can be studied as a function of the hard scale in this process given by the mass of the vector meson M_V^2 in the photoproduction case or Q^2 (or more precisely a combination of Q^2 and M_V^2) in the case of the diffractive DIS production of vector mesons, as well as the energy W of the photon-proton system available in the process which is closely related to x.

The differential cross section for elastic vector meson production can be expressed in the following form:

$$\frac{d\sigma^{\gamma^* p \to J/\psi p}}{dt} = \frac{1}{16\pi} |\mathcal{A}(x, Q, \Delta)|^2 , \qquad (3.23)$$

where the amplitude for the process of elastic diffractive vector meson production in the high energy limit, in the dipole picture, is given by

$$\mathcal{A}(x, Q, \Delta) = \sum_{h\bar{h}} \int d^2\mathbf{r} \int dz \Psi^*_{h\bar{h}}(z, \mathbf{r}, Q) \, \mathcal{N}(x, \mathbf{r}, \Delta) \, \Psi^V_{h\bar{h}}(z, \mathbf{r}) . \qquad (3.24)$$

In the above formula, $\Psi^*_{h\bar{h}}(z, \mathbf{r}, Q)$ is the photon wave function which describes the splitting of the virtual photon γ^* into a $q\bar{q}$ pair. This wave funtion can be calculated in perturbative QCD. The function $\Psi^V_{h\bar{h}}(z, \mathbf{r})$ is the wave function of the vector meson. Finally, $\mathcal{N}(x, \mathbf{r}, \Delta)$ is the dipole amplitude which contains all the information about the interaction of the quark-antiquark dipole with the target. The formula (3.24) can be interpreted as the process of fluctuation of the virtual photon into a $q\bar{q}$ pair, which subsequently interacts with the target through the dipole amplitude $\mathcal{N}$ and then forms the vector meson, given by the amplitude Ψ^V, see Fig. 3.22, right plot. The two integrals in the definition Eq. (3.24) are performed over the dipole size which is denoted by $\mathbf{r}$, and z which is the longitudinal momentum fraction of the photon carried by the quark. The scattering amplitude depends on the value of the momentum transfer Δ, which is related to the Mandelstam variable $t = -\Delta^2$. The sum is performed over the helicity states of the quark and antiquark.

The dipole amplitude $\mathcal{N}(x, \mathbf{r}, \Delta)$ can be related to the dipole amplitude in coordinate space through the appropriate Fourier transform

$$N(x, \mathbf{r}, \mathbf{b}) = \int d^2\Delta \, e^{i\Delta \cdot \mathbf{b}} \mathcal{N}(x, \mathbf{r}, \Delta) . \qquad (3.25)$$

We stress that $\mathbf{r}$ and $\mathbf{b}$ are two different transverse sizes here. The dipole size $\mathbf{r}$ is conjugate to the transverse momentum of the partons $\mathbf{k}$, whereas the impact parameter is roughly the distance between the centre of the scattering target to the centre-of-mass of the quark-antiquark dipole and is related to the Fourier conjugate variable, the momentum transfer Δ.

The dipole amplitude $N(x, \mathbf{r}, \mathbf{b})$ contains rich information about the dynamics of the hadronic interaction. It is a 5-dimensional function and it depends on the longitudinal momentum fraction, and two two-dimensional coordinates. The dependence on the longitudinal momentum fraction is obviously related to the evolution with the centre-of-mass energy of the process, while the dependence on $\mathbf{b}$ provides information about the spatial distribution of the partons in the target. The dipole amplitude is related to the distribution of gluons in impact parameter

space. The dipole amplitude has a nice property that its value should be bounded from above by the unitarity requirement $N \leq 1$. The complicated dependence on energy, dipole size and impact parameter of this amplitude can provide a unique insight into the dynamics of QCD, and on the approach to the dense partonic regime. Besides, from Eqs. (3.23),(3.24) and (3.25) it is evident that the information about the spatial distribution in impact parameter $\mathbf{b}$ is related through the Fourier transform to the dependence of the cross section on the momentum transfer $t = -\Delta^2$.

To see how the details of the distribution, and in particular the approach to unitarity, can be studied through the VM elastic production, calculations based on the dipole model were performed [111], and extended to energies which can be reached at the LHeC as well as the FCC-eh. The parameterisations used in the calculation were the so-called IP-Sat [112, 113] and b-CGC [114] models. In both cases the impact parameter dependence has to be modelled phenomenologically. In the IP-Sat model the dipole amplitude has the following form

$$N(x, \mathbf{r}, \mathbf{b}) \;=\; 1 - \exp\left[-\frac{\pi^2 r^2}{2N_c} \alpha_s(\mu^2) x g(x, \mu^2) T_G(b) \right] \;, \tag{3.26}$$

where $xg(x, \mu^2)$ is the collinear gluon density, evolved using LO DGLAP (without quarks), from an initial scale μ_0^2 up to the scale μ^2 set by the dipole size $\mu^2 = \frac{4}{r^2} + \mu_0^2$. $\alpha_s(\mu^2)$ is the strong coupling. The parameterisation of the gluon density at the initial scale μ_0^2 is given by

$$xg(x, \mu_0^2) = A_g x^{-\lambda_g} (1 - x)^{5.6} \;, \tag{3.27}$$

and the impact parameter profile for the gluon by

$$T_G(b) \;=\; \frac{1}{2\pi B_G} \exp(-b^2/2B_G) \;. \tag{3.28}$$

An alternative parameterisation is given by the b-CGC model [114] which has the form

$$N(x, \mathbf{r}, \mathbf{b}) \;=\; \begin{cases} N_0 \left(\frac{rQ_s}{2} \right)^{2\gamma_{\mathrm{eff}}} & \text{for} \quad rQ_s \leq 2 \;, \\ 1 - \exp(-\mathcal{A} \ln^2(\mathcal{B} r Q_s)) & \text{for} \quad rQ_s > 2 \;. \end{cases} \tag{3.29}$$

Here the effective anomalous dimension γ_{eff} and the saturation scale Q_s of the proton explicitly depend on the impact parameter and are defined as

$$\begin{aligned} \gamma_{\mathrm{eff}} &= \gamma_s + \frac{1}{\kappa \lambda \ln 1/x} \ln \left(\frac{2}{rQ_s} \right) \;, \\ Q_s(x, b) &= \left(\frac{x_0}{x} \right)^{\lambda/2} \exp\left[-\frac{b^2}{4\gamma_s B_{\mathrm{CGC}}} \right] \quad \mathrm{GeV} \;, \end{aligned} \tag{3.30}$$

where $\kappa = \chi''(\gamma_s)/\chi'(\gamma_s)$, with $\chi(\gamma)$ being the leading-logarithmic BFKL kernel eigenvalue function [115]. The parameters $\mathcal{A}$ and $\mathcal{B}$ in Eq.(3.29) are determined uniquely from the matching of the dipole amplitude and its logarithmic derivatives at the limiting value of $rq_s = 2$. The b-CGC model is constructed by smoothly interpolating between two analytically known limiting cases [114], namely the solution of the BFKL equation in the vicinity of the saturation line for small dipole sizes $r < 2/Q_s$, and the solution of the BK equation deep inside the saturation region for large dipole sizes $r > 2/Q_s$.

The parameters μ_0, A_g, λ_g of the IP-Sat model and $N_0, \gamma_s, x_0 \lambda$ of the b-CGC model were fitted to obtain the best description of the inclusive data for the structure function F_2 at HERA. The

Figure 3.23: Differential cross section for the elastic J/ψ production as a function of $|t|$ within the IP-Sat (saturation), b-CGC and 1-Pomeron models at a fixed $W\gamma p = 1\,\text{TeV}$, which corresponds to the LHeC kinematics, and for two different values of photon virtuality $Q = 0$ and $Q^2 = 10\ \text{GeV}^2$. The thickness of points includes the uncertainties associated with the freedom to choose different values for the charm quark mass within the range $m_c = 1.2 - 1.4\ \text{GeV}$.

slope parameters B_g and B_{CGC}, which control the b-dependence in both models, were fitted to obtain the best description of elastic diffractive J/ψ production, in particular its t-dependence, at small values of t.

In Figs. 3.23 and 3.24 we show the simulated differential cross section $d\sigma/dt$ as a function of $|t|$ and study its variation with energy and virtuality, and its model dependence. First, in Fig. 3.23 we show the differential cross section as a function of t for fixed energy $W = 1\,\text{TeV}$, in the case of the photoproduction of J/ψ (left plot) and for the case of DIS with $Q^2 = 10\,\text{GeV}^2$ (right plot). The energy W corresponds to the LHeC kinematics. There are three different calculations in each plot, using the IP-sat model, the b-CGC model and the 1-Pomeron approximation. The last one is obtained by keeping just the first non-trivial term in the expansion of the eikonalised formula of the IP-Sat amplitude (3.26). First, let us observe that all three models coincide for very low values of t, where the dependence on t is exponential. This is because for low $|t|$, relatively large values of impact parameter are probed in Eq. (3.24) where the amplitude is small, and therefore the tail in impact parameter is Gaussian in all three cases. Since the Fourier transform of the Gaussian in b is an exponential in t, the result at low t follows. On the other hand, the three scenarios differ significantly for large values of $|t|$. In the case of the 1-Pomeron approximation the dependence is still exponential, without any dips, which is easily understood since the impact parameter profile is perfectly Gaussian in this case. For the two other scenarios, dips in $d\sigma/dt$ as a function in t emerge. They signal the departure from the Gaussian profile in b for small values of b where the system is dense. A similar pattern can be observed when performing the Fourier transform of the Wood-Saxon distribution, which is the typical distribution used for the description of the matter density in nuclei. When Q^2 is increased the pattern of dips also changes. This is illustrated in Fig. 3.23. It is seen that the dips move to higher values of $|t|$ for DIS than for photoproduction. This can be understood from the dipole formula Eq. (3.24) which contains the integral over the dipole size. Larger values of Q^2 select

smaller values of dipole size r, where the amplitude is smaller and thus in the dilute regime, where the profile in b is again Gaussian. On the other hand, small scales select large dipole sizes for which the dipole amplitude is larger and thus the saturation effects more prominent, leading to the distortion of the impact parameter profile and therefore to the emergence of dips in the differential cross section $d\sigma/dt$ when studied as a function of t.
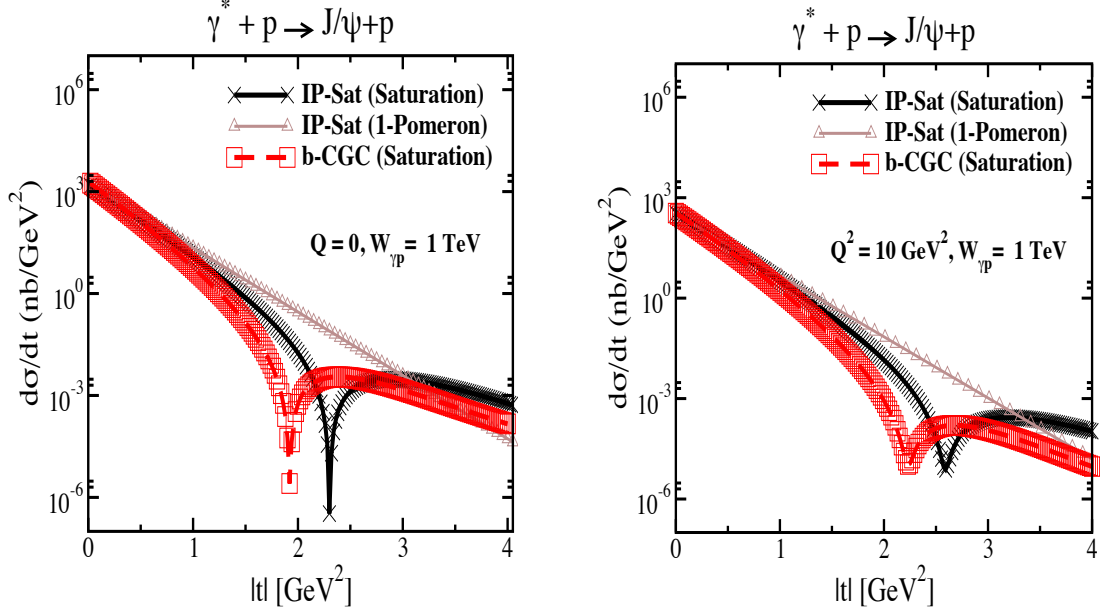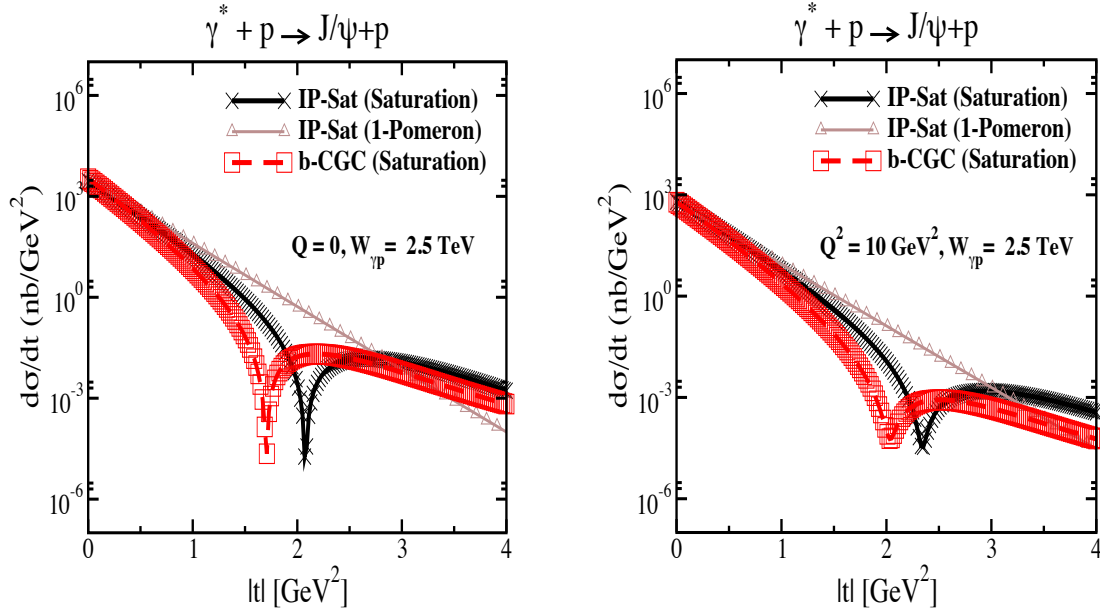

Figure 3.24: Differential cross section for elastic J/ψ production as a function of $|t|$ within the IP-Sat (saturation), b-CGC and 1-Pomeron models at a fixed $W\gamma p = 2.5$ TeV, which corresponds to the region that can be explored by FCC-eh, and for two different values of photon virtuality $Q = 0$ (left plot) and $Q^2 = 10$ GeV^2 (right plot). The thickness of points includes the uncertainties associated with the freedom to choose different values for the charm quark mass within the range $m_c = 1.2 - 1.4$ GeV .

In Fig. 3.24 we show the same calculation but for even higher energy $W = 2.5$ TeV, which could be explored in the FCC-eh. In this case we see that the dips move to lower values of $|t|$. This can be easily understood, as with increasing energy the dipole scattering amplitude increases, and thus the dilute-dense boundary shifts to larger values of b, meaning that the deviation from the exponential fall off occurs for smaller values of $|t|$. Similar studies [111] show also the change of the position of the dips with the mass of the vector meson: for lighter vector mesons like ρ, ω, ϕ the dips occur at smaller t than for the heavier vector mesons J/ψ or Υ. We note that, of course, the positions of the dips depend crucially on the details of the models, which are currently not constrained by the existing HERA data. We also note the sizeable uncertainties due to the charm quark mass (the fits to inclusive HERA data from which parameters of the models have been extracted are performed at each fixed value of the charm mass that is then used to compute exclusive J/ψ production).

We thus see that the precise measurement of the t-slope in the elastic production of vector mesons at the LHeC, and its variation with x and scales, provide a unique opportunity to explore the transition between the dilute and dense partonic regimes. As mentioned earlier, elastic diffractive production is one among several different measurements which can be performed to explore the 3D structure of the hadron. Another one is Deeply Virtual Compton Scattering which is a process sensitive to the spatial distribution of quarks inside the hadron. Previous preliminary analyses [1] indicate a huge potential of LHeC for the measurement of DVCS. Another example of a process that could be studied at the LHeC, is diffractive exclusive dijet production. It

has been suggested [116] that this process is sensitive to the Wigner function, and that the transverse momentum and spatial distribution of partons can be extracted by measuring this process. The transverse momentum of jets would be sensitive to the transverse momentum of the participating partons, whereas the momentum transfer of the elastically scattered proton would give a handle on the impact parameter distribution of the partons in the target [117–119], thus giving a possibility to extract information about the Wigner distribution.

So far we have referred to coherent diffraction, i.e. to a scenario in which the proton remains intact after the collision. There also exists incoherent diffraction, where the proton gets excited into some state with the quantum numbers of the proton and separated from the rest of the event by a large rapidity gap. In order to apply the dipole formalism to the incoherent case, see Sec. 6.3.1 where the formulae applicable for both protons and nuclei are shown. Here one must consider a more involved structure of the proton (e.g. as composed by a fixed [120–123] or a growing number with $1/x$ of hot spots [124–126]). As discussed in Sec. 6.3.1, coherent diffraction is sensitive to the gluon distribution in transverse space, while incoherent diffraction is particularly sensitive to fluctuations of the gluon distribution. A prediction of the model with a growing number of hot spots, both in models where this increasing number is implemented by hand [124–126] and in those where it is dynamically generated [123] from a fixed number at larger x, is that the ratio of incoherent to coherent diffraction will decrease with W, and that this decrease is sensitive to the details of the distribution of hot spots, and thus, to the fluctuations of the gluon distribution in transverse space. In order to check these ideas, both the experimental capability to separate coherent from incoherent diffraction and a large lever arm in W, as available at the LHeC, are required.

In conclusion, measurements at the LHeC (particularly exclusive diffractive production of vector mesons, photons and other final states like dijets) will offer unprecedented opportunities to unravel the three-dimensional structure of hadrons in a kinematic region complementary to that at the EIC. Note that, such structure varies with x or energy, so its measurement at small enough x is key as input for both analytic calculations and Monte Carlo simulators at high energy hadron colliders. And the large lever arms both in x and Q^2, as those offered by the LHeC, are required to understand the perturbative evolution of such quantities, as much as it is required for collinear PDFs. Ultraperipheral collisions at the LHC, see Refs. [127, 128] and references therein, offer an alternative albeit less precise and for photoproduction.

Chapter 4

Exploration of Quantum Chromodynamics

The gauge theory formalism of Quantum Chromodynamics (QCD) provides a very successful description of strong interactions between confined partons. Despite the undoubted success of QCD, the strong force still remains one of the least known fundamental sectors of (particle) physics which needs to be explored much deeper.

For an improved understanding of strong interactions and to answer a variety of those open questions additional measurements with highest precision have to be performed. At the LHeC, deep-inelastic electron-proton and lepton-nucleus reactions will extend tests of QCD phenomena to a new and yet unexplored domain up to the TeV scale and to x values as low as 10^{-6}, and QCD measurements can be performed with very high experimental precision. This is because the proton is a *strongly* bound system and in deep-inelastic scattering (DIS) the exchanged *colourless* photon (or Z) between the electron and the parton inside the proton acts as a neutral observer with respect to the phenomena of the strong force. In addition, the over-constrained kinematic system in DIS allows for precise (*in-situ*) calibrations of the detector to measure the kinematics of the scattered lepton, and, more importantly here, also the hadronic final state. In DIS, in many cases, the virtuality of the exchanged γ/Z boson often provides a reasonable scale to stabilise theoretical predictions.

In this Chapter, selected topics of QCD studies at the LHeC are discussed.

4.1 Determination of the strong coupling constant

Quantum Chromodynamics (QCD) [129, 130] has been established as the theory of strong interactions within the Standard Model of particle physics. While there are manifold aspects both from the theoretical and from the experimental point-of-view, by far the most important parameter of QCD is the coupling strength which is most commonly expressed at the mass of the Z boson, M_Z, as $\alpha_\mathrm{s}(M_\mathrm{Z})$. Its (renormalisation) scale dependence is given by the QCD gauge group SU(3) [131, 132]. Predictions for numerous processes in e^+e^-, pp or ep collisions are then commonly performed in the framework of perturbative QCD, and (the lack of) higher-order QCD corrections often represent limiting aspects for precision physics. Therefore, the determination of the strong coupling constant $\alpha_\mathrm{s}(M_\mathrm{Z})$ constitutes one of the most crucial tasks for future precision physics, while at the same time the study of the scale dependence of α_s provides

an inevitable test of the validity of QCD as the theory of strong interactions and the portal for GUT theories.

Different processes and methodologies can be considered for a determination of $\alpha_s(M_Z)$ (see e.g. reviews [133–135]). Since QCD is an asymptotically free theory, with free behaviour at high scales but confinement at low scales, a high sensitivity to the value of $\alpha_s(M_Z)$ is naturally obtained from low-scale measurements. However, the high-scale behaviour must then be calculated by solving the renormalisation group equation, which implies the strict validity of the theory and an excellent understanding of all subleading effects, such as the behaviour around quark-mass thresholds.

Precision measurements at the LHeC offer the unique opportunity to exploit many of these aspects. Measurements of jet production cross sections or inclusive NC and CC DIS cross sections provide a high sensitivity to the value of $\alpha_s(M_Z)$, since these measurements can be performed at comparably low scales and with high experimental precision. At the same time, the LHeC provides the opportunity to test the running of the strong coupling constant over a large kinematic range. In this Section, the prospects for a determination of the strong coupling constant with inclusive jet cross sections and with inclusive NC/CC DIS cross sections are studied.

4.1.1 Strong coupling from inclusive jet cross sections

The measurement of inclusive jet or di-jet production cross sections in NC DIS provides a high sensitivity to the strong coupling constant and to the gluon PDF of the proton. This is because jet cross sections in NC DIS are measured in the Breit reference frame [136], where the virtual boson γ^* or Z collides head-on with the struck parton from the proton and the outgoing jets are required to have a non-zero transverse momentum in that reference frame. The leading order QCD diagrams are QCD Compton and boson-gluon fusion and are both $\mathcal{O}(\alpha_s)$, see Fig. 4.1.
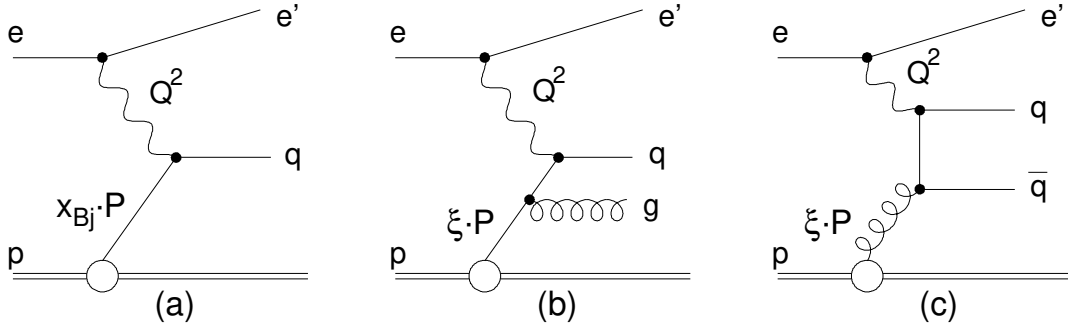
Figure 4.1: Leading order diagrams for inclusive DIS (a) and jet production (b,c) in the Breit frame (taken from Ref. [137]).

At HERA, jets are most commonly defined by the longitudinally invariant k_t jet algorithm [138] with a distance parameter $R = 1.0$ [137, 139–155]. This provides an infrared safe jet definition and the chosen distance parameter guarantees a small dependence on non-perturbative effects, such as hadronisation. Differently than in pp at the LHC [156–159], jet algorithms at the LHeC do not require any pile-up subtraction and any reduction of the dependence on minimum bias or underlying event, due to the absence of such effects. Therefore, for this study we adopt the choices made at HERA.
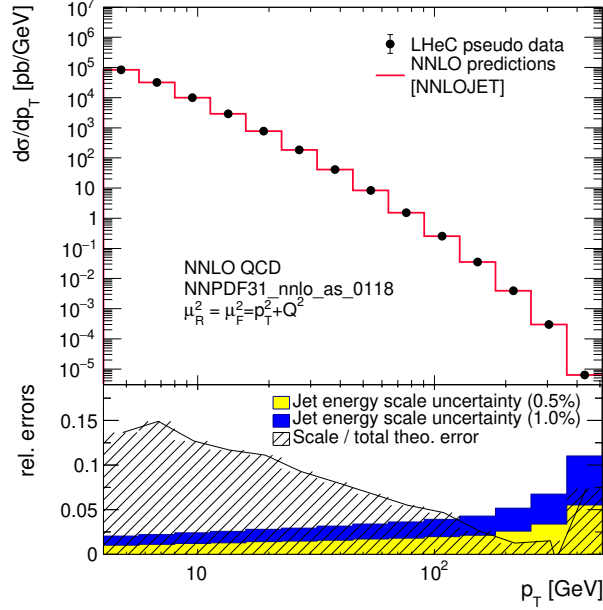
Figure 4.2: Inclusive jet cross sections calculated in NNLO QCD as a function of the jet transverse momentum in the Breit frame, p_T. The shaded area indicates NNLO scale uncertainties and the yellow band shows the estimated experimental jet energy scale uncertainty (JES) of 0.5 %. The blue band shows a very conservative assumption on the JES of 1 %.

In Fig. 4.2 the next-to-next-to-leading order QCD (NNLO) predictions [160, 161] for cross sections for inclusive jet production in NC DIS as a function of the transverse momentum of the jets in the Breit frame are displayed. The calculations are performed for an electron beam energy of $E_e = 60$ GeV and include γ/Z and Z exchange terms and account for the electron polarisation $P_e = -0.8$. The NC DIS kinematic range is set to $Q^2 > 4$ GeV^2. The calculations are performed using the NNLOJET program [162] interfaced to the APPLfast library [163–165] which provides a generic interface to the APPLgrid [166, 167] and fastNLO [168, 169] interpolation grid code.

The kinematically accessible range in jet-p_T ranges over two orders of magnitude, $4 < p_T \lesssim 400$ GeV. The size of the cross section extends over many orders in magnitude, thus imposing challenging demands on LHeC experimental conditions, triggers and DAQ bandwidth, calibration, and data processing capabilities. The scale uncertainty of the NNLO predictions is about 10 % at low values of p_T and significantly decreases with increasing values of p_T. Future improved predictions will further reduce these theoretical uncertainties.

For the purpose of estimating the uncertainty of $\alpha_s(M_Z)$ in a determination from inclusive jet cross sections at the LHeC, double-differential cross sections as a function of Q^2 and p_T with a full set of experimental uncertainties are generated. Altogether 509 cross section values are calculated in the kinematic range $8 < Q^2 < 500\,000$ GeV^2 and $4 < p_T < 512$ GeV, and the bin grid is similar to the ones used by CMS, H1 or ZEUS [44, 156, 165, 170]. The various error sources considered are summarised in Tab. 4.1. The uncertainties related to the reconstruction of the NC DIS kinematic variables, Q^2, y and x_{bj}, are similar to the estimates for the inclusive NC DIS cross sections (see section 3.2). For the reconstruction of hadronic final state particles which are the input to the jet algorithm, jet energy scale uncertainty (JES), calorimetric noise and the polar angle uncertainty are considered. The size of the uncertainties is gauged with achieved values by H1, ZEUS, ATLAS and CMS [146, 154, 171, 172]. The size of the dominant JES one is assumed to be 0.5 % for reconstructed particles in the laboratory rest frame, yielding an uncertainty of

0.2–4.4 % on the cross section after the boost to the Breit frame. A JES uncertainty of 0.5 % is well justified by improved calorimeters, since already H1 and ZEUS reported uncertainties of 1 % [146, 154, 173], and ATLAS and CMS achieved 1 % over a wide range in p_T [171, 172], albeit the presence of pile-up and the considerably more complicated definition of a reference object for the in-situ calibration. The size of the JES uncertainty is also displayed in Fig. 4.2. The calorimetric noise of ± 20 MeV on every calorimeter cluster, as reported by H1, yields an uncertainty of up to 0.7 % on the jet cross sections. A minimum size of the statistical uncertainty of 0.15 % is imposed for each cross section bin. An overall normalisation uncertainty of 1.0 % is assumed, which will be mainly dominated by the luminosity uncertainty. In addition, an uncorrelated uncertainty component of 0.6 % collects various smaller error sources, such as for instance radiative corrections, unfolding or model uncertainties. Studies on the size and the correlation model of these uncertainties are performed below.

Exp. uncertainty	Shift	Size on σ [%]
Statistics with $1\,\mathrm{ab}^{-1}$	min. 0.15 %	0.15 –5
Electron energy	0.1 %	0.02 –0.62
Polar angle	2 mrad	0.02 –0.48
Calorimeter noise	± 20 MeV	0.01 –0.74
Jet energy scale (JES)	0.5 %	0.2 –4.4
Uncorrelated uncert.	0.6 %	0.6
Normalisation uncert.	1.0 %	1.0

Table 4.1: Anticipated uncertainties of inclusive jet cross section measurements at the LHeC.

The value and uncertainty of $\alpha_s(M_Z)$ is obtained in a χ^2-fit of NNLO predictions [160, 161] to the simulated data with $\alpha_s(M_Z)$ being a free fit parameter. The methodology follows closely analyses of HERA jet data [165, 170] and the χ^2 quantity is calculated from relative uncertainties, i.e. those of the right column of Tab. 4.1. The predictions for the cross section σ account for both α_s-dependent terms in the NNLO calculations, i.e. in the DGLAP operator and the hard matrix elements, by using

$$\sigma = f_{\mu_0} \otimes P_{\mu_0 \to \mu_F}(\alpha_s(M_z)) \otimes \hat{\sigma}(\alpha_s(M_z), \mu) \,, \tag{4.1}$$

where f_{μ_0} are the PDFs at a scale of $\mu_0 = 30$ GeV, and $P_{\mu_0 \to \mu_F}$ denotes the DGLAP operator, which is dependent on the value of $\alpha_s(M_Z)$. The α_s uncertainty is obtained by linear error propagation and is validated with a separate study of the $\Delta\chi^2 = 1$ criterion.

In the fit of NNLO QCD predictions to the simulated double-differential LHeC inclusive jet cross sections an uncertainty of

$$\Delta\alpha_s(M_Z)(\text{jets}) = \pm 0.00013_{(\text{exp})} \pm 0.00010_{(\text{PDF})} \tag{4.2}$$

is found. The PDF uncertainty is estimated from a PDF set obtained from LHeC inclusive DIS data (see Sec. 3.3). These uncertainties promise a determination of $\alpha_s(M_Z)$ with the highest precision and would represent a considerable reduction of the current world average value with a present uncertainty of ± 0.00110 [134].

The uncertainty of α_s is studied for different values of the experimental uncertainties for the inclusive jet cross section measurement and for different assumption on bin-to-bin correlations, expressed by the correlation coefficient ρ, of individual uncertainty sources, as shown in Fig. 4.3. It is observed that, even for quite conservative scenarios, $\alpha_s(M_Z)$ will be determined with an uncertainty smaller than 2 ‰. For this, it is important to keep the size of the uncorrelated
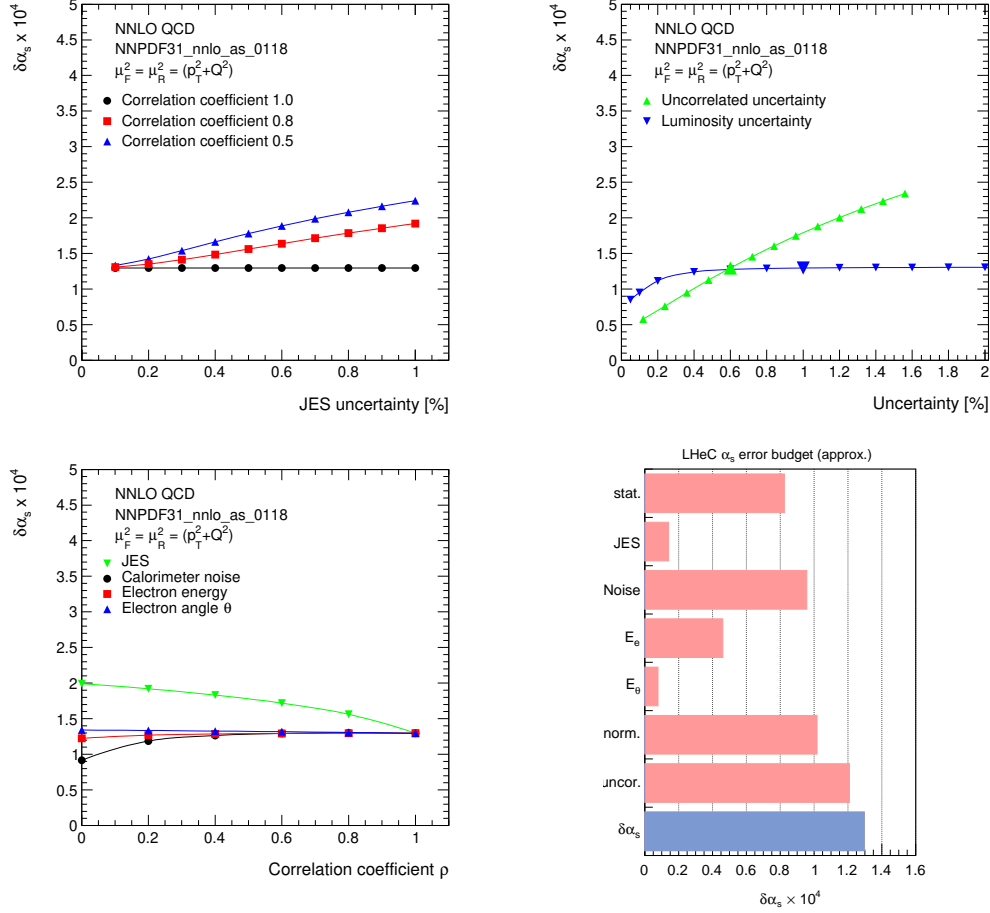
Figure 4.3: Studies of the size and correlations of experimental uncertainties impacting the uncertainty of $\alpha_s(M_Z)$. Top left: Study of the value of the correlation coefficient ρ for different systematic uncertainties. Common systematic uncertainties are considered as fully correlated, $\rho = 1$. Top right: Size of the JES uncertainty for three different values of ρ_{JES}. Bottom left: Impact of the uncorrelated and normalisation uncertainties on $\Delta\alpha_s(M_Z)$. Bottom right: Contribution of individual sources of experimental uncertainty to the total experimental uncertainty of $\alpha_s(M_Z)$.

uncertainty or the uncorrelated components of other systematic uncertainties under good control. This is also visible from Fig. 4.3 (bottom right), where the contributions of the individual uncertainty sources to the total uncertainty of $\alpha_s(M_Z)$ are displayed, and it is seen that the uncorrelated and the normalisation uncertainty are the largest individual uncertainty components. It is further observed, that the size of the statistical uncertainty (stat.) is non-negligible, which is, however, strongly dependent on the *ad hoc* assumption on the minimum size of $0.15\,\%$. The noise uncertainty contributes mainly to jets at low-p_{T}, and since these have a particular high sensitivity to $\alpha_s(M_Z)$, due to their low scale μ_{R}. It is of great importance to keep this experimental uncertainty well under control, or make better use of track-based information for the measurment of jets.

In the present formalism theoretical uncertainties from scale variations of the NNLO predictions amount to about $\Delta\alpha_s(M_Z) = 0.0035\,(\mathrm{NNLO})$. These can be reduced with suitable cuts in p_{T} or Q^2 to about $\Delta\alpha_s(M_Z) \approx 0.0010$. However, it is expected that improved predictions, e.g. with resummed contributions or N^{3}LO predictions will significantly reduce these uncertainties in the future. Uncertainties on non-perturbative hadronisation effects will have to be considered as

well, but these will be under good control due to the measurements of charged particle spectra at the LHeC and improved phenomenological models.

4.1.2 Pinning Down α_{s} with Inclusive and Jet LHeC Data

The dependence of the coupling strength as a function of the renormalisation scale μ_{R} is predicted by QCD, which is often called the *running* of the strong coupling. Its study with experimental data represents an important consistency and validity test of QCD. Using inclusive jet cross sections the running of the strong coupling can be tested by determining the value of α_{s} at different values of μ_{R} by grouping data points with similar values of μ_{R} and determining the value of $\alpha_{\mathrm{s}}(\mu_{\mathrm{R}})$ from these subsets of data points. The assumptions on the running of $\alpha_{\mathrm{s}}(\mu_{\mathrm{R}})$ are then imposed only for the limited range of the chosen interval, and not to the full measured interval as in the previous study. Here we set $\mu_{\mathrm{R}}^2 = Q^2 + p_{\mathrm{T}}^2$ [1]. The experimental uncertainties from the fits to subsets of the inclusive jet pseudodata are displayed in Fig. 4.4. These results
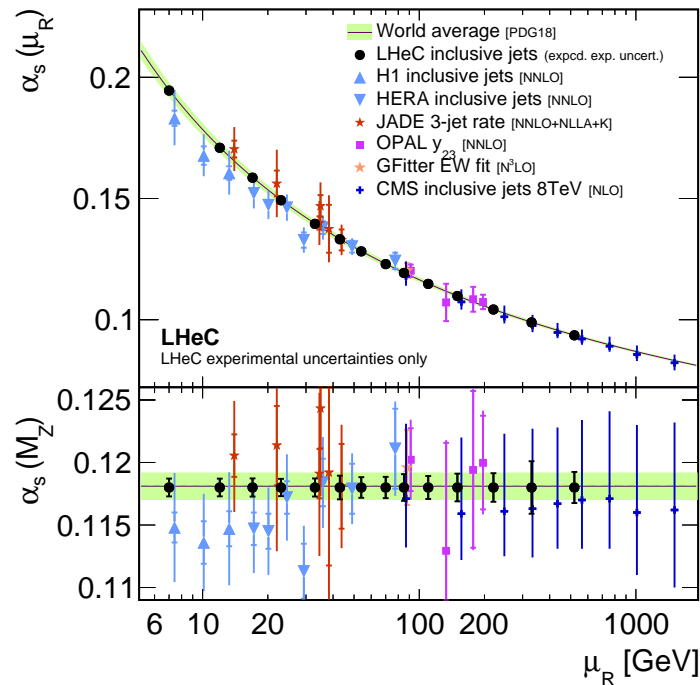
Figure 4.4: Uncertainties of $\alpha_s(M_Z)$ and corresponding $\alpha_s(\mu_R)$ in a determination of α_s using LHeC inclusive jet cross sections at different values of $\mu_R^2 = Q^2 + p_T^2$. Only experimental uncertainties are shown for LHeC and are compared with a number of presently available measurements and the world average value.

demonstrate a high sensitivity to α_s over two orders of magnitude in renormalisation scale up

---

[1] The choice of the scales follows a *conventional* scale setting procedure and uncertainties for the scale choice and for unknown higher order terms are estimated by varying the scales. Such variations are sensitive only to the terms which govern the behaviour of the running coupling, and may become unreliable due to renormalons [174]. An alternative way to fix the scales is provided by the Principle of Maximum Conformality (PMC) [175–179]. The PMC method was recently applied to predictions of event shape observables in $e^+e^- \to$ hadrons [180]. When applying the PMC method to observables in DIS, the alternative scale setting provides a profound alternative to verify the running of $\alpha_{\mathrm{s}}(\mu_{\mathrm{R}})$. Such a procedure could be particularly relevant for DIS event shape observables, where the leading-order terms are insensitive to α_{s} and conventional scale choices may not be adequately related to the α_s-sensitive higher order QCD corrections.

to values of about $\mu_{\mathrm{R}} \approx 500\,\mathrm{GeV}$. In the range $6 < \mu_{\mathrm{R}} \lesssim 200\,\mathrm{GeV}$ the experimental uncertainty is found to be smaller than the expectation from the world average value [181]. This region is of particular interest since it connects the precision determinations from lattice calculations [182] or τ decay measurements [183], which are at low scales $\mathcal{O}(\mathrm{GeV})$, to the measurements at the Z pole [184] and to the applications to scales which are relevant for the LHC, e.g. for Higgs or top-quark physics or high-mass searches. This kinematic region of scales $\mathcal{O}(10\,\mathrm{GeV})$ cannot be accessed by (HL-)LHC experiments because of limitations due to pile-up and underlying event [185].

Inclusive DIS cross sections are sensitive to $\alpha_{\mathrm{s}}(M_{\mathrm{Z}})$ through higher-order QCD corrections, contributions from the F_L structure function and the scale dependence of the cross section at high x (*scaling violations*). The value of $\alpha_{\mathrm{s}}(M_{\mathrm{Z}})$ can then be determined in a combined fit of the PDFs and $\alpha_{\mathrm{s}}(M_{\mathrm{Z}})$ [170]. While a simultaneous determination of $\alpha_s(M_{\mathrm{Z}})$ and PDFs is not possible with HERA inclusive DIS data alone due to its limited precision and kinematic coverage [44, 170], the large kinematic coverage, high precision and the integrated luminosity of the LHeC data will allow for the first time such an α_{s} analysis.

For the purpose of the determination of $\alpha_{\mathrm{s}}(M_{\mathrm{Z}})$ from inclusive NC/CC DIS data, a combined PDF+α_{s} fit to the simulated data is performed, similar to the studies presented above, in Chapter 3. Other technical details are outlined in Ref. [170]. In this fit, however, the numbers of free parameters of the gluon parameterisation is increased, since the gluon PDF and $\alpha_{\mathrm{s}}(M_{\mathrm{Z}})$ are highly correlated and LHeC data are sensitive to values down to $x < 10^{-5}$, which requires additional freedom for the gluon parameterisation. The inclusive data are restricted to $Q^2 \geq 5\,\mathrm{GeV}^2$ in order to avoid a region where effects beyond fixed-order perturbation theory may become sizeable [44, 186].

Exploiting the full LHeC inclusive NC/CC DIS data with $E_e = 50\,\mathrm{GeV}$, the value of $\alpha_{\mathrm{s}}(M_{\mathrm{Z}})$ can be determined with an uncertainty $\Delta\alpha_{\mathrm{s}}(M_{\mathrm{Z}}) = \pm 0.00038$. With a more optimistic assumption on the dominant uncorrelated uncertainty of $\delta\sigma_{(\mathrm{uncor.})} = 0.25\,\%$, an uncertainty as small as

$$\Delta\alpha_{\mathrm{s}}(M_{\mathrm{Z}})(\mathrm{incl.\ DIS}) = \pm 0.00022_{(\mathrm{exp+PDF})} \qquad (4.3)$$

is achieved. This would represent a considerable improvement over the present world average value. Given these small uncertainties, theoretical uncertainties from missing higher orders or heavy quark effects have to be considered in addition. In a dedicated study, the fit is repeated with a reduced data set which can be accumulated already during a single year of operation [2], corresponding to about $\mathcal{L} \sim 50\,\mathrm{fb}^{-1}$. Already these data will be able to improve the world average value. These studies are displayed in Fig. 4.5.

High sensitivity to $\alpha_{\mathrm{s}}(M_{\mathrm{Z}})$ and an optimal treatment of the PDFs is obtained by using inclusive jet data together with inclusive NC/CC DIS data in a combined determination of $\alpha_{\mathrm{s}}(M_{\mathrm{Z}})$ and the PDFs. The jet data will provide an enhanced sensitivity to $\alpha_{\mathrm{s}}(M_{\mathrm{Z}})$, while inclusive DIS data has the highest sensitivity to the determination of the PDFs. In such combined QCD analyses, also heavy quark data may be further analysed to determine m_c and m_b. However, since jet cross sections have sufficiently high scale ($p_{\mathrm{T}} \gg m_b$) these are fairly insensitive to the actual value of the heavy quark masses. Contrary, heavy quark data is predominantly sensitive to the quark mass parameters rather than to $\alpha_{\mathrm{s}}(M_{\mathrm{Z}})$, and their correlation is commonly found to be small in such combined analyses, see e.g. Ref [52]. Infact, at LHeC the masses of charm and bottom quarks can be determined with high precision and uncertainties of $3\,\mathrm{MeV}$ and $10\,\mathrm{MeV}$ are expected, respectively [1]. Therefore, for our sole purpose of estimating the uncertainty of

---

[2] Two different assumptions are made. One fit is performed with only electron data corresponding to $\mathcal{L} \sim 50\,\mathrm{fb}^{-1}$, and an alternative scenario considers further positron data corresponding to $\mathcal{L} \sim 1\,\mathrm{fb}^{-1}$.
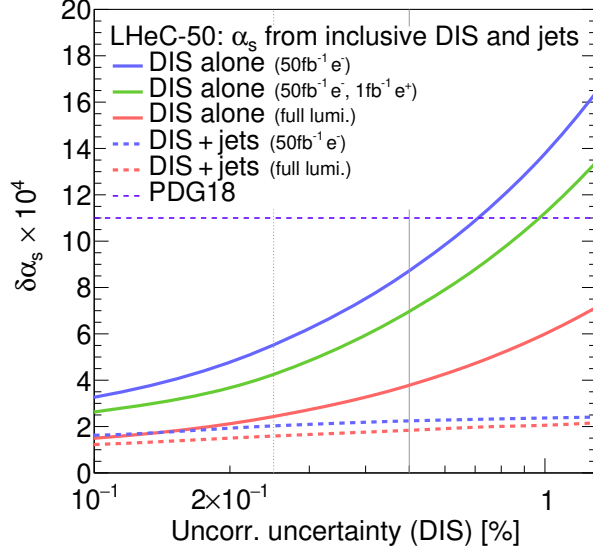
Figure 4.5: Uncertainties of $\alpha_s(M_Z)$ from simultaneous fits of $\alpha_s(M_Z)$ and PDFs to inclusive NC/CC DIS data as a function of the size of the uncorrelated uncertainty of the NC/CC DIS data. The full lines indicate the uncertainties obtained with different assumptions on the data taking scenario and integrated luminosity. The dashed lines indicate results where, additionally to the inclusive NC/CC DIS data, inclusive jet cross section data are considered.

$\alpha_s(M_Z)$ from LHeC data, we do not consider heavy quark data, nor free values of m_c or m_b in the analysis, and we leave the outcome of such a complete QCD analysis to the time when real data are available and the actual value of the parameters are of interest. At this time, also better theoretical predictions will be used, including higher order corrections, heavy quark mass effects or higher-twist terms, as can be expected from steady progress [187–192].

For this study, the double-differential inclusive jet data as described above, and additionally the inclusive NC/CC DIS data with $E_e = 50\,\text{GeV}$ as introduced in Sec. 3.2, are employed. Besides the normalisation uncertainty, all sources of systematic uncertainties are considered as uncorrelated between the two processes. A fit of NNLO QCD predictions to these data sets is then performed, and $\alpha_s(M_Z)$ and the parameters of the PDFs are determined. The methodology follows closely the methodology sketched in Sect. 3. Using inclusive jet and inclusive DIS data in a single analysis, the value of $\alpha_s(M_Z)$ is determined with an uncertainty of

$$\Delta\alpha_s(M_Z)(\text{incl. DIS \& jets}) = \pm 0.00018_{(\text{exp+PDF})} . \tag{4.4}$$

This result will improve the world average value considerably. However, theoretical uncertainties are not included and new mathematical tools and an improved understanding of QCD will be needed in order to achieve small values similar to the experimental ones. The dominant sensitivity in this study arises from the jet data. This can be seen from Fig. 4.5, where $\Delta\alpha_s(M_Z)$ changes only moderately with different assumptions imposed on the inclusive NC/CC DIS data. Assumptions made for the uncertainties of the inclusive jet data have been studied above, and these results can be translated easily to this PDF+α_s fit.

The expected values for $\alpha_s(M_Z)$ obtained from inclusive jets or from inclusive NC/CC DIS data are compared in Fig. 4.6 with present determinations from global fits based on DIS data (called *PDF fits*) and the world average value [134]. It is observed that LHeC will have the potential to improve considerably the world average value. Already after one year of data taking, the
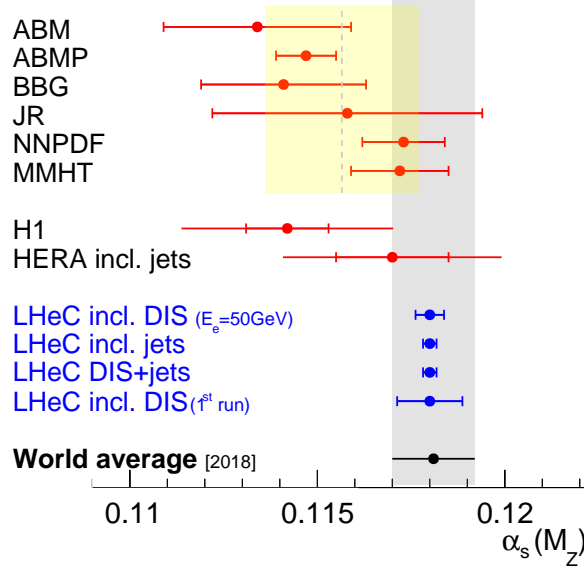
Figure 4.6: Summary of $\alpha_s(M_Z)$ values in comparison with present values.

experimental uncertainties of the NC/CC DIS data are competitive with the world average value. The measurement of jet cross sections will further improve that value (not shown).

Furthermore, LHeC will be able to address a long standing puzzle. All α_s determinations from global fits based on NC/CC DIS data find a lower value of $\alpha_s(M_Z)$ than determinations in the lattice QCD framework, from τ decays or in a global electroweak fit. With the expected precision from LHeC this discrepancy will be resolved.

4.1.3 Strong coupling from other processes

A detailed study for the determination of $\alpha_s(M_Z)$ from NC/CC DIS and from inclusive jet data was presented in the previous paragraphs. However, a large number of additional processes and observables that are measured at the LHeC can also be considered for a determination of $\alpha_s(M_Z)$. Suitable observables or processes are di-jet and multi-jet production, heavy flavour production, jets in photoproduction or event shape observables. These processes all exploit the α_s dependence of the hard interaction. Using suitable predictions, also *softer* processes can be exploited for an α_s determination. Examples could be jet shapes or other substructure observables, or charged particle multiplicities.

Since $\alpha_s(M_Z)$ is a parameter of a phenomenological model, the total uncertainty of $\alpha_s(M_Z)$ is always a sum of experimental and theoretical uncertainties which are related to the definition of the observable and to the applied model, e.g. hadronisation uncertainties, diagram removal/sub-traction uncertainties or uncertainties from missing higher orders. Therefore, credible prospects for the total uncertainty of $\alpha_s(M_Z)$ from other observables or processes altogether are difficult to predict, even more since LHeC will explore a new kinematic regime that was previously unmeasured.

In a first approximation, for any process the sensitivity to $\alpha_s(M_Z)$ scales with the order n of α_s in the leading-order diagram, α_s^n. The higher the power n the higher the sensitivity to $\alpha_s(M_Z)$.

Consequently, the experimental uncertainty of an α_{s} fit may reduce with increasing power n. Already at HERA three-jet cross section were proven to have a high sensitivity to $\alpha_{\mathrm{s}}(M_{\mathrm{Z}})$ albeit their sizeable statistical uncertainties [137, 147]. At the LHeC, due to the higher $\sqrt{s}$ and huge integrated luminosity, as well as the larger acceptance of the detector, three-, four- or five-jet cross sections represent highly sensitive observables for a precise determination of $\alpha_{\mathrm{s}}(M_{\mathrm{Z}})$, and high experimental precision can be achieved. In these cases, fixed order pQCD predictions may become limiting factors, since they are more complicated for large n.

Di-jet observables are expected to yield a fairly similar experimental uncertainty than inclusive jet cross sections, as studied in the previous paragraphs, since both have $n = 1$ at LO. However, their theoretical uncertainties may be smaller, since di-jet observables are less sensitive to additional higher-order radiation, in particular at lower scales where $\alpha_{\mathrm{s}}(\mu_{\mathrm{R}})$ is larger.

Event shape observables in DIS exploit additional radiation in DIS events (see e.g. review [193] or HERA measurements [194, 195]). Consequently, once measured at the LHeC the experimental uncertainties of $\alpha_{\mathrm{s}}(M_{\mathrm{Z}})$ from these observables are expected to become very similar to that in Eq. (4.4), since both the event sample and the process is similar to the inclusive jet cross sections [3]. However, different reconstruction techniques of the observables may yield reduced experimental uncertainties, and the calculation of event shape observables allow for the resummation of large logarithms, and steady theoretical advances promise small theoretical uncertainties [196–202].

Jet production cross sections in photoproduction represents a unique opportunity for another precision determination of $\alpha_{\mathrm{s}}(M_{\mathrm{Z}})$. Such measurements have been performed at HERA [203–206]. The sizeable photoproduction cross section provides a huge event sample, which is statistically independent from NC DIS events, and already the leading-order predictions are sensitive to $\alpha_{\mathrm{s}}(M_{\mathrm{Z}})$ [207]. Also its running can be largely measured since the scale of the process is well estimated by the transverse momentum of the jets $\mu_R \sim p_{\mathrm{T}}^{\mathrm{jet}}$. Limiting theoretical aspects are due to the presence of a quasi-real photon and the poorly known photon PDF [208, 209].

A different class of observables represent heavy flavour (HF) cross sections, which are discussed in Sec. 3.3.5. Due to flavour conservation, these are commonly proportional to $\mathcal{O}(\alpha_{\mathrm{s}}^1)$ at leading-order. However, when considering inclusive HF cross sections above the heavy quark mass threshold heavy quarks can be factorised into the PDFs, and the leading structure functions $F_2^{c,b}$ are sensitive to α_{s} only beyond the LO approximation (see reviews [80, 81], recent HERA measurements [64, 210] and references therein). The presence of the heavy quark mass as an additional scale stabilises perturbative calculations, and reduced theoretical uncertainties are expected.

At the LHeC the structure of jets and the formation of hadrons can be studied with unprecedented precision. This is so because of the presence of a single hadron in the initial state. Therefore, limiting effects like the underlying event or pile-up are absent or greatly diminished. Precise measurements of jet shape observables, or the study of jet substructure observables [211], are highly sensitive to the value of $\alpha_{\mathrm{s}}(M_{\mathrm{Z}})$, because parton shower and hadronisation take place at lower scales where the strong coupling becomes large and an increased sensitivity to $\alpha_{\mathrm{s}}(M_{\mathrm{Z}})$ is attained [163, 212].

Finally, also the determination of $\alpha_{\mathrm{s}}(M_{\mathrm{Z}})$ from inclusive NC DIS cross sections can be improved. For NC DIS the dominant sensitivity to α_{s} arises from the F_L structure function and from scaling violations of F_2 at lower values of Q^2 but at very high values of x. Dedicated measurements of

---

[3]It shall be noted, that event shape observables in NC DIS can be defined in the laboratory rest frame or the Breit frame.

these kinematic regions will further improve the experimental uncertainties from the estimated values in Eq. (4.3).

4.2 Discovery of New Strong Interaction Dynamics at Small x

The LHeC machine will offer access to a completely novel kinematic regime of DIS characterised by very small values of x. From the kinematical plane in (x, Q^2) depicted in Fig. 1.1, it is clear that the LHeC will be able to probe Bjorken-x values as low as 10^{-6} for perturbative values of Q^2. At low values of x various phenomena may occur which go beyond the standard collinear perturbative description based on DGLAP evolution. Since the seminal works of Balitsky, Fadin, Kuraev and Lipatov [115, 213, 214] it has been known that, at large values of centre-of-mass energy $\sqrt{s}$ or, to be more precise, in the Regge limit, there are large logarithms of energy which need to be resummed. Thus, even at low values of the strong coupling α_s, logarithms of energy $\ln s$ may be sufficiently large, such that terms like $(\alpha_s \ln s)^n$ will start to dominate the cross section.

In addition, other novel effects may appear in the low x regime, which are related to the high gluon densities. At large parton densities the recombination of the gluons may become important in addition to the gluon splitting. This is known as the parton saturation phenomenon in QCD, and is deeply related to the restoration of the unitarity in QCD. As a result, the linear evolution equations will need to be modified by the additional nonlinear terms in the gluon density. In the next two subsections we shall explore the potential and sensitivity of the LHeC to these small x phenomena in ep collisions. Note also that, being a density effect, the non-linear phenomena leading to parton saturation are enhanced by increasing the mass number of the nucleus in eA. Chapter 6, devoted to the physics opportunities with eA collisions at the LHeC, discusses this aspect, see also Ref. [1].

4.2.1 Resummation at small x

The calculation of scattering amplitudes in the high-energy limit and the resummation of $(\alpha_s \ln s)^n$ series in the leading logarithmic order was performed in Refs. [115, 213, 214] and it resulted in the famous BFKL evolution equation. This small x evolution equation, written for the so-called gluon Green's function or the unintegrated gluon density, is a differential equation in $\ln 1/x$. An important property of this equation is that it keeps the transverse momenta unordered along the gluon cascade. This has to be contrasted with DGLAP evolution which is differential in the hard scale Q^2 and relies on the strong ordering in the transverse momenta of the exchanged partons in the parton cascade. The solution to the BFKL equation is a gluon density which grows sharply with decreasing x, as a power i.e. $\sim x^{-\omega_{IP}}$, where ω_{IP} is the hard Pomeron intercept, and in the leading logarithmic approximation equals $\frac{N_c \alpha_s}{\pi} 4 \ln 2$, which gives a value of about 0.5 for typical values of the strong coupling. The leading logarithmic (LLx) result yielded a growth of the gluon density which was too steep for the experimental data at HERA. The next-to-leading logarithmic (NLLx) calculation performed in the late 90s [215, 216] resulted in large negative corrections to the LLx value of the hard Pomeron intercept and yielded some instabilities in the cross section [217–220] and it is important to account for subleading effects, since these are large [221, 222].

The appearance of the large negative corrections at NLLx motivated the search for the appropriate resummation which would stabilize the result. It was understood very early that the large

corrections which appear in BFKL at NLLx are mostly due to the kinematics [223–225] as well as DGLAP terms and the running of the strong coupling. First attempts at combining the BFKL and DGLAP dynamics together with the proper kinematics [226–228] yielded encouraging results, and allowed a description of HERA data on structure functions with good accuracy. The complete resummation program was developed in a series of works [229–245]. In these works the resummation for the gluon Green's function and the splitting functions was developed.

The low-x resummation was recently applied to the description of structure function data at HERA using the methodology of NNPDF [246]. It was demonstrated that the resummed fits provide a better description of the structure function data than the pure DGLAP based fits at fixed NNL order. In particular, it was shown that the χ^2 of the fits does not vary appreciably when more small x data are included in the case of the fits which include the effects of the small-x resummation. On the other hand, the fits based on NNLO DGLAP evolution exhibit a worsening of their quality in the region of low x and low to moderate values of Q^2. This indicates that there is some tension in the fixed order fits based on DGLAP, and that resummation alleviates it. In addition, it was shown that the description of the longitudinal structure function F_L from HERA data is improved in the fits with the small x resummation. This analysis suggests that the small x resummation effects are indeed visible in the HERA kinematic region. Such effects will be strongly magnified at the LHeC, which probes values of x more than one order of magnitude lower than HERA. The NNPDF group also performed simulation of the structure functions F_2 and F_L with and without resummation in the LHeC range as well as for the next generation electron-hadron collider FCC-eh [246]. The predictions for the structure functions as a function of x for fixed values of Q^2 are shown in Figs. 4.7.
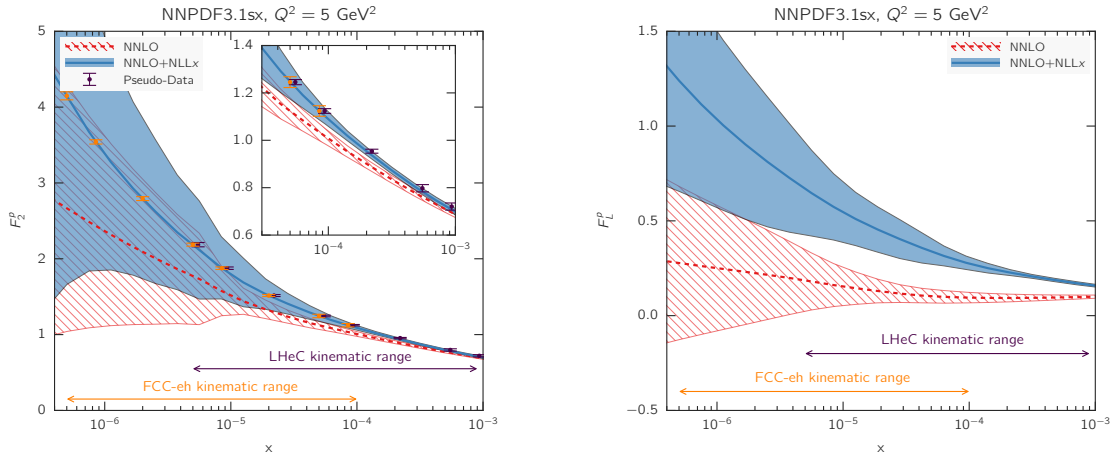
Figure 4.7: Predictions for the F_2 and F_L structure functions using the NNPDF3.1sx NNLO and NNLO+NLLx fits at $Q^2 = 5\,\mathrm{GeV}^2$ for the kinematics of the LHeC and FCC-eh. In the case of F_2, we also show the expected total experimental uncertainties based on the simulated pseudodata, assuming the NNLO+NLLx values as the central prediction. A small offset has been applied to the LHeC pseudodata as some of the values of x overlap with the FCC-eh pseudodata points. The inset in the left plot shows a magnified view in the kinematic region $x > 3 \times 10^{-5}$, corresponding to the reach of HERA data. Figure taken from Ref. [246].

The simulations were done using APFEL [247] together with the HELL package [248] which implements the small x resummation. From Fig. 4.7 it is clear that LHeC will have much higher sensitivity to discriminate between fixed order and resummed scenarios than the HERA collider, with even better discrimination at the FCC-eh. The differences between the central values for the two predictions are of the order of 15% for the case of F_2 and this is much larger than

the projected error bar on the reduced cross section or structure function F_2 which could be measured at LHeC. For comparison, the simulated pseudodata for F_2 are shown together with the expected experimental uncertainties. The total uncertainties of the simulated pseudodata are at the few percent level at most, and are therefore much smaller than the uncertainties coming from the PDFs in most of the kinematic range.

It is evident that fits to the LHeC data will have power to discriminate between the different frameworks. In the right plot in Fig. 4.7, the predictions for the longitudinal structure function are shown. We see that in the case of the F_L structure function, the differences between the fixed order and resummed predictions are even larger, consistently over the entire range of x. This indicates the importance of the measurement of the longitudinal structure function F_L which can provide further vital constraints on the QCD dynamics in the low x region due to its sensitivity to the gluon density in the proton.

To further illustrate the power of a high energy DIS collider like the LHeC in exploring the dynamics at low x, fits which include the simulated data were performed. The NNLO+NLLx resummed calculation was used to obtain the simulated pseudodata, both for the LHeC, in a scenario of a 60 GeV electron beam on a 7 TeV proton beam as well as in the case of the FCC-eh scenario with a 50 TeV proton beam. All the experimental uncertainties for the pseudodata have been added in quadrature. Next, fits were performed to the DIS HERA as well as LHeC and FCC-eh pseudodata using the theory with and without the resummation at low x. Hadronic data like jet, Drell-Yan or top, were not included for this analysis but, as demonstrated in [246], these data do not have much of the constraining power at low x, and therefore the results of the analysis at low x are independent of the additional non-DIS data sets. The quality of the fits characterised by the χ^2 was markedly worse when the NNLO DGLAP framework was used to fit the HERA data and the pseudodata from LHeC and/or FCC-eh than was the case with resummation. To be precise, the χ^2 per degree of freedom for the HERA data set was equal to 1.22 for the NNLO fit, and 1.07 for the resummed fit. For the case of the LHeC/FCC-eh the χ^2 per degree of freedom was equal to 1.71/2.72 and 1.22/1.34 for NNLO and NNLO+resummation fits, respectively. These results demonstrate the huge discriminatory power of the new DIS machines between the DGLAP and resummed frameworks, and the large sensitivity to the low x region while simultaneously probing low to moderate Q^2 values.
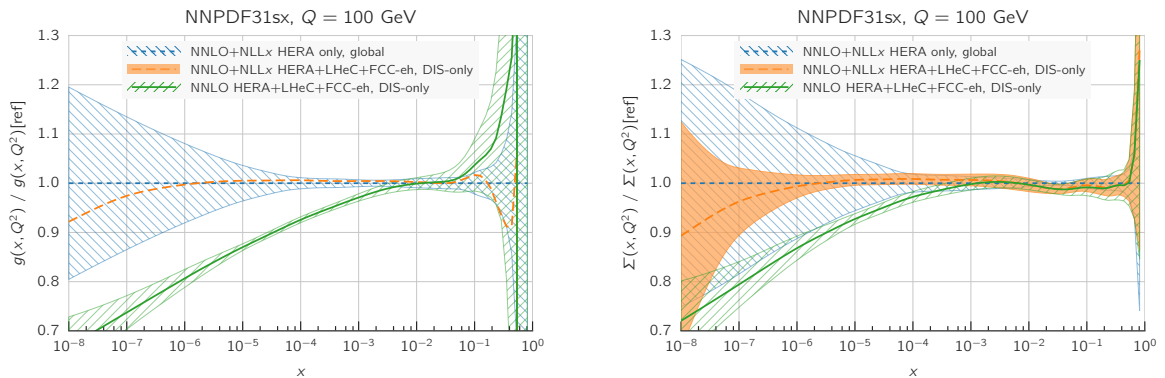
Figure 4.8: Comparison between the gluon (left plot) and the quark singlet (right plot) PDFs in the NNPDF3.1sx NNLO+NNLx fits without (blue hatched band) and with the LHeC+FCC-eh pseudodata (orange band) on inclusive structure functions. For completeness, we also show the results of the corresponding NNPDF3.1sx NNLO fit with LHeC+FCC-eh pseudodata (green hatched band). Figure taken from Ref. [246].

In Fig. 4.8 the comparison of the gluon and quark distributions from the NNLO + NLLx fits is

shown at $Q = 100$ GeV as a function of x, with and without including the simulated pseudodata from LHeC as well as FCC-eh. The differences at large x are due to the fact that only DIS data were included in the fits, and not the hadronic data. The central values of the extracted PDFs using only HERA or using HERA and the simulated pseudodata coincide with each other, but a large reduction in uncertainty is visible when the new data are included. The uncertainties from the fits based on the HERA data only increase sharply already at $x \sim 10^{-4}$. On the other hand, including the pseudodata from LHeC and/or FCC-eh can extend this regime by order(s) of magnitude down in x. Furthermore, fits without resummation, based only on NNLO DGLAP, were performed to the HERA data and the pseudodata. We see that in this case the extracted gluon and singlet quark densities differ significantly from the fits using the NNLO+NLLx. Already at $x = 10^{-4}$ the central values of the gluon differ by 10% and at $x = 10^{-5}$, which is the LHeC regime, the central values for the gluon differ by 15%. This difference is much larger than the precision with which the gluon can be extracted from the DIS data, which is of the order of $\sim 1\%$.

The presented analysis demonstrates that the fixed order prediction based on the DGLAP evolution would likely fail to describe accurately the structure function data in the new DIS machines and that in that regime new dynamics including resummation are mandatory for quantitative predictions. Therefore, the LHeC machine has an unprecedented potential to pin down the details of the QCD dynamics at low values of Bjorken x.

4.2.2 Disentangling non-linear QCD dynamics at the LHeC

As mentioned previously the kinematic extension of the LHeC will allow unprecedented tests of the strong interaction in the extremely low x region, and allow for the tests of the novel QCD dynamics at low x. The second effect, in addition to resummation, that may be expected is the parton saturation phenomenon, which may manifest itself as the deviation from the linear DGLAP evolution, and the emergence of the saturation scale.

In particular, it has been argued that the strong growth of the gluon PDF at small-x should eventually lead to gluon recombination [249] to avoid violating the unitary bounds. The onset of such non-linear dynamics, also known as saturation, has been extensively searched but so far there is no conclusive evidence of its presence, at least within the HERA inclusive structure function measurements. In this context, the extended kinematic range of the LHeC provides unique avenues to explore the possible onset of non-linear QCD dynamics at small-x. The discovery of saturation, a radically new regime of QCD, would then represent an important milestone in our understanding of the strong interactions.

The main challenge in disentangling saturation lies in the fact that non-linear corrections are expected to be moderate even at the LHeC, since they are small (if present at all) in the region covered by HERA. Therefore, great care needs to be employed in order to separate such effects from those of standard DGLAP linear evolution. Indeed, it is well known that HERA data at small-x in the perturbative region can be equally well described, at least at the qualitative level, both by PDF fits based on the DGLAP framework as well as by saturation-inspired models. However, rapid progress both in theory calculations and methodological developments have pushed QCD fits to a new level of sophistication, and recently it has been shown that subtle but clear evidence of BFKL resummation at small-x is present in HERA data, both for inclusive and for heavy quark structure functions [250, 251]. Such studies highlight how it should be possible to tell apart non-linear from linear dynamics using state-of-the-art fitting methods even if these are moderate, provided that they are within the LHeC reach.

Here we want to assess the sensitivity of the LHeC to detect the possible onset of non-linear saturation dynamics. This study will be carried out by generalising a recent analysis [59] that quantified the impact of LHeC inclusive and semi-inclusive measurements on the PDF4LHC15 PDFs [252, 253] by means of Hessian profiling [254]. There, the LHeC pseudodata was generated assuming that linear DGLAP evolution was valid in the entire LHeC kinematic range using the PDF4LHC15 set as input. To ascertain the possibility of pinning down saturation at the LHeC, here we have revisited this study but now generating the LHeC pseudodata by means of a saturation-inspired calculation. By monitoring the statistical significance of the tension that will be introduced (by construction) between the saturation pseudodata and the DGLAP theory assumed in the PDF fit, we aim to determine the likelihood of disentangling non-linear from linear evolution effects at the LHeC. See also [255] for previous related studies along the same direction.

Analysis settings

In this study we adopt the settings of [59, 256], to which we refer the interested reader for further details. In Ref. [59] the impact on the proton PDFs of inclusive and semi-inclusive neutral-current (NC) and charged current (CC) DIS structure functions from the LHeC was quantified. These results were then compared with the corresponding projections for the PDF sensitivity of the High-Luminosity upgrade of the LHC (HL-LHC). In Fig. 3.4 the kinematic range in the (x, Q^2) plane of the LHeC pseudodata employed in that analysis is displayed, which illustrated how the LHeC can provide unique constraints on the behaviour of the quark and gluon PDFs in the very small-x region.

Since non-linear dynamics are known to become sizeable only at small-x, for the present analysis it is sufficient to consider the NC e^-p inclusive scattering cross sections from proton beam energies of $E_p = 7\,\text{TeV}$ and $E_p = 1\,\text{TeV}$. In Fig. 4.9 we show the bins in (x, Q^2) for which LHeC pseudodata for inclusive structure functions has been generated according to a saturation-based calculation. Specifically, we have adopted here the DGLAP-improved saturation model of Ref. [257], in which the scattering matrix is modelled through eikonal iteration of two gluon exchanges. This model was further extended to include heavy flavour in Ref. [258]. The specific parameters that we use were taken from Fit 2 in Ref. [259], where parameterisations are provided that can be used for $x < 0.01$ and $Q^2 < 700\,\text{GeV}^2$. These parameters were extracted from a fit to the HERA legacy inclusive structure function measurements [44] restricted to $x < 0.01$ and $0.045 < Q^2 < 650\,\text{GeV}^2$. In contrast to other saturation models, the one we assume here [259] provides a reasonable description for large Q^2 in the small x region, where it ensure a smooth transition to standard fixed-order perturbative results.

Note that the above discussion refers only to the generated LHeC pseudodata: all other aspects of the QCD analysis of Ref. [59] are left unchanged. In particular, the PDF profiling will be carried out using theory calculations obtained by means of DGLAP evolution with the NNLO PDF4LHC15 set (see also Ref. [260]), with heavy quark structure functions evaluated by means of the FONLL-B general-mass variable flavour number scheme [88]. In order to ensure consistency with the PDF4LHC15 prior, here we will replace the DGLAP pseudodata by the saturation calculation only in the kinematic region for $x \lesssim 10^{-4}$, rather than for all the bins indicated in red in Fig. 4.9. The reason for this choice is that PDF4LHC15 already includes HERA data down to $x \simeq 10^{-4}$ which is successfully described via the DGLAP framework, and therefore if we assume departures from DGLAP in the LHeC pseudodata this should only be done for smaller values of x.
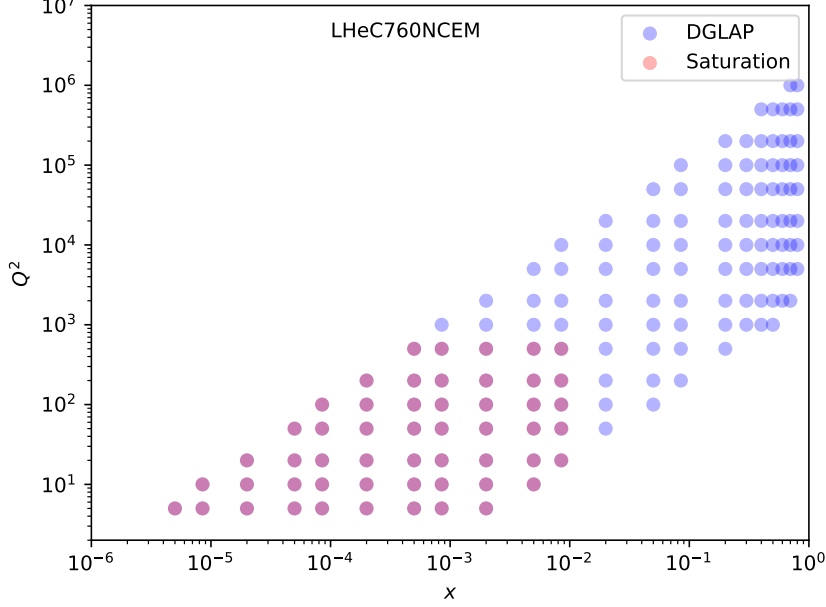
Figure 4.9: The kinematic coverage of the NC $e^- p$ scattering pseudodata at the LHeC, where the blue (red) points indicate those bins for which DGLAP (saturation) predictions are available.

Results and discussion

Using the analysis settings described above, we have carried out the profiling of PDF4LHC15 with the LHeC inclusive structure function pseudodata, which for $x \leq 10^{-4}$ ($x > 10^{-4}$) has been generated using the GBW saturation (DGLAP) calculations, and compare them with the results of the profiling where the pseudodata follows the DGLAP prediction. We have generated $N_{\exp} = 500$ independent sets LHeC pseudodata, each one characterised by different random fluctuations (determined by the experimental uncertainties) around the underlying central value.

To begin with, it is instructive to compare the data versus theory agreement, χ^2/n_{dat}, between the pre-fit and post-fit calculations, in order to assess the differences between the DGLAP and saturation cases. In the upper plots of Fig. 4.10 we show the distributions of pre-fit and post-fit values of χ^2/n_{dat} for the $N_{\exp} = 500$ sets of generated LHeC pseudodata. We compare the results of the profiling of the LHeC pseudodata based on DGLAP calculations in the entire range of x with those where the pseudodata is based on the saturation model in the region $x < 10^{-4}$. Then in the bottom plot we compare of the post-fit χ^2 distributions between the two scenarios. Note that in these three plots the ranges in the x axes are different.

From this comparison we can observe that for the case where the pseudodata is generated using a consistent DGLAP framework (PDF4LHC15) as the one adopted for the theory calculations used in the fit, as expected the agreement is already good at the pre-fit level, and it is further improved at the post-fit level. However the situation is rather different in the case where a subset of the LHeC pseudodata is generated using a saturation model: at the pre-fit level the agreement between theory and pseudodata is poor, with $\chi^2/n_{\mathrm{dat}} \simeq 7$. The situation markedly improves at the post-fit level, where now the χ^2/n_{dat} distributions peaks around 1.3. This result implies that the DGLAP fit manages to absorb most of the differences in theory present in the saturation pseudodata. This said, the DGLAP fit cannot entirely *fit away* the non-linear corrections: as shown in the lower plot of Fig. 4.10, even at the post-fit level one can still tell apart the χ^2/n_{dat} distributions between the two cases, with the DGLAP (saturation) pseudodata
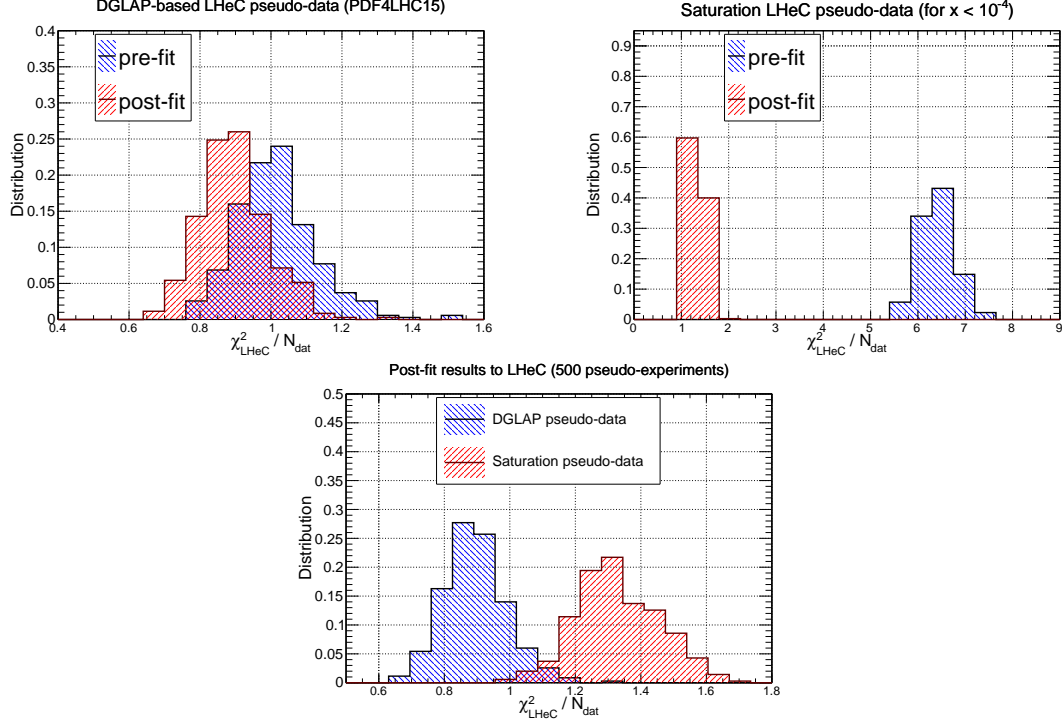
Figure 4.10: Upper plots: the distribution of pre-fit and post-fit values of χ^2/n_{dat} for the $N_{\text{exp}} = 500$ sets of generated LHeC pseudodata. We compare the results of the profiling of the LHeC pseudodata based on DGLAP calculations in the entire range of x (left) with those where the pseudodata is based on the saturation model in the region $x < 10^{-4}$ (right plot). Bottom plot: comparison of the post-fit χ^2/n_{dat} distributions between these two scenarios for the pseudodata generation.

peaking at around 0.9 (1.3). This comparison highlights that it is not possible for the DGLAP fit to completely absorb the saturation effects into a PDF redefinition.

In order to identify the origin of the worse agreement between theory predictions and LHeC pseudodata in the saturation case, it is illustrative to take a closer look at the pulls defined as

$$P(x, Q^2) = \frac{\mathcal{F}_{\text{dat}}(x, Q^2) - \mathcal{F}_{\text{fit}}(x, Q^2)}{\delta_{\text{exp}} \mathcal{F}(x, Q^2)}, \tag{4.5}$$

where $\mathcal{F}_{\text{fit}}$ is the central value of the profiled results for the observable $\mathcal{F}$ (in this case the reduced neutral current DIS cross section), $\mathcal{F}_{\text{dat}}$ is the corresponding central value of the pseudodata, and $\delta_{\text{exp}} \mathcal{F}$ represents the associated total experimental uncertainty. In Fig. 4.11 we display the pulls between the post-fit prediction and the central value of the LHeC pseudodata for different bins in Q^2. We compare the cases where the pseudodata has been generated using a consistent theory calculation (DGLAP) with that based on the GBW saturation model.

The comparisons in Fig. 4.11 show first of all that in the DGLAP case the pulls are $\mathcal{O}(1)$ in the entire kinematical range. This is of course expected, given that the LHeC pseudodata is generated using the same theory as the one subsequently used for the fit. In the case where the pseudodata has been partially generated with the saturation calculation, on the other hand, one finds a systematic tension between the theory used for the fit (DGLAP) and the one used to generate the pseudodata (saturation). Indeed, we find that at the smallest values of x the theory prediction overshoots the data by a significant amount, while at higher x the opposite behaviour takes place. One can also see that in the region $10^{-4} \lesssim x \lesssim 10^{-3}$ the fit undershoots the pseudodata by a large amount.
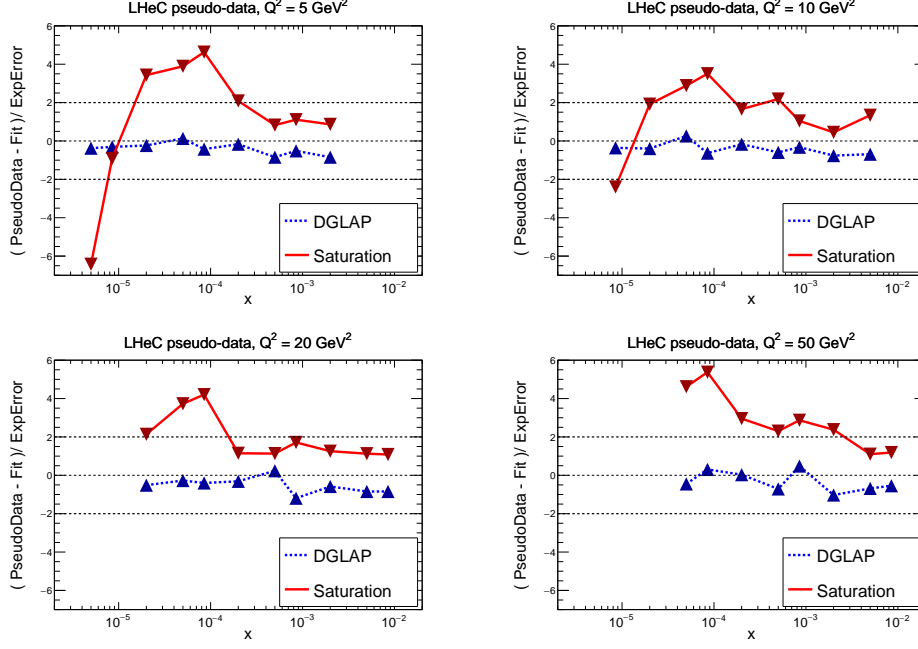
Figure 4.11: The pulls between the central value of the LHeC pseudodata and post-fit prediction, Eq. (4.5), for four different bins in Q^2. We compare the results of the profiling where the LHeC pseudodata has been generated using a consistent DGLAP theory with that partially based on the saturation calculations.

These comparisons highlight how a QCD fit to the saturation pseudodata is obtained as a compromise between opposite trends: the theory wants to overshoot the data at very small x and undershoot it at larger values of x. These tensions result in a distorted fit, explaining the larger χ^2/n_{dat} values as compared to the DGLAP case. Such a behaviour can be partially traced back by the different scaling in Q^2 between DGLAP and GBW: while a different x dependence could eventually be absorbed into a change of the PDFs at the parameterisation scale Q_0, this is not possible with a Q^2 dependence.

The pull analysis of Fig. 4.11 highlights how in order to tell apart linear from non-linear QCD evolution effects at small-x it would be crucial to ensure a lever arm in Q^2 as large as possible in the perturbative region. This way it becomes possible to disentangle the different scaling in Q^2 for the two cases. The lack of a sufficiently large lever arm in Q^2 at HERA at small x could explain in part why both frameworks are able to describe the same structure function measurements at the qualitative level. Furthermore, we find that amplifying the significance of these subtle effects can be achieved by monitoring the χ^2 behaviour in the Q^2 bins more affected by the saturation corrections. The reason is that the total χ^2, such as that reported in Fig. 4.10, is somewhat less informative since the deviations at small-Q are washed out by the good agreement between theory and pseudodata in the rest of the kinematical range of the LHeC summarised in Figs. 3.4 and 4.9.

To conclude this analysis, in Fig. 4.12 we display the comparison between the PDF4LHC15 baseline with the results of the PDF profiling of the LHeC pseudodata for the gluon (left) and quark singlet (right) for $Q = 10\,\mathrm{GeV}$. We show the cases where the pseudodata is generated using DGLAP calculations and where it is partially based on the GBW saturation model (for $x \lesssim 10^{-4}$). We find that the distortion induced by the mismatch between theory and pseudodata in the saturation case is typically larger than the PDF uncertainties expected once the LHeC constraints are taken into account. While of course in a realistic situation such a comparison

would not be possible, the results of Fig. 4.12 show that saturation-induced effects are expected to be larger than the typical PDF errors in the LHeC era, and thus that it should be possible to tell them apart using for example tools such as the pull analysis of Fig. 4.11 or other statistical methods.
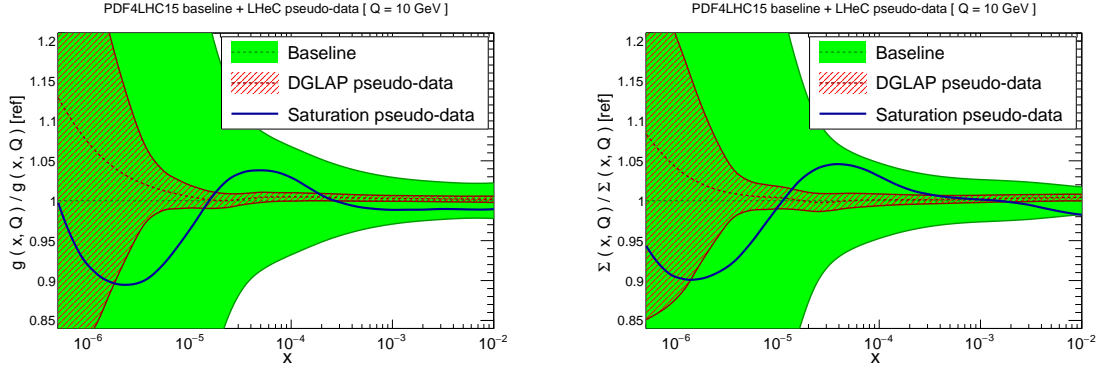
Figure 4.12: Comparison between the PDF4LHC15 baseline (green band) with the results of the profiling of the LHeC pseudodata for the gluon (left) and quark singlet (right) for $Q = 10 \,\mathrm{GeV}$. We show the cases where the pseudodata is generated using DGLAP calculations (red hatched band) and where it is partially based on the GBW saturation model (blue curve).

Summary

Here we have assessed the feasibility of disentangling DGLAP evolution from non-linear effects at the LHeC. By means of a QCD analysis where LHeC pseudodata is generated using a saturation model, we have demonstrated that the LHeC should be possible to identify non-linear effects with large statistical significance, provided their size is the one predicted by current calculations such as the that of [259] that have been tuned to HERA data. A more refined analysis would require to study whether or not small-x BFKL resummation effects can partially mask the impact of non-linear dynamics, though this is unlikely since the main difference arises in their Q^2 scaling. The discovery of non-linear dynamics would represent an important milestone for the physics program of the LHeC, demonstrating the onset of a new gluon-dominated regime of the strong interactions and paving the way for detailed studies of the properties of this new state of matter. Such discovery would have also implications outside nuclear and particle physics, for instance it would affect the theory predictions for the scattering of ultra-high energy neutrinos with matter [261].

4.2.3 Low x and the Longitudinal Structure Function F_L

DIS Cross Section and the Challenge to Access F_L

The inclusive, deep inelastic electron-proton scattering cross section at low $Q^2 \ll M_Z^2$,

$$\frac{Q^4 x}{2\pi\alpha^2 Y_+} \cdot \frac{d^2\sigma}{dx dQ^2} = \sigma_r \simeq F_2(x, Q^2) - f(y) \cdot F_L(x, Q^2) = F_2 \cdot \left(1 - f(y)\frac{R}{1+R}\right) \qquad (4.6)$$

is defined by two proton structure functions, F_2 and F_L, with $y = Q^2/sx$, $Y_+ = 1 + (1-y)^2$ and $f(y) = y^2/Y_+$. The cross section may also be expressed [262] as a sum of two contributions, $\sigma_r \propto (\sigma_T + \epsilon\sigma_L)$, referring to the transverse and longitudinal polarisation state of the exchanged

boson, with ϵ characterising the ratio of the longitudinal to the transverse polarisation. The ratio of the longitudinal to transverse cross sections is termed

$$R(x, Q^2) = \frac{\sigma_L}{\sigma_T} = \frac{F_L}{F_2 - F_L}, \qquad (4.7)$$

which is related to F_2 and F_L as given above. Due to the positivity of the cross sections $\sigma_{L,T}$ one observes that $F_L \leq F_2$. The reduced cross section σ_r, Eq. (4.6), is therefore a direct measure of F_2, apart from a limited region of high y where a contribution of F_L may be sizeable. To leading order, for spin $1/2$ particles, one expected $R = 0$. The initial measurements of R at SLAC [263, 264] showed that R was indeed small, $R \simeq 0.18$, which was taken as evidence for quarks to carry spin $1/2$.

The task to measure F_L thus requires to precisely measure the inclusive DIS cross section near to $y = 1$ and to then disentangle the two structure functions by exploiting the $f(y) = y^2/Y_+$ variation which depends on x, Q^2 and s. By varying the centre-of-mass (cms) beam energy, s, one can disentangle F_2 and F_L obtaining independent measurements at each common, fixed point of x, Q^2. This is particularly challenging not only because the F_L part is small, calling for utmost precision, but also because it requires to measure at high y. The inelasticity $y = 1 - E'/E_e$, however, is large only for scattered electron energies E'_e much smaller than the electron beam energy E_e, for example $E'_e = 2.7\,\mathrm{GeV}$ for $y = 0.9$ at HERA [4]. In the region where E' is a few GeV only, the electron identification becomes a major problem and the electromagnetic ($\pi^0 \to \gamma\gamma$) and hadronic backgrounds, mainly from unrecognised photoproduction, rise strongly.
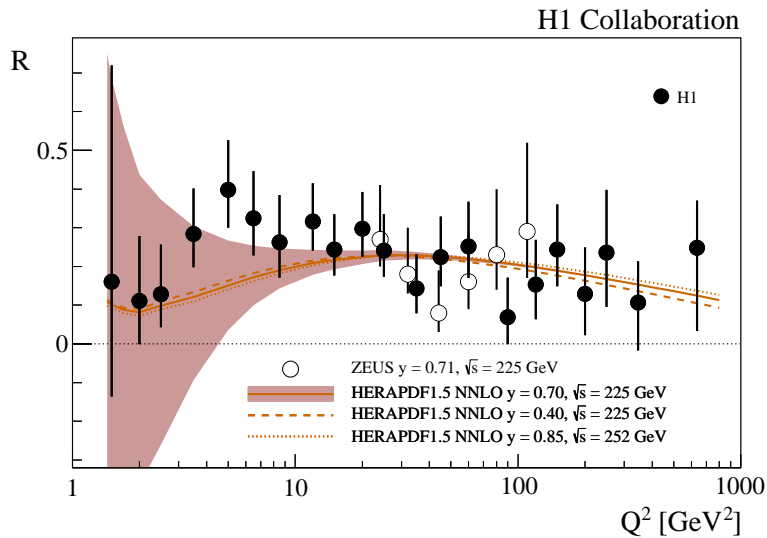
Figure 4.13: Measurement of the structure function ratio $R = F_L/(F_2 - F_L)$ by H1 (solid points) and ZEUS (open circles), from a variation of proton beam energy in the final half year of HERA operation. The curve represents an NNLO QCD fit analysis of the other HERA data. This becomes uncertain for Q^2 below $10\,\mathrm{GeV}^2$ where the Q^2 dependence of F_2 at HERA does not permit an accurate determination of the gluon density which dominates the prediction on F_L.

The history and achievements on F_L, the role of HERA and the prospects as sketched in the CDR of the LHeC, were summarised in detail in [53]. The measurement of F_L at HERA [265] was given very limited time and it collected about 5.9 and $12.2\,\mathrm{pb}^{-1}$ of data at reduced beam

---

[4]The nominal electron beam energy E_e at the LHeC is doubled as compared to HERA. Ideally one would like to vary the proton beam energy in an F_L measurement at the LHeC, which yet would affect the hadron collider operation. In the present study it was therefore considered to lower E_e which may be done independently of the HL-LHC.

energies which were analysed together with about $100\,\mathrm{pb}^{-1}$ at nominal HERA energies. The result may well be illustrated with the data obtained on the ratio $R(x, Q^2)$ shown in Fig. 4.13. To good approximation, $R(x, Q^2)$ is a constant which was determined as $R = 0.23 \pm 0.04$, in good agreement with the SLAC values of $R \simeq 0.18$ despite the hugely extended kinematic range. The rather small variation of R towards small x, at fixed $y = Q^2/sx$, may appear to be astonishing as one observed F_2 to strongly rise towards low x. A constant R of e.g. 0.25 means that $F_2 = (1 + R)F_L/R$ is five times larger than F_L, and that they rise together, as they have a common origin, the rise of the gluon density. This can be understood in approximations to the DGLAP expression of the Q^2 derivative of F_2 and the so-called Altarelli-Martinelli relation of F_L to the parton densities [266, 267], see the discussion in Ref. [53]. The resulting H1 value also obeyed the condition $R \leq 0.37$, which had been obtained in a rigorous attempt to derive the dipole model for inelastic DIS [268].

Parton Evolution at Low x

Parton distributions are to be extracted from experiment as their x dependence and flavour sharing are not predicted in QCD. They acquire a particular meaning through the theoretical prescription of their kinematic evolution. PDFs, as they are frequently used for LHC analyses, are predominantly defined through the now classic DGLAP formalism, in which the Q^2 dependence of parton distributions is regulated by splitting functions while the DIS cross section, determined by the structure functions, is calculable by folding the PDFs with coefficient functions. Deep inelastic scattering is known to be the most suited process to extract PDFs from the experiment, for which the HERA collider has so far delivered the most useful data. Through factorisation theorems the PDFs are considered to be universal such that PDFs extracted in ep DIS shall be suited to describe for example Drell-Yan scattering cross sections in pp at the LHC. This view has been formulated to third order pQCD already and been quite successful in the interpretation of LHC measurements, which by themselves also constrain PDFs in parton-parton scattering sub-processes.

As commented in Sec. 4.2.1, the question has long been posed about the universal validity of the DGLAP formalism, especially for the region of small Bjorken x where logarithms $\propto \ln(1/x)$ become very sizeable. This feature of the perturbation expansion is expected to significantly modify the splitting functions. This in turn changes the theory underlying the physics of parton distributions, and predictions for the LHC and its successor will correspondingly have to be altered. This mechanism, for an equivalent Q^2 of a few GeV^2, is illustrated in Fig. 4.14, taken from Ref. [251]. It shows the x dependence of the gluon-gluon and the quark-gluon splitting functions, P_{gg} and P_{qg}, calculated in DGLAP QCD. It is observed that at NNLO P_{gg} strongly decreases towards small x, becoming smaller than P_{qg} for x below 10^{-4}. Resummation of the large $\ln(1/x)$ terms, see Ref. [251], here performed to next-to-leading log x, restores the dominance of the gg splitting over the qg one. Consequently, the gluon distribution in the resummed theory exceeds the one derived in pure DGLAP. While this observation has been supported by the HERA data, it yet relies on limited kinematic coverage and precision. The LHeC will examine this in detail, at a hugely extended range and is thus expected to resolve the long known question about the validity of the BFKL evolution and the transition from DGLAP to BFKL as x decreases while Q^2 remains large enough for pQCD to apply.
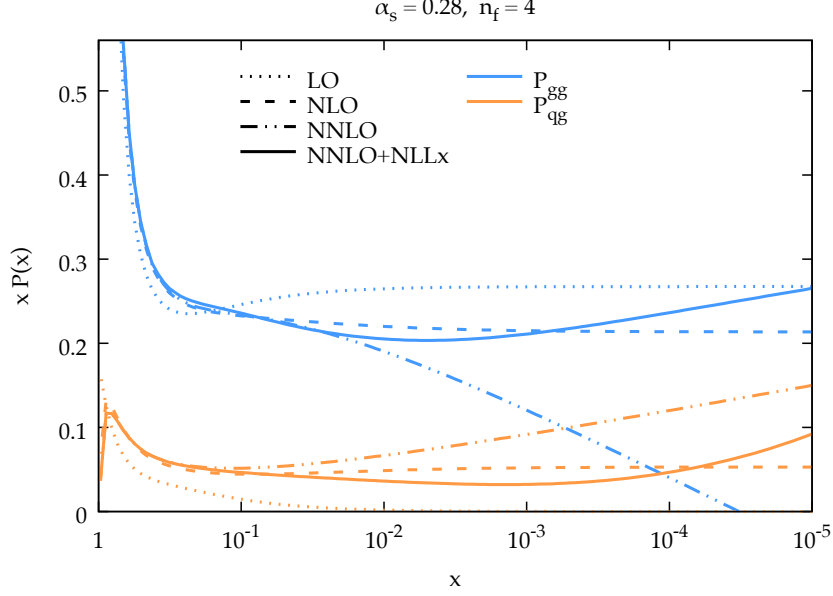
Figure 4.14: Calculation of splitting functions P_{gg} (top, blue) and P_{qg} (bottom, brown) in resummed NNLO (solid) as compared to non-resummed calculations at LO (dotted), NLO (dashed) and NNLO (dashed-dotted) as functions of x for $n_f = 4$ at a large value of α_s corresponding to a Q^2 of a few GeV^2, from Ref. [251]. The resummed calculation is seen to restore the dominance of P_{gg} over P_{qg} as x becomes small (towards the right side), which is violated at NNLO.

Kinematics of Higgs Production at the HL-LHC

The clarification of the evolution and the accurate and complete determination of the parton distributions is of direct importance for the LHC. This can be illustrated with the kinematics of Higgs production at HL-LHC which is dominated by gluon-gluon fusion. With the luminosity upgrade, the detector acceptance is being extended into the forward region to pseudorapidity values of $|\eta| = 4$, where $\eta = \ln \tan \theta/2$ is a very good approximation of the rapidity. In Drell-Yan scattering of two partons with Bjorken x values of $x_{1,2}$ these are related to the rapidity via the relation $x_{1,2} = \exp(\pm\eta) \cdot M/\sqrt{s}$ where $\sqrt{s} = 2E_p$ is the cms energy and M the mass of the produced particle. It is interesting to see that $\eta = \pm 4$ corresponds to $x_1 = 0.5$ and $x = 0.00016$ for the SM Higgs boson of mass $M = 125$ GeV. Consequently, Higgs physics at the HL-LHC will depend on understanding PDFs at high x, a challenge resolved by the LHeC too, and on clarifying the evolution at small x. At the FCC-hh, in its 100 TeV energy version, the small x value for $\eta = 4$ will be as low as $2 \cdot 10^{-5}$. Both the laws of QCD and the resulting phenomenology of particle production at the HL-LHC and its successor demand to clarify the evolution of the parton contents at small x as a function of the resolution scale Q^2 [269–271]. This concerns in particular the unambiguous, accurate determination of the gluon distribution, which dominates the small-x parton densities and as well the production of the Higgs boson in pp scattering.

Indications for Resummation in H1 F_L Data

The simultaneous measurement of the two structure functions F_2 and F_L is the cleanest way to establish new parton dynamics at low x. This holds because their independent constraints on the dominating gluon density at low x ought to lead to consistent results. In other words, one may constrain all partons with a complete PDF analysis of the inclusive cross section in

the kinematic region where its F_L part is negligible and confront the F_L measurement with this result. A significant deviation from F_L data signals the necessity to introduce new, non-DGLAP physics in the theory of parton evolution, especially at small x. The salient value of the F_L structure function results from its inclusive character enabling a clean theoretical treatment as has early on been recognised [266, 267]. This procedure has recently been illustrated [251] using the H1 data on F_L [272] which are the only accurate data from HERA at smallest x. The
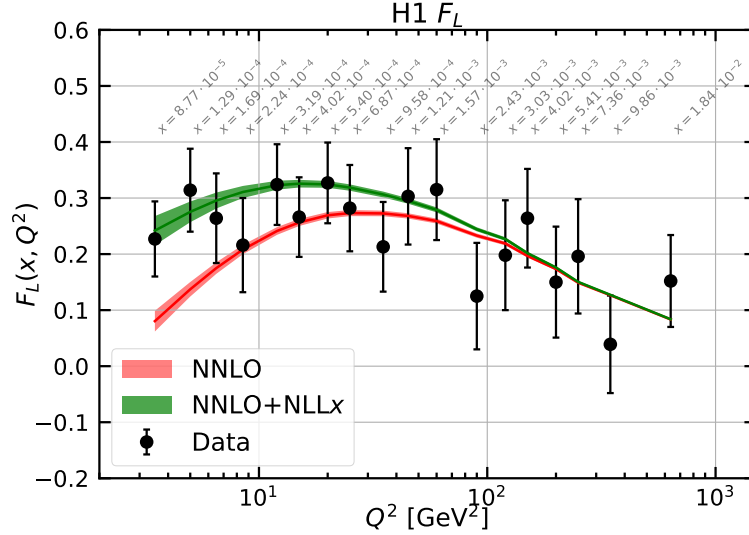
Figure 4.15: Measurement of the longitudinal structure function F_L, obtained as an average results over a number of x dependent points at fixed Q^2, plotted vs Q^2 with the corresponding x values indicated in grey. Red curve: NNLO fit to the H1 cross section data; green curve: NNLO fit including NLLx resummation, from Ref. [251].

result is shown in Fig. 4.15. One observes the trend described above: the resummed prediction is higher than the pure NNLO curve, and the description at smallest x, below $5 \cdot 10^{-4}$, appears to be improved. The difference between the two curves increases as x decreases. However, due to the peculiarity of the DIS kinematics, which relates x to Q^2/sy, one faces the difficulty of Q^2 decreasing with x at fixed s for large $y \geq 0.6$, which is the region of sensitivity to F_L. Thus one not only wishes to improve substantially the precision of the F_L data but also to increase substantially s in order to avoid the region of non-perturbative behaviour while testing theory at small x. This is the double and principal advantage which the LHeC offers - a much increased precision and more than a decade of extension of kinematic range.

The Longitudinal Structure Function at the LHeC

Following the method described above, inclusive cross section data have been simulated for $E_p = 7\,\mathrm{TeV}$ and three electron beam energies E_e of 60, 30 and 20 GeV. The assumed integrated luminosity values are 10, 1 and again $1\,\mathrm{fb}^{-1}$, respectively. These are about a factor of a hundred larger than the corresponding H1 luminosities. At large y, the kinematics is best reconstructed using the scattered electron energy, E'_e, and polar angle, θ_e. The experimental methods to calibrate the angular and energy measurements are described in [265]. For the present study similar results are assumed: for E'_e a scale uncertainty of 0.5 % at small y (compared to 0.2 % with H1) rising linearly to 1.2 %, in the range of $y = 0.4$ to 0.9. For the polar angle, given the superior quality of the anticipated LHeC Silicon tracker as compared to the H1 tracker,

it is assumed that θ_e may be calibrated to $0.2\,\mathrm{mrad}$, as compared to $0.5\,\mathrm{mrad}$ at H1. The residual photo-production background contamination is assumed to be $0.5\,\%$ at largest y, twice better than with H1. There is further an assumption made on the radiative corrections which are assumed to be uncertain to $1\,\%$ and treated as a correlated error. The main challenge is to reduce the uncorrelated uncertainty, which here was varied between 0.2 and $0.5\,\%$. This is about ten to three times more accurate than the H1 result which may be a reasonable assumption: the hundred fold increase in statistics sets a totally different scale to the treatment of uncorrelated uncertainties, as from imperfect simulations, trigger efficiency or Monte Carlo statistics. It is very difficult to transport previous results to the modern and future conditions. It could, however, be an important fix point if one knows that the most precise measurement of Z boson production by ATLAS at the LHC had a total systematic error of just $0.5\,\%$ [273].
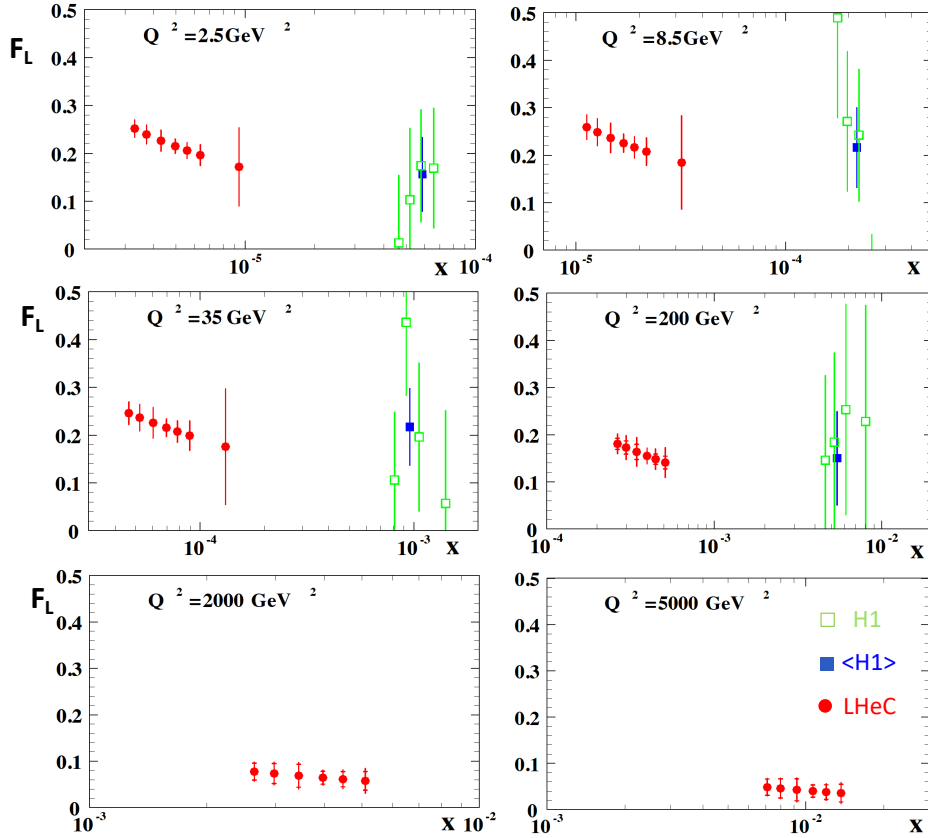
Figure 4.16: H1 measurement and LHeC simulation of data on the longitudinal structure function $F_L(x, Q^2)$. Green: Data by H1, for selected Q^2 intervals from Ref. [272]; Blue: Weighted average of the (green) data points at fixed Q^2; Red: Simulated data from an F_L measurement at the LHeC with varying beam energy, see text. The H1 error bars denote the total measurement uncertainty. The LHeC inner error bars represent the data statistics, visible only for $Q^2 \geq 200\,\mathrm{GeV}^2$, while the outer error bars are the total uncertainty. Since the F_L measurement is sensitive only at high values of inelasticity, $y = Q^2/sx$, each Q^2 value is sensitive only to a certain limited interval of x values which increase with Q^2. Thus each panel has a different x axis. The covered x range similarly varies with s, i.e. H1 x values are roughly twenty times larger at a given Q^2. There are no H1 data for high Q^2, beyond $1000\,\mathrm{GeV}^2$, see Ref. [272].

The method here used is that of a simple straight-line fit of $\sigma_r = F_2 - f(y)F_L$ (Eq. (4.6)), in which F_L is obtained as the slope of the $f(y)$ dependence [5]. The predictions for F_2 and F_L were

---

[5] Better results were achieved by H1 using a χ^2 minimisation technique, see Ref. [274], which for the rough

obtained using LO formulae for the PDF set of MSTW 2008. In this method any common factor does not alter the absolute uncertainty of F_L. This also implies that the estimated absolute error on F_L is independent of whether F_L is larger or smaller than here assumed. For illustration, F_L was scaled by a factor of two. Since $f(y) \propto y^2$, the accuracy is optimised with a non-linear choice of lowered beam energies. The fit takes into account cross section uncertainties and their correlations, calculated numerically following [58, 275], by considering each source separately and adding the results of the various correlated sources to one correlated systematic error which is added quadratically to the statistical and uncorrelated uncertainties to obtain one total error.

The result is illustrated in Fig. 4.16 presenting the x-dependent results, for some selected Q^2 values, of both H1, with their average over x, and the prospect LHeC results. It reflects the huge extension of kinematic range, towards low x and high Q^2 by the LHeC as compared to HERA. It also illustrates the striking improvement in precision which the LHeC promises to provide. The F_L measurement will cover an x range from $2 \cdot 10^{-6}$ to above $x = 0.01$. Surely, when comparing with Fig. 4.15, one can safely expect that any non-DGLAP parton evolution would be discovered with such data, in their combination with a very precise F_2 measurement.

A few comments are in order on the variation of the different error components with the kinematics, essentially Q^2 since the whole F_L sensitivity is restricted to high y which in turn for each Q^2 defines a not wide interval of x values covered. One observes in Fig. 4.16 that the precision is spoiled towards large $x \propto 1/y$, see e.g. the result for $Q^2 = 8.5\,\mathrm{GeV}^2$. The assumptions on the integrated luminosity basically define a Q^2 range for the measurement. For example, the statistical uncertainty for $Q^2 = 4.5\,\mathrm{GeV}^2$ and $x = 10^{-5}$, a medium x value at this Q^2 interval, is only $0.6\,\%$ (or 0.001 in absolute for $F_L = 0.22$). At $Q^2 = 2000\,\mathrm{GeV}^2$ it rises to $21\,\%$ (or 0.012 for $F_L = 0.064$). One thus can perform the F_L measurement at the LHeC, with a focus on only small x, with much less luminosity than the $1\,\mathrm{fb}^{-1}$ here used. The relative size of the various systematic error sources also varies considerably, which is due to the kinematic relations between angles and energies and their dependence on x and Q^2. This is detailed in [58]. It implies, for example, that the $0.2\,\mathrm{mrad}$ polar angle scale uncertainty becomes the dominant error at small Q^2, which is the backward region where the electron is scattered near the beam axis in the direction of the electron beam. For large Q^2, however, the electron is more centrally scattered and the θ_e calibration requirement may be more relaxed. The E'_e scale uncertainty has a twice smaller effect than that due to the θ_e calibration at lowest Q^2 but becomes the dominant correlated systematic error source at high Q^2. The here used overall assumptions on scale uncertainties are therefore only rough first approximations and would be replaced by kinematics and detector dependent requirements when this measurement may be pursued. These could also exploit the cross calibration opportunities which result from the redundant determination of the inclusive DIS scattering kinematics through both the electron and the hadronic final state. This had been noted very early at HERA times, see Ref. [55, 57, 275] and was worked out in considerable detail by both H1 and ZEUS using independent and different methods. A feature used by H1 in their F_L measurement includes a number of decays such as $\pi^0 \to \gamma\gamma$ and $J/\psi \to e^+ e^-$ for calibrating the low energy measurement or $K_s^0 \to \pi^+ \pi^-$ and $\Lambda \to p\pi$ for the determination of tracker scales, see Ref. [265].

It is obvious that the prospect to measure F_L as presented here is striking. For nearly a decade, Guido Altarelli was a chief theory advisor to the development of the LHeC. In 2011, he publishes an article [274], in honour of Mario Greco, about *The Early Days of QCD (as seen from Rome)* in which he describes one of his main achievements [266], and persistent irritation, regarding the longitudinal structure function, F_L, and its measurement: ... *The present data, recently*

<hr/>

estimate on the projected F_L uncertainty at the LHeC has not been considered.

obtained by the H1 experiment at DESY, are in agreement with our [!this] LO QCD prediction but the accuracy of the test is still far from being satisfactory for such a basic quantity. The LHeC developments had not been rapid enough to let Guido see results of much higher quality on F_L with which the existence of departures from the DGLAP evolution, to high orders pQCD, may be expected to most safely be discovered.

4.2.4 Associated jet final states at low x

The dynamical effects from resummation or nonlinear corrections which we have discussed above can arise at the LHeC not only in the inclusive structure functions, as we have illustrated so far, but also in more exclusive observables describing the structure of the jet final states associated to low-x DIS.

Baseline predictions for jet final states in DIS are obtained from perturbative finite-order calculations (see e.g. [201, 276] for third-order calculations), supplemented by parton-shower Monte Carlo generators for realistic event simulation (as e.g. in [200]). But owing to the large phase space opening up at LHeC energies and the complex kinematics possibly involving multiple hard scales, jet events are potentially sensitive to soft-gluon coherence effects of initial-state radiation [223, 277–279], which go beyond finite-order perturbative evaluations and collinear parton showers, and show up as logarithmic $x \to 0$ corrections to all orders of perturbation theory. These corrections can be resummed, and combined with large-x contributions, via CCFM exclusive evolution equations [223, 277], and affect the structure of jet multiplicities and angular jet correlations [279] as well as heavy quark distributions [278]. Observables based on forward jets, transverse energy flow, angle and momentum correlations constitute probes of low-x dynamics in DIS final states [280–282]. Phenomenological studies started with HERA [283–285] and will continue with the LHeC.

Computational tools are being developed to address the structure of multi-jet final states by including low-x dynamical effects. These include CCFM Monte Carlo tools [286, 287], off-shell matrix element parton-level generators [288, 289], BFKL Monte Carlo generators [290–292]. Fig. 4.17 gives an example of transverse momentum correlations in DIS di-jet and three-jet final states computed with the Monte Carlo [286], compared with the measurements [293].

Furthermore, exclusive parton branching formalisms are being proposed in which not only gluon distributions but also quark distributions are treated at unintegrated level in transverse momentum [295–297]. This is instrumental in connecting low-x approaches with DGLAP approaches to parton showers beyond leading order [298, 299]. Applications of these new developments have so far been mostly carried out for final states in hadron-hadron collisions, while extensions to lepton-hadron collisions are underway. Fig. 4.18 gives examples of transverse momentum spectra in low-mass Drell-Yan lepton pair production computed in [300] by the parton branching (PB) method [296], compared with the measurements [301] and [302].

4.2.5 Relation to Ultrahigh Energy Neutrino and Astroparticle physics

The small-x region probed by the LHeC is also very important in the context of ultra-high energy neutrino physics and astroparticle physics. Highly energetic neutrinos provide a unique window into the Universe, due to their weak interaction with matter, for a review see for example [303]. They can travel long distances from distant sources, undeflected by the magnetic fields inside and in between galaxies, and thus provide complementary information to cosmic rays, gamma
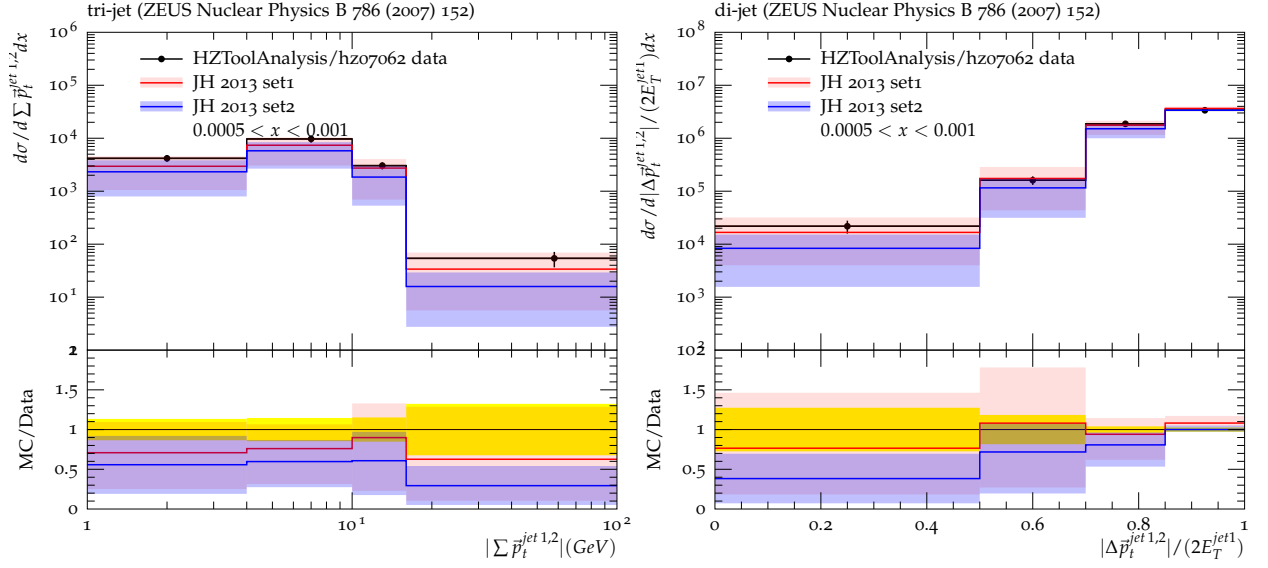
Figure 4.17: Momentum correlations in DIS multi-jet final states at low x computed from the CCFM Monte Carlo [286] with TMD parton densities JH2013 [294], compared with the measurements [293]: (left) tri-jets; (right) di-jets.

rays and gravitational wave signals. The IceCube observatory on Antarctica [304] is sensitive to neutrinos with energies from $100\,\mathrm{GeV}$ up (above $10\,\mathrm{GeV}$ with the use of their Deep Core detector). Knowledge about low-x physics becomes indispensable in two contexts: neutrino interactions and neutrino production. At energies beyond the TeV scale the dominant part of the cross section is due to the neutrino DIS CC and NC interaction with the hadronic targets [303].

In Fig. 4.19 we show the charged current neutrino cross section as a function of the neutrino energy for an isoscalar target (in the laboratory frame where the target is at rest), using a calculation [305] based on the resummed model in [228]. We see that at energies below $\sim 50\,\mathrm{TeV}$ the cross section grows roughly linearly with energy, and in this region it is dominated by contributions from the large-x valence region. Beyond that energy the neutrino cross section grows slower, roughly as a power $\sim E_\nu^\lambda$ with $\lambda \simeq 0.3$. This high energy behaviour is totally controlled by the small-x behaviour of the parton distributions. The dominance of the sea contributions to the cross section is clearly seen in Fig. 4.19. To illustrate more precisely the contributing values of x and Q^2, in Fig. 4.20 we show the differential cross section for the CC interaction $xQ^2 d\sigma^{CC}/dx dQ^2$ for a neutrino energy $E_\nu = 10^{11}$ GeV (in the frame where the hadronic target is at rest). We see a clear peak of the cross section at roughly a value of $Q^2 = M_W^2$ and an x value

$$x \simeq \frac{M_W^2}{2 M E_\nu} \, , \tag{4.8}$$

which in this case is about 3×10^{-8}. We note that IceCube extracted the DIS cross section from neutrino observations [306] in the region of neutrino energies $10 - 1000\,\mathrm{TeV}$. The extraction is consistent, within the large error bands, with the predictions based on the QCD, like those illustrated in Fig. 4.19. It is important to note that the IceCube extraction is limited to these energies by the statistics due to the steeply falling flux of neutrinos at high energy. We thus see that the neutrino interaction cross section at high energies is sensitive to a region which is currently completely unconstrained by existing precision DIS data.

Another instance where dynamics at low x are crucial for neutrino physics is in understanding the mechanisms of ultra-high energy neutrino production. The neutrinos are produced in
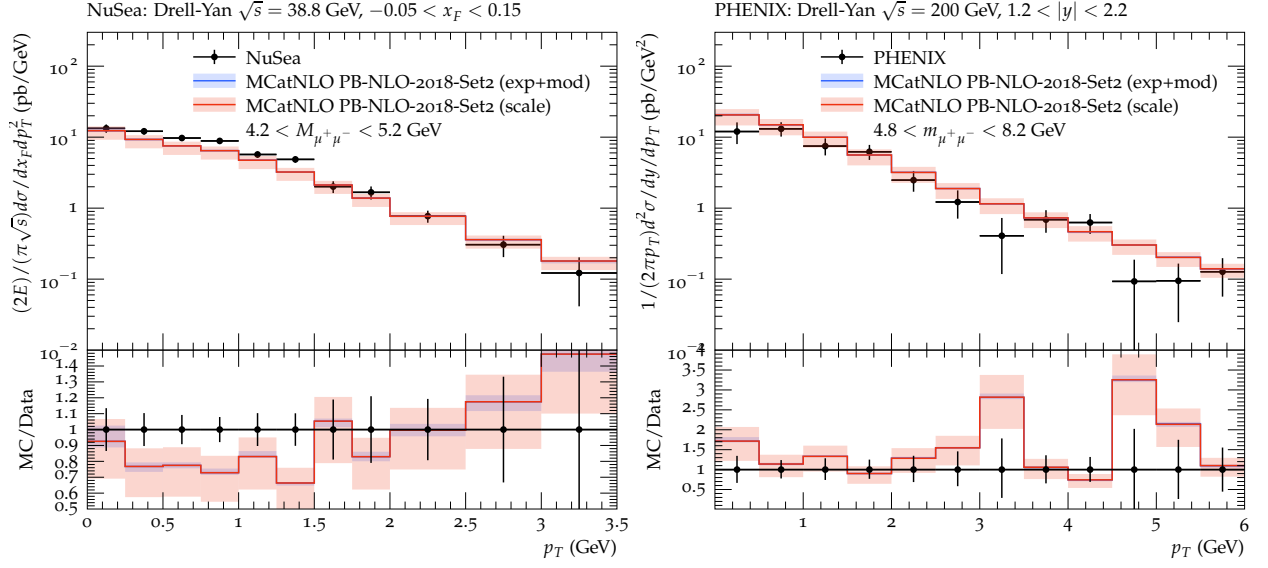
Figure 4.18: Transverse momentum spectra in low-mass Drell-Yan lepton pair production [300] from the parton branching (PB) method, compared with (left) NuSea measurements [301] and (right) PHENIX measurements [302].
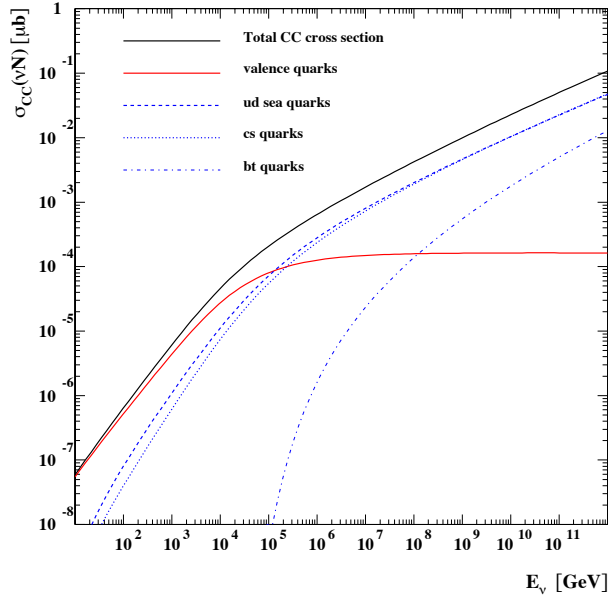
Figure 4.19: Charged current cross section for the neutrino - nucleon interaction on a isoscalar target as a function of neutrino energy. The total CC cross section is broken down into several contributions due to valence, up-down,strange-charm and bottom-top quarks. The calculation was based on Ref. [305].

interactions which involve hadrons, either in γp or in pp interactions. They emerge as decay products of pions, kaons and charmed mesons, and possibly beauty mesons if the energy is high enough [307]. For example, in the atmosphere neutrinos are produced in the interactions of the highly energetic cosmic rays with nitrogen and oxygen nuclei. The lower energy part of the atmospheric neutrino spectrum, up to about 100 TeV or so, is dominated by the decay of pions and kaons. This is called the conventional atmospheric neutrino flux. Above that energy the
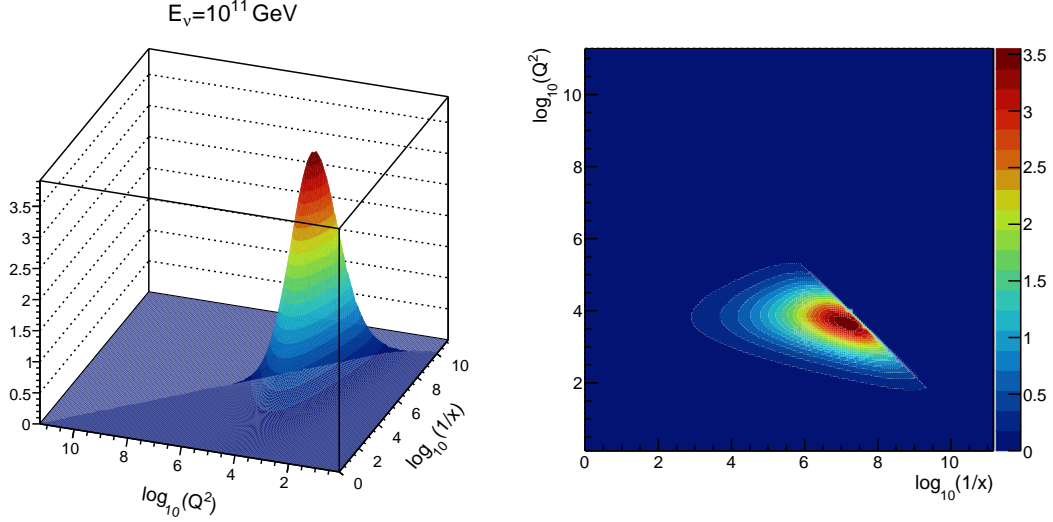
Figure 4.20: Differential charged current neutrino cross section $10^5 \cdot x Q^2 d\sigma^{CC}/dx dQ^2$ [nb] as a function of Q^2 and x for fixed neutrino energy $E_\nu = 10^{11}$ GeV. Left: surface plot; right: contour plot.

neutrino flux is dominated by the decay of the shorter-lived charmed mesons. Thus, this part of the neutrino flux is called the prompt-neutrino flux. The reason why the prompt-neutrino flux dominates at high energies is precisely related to the life-time of the intermediate mesons (and also baryons like Λ_c). The longer lived pions and kaons have a high probability of interacting before they decay, thus degrading their energy and leading to a steeply falling neutrino flux. The cross section for the production of charmed mesons is smaller than that for pions and kaons, but the charmed mesons $D^\pm, D^0, D_s$ and baryon Λ_c live shorter than pions and kaons, and thus decay prior to any interaction. Thus, at energies about 100 TeV the prompt neutrino flux will dominate over the conventional atmospheric neutrino flux. Therefore, the knowledge of this part of the spectrum is essential as it provides a background for the sought-after astrophysical neutrinos [308]. Charmed mesons in high energy hadron-hadron interactions are produced through gluon-gluon fusion into $c\bar{c}$ pairs, where one gluon carries rather large x and the other one carries very small x. Since the scales are small, of the order of the charm masses, the values of the longitudinal momentum fractions involved are also very small and thus the knowledge of the parton distributions in this region is essential [309]. The predictions for the prompt neutrino flux become extremely sensitive to the behaviour of the gluon distribution at low x (and low Q^2), where novel QCD phenomena like resummation as well as gluon saturation are likely to occur [310].

In addition, the LHeC measurements could help pin down one enduring mystery - what is the composition of the most energetic cosmic rays? The best measurements of composition at energies above 10^{18} eV are based on studies of how showers develop in the atmosphere. The main observable is the depth (in the atmosphere) of shower maximum - so called $X_{\max}$. The absolute value of $X_{\max}$ and the elongation rate $dX_{\max}/dE$ of cosmic-rays depends on the assumed details of the hadronic physics. A change in the elongation rate, observed by the Auger observatory has often been interpreted as a signature for composition change (i.e. from mostly protons to mostly iron) with increasing energy [311, 312]. However, new hadronic phenomena, such as a color glass condensate, might also lead to a change in the elongation rate. Seeing saturation in a Large Hadron electron Collider would help select between these two options [313, 314].

Finally, the low-x dynamics will become even more important at the HL-LHC and FCC hadron

colliders, see Sect. 9.6. With increasing centre-of-mass energy, hadron colliders will probe values of x previously unconstrained by HERA data. It is evident that all the predictions in pp interactions at high energy will heavily rely on the PDF extrapolations to the small x region which carry large uncertainties. As discussed in detail in this Section, resummation will play an increasingly important role in the low x region of PDFs. A precision DIS machine is thus an indispensable tool for constraining the QCD dynamics at low x with great precision as well as for providing complementary information and independent measurements to hadronic colliders.

4.3 Diffractive Deep Inelastic Scattering at the LHeC

4.3.1 Introduction and Formalism

An important discovery of HERA was the observation of a large ($\sim 10\,\%$) fraction of diffractive events in DIS [315, 316]. In these events the proton stays intact or dissociates into a state with the proton quantum numbers, despite undergoing a violent, highly energetic collision, and is separated from the rest of the produced particles by a large rapidity gap. In a series of ground-breaking papers (see Ref. [317] for a review), the HERA experiments determined the deep inelastic structure of the t-channel exchange in these events in the form of diffractive parton densities.

The precise measurement of diffraction in DIS is of great importance for our understanding of the strong interaction. First, the mechanism through which a composite strongly interacting object interacts perturbatively while keeping colour neutrality [318–324] offers information about the confinement mechanism. Second, diffraction is known to be highly sensitive to the low-x partonic content of the proton and its evolution with energy [325–328] and it therefore has considerable promise to reveal deviations from standard linear evolution through higher twist effects or, eventually, non-linear dynamics. Third, it allows checks of basic theory predictions such as the relation between diffraction in ep scattering and nuclear shadowing [329]. Finally, the accurate extraction of diffractive parton distribution functions facilitates tests of the range of validity of perturbative factorisation [330–332]. The potential studies of inclusive diffraction that would be possible at the LHeC are presented here (see Ref. [333] for further details). They substantially extend the kinematic coverage of the HERA analyses, leading to much more detailed tests of theoretical ideas than have been possible hitherto. Although we work here at NLO of QCD, it is worth noting that similar analyses in the HERA context have recently extended to NNLO [334].

In Fig. 4.21 we show a diagram depicting a neutral current diffractive deep inelastic event. Charged currents could also be considered and were measured at HERA [335] but with large statistical uncertainties and in a very restricted region of phase space. Although they could be measured at both the LHeC and the FCC-eh with larger statistics and more extended kinematics, in this first study we limit ourselves to neutral currents. The incoming electron or positron, with four momentum k, scatters off the proton, with incoming four momentum p, and the interaction proceeds through the exchange of a virtual photon with four-momentum q. The kinematic variables for such an event include the standard deep inelastic variables

$$Q^2 = -q^2 \,, \qquad x = \frac{-q^2}{2p \cdot q} \,, \qquad y = \frac{p \cdot q}{p \cdot k} \,, \tag{4.9}$$

where Q^2 describes the photon virtuality, x is the Bjorken variable and y the inelasticity of the process. In addition, the variables

$$s = (k + p)^2 \,, \qquad W^2 = (q + p)^2 \,, \tag{4.10}$$
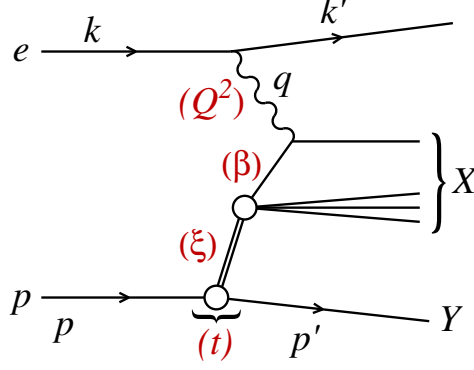
Figure 4.21: A diagram of a diffractive NC event in DIS together with the corresponding variables, in the one-photon exchange approximation. The large rapidity gap is between the system X and the scattered proton (or its low mass excitation) Y.

are the electron-proton centre-of-mass energy squared and the photon-proton centre-of-mass energy squared, respectively. A distinguishing feature of the diffractive event $ep \to eXY$ is the presence of the large rapidity gap between the diffractive system, characterised by the invariant mass M_X and the final proton (or its low-mass excitation) Y with four momentum p'. In addition to the standard DIS variables listed above, diffractive events are also characterised by an additional set of variables defined as

$$t = (p - p')^2, \qquad \xi = \frac{Q^2 + M_X^2 - t}{Q^2 + W^2}, \qquad \beta = \frac{Q^2}{Q^2 + M_X^2 - t}. \qquad (4.11)$$

In the above t is the squared four-momentum transfer at the proton vertex, ξ (alternatively denoted by x_{IP}) can be interpreted as the momentum fraction of the *diffractive exchange* with respect to the hadron, and β is the momentum fraction of the parton with respect to the diffractive exchange. The two momentum fractions combine to give Bjorken-x, $x = \beta\xi$.

The kinematic range in (β, Q^2, ξ) that we consider at the LHeC is restricted by the following cuts:

- $Q^2 \geq 1.8\,\text{GeV}^2$: due to the fact that the initial distribution for the DGLAP evolution is parameterised at $\mu_0^2 = 1.8\,\text{GeV}^2$. The renormalisation and factorisation scales are taken to be equal to Q^2.

- $\xi < 0.4$: constrained by physical and experimental limitations. This rather high ξ value is an experimental challenge and physically enters the phase-space region where the Pomeron contribution should become negligible compared with sub-leading exchanges. Within the two-component model, see Eq. (4.16) below, at high ξ the cross section is dominated by the secondary Reggeon contribution, which is poorly fixed by the HERA data. We present this high ξ (> 0.1) region for illustrative purpose and for the sake of discussion of the fit results below.

In Fig. 4.22 the accessible kinematic range in (x, Q^2) is shown for three machines: HERA, LHeC and FCC-eh. For the LHeC design the range in x is increased by a factor ~ 20 over HERA and the maximum available Q^2 by a factor ~ 100. The FCC-eh machine would further increase this range with respect to LHeC by roughly one order of magnitude in both x and Q^2. We also show the EIC kinematic region for comparison. The three different machines are clearly complementary in their kinematic coverage, with LHeC and EIC adding sensitivity at lower and higher x than HERA, respectively.
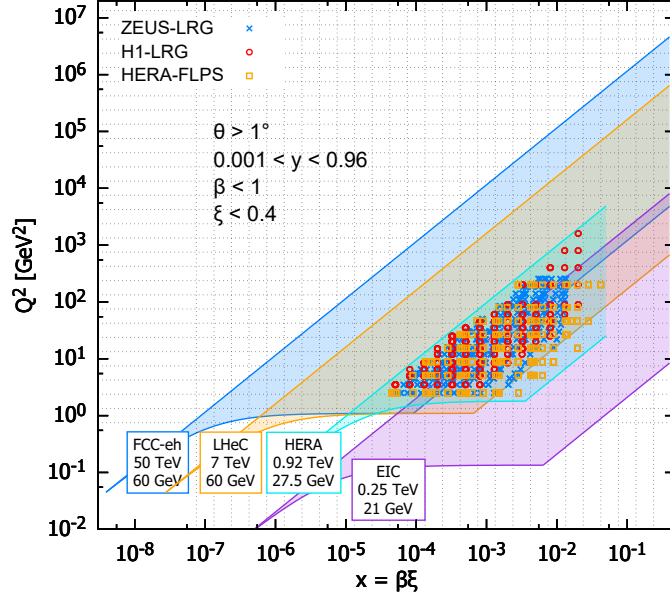
Figure 4.22: Kinematic phase space for inclusive diffraction in (x, Q^2) for the EIC (magenta region), the LHeC (orange region) and the FCC-eh (dark blue region) as compared with the HERA data (light blue region, ZEUS-LRG [336], H1-LRG [337], HERA-FLPS [338]). The acceptance limit for the electron in the detector design has been assumed to be $1°$, and we take $\xi < 0.4$.

In Fig. 4.23 the phase space in (β, Q^2) is shown for fixed ξ for the LHeC. The LHeC machine probes very small values of ξ, reaching 10^{-4} with a wide range of β. Of course, the ranges in β and ξ are correlated since $x = \beta\xi$. Therefore, for small values of ξ only large values of β are accessible while for large ξ the range in β extends to very small values.

Diffractive cross sections in the neutral current case can be presented in the form of the reduced cross sections integrated over t [335]:

$$\frac{d^3\sigma^{\mathrm{D}}}{d\xi d\beta dQ^2} = \frac{2\pi\alpha_{\mathrm{em}}^2}{\beta Q^4} Y_+ \, \sigma_{\mathrm{red}}^{\mathrm{D}(3)} \,, \tag{4.12}$$

where $Y_+ = 1 + (1-y)^2$ and the reduced cross sections can be expressed in terms of two diffractive structure functions F_2^{D} and $F_{\mathrm{L}}^{\mathrm{D}}$. In the one-photon approximation, the relations are

$$\sigma_{\mathrm{red}}^{\mathrm{D}(3)} = F_2^{\mathrm{D}(3)}(\beta, \xi, Q^2) - \frac{y^2}{Y_+} F_{\mathrm{L}}^{\mathrm{D}(3)}(\beta, \xi, Q^2) \,. \tag{4.13}$$

In this analysis we neglect Z^0 exchange, though it should be included in future studies.

Both $\sigma_{\mathrm{red}}^{\mathrm{D}(3)}$ and $\sigma_{\mathrm{red}}^{\mathrm{D}(4)}$ have been measured at the HERA collider [315, 316, 335–337, 339–342] and used to obtain QCD-inspired parameterisations.

The standard perturbative QCD approach to diffractive cross sections is based on collinear factorisation [330–332]. It was demonstrated that, similarly to the inclusive DIS cross section, the diffractive cross section can be written, up to terms of order $\mathcal{O}(\Lambda^2/Q^2)$, where Λ is the hadronic scale, in a factorised form

$$d\sigma^{ep \to eXY}(\beta, \xi, Q^2, t) = \sum_i \int_\beta^1 dz \, d\hat{\sigma}^{ei}\left(\frac{\beta}{z}, Q^2\right) f_i^{\mathrm{D}}(z, \xi, Q^2, t) \,, \tag{4.14}$$
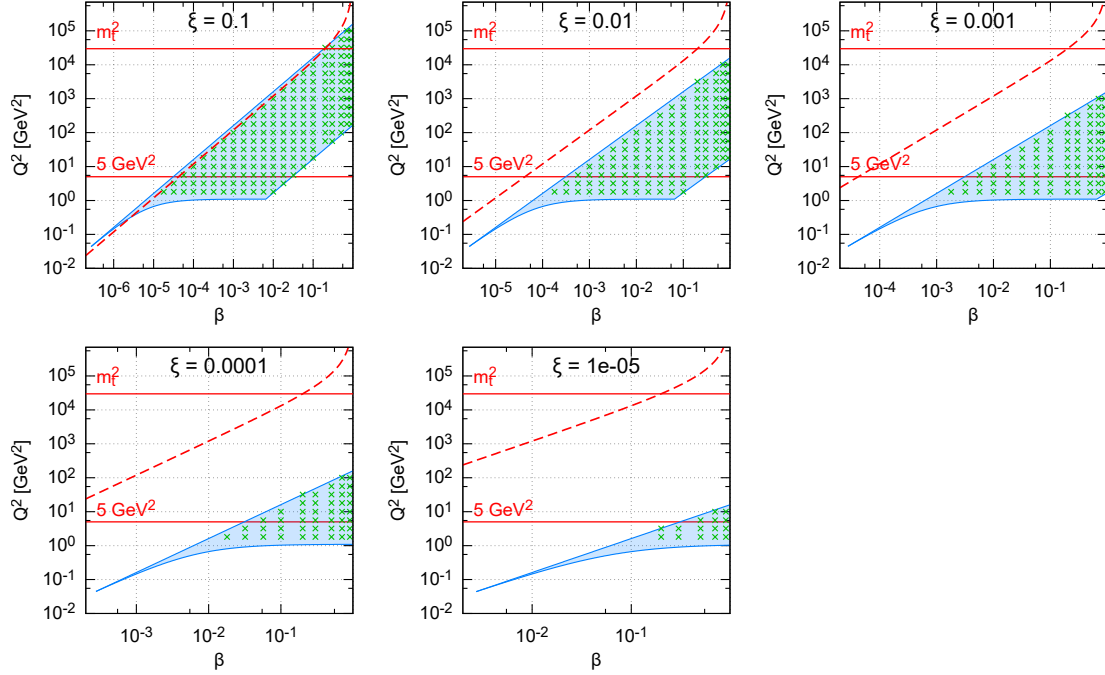
Figure 4.23: Kinematic phase space for inclusive diffraction in (β, Q^2) for fixed values of ξ for the LHeC design. The horizontal lines indicate correspondingly, $Q^2 = 5$ GeV^2, the lowest data value for the DGLAP fit performed in this study and m_t^2 the 6-flavour threshold. The dashed line marks the kinematic limit for $t\bar{t}$ production.

where the sum is performed over all parton flavours (gluon, d-quark, u-quark, etc.). The hard scattering partonic cross section $d\hat{\sigma}^{ei}$ can be computed perturbatively in QCD and is the same as in the inclusive deep inelastic scattering case. The long distance part f_i^{D} corresponds to the diffractive parton distribution functions, which can be interpreted as conditional probabilities for partons in the proton, provided the proton is scattered into the final state system Y with specified 4-momentum p'. They are evolved using the DGLAP evolution equations [343–346] similarly to the inclusive case. The analogous formula for the t-integrated structure functions reads

$$F_{2/\mathrm{L}}^{\mathrm{D}(3)}(\beta, \xi, Q^2) = \sum_i \int_\beta^1 \frac{dz}{z} \, C_{2/\mathrm{L},i}\Big(\frac{\beta}{z}\Big) \, f_i^{\mathrm{D}(3)}(z, \xi, Q^2) \, , \tag{4.15}$$

where the coefficient functions $C_{2/\mathrm{L},i}$ are the same as in inclusive DIS.

Fits to the diffractive structure functions usually [335, 341] parameterise the diffractive PDFs in a two component model, which is a sum of two diffractive exchange contributions, $I\!\!P$ and $I\!\!R$:

$$f_i^{\mathrm{D}(4)}(z, \xi, Q^2, t) = f_{I\!\!P}^p(\xi, t) \, f_i^{I\!\!P}(z, Q^2) + f_{I\!\!R}^p(\xi, t) \, f_i^{I\!\!R}(z, Q^2) \, . \tag{4.16}$$

For both of these terms proton vertex factorisation is separately assumed, meaning that the diffractive exchange can be interpreted as colourless objects called a *Pomeron* or a *Reggeon* with parton distributions $f_i^{I\!\!P, I\!\!R}(\beta, Q^2)$. The flux factors $f_{I\!\!P, I\!\!R}^p(\xi, t)$ represent the probability that a Pomeron/Reggeon with given values ξ, t couples to the proton. They are parameterised using the form motivated by Regge theory,

$$f_{I\!\!P, I\!\!R}^p(\xi, t) = A_{I\!\!P, I\!\!R} \frac{e^{B_{I\!\!P, I\!\!R} t}}{\xi^{2\alpha_{I\!\!P, I\!\!R}(t) - 1}} \, , \tag{4.17}$$

103

with a linear trajectory $\alpha_{\mathbb{P},\mathbb{R}}(t) = \alpha_{\mathbb{P},\mathbb{R}}(0) + \alpha'_{\mathbb{P},\mathbb{R}} t$. The diffractive PDFs relevant to the t-integrated cross sections read

$$f_i^{\mathrm{D(3)}}(z,\xi,Q^2) = \phi_{\mathbb{P}}^p(\xi)\, f_i^{\mathbb{P}}(z,Q^2) + \phi_{\mathbb{R}}^p(\xi)\, f_i^{\mathbb{R}}(z,Q^2) \,, \tag{4.18}$$

with

$$\phi_{\mathbb{P},\mathbb{R}}^p(\xi) = \int dt\, f_{\mathbb{P},\mathbb{R}}^p(\xi,t) \,. \tag{4.19}$$

Note that, the notions of *Pomeron* and *Reggeon* used here to model hard diffraction in DIS are, in principle, different from those describing the soft hadron-hadron interactions; in particular, the parameters of the fluxes may be different.

The diffractive parton distributions of the Pomeron at the initial scale $\mu_0^2 = 1.8\,\mathrm{GeV}^2$ are parameterised as

$$z f_i^{\mathbb{P}}(z,\mu_0^2) = A_i z^{B_i}(1-z)^{C_i} \,, \tag{4.20}$$

where i is a gluon or a light quark and the momentum fraction $z = \beta$ in the case of quarks. In the diffractive parameterisations the contributions of all the light quarks (anti-quarks) are assumed to be equal. For the treatment of heavy flavours, a variable flavour number scheme (VFNS) is adopted, where the charm and bottom quark DPDFs are generated radiatively via DGLAP evolution, and no intrinsic heavy quark distributions are assumed. The structure functions are calculated in a General-Mass Variable Flavour Number scheme (GM-VFNS) [347, 348] which ensures a smooth transition of $F_{2,\mathrm{L}}$ across the flavour thresholds by including $\mathcal{O}(m_h^2/Q^2)$ corrections. The parton distributions for the Reggeon component are taken from a parameterisation which was obtained from fits to the pion structure function [349, 350].

In Eq. (4.16) the normalisation factors of fluxes, $A_{\mathbb{P},\mathbb{R}}$ and of DPDFs, A_i enter in the product. To resolve the ambiguity we fix[6] $A_{\mathbb{P}}$ and use $f_i^{\mathbb{R}}(z,Q^2)$ normalised to the pion structure function, which results in A_i and $A_{\mathbb{R}}$ being well defined free fit parameters. For full details, see Ref. [333].

4.3.2 Pseudodata for diffractive structure functions

The reduced cross sections are extrapolated using the ZEUS-SJ DPDFs. Following the scenario of the ZEUS fit [341] we work within the VFNS scheme at NLO accuracy. The transition scales for DGLAP evolution are fixed by the heavy quark masses, $\mu^2 = m_h^2$ and the structure functions are calculated in the Thorne–Roberts GM-VFNS [351]. The Reggeon PDFs are taken from the GRV pion set [350], the numerical parameters are taken from Tables 1 and 3 of Ref. [341], the heavy quark masses are $m_c = 1.35\,\mathrm{GeV}, m_b = 4.3\,\mathrm{GeV}$, and $\alpha_{\mathrm{s}}(M_Z^2) = 0.118$.

The pseudodata were generated using the extrapolation of the fit to HERA data, which provides the central values, amended with a random Gaussian smearing with standard deviation corresponding to the relative error δ. An uncorrelated 5% systematic error was assumed giving a total uncertainty

$$\delta = \sqrt{\delta_{\mathrm{sys}}^2 + \delta_{\mathrm{stat}}^2} \,. \tag{4.21}$$

The statistical error was computed assuming a very modest integrated luminosity of $2\,\mathrm{fb}^{-1}$, see Ref. [35, 36]. For the binning adopted in this study, the statistical uncertainties have a very small effect on the uncertainties in the extracted DPDFs. Obviously, a much larger luminosity would allow a denser binning that would result in smaller DPDF uncertainties.

---

[6]Here, as in the HERA fits, $A_{\mathbb{P}}$ is fixed by normalizing $\phi_{\mathbb{P}}^p(0.003) = 1$.

In Fig. 4.24 we show a subset of the simulated data for the diffractive reduced cross section $\xi\sigma_{\rm red}$ as a function of β in selected bins of ξ and Q^2 for the LHeC. For the most part the errors are very small, and are dominated by the systematics. The breaking of Regge factorisation evident at large ξ comes from the large Reggeon contribution in that region, whose validity could be further investigated at the LHeC.
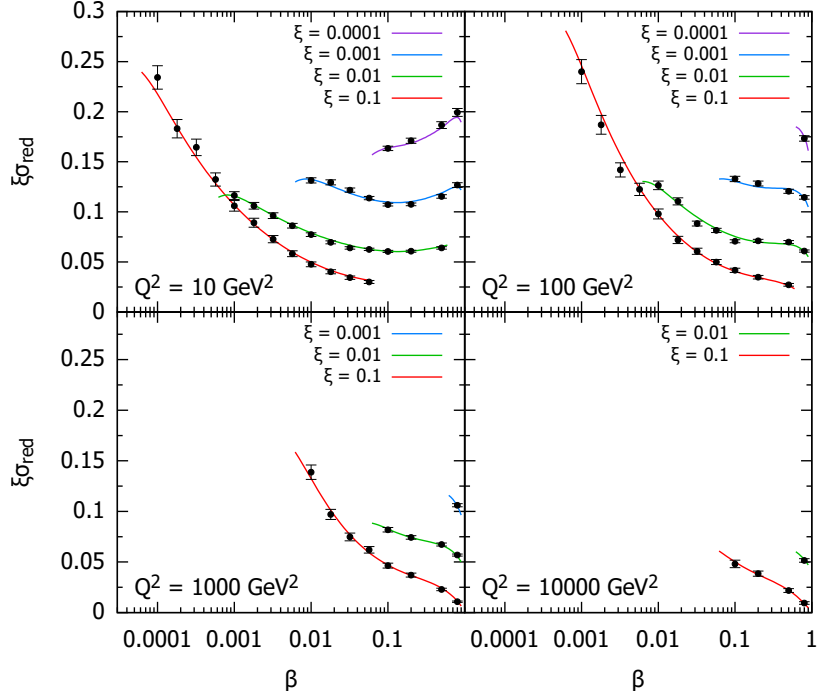
Figure 4.24: Selected subset of the simulated data for the diffractive reduced cross section as a function of β in bins of ξ and Q^2 for *ep* collisions at the LHeC. The curves for $\xi = 0.01, 0.001, 0.0001$ are shifted up by 0.04, 0.08, 0.12, respectively.

4.3.3 Potential for constraining diffractive PDFs at the LHeC and FCC-eh

With the aim of establishing the experimental precision with which DPDFs could be extracted when LHeC data become available, we generate the central values of the pseudodata using the central set of the ZEUS-SJ fit that are distributed according to a Gaussian with experimental width given by Eq. (4.21), that also provides the uncertainty in the pseudodata. We then include the pseudodata in a fit alongside the existing HERA data using the same functional form and, as expected, obtain a $\chi^2/\mathrm{ndf} \sim 1$, which demonstrates the consistency of the approach.

To evaluate the experimental precision with which the DPDFs can be determined, several pseudodata sets, corresponding to independent random error samples, were generated. Each pseudodata set was fitted separately. The minimal value of Q^2 for the data considered in the fits was set to $Q^2_{\rm min} = 5\,{\rm GeV}^2$. The reason for this cut-off is to show the feasibility of the fits including just the range in which standard twist-2 DGLAP evolution is expected to be trustable. At HERA, the $Q^2_{\rm min}$ values giving acceptable DGLAP (twist-2) fits were $8\,{\rm GeV}^2$ [335] and $5\,{\rm GeV}^2$ [336] for H1 and ZEUS, respectively. The maximum value of ξ was set by default to $\xi_{\rm max} = 0.1$, above which the cross section starts to be dominated by the Reggeon exchange. The binning adopted in this study corresponds roughly to 4 bins per order of magnitude in each of ξ, β, Q^2. For $Q^2_{\rm min} = 5\,{\rm GeV}^2$, $\xi_{\rm max} = 0.1$ and below the top threshold this results in 1229 and 1735 pseudo-

data points for the LHeC and FCC-eh, respectively. The top-quark region adds 17 points for the LHeC and 255 for FCC-eh. Lowering $Q^2_{\min}$ down to $1.8\,\mathrm{GeV}^2$ we get 1589 and 2171 pseudodata points, while increasing ξ up to 0.32 adds around 180 points for both proposed machines.

The potential for determination of the gluon DPDF was investigated by fitting the inclusive diffractive DIS pseudodata with two models with different numbers of parameters, named S and C (see Ref. [333]) with $\alpha_{IP,IR}(0)$ fixed, in order to focus on the shape of the Pomeron's PDFs. At HERA, both S and C fits provide equally good descriptions of the data with $\chi^2/\mathrm{ndf} = 1.19$ and 1.18, respectively, despite different gluon DPDF shapes. The LHeC pseudodata are much more sensitive to gluons, resulting in χ^2/ndf values of 1.05 and 1.4 for the S and C fits, respectively. This motivates the use of the larger number of parameters in the fit-S model, which we employ in the following studies. It also shows clearly the potential of the LHeC and the FCC-eh to better constrain the low-x gluon and, therefore, unravel eventual departures from standard linear evolution.
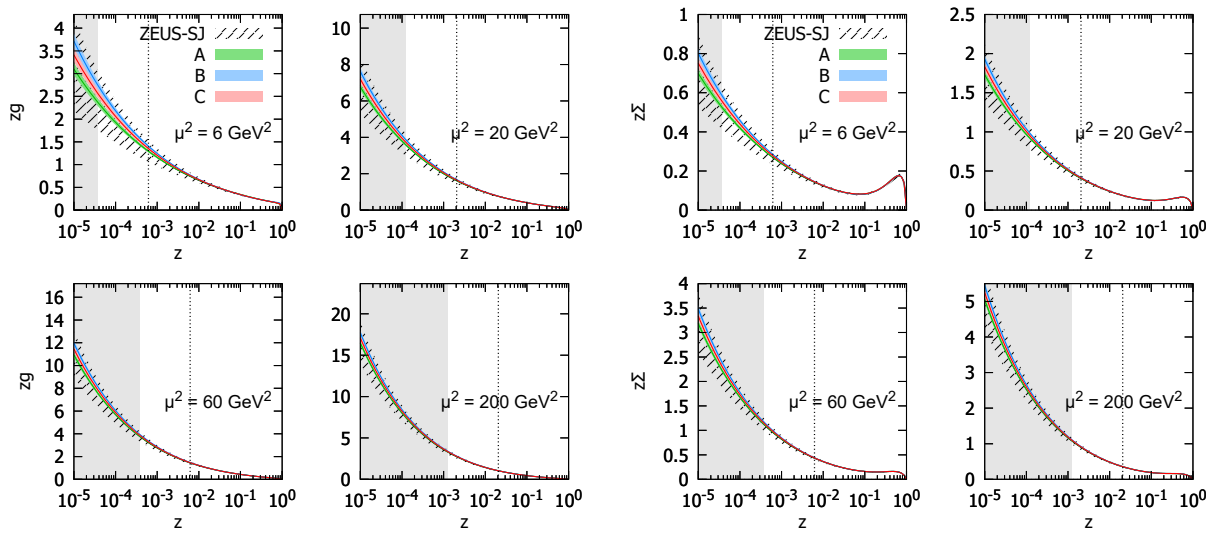
Figure 4.25: Diffractive PDFs for gluon and quark in the LHeC kinematics as a function of momentum fraction z for fixed values of scale μ^2. Results of fits to three (A,B,C) pseudodata replicas are shown together with the experimental error bands. For comparison, the extrapolated ZEUS-SJ fit is also shown (black) with error bands marked with the hatched pattern. The vertical dotted lines indicate the HERA kinematic limit. The bands indicate only the experimental uncertainties.

In Fig. 4.25 the diffractive gluon and quark distributions are shown for the LHeC and FCC-eh, respectively, as a function of momentum fraction z for fixed scales $\mu^2 = 6, 20, 60, 200\,\mathrm{GeV}^2$. The bands labelled A, B, C denote fits to three statistically independent pseudodata replicas, obtained from the same central values and statistical and systematic uncertainties. Hereafter the uncertainty bands shown correspond to $\Delta\chi^2 = 2.7$ (90 % CL). Also the extrapolated ZEUS-SJ DPDFs are shown with error bands marked by the '/' hatched area. Note that the depicted uncertainty bands come solely from experimental errors, neglecting theoretical sources, such as fixed input parameters and parameterisation biases. The extrapolation beyond the reach of LHeC/FCC-eh is marked in grey and the HERA kinematic limit is marked with the vertical dotted line. The stability of the results with respect to the independent pseudodata replicas used for the analysis is evident, so in the following only one will be employed. The low x DPDF determination accuracy improves with respect to HERA by a factor of 5–7 for the LHeC and 10–15 for the FCC-eh and completely new kinematic regimes are accessed.

For a better illustration of the precision, in Fig. 4.26 the relative uncertainties are shown for

parton distributions at different scales. The different bands show the variation with the upper cut on the available ξ range, from 0.01 to 0.32. In the best constrained region of $z \simeq 0.1$, the precision reaches the 1% level. We observe only a modest improvement in the achievable accuracy of the extracted DPDFs with the change of ξ by an order of magnitude from 0.01 to 0.1. An almost negligible effect is observed when further extending the ξ range up to 0.32. This is encouraging, since the measurement for the very large values of ξ is challenging. It reflects the dominance of the secondary Reggeon in this region. We stress again that only experimental errors are included in our uncertainty bands. Neither theoretical uncertainties nor the parameterisation biases are considered. For a detailed discussion of this and other aspects of the fits, see Ref. [333].
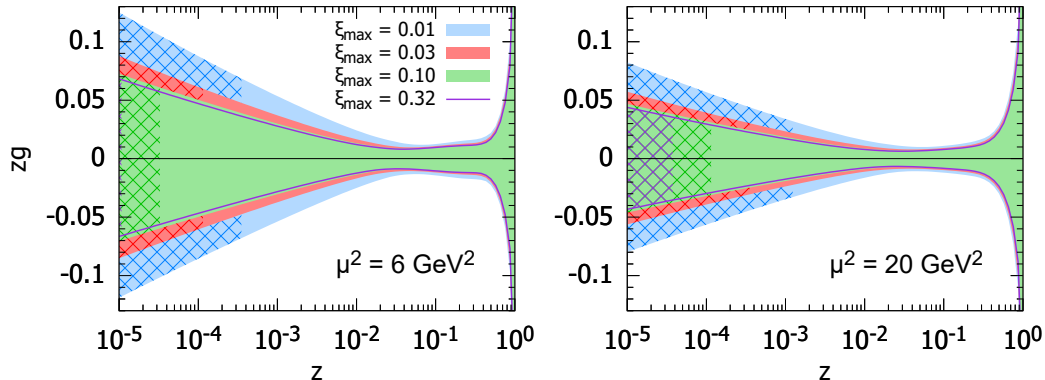
Figure 4.26: Relative uncertainties on the diffractive gluon PDFs for the LHeC kinematics. Two different choices of scales are considered $\mu^2 = 6$ and $\mu^2 = 20\,\mathrm{GeV}^2$. The blue, red, green bands and magenta line correspond to different maximal values of $\xi = 0.01, 0.03, 0.1, 0.32$, respectively. The cross-hatched areas show kinematically excluded regions. The bands indicate only the experimental uncertainties, see the text.

4.3.4 Hadronic Final States in Diffraction and hard rapidity gap processes

Various diffractive processes offer unique opportunity to investigate the factorisation properties and can help to disentangle DGLAP vs BFKL dynamics.

The factorisation properties of diffractive DIS were a major topic of study at HERA [317] and are highly relevant to the interpretation of diffractive processes at the LHC [352]. A general theoretical framework is provided by the proof [330] of a hard scattering collinear QCD factorisation theorem for semi-inclusive DIS scattering processes such as $ep \rightarrow epX$. This implies that the DPDFs extracted in fits to inclusive diffractive DIS may be used to predict perturbative cross sections for hadronic final state observables such as heavy flavour or jet production. Testing this factorisation pushes at the boundaries of applicability of perturbative QCD and will be a major topic of study at the LHeC.

Tests of diffractive factorisation at HERA are strongly limited by the kinematics. The mass of the dissociation system X is limited to approximately $M_X < 30\,\mathrm{GeV}$, which implies for example that jet transverse momenta cannot be larger than about 15 GeV and more generally leaves very little phase space for any studies at perturbative scales. As well as restricting the kinematic range of studies, this restriction also implied large hadronisation and scale uncertainties in theoretical predictions, which in turn limit the precision with which tests can be made.

The higher centre-of-mass energy of the LHeC opens up a completely new regime for diffractive

hadronic final state observables in which masses and transverse momenta are larger and theoretical uncertainties are correspondingly reduced. For example, M_X values in excess of $250\,\text{GeV}$ are accessible, whilst remaining in the region $\xi < 0.05$ where the leading diffractive (pomeron) exchange dominates. The precision of tests is also improved by the development of techniques for NNLO calculations for diffractive jets [353].

Fig. 4.27 shows a simulation of the expected diffractive jet cross section at the LHeC, assuming DPDFs extrapolated from H1 at HERA [335], using the NLOJET++ framework [354]. An integrated luminosity of $100\,\text{fb}^{-1}$ is assumed and the kinematic range considered is $Q^2 > 2\,\text{GeV}^2$, $0.1 < y < 0.7$ and scattered electron angles larger than $1°$. Jets are reconstructed using the k_T algorithm with $R = 1$. The statistical precision remains excellent up to jet transverse momenta of almost $50\,\text{GeV}$ and the theoretical scale uncertainties (shaded bands) are substantially reduced compared with HERA measurements. Comparing a measurement of this sort of quality with predictions refined using DPDFs from inclusive LHeC data would clearly provide an exacting test of diffractive factorisation.
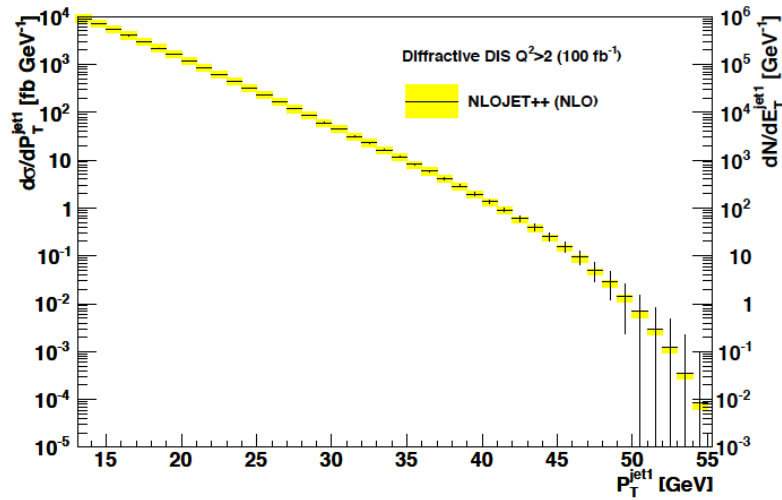
Figure 4.27: Simulated diffractive dijet cross section as a function of leading jet transverse momentum in the kinematic range $Q^2 > 2\,\text{GeV}^2$ and $0.1 < y < 0.7$, with scattered electron angles in excess of $1°$. The error bars indicate predicted statistical uncertainties for a luminosity of $100\,\text{fb}^{-1}$. The coloured bands correspond to theoretical uncertainties when varying the renormalisation and factorisation scales by factors of 2.

Further interesting hadronic final state observables that were studied at HERA and could be extended at the LHeC include open charm production, thrust and other event shapes, charged particle multiplicities and energy flows. In addition, the LHeC opens up completely new channels, notably diffractive beauty, W and Z production, the latter giving complementary sensitivity to the quark densities to that offered by inclusive diffraction.

Of separate interest are hard rapidity gap processes, for example $\gamma^* p \to J/\psi + \text{rapidity gap}(\Delta y) + Y$ at large $-t \gg 1\,\text{GeV}^2$. In such processes DGLAP evolution is strongly suppressed and therefore this is an ideal laboratory to investigate BFKL dynamics. The dependence of the process on Δy is expected to be given by $\sigma \sim \Delta y^{2\omega_P(t)}$. Here, the effective pomeron trajectory is parameterized as $\alpha_P(t) = 1 + \omega(t)$. The current models give ω between 0.5 (LO BFKL) and $\omega = 0.2 - 0.3$ for the resummed BFKL. With a proper large acceptance detector one would be able to study dependence on Δy in a wide rapidity interval as well as the dependence on the momentum transfer t. Hence this process offers a powerful test for the theoretical predictions of the properties of the BFKL pomeron.

4.4 Theoretical Developments

4.4.1 Prospects for Higher Order pQCD in DIS

With its large anticipated luminosity, the LHeC will be able to perform highly precise measurements for a wide variety of final states in deep inelastic scattering, often exploring novel kinematical ranges, challenging the theory of QCD at an unprecedented level of accuracy, and enabling precision determinations of QCD parameters and of the proton's parton structure. For this program to succeed, it will be mandatory to be able to confront the LHeC precision data with equally precise theoretical predictions.

In the Standard Model, these predictions can be obtained through a perturbative expansion to sufficiently high order. These calculations are performed in the larger framework of QCD factorisation [38] and exploit the process-independence of parton distributions, whose evolution is controlled by the DGLAP equations. The DGLAP splitting functions are known to NNLO level for already quite some time [355, 356], and important progress has been made recently towards their N3LO terms [92, 93]. Moreover, mixed QCD/QED corrections to them have been derived [357], enabling a consistent combination of QCD and electroweak effects.

The physics opportunities that are offered already by the HERA legacy data set have motivated substantial recent activity in precision QCD calculations for deeply inelastic processes. At the inclusive level, the QCD coefficients for the inclusive DIS structure functions are known to three loops (N3LO) for some time [358], they were improved upon recently by the computation of heavy quark mass effects [359, 360]. Fully differential predictions for final states with jets, photons, heavy quarks or hadrons are generally available to NLO in QCD, often dating back to the HERA epoch. Technical developments that were made in the context of fully differential higher-order QCD calculations for LHC processes have enabled substantial advances in the theory precision of DIS jet cross sections. Fully differential predictions for single jet production are now available to NNLO [199] and N3LO [201, 276] for neutral-current and charged current DIS, and two-jet production [160, 161, 361] has been computed to NNLO. The latter calculations are performed with fully differential parton-level final state information, thereby allowing their extension to jet production in diffractive DIS [353] and to DIS two-parton event shapes [202]. The newly derived NNLO jet cross sections were partly used in the projections for LHeC precision jet studies in Sections 4.1.2 and 4.3.4 above.

NLO calculations have been largely automated in QCD [362–364] and the electroweak theory [365, 366], and are now available in multi-purpose event generator programs [367–369] for processes of arbitrary multiplicity. These can be combined with parton shower approximations to provide NLO-accurate predictions for fully exclusive final states. Although most of the applications of these tools were to hadron collider observables, they are also ready to be used for DIS processes [200], thereby offering novel opportunities for precision studies for LHeC. In this context, electroweak corrections may become particularly crucial for high-mass final states at the LHeC, and have been largely unexplored up to now. A similar level of automation has not yet been reached so far at NNLO, where calculations are performed on a process-by-process basis. For DIS processes, fully differential NNLO calculations for three-jet final states or for heavy quark production could become feasible in the near-term future. Moreover, a whole set of calculations at this order for specific final states (involving jets, vector bosons or heavy quarks) in photoproduction could be readily taken over by adapting the respective hadron collider results.

The all-order resummation of large logarithmic corrections to hadron collider processes has made very substantial advances in the recent past, owing to the emergence of novel systematic

frameworks from soft-collinear effective theory, or in momentum space resummation. As a result, threshold logarithms and transverse-momentum logarithms in benchmark hadron collider processes can now be resummed up to the third subleading logarithmic order (N3LL). A similar accuracy has been reached for selected event shapes in electron-position annihilation. For DIS event shapes, currently available predictions include only up to NLL resummation [370]. With the newly available frameworks, they could be improved by two more logarithmic orders, as demonstrated in exploratory work on the DIS one-jettiness event shape [197, 198]. Applications of this framework to final states in DIS the small-x limit (see Section 4.2) are largely unexplored, and may provide important novel insights into the all-order dynamics in the high-energy limit.

The full exploitation of future LHeC data will require novel precision calculations for a variety of benchmark processes, often combining fixed-order, resummation and parton shower event generation to obtain theory predictions of matching accuracy. Recent advances in calculational techniques and an increasing degree of automation will help to enable this progress. A close interplay between experiment and theory will then be crucial to combine data and predictions into precision measurements of physics parameters and into probes of fundamental particle dynamics.

4.4.2 Theoretical Concepts on the Light Cone

Intrinsic Heavy Quark Phenomena

One of the most interesting nonperturbative quantum field theoretic aspects of hadron light front wavefunctions in QCD are the intrinsic heavy-quark Fock states [371–373]. Consider a heavy-quark loop insertion to the proton's self-energy. The heavy-quark loop can be attached by gluons to just one valence quark. The cut of such diagrams yields the standard DGLAP gluon splitting contribution to the proton's heavy quark structure function. In this case, the heavy quarks are produced at very small x. However, the heavy quark loop can also be attached to two or more valence quarks in the proton self-energy. In the case of QED this corresponds to the light-by-light lepton loop insertion in an atomic wavefunction. In the case of QCD, the heavy quark loop can be attached by three gluons to two or three valence quarks in the proton self-energy. This is a non-Abelian insertion to the hadron's self-energy. The cut of such diagrams gives the *intrinsic* heavy-quark contribution to the proton's light-front wavefunction. In the case of QCD, the probability for an intrinsic heavy $Q\bar{Q}$ pair scales as $\frac{1}{M_Q^2}$; this is in contrast to heavy $\ell\bar{\ell}$ lepton pairs in QED where the probability for heavy lepton pairs in an atomic wavefunction scales as $\frac{1}{M_\ell^4}$. This difference in heavy-particle scaling in mass distinguishes Abelian from non-Abelian theories.

A basic property of hadronic light-front wavefunctions is that they have strong fall-off with the invariant mass of the Fock state. For example, the Light-Front Wave Functions (LFWFs) of the colour-confining AdS/QCD models [374] $\mathcal{M}^2 = [\sum_i k_i^\mu]^2$ of the Fock state constituents. This means that the probability is maximised when the constituents have equal true rapidity, i.e. $x_i \propto (\vec{k}_{\perp i}^2 + m_i^2)^{1/2}$. Thus the heavy quarks carry most of the momentum in an intrinsic heavy quark Fock state. For example, the charm quark in the intrinsic charm Fock state $|uudc\bar{c}\rangle$ of a proton carries about 40 % of the proton's momentum: $x_c \sim 0.4$. After a high-energy collision, the co-moving constituents can then recombine to form the final state hadrons. along the proton. Thus, in a ep collision the comoving udc quarks from the $|uudc\bar{c}\rangle$ intrinsic 5-quark Fock state can recombine to a Λ_c, where $x_{\Lambda_c} = x_c + x_u + x_d \sim 0.5$. Similarly, the comoving dcc in the $|uudc\bar{c}c\bar{c}\rangle$ intrinsic 7-quark Fock state can recombine to a $\Xi(ccd)^+$, with $x_{\Xi(ccd)} = x_c + x_c + x_d \sim 0.9$.

Therefore, in the intrinsic heavy quark model the wavefunction of a hadron in QCD can be represented as a superposition of Fock state fluctuations, e.g. $|n_V\rangle$, $|n_V g\rangle$, $|n_V Q\overline{Q}\rangle$, ... components where $n_V \equiv dds$ for Σ^-, uud for proton, $\overline{u}d$ for π^- and $u\overline{d}$ for π^+. Charm hadrons can be produced by coalescence in the wavefunctions of the moving hadron. Doubly-charmed hadrons require fluctuations such as $|n_V c\overline{c}c\overline{c}\rangle$. The probability for these Fock state fluctuations to come on mass shell is inversely proportional to the square of the quark mass, $\mathcal{O}(m_Q^{-2n})$ where n is the number of $Q\overline{Q}$ pairs in the hadron. Thus the natural domain for heavy hadrons produced from heavy quark Fock states is $\vec{k}_{\perp Q}^2 \sim m_Q^2$ and high light-front momentum fraction x_Q [371, 372, 372, 373]. For example, the rapidity regime for double-charm hadron production $y_{ccd} \sim 3$ at low energies is well within the kinematic experiment domain of a fixed target experiment such as SELEX at the Tevatron [375]. Note that the intrinsic heavy-quark mechanism can account for many previous observations of forward heavy hadron production single and double J/ψ production by pions observed at high $x_F > 0.4$ in the low energy fixed target NA3 experiment, the high x_F production of $pp \to \Lambda_c, +X$ and $pp \to \Lambda_b + X$ observed at the ISR; single and double $\Upsilon(b\overline{b})$ production, as well as *quadra-bottom* tetraquark $[bb\overline{b}\overline{b}]$ production observed recently by the AnDY experiment at RHIC [376]. In addition the EMC collaboration observed that the charm quark distribution in the proton at $x = 0.42$ and $Q^2 = 75\,\text{GeV}^2$ is 30 times larger that expected from DGLAP evolution. All of these experimental observations are naturally explained by the intrinsic heavy quark mechanism. The SELEX observation [375] of double charm baryons at high x_F reflects production from double intrinsic heavy quark Fock states of the baryon projectile. Similarly, the high x_F domain – which would be accessible at forward high x_F – is the natural production domain for heavy hadron production at the LHeC.

The production of heavy hadrons based on intrinsic heavy quark Fock states is thus remarkable efficient and greatly extends the kinematic domain of the LHeC, e.g. for processes such as $\gamma^* b \to Z^0 b$. This is in contrast with the standard production cross sections based on gluon splitting, where only a small fraction of the incident momentum is effective in creating heavy hadrons.

Light-Front Holography and Superconformal Algebra

The LHeC has the potential of probing the high mass spectrum of QCD, such as the spectroscopy and structure of hadrons consisting of heavy quarks. Insights into this new domain of hadron physics can now be derived by new non-perturbative colour-confining methods based on light-front (LF) holography. A remarkable feature is universal Regge trajectories with universal slopes in both the principal quantum number n and internal orbital angular momentum L. A key feature is di-quark clustering and supersymmetric relations between the masses of meson, baryons, and tetraquarks. In addition the running coupling is determined at all scales, including the soft domain relevant to rescattering corrections to LHeC processes. The combination of lightfront holography with superconformal algebra leads to the novel prediction that hadron physics has supersymmetric properties in both spectroscopy and dynamics.

Light-front holography and recent theoretical advances   Five-dimensional AdS$_5$ space provides a geometrical representation of the conformal group. Remarkably, AdS$_5$ is holographically dual to $3 + 1$ spacetime at fixed LF time τ [377]. A colour-confining LF equation for mesons of arbitrary spin J can be derived from the holographic mapping of the *soft-wall model* modification of AdS$_5$ space for the specific dilaton profile $e^{+\kappa^2 z^2}$, where z is the fifth dimension variable of the five-dimensional AdS$_5$ space. A holographic dictionary maps the fifth dimension

z to the LF radial variable ζ, with $\zeta^2 = b_\perp^2(1-x)$. The same physics transformation maps the AdS$_5$ and $(3+1)$ LF expressions for electromagnetic and gravitational form factors to each other [378].

A key tool is the remarkable dAFF principle [379] which shows how a mass scale can appear in a Hamiltonian and its equations of motion while retaining the conformal symmetry of the action. When applying it to LF holography, a mass scale κ appears which determines universal Regge slopes, and the hadron masses. The resulting *LF Schrödinger Equation* incorporates colour confinement and other essential spectroscopic and dynamical features of hadron physics, including Regge theory, the Veneziano formula [380], a massless pion for zero quark mass and linear Regge trajectories with the universal slope in the radial quantum number n and the internal orbital angular momentum L. The combination of LF dynamics, its holographic mapping to AdS$_5$ space, and the dAFF procedure provides new insight into the physics underlying colour confinement, the non-perturbative QCD coupling, and the QCD mass scale. The $q\bar{q}$ mesons and their valence LFWFs are the eigensolutions of the frame-independent a relativistic bound-state LF Schrödinger equation.

The mesonic $q\bar{q}$ bound-state eigenvalues for massless quarks are $M^2(n,L,S) = 4\kappa^2(n+L+S/2)$. This equation predicts that the pion eigenstate $n=L=S=0$ is massless for zero quark mass. When quark masses are included in the LF kinetic energy $\sum_i \frac{k_{\perp i}^2 + m^2}{x_i}$, the spectroscopy of mesons are predicted correctly, with equal slope in the principal quantum number n and the internal orbital angular momentum L. A comprehensive review is given in Ref. [377].

The QCD Running Coupling at all Scales from Light-Front Holography The QCD running coupling $\alpha_s(Q^2)$ sets the strength of the interactions of quarks and gluons as a function of the momentum transfer Q (see Sec. 4.1). The dependence of the coupling Q^2 is needed to describe hadronic interactions at both long and short distances [381]. It can be defined [382] at all momentum scales from a perturbatively calculable observable, such as the coupling $\alpha_s^{g_1}(Q^2)$, which is defined using the Bjorken sum rule [383], and determined from the sum rule prediction at high Q^2 and, below, from its measurements [384–386]. At high Q^2, such *effective charges* satisfy asymptotic freedom, obey the usual pQCD renormalisation group equations, and can be related to each other without scale ambiguity by commensurate scale relations [387].

The high Q^2 dependence of $\alpha_s^{g_1}(Q^2)$ is predicted by pQCD. In the small Q^2 domain its functional behaviour can be predicted by the dilaton $e^{+\kappa^2 z^2}$ soft-wall modification of the AdS$_5$ metric, together with LF holography [388], as $\alpha_s^{g_1}(Q^2) = \pi e^{-Q^2/4\kappa^2}$. The parameter κ determines the mass scale of hadrons and Regge slopes in the zero quark mass limit, and it was shown that it can be connected to the mass scale Λ_s, which controls the evolution of the pQCD coupling [388–390]. Measurements of $\alpha_s^{g_1}(Q^2)$ [391,392] are remarkably consistent with this predicted Gaussian form, and a fit gives $\kappa = 0.513 \pm 0.007\,\text{GeV}$, see Fig. 4.28.

The matching of the high and low Q^2 regimes of $\alpha_s^{g_1}(Q^2)$ determines a scale Q_0, which sets the interface between perturbative and non-perturbative hadron dynamics. This connection can be done for any choice of renormalisation scheme and one obtains an effective QCD coupling at all momenta. In the $\overline{\text{MS}}$ scheme one gets $Q_0 = 0.87 \pm 0.08\,\text{GeV}$ [393]. The corresponding value of $\Lambda_{\overline{\text{MS}}}$ agrees well with the measured world average value and its value allows to compute hadron masses using the AdS/QCD superconformal predictions for hadron spectroscopy. The value of Q_0 can further be used to set the factorisation scale for DGLAP evolution [344–346] or the ERBL evolution of distribution amplitudes [394,395]. The use of the scale Q_0 to resolve the factorisation scale uncertainty in structure functions and fragmentation functions, in combination with the

scheme-independent *principle of maximum conformality* (PMC) [178] for setting renormalisation scales, can greatly improve the precision of pQCD predictions for collider phenomenology at LHeC and HL-LHC.
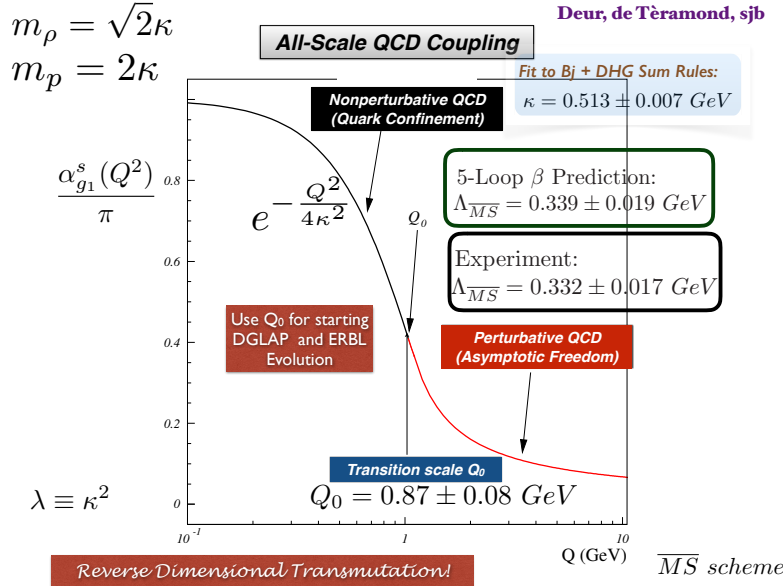
Figure 4.28: Prediction for the running coupling $\alpha_s^{g_1}(Q^2)$ at all scales. At lower Q^2 predictions are obtained from LF Holography and at higher Q^2 from perturbative QCD. The magnitude and derivative of the perturbative and non-perturbative coupling are matched at the scale Q_0. This matching connects the perturbative scale $\Lambda_{\overline{MS}}$ to the non-perturbative scale κ which underlies the hadron mass scale.

Superconformal Algebra and Hadron Physics with LHeC data If one generalises LF holography using *superconformal algebra* the resulting LF eigensolutions yield a unified Regge spectroscopy of mesons, baryons and tetraquarks, including remarkable supersymmetric relations between the masses of mesons and baryons of the same parity [7] [396, 397]. This generalisation further predicts hadron dynamics, including vector meson electroproduction, hadronic LFWFs, distribution amplitudes, form factors, and valence structure functions [398, 399]. Applications to the deuteron elastic form factors and structure functions are given in Refs. [400, 401]

The eigensolutions of superconformal algebra predict the Regge spectroscopy of mesons, baryons, and tetraquarks of the same parity and twist as equal-mass members of the same 4-plet representation with a universal Regge slope [402–404]. A comparison with experiment is shown in Fig. 4.29. The $q\bar{q}$ mesons with orbital angular momentum $L_M = L_B + 1$ have the same mass as their baryonic partners with orbital angular momentum L_B [402, 405].

The predictions from LF holography and superconformal algebra can also be extended to mesons, baryons, and tetraquarks with strange, charm and bottom quarks. Although conformal symmetry is strongly broken by the heavy quark masses, the basic underlying supersymmetric mechanism, which transforms mesons to baryons (and baryons to tetraquarks), still holds and gives remarkable mass degeneracy across the entire spectrum of light, heavy-light and double-heavy hadrons.

---

[7] QCD is not supersymmetrical in the usual sense, since the QCD Lagrangian is based on quark and gluonic fields, not squarks or gluinos. However, its hadronic eigensolutions conform to a representation of superconformal algebra, reflecting the underlying conformal symmetry of chiral QCD and its Pauli matrix representation.
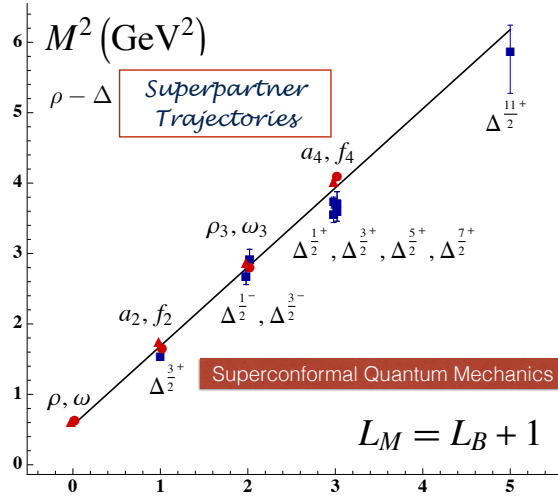
Figure 4.29: Comparison of the ρ/ω meson Regge trajectory with the $J = 3/2$ Δ baryon trajectory. Superconformal algebra predicts the mass degeneracy of the meson and baryon trajectories if one identifies a meson with internal orbital angular momentum L_M with its superpartner baryon with $L_M = L_B + 1$. See Refs. [402, 405].

The 4-plet symmetry of quark-antiquark mesons, quark-diquark baryons, and diquark-antidiquark tetraquarks are important predictions by superconformal algebra [393, 396]. Recently the AnDY experiment at RHIC has reported the observation of a state at $18\,\mathrm{GeV}$ which can be identified with the $[bb][\bar{b}\bar{b}]$ tetraquark [376]. The states with heavy quarks such as the $[bb][\bar{b}\bar{b}]$ tetraquark can be produced at the LHeC, especially at high x_F along the proton beam direction. New measurements at the LHeC are therefore inevitable to manifest the superconformal nature of hadronic bound states.

Chapter 5

Electroweak and Top Quark Physics

5.1 Electroweak Physics with Inclusive DIS data

With the discovery of the Standard Model (SM) Higgs boson at the CERN LHC experiments and subsequent measurements of its properties, all fundamental parameters of the SM have now been measured directly and with remarkable precision. To further establish the validity of the theory of electroweak interactions [25,406–409], validate the mechanism of electroweak symmetry breaking and the nature of the Higgs sector [410–412], new electroweak measurements have to be performed at highest precision. Such high-precision measurements can be considered as a portal to new physics, since non-SM contributions, as for instance loop-insertions, may cause significant deviations for some precisely measurable and calculable observables. At the LHeC, the greatly enlarged kinematic reach to higher mass scales in comparison to HERA [413–415] and the large targeted luminosity will enable electroweak measurements in ep scattering with higher precision than ever before.

In this section the sensitivity of inclusive DIS cross sections to electroweak parameters is discussed. An extended analysis and a more comprehensive discussion is found in Ref. [416], and some aspects are described in the following. The direct production of W and Z bosons is discussed in the subsequent section.

5.1.1 Electroweak effects in inclusive NC and CC DIS cross sections

Electroweak NC interactions in inclusive $e^\pm p$ DIS are mediated by exchange of a virtual photon (γ) or a Z boson in the t-channel, while CC DIS is mediated exclusively by W-boson exchange as a purely *weak* process. Inclusive NC DIS cross sections are expressed in terms of generalised structure functions $\tilde{F}_2^\pm$, $x\tilde{F}_3^\pm$ and $\tilde{F}_L^\pm$ at EW leading order (LO) as

$$\frac{d^2\sigma^{\mathrm{NC}}(e^\pm p)}{dx dQ^2} = \frac{2\pi\alpha^2}{xQ^4} \left[Y_+ \tilde{F}_2^\pm(x, Q^2) \mp Y_- x\tilde{F}_3^\pm(x, Q^2) - y^2 \tilde{F}_L^\pm(x, Q^2) \right] , \qquad (5.1)$$

where α denotes the fine structure constant. The terms $Y_\pm = 1 \pm (1-y)^2$, with $y = Q^2/sx$, describe the helicity dependence of the process. The generalised structure functions are separated into contributions from pure γ- and Z-exchange and their interference [96,134]:

$$\tilde{F}_2^\pm = F_2 - (g_V^e \pm P_e g_A^e)\kappa_Z F_2^{\gamma Z} + [(g_V^e g_V^e + g_A^e g_A^e) \pm 2P_e g_V^e g_A^e] \kappa_Z^2 F_2^Z , \qquad (5.2)$$

$$\tilde{F}_3^\pm = -(g_A^e \pm P_e g_V^e)\kappa_Z F_3^{\gamma Z} + [2g_V^e g_A^e \pm P_e(g_V^e g_V^e + g_A^e g_A^e)] \kappa_Z^2 F_3^Z . \qquad (5.3)$$

Similar expressions hold for $\tilde{F}_L$. In the naive quark-parton model, which corresponds to the LO QCD approximation, the structure functions are calculated as

$$\left[F_2, F_2^{\gamma Z}, F_2^Z\right] = x \sum_q \left[Q_q^2, 2Q_q g_V^q, g_V^q g_V^q + g_A^q g_A^q\right] \{q + \bar{q}\} \ , \tag{5.4}$$

$$x \left[F_3^{\gamma Z}, F_3^Z\right] = x \sum_q \left[2Q_q g_A^q, 2g_V^q g_A^q\right] \{q - \bar{q}\} \ , \tag{5.5}$$

representing two independent combinations of the quark and anti-quark momentum distributions, xq and $x\bar{q}$. In Eq. (5.3), the quantities g_V^f and g_A^f stand for the vector and axial-vector couplings of a fermion ($f = e$ or $f = q$ for electron or quark) to the Z boson, and the coefficient κ_Z accounts for the Z-boson propagator including the normalisation of the weak couplings. Both parameters are fully calculable from the electroweak theory. The (effective) coupling parameters depend on the electric charge, Q_f and the third component of the weak-isospin, $I_{L,f}^3$. Using $\sin^2\theta_W = 1 - \frac{M_W^2}{M_Z^2}$, one can write

$$g_V^f = \sqrt{\rho_{NC,f}} \left(I_{L,f}^3 - 2Q_f \kappa_{NC,f} \sin^2\theta_W\right) \ , \quad \text{and} \tag{5.6}$$

$$g_A^f = \sqrt{\rho_{NC,f}} \, I_{L,f}^3 \qquad\qquad\qquad \text{with } f = (e, u, d) \ . \tag{5.7}$$

The parameters $\rho_{NC,f}$ and $\kappa_{NC,f}$ are calculated as real parts of complex form factors which include the higher-order loop corrections [417–419]. They contain non-leading flavour-specific components.

Predictions for CC DIS are written in terms of the CC structure functions W_2, xW_3 and W_L and higher-order electroweak effects are collected in two form factors $\rho_{CC,eq}$ and $\rho_{CC,e\bar{q}}$ [420, 421].

In this study, the on-shell scheme is adopted for the calculation of higher-order corrections. This means that the independent parameters are chosen as the fine structure constant α and the masses of the weak bosons, the Higgs boson and the fermions. The weak mixing angle is then fixed and G_F is a prediction, whose higher-order corrections are included in the well-known correction factor Δr [422–424] (see discussion of further contributions in Ref. [134]).

The predicted single-differential inclusive NC and CC DIS cross sections for polarised e^-p scattering as a function of Q^2 are displayed in Fig. 5.1. For NC DIS and at higher Q^2, electroweak effects are important through γZ interference and pure Z-exchange terms and the polarisation of the LHeC electron beam of $P_e = \pm0.8$ will considerably alter the cross sections. For CC DIS, the cross section scales linearly with P_e. Two different electron beam energies are displayed in Fig. 5.1, and albeit the impact of a reduction from $E_e = 60$ to $50\,\text{GeV}$ appears to be small, a larger electron beam energy would yield higher precision for the measurement of electroweak parameters, since these are predominantly sensitive to the cross sections at highest scales, as will be shown in the following.

5.1.2 Methodology of a combined EW and QCD fit

A complete electroweak analysis of DIS data has to consider PDFs together with electroweak parameters [426]. In this study, the uncertainties of electroweak parameters are obtained in a combined fit of electroweak parameters and the PDFs, and the inclusive NC and CC DIS pseudodata (see Sec. 4.3.2) are explored as input data. The PDFs are parameterised with 13 parameters at a starting scale Q_0^2 and NNLO DGLAP evolution is applied [47, 48]. In this way, uncertainties from the PDFs are taken into account, which is very reasonable, since the
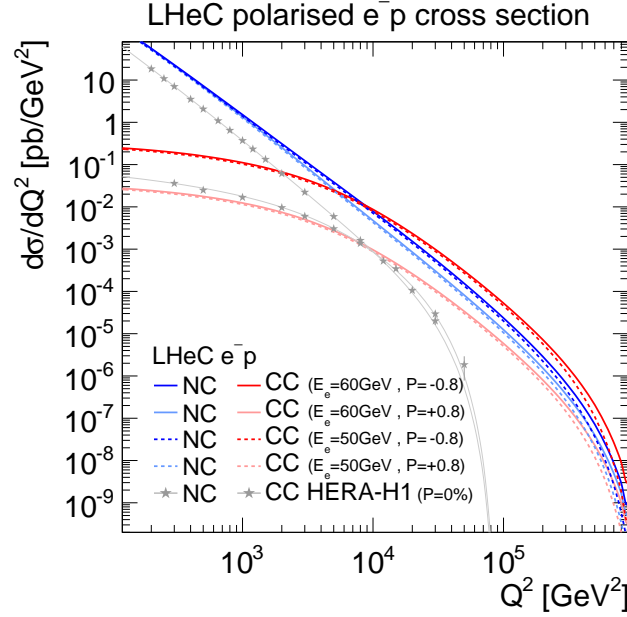
Figure 5.1: Single differential cross sections for polarised e^-p NC and CC DIS at LHeC for two different electron beam energies (E_e). Cross sections for longitudinal electron beam polarisations of $P_e = -0.8$ and $+0.8$ are displayed. For comparison also measurements at centre-of-mass energies of $\sqrt{s} = 920\,\text{GeV}$ by H1 at HERA for unpolarised ($P_e = 0\,\%$) electron beams are displayed [425].

PDFs will predominantly be determined from those LHeC data in the future. The details of the PDF fit are altogether fairly similar to the PDF fits outlined in Chapter. 3. Noteworthy differences are that additionally EW effects are included into the calculation by considering the full set of 1-loop electroweak corrections [427], and the χ^2 quantity [146], which is input to the minimisation and error propagation, is based on normal-distributed relative uncertainties. In this way, a dependence on the actual size of the simulated cross sections is avoided. The size of the pseudodata are therefore set equivalent to the predictions [428].

5.1.3 Weak boson masses M_W and M_Z

The expected uncertainties for a determination of the weak boson masses, M_W and M_Z, are determined in the PDF+EW-fit, where one of the masses is determined together with the PDFs, while the other mass parameter is taken as external input. The expected uncertainties for M_W are

$$\Delta M_W(\text{LHeC-60}) = \pm 8_{(\text{exp})} \pm 5_{(\text{PDF})}\,\text{MeV} = 10_{(\text{tot})}\,\text{MeV} \quad \text{and} \tag{5.8}$$
$$\Delta M_W(\text{LHeC-50}) = \pm 9_{(\text{exp})} \pm 8_{(\text{PDF})}\,\text{MeV} = 12_{(\text{tot})}\,\text{MeV}$$

for LHeC with $E_e = 60\,\text{GeV}$ or $50\,\text{GeV}$, respectively. The breakdown into experimental and PDF uncertainties is obtained by repeating the fit with PDF parameters fixed. These uncertainties are displayed in Fig. 5.2 and compared to the values obtained by LEP2 [430], Tevatron [429], ATLAS [431] and the PDG value [181]. The LHeC measurement will become the most precise measurement from one single experiment and will greatly improve over the best measurement achieved by H1, which was $M_W(\text{H1}) = 80.520 \pm 0.115\,\text{GeV}$ [415]. If the dominating uncorrelated

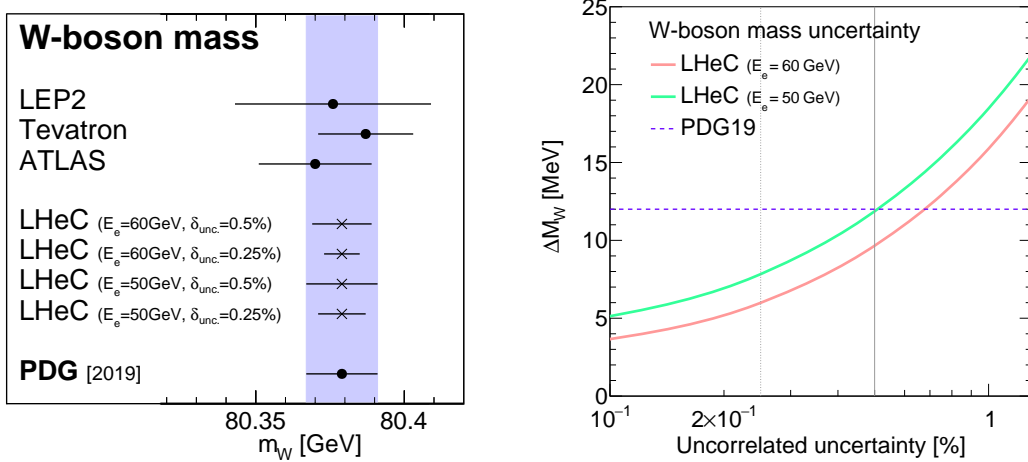**Figure 5.2:** Left: Measurements of the W-boson mass assuming fixed values for the top-quark and Z-boson masses at the LHeC for different scenarios in comparison with today's measurements [429–431] and the world average value (PDG19) [181]. For LHeC, prospects for $E_e = 60\,\text{GeV}$ and $50\,\text{GeV}$ are displayed, as well as results for the two scenarios with 0.5% or 0.25% uncorrelated uncertainty (see text). Right: Comparison of the precision for M_W for different assumptions of the uncorrelated uncertainty of the pseudodata. The uncertainty of the world average value is displayed as horizontal line. The nominal (and alternative) size of the uncorrelated uncertainty of the inclusive NC/CC DIS pseudodata is indicated by the vertical line (see text).

uncertainties can be reduced from the prospected 0.5% to 0.25%[1], a precision for M_W of up to

$$\Delta M_W(\text{LHeC-60}) = \pm 5_{(\text{exp})} \pm 3_{(\text{PDF})}\,\text{MeV} = 6_{(\text{tot})}\,\text{MeV}\quad\text{and} \tag{5.9}$$
$$\Delta M_W(\text{LHeC-50}) = \pm 6_{(\text{exp})} \pm 6_{(\text{PDF})}\,\text{MeV} = 8_{(\text{tot})}\,\text{MeV}$$

for LHeC-60 and LHeC-50 may be achieved, respectively. A complete dependence of the expected total experimental uncertainty ΔM_W on the size of the uncorrelated uncertainty component is displayed in Fig. 5.2, and with a more optimistic scenario an uncertainty of up to $\Delta M_W \approx 5\,\text{MeV}$ can be achieved. In view of such a high accuracy, it will be important to study carefully theoretical uncertainties. For instance the parameteric uncertainty due to the dependence on the top-quark mass of $0.5\,\text{GeV}$ will yield an additional error of $\Delta M_W = 2.5\,\text{MeV}$. Also higher-order corrections, at least the dominating 2-loop corrections in DIS will have to be studied and kept under control. Then, the prospected determination of the W-boson mass from LHeC data will be among the most precise determinations and significantly improve the world average value of M_W. It will also become competitive with its prediction from global EW fits with present uncertainties of about $\Delta M_W = 7\,\text{MeV}$ [181, 432, 433].

While the determination of M_W from LHeC data is competitive with other measurements, the experimental uncertainties of a determination of M_Z are estimated to be about $11\,\text{MeV}$ and $13\,\text{MeV}$ for LHeC-60 and LHeC-50, respectively. Therefore, the precision of the determination of M_Z at LHeC cannot compete with the precise measurements at the Z-pole by LEP+SLD and future e^+e^- colliders may even improve on that.

A simultaneous determination of M_W and M_Z is displayed in Fig. 5.3 (left). Although the precision of these two mass parameters is only moderate, a meaningful test of the high-energy

---

[1]Due to performance reasons, the pseudodata are generated for a rather coarse grid. With a binning which is closely related to the resolution of the LHeC detector, much finer grids in x and Q^2 are feasible. Already such a change would alter the uncertainties of the fit parameters. However, such an effect can be reflected by a changed uncorrelated uncertainty, and a value of 0.25% appears like an optimistic, but achievable, alternative scenario.
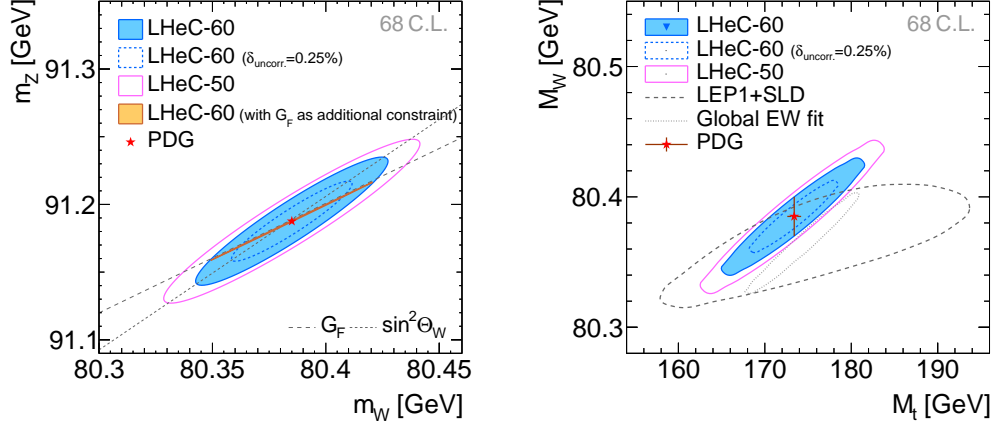
Figure 5.3: Simultaneous determination of the top-quark mass M_t and W-boson mass M_W from LHeC-60 or LHeC-50 data (left). Simultaneous determination of the W-boson and Z-boson masses from LHeC-60 or LHeC-50 data (right).

behaviour of electroweak theory is obtained by using G_F as additional input: The high precision of the G_F measurement [434] yields a very shallow error ellipse and a precise test of the SM can be performed with only NC and CC DIS cross sections alone. Such a fit determines and simultaneously tests the high-energy behaviour of electroweak theory, while using only low-energy parameters α and G_F as input (plus values for masses like M_t and M_H needed for loop corrections).

5.1.4 Further mass determinations

Inclusive DIS data are sensitive to the top-quark mass M_t indirectly through radiative corrections. M_t-dependent terms are dominantly due to corrections from the gauge boson self-energy corrections. They are contained in the ρ and κ parameters and in the correction factor Δr. The leading contributions are proportional to M_t^2. This allows for an indirect determination of the top-quark mass using LHeC inclusive DIS data, and a determination of M_t will yield an uncertainty of $\Delta M_t = 1.8\,\text{GeV}$ to $2.2\,\text{GeV}$. Assuming an uncorrelated uncertainty of the DIS data of $0.25\,\%$ the uncertainty of M_t becomes as small as

$$\Delta M_t = 1.1 \ \text{ to } \ 1.4\,\text{GeV} \tag{5.10}$$

for 60 and 50 GeV electron beams, respectively. This would represent a very precise indirect determination of the top-quark mass from purely electroweak corrections and thus being fully complementary to measurements based on real t-quark production, which often suffer from sizeable QCD corrections. The precision achievable in this way will be competitive with indirect determinations from global EW fits after the HL-LHC [435].

More generally, and to some extent depending on the choice of the renormalisation scheme, the leading self-energy corrections are proportional to $\frac{M_t^2}{M_W^2}$ and thus a simultaneous determination of M_t and M_W is desirable. The prospects for a simultaneous determination of M_t and M_W is displayed in Fig. 5.3 (right). It is remarkable that the precision of the LHeC is superior to that of the LEP+SLD combination [436]. In an optimistic scenario an uncertainty similar to the global electroweak fit [433] can be achieved. In a fit without PDF parameters similar uncertainties are found (not shown), which illustrates that the determination of EW parameters is to a large extent independent of the QCD phenomenology and the PDFs.
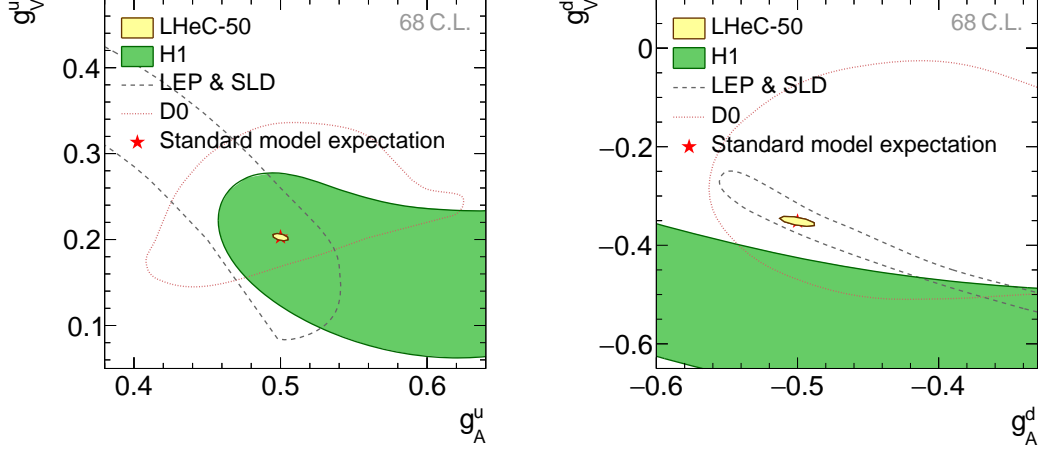
Figure 5.4: Weak NC vector and axial-vector couplings of u-type (left) and d-type quarks (right) at 68 % confidence level (C.L.) for simulated LHeC data with $E_e = 50\,\mathrm{GeV}$. The LHeC expectation is compared with results from the combined LEP+SLD experiments [436], a single measurement from D0 [437] and one from H1 [415]. The standard model expectations are diplayed by a red star, partially hidden by the LHeC prospects.

The subleading contributions to self-energy corrections have a Higgs-boson mass dependence and are proportional to $\log \frac{M_H^2}{M_W^2}$. When fixing all other EW parameters the Higgs boson mass could be constrained indirectly through these loop corrections with an experimental uncertainty of $\Delta m_H = {}^{+29}_{-23}$ to ${}^{+24}_{-20}\,\mathrm{GeV}$ for different LHeC scenarios, which is again similar to the indirect constraints from a global electroweak fit [433], but not competitive with direct measurements.

5.1.5 Weak Neutral Current Couplings

The vector and axial-vector couplings of up-type and down-type quarks to the Z, g_V^q and g_A^q, see Eq. (5.7), are determined in a fit of the four coupling parameters together with the PDFs.

Coupling	PDG	Expected uncertainties		
parameter	value	LHeC-60	LHeC-60 ($\delta_{\mathrm{uncor.}}{=}0.25\,\%$)	LHeC-50
g_A^u	$0.50\ {}^{+0.04}_{-0.05}$	0.0022	0.0015	0.0035
g_A^d	$-0.514\ {}^{+0.050}_{-0.029}$	0.0055	0.0034	0.0083
g_V^u	$0.18\ \pm 0.05$	0.0015	0.0010	0.0028
g_V^d	$-0.35\ {}^{+0.05}_{-0.06}$	0.0046	0.0027	0.0067

Table 5.1: Light-quark weak NC couplings $(g_A^u, g_A^d, g_V^u, g_V^d)$ and their currently most precise values from the PDG [181] compared with the prospected uncertainties for different LHeC scenarios. The LHeC prospects are obtained in a simultaneous fit of the PDF parameters and all four coupling parameters determined at a time.

The resulting uncertainties are collected in Tab. 5.1. The two-dimensional uncertainty contours at 68 % confidence level obtained from LHeC data with $E_e = 50\,\mathrm{GeV}$ are displayed in Fig. 5.4 for the two quark families and compared with available measurements. While all the current determinations from e^+e^-, ep or $p\bar{p}$ data have a similar precision, the future LHeC data will greatly improve the precision of the weak neutral-current couplings and expected uncertainties are an order of magnitude smaller than the currently most precise ones [181]. An increased
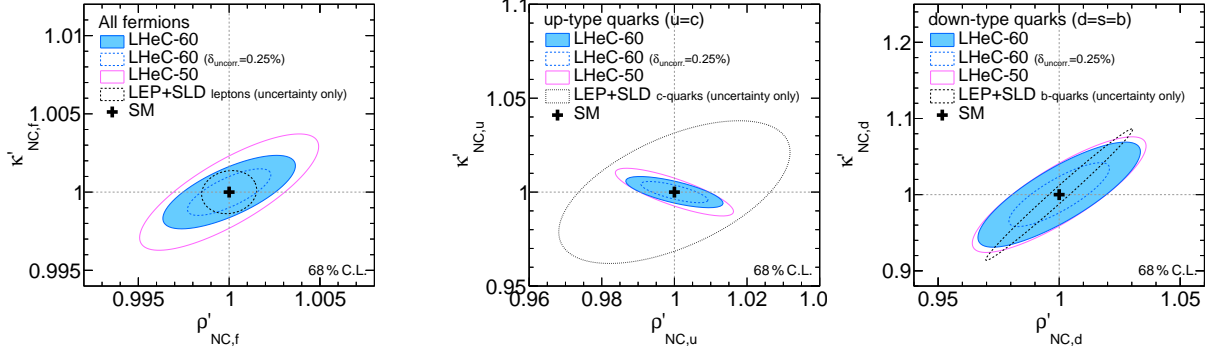
Figure 5.5: Expectations at 68 % confidence level for the determination of the ρ'_{NC} and κ'_{NC} parameters assuming a single anomalous factor equal for all fermions (left). The results for three different LHeC scenarios are compared with the achieved uncertainties from the LEP+SLD combination [436] for the determination the respective leptonic quantities. Right: uncertainties for the simultaneous determination of the anomalous form factors for u and d-type quarks, assuming known values for the electron parameters. The values are compared with uncertainties reported by LEP+SLD for the determination of the values $\rho_{\mathrm{NC},(c,b)}$ and $\sin\theta_{\mathrm{W}}^{\mathrm{eff},(c,b)}$ for charm or bottom quarks, respectively.

electron beam energy of $E_e = 60\,\mathrm{GeV}$ or improved experimental uncertainties would further improve this measurement.

The determination of the couplings of the electron to the Z boson, g_V^e and g_A^e, can be determined at the LHeC with uncertainties of up to $\Delta g_V^e = 0.0013$ and $\Delta g_A^e = \pm 0.0009$, which is similar to the results of a single LEP experiment and about a factor three larger than the LEP+SLD combination [436].

5.1.6 The neutral-current ρ_{NC} and κ_{NC} parameters

Beyond Born approximation, the weak couplings are subject to higher-order loop corrections. These corrections are commonly parameterised by quantities called ρ_{NC}, κ_{NC} and ρ_{CC}. They are sensitive to contributions beyond the SM and the structure of the Higgs sector. It is important to keep in mind that these effective coupling parameters depend on the momentum transfer and are, indeed, form factors rather than constants. It is particularly interesting to investigate the so-called effective weak mixing angle defined as $\sin^2\theta_{\mathrm{W}}^{\mathrm{eff}} = \kappa_{\mathrm{NC}}\sin^2\theta_{\mathrm{W}}$. At the Z-pole it is well accessible through asymmetry measurements in e^+e^- collisions. In DIS at the LHeC, the scale dependence of the effective weak mixing angle is not negligible. It can be determined only together with the ρ parameter due to the Q^2 dependence and the presence of the photon exchange terms. Therefore, we introduce (multiplicative) anomalous contributions to these factors, denoted as $\rho'_{\mathrm{NC,CC}}$ and κ'_{NC}, and test their agreement with unity (for more details see Ref. [415]), and uncertainties of these parameters are obtained in a fit together with the PDFs. The two-dimensional uncertainty contours of the anomalous form factors $\rho'_{\mathrm{NC},f}$ and $\kappa'_{\mathrm{NC},f}$ are displayed for three different LHeC scenarios in Fig. 5.5 (left), and compared with uncertainties from the LEP+SLD combination [2] [436]. It is found that these parameters can be determined with very high experimental precision.

---

[2]Since in the LEP+SLD analysis the values of ρ_{NC} and $\kappa_{\mathrm{NC}}\sin^2\theta_{\mathrm{W}}$ are determined, we compare only the size of the uncertainties in these figures. Furthermore it shall be noted, that LEP is mainly sensitive to the parameters of leptons or heavy quarks, while LHeC data is more sensitive to light quarks (u,d,s), and thus the LHeC measurements are highly complementary.
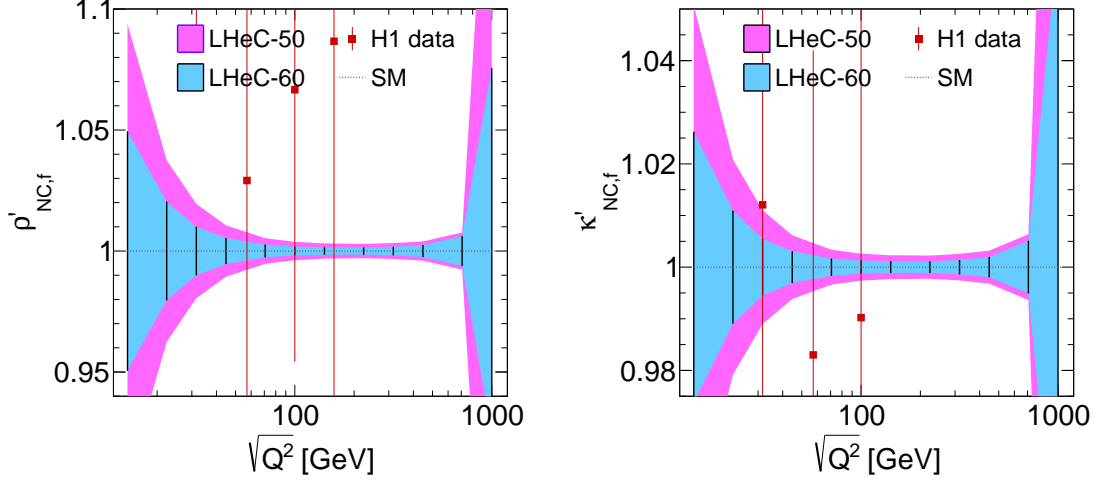
Figure 5.6: Test of the scale dependence of the anomalous ρ and κ parameters for two different LHeC scenarios. For the case of LHeC-60, i.e. $E_e = 60\,\text{GeV}$, we assume an uncorrelated uncertainty of $0.25\,\%$. The uncertainties of the parameter $\kappa'_{\text{NC,f}}$ can be interpreted as sensitivity to the scale-dependence of the weak mixing angle, $\sin\theta_{\text{W}}^{\text{eff}}(\mu)$.

Assuming the couplings of the electron are given by the SM, the anomalous form factors for the two quark families can be determined and results are displayed in Fig. 5.5 (right). Since these measurements represent unique determinations of parameters sensitive to the light-quark couplings, we can compare only with nowadays measurements of the parameters for heavy-quarks of the same charge and it is found that the LHeC will provide high-precision determinations of the ρ'_{NC} and κ'_{NC} parameters.

A meaningful test of the SM can be performed by determining the effective coupling parameters as a function of the momentum transfer. In case of κ'_{NC}, this is equivalent to measuring the running of the effective weak mixing angle, $\sin\theta_{\text{W}}^{\text{eff}}(\mu)$ (see also Sec. 5.1.7). However, DIS is quite complementary to other measurements since the process is mediated by space-like momentum transfer, i.e. $q^2 = -Q^2 < 0$ with q being the boson four-momentum. Prospects for a determination of ρ'_{NC} or κ'_{NC} at different Q^2 values are displayed in Fig. 5.6 and compared to results obtaind by H1. The value of $\kappa'_{\text{NC}}(\mu)$ can be easily translated to a measurement of $\sin\theta_{\text{W}}^{\text{eff}}(\mu)$. From Fig. 5.6 one can conclude that this quantity can be determined with a precision of up to $0.1\,\%$ and better than $1\,\%$ over a wide kinematic range of about $25 < \sqrt{Q^2} < 700\,\text{GeV}$.

5.1.7 The effective weak mixing angle $\sin^2\theta_{\text{W}}^{\text{eff},\ell}$

The leptonic effective weak mixing angle is defined as $\sin^2\theta_{\text{W}}^{\text{eff},\ell}(\mu^2) = \kappa_{\text{NC},\ell}(\mu^2)\sin^2\theta_{\text{W}}$. Due to its high sensitivity to loop corrections it represents an ideal quantity for precision tests of the Standard Model. Its value is scheme dependent and it exhibits a scale dependence. Near the Z pole, $\mu^2 = M_Z^2$, its value was precisely measured at LEP and at SLD. Those analyses were based on the measurement of asymmetries and their interpretation in terms of the leptonic weak mixing angle was simplified by the fact that many non-leptonic corrections and contributions from box graphs cancel or can be taken into account by subtracting their SM predictions. The highest sensitivity to $\sin^2\theta_{\text{W}}^{\text{eff},\ell}(M_Z)$ to date arises from a measurement of $A_{\text{fb}}^{0,b}$ [436], where the non-universal flavour-specific corrections to the quark couplings are taken from the SM and consequently these measurements are interpreted to be sensitive only to the universal, i.e.

Fit parameters	Parameter of interest	SM value	Expected uncertainties			
			LHeC-50 ($\delta_{\text{uncor.}} = 0.50\,\%$)	LHeC-60	LHeC-50 ($\delta_{\text{uncor.}} = 0.25\,\%$)	LHeC-60
$\kappa'_{\text{NC},f}$, PDFs	$\sin^2\theta_{\text{W}}^{\text{eff},\ell}(M_Z^2)$	0.23154	0.00033	0.00025	0.00022	0.00015
$\kappa'_{\text{NC},f}$, $\rho'_{\text{NC},f}$, PDFs	$\sin^2\theta_{\text{W}}^{\text{eff},\ell}(M_Z^2)$	0.23154	0.00071	0.00036	0.00056	0.00023
$\kappa'_{\text{NC},e}$, PDFs	$\sin^2\theta_{\text{W}}^{\text{eff},e}(M_Z^2)$	0.23154	0.00059	0.00047	0.00038	0.00028
$\kappa'_{\text{NC},e}$, $\kappa'_{\text{NC},u}$, $\kappa'_{\text{NC},d}$, PDFs	$\sin^2\theta_{\text{W}}^{\text{eff},e}(M_Z^2)$	0.23154	0.00111	0.00095	0.00069	0.00056
$\kappa'_{\text{NC},f}$	$\sin^2\theta_{\text{W}}^{\text{eff},\ell}(M_Z^2)$	0.23154	0.00028	0.00023	0.00017	0.00014

Table 5.2: Determination of $\sin^2\theta_{\text{W}}^{\text{eff},\ell}(M_Z^2)$ with inclusive DIS data at the LHeC for different scenarios. Since the value of the effective weak mixing angle at the Z pole cannot be determined directly in DIS, a fit of the $\kappa'_{\text{NC},f}$ parameter is performed instead and its uncertainty is translated to $\sin^2\theta_{\text{W}}^{\text{eff},\ell}(M_Z^2)$. Different assumptions on the fit parameters are studied, and results include uncertainties from the PDFs. Only the last line shows results where the PDF parameters are kept fixed. See text for more details.

flavour-independent [3], non-SM contributions to κ_{NC}. Applying this assumption also to the DIS cross sections, the determination of $\kappa'_{\text{NC},f}$ can directly be interpreted as a sensitivity study of the leptonic effective weak mixing angle $\sin^2\theta_{\text{W}}^{\text{eff},\ell}$.

The prospects for a determination of $\sin^2\theta_{\text{W}}^{\text{eff},\ell}$ are listed in Tab. 5.2. Two fits have been studied: one with a fixed parameter ρ'_{NC} and one where $\sin^2\theta_{\text{W}}^{\text{eff},\ell}$ is determined together with ρ'_{NC} (see Fig. 5.5 (left)). At the LHeC, it will be possible to determine the value of $\sin^2\theta_{\text{W}}^{\text{eff},\ell}(M_Z^2)$ with an experimental uncertainty of up to

$$\Delta\sin^2\theta_{\text{W}}^{\text{eff},\ell} = \pm 0.00015\,, \tag{5.11}$$

where PDF uncertainties are already included. If the PDF parameters are artificially kept fixed, the uncertainties are of very similar size, which demonstrates that these measurements are fairly insensitive to the QCD effects and the PDFs. The uncertainties are compared [4] to recent average values in Fig. 5.7. One can see that the LHeC measurement has the potential to become the most precise single measurement in the future with a significant impact to the world average value. It is obvious that a conclusive interpretation of experimental results with such a high precision will require correspondingly precise theoretical predictions, and the investigation of two-loop corrections for DIS will become important.

This LHeC measurement will become competitive with measurements at the HL-LHC [185]. Since in pp collisions one of the dominant uncertainties is from the PDFs [440, 441, 444–446], future improvements can (only) be achieved with a common analysis of LHeC and HL-LHC data. Such a study will yield highest experimental precision and the challenging theoretical and experimental aspects for a complete understanding of such an analysis will deepen our understanding of the electroweak sector.

It may be further of interest, to determine the value of the effective weak mixing angle of the electron separately in order to compare with measurements in pp and test furthermore lepton-

---

[3]Flavour-specific tests have been discussed to some extent in the previous Section.

[4] It shall be noted, that in order to compare the LHeC measurements with the Z-pole measurements at $\mu^2 = M_Z^2$ in a conclusive way, one has to assume the validity of the SM framework. In particular the scale-dependence of $\kappa_{\text{NC},\ell}$ must be known in addition to the flavour-specific corrections. On the other hand, the scale dependence can be tested itself with the LHeC data which cover a large range of space-like Q^2. In this aspect, DIS provides a unique opportunity for precision measurements in the space-like regime ($\mu^2 < 0$) as has been discussed in the previous Section, see Fig. 5.6 (right).
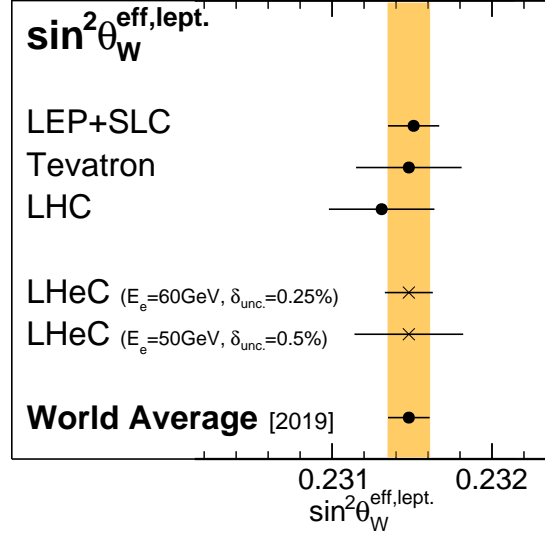
Figure 5.7: Comparison of the determination of $\sin^2 \theta_{\mathrm{W}}^{\mathrm{eff},\ell}(M_Z^2)$ from LHeC inclusive DIS data with recent averaged values. Results from LEP+SLC [436], Tevatron [438], LHC [439–442] and the world average value [442] are all obtained from a combination of various separate measurements (not shown individually) (see also Ref. [443] for additional discussions). For LHeC, the experimental and PDF uncertainties are displayed.

specific contributions to $\kappa_{\mathrm{NC,lept.}}$. Such fits are summarised in Table 5.2 and a reasonable precision is achieved with LHeC.

The measurement of the weak mixing angle can be performed in sub-regions of Q^2 due to the wide kinematic range accessible at the LHeC. The relative uncertainties for the determination of the weak mixing angle for different Q^2 intervals is displayed in Fig. 5.8. We find that the weak mixing angle can be determined in the range of about $25 < \sqrt{Q^2} < 700\,\mathrm{GeV}$ with a precision better than 0.1 %. If a calculation of DIS cross sections including higher-order EW corrections in the $\overline{\mathrm{MS}}$ scheme is available, these relative uncertainties can be mapped into a test of the running of the weak mixing angle. Note, that in DIS the scattering process is mediated by boson exchange with spacelike momenta and is therefore complementary to other measurements since the scale is $\mu^2 = -Q^2$.

5.1.8 Electroweak effects in charged-current scattering

The charged-current sector of the SM can be uniquely measured at high scales over many orders of magnitude in Q^2 at the LHeC, due to the excellent tracking detectors, calorimetry, and high-bandwidth triggers. Similarly as in the NC case, the form factors of the effective couplings of the fermions to the W boson can be measured. In the SM formalism, only two of these form factors are present, $\rho_{\mathrm{CC},eq}$ and $\rho_{\mathrm{CC},e\bar{q}}$. We thus introduce two anomalous modifications to them, $\rho_{\mathrm{CC},(eq/e\bar{q})} \to \rho'_{\mathrm{CC},(eq/e\bar{q})}\rho_{\mathrm{CC},(eq/e\bar{q})}$ (see Ref. [415]). The prospects for the determination of these parameters are displayed in Fig. 5.9, and it is found, that with the LHeC these parameters can be determined with a precision up to 0.2–0.3 %. Also their Q^2 dependence can be uniquely studied with high precision up to $\sqrt{Q^2}$ values of about $400\,\mathrm{GeV}$.

124
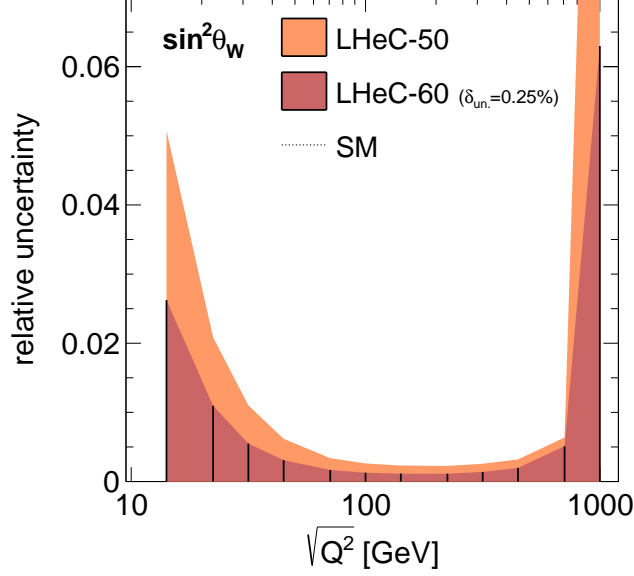
Figure 5.8: Expected uncertainties of the weak mixing angle determined in sub-regions of Q^2. Two scenarios for the simulation of LHeC inclusive NC/CC DIS data are considered.
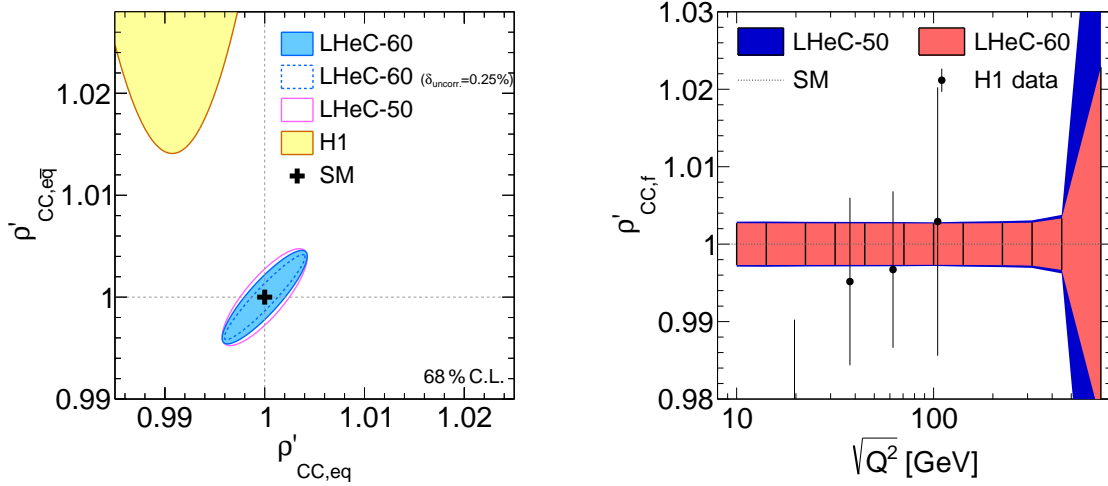
Figure 5.9: Left: anomalous modifications of the charged current form factors $\rho'_{\mathrm{CC},eq}$ and $\rho'_{\mathrm{CC},e\bar{q}}$ for different LHeC scenarios in comparison with the H1 measurement [415]. Right: scale dependent measurement of the anomalous modification of the charged current form factor $\rho'_{\mathrm{CC}}(Q^2)$, assuming $\rho'_{\mathrm{CC},eq} = \rho'_{\mathrm{CC},e\bar{q}} = \rho'_{\mathrm{CC}}$.

5.1.9 Conclusion

With LHeC inclusive NC and CC DIS data, unique measurements of electroweak parameters can be performed with highest precision. Since inclusive DIS is mediated through space-like momentum transfer (t-channel exchange) the results are often complementary to other experiments, such as pp or e^+e^- collider experiments, where measurements are performed in the time-like regime and most often at the Z peak. Among many other quantities, measurements of the weak couplings of the light quarks, u and d, or their anomalous form factors $\rho'_{\mathrm{NC},u/d}$ and $\kappa'_{\mathrm{NC},u/d}$,

can be performed uniquely due to the important contributions of valence quarks in the initial state. Also scale dependent measurements of weak interactions can be performed over a large range in $\sqrt{Q^2}$, which provides an interesting portal to BSM physics. The W boson mass can be determined with very small experimental uncertainties, such that theoretical uncertainties are expected to become more important than experimental uncertainties. While the parameters of the PDFs are determined together with the EW parameters in the present study, it is found that the PDFs do not induce a limitation of the uncertainties. Considering the dominating top-quark mass dependence of higher-order electroweak effects, one can realise that the LHeC will be competitive with the global electroweak fit after the HL-LHC era [185, 435].

Besides proving its own remarkable prospect on high-precision electroweak physics, the LHeC will further significantly improve the electroweak measurements in pp collisions at the LHC by reducing the presently sizeable influence of PDF and α_s uncertainties. This is discussed in Sec. 9.

5.2 Direct W and Z Production and Anomalous Triple Gauge Couplings

5.2.1 Direct W and Z Production

The direct production of single W and Z bosons as a crucial signal represents an important channel for EW precision measurements. The production of W bosons has been measured at $\sqrt{s} \simeq 320\,\mathrm{GeV}$ at HERA [447–449]. With the full $e^{\pm}p$ data set collected by the H1 and ZEUS experiments together, corresponding to an integrated luminosity of about $\mathcal{L} \sim 1\,\mathrm{fb}^{-1}$, a few dozens of W boson event candidates have been identified in the e, μ or τ decay channel.

Detailed studies of direct W/Z production in ep collisions at higher centre-of-mass energies have been presented in the past, see Refs. [450–452]. These theoretical studies were performed for a proton beam energy of $E_p = 8\,\mathrm{TeV}$ and electron beam energies of $E_e = 55\,\mathrm{GeV}$ or $100\,\mathrm{GeV}$, which correspond to a very similar centre-of-mass energy as the LHeC. Measurements at the LHeC will benefit considerably from the large integrated luminosity, in comparison to earlier projections.

The W or Z direct production in e^-p collisions can be classified into five processes

$$
\begin{aligned}
e^-p \to e^- W^+ j, \quad & e^-p \to e^- W^- j, \\
e^-p \to \nu_e^- W^- j, \quad & e^-p \to \nu_e^- Z j
\end{aligned}
\tag{5.12}
$$

and

$$
e^-p \to e^- Z j,
\tag{5.13}
$$

where j denotes the hadronic the final state (i.e. the *forward jet*). According to the above classification, the four processes in Eq. (5.12) can be used to study Tripe Gauge Couplings (TGCs), e.g. $WW\gamma$ and WWZ couplings, since some contributing diagrams represent Vector Boson Fusion (VBF) processes. The process shown in Eq. (5.13) does not contain any TGC vertex. The processes for positron-proton collisions can be easily derived from Eqs. (5.12) and (5.13), but are not discussed further here due to the small integrated luminosity of the LHeC e^+p data.

The MadGraph5_v2.4.2 program [367] is employed for matrix element calculation and event generation and the PDF NNPDF23_nlo_as_0119_qed [453] is used. Technical cuts on the transverse

momentum of the outgoing scattered lepton, p_T^ℓ, of $10\,\text{GeV}$ or alternatively $5\,\text{GeV}$, are imposed and other basic cuts are $p_T^j > 20\,\text{GeV}$, $|\eta_{e,j}| < 5$ and $\Delta R_{ej} < 0.4$. The resulting Standard Model total cross sections of the above processes are listed in Tab. 5.3.

Process	$E_e = 50\,\text{GeV}, E_p = 7\,\text{TeV}$ $p_T^e > 10\,\text{GeV}$	$E_e = 60\,\text{GeV}, E_p = 7\,\text{TeV}$ $p_T^e > 10\,\text{GeV}$	$E_e = 60\,\text{GeV}, E_p = 7\,\text{TeV}$ $p_T^e > 5\,\text{GeV}$
$e^- W^+ j$	$1.00\,\text{pb}$	$1.18\,\text{pb}$	$1.60\,\text{pb}$
$e^- W^- j$	$0.930\,\text{pb}$	$1.11\,\text{pb}$	$1.41\,\text{pb}$
$\nu_e^- W^- j$	$0.796\,\text{pb}$	$0.956\,\text{pb}$	$0.956\,\text{pb}$
$\nu_e^- Z j$	$0.412\,\text{pb}$	$0.502\,\text{pb}$	$0.502\,\text{pb}$
$e^- Z j$	$0.177\,\text{pb}$	$0.204\,\text{pb}$	$0.242\,\text{pb}$

Table 5.3: The SM predictions of direct W and Z production cross sections in $e^- p$ collisions for different collider beam energy options, E_e, and final state forward electron transverse momentum cut, p_T^e. Two different electron beam energy options are considered, $E_e = 50\,\text{GeV}$ and $60\,\text{GeV}$.

The process with the largest production cross section in $e^- p$ scattering is the single W^+ boson production. This will be the optimal channel of both the SM measurement and new physics probes in the EW sector. Also, this channel is experimentally preferred since the W^+ is produced in NC scattering, so the beam electron is measured in the detector, and the W-boson has opposite charge to the beam lepton and thus in a leptonic decay an opposite charge lepton and missing transverse momentum is observed. Altogether, it is expected that a few million of direct W-boson events are measured at LHeC.

Several 10^5 direct Z events are measured, which corresponds approximately to the size of the event sample of the SLD experiment [436], but at the LHeC these Z bosons are predominantly produced in VBF events.

All these total cross sections increase significantly with smaller transverse momentum of the outgoing scattered lepton. Therefore it will become important to decrease that threshold with dedicated electron taggers, see Chapter 12.

5.2.2 Anomalous Triple Gauge Couplings

The measurement of gauge boson production processes provides a precise measurement of the triple gauge boson vertex. The measurement is sensitive to new physics contributions in *anomalous* Tripe Gauge Couplings (aTGC). The LHeC has advantages of a higher centre-of-mass energy and easier kinematic analysis in the measurement of aTGCs.

In the effective field theory language, aTGCs in the Lagrangian are generally parameterised as

$$
\begin{aligned}
\mathcal{L}_{TGC}/g_{WWV} &= ig_{1,V}(W^+_{\mu\nu}W^-_\mu V_\nu - W^-_{\mu\nu}W^+_\mu V_\nu) + i\kappa_V W^+_\mu W^-_\nu V_{\mu\nu} + \frac{i\lambda_V}{M_W^2}W^+_{\mu\nu}W^-_{\nu\rho}V_{\rho\mu} \\
&+ g_5^V \epsilon_{\mu\nu\rho\sigma}(W^+_\mu \overleftrightarrow{\partial}_\rho W^-_\nu)V_\sigma - g_4^V W^+_\mu W^-_\nu (\partial_\mu V_\nu + \partial_\nu V_\mu) \\
&+ i\tilde{\kappa}_V W^+_\mu W^-_\nu \tilde{V}_{\mu\nu} + \frac{i\tilde{\lambda}_V}{M_W^2}W^+_{\lambda\mu}W^-_{\mu\nu}\tilde{V}_{\nu\lambda},
\end{aligned} \tag{5.14}
$$

where $V = \gamma, Z$. The gauge couplings $g_{WW\gamma} = -e$, $g_{WWZ} = -e\cot\theta_W$ and the weak mixing angle θ_W are from the SM. $\tilde{V}_{\mu\nu}$ and $A\overleftrightarrow{\partial}_\mu B$ are defined as $\tilde{V}_{\mu\nu} = \frac{1}{2}\epsilon_{\mu\nu\rho\sigma}V_{\rho\sigma}$, $A\overleftrightarrow{\partial}_\mu B = A(\partial_\mu B) - (\partial_\mu A)B$, respectively. There are five aTGCs ($g_{1,Z}$, κ_V, and λ_V) conserving the C and CP

condition with electromagnetic gauge symmetry requires $g_{1,\gamma} = 1$. Only three of them are independent because $\lambda_Z = \lambda_\gamma$ and $\Delta\kappa_Z = \Delta g_{1,Z} - \tan^2\theta_W \Delta\kappa_\gamma$ [454–456]. The LHeC can set future constraints on $\Delta\kappa_\gamma$ and λ_γ.

In the direct Z/γ production process, the anomalous WWZ and $WW\gamma$ couplings can be separately measured without being influenced by their interference [457, 458]. In the direct W production process, both the deviation in signal cross section and the kinematic distributions can effectively constrain the $WW\gamma$ aTGC, while anomalous WWZ contribution in this channel is insensitive as a result of the suppression from Z boson mass [459–461].
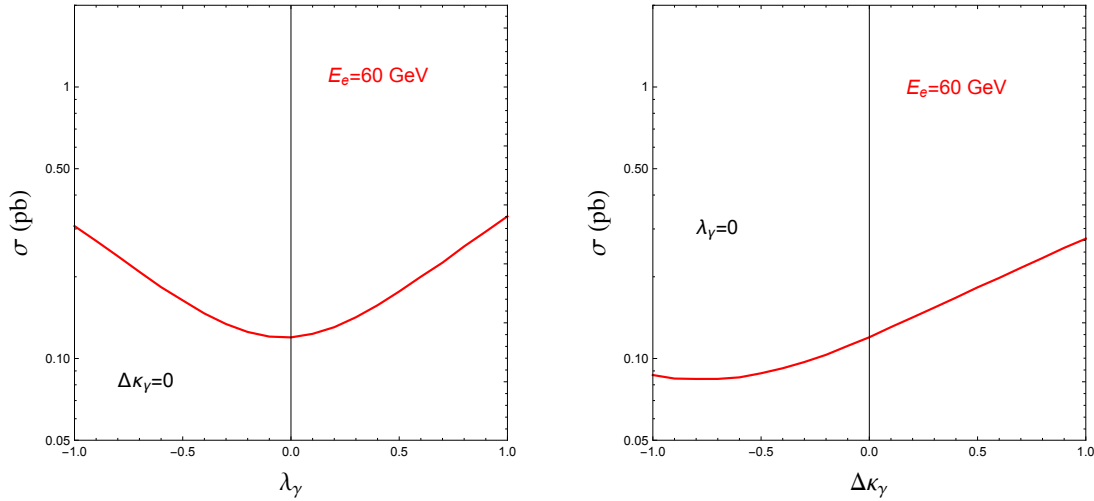

Figure 5.10: Total cross sections of the $e^-p \to e^-\mu^+\nu_\mu j$ process with varying λ_γ (left plot) and $\Delta\kappa_\gamma$ (right plot).

The W decay into muon channel is the expected optimal measurement for the anomalous $WW\gamma$ coupling because of the discrimination of final states and mistagging efficiencies [459]. Fig. 5.10 shows the cross section of single W^+ production process followed by $W^+ \to \mu^+\nu_\mu$ decay, with different λ_γ and $\Delta\kappa_\gamma$ values. Large anomalous coupling leads to measurable deviation to the SM prediction. The cross section increases monotonically with $\Delta\kappa_\gamma$ and the absolute value of λ_γ within the region of $-1.0 \leq \lambda_\gamma/\Delta\kappa_\gamma \leq 1.0$.

Kinematic analysis is necessary for the precise aTGC measurement. At LHeC, the $e^-p \to e^-W^\pm j$ process with leptonic W boson decay can be fully reconstructed because the undetected neutrino information is reconstructed either with energy-momentum conservation or the recoil mass method. This allows to use angular correlation observables, which are sensitive to the W boson polarisation. Helicity amplitude calculation indicates that a non-SM value of λ_γ leads to a significant enhancement in the transverse polarisation fraction of the W boson in the $e^-p \to e^-W^+j$ process, while a non-SM value of $\Delta\kappa_\gamma$ leads to enhancement in the longitudinal component fraction [450]. The angle $\theta_{\ell W}$ is defined as the angle between the decay product lepton ℓ in the W rest frame and W moving direction in the collision rest frame. Making use of the energetic final states in the forward direction, a second useful angle $\Delta\phi_{ej}$ is defined as the separation of final state jet and electron on the azimuthal plane. In an optimised analysis, assuming an integrated luminosity of $1\,\mathrm{ab}^{-1}$, the observable $\Delta\phi_{ej}$ can impose stringent constraints on both λ_γ and $\Delta\kappa_\gamma$, and uncertainties within $[-0.007, 0.0056]$ and $[-0.0043, 0.0054]$ are achieved, respectively. The $\cos\theta_{\mu W}$ observable is also sensitive to $\Delta\kappa_\gamma$ at the same order, but fails to constrain λ_γ. The analysis is described in detail in Ref. [459].

Fig. 5.11 shows the two-parameter aTGC constraint on the λ_γ–$\Delta\kappa_\gamma$ plane based on a χ^2 analysis
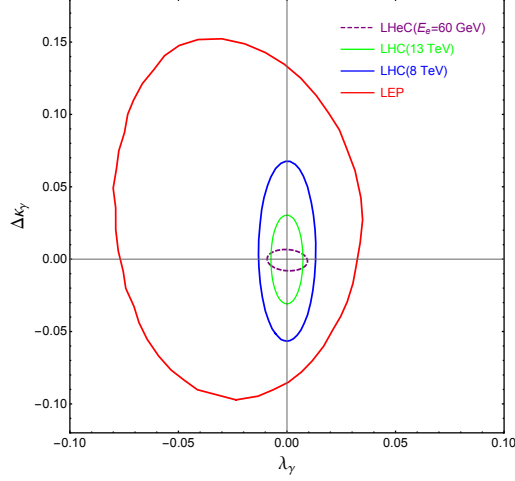
Figure 5.11: The 95% C.L. exclusion limit on the $\Delta\kappa_\gamma$-λ_γ plane. The purple dashed contour is the projected LHeC exclusion limit with $1\,\mathrm{ab}^{-1}$ integrated luminosity [459]. The blue, green and red contours are current bounds from LHC [462, 463] and LEP [464].

of $\Delta\phi_{ej}$ at parton-level and assuming an electron beam energy of $E_e = 60\,\mathrm{GeV}$. When comparing with the current LHC (blue and green) and LEP (red) bounds, the LHeC has the potential to significantly improve the constraints, in particular on the $\Delta\kappa_\gamma$ parameter. The polarised electron beam is found to improve the aTGC measurement [458, 461]. In consideration of the *realistic* analysis at detector level, one expects 2-3 ab^{-1} integrated luminosity to achieve same results [459].

One uncertainty in the aTGC measurement at the (HL-)LHC comes from the PDF uncertainty. Future LHeC PDF measurement will improve the precision of aTGC measurement in the $x \simeq \mathcal{O}(10^{-2})$ region.

5.3 Top Quark Physics

SM top quark production at a future ep collider is dominated by single top quark production, mainly via CC DIS production. An example graph is shown in Fig. 5.12 (left). The total cross section is $1.89\,\mathrm{pb}$ at the LHeC [465] and with an electron beam energy of $60\,\mathrm{GeV}$, and an LHC proton beam of $7\,\mathrm{TeV}$, leading to a centre-of-mass energy of $1.3\,\mathrm{TeV}$, respectively. The other important top quark production mode is $t\bar{t}$ photoproduction with a total cross section of $0.05\,\mathrm{pb}$ at the LHeC [466]. An example graph is shown in Fig. 5.12 (right). This makes a future LHeC a top quark factory and an ideal tool to study top quarks with a high precision, and to analyse in particular their electroweak interaction. Selected highlights in top quark physics are summarised here.

5.3.1 *Wtq* Couplings

The top quark couplings with gauge bosons can be modified significantly in models with new top (or third generation) partners, such as in some extensions of the minimal supersymmetric standard model, in little Higgs models, top-color models, top seesaw, top compositeness, and
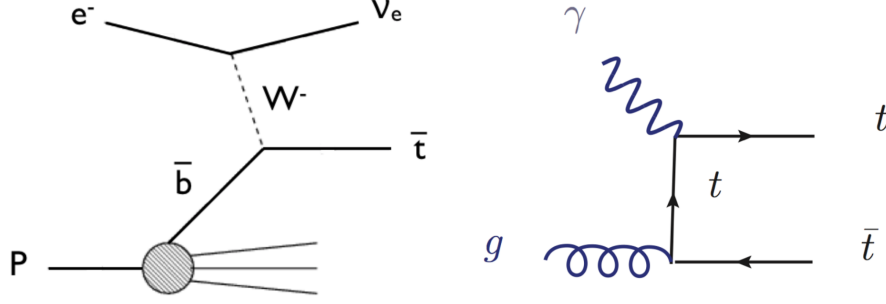
Figure 5.12: Example graphs for CC DIS top quark production (left) and top quark photoproduction (right).

others. Testing them is therefore of utmost importance to find out whether there are other sources of electroweak symmetry breaking that are different from the standard Higgs mechanism.

One flagship measurement is the direct measurement of the CKM matrix element $|V_{tb}|$, i.e. without making any model assumptions such as on the unitarity of the CKM matrix or the number of quark generations. An elaborate analysis of the single top quark CC DIS process at the LHeC including a detailed detector simulation using the DELPHES package [467] shows that already at $100\,\mathrm{fb}^{-1}$ of integrated luminosity an uncertainty of 1% can be expected. This compares to a total uncertainty of 4.1 % of the currently most accurate result at the LHC Run-I performed by the CMS experiment [468].

The same analysis [465] can also be used to search for anomalous left- and right-handed Wtb vector (f_1^L, f_1^R) and tensor (f_2^L, f_2^R) couplings analyzing the following effective Lagrangian:

$$\mathcal{L}_{Wtb} = -\frac{g}{\sqrt{2}}\bar{b}\gamma^\mu V_{tb}(f_1^L P_L - f_1^R P_R)tW_\mu^- - \frac{g}{\sqrt{2}}\bar{b}\frac{i\sigma^{\mu\nu}q_\nu}{M_W}(f_2^L P_L - f_2^R P_R)tW_\mu^- + h.c. \quad (5.15)$$

In the SM $f_1^L = 1$ and $f_1^R = f_2^L = f_2^R = 0$. The effect of anomalous Wtb couplings is consistently evaluated in the production and the decay of the antitop quark, cf. Fig. 5.12 (left).[5] Using hadronic top quark decays only, the expected accuracies in a measurement of these couplings as a function of the integrated luminosity are presented in Fig. 5.13, derived from expected 95% C.L. limits on the cross section yields. The couplings can be measured with accuracies of 1 % for the SM f_1^L coupling determining $|V_{tb}|$ (as discussed above) and of 4 % for f_2^L, 9 % for f_2^R, and 14% for f_1^R at 1 ab^{-1}.

Similarly, the CKM matrix elements $|V_{tx}|$ ($x = d, s$) can be extracted using a parameterisation of deviations from their SM values with very high precision through W boson and bottom (light) quark associated production channels, where the W boson and b-jet (light jet $j = d, s$) final states can be produced via s-channel single top quark decay or t-channel top quark exchange as outlined in [470]. As an example, analysing the processes

Signal 1: $pe^- \to \nu_e\bar{t} \to \nu_e W^-\bar{b} \to \nu_e\ell^-\nu_\ell\bar{b}$

Signal 2: $pe^- \to \nu_e W^- b \to \nu_e\ell^-\nu_\ell b$

Signal 3: $pe^- \to \nu_e\bar{t} \to \nu_e W^- j \to \nu_e\ell^-\nu_\ell j$

---

[5]Further studies of the top quark charged current coupling can be found in [469]There, a more general framework is employed using the full basis of $SU(2)_L \times U(1)$ operators, including the relevant four-fermion ones.

in an elaborate analysis including a detailed detector simulation using the DELPHES package [467], the expected accuracies on $|V_{td}|$ and $|V_{ts}|$ at the 2σ confidence level (C.L.) are shown as a function of the integrated luminosity in Fig. 5.14. At $1\,\mathrm{ab}^{-1}$ of integrated luminosity and an electron polarisation of $80\,\%$, the 2σ limits improve on existing limits from the LHC [471] (interpreted by [472]) by a factor of ≈ 3.5. Analyzing Signal 3 alone, and even more when combining Signals 1, 2 and 3, will allow for the first time to achieve an accuracy of the order of the actual SM value of $|V_{ts}^{\mathrm{SM}}| = 0.04108^{+0.0030}_{-0.0057}$ as derived from an indirect global CKM matrix fit [473], and will therefore represent a direct high precision measurement of this important top quark property. In these studies, upper limits at the 2σ level down to $|V_{ts}| < 0.06$, and $|V_{td}| < 0.06$ can be achieved.

5.3.2 Top Quark Polarisation

Single top quarks produced via the $e^+p \to t\bar{\nu}$ processes possess a high degree of spin polarisation in terms of a basis which decomposes the top quark spin in its rest frame along the direction of the incoming e beam [474]. It has been investigated for $\sqrt{s} = 1.6\,\mathrm{TeV}$ in e^+p scattering, that the spin fraction defined as the ratio of the polarised cross section to the unpolarised one, reaches 96% allowing a detailed study of top quark spin and polarisation. Exploring the angle between the momentum direction of the charged lepton from top quark decay and the spin quantisation axis in the top quark rest frame, anomalous Wtb couplings can be tested. Assuming a total systematic uncertainty of 10% the expected sensitivity for $\sqrt{s} = 1.6\,\mathrm{TeV}$ reaches $\pm 3\%$ for f_2^L, and $\pm 7\%$ for f_2^R as defined in Eq. (5.15).

5.3.3 Top-γ and Top-Z Couplings

The LHeC is particularly well suited to measure the $t\bar{t}\gamma$ vertex, since in photoproducton of top quark pairs (see Fig. 5.12, right) the highly energetic incoming photon only couples to the top quark, and therefore the cross section directly depends on the $t\bar{t}\gamma$ vertex. This provides a direct
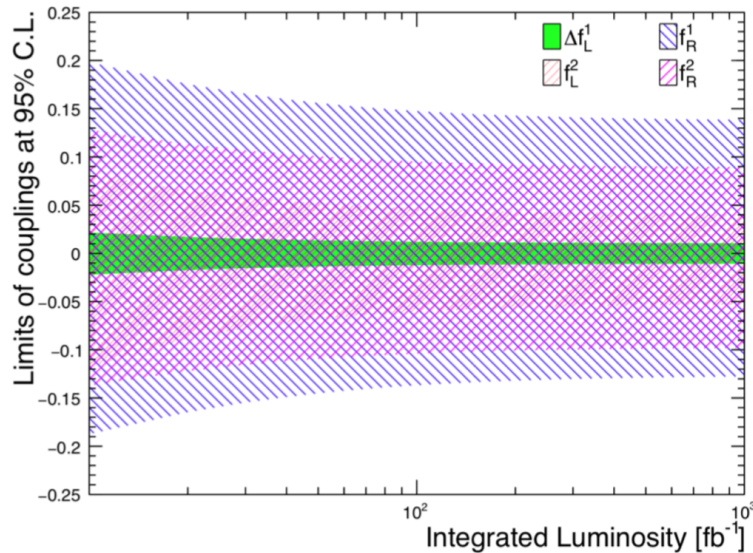

Figure 5.13: Expected sensitivities as a function of the integrated luminosity on the SM and anomalous Wtb couplings [465].
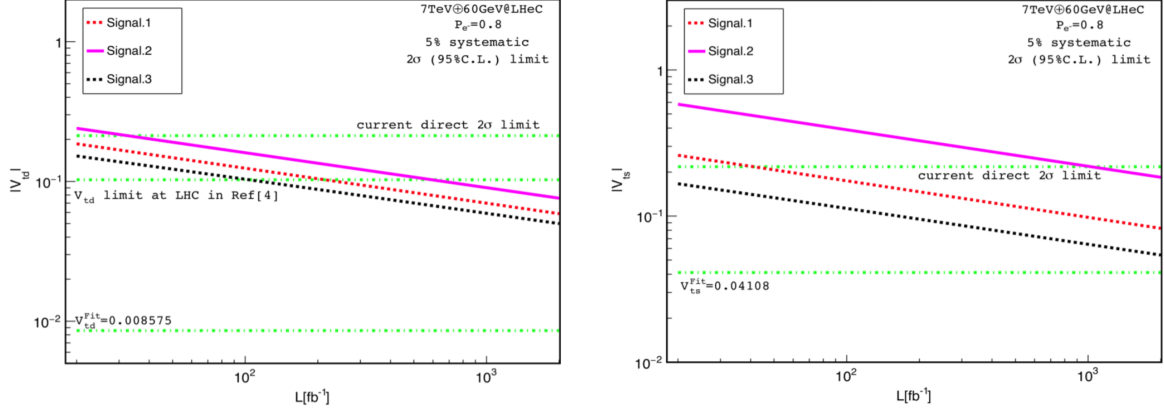
Figure 5.14: Expected sensitivities as a function of the integrated luminosity on on $|V_{td}|$ (left) and $|V_{ts}|$ (right) [470].

measurement of the coupling between the top quark and the photon and therefore of another important top quark property, the top quark charge. In contrast, at the LHC the $t\bar{t}\gamma$ vertex vertex is probed in $t\bar{t}\gamma$ production, where the final state photon can also be produced from other vertices than the $t\bar{t}\gamma$ vertex, such as from initial state radiation or from radiation off charged top quark decay products.

The LHeC also provides a high potential for measuring the $t\bar{t}\gamma$ magnetic and electric dipole moments (MDM and EDM, respectively) in $t\bar{t}$ production [466]. In an effective Lagrangian framework, effective $t\bar{t}\gamma$ couplings can be written in terms of form factors:

$$\mathcal{L}_{Wtb} = e\,\bar{t}\left(Q_t\gamma^\mu A_\mu + \frac{1}{4\,m_t}\sigma^{\mu\nu}F_{\mu\nu}\left(\kappa + i\tilde{\kappa}\gamma_5\right)\right)t \ + h.c. \tag{5.16}$$

with the anomalous MDM of the top quark, κ, and the EDM of the top quark, $\tilde{\kappa}$. The top quark charge is given by eQ_t.

By solely measuring the $t\bar{t}$ production cross section, remarkably tight bounds can be derived on the MDM and the EDM of the top quark as presented in Fig. 5.15. In this parton level study, for the computation of the cross section a set of appropriate phase-space cuts are imposed on the final-state momenta. Applying further cuts to remove the background will result in a substantial reduction of the signal. It is therefore assumed that this would lead to a statistical uncertainty of about 8%, represented by the dark inner ring in Fig. 5.15. To include uncertainties due to mistagging and to allow for other unspecified sources of systematic uncertainty, it is assumed that the total uncertainty will be about 16% corresponding to the full ring in Fig. 5.15. This would yield bounds of $-0.13 < \kappa < 0.18$, and $|\tilde{\kappa}| < 0.38$, respectively, at the 2σ C.L. Figure 5.15 shows that the LHeC could greatly improve the limits imposed by the indirect constraints from $b \to s\gamma$, and even the limits imposed by a future measurement of $t\bar{t}\gamma$ production at the LHC at $\sqrt{s} = 14\,\text{TeV}$.

Furthermore, the deep inelastic scattering (DIS) regime of $t\bar{t}$ production will allow to probe the $t\bar{t}Z$ coupling, albeit with less sensitivity [466].

5.3.4 Top-Higgs Coupling

The CP-nature of the top-Higgs coupling can be analysed at the LHeC in $ep \rightarrow \bar{t}H$ production exploring the top quark polarisation and other angular variables such as the rapidity difference between the single top quark and the Higgs boson. Measuring just the fiducial inclusive production cross section gives already a powerful probe of the CP properties of the $t\bar{t}H$ coupling [476]. Further details are given in Section 7.5.

5.3.5 Top Quark PDF and the Running of α_s

Parton distributions are usually released in a variable-flavor number scheme, in which the number of active flavors changes as the scale is raised [252]. However, $n_f = 5$ is normally taken by default as a maximum number of flavors, even though in some PDF releases $n_f = 6$ PDF sets are also made available [477]. The top PDF is unlikely to be required for precision phenomenology, even at very high scales, because the top threshold is high enough that collinear resummation is not necessary up to extremely large scales: indeed $\frac{\alpha_s(M_t^2)}{\pi} \ln \frac{Q^2}{m_t^2} \sim \frac{1}{2}$ only for $Q \gtrsim 10^6 \, m_t$. On the other hand, the use of $n_f = 6$ active flavors in the running of α_s is important for precision phenomenology, since the value of α_s with five and six active flavors already differ by about 2% at the TeV scale [478]. Investigations of the top quark structure inside the proton are also discussed in Refs. [1, 40].
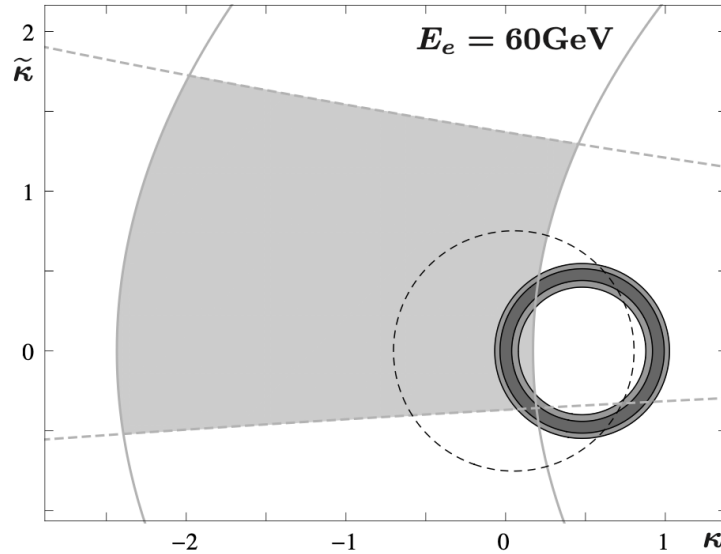
Figure 5.15: Allowed region of the magnetic dipole moment κ and the electric dipole moment $\tilde{\kappa}$ of the top quark as expected in a measurement of the photoproduction cross section $\sigma(e(\gamma)p(g) \rightarrow t\bar{t})$ in semileptonic final states, assuming an experimental uncertainty of 8% (dark grey), and of 16% (dark+medium grey) [466]. Light gray area: region allowed by the measurements of the branching ratio (solid gray lines) and the CP asymmetry (dashed gray lines) of $B \rightarrow X_s\gamma$ [475]. Black dashed line: region allowed by a hypothetical experimental result for $\sigma(pp \rightarrow t\bar{t}\gamma)$ utilizing semileptonic final states at the LHC at $\sqrt{s} = 14 \, \text{TeV}$ with phase-space cuts as defined in equations (5), (6) of Ref. [475] (including $E_T^\gamma > 10 \, \text{GeV}$), and assuming an experimental uncertainty of 5%.
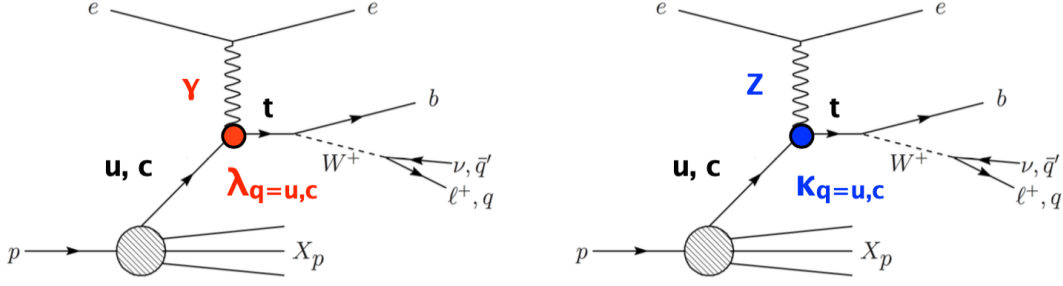
Figure 5.16: Example graphs for single top quark production via FCNC $tq\gamma$ (left) and tuZ (right) couplings.

5.3.6 FCNC Top Quark Couplings

Like all the Flavour Changing Neutral Currents (FCNCs) the top quark FCNC interactions are also extremely suppressed in the SM, which renders them a good test of new physics. The contributions from FCNC to top interactions can be parameterised via an effective theory and studied by analysing specific processes.

Single top quark NC DIS production can be used to search for FCNC $tu\gamma$, $tc\gamma$, tuZ, and tcZ couplings [479, 480] as represented by the Lagrangian

$$\mathcal{L}_{\text{FCNC}} = \sum_{q=u,c} \left(\frac{g_e}{2m_t} \bar{t}\sigma^{\mu\nu}(\lambda_q^L P_L + \lambda_q^R P_R)q A_{\mu\nu} + \frac{g_W}{4c_W m_Z} \bar{t}\sigma^{\mu\nu}(\kappa_q^L P_L + \kappa_q^R P_R)q Z_{\mu\nu} \right) + h.c. \; ,$$
(5.17)

where g_e (g_W) is the electromagnetic (weak) coupling constant, c_W is the cosine of the weak mixing angle, $\lambda_q^{L,R}$ and $\kappa_q^{L,R}$ are the strengths of the anomalous top FCNC couplings (the values of these couplings vanish at the lowest order in the SM). Top FCNC couplings as introduced in Eq. (5.17) would lead to Feynman graphs as shown in Fig. 5.16.

In an elaborate analysis, events including at least one electron and three jets (hadronic top quark decay) with high transverse momentum and within the pseudorapidity acceptance range of the detector are selected. The distributions of the invariant mass of two jets (reconstructed W boson mass) and an additional jet tagged as b-jet (reconstructed top quark mass) are used to further enhance signal over background events, mainly given by $W + $ jets production. Signal and background interference effects are included. A detector simulation with DELPHES [467] is applied.

The expected limits on the branching ratios $\text{BR}(t \to q\gamma)$ and $\text{BR}(t \to qZ)$ as a function of the integrated luminosity at the 2σ C.L. are presented in Fig. 5.17 (left). Assuming an integrated luminosity of $1\,\text{ab}^{-1}$, limits of $\text{BR}(t \to q\gamma) < 1 \cdot 10^{-5}$ and $\text{BR}(t \to qZ) < 4 \cdot 10^{-5}$ are expected. This level of precision is close to actual predictions of concrete new phenomena models, such as SUSY, little Higgs, and technicolour, that have the potential to produce FCNC top quark couplings. The expected limits will improve on existing limits from the LHC by one order of magnitude [14]. They will be similar to limits expected from the High Luminosity-LHC (HL-LHC) with $3000\,\text{fb}^{-1}$ [185], and will improve limits from the International Linear Collider (ILC) with $500\,\text{fb}^{-1}$ at $\sqrt{s} = 250\,\text{GeV}$ [481, 482] by an order of magnitude (see also Fig. 5.19). Figure 5.17 (right) shows how the sensitivity on $\text{BR}(t \to q\gamma)$ and $\text{BR}(t \to qZ)$, respectively, changes as a function of the centre-of-mass energy. At a future FCC-ep [14] with, for example, an electron beam energy of $60\,\text{GeV}$, and a proton beam energy of $50\,\text{TeV}$, leading to a centre-of-

mass energy of 3.5 TeV, the sensitivity to FCNC $tq\gamma$ couplings even exceed expected sensitivities from the HL-LHC with 3000 fb^{-1} at $\sqrt{s} = 14$ TeV [185].
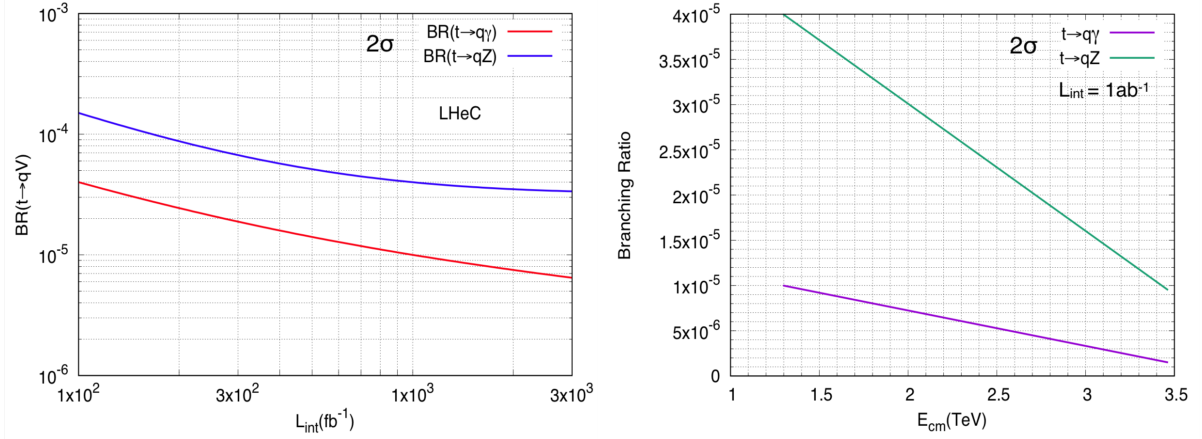

Figure 5.17: Expected sensitivities as a function of the integrated luminosity on FCNC $t \to qV$ branching ratios (left) [479, 480]. The expected upper limits on FCNC $t \to qV$ branching ratios are also shown as a function of the centre-of-mass-energy (right).

A further study of the top quark FCNC through Z-boson has been performed in Ref. [483] for the LHeC including a DELPHES [467] detector simulation. The effective couplings for FCNC processes are of vector and tensor in nature, the latter corresponding to those in Eq. (5.17). The effect of these couplings is probed in the single top quark production (see Fig. 5.16 right). It is shown that the polar angle (θ) of the electrons coming out of the primary vertex in association with the top quark polarisation asymmetries constructed from the angular distribution of the secondary lepton arising from the top decay, allow to distinguish the Lorentz structure of the couplings. From a multi-parameter analysis, a reach of the $\mathcal{O}(10^{-2})$ in the case of vector couplings and $0.1 - 0.5$ TeV^{-1} in case of tensor couplings are obtained at an integrated luminosity of 2 ab^{-1} for 95% C.L.

Another example for a sensitive search for anomalous top quark couplings is the one for FCNC tqH couplings as defined in

$$\mathcal{L}_{\text{FCNC}} = \kappa_{tuH}\, \bar{t}uH + \kappa_{tcH}\, \bar{t}cH + h.c. \tag{5.18}$$

This can be studied in CC DIS production as shown in Fig. 5.18 (left), where singly produced top anti-quarks could decay via such couplings into a light up-type anti-quark and a Higgs boson decaying into a bottom quark-antiquark pair, $e^-p \to \nu_e \bar{t} \to \nu_e H\bar{q} \to \nu_e b\bar{b}\bar{q}$ [484]. Another signal involves the FCNC tqH coupling in the production vertex, i.e. a light quark from the proton interacts via t-channel top quark exchange with a W boson radiated from the initial electron producing a b quark and a Higgs boson decaying into a bottom quark-antiquark pair, $e^-p \to \nu_e Hb \to \nu_e b\bar{b}b$ [484]. This channel is similar in sensitivity to the previous one due to the clean experimental environment when requiring three identified b-jets. Largest backgrounds are given by $Z \to b\bar{b}$, SM $H \to b\bar{b}$, and single top quark production with hadronic top quark decays. A 5% systematic uncertainty for the background yields is added. Furthermore, the analysis assumes parameterised resolutions for electrons, photons, muons, jets and unclustered energy using typical parameters taken from the ATLAS experiment. Furthermore, a b-tag rate of 60%, a c-jet fake rate of 10%, and a light-jet fake rate of 1% is assumed. The selection is optimised for the different signal contributions separately. Fig. 5.18 (right), shows the expected upper limit on the branching ratio Br($t \to Hu$) with 1σ, 2σ, 3σ, and 5σ C.L. as a function of

Figure 5.18: Example Feynman graph for associated single top quark and Higgs boson production via FCNC tqH couplings (left). Expected sensitivities as a function of the integrated luminosity on FCNC $t \to uH$ branching ratios [484] (right).

the integrated luminosity for the $e^-p \to \nu_e \bar{t} \to \nu_e H \bar{q} \to \nu_e b \bar{b}$ signal process. For an integrated luminosity of $1\,\text{ab}^{-1}$, upper limits of $\text{Br}(t \to Hu) < 0.15 \cdot 10^{-3}$ are expected at the 2σ C.L.

In Fig. 5.19 the different expected limits on various FCNC top quark couplings from the LHeC are summarised, and compared to results from the LHC and the HL-LHC. This clearly shows the competitiveness of the LHeC results, and documents the complementarity of the results gained at different colliders.

5.3.7 Other Top Quark Property Measurements and Searches for New Physics

Other exciting results not presented here involve, for example, the study of the CP-nature in $t\bar{t}H$ production [476] (see Section 7.5), searches for anomalous $t\bar{t}\gamma$ and $t\bar{t}Z$ chromoelectric and chromomagnetic dipole moments in $t\bar{t}$ production [466], the study of top quark spin and polarisation [474], and the investigation of the top quark structure function inside the proton [1, 40].

5.3.8 Summary of Top Quark Physics

Top quark physics at the LHeC represents a very rich and diverse field of research involving high precision measurements of top quark properties, and sensitive searches for new physics. In particular the top couplings to the photon, the W boson and possible FCNC interactions can be studied in a uniquely clean environment. One signature analysis is the expected direct measurement of the CKM matrix element $|V_{tb}|$ with a precision of less than $1\,\%$ in CC DIS. In top quark pair photoproduction the magnetic and electric dipole moments of the top quark can be probed directly with higher sensitivity than indirect limits from $b \to s\gamma$ and the potential limits from the LHC through $t\bar{t}\gamma$ production. Furthermore, FCNC top quark couplings can be studied with a precision high enough to explore those couplings in a regime that might be affected by actual new phenomena models, such as SUSY, little Higgs, and technicolour.

It has been shown [14], that results from future e^+e^--colliders, eh-colliders, and hh-colliders deliver complimentary information and will therefore give us a more complete understanding of
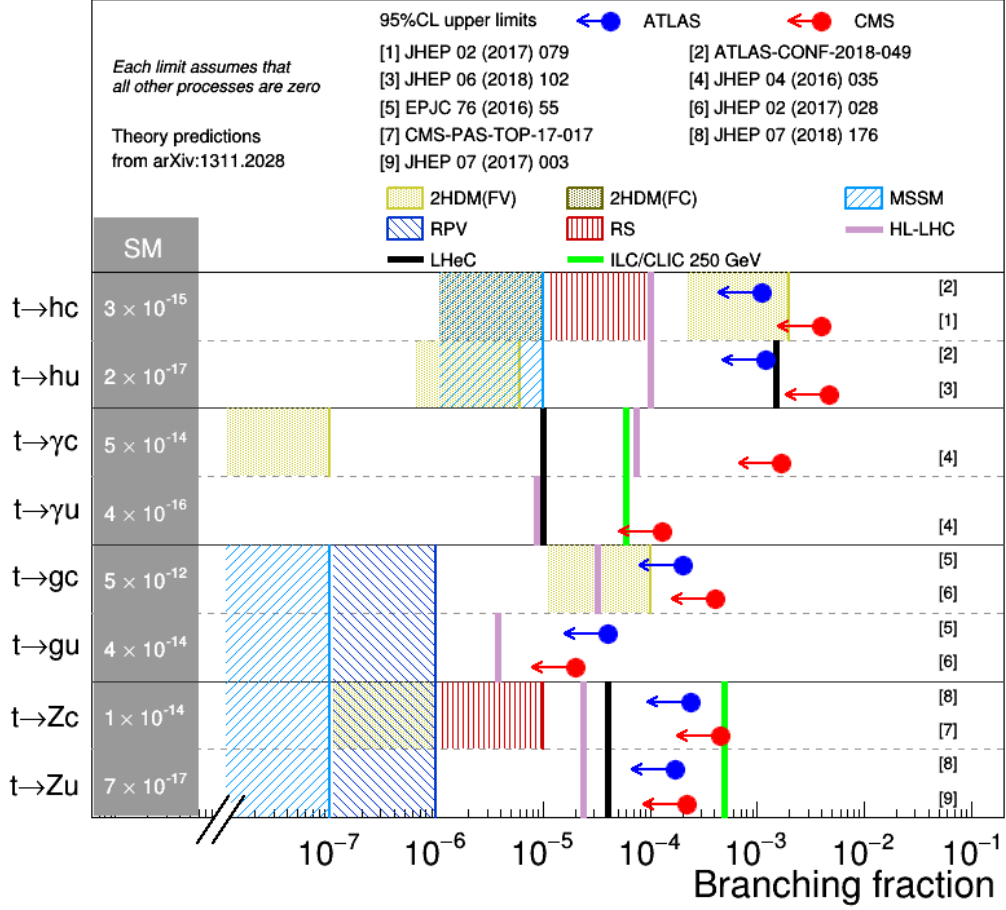
Figure 5.19: Summary of 95% C.L. limits on top quark branching fractions in searches for FCNC in top quark production or decays. The LHeC results (black lines) are compared to current LHC limits (blue and red dots), to HL-LHC predictions with $3000\,\text{fb}^{-1}$ at $\sqrt{s} = 14\,\text{TeV}$ [185] (magenta lines), and to predictions from a future ILC collider with $500\,\text{fb}^{-1}$ at $\sqrt{s} = 250\,\text{GeV}$ [481, 482] (green lines). The results are also compared to various theory predictions (hached areas).

the properties of the heaviest elementary particle known to date, and of the top quark sector in general.

Chapter 6

Nuclear Particle Physics with Electron-Ion Scattering at the LHeC

6.1   Introduction

The LHeC accelerator, in addition to being a powerful machine for exploring proton structure, will allow for the first time studies of DIS off nuclei in a collider mode at the energy frontier. The nuclear structure has been previously studied in fixed target experiments with charged lepton and neutrino beams, see [68–70, 485–494] and references therein. Due to the energy limitations of the machines operating in this mode, the kinematic range covered by these experiments is rather narrow, mostly limited to relatively large values of $x \geq 0.01$ and low to moderate Q^2, in the range $Q^2 < 100\,\text{GeV}^2$. The precise kinematic range covered by experiments is shown in Fig. 6.1, where the DIS experiments overlap to a large degree with the data from hadronic collisions using the Drell-Yan (DY) process. These fixed target DIS and DY data dominate the data sets used in the fits for the nuclear parton distribution functions. In addition, in some analyses of nuclear PDFs, data on inclusive single hadron production in dAu collisions at RHIC and on EW bosons and dijets in pPb collisions at the LHC are included.

As is clear from Fig. 6.1, the LHeC will be able to cover a very large range in (x, Q^2) in eA, previously unexplored in experiments. It will extend the range in x down to $\sim 10^{-6}$ and have a huge lever arm in Q^2 from very low values up to $\sim 10^6\,\text{GeV}^2$. It will also be complementary to the EIC [100] machine, extending the range in x and Q^2 by about two orders of magnitude with respect to it. The extension of these ranges will be even larger at the FCC-eh.

Due to large statistics and modern, specialised detectors, it will be possible to study nuclear structure at the LHeC with unprecedented precision in a kinematical range far wider than previously possible and with the controlled systematics of one single experiment. There are a large number of important physics topics that can be addressed in eA collisions at the LHeC:

- A precise determination of nuclear parton densities for a single nucleus (lead, and eventually lighter ions) will be possible. In particular, the current huge uncertainties in nuclear gluon and sea quark densities at low x will be dramatically improved using the data from the LHeC. In analogy to the proton PDF extraction described in previous sections, full flavour decomposition in the nuclear case could be achieved using both NC and CC data with heavy flavour identification.

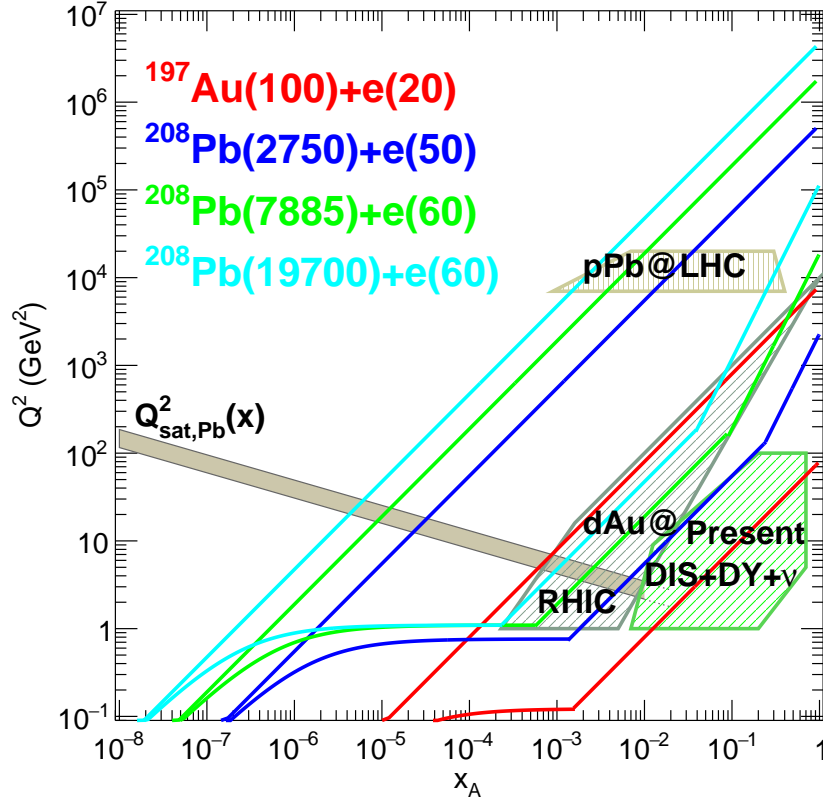- Precision measurement of semi-inclusive and exclusive processes will enable an exploration

Figure 6.1: Kinematic regions in the $x - Q^2$ plane explored by different data sets (charged lepton and neutrino DIS, DY, dAu at RHIC and pPb at the LHC) used in present nPDF analyses [495], compared to the ones achievable at the EIC (red), the LHeC (ERL against the HL-LHC beams, dark blue) and two FCC-eh versions (with Pb beams corresponding to proton energies $E_p = 20\,\mathrm{TeV}$ - green and $E_p = 50\,\mathrm{TeV}$ - light blue). Acceptance of the detector for the electrons is taken to be $1° < \theta < 179°$, and $0.01(0.001) < y < 1$ for the EIC (all other colliders). The saturation scale Q_{sat} shown here for indicative purposes only, see also [496], has been drawn for a Pb nucleus considering an uncertainty ~ 2 and a behaviour with energy following the model in [497]. Note that it only indicates a region where saturation effects are expected to be important but there is no sharp transition between the linear and non-linear regimes.

of new details of the nuclear structure. Similarly to the proton case, DVCS and exclusive vector-meson production will provide unique insight into 3D nuclear structure.

- The LHeC will offer unprecedented opportunities to extract diffractive parton densities in nuclei for the first time. A first detailed analysis [333] indicates that the achievable precision on diffractive PDFs in nuclei will be comparable to that possible in the proton case. The measurements of diffraction on protons and nuclei as well as the inclusive structure functions in the nuclear case will allow us to explore the very important relation between nuclear shadowing and diffraction [498].

- The LHeC will be able to test and establish or exclude the phenomenon of parton saturation at low x in protons and nuclei. According to the Color Glass Condensate framework [499, 500], parton saturation is a density effect that can be achieved in two ways, either by decreasing the value of x or by increasing the size of the target by increasing A. The LHeC will be a unique machine to address both of their variations, such that the ideas of saturation could be precisely tested. It will be possible to search for parton saturation in

a variety of ways which include, among others, the search for tensions in DGLAP fits, the study of the diffraction, in particular the ratios of diffractive to inclusive cross sections, and the study of particle azimuthal de-correlations.

- Finally, the LHeC machine in eA mode will have a huge impact onto physics explored in pA and AA collisions, see Sec. 9.7, where it will provide vital input and constraints on the 'baseline' initial state in nuclear collisions, measurements of the impact of a cold nuclear medium on hard probes and effects of hadronisation. It will also explore the initial state correlations on the final state observables relevant for understanding collectivity in small systems explored in pp or pA collisions.

As commented below, these aims will require an experimental apparatus with large rapidity coverage and associated forward and backward electron, photons, hadron and nuclear detectors. In addition the detector design should allow to precisely measure diffractive events in eA and allow the clean separation of radiative events, most important for the case of DVCS and exclusive diffraction.

Photonuclear interactions at high energies can also be studied through ultraperipheral collisions at RHIC and the LHC [127, 128, 314, 501] that offer an alternative although with less precision. This is briefly discussed in Chapter 9 where the relation between the LHeC and the HL-LHC is presented.

In this Chapter we do not address issues on the nuclear modification on jet yields and fragmentation that are expected to show dramatic effects and to be of great importance for heavy-ion collisions. All these aspects were previously discussed in Ref. [1]. Besides, electron-deuteron collisions that offer additional possibilities for determining proton and neutron parton densities, and for studying weak interactions with neutron targets at high energies, are not considered here, see Ref. [1] where an analysis of parton densities in eD collisions can be found.

6.2 Nuclear Parton Densities

PDFs are essential ingredients in our understanding of the dynamics of the strong interaction. First, they encode important information about the structure of hadrons [502, 503]. Second, they are indispensable for the description of hadronic collisions within standard collinear factorisation [38]. Concerning nuclei, it has been known for more than 40 years that structure functions are strongly affected by the nuclear environment [493, 494] so that they cannot be interpreted as a simple superposition of structure functions of free nucleons. In the standard approach, within collinear factorization, the nuclear modification is included in the parametrisation of the parton densities. This means that the parton densities in a bound nucleon are different from those in a free nucleon, and the difference is encoded in the non-perturbative initial conditions of the parton densities at some low, initial scale Q_0^2. The present status of nuclear parton densities (nPDFs), see for example [504, 505], can be summarised as follows:

- Modern analyses [495, 506–508] are performed at next-to-leading order (NLO) and next-to-next-to-leading order (NNLO) [509, 510]. Differences between the different groups mainly arise from the different sets of data included in the analyses [1] and from the different functional forms employed for the initial conditions.

---

[1]The main difference lies in the use or not of neutrino-Pb cross sections (whose usage has been controversial [511–513], particularly the NuTeV data [69] from the Fe nucleus) from CHORUS and $\pi^{0,\pm}$ transverse momentum spectra from dAu collisions at the Relativistic Heavy Ion Collider (RHIC).

- Many sets of data are presented as ratios of cross section for a given nucleus over that in deuterium, which is loosely bound and isoscalar. Therefore, it has become customary to work in terms of ratios of nPDFs:

$$R_i(x, Q^2) = \frac{f_i^{\mathrm{A}}(x, Q^2)}{A f_i^p(x, Q^2)} \ , \quad i = u, d, s, c, b, g, \ldots, \tag{6.1}$$

with $f_i^{p(\mathrm{A})}(x, Q^2)$ the corresponding parton density in a free proton p or in nucleus A. These nuclear modification factors are parametrised at initial scale Q_0^2 (assuming isospin symmetry to hold). The nPDFs are then obtained multiplying the nuclear modification factors by some given set of free proton PDFs.

- The available data come from a large variety of nuclei and the number of data points for any of them individually is very small compared to the proton analyses. In particular, for the Pb nucleus there are less than 50 points coming from the fixed target DIS and DY experiments and from particle production data in pPb collisions at the LHC. The fit for a single nucleus is therefore impossible and the modelling of the A-dependence of the parameters in the initial conditions becomes mandatory [495, 508]. The most up to date analyses include between 1000 and 2000 data points for 14 nuclei.

- The kinematic coverage in Q^2 and x with existing data is very small compared to that of present hadronic colliders. The ultimate precision and large coverage of the kinematic plane for nPDFs can only be provided by a high energy electron-ion collider. Meanwhile, the only experimental collision system where nPDFs can be currently constrained are hadronic and ultraperipheral collisions (UPCs). It is important to stress that extracting PDFs from these collisions presents many theoretical challenges. These are related to the question of applicability of collinear factorization for nuclear collisions, higher twist effects, scale choices and other theoretical uncertainties.

All parton species are very weakly constrained at small $x < 10^{-2}$ [514], gluons are poorly known at large $x > 0.2$, and the flavour decomposition is largely unknown - a natural fact for u and d due to the approximate isospin symmetry in nuclei [2]. The impact of presently available LHC data, studied using reweighting [254, 515] in [516, 517] and included in the fit in [495], is quite modest with some constrains on the gluon and the strange quark in the region $0.01 < x < 0.3$. On the other hand, theoretical predictions for nuclear shadowing of quark and gluon PDFs based on s-channel unitarity and diffractive nucleon PDFs are available down to $x \sim 10^{-4} - 10^{-5}$ [498, 518–520]. Predictions on the flavour dependence of nuclear effects in the antishadowing region [521] cannot be confirmed with present data.

Future runs at the LHC will offer some further possibilities for improving our knowledge on nPDFs [501]. However, the ideal place to determine parton densities is DIS, either at the Electron Ion Collider (EIC) [100] in the USA or, in a much larger kinematic domain (see Fig. 6.1), at the LHeC. DIS measurements in such configurations offer unprecedented possibilities to enlarge our knowledge of parton densities through a complete unfolding of all flavours.

In the following, we show the possibilities for constraining the PDFs for a Pb nucleus at the LHeC. In the next subsection, Subsec. 6.2.1, we discuss the corresponding pseudodata for the inclusive cross section in electron-nucleus scattering. Next, in Subsec. 6.2.2 we discuss how the pseudodata will be introduced in a global nPDF fit. Finally, in Subsec. 6.2.3 it is demonstrated how the PDFs of Pb can be extracted with a very good precision from the LHeC data only, without requiring any other set of data.

---

[2]The u-d difference is suppressed by a factor $2Z/A - 1$.

6.2.1 Pseudodata

The LHeC provides measurements of eA scattering cross sections in the deep inelastic scattering region $Q^2 > 1 \, \text{GeV}^2$ reaching values of Q^2 up to about $5 \cdot 10^5 \, \text{GeV}^2$ and corresponding x values between a few times 10^{-6} and near to $x = 1$. This enables the determination of a complete set of nPDFs in ePb scattering at the LHeC from the inclusive neutral and charged current cross sections with a clean separation of up and down valence and sea quark distributions. The very high Q^2 region which reaches much beyond the W mass squared makes the CC measurements extremely valuable for the separation of different flavours when taken together with the NC, from photon and Z boson exchange. Charm tagging in CC determines the anti-strange quark distribution in a wide kinematic range to typically $10 - 20\,\%$ precision, while charm and beauty tagging in NC provide high precision determinations of xc and xb from nuclei. Using coherent data from just this one experiment the uncertainties of these nPDFs will follow from a straightforward $\Delta\chi^2 = 1$ criterion.

The QCD analyses of pseudo LHeC cross section data illustrated subsequently employ sets of simulated NC and CC measurements under assumptions on precision which are summarised in Table 6.1, see Ref. [522]. The cross section simulation was done numerically employing derivative formulae from [58] and found to compare well to a detailed Monte Carlo simulation when tested for the conditions of the H1 experiment. The assumptions made are all reasonable when comparing with the H1 achievements, allowing for further improvements owing to new detector techniques and higher statistics. The control of radiative corrections in eA scattering is a special challenge as these grow $\propto Z^2$. The LHeC detector thus needs to be equipped with reliable photon detectors and the exploitation of the energy-momentum conservation, via the $E - p_z$ cut, should further reduce the effect of photon radiation to a few per cent level. It is also to be noted that the semi-inclusive measurements of the s, c and b quark distributions carry additional uncertainties for tagging, acceptance and background influences.

Source of uncertainty	Error on the source or cross section
Scattered electron energy scale	$0.1\,\%$
Scattered electron polar angle	$0.1 \, \text{mrad}$
Hadronic energy scale	$0.5\,\%$
Calorimeter noise ($y < 0.01$)	1–$3\,\%$
Radiative corrections	1–$2\,\%$
Photoproduction background	$1\,\%$
Global efficiency error	$0.7\,\%$

Table 6.1: Summary of assumed systematic uncertainties for future inclusive cross section measurements at the LHeC.

Fig. 6.2 illustrates the kinematic reach of the NC+CC pseudodata at the LHeC and the FCC-eh, in ep and ePb collisions (for per nucleon integrated luminosities ≤ 1 and $10 \, \text{fb}^{-1}$ respectively). In addition to inclusive data, semi-inclusive measurements with flavour sensitivity are also included. They will allow us to determine the strange, charm and beauty (also the top) PDFs. The principal technique is charm tagging (in CC for xs, in NC for xc) and beauty tagging (in NC for xb). The beam spot of the LHeC has a transverse extension of about $(7 \, \mu\text{m})^2$. Modern Si detectors have a resolution of a few microns to be compared with typical decay lengths of charm and beauty particles of hundreds of μm. The experimental challenges then are the beam pipe radius, coping at the LHeC with strong synchrotron radiation effects, and the forward tagging acceptance, similar to the HL-LHC challenges.
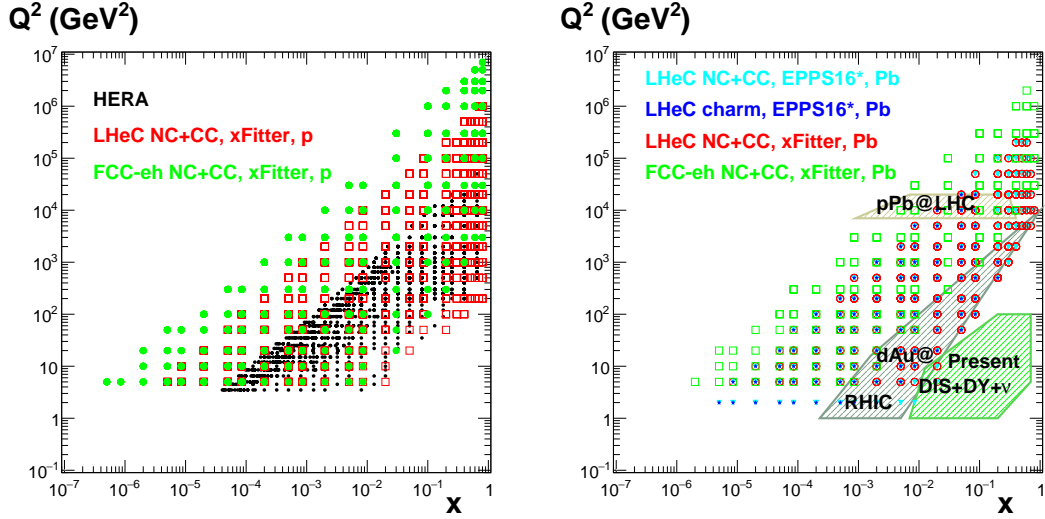
Figure 6.2: Left: kinematic $x - Q^2$ plot of the NC+CC pseudodata on a proton at the LHeC (red symbols) and the FCC-eh (green symbols) used in the *xFitter* analysis in Section 6.2.3; data used in analysis at HERA (black symbols) are shown for comparison. Right: kinematic $x - Q^2$ plot of the pseudodata on Pb used in the EPPS16 analysis at the LHeC (NC+CC, light blue symbols, and charm, dark blue symbols) in Section 6.2.2, and in the *xFitter* analysis in Subsec. 6.2.3 (at the LHeC, red symbols, and the FCC-eh, green symbols); the regions explored by currently available data sets (charged lepton and neutrino DIS, DY, dAu at RHIC and pPb at the LHC) used in present nPDF analyses [495] are shown for comparison.

A study was made of the possible measurements of the anti-strange density in nuclei (see Fig. 6.3) using impact parameter tagging in eA CC scattering, and of the charm and beauty structure functions in NC (see Fig. 6.4). Following experience on heavy flavour tagging at HERA and
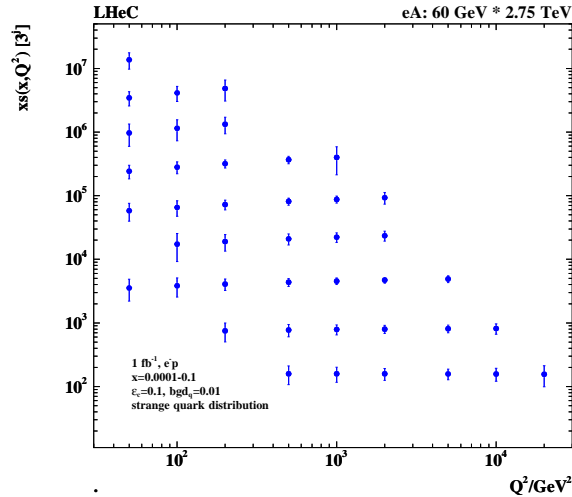

Figure 6.3: Simulation of the measurement of the (anti)-strange quark distribution $x\bar{s}(x, Q^2)$ in charged current eA scattering through the t-channel reaction $W^-\bar{s} \to c$. The data are plotted with full systematic and statistical errors added in quadrature.

ATLAS, assumptions were made on the charm and beauty tagging efficiencies to be 10 % and 60 %, respectively. The light quark background in the charm analysis is assumed to be controllable to per cent level, while the charm background in the beauty tagging sample is assumed
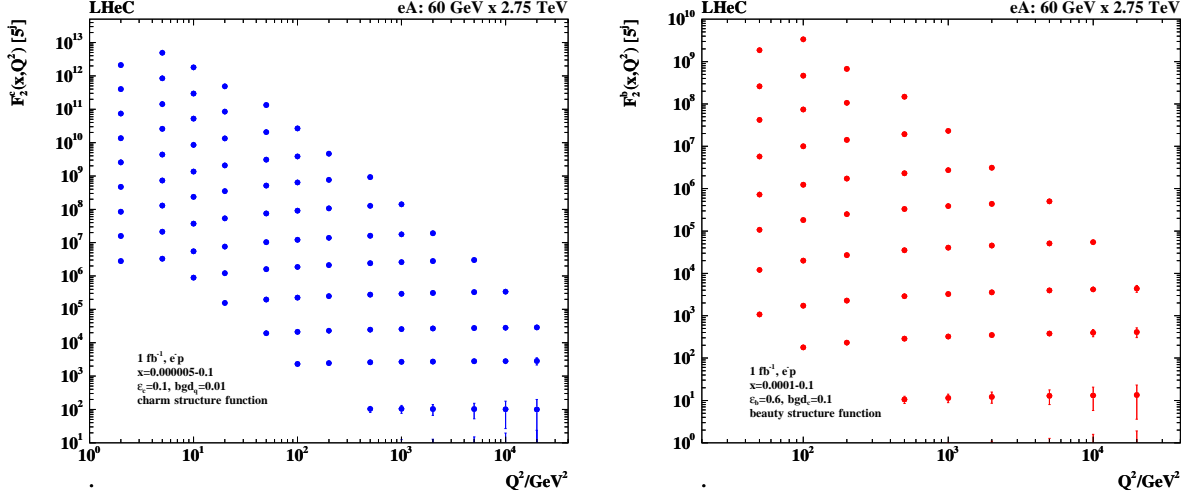
Figure 6.4: Left: Simulation of the measurement of the charm quark distribution expressed as $F_2^c = e_c^2 x(c + \bar{c})$ in neutral current eA scattering; Right: Simulation of the measurement of the bottom quark distribution expressed as $F_2^b = e_b^2 x(b + \bar{b})$ in neutral current eA scattering. The data are plotted with full systematic and statistical errors added in quadrature.

to be 10 %. The tagging efficiencies and background contaminations affect the statistical error. Moreover, an additional systematic error is assumed in the simulated NC (CC) measurements of 3 (5) %. These result in very promising measurements of the heavier quark distributions: to about $10 - 20$ % total uncertainty on the strange and $3 - 5$ % on the charm and beauty measurements, for typically x between 10^{-4} and 0.1 and Q^2 extending from below threshold m_Q^2 up to a few times $10^4 \, \mathrm{GeV}^2$. The knowledge of the heavy quark densities is of prime relevance for understanding nuclear structure and the development of QCD as has often been emphasised.

6.2.2 Nuclear gluon PDFs in a global-fit context

To illustrate the impact of the LHeC ePb pseudodata in the global context, they have been added [523] into the EPPS16 global analysis of nuclear PDFs [495]. The EPPS16 strategy is to parametrise the nuclear modification ratios $R_i(x, Q^2)$ between the bound-proton PDFs $f_i^{\mathrm{p}/Pb}$ and proton PDFs f_i^{p},

$$R_i(x, Q^2) \equiv \frac{f_i^{\mathrm{p}/Pb}(x, Q^2)}{f_i^{\mathrm{p}}(x, Q^2)} \ , \tag{6.2}$$

at the charm mass threshold $Q^2 = m_{charm}^2 = (1.3 \, \mathrm{GeV})^2$. At higher Q^2 the nuclear PDFs are obtained by solving the standard DGLAP evolution equations at next-to-leading order in QCD. As the LHeC pseudodata reach to significantly lower x than the data that were used in the EPPS16 analysis, an extended small-x parametrisation was used for gluons, see Figure 6.5. The framework is almost identical to that in Ref. [524]. The introduced functional form allows for rather wild – arguably unphysical – behaviour at small-x where e.g. significant enhancement is allowed. This is contrary to the theoretical expectations from the saturation conjecture and looks also to be an improbable scenario given the recent LHCb D and B meson measurements [525,526] which impressively indicate [527] gluon shadowing down to $x \sim 10^{-5}$ at interaction scales as low as $Q^2 \sim m_{charm}^2$. On the other hand, given that there are no prior DIS measurements in this kinematic range for nuclei other than the proton, and that the D and B meson production in

pPb collisions could be affected by strong final-state effects (which could eventually be resolved by e.g. measurements of forward prompt photons [528] in pPb), we hypothesise that any kind of behaviour is possible at this stage. Anyway, with the extended parametrisation – called here EPPS16* – the uncertainties in the small-x regime get significantly larger than in the standard EPPS16 set. This is reflected as significantly larger PDF error bands in comparison to the projected LHeC pseudodata. It is shown in Figure 6.6 where EPPS16* predictions are compared with the LHeC pseudodata for inclusive NC and CC reactions, as well as charm production in neutral-current scattering. The uncertainties are estimated using the Hessian method [529] and the same overall tolerance $\Delta\chi^2 = 52$ as in the EPPS16 analysis has been used when defining the error bands. Because there are no small-x data constraints for gluons, the gluon uncertainty is enormous and the Hessian method used for estimating the uncertainties is not particularly accurate, i.e. the true $\Delta\chi^2 = 52$ error bands are likely to be even larger. At some point the downward uncertainty will be limited by positivity constraints e.g. for F_L, but will depend strongly on which Q^2 is used to set the positivity constraints (e.g. in the EPPS16 analysis F_L is required to remain positive at $Q^2 = m_{charm}^2$).
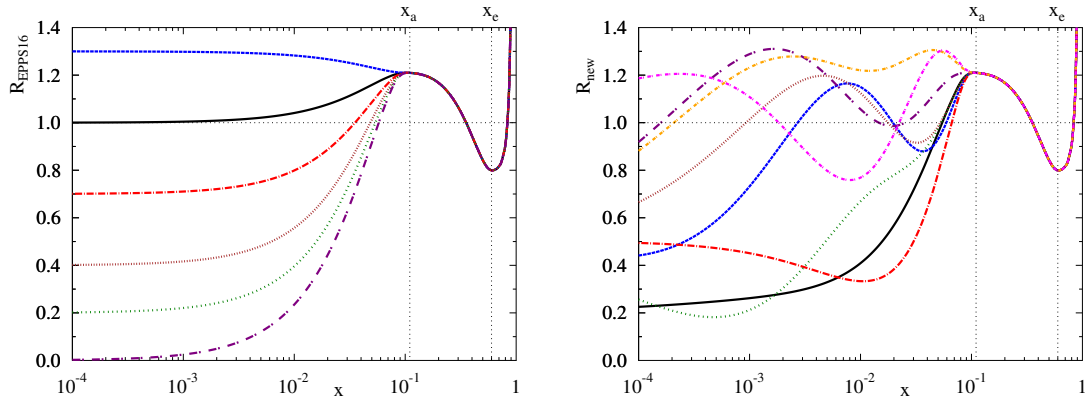

Figure 6.5: Left: Illustration of the functional behaviours allowed at small x in the EPPS16 analysis. Right: Illustration of the possible functional variations at small x in the extended parametrisation that we employ here.

Upon including the LHeC ePb pseudodata in the fit, the new nPDFs adapt to reproduce the pseudodata and their uncertainties are greatly reduced, as shown in Figure 6.7. The overall tolerance has been kept fixed to the default value $\Delta\chi^2 = 52$. The impact on the nuclear modification of the gluon PDF is illustrated in Figure 6.8 at two values of Q^2: $Q^2 = 1.69\,\text{GeV}^2$ (the parametrisation scale) and $Q^2 = 10\,\text{GeV}^2$. Already the inclusive pseudodata are able to reduce the small-x gluon uncertainty quite significantly, and the addition of the charm data promises an even more dramatic reduction in the errors. The analysis indicates that the LHeC will nail the nuclear gluon PDF to a high precision down to x of at least 10^{-5}.

6.2.3 nPDFs from DIS on a single nucleus

Another approach that becomes possible with the large kinematic coverage and volume of data for a single nucleus, Pb, at the LHeC and FCC-eh, is to perform a fit to only Pb data in order to extract the Pb PDFs, removing the need to interpolate between different nuclei. Then the corresponding ratios or nuclear modification factors for each parton species can be obtained using either a proton PDF set from a global fit or, as we do here (see [14, 530, 531]), from a fit to proton LHeC and FCC-eh pseudodata. In this way, there will be no need to introduce a
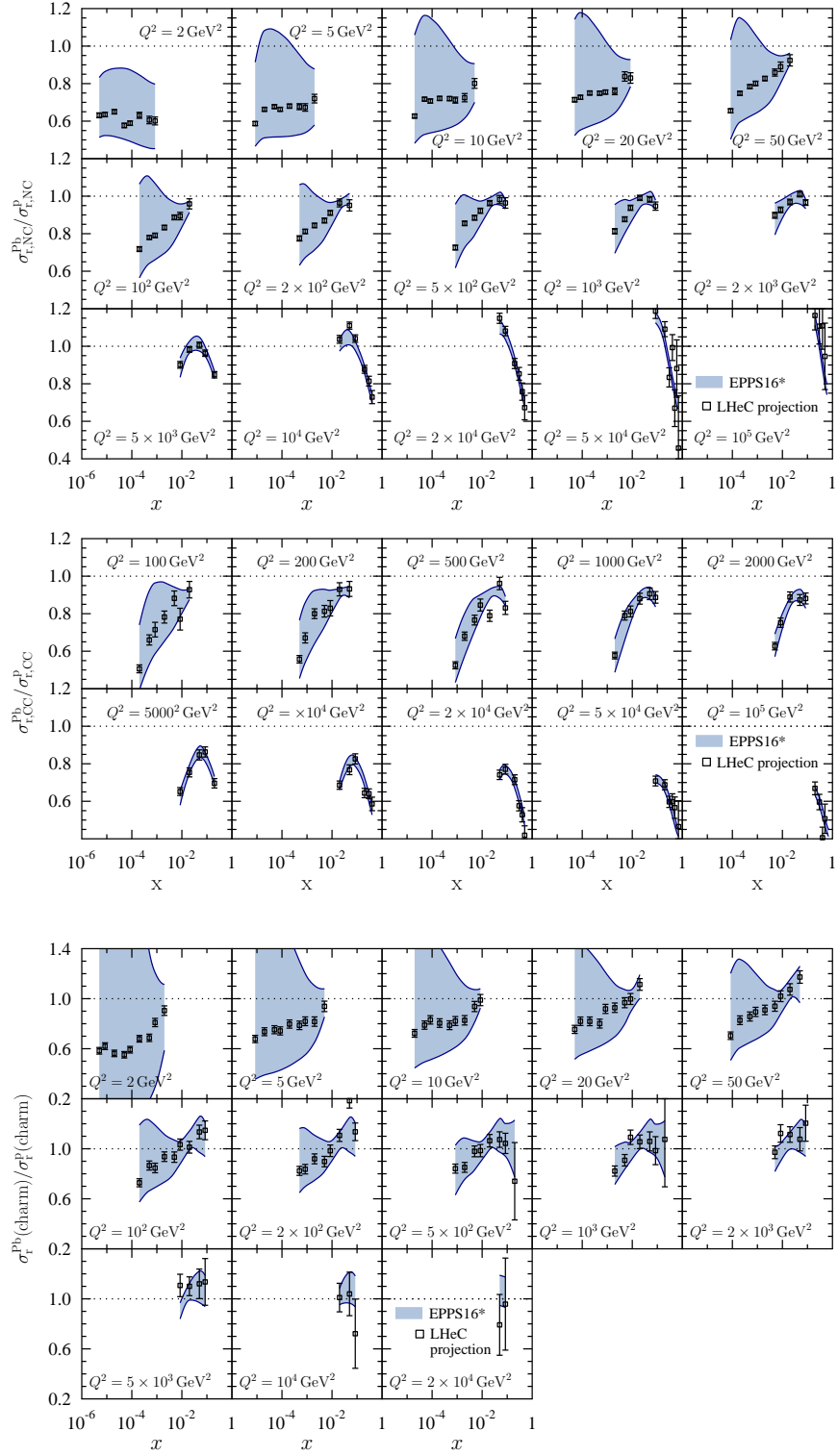
Figure 6.6: Top: Simulated ratios of neutral-current reduced cross sections between ePb and ep collisions compared with the predictions from a EPPS16-type global fit of nuclear PDFs using an extended parametrisation for gluons. Middle: Charged-current cross section ratios. Bottom: Neutral-current charm-production cross section ratios.
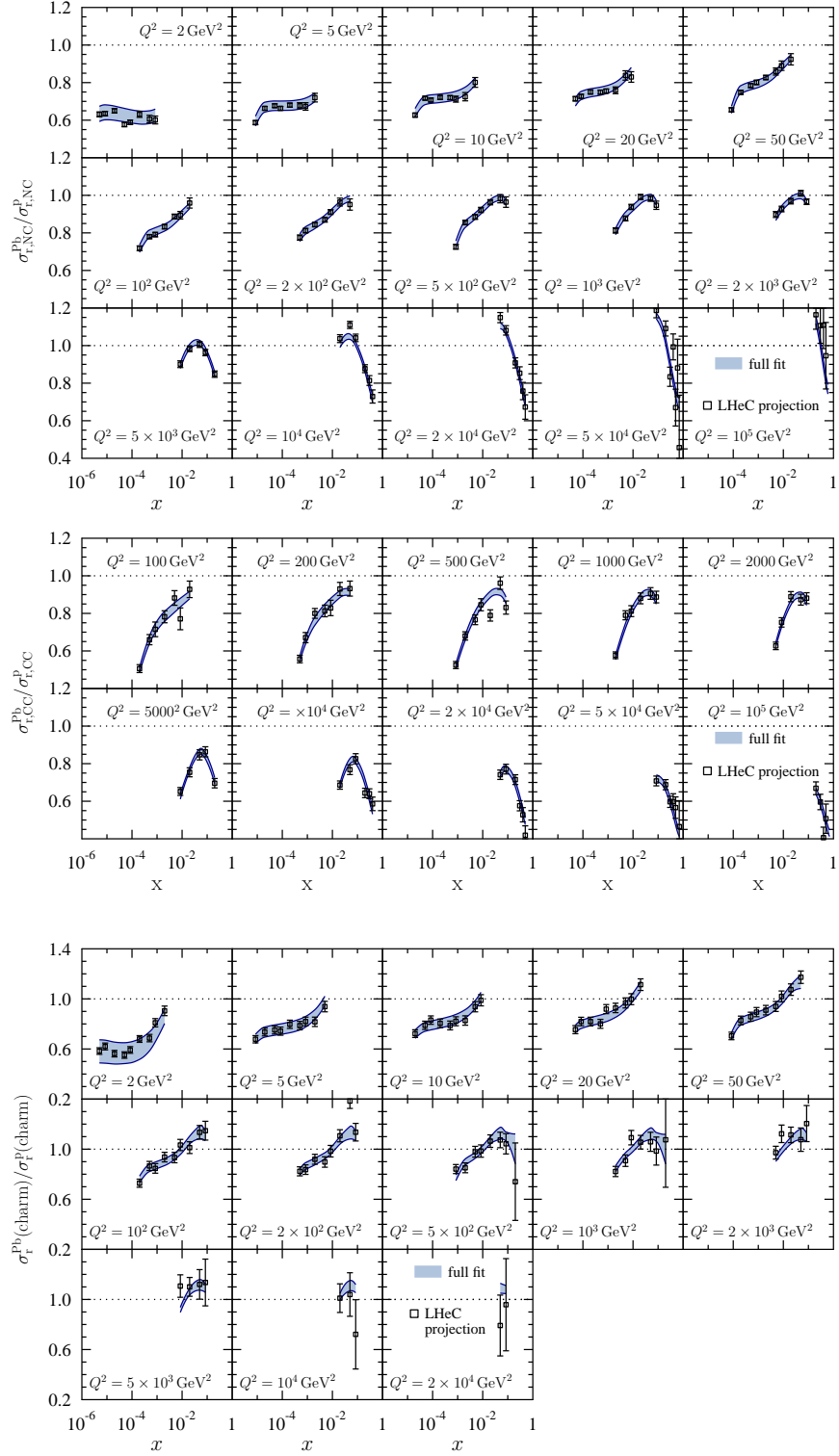
Figure 6.7: As Figure 6.6 but with fit results after including the LHeC pseudodata in the global analysis.
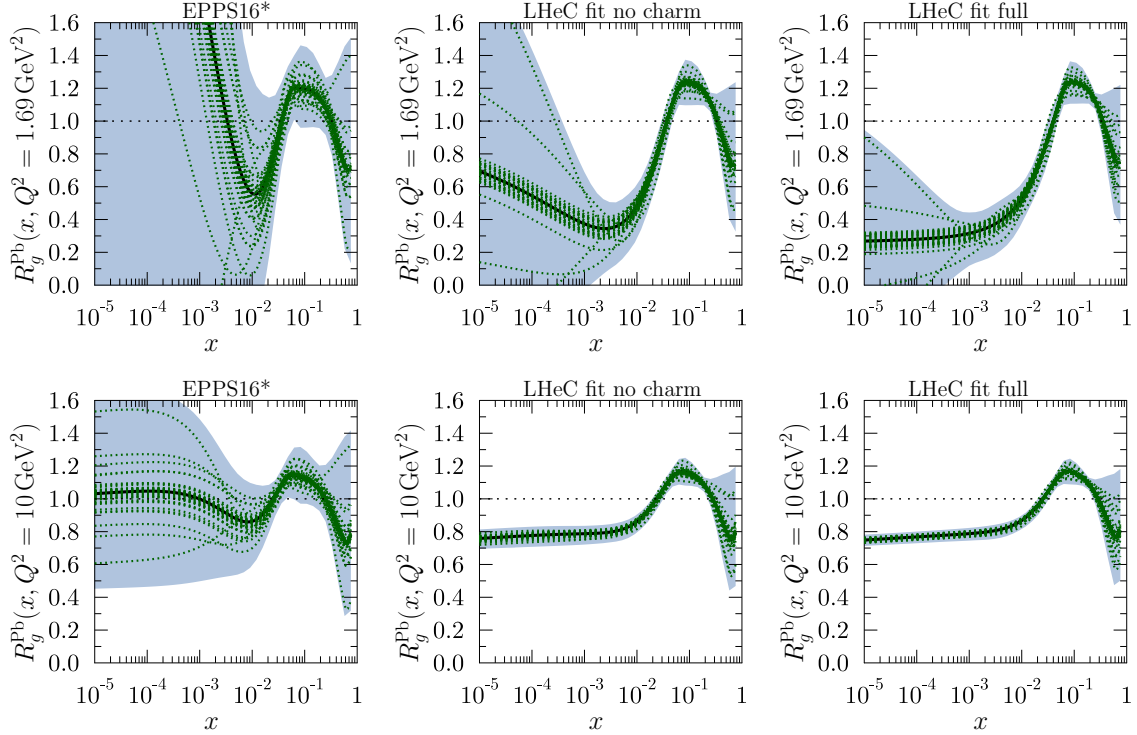
Figure 6.8: Upper panels: The gluon nuclear modification for the Pb nucleus at $Q^2 = 1.69\,\mathrm{GeV}^2$ in EPPS16* (left), LHeC analysis without charm pseudodata (middle), and full LHeC analysis (right). The blue bands mark the total uncertainty and the green dotted curves correspond to individual Hessian error sets. Lower panels: As the upper panels but at $Q^2 = 10\,\mathrm{GeV}^2$.

nuclear size dependence in the parameters for the initial condition for DGLAP evolution. Such nPDFs can then be used for comparing to those obtained from global fits and for precision tests of collinear factorisation in nuclear collisions.

The fits are performed using *xFitter* [532], where 484 (150) NC+CC Pb data points at the LHeC (FCC-eh) have been used in the fitted region $Q^2 > 3.5\,\mathrm{GeV}^2$, see Fig. 6.2. A HERAPDF2.0-type parametrisation [44] has been employed to provide both the central values for the reduced cross sections (therefore, the extracted nuclear modification factors are centered at 1) and the fit functional form; in this way, neither theory uncertainties (treatment of heavy flavours, value of α_s, order in the perturbative expansion) nor the uncertainty related to the functional form of the initial condition – parametrisation bias – are considered in our study, in agreement with our goal of estimating the *ultimate achievable experimental* precision in the extraction of nPDFs. We have worked at NNLO using the Roberts-Thorne improved heavy quark scheme, and $\alpha_s(m_Z^2) = 0.118$. The treatment of systematics and the tolerance $\Delta\chi^2 = 1$ are identical to the approach in the HERAPDF2.0 fits, as achievable in a single experiment.

The results for the relative uncertainties in the nuclear modification factors are shown in Figs. 6.9, 6.10 and 6.11 for valence, sea and gluon, respectively. The uncertainties in these plots reflect the assumed uncertainties in the pseudodata, both statistics (mainly at large x) and systematics from detector efficiencies, radiative corrections, etc., see Sec. 6.2.1. As expected, the uncertainty in the extraction of the valence at small x is sizeably larger than that for the sea and gluon.

While a very high precision looks achievable at the LHeC and the FCC-eh, for the comparison with EPPS16 (or any other global fit) shown in the plots and with previous results including
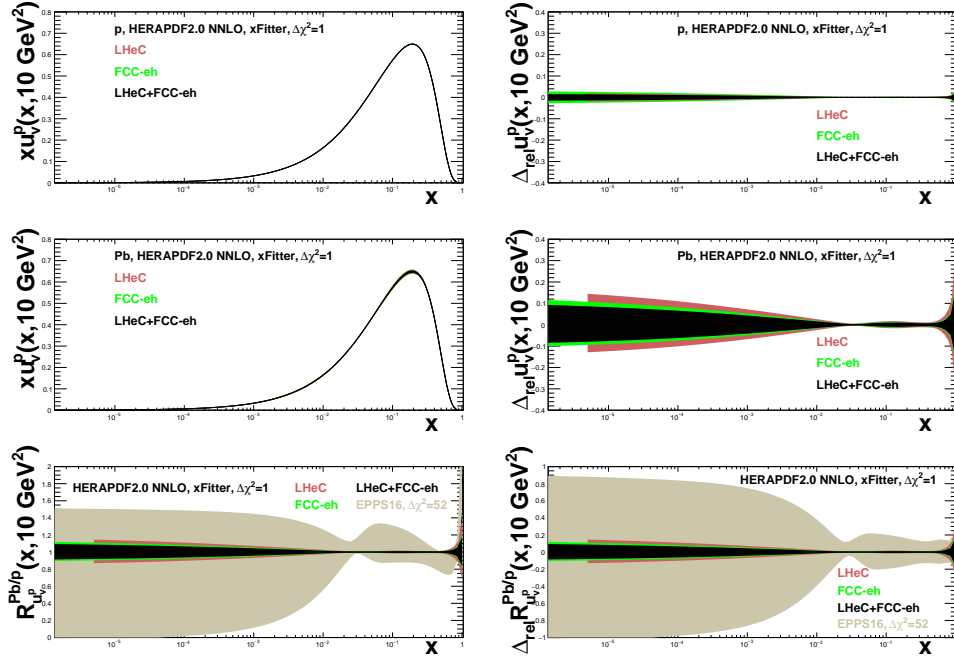
Figure 6.9: Distributions (left) and their relative uncertainties (right) of the valence u-quark density in the proton (top), Pb (middle) and the corresponding nuclear modification factor (bottom) in an analysis of ep and ePb LHeC and FCC-eh NC plus CC pseudodata using *xFitter* (both a single set of data and all combined), compared to the results of EPPS16 [495], see the text for details.
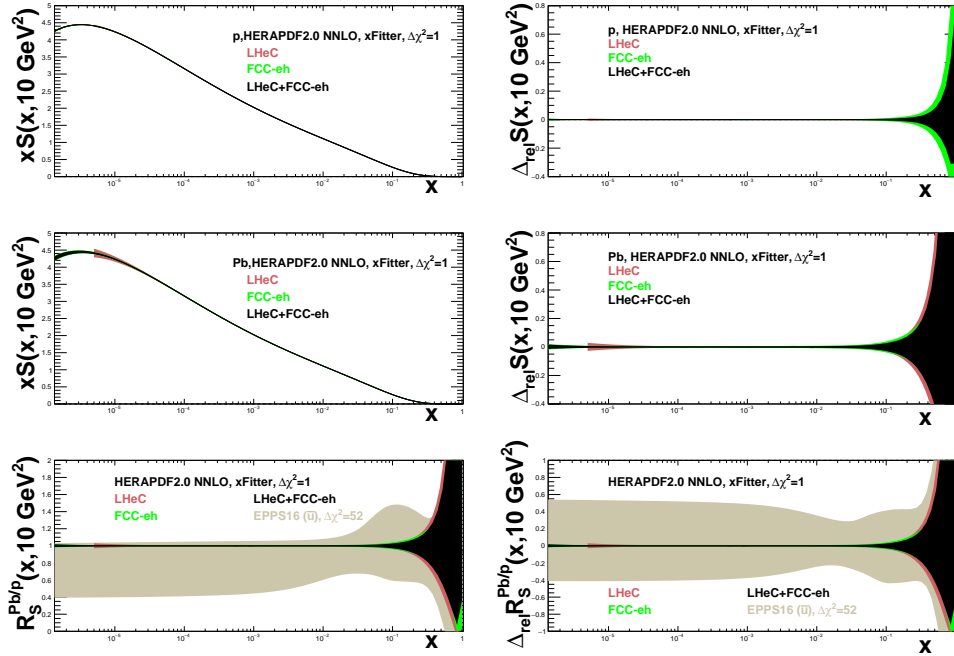

Figure 6.10: Distributions (left) and their relative uncertainties (right) of the sea quark density in the proton (top), Pb (middle) and the corresponding nuclear modifications factor (bottom) in an analysis of ep and ePb LHeC and FCC-eh NC plus CC pseudodata using *xFitter* (both a single set of data and all combined), compared to the results of EPPS16 [495] for $\bar{u}$, see the text for details.
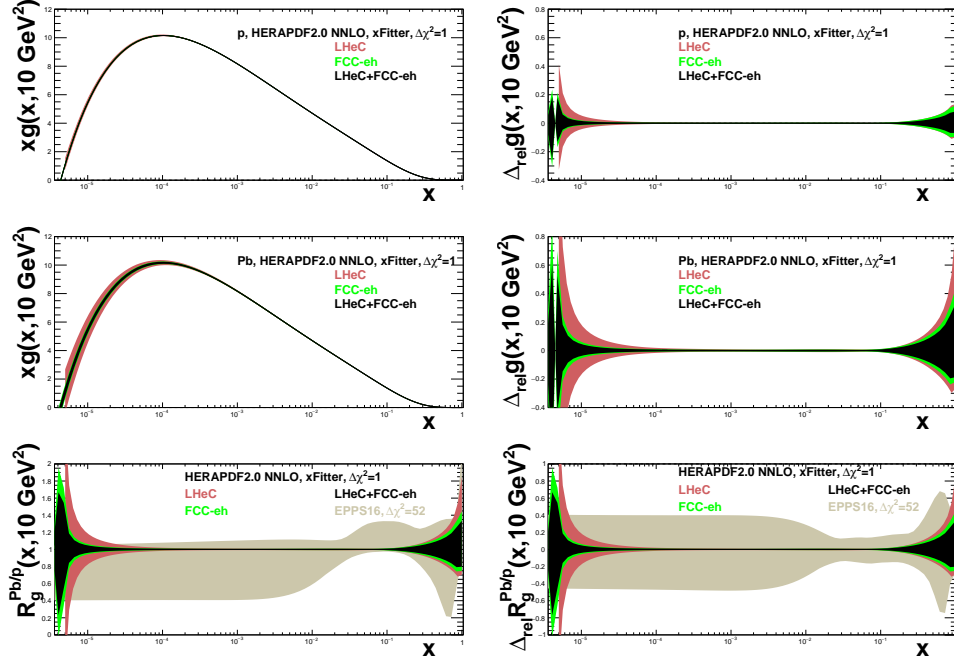
149

Figure 6.11: Distributions (left) and their relative uncertainties (right) of the gluon density in the proton (top), Pb (middle) and the corresponding nuclear modifications factor (bottom) in an analysis of ep and ePb LHeC and FCC-eh NC plus CC pseudodata using *xFitter* (both a single set of data and all combined), compared to the results of EPPS16 [495], see the text for details.

LHeC pseudodata in that setup, see Sect. 6.2.2 and [523,524], some caution is required. First, the effective EPPS16 tolerance criterion $\Delta\chi^2 \simeq 52$ implies that naively the uncertainty bands should be compared after rescaling by a factor $\sqrt{52}$. Second, the treatment of systematics is rather different, considering correlations in the *xFitter* exercise and taking them as fully uncorrelated (and added quadratically to the statistical ones) in the EPPS16 approach. Finally, EPPS16 uses parametrisations for the nuclear modification factors for different parton species while in *xFitter* just the (n)PDF combinations that enter the reduced cross sections are parametrised and employed for the fit [3]. With all these considerations in mind, the results shown in this Section are fully compatible with those in the previous one.

6.3 Nuclear diffraction

In Sec. 3.4 we have discussed specific processes which will probe the details of the 3D structure of the proton. The same processes can be studied in the context of electron-ion scattering and used to learn about the partonic structure of nuclei. Inclusive diffraction on nuclei can provide important information about the nuclear diffractive parton distribution similarly to the diffraction on the proton, see Sec. 4.3. Diffractive vector meson production can be studied in the nuclear case as well, e.g. within the framework of the dipole model suitable for high energy and including non-linear effects in density. In the nuclear case though, one needs to make a distinction between coherent and incoherent diffraction. In the coherent process, the nucleus

---

[3]In this respect let us note that, in analogy to proton PDFs, a full flavour decomposition can be achieved using both NC and CC with heavy flavour identification that will verify the existing ideas on flavour dependence of nuclear effects on parton densities [521].

scatters elastically and stays intact after the collision. In incoherent diffraction, the nucleus breaks up, and individual nucleons can be set free. Still, there will be a large rapidity gap between the produced diffractive system and the dissociated nucleus. It is expected that this process will dominate the diffractive cross section for medium and large values of momentum transfer. It is only in the region of small values of momentum transfer where elastic diffraction is the dominant contribution. Dedicated instrumentation in the forward region must be constructed in order to clearly distinguish between the two scenarios, see Chapter 10.

6.3.1 Exclusive vector meson diffraction

Calculations for the case of Pb for the coherent diffractive J/ψ production were performed using the dipole model [122], see Sec. 3.4. In order to apply the dipole model calculation to the nuclear case, one takes the independent scattering approximation that is Glauber theory [533]. The dipole amplitude can then be represented in the form

$$N_A(x, \mathbf{r}, \mathbf{b}) = 1 - \prod_{i=1}^{A} \left[1 - N(x, \mathbf{r}, \mathbf{b} - \mathbf{b}_i) \right] . \tag{6.3}$$

Here $N(x, \mathbf{r}, \mathbf{b} - \mathbf{b}_i)$ is the dipole amplitude for the nucleon (see Sec. 3.4) and $\mathbf{b}_i$ denotes the transverse positions of the nucleons in the nucleus. The interpretation of Eq. (6.3) is that $1 - N$ is the probability not to scatter off an individual nucleon, and thus $\prod_{i=1}^{A} \left[1 - N(\mathbf{r}, \mathbf{b} - \mathbf{b}_i, x) \right]$ is the probability not to scatter off the entire nucleus.

In addition, the following simulation includes the fluctuations of the density profile in the proton, following the prescription given in [120–122]. To include these proton structure fluctuations one assumes that the gluonic density of the proton in the transverse plane is distributed around three constituent quarks (hot spots). These hot spots are assumed to be Gaussian. In practical terms one replaces the proton profile $T_p(\mathbf{b})$

$$T_p(\mathbf{b}) = \frac{1}{2\pi B_p} e^{-b^2/(2B_p)} , \tag{6.4}$$

that appears in each individual nucleon scattering probability $N(x, \mathbf{r}, \mathbf{b} - \mathbf{b}_i)$ by the function

$$T_p(\mathbf{b}) = \sum_{i=1}^{3} T_q(\mathbf{b} - \mathbf{b}_{q,i}) , \tag{6.5}$$

where the 'quark' density profile is given by

$$T_q(\mathbf{b}) = \frac{1}{2\pi B_q} e^{-b^2/(2B_q)} . \tag{6.6}$$

Here $\mathbf{b}_{q,i}$ are the location of the hotspots that are sampled from a two dimensional Gaussian distribution whose width is given by parameter B_{qc}. The free parameters B_q and B_{qc} were obtained in [121] by comparing with HERA data on coherent and incoherent J/ψ production at a photon-proton centre-of-mass energy $W = 75\,\text{GeV}$, corresponding to fractional hadronic target energy loss $x_{IP} = 10^{-3}$. The proton fluctuation parameters obtained are $B_{qc} = 3.3\,\text{GeV}^{-2}$ and $B_q = 0.7\,\text{GeV}^{-2}$.

The results for the differential cross section at $t = 0$ for coherent production of J/ψ as a function of (virtual) photon-proton energy W for fixed values of Q^2 are shown in Figs. 6.12

and Figs. 6.13. The calculations for Pb are compared to those on the proton target. We see that the cross sections for the nuclear case increase with energy slower than for the proton case and are always smaller. Note that, we have already rescaled the diffractive cross section by a factor A^2, as appropriate for comparison of the diffractive cross section on the proton and nucleus. In the absence of nuclear corrections their ratio should be equal to 1. The differences between the scattering off a nucleus and a proton are also a function of Q^2. They are larger for smaller values of Q^2 and for photoproduction. This is understood from the dipole formulae, see Eqs. (3.23), (3.24), (3.25). As explained previously, larger values of scale Q^2 select smaller size dipoles, for which the density effects are smaller. Similarly, the differences between the lead and proton cases are larger for higher energies. This is because the dipole amplitude grows with decreasing values of x which are probed when the energy is increased, and thus the non-linear density effects are more prominent at low values of x and Q^2.
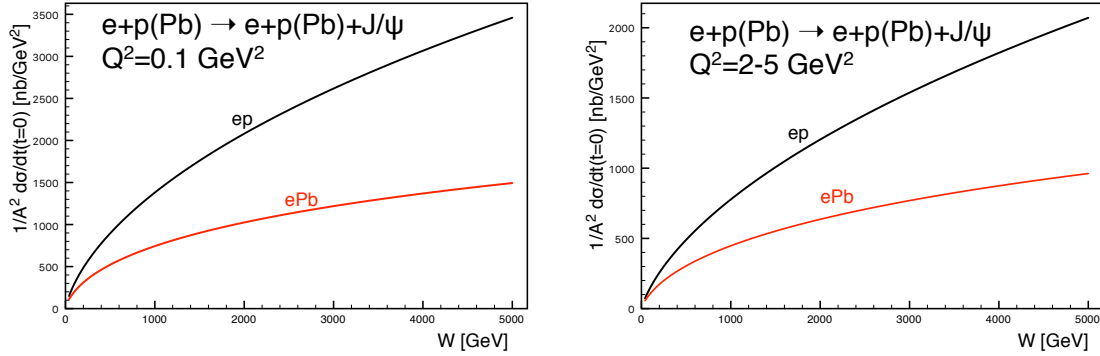

Figure 6.12: Cross section for the coherent diffractive production of the vector meson J/ψ in ePb (red solid curves) and ep (black solid curves) collisions, as a function of the energy W. Left: photoproduction case $Q^2 \simeq 0$, right: $Q^2 = 2 - 5$ GeV^2
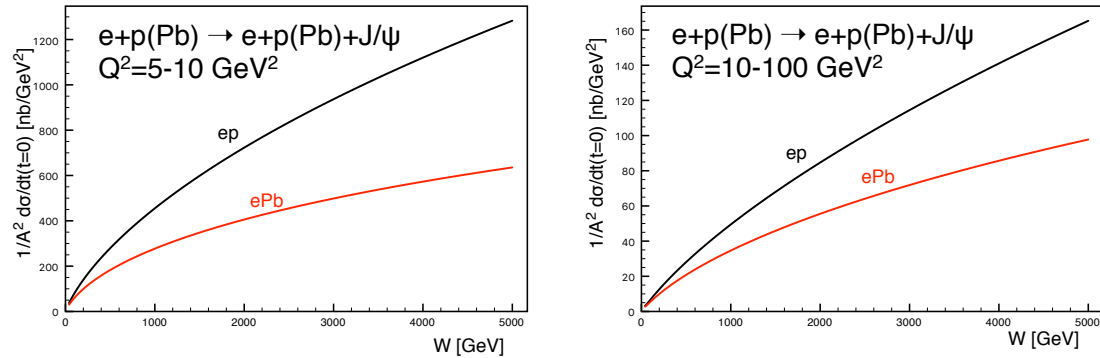

Figure 6.13: Cross section for the coherent diffractive production of the vector meson J/ψ in ePb (red solid curves) and ep (black solid curves) collisions, as a function of the energy W. Left: $Q^2 = 5-10$ GeV^2, right: $Q^2 = 10 - 100$ GeV^2.

These findings can be summarised by inspecting the ratio of the cross sections, presented as a function of x defined as[4]

$$x = \frac{Q^2 + m_{J/\psi}^2}{Q^2 + W^2 + m_{J/\psi}^2 - m_N^2} \tag{6.7}$$

---

[4]This choice to translate W and Q^2 into x in the dipole model calculations differs from others in the literature but the difference is only significative at large x where the dipole model is not applicable.

which is shown in Fig. 6.14. We observe that the ratio is smaller for smaller values of Q^2, and it decreases for decreasing values of x. The results from the dipole model calculations are
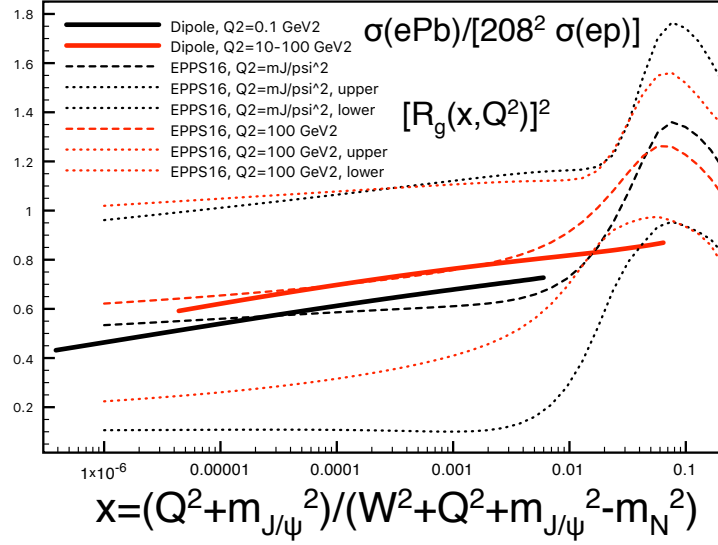

Figure 6.14: Ratio of coherent J/ψ production diffractive cross sections for Pb and proton as a function of the variable x (defined in Eq. (6.7) for the dipole model results). Solid lines: dipole model calculation, for $Q^2 = 0.1$ GeV^2 (black) and $Q^2 = 10 - 100$ GeV^2 (red). Dotted and dashed lines correspond to the nuclear ratio for the gluon density squared using the EPPS16 parametrisation [495] of the nuclear parton distribution functions. Black and red dashed lines are the central sets for $Q^2 = M_{J/\psi}^2$ and $Q^2 = 100$ GeV^2. The dotted lines correspond to the low and high edges of the Hessian uncertainty in the EPPS16 parametrisation. The difference between the two dotted lines is thus indicative of the parametrisation uncertainty for the nuclear ratio. These ratios, that can also be measured in ultraperipheral collisions [127], are larger that the values $0.2 - 0.4$ at $x \simeq 10^{-5}$ predicted by the relation between diffraction and nuclear shadowing [498].

compared with the ratio of the gluon density squared (evaluated at x and Q^2) obtained from the nuclear PDFs using the EPPS16 set [495]. The reason why one can compare the diffractive cross section ratios with the ratios for the gluon density squared can be understood from Eqs. (3.23) and (3.24). The diffractive amplitude is proportional to the gluon density $xg(x, Q^2)$. On the other hand the diffractive cross section is proportional to the amplitude squared, thus having enhanced sensitivity to the gluon density. The nuclear PDFs have large uncertainties, which is indicated by the region between the two sets of dotted lines. The EPPS16 parametrisation is practically unconstrained in the region below $x = 0.01$. Nevertheless, the estimate based on the dipole model calculation and the central value of the EPPS16 parametrisation are consistent with each other. This strongly suggests that it will be hard to disentangle nuclear effects from saturation effects and that only through a detailed combined analysis of data on the proton and the nucleus firm conclusions can be established on the existence of a new non-linear regime of QCD.

The differential cross section $d\sigma/dt$ as a function of the negative four momentum transfer squared $-t$ for the case of coherent and incoherent production is shown in Fig. 6.15. Coherent and incoherent diffraction cross sections are computed from the dipole model in the following way. The coherent diffractive cross section is obtained by averaging the diffractive scattering amplitude over the target configurations and taking the square

$$\frac{d\sigma}{dt} = \frac{1}{16\pi} |\langle \mathcal{A}(x, Q, \Delta) \rangle|^2 \ . \tag{6.8}$$
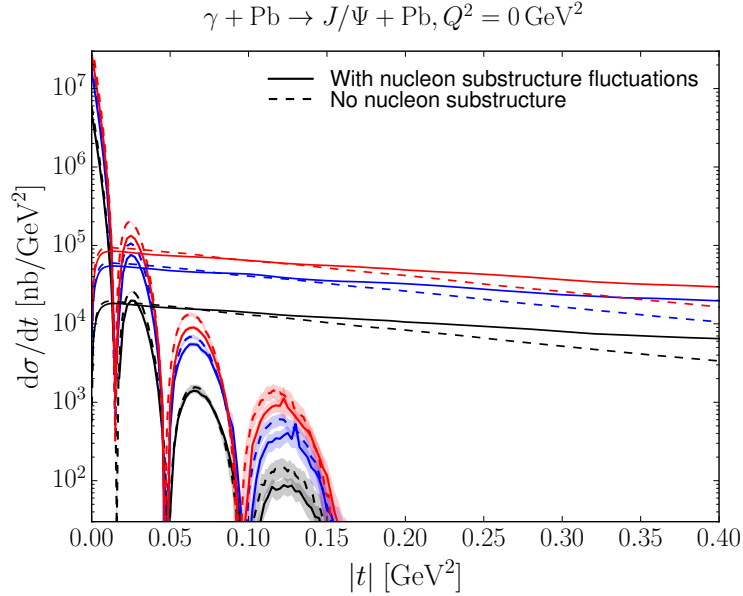
$$\gamma + \mathrm{Pb} \to J/\Psi + \mathrm{Pb}, Q^2 = 0\,\mathrm{GeV}^2$$

Figure 6.15: The differential cross sections for coherent and incoherent production of J/ψ in ePb as a function of the negative four momentum transfer squared $-t$, for photoproduction, $Q^2 = 0$. The lines showing dips are for coherent production, and those extending to large $|t|$ are for incoherent. The solid (dashed) lines are the results with (without) nucleon substructure fluctuations. Black, blue, red are for $W = 0.1, 0.813, 2.5\,\mathrm{TeV}$, respectively.

Here the brackets $\langle \ldots \rangle$ refer to averages over different configurations of the target. The incoherent cross section is obtained by subtracting the coherent cross section from the total diffractive cross section. It is standardly assumed that it takes the form of a variance of the diffractive scattering amplitude

$$\frac{d\sigma}{dt} = \frac{1}{16\pi}\left(\langle|\mathcal{A}(x,Q,\Delta)|\rangle^2 - |\langle\mathcal{A}(x,Q,\Delta)\rangle|^2\right), \qquad (6.9)$$

which should be valid for small $|t|$. The t dependence, and the relation between the impact parameter and t through the Fourier transform, makes diffractive scattering a sensitive probe of the internal geometric structure of hadrons and nuclei, see Ref. [534] for an extraction of the transverse profile of the nucleus in ultraperipheral collisions at RHIC; also Ref. [535] for an study for the EIC. In particular, because the incoherent cross section has the form of a variance of the amplitude, it is sensitive to the amount of fluctuations in impact parameter space.

The results in Fig. 6.15 (results for higher Q^2 are very similar) indicate that the incoherent production is dominant for most values of $-t$, except for the very small momentum transfers, about $|t| < 0.02\,\mathrm{GeV}^2$. Thus, dedicated instrumentation which will allow us to distinguish between the two cases is essential if one wants to measure the coherent process in a reasonably wide range of $|t|$. As in the proton case, the coherent t distribution exhibits characteristic dips. However, in the case of the nuclear targets the dips occur for much smaller values of t. This is related to the much larger value of the dipole amplitude for a wide range of impact parameters in the case of nuclear targets compared to the proton case.

Another interesting aspect, see Sec. 3.4, is the effect of the transverse structure of the target in nuclear coherent and incoherent diffraction [536]. For example, in the formulation shown above [122] a fixed number of hot spots was considered, while in [126] (see also [123] for a realisation using small-x evolution) a growing number with $1/x$ is implemented. In both cases,

the ratio of incoherent to coherent diffraction decreases with W, being smaller for larger nuclei. This decrease is sensitive to the details of the distribution of hot spots - thus, to the fluctuations of the gluon distribution in transverse space. It also shows interesting dependencies on the mass of the produced vector meson and on Q^2, resulting in the ratio being smaller for lighter vector mesons and for lower Q^2. Besides, the hot spot treatment also has some effects on the distributions in momentum transfer, see Fig. 6.15. In order to check these ideas, both the experimental capability to separate coherent form incoherent diffraction, and a large lever arm in W and Q^2 as available at the LHeC, are required.

We thus conclude that by investigating coherent and incoherent diffractive scattering on nuclei, one gets unique insight into the spatial structure of matter in nuclei. On the one hand, the coherent cross section, which is obtained by averaging the amplitude before squaring it, is sensitive to the average spatial density distribution of gluons in transverse space. On the other hand, the incoherent cross section, which is governed by the variance of the amplitude with respect to the initial nucleon configurations of the nucleus, measures fluctuations of the gluon density inside the nucleus. In the case of a nucleus, the diffractive production rate is controlled by two different scales related to the proton and nucleus size. At momentum scales corresponding to the nucleon size $|t| \sim 1/R_p^2$ the diffractive cross section is almost purely incoherent. The t-distribution in coherent diffractive production off the nucleus gives rise to a dip-type structure for both saturation and non-saturation models, while in the case of incoherent production at small $|t|$, both saturation and non-saturation models do not lead to dips [122]. This is in drastic contrast to the diffractive production off the proton where only saturation models lead to a dip-type structure in the t-distribution at values of $|t|$ that can be experimentally accessible. Therefore, diffractive production offers a unique opportunity to measure the spatial distribution of partons in the protons and nuclei. It is also an excellent tool to investigate the approach to unitarity in the high energy limit of QCD.

While we have focused here on J/ψ production, lighter vector mesons like ρ, ω, ϕ could also be studied. They should show a different Q^2 dependence and their larger sizes would make them lie closer to the black disk regime. Also the dominance of two-jet events in photoproduction would provide sensitivity to the approach to the unitarity limit [498].

6.3.2 Inclusive diffraction on nuclei

In Sec. 4.3, a study of the prospects for extracting diffractive parton densities in the proton was presented following [333]. Similar considerations apply to diffraction in eA as to ep collisions. The main difference is the larger contribution from incoherent diffraction [5] $e + A \to e + X + A^*$ than from coherent diffraction $e + A \to e + X + A$, the former dominating for $|t|$ larger than a few hundredths of a GeV^2. In the following we focus on coherent diffraction, which could be distinguished from the incoherent case using forward detectors [1].

Assuming the same framework (collinear factorization for hard diffraction, such that Eq. (4.14), and Regge factorization, Eq. (4.16) as introduced for ep in Sec. 4.3 also hold for eA), nuclear diffractive PDFs (nDPDFs) can be extracted from the diffractive reduced cross sections. It should be noted that such nDPDFs have never been measured. With the same electron energy $E_e = 60\,\mathrm{GeV}$ and nuclear beams with $E_N = 2.76\,\mathrm{TeV}$/nucleon for the LHeC, the kinematic coverage is very similar to that shown in Fig. 4.22. For details, see Ref. [333].

---

[5] A^* denotes a final state in which the nucleus has dissociated to a system of at least two hadrons, but the rapidity gap signature that defines the diffractive event is still present.
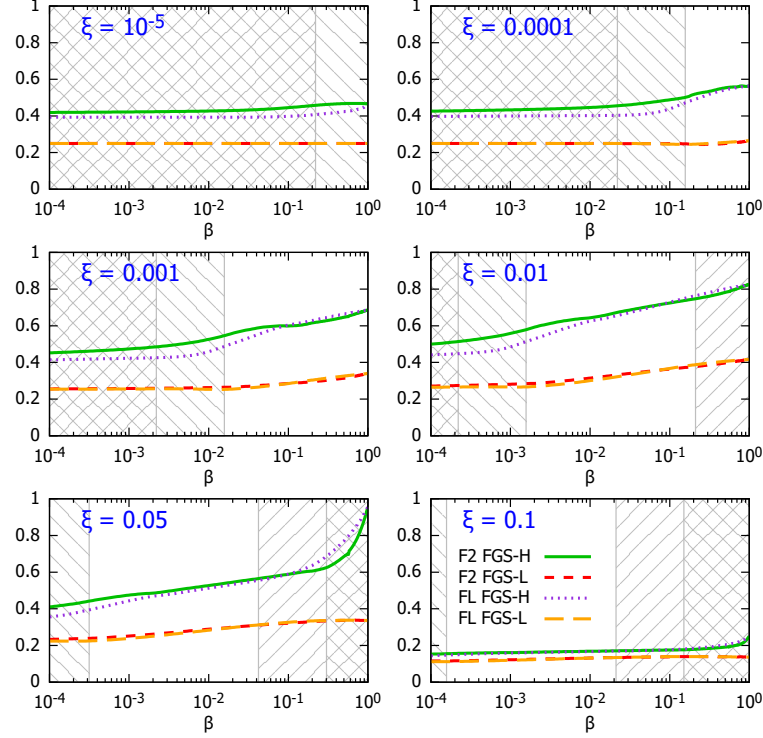
Figure 6.16: Nuclear modification factor, Eq. (6.10), for $F_2^{D(3)}$ and $F_L^{D(3)}$ in ^{208}Pb versus β, at $Q^2 = 10\,\mathrm{GeV}^2$ and for different ξ, for the models H and L in [498]. The '\' and '/' hatched areas show kinematically excluded regions for $E = 2.76$ and $19.7\,\mathrm{TeV/nucleon}$, respectively.

The nuclear modification factors for $F_2^{D(3)}$ and $F_L^{D(3)}$ from the FGS models [498] are shown in Fig. 6.16 where, in analogy to Eq. (6.1), the diffractive nuclear modification factor reads

$$R_k^A(\beta, \xi, Q^2) = \frac{f_{k/A}^{D(3)}(\beta, \xi, Q^2)}{A\, f_{k/p}^{D(3)}(\beta, \xi, Q^2)} \ . \tag{6.10}$$

The model in [498] employs Gribov inelastic shadowing [329] which relates diffraction in ep to nuclear shadowing for total and diffractive eA cross sections. It assumes that the nuclear wave function squared can be approximated by the product of one-nucleon densities, neglects the t-dependence of the diffractive γ^*-nucleon amplitude compared to the nuclear form factor, introduces a real part in the amplitudes [537], and considers the colour fluctuation formalism for the inelastic intermediate nucleon states [538]. There are two variants of the model, named H and L, corresponding to different strengths of the colour fluctuations, giving rise to larger and smaller probabilities for diffraction in nuclei with respect to that in proton, respectively. Results from both model versions are shown in Figs. 6.16 and 6.17.

The pseudodata for the reduced cross sections are generated assuming $5\,\%$ systematic error and statistic errors calculated for the integrated luminosity of $2\,\mathrm{fb}^{-1}$. A selected subset of the simulated data is shown in Fig. 6.17. The large kinematic coverage and small uncertainty (dominated by the assumed systematics) illustrated in this figure compared to Fig. 4.24 make it clear that an accurate extraction of nDPDFs in ^{208}Pb in an extended kinematic region, similar to that shown in Figs. 4.25 and 4.26, will be possible.
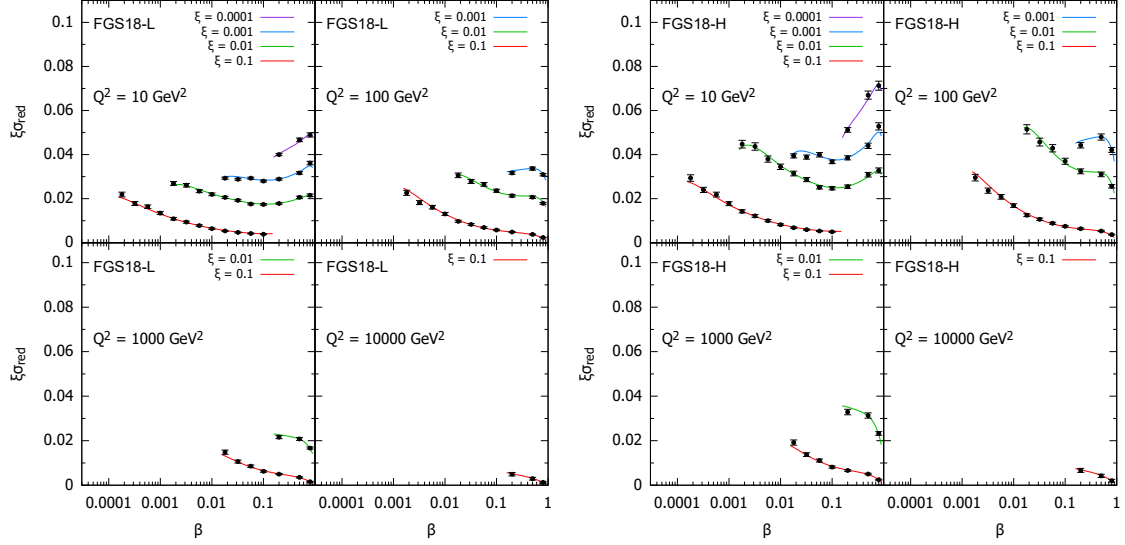
Figure 6.17: An indicative subset of simulated data for the diffractive reduced cross section as a function of β in bins of ξ and Q^2 for $e\,^{208}$Pb collisions at the LHeC, in the models in [498]. The curves for $\xi = 0.01, 0.001, 0.0001$ are shifted up by $0.01, 0.02, 0.03$, respectively.

6.4   New Dynamics at Small x with Nuclear Targets

As discussed in Sec. 4.2.1, theoretical expectations [500] indicate that fixed-order perturbation theory leading to the DGLAP evolution equations should eventually fail. When x decreases, $\alpha_s \ln 1/x$ becomes large and these large logarithms must be resummed, leading to the BFKL equation. Furthermore, when the parton density becomes large, the linear approximation that underlies both DGLAP and BFKL breaks, and non-linear processes must be taken into account to compute parton evolution. The CGC [499] offers a non-perturbative but weak coupling effective theory to treat dense parton systems in a systematic and controlled way. One of the important predictions of the CGC is that in a dense parton system saturation occurs leading to the emergence of a new dynamical scale – the saturation scale Q_{sat}, which increases with the energy.

The parton density in a hadron becomes high both through evolution – when energy or $1/x$ becomes large, and/or when partons are accumulated by overlapping nucleons – when mass number A becomes large in a nucleus. In the nucleus rest frame, the virtual photon fluctuations at small $x < (2m_N R_A)^{-1}$, with m_N the nucleon mass and R_A the nuclear radius, acquire a lifetime larger than the time taken to traverse the nucleus and, thus, all partons within a transverse area $\sim 1/Q^2$ are simultaneously probed. Actually, the parameter determining the transition between linear and non-linear dynamics is the parton density and, therefore, the onset of this new regime of QCD and its explanation must be tested, as commented in [1], exploring both decreasing values of x and increasing values of A in a kinematic $x - Q^2$ region where, in order to be sensitive to differences in evolution, enough lever arm in $Q^2 \gg \Lambda_{\text{QCD}}^2$ at small x is available. The saturation scale Q_{sat} that characterises the typical gluon momentum in a saturated hadron wave function increases with nuclear size, $Q_{sat}^2 \propto A^{1/3}$. Therefore, in eA collisions the perturbatively saturated regime is achieved at parametrically larger x than in a proton – a prediction not only of the CGC but of all multiple scattering models that anticipate an approach to the black disk, unitarity limit.

157

The opportunities to establish the existence of saturation in lepton-nucleus collisions are numerous. They include inclusive observables, both total and diffractive cross sections, and less inclusive ones like correlations:

- Tension in DGLAP fits for inclusive observables: As discussed in [1,255] and in Sec. 4.2.2, deviations from fixed-order perturbation theory can be tested by the tension that would appear in the description within a DGLAP fit of observables with different sensitivities to the sea and the glue, for example F_2 and F_L (or reduced cross sections at different energies) or $F_2^{\text{inclusive}}$ and $F_2^{\text{heavy quarks}}$. In [539], such an exercise was performed considering F_2 and F_L pseudodata for eAu collisions at the EIC [100] using reweighting techniques. While the results for EIC energies are shown not to be conclusive due to the reduced lever arm in $Q^2 > Q_{sat}^2 \gg \Lambda_{\text{QCD}}^2$, the much larger centre-of-mass energies at the LHeC (and FCC-eh) should make possible a search for tensions between different observables.

- Saturation effects in diffraction: A longstanding prediction of saturation [106, 540, 541] is a modification of the diffractive cross section in nuclei with respect to protons, with a suppression (enhancement) at small (large) β due to the approach of the nucleus to the black disk limit, where elastic and diffractive scattering become maximal, and the behaviour of the different Fock components of the virtual photon wave function. Such effects can also be discussed in terms of a competition of nuclear shadowing with the probability that the event remains diffractive in the multiple scattering process [498]. This leads to the generic expectation of an enhancement of the ratio of the coherent diffractive cross section in nucleus over that in protons, in non-linear approaches with respect to linear ones [100].

- Correlations: Correlations have been considered for a long time as sensitive probes of the underlying production dynamics. For example, the cross section for the production of two jets with the same hardness and widely separated in rapidity, called Mueller-Navelet jets [542], was proposed as a test of BFKL versus DGLAP dynamics, but the effect of saturation has not been widely studied although it has the large potentiality of differentiating linear resummation from non-linear saturation where non-trivial nuclear effects could appear. Correlations between jets were analysed in [1] for the LHeC kinematics, both in inclusive and diffractive events, see the formalism in [543]. On the other hand, the azimuthal decorrelation of particles and jets when saturation effects are at work – at small x, studied by the difference between collisions involving proton and nuclei, was proposed long ago in dAu collisions at the Relativistic Hadron Collider [544, 545]. It was studied in [1] for the LHeC kinematics, see recent developments in [546] and the extension to forward dijet production in [547]. It could also be analysed in ultraperipheral collisions at the LHC, see Sec. 9.7.

6.5   Collective effects in dense environments – the 'ridge'

One of the most striking discoveries [548] at the LHC is, that in all collision systems, from small (pp and pA) to large (AA), many of the features that are considered as indicative of the production of a dense hot partonic medium are observed (see e.g. reviews [549–551] and references therein). The most celebrated of such features is the long rapidity range particle correlations collimated in azimuth, named the 'ridge', shown in Fig. 6.18. The dynamics underlying this phenomena, either the formation of QGP and the existence of strong final state interactions, or some initial state dynamics that leaves imprint on the final observables, is under discussion [552].

While observed in photoproduction on Pb in UPCs at the LHC [553], its existence in smaller systems like e^+e^- [554] at LEP and ep at HERA [555] has been scrutinised, but the results are not conclusive.
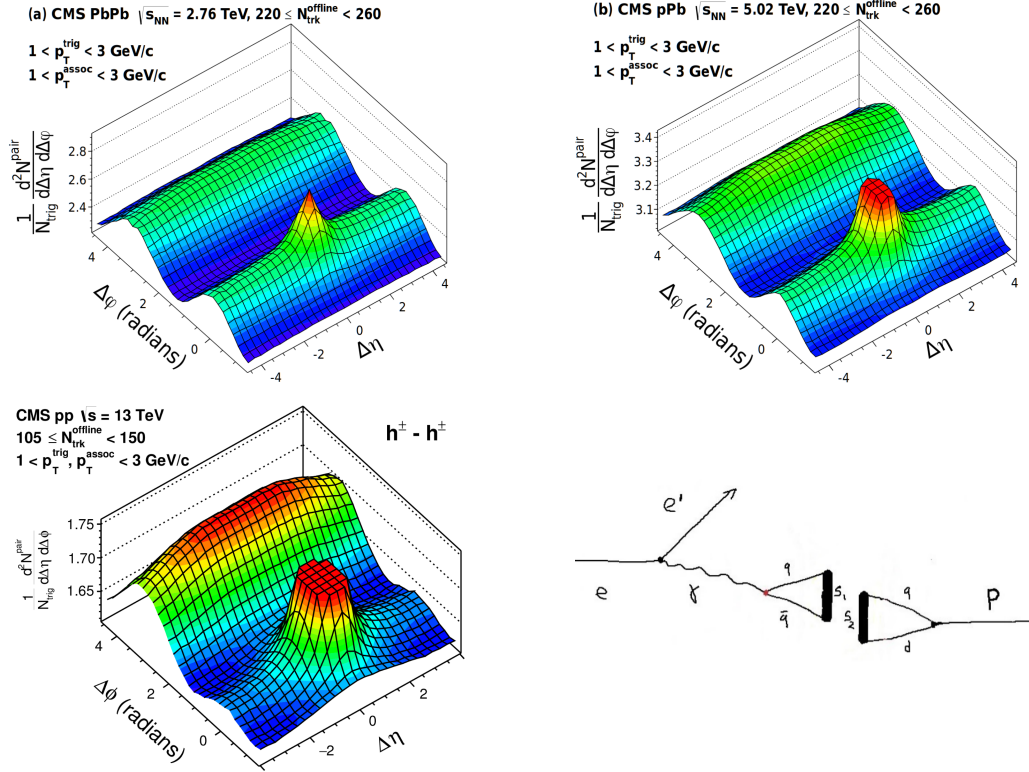

Figure 6.18: Left and top right: Collective effects seen in high-multiplicity two-particle azimuthal correlation, as observed by CMS in PbPb, pPb [556], and pp [557] collisions. Bottom right: Schematic illustration for the production of *ridge*-like effects in ep or eA scattering at the LHeC [558].

In this respect, measurements in ep and eA collisions at the LHeC at considerable centre-of-mass energies will offer crucial additional information. For example, the collision of the virtual photon with the proton at the LHeC can be considered as a high energy collision of two jets or 'flux tubes', as discussed in Refs. [558, 559] and illustrated in Fig. 6.18. This can lead to the production of 'ridges' and other novel configurations of gluons and quarks and will be measured uniquely at the LHeC.

6.6 Novel QCD Nuclear Phenomena at the LHeC

Beyond the topics discussed above there are many novel phenomena which can be explored in eA collisions at LHeC or FCC-eh, in a high energy regime and using dedicated instrumentation. We shall briefly review some of these phenomena, which can be understood utilizing the light-front framework of QCD, for a review see [560].

One of the most important theoretical tools in high energy physics is Dirac's light-front (LF) time: $\tau = x^+ = t + z/c$, the time along the light-front [561], a concept which allows all of the tools and insights of Schrödinger's quantum mechanics and the Hamiltonian formalism to be applied to relativistic physics [560]. When one takes a photograph, the object is observed at a

fixed LF time. Similarly, Compton $\gamma p \to \gamma' p''$ and deep-inelastic lepton-proton scattering are measurements of proton structure at fixed LF time. Unlike ordinary *instant time t*, physics at fixed τ is Poincaré invariant; i.e. independent of the observer's Lorentz frame. Observations at fixed τ are made within the causal horizon. LF time τ reduces to ordinary time t in the nonrelativistic limit $c \to \infty$.

The LF wavefunctions (LFWF) of hadrons are superpositions of $\Psi_n^H(x_i, \vec{k}_{\perp i}, \lambda_i) = <\Psi_H|n>$, the Fock state projections of the eigensolution of the QCD LF Hamiltonian $H_{QCD}|\Psi_H>= M_H^2 \Psi_H>$. They encode the underlying structure of bound states in quantum field theory and underlie virtually every observable in hadron physics. Hadronic LFWFs can also be measured directly by the Ashery method [562], the coherent diffractive dissociation of high energy hadrons into jets [563, 564]. In the diffractive dissociation of a high energy hadron into quark and gluon jets by two-gluon exchange, the cross-section measures the square of the second transverse derivative of the projectile LFWF. Similarly, the dissociation of a high energy atom such as positronium or *true muonium* ($[\mu^+\mu^-]$) can be used to measure the transverse derivative of its LFWFs.

Hadronic LFWFs are defined at fixed $\tau = -x^+ = t + z/c$; they are thus off-shell in the total $P^- = P^0 - P^z$, not energy P^0 [560]. Thus LFWFs are also off-shell in $\mathcal{M}^2 = P^+ P^- - P_\perp^2 = [\sum_i k_i^\mu]^2 = \sum_i \frac{k_\perp^2 + m^2}{x}_i$, the invariant mass squared of the constituents in the n-particle Fock state. LFWFs are thus functions of the invariant mass squared of the constituents in the Fock state. For a two-particle Fock state, $\mathcal{M}^2 = \frac{k_\perp^2 + m^2}{x(1-x)}$. Thus, the constituent transverse momenta $k_{\perp i}^2$ do appear alone as a separate factor in the LFWF; the transverse momenta are always coupled to the longitudinal LF momentum fractions x_i. This is the light-front version of rotational invariance. Only positive $k_i^+ = k_i^0 + k_i^z \geq 0$ and $0 \leq x_i = \frac{k_i^+}{P^+} \leq 1$ appear, where $\sum_i x_i = 1$. In addition, $J^z = \sum_i L_i^z + S_i^z$, as well as $P^+ = \sum_i k_i^+$ and $\vec{P}_\perp = \sum_i \vec{k}_{\perp i}$ are conserved at every vertex – essential covariant kinematical constraints. A remarkable property: the anomalous gravitomagnetic moment of every LF Fock state vanishes at $Q^2 = 0$. The LFWFs of bound states are off-shell in $P^- = \sum_i k_i^-$, but they tend to be maximal at minimal off-shellness; i.e. minimal invariant mass. In fact, in the holographic LFWFs where colour is confined, the LFWFs of hadrons have fast Gaussian fall-off in invariant mass. This feature also underlie intrinsic heavy quark Fock states: the LFWFs have maximal support when all of the constituents have the same rapidity y_i; i.e. $x_i \propto \sqrt{m_i^2 + k_{\perp i}^2}$. Thus the heavy quarks have the highest momentum fractions x_i.

Conversely, light-front wavefunctions provide the boost-invariant transition amplitude which convert the free quark and gluons into the hadronic eigenstates of QCD. Thus, knowing the LFWFs allows one to compute *hadronization at the amplitude level* – how the coloured quarks and gluons produced in a deep inelastic scattering event $ep \to e'X$ at the LHeC are confined and emerge as final-state hadrons.

The LF formalism leads to many novel nuclear phenomena, such as *hidden colour* [565] *colour transparency* [566], *nuclear-bound quarkonium* [567], *nuclear shadowing and antishadowing* of nuclear structure functions, etc. For example, there are five distinct colour-singlet QCD Fock state representations of the six colour-triplet quarks of the deuteron. These hidden-colour Fock states become manifest when the deuteron fluctuates to a small transverse size, as in measurements of the deuteron form factor at large momentum transfer. One can also probe the hidden-colour Fock states of the deuteron by studying the final state of the dissociation of the deuteron in deep inelastic lepton scattering at the LHeC $eD \to e'X$, where X can be $\Delta^{++} + \Delta^-$, six quark jets, or other novel colour-singlet final states.

The LF wave functions provide the input for scattering experiments at the amplitude level, encoding the structure of a projectile at a single light-front time τ [560]. For example, consider photon-ion collisions. The incoming photon probes the finite size structure of the incoming nucleus at fixed LF time, like a photograph – not at a fixed instant time, which is acausal. Since the nuclear state is an eigenstate of the LF Hamiltonian, its structure is independent of its momentum, as required by Poincaré invariance. One gets the same answer in the ion rest frame, the CM frame, or even if the incident particles move in the same direction, but collide transversely. There are no colliding *pancakes* using the LF formalism.

The resulting photon-ion cross-section is not point-like; it is shadowed: $\sigma(\gamma A \to X) = A^\alpha \sigma(\gamma N \to X)$, where A is the mass number of the ion, N stands for a nucleon, and the power $\alpha \approx 0.8$ reflects Glauber shadowing [568]. The shadowing stems from the destructive interference of two-step and one-step amplitudes, where the two-step processes involve diffractive reactions on a front-surface nucleon which shadows the interior nucleons. Thus the photon interacts primarily on the front surface. Similarly, a high energy ion-ion collision $A_1 + A_2 \to X$ involves the overlap of the incident frame-independent LFWFs. The initial interaction on the front surface of the colliding ions can resemble a shock wave.

In the case of a deep inelastic lepton-nucleus collision $\gamma^* A \to X$, the two-step amplitude involves a leading-twist diffractive deep inelastic scattering (DDIS) $\gamma^* N_1 \to V^* N_1$ on a front surface nucleon N_1 and then the on-shell propagation of the vector system V^* to a downstream nucleon N_2 where it interacts inelastically: $V^* N_2 \to X$. If the DDIS involves Pomeron exchange, the two-step amplitude interferers destructively with the one-step amplitude $\gamma^* N_1 \to X$ thus producing shadowing of the nuclear parton distribution function at low $x < 0.1$. On the other hand, if the DDIS process involves $I = 1$ Reggeon exchange, the interference is constructive, producing *flavour-dependent* leading-twist antishadowing [568] in the domain $0.1 < x < 0.2$.

One can also show that the Gribov-Glauber processes, which arise from leading-twist diffractive deep inelastic scattering on nucleons and underly the shadowing and antishadowing of nuclear structure functions [568], prevent the application of the operator product expansion to the virtual Compton scattering amplitude $\gamma^* A \to \gamma^* A$ on nuclei and thus negate the validity of the momentum sum rule for deep inelastic nuclear structure functions [569].

Chapter 7

Higgs Physics with LHeC

7.1 Introduction

The Higgs boson was discovered in 2012 by ATLAS [570] and CMS [571] at the Large Hadron Collider (LHC). It is the most recently discovered and least explored part of the Standard Model. The Higgs Boson (H) is of fundamental importance. It is related to the mechanism predicted by [411, 412, 572] and independently by [573]], in which the intermediate vector bosons of the spontaneously broken electroweak symmetry acquire masses [1] while the photon remain massless. Fermions obtain a mass via the Yukawa couplings with the Higgs field. Following the discovery of the Higgs boson, its physics and thorough exploration has become a central theme of the physics programme at the LHC. Any high-energy future collider project, beginning with the high luminosity upgrade of the Large Hadron Collider, the HL-LHC, underway to collect data in a decade hence, has put the potential to precisely study the properties of the Higgs boson into its center of attention, for understanding its characteristics and hoping to open a new window into physics extending beyond the Standard Model, see for example [574, 575]. In this section we present the potential to explore the SM Higgs physics at the LHeC and to certain extent at FCC-eh also.

A first challenge on the physics of the Higgs boson is to establish whether it indeed satisfies the properties inherent to the Standard Model (SM) regarding its production and decay mechanisms. The SM neutral H boson decays into pairs of fermions, $f\bar{f}$. The dominant decay is $H \to b\bar{b}$ with a branching fraction of about 58 %. The branching scales with the square of the fermion mass, m_f^2. The next prominent fermionic decay therefore is $H \to \tau^+\tau^-$ with 6.3 % followed by the charm decay with a predicted branching fraction of 2.9 %. The Higgs boson also decays into pairs of W and Z bosons at a rate of 21.5 % and 2.6 %, respectively. Loop diagrams enable the decay into gluon and photon pairs with a branching of 8.2 and 0.2 %, respectively. The seven most frequent decay channels, ordered according to descending branching fractions, thus are into $b\bar{b}$, W^+W^-, gg, $\tau^+\tau^-$, $c\bar{c}$, ZZ and $\gamma\gamma$. Together these are predicted to represent a total SM branching fraction of 99.9 %. At the LHC these and rarer decays can be reconstructed, with the exception of the charm decay for reasons of prohibitive combinatorial background. The

---

[1]The mass of the W boson, M_W, is generated through the vacuum expectation value, η, of the Higgs field (Φ) and given by the simple relation $M_W = g\eta/\sqrt{2}$ where g is the weak interaction coupling. Here $\eta = \sqrt{-\mu^2/2\lambda}$ with the two parameters of the Higgs potential that is predicted to be $V = -\mu^2\Phi^+\Phi - \lambda(\Phi^+\Phi)^2$. The Higgs mass is given as $M_H = 2\eta\sqrt{\lambda}$ while the mass of the Z boson is related to M_W with the electroweak mixing angle, $M_Z = M_W/\cos\Theta_W$.

main purpose of this paper is to evaluate the prospects for precisely measuring these channels in electron-proton scattering.

7.2 Higgs Production in Deep Inelastic Scattering

In deep inelastic electron-proton scattering, the Higgs boson is predominantly produced through WW fusion in charged current DIS (CC) scattering, Fig. 1. The next large Higgs production mode in ep is $ZZ \to H$ fusion in neutral current DIS (NC) scattering, Fig. 1, which has a smaller but still sizable cross section. These ep Higgs production processes are very clean for a number
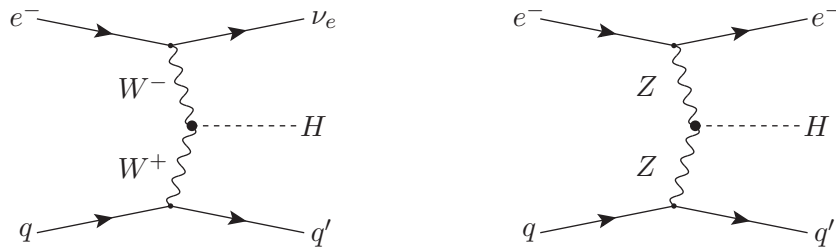

Figure 7.1: Higgs boson production in charged (left) and neutral (right) current deep inelastic electron-proton scattering to leading order.

of reasons:

- even at the high luminosity of $10^{34} \, \text{cm}^{-2}\text{s}^{-1}$ the inclusive pileup is only 0.1 (1) for the LHeC (FCC-eh) and the final state signature therefore free from event overlap, in contrast to the HL-LHC where it will typically be 150;

- in ep, contrary to pp, there is no initial nor final state colour (re)connection;

- the higher-order corrections are small. For the total CC process they were estimated [576] to be of the order of only 1 % for the QCD part, subject to cut dependencies yielding shape changes up to 20 %, and -5 % for the QED part (with a weak dependence on the PDF choice). The smallness of the QCD corrections was attributed mainly to the absorption of gluon and quark radiation effects in the evolution of the parton distributions (PDFs) [576]. The PDFs will be measured with very high precision at any of the ep colliders here considered, see Chapter 3, thus allowing a unique self-consistency of Higgs cross section measurements.

The NC reaction is even cleaner than the CC process as the scattered electron fixes the kinematics more accurately than the missing energy. While in pp both WW and ZZ processes are hardly distinguishable, in ep they uniquely are, which provides an important, precise constraint on the WWH and ZZH couplings.

7.2.1 Kinematics of Higgs Production

At HERA the kinematics was conveniently reconstructed through event-wise measurements of Q^2 and y. The reconstruction of the kinematics in charged currents uses the inclusive hadronic final state measurements. Based on the energies E'_e and E_h and the polar angles Θ_e and Θ_h

of the scattered electron and the hadronic final state, respectively, one obtains a redundant determination of the kinematics in neutral current scattering. This permits a cross calibration of calorimetric measurements, of the electromagnetic and hadronic parts and of different regions of the detector, which is a major means to achieve superb, sub-percent precision in ep collider measurements. Methods have been developed to optimise the kinematics reconstruction and maximise the acceptance by exploiting the redundant determination of the scattering kinematics, see for example [56]. The basic DIS kinematic distributions of Q^2, x and y for Higgs production at $\sqrt{s} = 3.5$ TeV are illustrated in Fig. 7.2. The average Q^2 and x values probed are $Q^2 \approx$
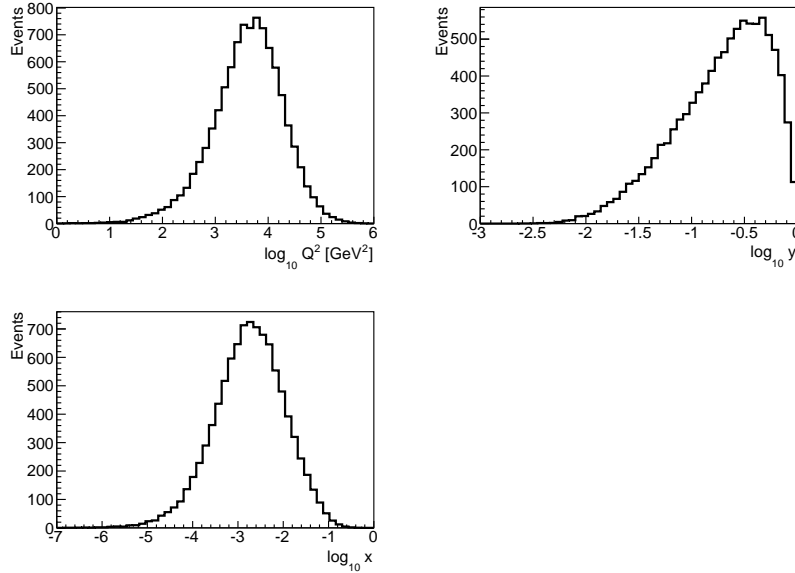

Figure 7.2: Distributions for $ep \to \nu HX$ events, at parton-level, for the negative 4-momentum transfer squared, Q^2 (top left), Bjorken x (bottom left) and the inelasticity $y = Q^2/sx$ (top right) at $\sqrt{s} = 3.5$ TeV (FCC-eh). Events generated with MadGraph [367], see Tab. 7.1.

$2000\,\text{GeV}^2$, $x \approx 0.02$ at LHeC and $Q^2 \approx 6500\,\text{GeV}^2$, $x \approx 0.0016$ at FCC-eh.

As is described in this paper elsewhere, constraints for a large pseudorapidity or polar angle, $\eta = \ln \tan \theta/2$, acceptance of the apparatus arise i) for the backward region (the polar angle is defined w.r.t. the proton beam direction) from the need to reconstruct electrons at low Q^2 enabling low x physics and ii) for the forward region to cover a maximum region towards large x at medium Q^2 with the reconstruction of the hadronic final state. The acceptance therefore extends, for the LHeC, to pseudorapidities of $\eta = \pm 5$, which for the FCC-eh case is extended to $\eta = \pm 6$. The large acceptance is in particular suitable for the reconstruction of Vector-Boson-Fusion Higgs boson event signatures, see Fig. 7.3 for the typical pseudorapidity distributions of Higgs boson event signature in DIS at the most asymmetric FCC-eh collider configuration.

Geometric acceptances due to kinematic constraints in the pseudorapidity on the Higgs decay products for both LHeC and FCC-eh are further illustrated in Fig. 7.4. The acceptances are calculated for a basic selection of all final states with $p_T > 15$ GeV and a coverage of the forward jet up to $\eta = 5$ and $\eta = 6$, respectively, for both colliders. As seen from Fig. 7.4, the acceptances are higher for the less asymmetric LHeC beam configuration and about the same for hadronic calorimetry up to $\eta = 5$ and $\eta = 6$. Hence, the LHeC calorimeter is designed for $\eta = 5$. The optimal hadronic calorimetry coverage for FCC-eh is clearly $\eta = 6$ yielding significantly higher acceptances in comparison to an $\eta = 5$ calorimetry. From Fig. 7.4, it is apparent that for both collider configurations the Higgs decay products would require tagging capabilities up $\eta = 3.5$,
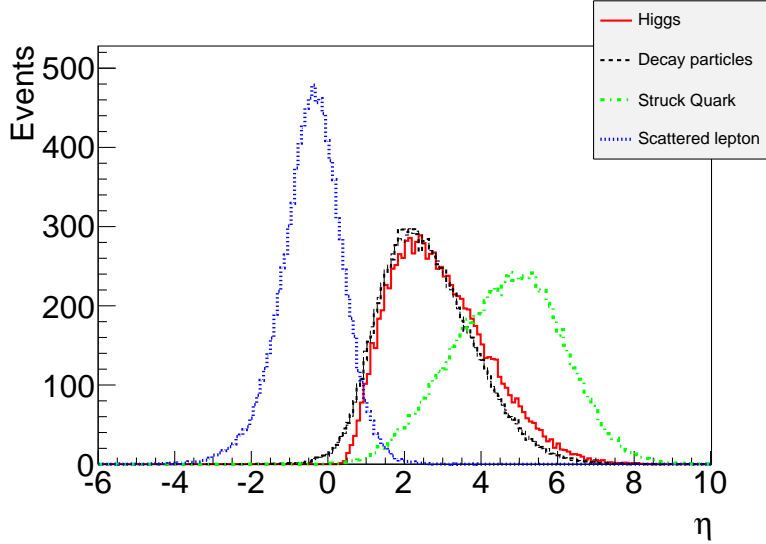
Figure 7.3: Pseudorapidity (η) distributions, at parton-level, characterising the Vector-Boson-Fusion production and decay of the Higgs boson to WW in DIS scattering at FCC-eh. The scattered lepton (blue) in the NC case (or missing energy for CC) has an average η of about -0.5, i.e. it is scattered somewhat backwards (in electron beam direction). The pseudorapidity distributions of the generated Higgs boson (red) and its decay particles (black) are very similar and peak at $\eta \simeq 2$. The struck quark, especially at the FCC-eh as compared to LHeC, generates a very forward jet requiring forward calorimetry up to $\eta \simeq 6$ as is foreseen in the FCC-eh detector design. Events are generated with MadGraph, see setup in Tab. 7.1.

e.g. for heavy flavour and tau decays. Suitably designed muon detectors covering $\eta = 4$ appear feasible for both collider configurations, those would result in high $H \rightarrow \mu\mu$ acceptances of about 72 % (63 %) for LHeC (FCC-eh) for selecting all final states with $p_T > 15$ GeV and a coverage of the forward jet up to $\eta = 5$ ($\eta = 6$). A further extension to a 1° muon acceptance, would change the acceptances marginally to 72.9 % (67.5 %) for LHeC (FCC-eh).

7.2.2 Cross Sections and Rates

The cross sections for Higgs production in CC and NC DIS e^- scattering of a 60 GeV electron beam with protons at three different energies, for LHeC, HE-LHeC and FCC-eh, are summarised in Tab. 7.1. The cross sections are calculated to leading order with MadGraph (MG5 v2.5.1) using the CTEQ6L1 proton PDF and $M_H = 125$ GeV. The CC e^-p cross section is directly proportional to the beam polarisation, P, as $\sigma_{CC} \propto (1 - P)$ while the NC cross section only weakly depends on the polarisation [96]. It is observed that the CC Higgs production cross section at LHeC is comparable to that of a 250 GeV e^+e^- collider. One thus expects, roughly, results of comparable sensitivity. The difference being that e^+e^- favours the H to ZZ couplings while ep is dominantly sensitive to $WW \rightarrow H$ production. This provides a fundamental complementarity between e^+e^- and ep collider Higgs physics.

The CC e^-p cross section is enlarged with the (negative) electron beam polarisation, P_e, while the NC cross section is less sensitive to P_e. The cross section at FCC-eh reaches values of pb. Combined with long operation time one reaches sub-permille precision of the Higgs couplings. Similarly, the HH cross section approaches 0.5 fb values only with the highest energy as expected for $\sqrt{s} > 3$ TeV FCC-eh or CLIC-ee colliders. A first cut-based study to access the Higgs self-
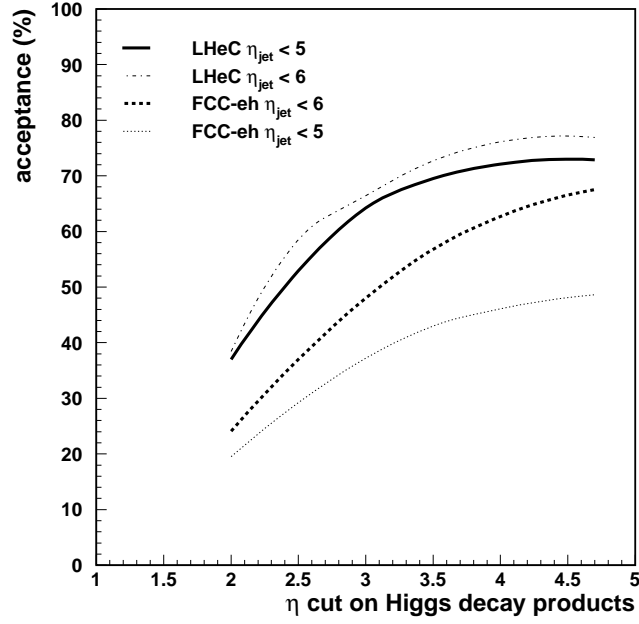
Figure 7.4: Acceptance of DIS Higgs candidates (y axis) in dependence on the pseudorapidity (η) cut requirement on the Higgs decay products (x axis) for two scenarios of the coverage of the hadronic final states. All final states are selected with $p_T > 15$ GeV. The forward jet is accepted up to $\eta = 5$ and $\eta = 6$ for LHeC (full and dashed-dotted lines), and FCC-eh (dotted and dashed lines), respectively. Calculations are at parton-level using MadGraph.

coupling at FCC-eh within 20% is detailed in Ref. [578]. Further prospects are not discussed here since measuring the HH coupling is one of the foremost tasks of HL-LHC and the FCC-hh [579].

The polarised e^+p cross section is calculated to be significantly smaller than the e^-p value, by a factor of $197/58 \simeq 6$ at the LHeC, mainly because the $W^-u \to \bar{d}$ reaction is more frequent than $W^+d \to u$. Furthermore, positron sources are currently considered to be much less intense (by a factor of about ten or even a hundred) than electron sources. It is desirable to take e^+p data at future ep colliders for electroweak physics but in the linac-ring version their amount will be limited and unlikely suitable for precision Higgs physics.

Table 7.2 provides an illustration of the statistics which is expected to be available in charged and neutral current scattering for nine decay channels ordered by their branching ratios for the nominal LHeC and FCC-eh configurations. The statistics at LHeC would be about ten times lower than that at FCC-eh since the cross section is diminished by $\simeq 1/5$ and due to a shorter expected running time, i.e. the integrated luminosity is assumed to be half of that at FCC-eh. Accessing rarer SM Higgs decay channels is the particular strength of luminous pp scattering at highest energies rather than that of anticipated ep or e^+e^- colliders. The signal strength and coupling analyses subsequently presented deal with the seven most frequent decays representing 99.9% of the SM Higgs decays. In addition, there is a significant potential for a measurement of the $H \to \mu\mu$ decay at the FCC-eh, which, as is seen in Tab. 7.2, may provide about 500 (45) events, from CC and NC DIS at FCC-eh (LHeC). Thus one may be able to measure this process to about 6% precision at the FCC-eh and 18% at LHeC.

Parameter	Unit	LHeC	HE-LHeC	FCC-eh	FCC-eh
E_p	TeV	7	13.5	20	50
$\sqrt{s}$	TeV	1.30	1.77	2.2	3.46
σ_{CC} $(P = -0.8)$	fb	197	372	516	1038
σ_{NC} $(P = -0.8)$	fb	24	48	70	149
σ_{CC} $(P = 0)$	fb	110	206	289	577
σ_{NC} $(P = 0)$	fb	20	41	64	127
HH in CC	fb	0.02	0.07	0.13	0.46

Table 7.1: Total cross sections, in fb, for inclusive Higgs production, $M_H = 125$ GeV, in charged and neutral current deep inelastic e^-p scattering for an unpolarised $(P = 0)$ and polarised $(P = -0.8)$ $E_e = 60$ GeV electron beam and four different proton beam energies, E_p, for LHeC, HE-LHeC and two FCC-eh versions. The c.m.s. energy squared in ep is $s = 4E_eE_p$. The last row shows the double-Higgs CC production cross sections in fb. The calculations are at LO QCD using the CTEQ6L1 PDF [577] and the default scale of MadGraph [367] with dependencies due to scale choices of 5-10 %.

		Number of Events			
		Charged Current		Neutral Current	
Channel	Fraction	LHeC	FCC-eh	LHeC	FCC-eh
$b\bar{b}$	0.581	114 500	1 208 000	14 000	175 000
W^+W^-	0.215	42 300	447 000	5 160	64 000
gg	0.082	16 150	171 000	2000	25 000
$\tau^+\tau^-$	0.063	12 400	131 000	1 500	20 000
$c\bar{c}$	0.029	5700	60 000	700	9 000
ZZ	0.026	5 100	54 000	620	7 900
$\gamma\gamma$	0.0023	450	5 000	55	700
$Z\gamma$	0.0015	300	3 100	35	450
$\mu^+\mu^-$	0.0002	40	410	5	70
σ [pb]		0.197	1.04	0.024	0.15

Table 7.2: Total event rates, and cross sections, for SM Higgs decays in the charged $(ep \to \nu HX)$ and neutral $(ep \to eHX)$ current production in polarised $(P = -0.8)$ electron-proton deep inelastic scattering at LHeC $(\sqrt{s} = 1.3$ TeV$)$ and FCC-eh $(\sqrt{s} = 3.5$ TeV$)$, for an integrated luminosity of 1 and 2 ab^{-1}, respectively. The branching fractions are taken from [580]. The estimates are at LO QCD using the CTEQ6L1 PDF and the default scale of MadGraph, see setup in Tab. 7.1.

7.3 Higgs Signal Strength Measurements

Standard Model Higgs production in deep inelastic ep scattering proceeds via Vector-Boson-Fusion in either charged or neutral current scattering as it is illustrated in Fig. 1. The scattering cross sections, including the decay of the Higgs boson into a pair of particles $A_i\bar{A}_i$ can be written as

$$\sigma^i_{CC} = \sigma_{CC} \cdot \frac{\Gamma^i}{\Gamma_H} \quad \text{and} \quad \sigma^i_{NC} = \sigma_{NC} \cdot \frac{\Gamma^i}{\Gamma_H}. \tag{7.1}$$

Here the ratio of the partial to the total Higgs decay width defines the branching ratio, br_i, for each decay into $A_i\bar{A}_i$. The ep Higgs production cross section and the O(1) ab^{-1} luminosity prospects enable to consider the seven most frequent SM Higgs decays, i.e. those into fermions $(b\bar{b}, c\bar{c}, \tau^+\tau^-)$ and into gauge particles $(WW, ZZ, gg, \gamma\gamma)$ with high precision at the LHeC and its higher energy versions.

In *ep* one obtains constraints on the Higgs production characteristics from CC and NC scattering, which probe uniquely either the HWW and the HZZ production, respectively. Event by event via the selection of the final state lepton which is either an electron (NC DIS) or missing energy (CC DIS) those production vertices can be uniquely distinguished, in contrast to *pp*. In e^+e^-, at the ILC, one has considered operation at $250\,\text{GeV}$ and separately at $500\,\text{GeV}$ to optimise the HZZ versus the HWW sensitive production cross section measurements [581]. For CLIC the c.m.s. energy may be set to $380\,\text{GeV}$ as a compromise working point for joint NC and CC measurements, including access to top production [582]. The salient advantage of the e^+e^- reaction, similarly considered for the more recent circular collider proposals, CEPC [18] and FCC-ee [15], stems from the kinematic constraint of the Higgs-strahlung, $e^+e^- \to Z^* \to ZH$, which determines the total Higgs production cross section independently of its decay.

The sum of the branching ratios for the seven Higgs decay channels here under study for *ep* adds up to $99.87\,\%$ of the total SM width [583]. As is discussed in Sect. 7.6, significant constraints of the $H \to invisible$ decay can be set with *ep* also albeit not being able to exclude exotic, unnoticed Higgs decays. The accurate reconstruction of all decays considered here will present a severe constraint on the total cross section and with that of the total decay width of the Higgs boson in the SM. For the evaluation of the measurement accuracy, the cross section measurement prospects for a decay channel i are presented here as relative signal strengths $\mu^i(NC, CC)$, obtained from division by the SM cross section.

Initially, detailed simulations and Higgs extraction studies for LHeC were made for the dominant $H \to b\bar{b}$ [584–588] and the challenging $H \to c\bar{c}$ [588–590] channels. The focus on the $H \to b\bar{b}$ decay has been driven not only by its dominance but as well by the difficulty of its accurate reconstruction at the LHC. It has been natural to extend this to the $H \to c\bar{c}$ which currently is considered to not be observable at the HL-LHC, for permutation and large background reasons. The results of the updated b and c decay studies, using cuts and boosted decision tree (BDT) techniques, are presented below.

A next detailed analysis has been performed for the $H \to W^+W^-$ decay. The total of the WW decays represents $21.5\,\%$ of the Higgs branching into SM particles. There is a special interest in its reconstruction in the DIS charged current reaction as this channel uniquely determines the HWW coupling to its fourth power. A complete signal and background simulation and eventual BDT analysis of the $H \to W^+W^-$ decay in charged currents has been performed which is subsequently described. Unlike at LHC, this uses the purely hadronic decays which in *pp* are very difficult to exploit.

Finally, as summarised below, an analysis using acceptance, efficiency and signal-to-background scale factors has been established for the residual four of the seven dominant decay channels, Tab. 7.2. This estimate could be successfully benchmarked with the detailed simulations for heavy quark and W decays. The present study therefore covers more than $99\,\%$ of the SM Higgs decays, which in *ep* are redundantly measured, in both neutral and charged current reactions. This opens interesting prospects for precision Higgs physics in *ep*, but as well in combination with *pp*, i.e. of LHeC with HL-LHC, and later of FCC-eh with FCC-hh.

7.3.1 Higgs Decay into Bottom and Charm Quarks

The Higgs boson decays dominantly into $b\bar{b}$ with a $58\,\%$ branching ratio in the SM. Its reconstruction at the LHC has been complicated by large combinatorial background. Recently this decay was established with signal strengths, relatively to the SM, of $\mu_{bb} = 1.01 \pm 0.12(stat) \pm^{0.16}_{0.15}(exp)$ by ATLAS [591] with a luminosity of $79.8\,\text{fb}^{-1}$ and of $\mu_{bb} = 1.01 \pm 0.22$ by CMS [592] with

a luminosity of $41.3\,\mathrm{fb}^{-1}$. This is a remarkable experimental LHC achievement since for long one expected to not be able to measure this decay to better than about 10 % at the future HL-LHC. Meanwhile this expectation has become more optimistic with the updated HL-LHC prospects [593], however, the most hopeful assumption for the $H \to c\bar{c}$ decay is a limit to two times the SM expectation.

Because of the special importance of determining the frequent $b\bar{b}$ decay most accurately, and with it the full set of SM branchings, the prime attention of the LHeC Higgs prospect studies has been given to those two channels. The first PGS detector-level study was published with the CDR [1] before the announcement of the discovery of the Higgs boson and assuming $M_H = 120$ GeV. This and subsequent analyses use samples generated by MadGraph5 [367], for both signal and background events with fragmentation and hadronization via PYTHIA 6.4 [594] in an ep customised programme version[2]. Subsequent analyses have been updated to $M_H = 125$ GeV and to state-of-the art fast detector simulation with DELPHES 3 [596] as testbed for ep detector configurations. Both cut-based and boosted decision tree (BDT) analyses were performed in independent evaluations.

As shown in the CDR, the $H \to b\bar{b}$ decay could be measured via applying classical kinematic selection requirements as follows:

- CC DIS kinematic cuts of $Q_h^2 > 500$ GeV^2, $y_h < 0.9$, missing energy $E_T^{\mathrm{miss}} > 30$ GeV, and no electrons in the final state to reject NC DIS;

- at least three anti-kt $R = 0.7$ jets with $p_T > 20$ GeV which are subject to further b-tagging requirements;

- a Higgs candidate from two b-tagged jets with b-tagging efficiencies of 60 to 75 %, charm (light quark) misidentification efficiencies of 10 to 5 % (1 %) ;

- rejection of single-top events via requiring a dijet W candidate mass of greater than 130 GeV and a three-jet top candidate mass of larger than 250 GeV using a combination with one of the b-jets of the Higgs mass candidate;

- a forward scattered jet with $\eta > 2$, and a large $\Delta\phi_{b,MET} > 0.2$ between the b-tagged jet and the missing energy.

The dominant backgrounds are CC DIS multijet and single top production, while CC Z, W and NC Z contributions are small. The background due to multijets from photoproduction, where $Q^2 \sim 0$, can be reduced considerably due to the tagging of the small angle scattered electron with an electron tagger. The result of a cut-based analysis is shown in Fig. 7.5 where clear Z and $H \to b\bar{b}$ peaks are seen. Assuming that the photoproduction background is vetoed with a 90 % efficiency, the resulting signal is shown in Fig. 7.5 corresponding to a SM $H \to b\bar{b}$ signal strength $\delta\mu/\mu$ of 2 % for an integrated luminosity of 1000 fb^{-1} and $P_e = -0.8$. This result is consistent with earlier analysis and robust w.r.t. the update of the Higgs mass from 120 to 125 GeV confirming the high $S/B > 1$ (see also Ref. [587] where an alternative approach to estimate the multijet photoproduction background gives a similar signal strength uncertainty). The result illustrates that even with harsh kinematic requirements and already a small luminosity of 100 fb^{-1}, this important decay channel could be measured to an uncertainty of about 6 %.

---

[2]The hadronic showering is not expected to change the kinematics of the DIS scattered lepton. This has been shown, see page 11 of Ref. [595], with the very good level of agreement of NC DIS electron kinematics with and without the ep-customized Pythia showering. Specifically, for 99.8 % of events the kinematics in the momentum vector components and for 98 % of the events the energy of the scattered electron remain unchanged.
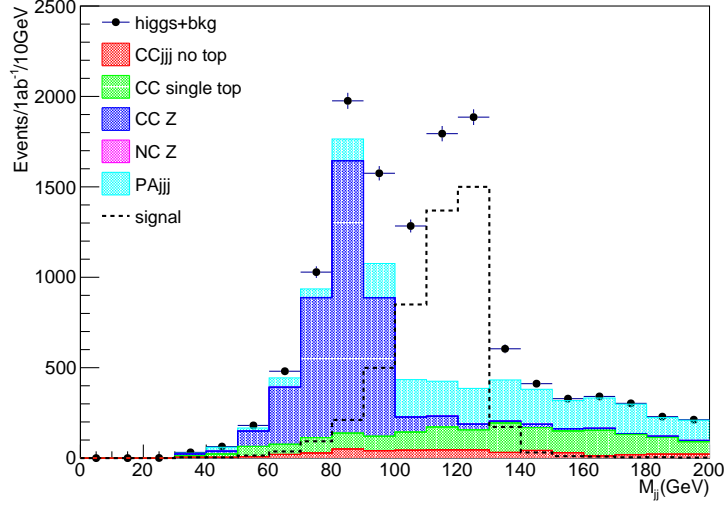
Figure 7.5: Invariant dijet mass distribution at DELPHES detector-level expected for 1 ab^{-1} and -80 % electron polarisation at LHeC. The S/B is about 2.9 for the events in the Higgs mass range of 100 to 130 GeV. Events are generated with MadGraph using $M_H = 125$ GeV and showered with PYTHIA 6.4, and subject to cut-based event selection criteria, see text for further details. Note that samples are generated with a minimum dijet mass cut of 60 GeV.

The stability of the cut-based results has been further shown for different hadronic calorimeter resolution setups

$$\frac{\sigma}{E} = \frac{a}{\sqrt{E}} \oplus b \quad \text{for} \quad |\eta| < |\eta_{\min}|, \tag{7.2}$$

$$\frac{\sigma}{E} = \frac{c}{\sqrt{E}} \oplus d \quad \text{for} \quad |\eta_{\min}| < |\eta| < 5, \tag{7.3}$$

where for $\eta_{\min} = 3$ the parameter b (d) is varied within 1 (3) and 7 (9) % for two resolution parameters a (c) of either 30 (60) and 35 (45) %. Alternatively, the central range was restricted to $\eta_{\min} = 2$ with parameter b (d) of 3 (5) % for resolution parameters a (c) of 35 (45) %. While using the same analysis cuts, the signal yields varied within 34 %, it could be shown that with adjusted set of cuts (notably the choices of cuts for Higgs mass range, $\Delta\phi_{b,MET}$, and forward η) the SM $H \to b\bar{b}$ signal strength $\delta\mu/\mu$ varied with a fractional uncertainty of at most 7 %.

The cut-based $H \to b\bar{b}$ signal strength analyses are suffering from rather low acceptance times selection efficiencies in the range of 3 to 4 % only. Modern state-of-the-art analysis techniques, e.g. as performed for finding $H \to b\bar{b}$ at the LHC regardless of the overwhelming QCD jet background, are based on neural networks in the heavy flavour tagging as well as in the analysis.

Boosted Decision Tree (BDT) $H \to b\bar{b}$ and $H \to c\bar{c}$ analyses using the Toolkit for Multivariate Data Analysis with ROOT (TMVA) [597] are performed using independently produced signal and background samples based on the same setup as for the cut-based analyses, see Fig. 7.5. Those analyses start with loose preselections of at least three anti-kt jets with $p_T > 15$ GeV without any further heavy flavour tagging in addition to the CC DIS kinematic cuts of $Q_h^2 > 400$ GeV^2, $y_h < 0.9$, and missing energy $E_T^{\text{miss}} > 20$ GeV. The invariant mass distributions using anti-kt $R = 0.5$ jets are illustrated in Fig. 7.6, where the mass distributions in the upper plots illustrate in particular the single top contributions and the subsequent significant Higgs signal loss if simple anti-top cuts would be applied. In the lower plot of Fig. 7.6 the invariant dijet
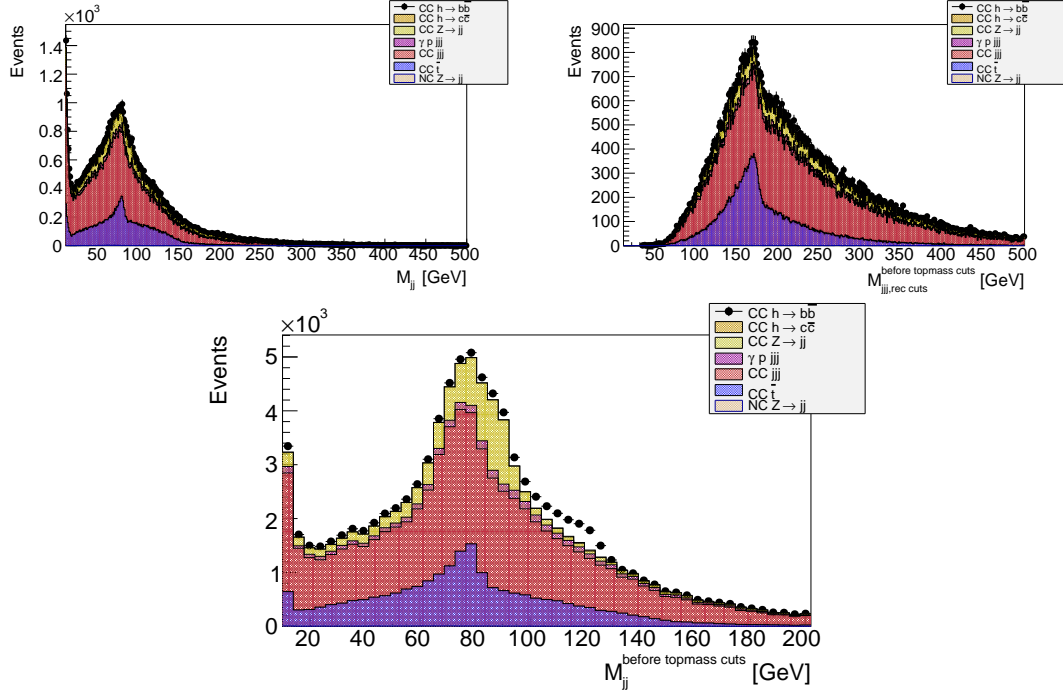
Figure 7.6: Invariant mass distributions at DELPHES detector level for an integrated luminosity of 100 fb^{-1} and -80% electron polarisation. Events passed preselection cuts of $Q_h^2 > 400$ GeV^2, $y_h < 0.9$, $E_T^{\mathrm{miss}} > 20$ GeV and at least three, flavour-untagged anti-kt $R = 0.5$ jets with $p_T > 15$ GeV. The different colours show the contributions per process, the photoproduction background (γp jjj) is assumed to be vetoed with 90%. Note that samples are generated with a minimum dijet mass cut of 60 GeV. Upper left: Invariant dijet mass, showing W candidates from single top production (blue), based on combining jets with second and third lowest $|\eta|$ values per event. Upper right: Invariant mass distribution combining the three highest p_T jets per event showing single top mass candidates (blue). Lower middle: Invariant dijet mass, showing Higgs candidates (black dots, including background), combining jets with the two lowest $|\eta|$ values per event.

mass distribution of untagged Higgs signal candidates is seen clearly above the background contributions in the expected mass range of 100 to 130 GeV. It is observed that the remaining background is dominated by CC multi-jets. The quantities represented in the three distributions of Fig. 7.6 are important inputs for the BDT neural network in addition to further variables describing e.g. the pseudorapidities of the Higgs and forward jet candidates including jet and track heavy flavour probabilities, see details below and further in Ref. [590].

As a novel element in these analyses, heavy flavour tagging based on track and jet probabilities has been implemented into the DELPHES detector analysis following the Tevatron D0 experimental ansatz described e.g. in Ref. [598]. The resulting b and c-jet efficiency versus the light jet misidentification efficiencies are illustrated in Fig. 7.7 for assumed nominal impact parameter resolution of 10 (5) μm for tracks with $0.5 < p_T < 5 \,(> 5)$ GeV and three choices of distance parameter $R = 0.5, 0.7, 0.9$ for the anti-kt jets. In particular for the charm tagging, impact parameters are studied with resolutions of 5 (2.5) μm (Half Vertex Resolution), 20 (10) μm (Double Vertex Resolution) for tracks with $0.5 < p_T < 5 \,(> 5)$ GeV within $|\eta| < 3.5$. For a conservative light jet efficiency of 5%, the b-jet tagging efficiency is rather robust around 60% for the considered nominal impact parameter performance and the three considered anti-kt distance parameters, in slight favour of the anti-kt $R = 0.5$ choice. For the expected charm tagging, however, an excellent impact parameter resolution and $R = 0.5$ jets give the best tagging efficiency of around 30%. This means a significant improvement e.g. w.r.t. a 23% charm tagging

efficiency for $R = 0.9$ jets at a nominal impact parameter resolution. These tagging efficiencies can be considered as realistic but rather conservative in particular for the remaining light jet efficiency which is expected to be about 0.1 % at a b-jet efficiency of 60 % using LHC-style neural network based taggers.
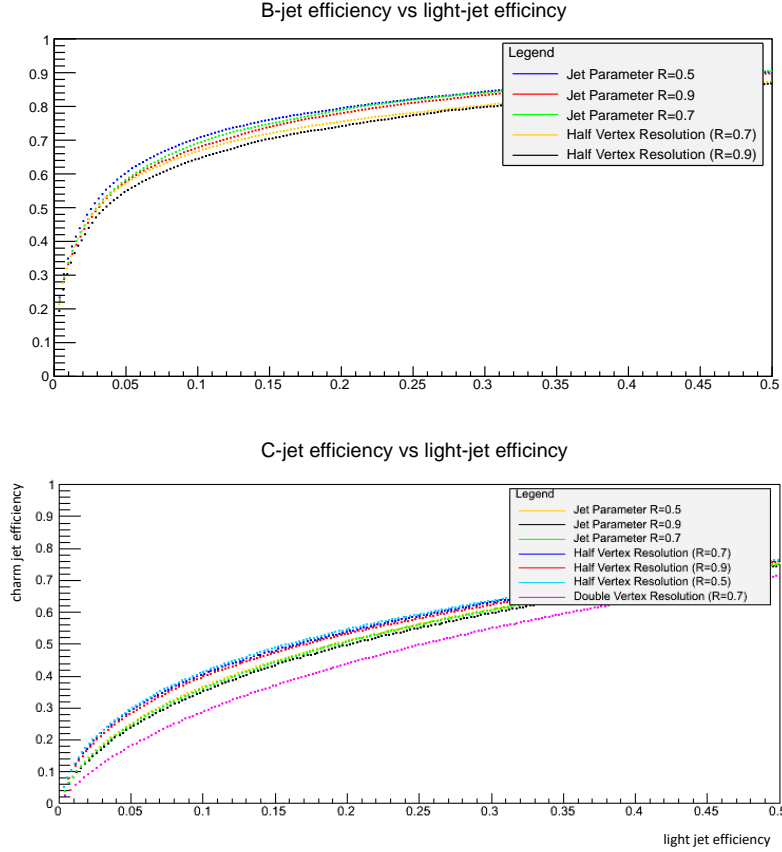

Figure 7.7: Expected average efficiency to tag a b-jet (upper plot) and charm-jet (lower plot) versus the light-jet efficiency (x-axis) based on Tevatron-style jet tagging [598]. Events are selected at DELPHES detector level using a CC multi-jet sample and for an integrated luminosity of 100 fb^{-1}. The coloured lines correspond to the choice of the anti-kt distance parameter R and different assumptions in the impact parameter resolution of 10 (5) μm (nominal, no text added in legend), 5 (2.5) μm (Half Vertex Resolution), 20 (10) μm (Double Vertex Resolution) for tracks with $0.5 < p_T < 5 (> 5)$ GeV within $|\eta| < 3.5$.

A series of BDT score tests has been performed using the preselected signal samples and CC multi-jet as the main background sample to determine the optimal combination of the impact resolution parameters while resolving the two jets from the Higgs decay in dependence of R. The resulting number of $H \to b\bar{b}(c\bar{c})$ signal events versus the BDT score is illustrated in Fig. 7.8, which shows the evident interplay between detector performance and the choice of jet parameters R, where the $R = 0.9$ anti-kt jets show the worst performance. At a score of BDT=0, the highest number of signal events are achieved for $R = 0.5$ anti-kt jets for both charm and beauty decays, where the effect of the impact resolution is much more stringent for the charm than for the beauty tagging. Following Fig. 7.8, the complete BDT-based $H \to b\bar{b}(c\bar{c})$ analyses are performed for anti-kt $R = 0.5$ jets and impact parameter resolution of 5 (2.5) μm (Half Vertex Resolution) for tracks with $0.5 < p_T < 5 (> 5)$ GeV within $|\eta| < 3.5$. The acceptance times efficiency values are about 28 % for the $H \to b\bar{b}$ and about 11 % for the $H \to c\bar{c}$ channel at BDT=0.
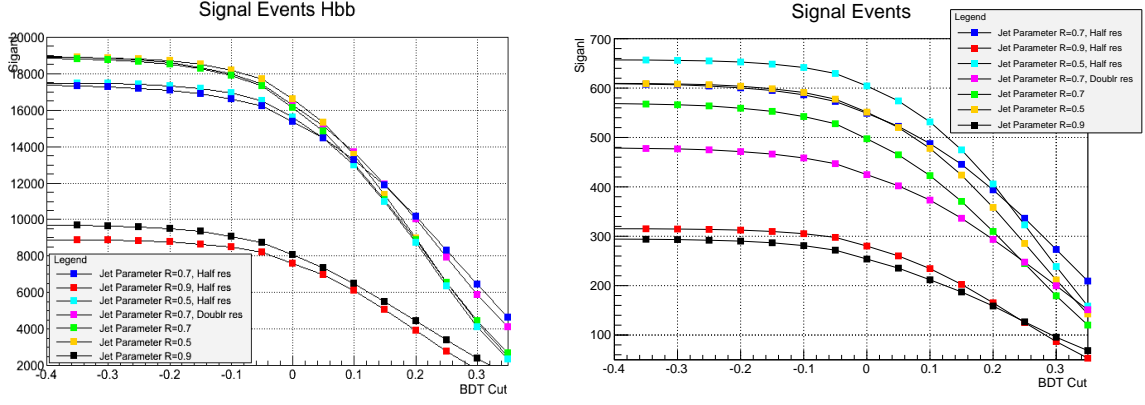
Figure 7.8: Expected $H \to b\bar{b}$ (left) and $H \to c\bar{c}$ (right) signal events as a function of the BDT score. Events are selected at DELPHES detector level for an integrated luminosity of 1 ab^{-1} and -80 % electron polarisation. The symbols correspond to the choice of the anti-kt distance parameter R and different assumptions in the impact parameter resolution of 10 (5) μm (nominal, no further text in legend added), 20 (10) μm (Doubl res), 5 (2.5) μm (Half res) for tracks with $0.5 < p_T < 5 \, (> 5)$ GeV within $|\eta| < 3.5$.

The results of the BDT $H \to b\bar{b}$ and $H \to c\bar{c}$ analyses, assuming that each background contribution is understood at the 2 % level via control regions and negligible statistical Monte Carlo uncertainties for the background predictions for the signal region, are shown in Fig. 7.9. Using these assumptions, the resulting signal strengths are 0.8 % for the $H \to b\bar{b}$ and 7.4 % for the $H \to c\bar{c}$ channel. For the latter, the SM Higgs decays, in particular $H \to b\bar{b}$, represent
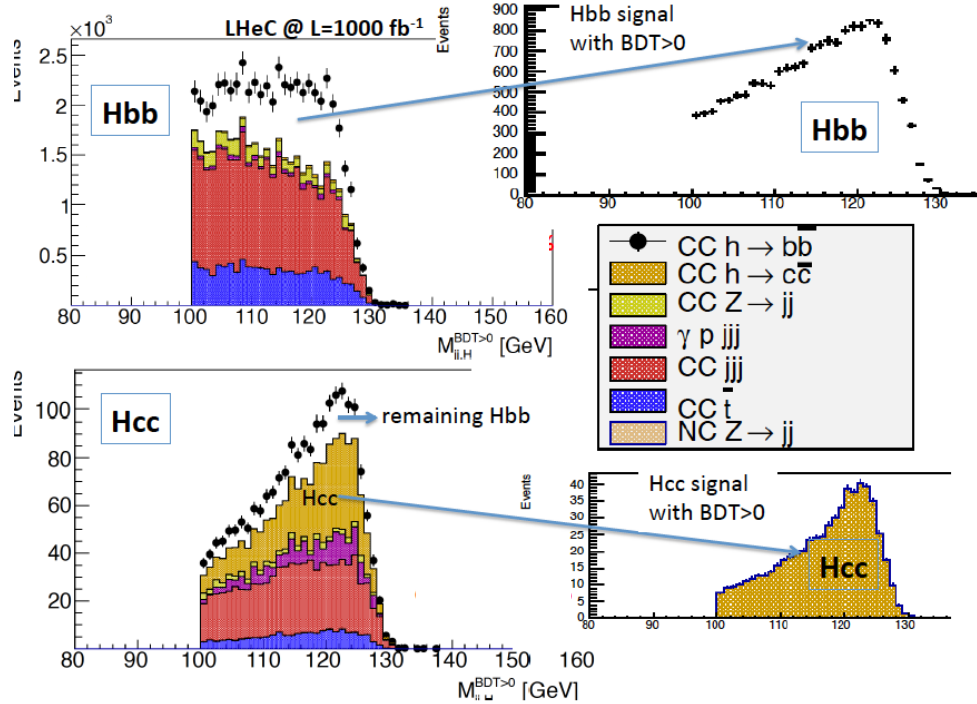

Figure 7.9: Result of the joint $H \to b\bar{b}$ and $H \to c\bar{c}$ analysis for an integrated luminosity of 1 ab^{-1} and -80 % electron polarisation at the LHeC. Left: Invariant mass distributions for the two channels with signal and background, see text. Right: Expected Higgs signal distributions after background subtraction. The background is assumed to be at the 2 % level via control region measurements.

also a part of the cc background contribution but can be controlled by the high precision of

the genuine bb result. Advanced analysis strategies to distinguish bb and cc SM Higgs decays via several layers of neural networks are discussed e.g. in Ref. [599] for an 250 GeV ILC and $M_H = 120$ GeV, where the expected $H \to c\bar{c}$ cross section is 6.9 fb for $M_H = 120$ GeV yields a signal strength uncertainty of 8.8 % in the ZH all hadronic channel ($Z \to q\bar{q}$) at an integrated luminosity of 250 fb^{-1}. The ILC charm cross section is quite similar to the 5.7 fb cross section for $M_H = 125$ GeV at LHeC. The number of preselected charm events and SM Higgs contributions for the ILC analysis are at a similar level as in this analysis, while the non-Higgs background at ILC is by a factor 6.8 larger than for the LHeC preselected events. Comparing the two results gives confidence into the expected $H \to c\bar{c}$ signal strength results at LHeC using the before mentioned assumptions.

In conclusion, Higgs to heavy flavour signal strength measurements require an excellent state-of-the-art calorimetry with high acceptance and excellent resolution as well as an impact parameter resolution as achieved e.g. with ATLAS inner b-layer. In addition, the details of the analysis strategy utilising neural network and advanced statistical methods (e.g. via RooStats/RooFit, see e.g. complex analysis methods using constraints via well measured control regions in signal fits [600]) will be important to control a high signal at low background yields where the latter is expected to be constrained via control regions to better than a few %.

7.3.2 Higgs Decay into WW

Inclusive charged current scattering, the CC production of the Higgs boson with a WW decay and the main backgrounds are illustrated in Fig. 7.10. The $ep \to \nu HX \to \nu W^*WX$ process with hadronic W decays, see Fig. 7.10 a, causes a final state which to lowest order comprises $4 + 1$ jets and the escaping neutrino identified via missing energy (MET). The pure hadronic WW Higgs decay has a branching ratio of about 45 %. Using MadGraph (MG5) and a version of PYTHIA, customised for ep DIS, events have been generated and analysed after passing a DELPHES description of the FCC-eh detector. The present study has been performed for the most asymmetric beam configuration of $E_e = 60$ GeV and $E_p = 50$ TeV yielding $\sqrt{s} = 3.5$ TeV.

The analysis has been focussed on requiring four fully resolved jets from the Higgs decay and at least one forward jet, where the jets are reconstructed using the anti-k_T algorithm with $R = 0.7$. Further event categories where the jets from the Higgs decay products may merge and yield either three or only two large-R jets in the final state have been not considered yet. However, as shown from state-of-the art LHC-style studies, those event categories and the use of e.g. dedicated top and W-tagging based on large-R jet substructures may give additional access to measure Higgs signal strengths.

The analysis requiring fully resolved jets from the $H \to W^*W \to 4j$ decay and at least one forward jet proceeds in the following steps:

- Study of the reconstructed event configuration and recognition of its characteristics for defining a set of loose cuts. These are: the p_T of any jet has to be larger than 6 GeV, the rapidity difference between the forward jet and the reconstructed 4-jet Higgs candidate to be larger than 1.5, the azimuthal difference between that Higgs candidate and either the forward jet or the scattered lepton (MET) to be larger than 1, two-jet masses of the virtual and the real W boson candidate to be larger than 12 GeV and below 90 GeV (Z mass).

- Verification of truth matching to check that the combinatorial association of jets reproduces the Higgs candidate (four jets) and its W (two jets) decays (see Fig. 7.11 and text).
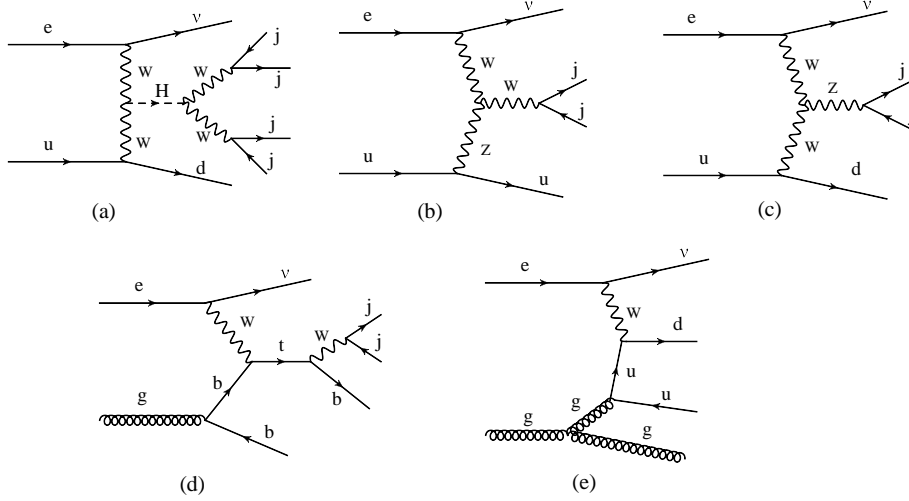
Figure 7.10: Typical lepton-parton diagrams relevant to the $H \to W^*W$ analysis: a) signal: CC DIS with a Higgs produced in the t-channel and its decay into a pair of W bosons which generates a four-jet final state, besides the forward jet. The other diagrams are examples to illustrate background channels which at higher orders, with extra emissions, may mimic the signal configuration: b) single W-boson production; c) single Z-boson production; d) single top-quark production; e) QCD multi-jet production.

- Application of this algorithm to the simulated background samples. The MadGraph single W, top and Z production samples are turned to multi-jet background through PYTHIA. The cross sections are reliably calculated as there is a hard scale available. The initial cuts reduce this background to about 3 % for single vector boson production and to 9 % for top.

- Due to the size of the $H b\bar{b}$ decay and jet radiation, there occurs a residual background from the Higgs itself which is also reduced to 3 % through the cuts.

- The final background is due to multi-jets. The MadGraph cross section for a 4+1 jet CC configuration is considered much too large in view of the cross section measurement results as a function of the jet number, both at HERA and the LHC, see for example [601]. The sample was thus scaled using a conservative α_s renormalisation to the inclusive cross section. The initial cuts reduce the multi-jet background to about 13 %.

- Following a detailed training study, a BDT analysis was used. This determined a final event number of about 12k for to a signal-to-background ratio of 0.23.

The result of this analysis translates to an estimated uncertainty on μ_{WW} of 1.9 % at FCC-eh. The 4-jet mass distribution after the BDT requirement exhibits a clear WW Higgs peak (see Fig. 7.11) which illustrates the suitability to use the electron-proton environment for Higgs measurements in indeed challenging final state configurations.

7.3.3 Accessing Further Decay Channels

Following the detailed studies of the $b\bar{b}$ and $c\bar{c}$ decay channels, presented above, a coarser analysis was established for other frequent decay channels both in NC and CC. Here acceptances and backgrounds were estimated with MadGraph, and efficiencies, distinguishing leptonic and hadronic decay channels for W, Z, and τ, were taken from prospective studies on Higgs coupling measurements at the LHC [602]. This provided a systematic scale factor, f, on the pure
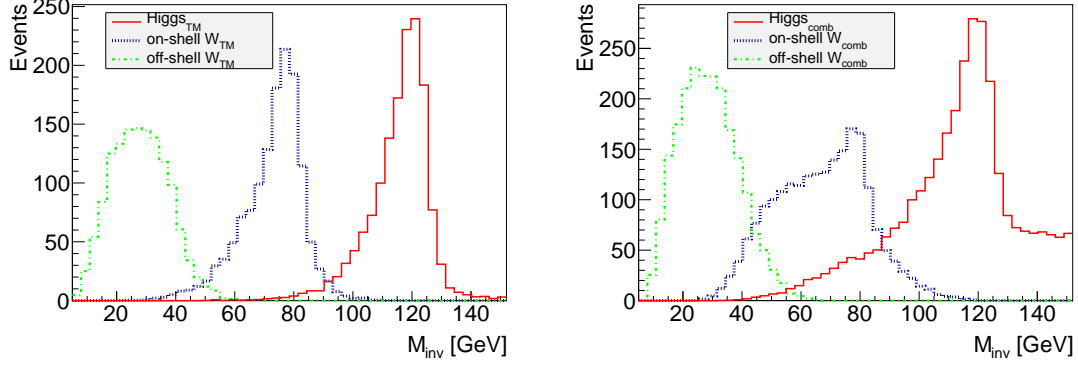
Figure 7.11: Reconstructed signal mass distributions (at DELPHES detector level) of truth matched events (left) and after the just combinatorial association of jets to the two W bosons forming Higgs candidates (right). Green: virtual W^* boson; blue: W boson; red: Higgs signal from W^*W reconstruction. It is observed that the combination causes some background while the respective signal peaks are clearly preserved with a purity of 68% that the correct forward jet is identified.

statistical error δ_s, which comprised the signal-to-background ratio, S/B, and the product of acceptance, A, and extra reconstruction efficiency ϵ, according to

$$f = \sqrt{\frac{1 + \frac{B}{S}}{A \cdot \epsilon}} \qquad (7.4)$$

The error on the signal strength μ_i for each of the Higgs decay channels i is determined as $\delta\mu_i/\mu_i = f_i \cdot \delta_s$.

Parameter	$b\bar{b}$	WW	gg	$\tau\tau$	cc	ZZ	$\gamma\gamma$
Branching fraction	0.581	0.215	0.082	0.063	0.029	0.026	0.0023
Statistical error (δ_s) [%]	0.09	0.15	0.24	0.28	0.41	0.43	1.41
Acceptance (A)	0.14	0.10	0.40	0.40	0.11	0.10	0.40
Signal/background (S/B)	9	0.2	0.1	0.2	0.43	0.33	0.5
Extra efficiency (ϵ)	1	0.3	0.5	0.43	1	0.5	0.7
Scale factor f	2.8	16	7.4	5.9	5.5	9.0	3.3

Table 7.3: Statistical uncertainty for the seven most abundant Higgs decay channels, for the charged current Higgs measurement prospects with the FCC-eh, together with their systematic scale factor f, Eq. 7.4, resulting from acceptance, background and efficiency effects as given. Note that the results for $b\bar{b}$ and $c\bar{c}$ are taken from the BDT analysis (Sect. 7.3.1) with efficiency 1. The WW result is replaced by the BDT analysis (Sect. 7.3.2) for quoting the expected signal strength uncertainty.

To good approximation these factors apply to LHeC, HE-LHeC and FCC-eh because the detector dimensions and acceptances scale with the proton energy, conceptually using the same technology and very similar resolution assumptions. Therefore there is one main matrix used for the subsequent experimental deterioration of the pure statistics precision, both for CC and NC. Future detailed analyses will lead to refining this expectation which for the current purpose was beyond the scope of the study. The results of the analysis of uncertainties are summarised in Tab. 7.3 for the CC channel at the FCC-eh. The resulting signal strength uncertainty values are provided in Tab. 7.4. Note that for the beauty, charm and WW channels the table contains the BDT analysis [3] results of Sect. 7.3.1 and Sect. 7.3.2, resp. The beauty and charm CC results

---

[3]This is in very good agreement with the scale factor method: for example, the WW result in Tab. 7.3 leads

Setup	$b\bar{b}$	$b\bar{b} \oplus$ Thy	WW	gg	$\tau\tau$	cc	ZZ	$\gamma\gamma$
LHeC NC	2.3	2.4	17	16	15	20	35	42
LHeC CC	0.80	0.94	6.2	5.8	5.2	7.1	12	15
HE-LHeC NC	1.15	1.25	8.9	8.3	7.5	10	17	21
HE-LHeC CC	0.41	0.65	3.2	3.0	2.7	3.6	6.2	7.7
FCC-eh NC	0.65	0.82	5.0	4.7	4.2	5.8	10	12
FCC-eh CC	0.25	0.56	1.9	1.8	1.6	2.2	3.8	4.6

Table 7.4: Summary of estimates on the experimental uncertainty of the signal strength μ, in per cent, for the seven most abundant Higgs decay channels, in charged and neutral currents for the LHeC, the HE-LHeC and the FCC-eh. The $b\bar{b}$ channel is the one which is most sensitive to theoretical uncertainties and for illustration is given two corresponding columns, see Sect. 7.3.4.

stem from the BDT analysis for LHeC and are applied to FCC-eh with a factor of about 1/3. The CC WW results are due to the FCC-eh BDT analysis and are used for LHeC, enlarged by a factor of 3.2, determined by the different cross sections and luminosities. For HE-LHC, the values are about twice as precise as the LHeC values because the cross section is enlarged by about a factor of two, see Tab. 7.1, and the integrated luminosity with $2\,\mathrm{ab}^{-1}$ twice that of the LHeC. All signal strength uncertainties, in both CC and NC, for the three collider configurations are shown in Fig. 7.12.
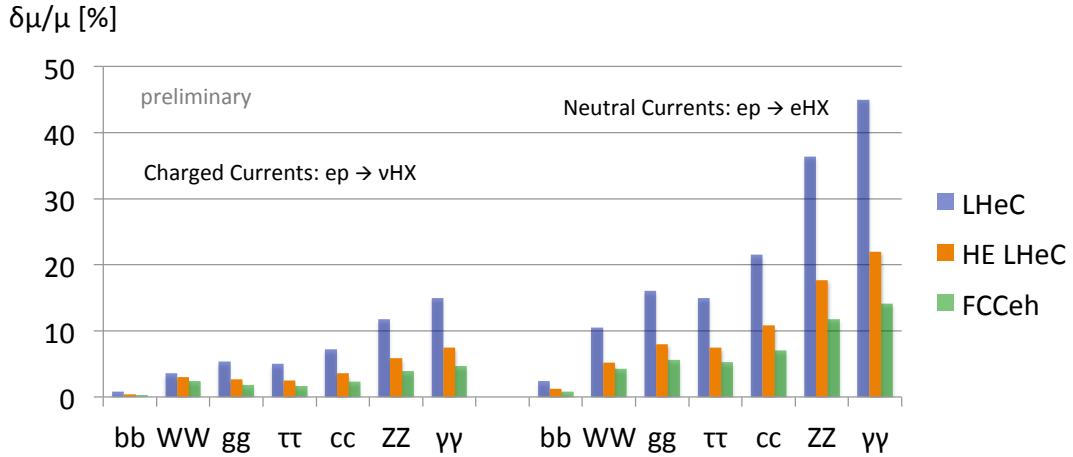

Figure 7.12: Uncertainties of signal strength determinations in the seven most abundant SM Higgs decay channels for the FCC-eh (green, $2\,\mathrm{ab}^{-1}$), the HE LHeC (brown, $2\,\mathrm{ab}^{-1}$) and LHeC (blue, $1\,\mathrm{ab}^{-1}$), in charged and neutral current DIS production.

7.3.4 Systematic and Theoretical Errors

The signal strength is expressed relatively to a theoretical calculation of the charged current Higgs cross section, including its decay into a chosen channel, according to

$$\mu = \frac{\sigma_{exp}}{\sigma_{thy}} = \frac{\sigma_{exp}}{\sigma_{Hty} \cdot br}. \tag{7.5}$$

Consequently one can decompose the (relative) error of μ into the genuine measurement error, denoted as $\delta\sigma_{exp}$, including a possible systematic error contribution, E, and two further

---

to a value of 2.1 % slightly worse than the BDT analysis.

components

$$\frac{\delta\mu}{\mu} = \left\{ \left(\frac{\delta\sigma_{exp}}{\sigma_{exp}}\right)^2 \cdot (1 \oplus E) + \left(\frac{\delta\sigma_{Hty}}{\sigma_{Hty}}\right)^2 + \left(\frac{\delta br}{br}\right)^2 \right\}^{1/2}, \tag{7.6}$$

which are due to imperfections to theoretically model the Higgs production cross section, σ_{Hty}, and uncertainties on the branching ratio, br, in the channel under study. Note, that the experimental uncertainty takes into account possible variations of the backgrounds which are estimated conservatively and thus represent more than genuine statistics.

The channel dependent signal strength uncertainties quoted in Tab. 7.4 are estimates of the first, experimental term in Eq. 7.6 neglecting extra systematic error effects. They are derived as stated above from the purely statistical error ($\delta_s = 1/\sqrt{N}$), its increase due to acceptance (A) and efficiency (ϵ) effects and, further, the modulation caused by the background-to-signal ratio (B/S). These factors are all involved in the BDT analysis but the scale factor equation, Eq. 7.4, may be used to estimate further systematic effects for any channel. From the relation

$$\frac{\delta\sigma_{exp}}{\sigma_{exp}} = \delta_s \cdot \sqrt{\frac{1 + B/S}{A \cdot \epsilon}} \tag{7.7}$$

the combined systematic error contribution, E, caused by variations Δ of A, ϵ and the background B can be estimated as

$$E = \frac{1}{2}\left\{ \left(\frac{\Delta A}{A}\right)^2 + \left(\frac{\Delta\epsilon}{\epsilon}\right)^2 + \left(\frac{\Delta B}{B} \cdot \frac{B/S}{1 + B/S}\right)^2 \right\}^{1/2}. \tag{7.8}$$

The formula shows that if the background-to-signal ratio is very small, then the background effect is suppressed $\propto B/S$. If it is larger than 1, the relative uncertainty of the background enters as an additional component of the signal strength error.

Given the fact that the experimental $H \rightarrow b\bar{b}$ result in the CC reaction is especially precise, compare Tab. 7.4, an estimate was performed of the systematic error in this channel. The following effects were included: a variation of the light-quark misidentification by a factor 3, a variation of the reduction of the photo-production via tagging between 2 % and 10 %, a variation of the combined acceptance times efficiency effect by 10 % and a variation of the hadronic energy resolution, studied in Ref. [585], leading to a 7 % signal variation. The overall effect of these contributions determines a systematic error of about 10 % on μ_{bb}, i.e. $\delta\mu/\mu = 0.80 \pm 0.09$ for $H \rightarrow b\bar{b}$ at the LHeC in the CC channel. Similar levels of uncertainty are expected to occur for other channels but have not been estimated to such detail as those channels are measured less precisely.

A separate effect arises from the measurement of the luminosity. While that will be measured about as accurate as 0.5 %, based on Bethe-Heitler scattering and its accurate description to higher-order QEDC [1], additionally it will be negligible to a good approximation: the LHeC, and its successors, will provide a very precise, determination of all parton distributions from the ep data alone. Any systematic mistake in the normalisation will therefore affect both the measured and the calculated cross section and drop out in their ratio μ.

A next uncertainty on the signal strength arises from the theoretical description of σ_{CCH} to which the measured cross section is normalised. From a simulation of the systematic uncertainties due to imperfect calibrations and extra efficiencies one may expect the cross section to be known to better than 1 %. The prediction will be available to N^{3}LO, α_s be determined to $0.1 - 0.2$ % precision, and it can be gauged with the inclusive cross section measurement. This

uncertainty, following Eq. 7.8, enters directly as a contribution to the μ measurement result. A 0.5 % uncertainty, as can be seen in Tab. 7.4, becomes noticeable in most of the $b\bar{b}$ results but is negligible for all other channels. In the present analysis values of 0.5 % and 1 % uncertainty have been considered and their effect on the κ result been evaluated, see Sect. 7.4.

A final uncertainty is caused by the branching fractions and their uncertainty. A recent uncertainty estimate [580] quotes on the here most relevant $H \to b\bar{b}$ branching ratio a theory contribution due to missing higher orders of 0.65 %, a parameterisation uncertainty depending on the quark masses of 0.73 %, and an α_s induced part of 0.78 %. The LHeC, or similarly the higher energy ep colliders, will determine the b mass (in DIS) to about 10 MeV and α_s to per mille precision [1] which would render corresponding uncertainty contributions to br_{bb} negligible. The genuine theoretical uncertainty would also be largely reduced with an extra order pQCD. In the subsequent study the contribution from the branching fraction uncertainty has been neglected. This may also be justified by the programme here sketched, and similarly for other future colliders: the ep colliders will measure the couplings, especially of the WW, bb and ZZ very precisely, which will enable an iterative treatment of the branching ratio uncertainties.

It may be noticed [580] that the α_s contribution to the $H \to gg$ branching fraction uncertainty is about 3.7 %, i.e. twice as large as the estimated signal strength measurement uncertainty of this channel at the FCC-eh. There arises another important benefit of the future ep colliders and their high precision DIS programme for precision Higgs physics at the combined ep & pp facilities.

7.4   Higgs Coupling Analyses

In order to quantify possible deviations from the SM expectation one may use the κ parameterisation framework, introduced in Ref. [603], which enables easy comparisons between different collider configurations independently of their ability to access the total Higgs decay width. It should be noted that there are differences between the results in the EFT and in the κ formalism [604]. Therefore, it would be very interesting to go beyond the κ framework also for the ep colliders here presented because out of the 2499 dimension-6 Wilson coefficients altogether $13 \cdot n_g^4 = 1053$ involve leptons and quarks [605], for $n_g = 3$ generations. This, however, has been beyond the scope of this study. In the following results are presented for the various ep collider configurations (Sect. 7.2.2).

The κ parameters are factors to the various Higgs couplings, equal to one in the SM, which scale $\sigma_{NC/CC}$ with $\kappa_{Z/W}^2$, the width Γ^i for a channel i with κ_i^2 and lead to replacing Γ_H by the sum $\Sigma_j \kappa_j \Gamma^j$, where we have assumed no non-SM H decays. This defines the following modifications of the cross sections (Eq. 7.1)

$$\sigma_{CC}^i = \sigma_{CC} \; br_i \cdot \kappa_W^2 \kappa_i^2 \frac{1}{\sum_j \kappa_j^2 br_j} \quad \text{and} \quad \sigma_{NC}^i = \sigma_{NC} \; br_i \cdot \kappa_Z^2 \kappa_i^2 \frac{1}{\sum_j \kappa_j^2 br_j}. \tag{7.9}$$

Dividing these expressions by the SM cross section predictions one obtains the variations of the relative signal strengths, μ^i, for charged and neutral currents and their κ dependence

$$\mu_{CC}^i = \kappa_W^2 \kappa_i^2 \frac{1}{\sum_j \kappa_j^2 br_j} \quad \text{and} \quad \mu_{NC}^i = \kappa_Z^2 \kappa_i^2 \frac{1}{\sum_j \kappa_j^2 br_j}. \tag{7.10}$$

With seven decay channels considered in CC and NC, one finds that for each of the ep collider configurations there exist eight constraints on κ_W and κ_Z and two on the other five κ parameters.

Using the signal strength uncertainties as listed in Tab. 7.4 fits to all seven channels, in NC and CC, are performed in a minimisation procedure to determine the resulting uncertainties for the κ parameters. These are done separately for each of the ep collider configurations with results listed in Tab. 7.5. A naive expectation would have been that $\delta\kappa \simeq \delta\mu/2$. Comparing the results, for example for LHeC (top rows), of the signal strengths (Tab. 7.4) with the κ fit results (Tab. 7.5) one observes that this relation holds approximately for the gg, $\tau\tau$, $c\bar{c}$, $\gamma\gamma$ channels. However, due to the dominance of $H \to b\bar{b}$ in the total H width and owing to the presence of the WWH and ZZH couplings in the initial state, there occurs a reshuffling of the precisions in the joint fit: κ_b is relatively less precise than μ_{bb} while both κ_W and κ_Z become more precise than naively estimated, even when one takes into account that the $H \to WW$ decay in CC measures κ_W^4. The seven channel results are displayed in Fig. 7.13.
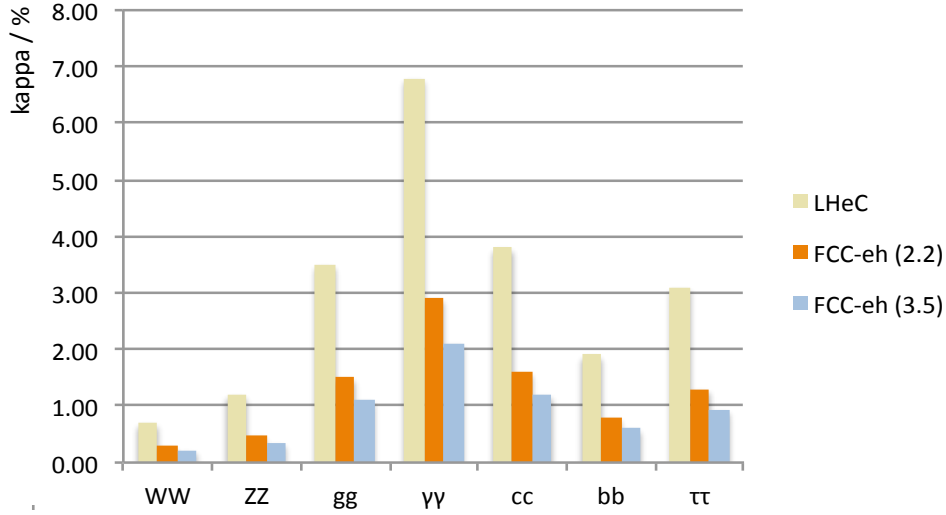

Figure 7.13: Summary of uncertainties of Higgs couplings from ep for the seven most abundant decay channels, for LHeC (gold), FCC-eh at 20 TeV proton energy (brown) and for $E_p = 50$ TeV (blue).

Setup	$b\bar{b}$	WW	gg	$\tau\tau$	cc	ZZ	$\gamma\gamma$
LHeC	1.9	0.70	3.5	3.1	3.8	1.2	6.8
HE-LHeC	1.0	0.38	1.8	1.6	1.9	0.6	3.5
FCC-eh	0.60	0.22	1.1	0.93	1.2	0.35	2.1

Table 7.5: Summary of κ uncertainty values as obtained from separate fits to the signal strength uncertainty estimates for the seven most abundant Higgs decay channels, in charged and neutral currents for the LHeC, the HE-LHeC and the FCC-eh, see text.

In the electroweak theory there is an interesting relation between the ratio of the W and Z couplings and the mixing angle,

$$\frac{\sigma(WW \to H \to AA)}{\sigma(ZZ \to H \to AA)} = \frac{\kappa_W^2}{\kappa_Z^2} = (1 - \sin^2\theta_W)^2 \qquad (7.11)$$

This relation can be particularly well tested with the ep colliders as they measure both WWH and ZZH in one experiment and common theoretical environment. If one assumes the WW and ZZ measurements to be independent, the resulting error on $\sin^2\theta_W \simeq 0.23$ is 0.003 for the

LHeC and 0.001 for FCC-eh. However, this probably is smaller because there exist correlations in the measurements which a genuine data based analysis would have to evaluate and take into account.

The effect of the theory uncertainties has been studied for the FCC-eh where the experimental precision is highest. Tab. 7.6 presents the results of a κ analysis using the CC and NC FCC-eh signal strength input (Tab. 7.4) neglecting the theoretical uncertainty and adding 0.5% or 1% in quadrature, to only μ_{bb} where it matters. This results in an about linear increase of the uncertainty for bb (by a factor of 1.5), WW (by 1.7) and ZZ (by 1.5), while all other κ uncertainties only slightly deteriorate. The effect of such uncertainties for LHeC is much smaller as the μ uncertainties are three times those of FCC-eh, see Tab. 7.4. Therefore, in the LHeC case, the theory uncertainties are neglected.

Setup	$b\bar{b}$	WW	gg	$\tau\tau$	cc	ZZ	$\gamma\gamma$
FCC-eh (no thy)	0.60	0.22	1.1	0.93	1.2	0.35	2.1
FCC-eh (0.5% thy)	0.72	0.28	1.1	1.0	1.2	0.41	2.2
FCC-eh (1.0% thy)	0.91	0.37	1.1	1.0	1.3	0.53	2.3

Table 7.6: Summary of κ uncertainty values as obtained from separate fits to the signal strength uncertainty estimates for the seven most abundant Higgs decay channels, in charged and neutral currents for the FCC-eh, with no theoretical uncertainty, half a per cent and one per cent uncertainty added.

An interesting question regards the role of the electron beam polarisation. Assuming a maximum polarisation of $P = -0.8$, the CC (NC) Higgs cross section is calculated to be 1.8 (1.09) times larger than that in unpolarised scattering. Therefore the signal CC and NC strength uncertainties scale like 1.34 and 1.09, respectively. This is studied for the LHeC. If the default fit is made, then the κ uncertainties quoted in Tab. 7.5 for bb, WW, gg, $\tau\tau$ and cc are enhanced by a factor of 1.28. This is due to the combined effect of CC and NC which diminishes the deterioration a bit, from 1.34 to 1.28. Thus, for example, the κ_W uncertainty moves from 0.7 to 0.9% in the unpolarised case. The uncertainty on κ_Z is enhanced only by a factor of 1.14, becoming 1.38 instead of 1.21 because the NC channel has a particularly strong effect on the ZZH coupling. Since the prospect to detect the $\gamma\gamma$ channel in NC is very poor, the κ_γ uncertainty is enlarged by the full CC factor of 1.34. It is for maximum precision very desirable to have the beam polarised. This, together with electroweak physics, represents an important reason to continue to develop high current polarised electron sources.

7.5 Measuring the Top-quark–Higgs Yukawa Coupling

Electron-proton collisions at high energy are known to provide a unique window of opportunity to perform precision measurements in the top sector [465]. This is due to the large cross-sections of the production of single top, which amounts to about $2\,\mathrm{pb}$ for $E_e = 60\,\mathrm{GeV}$ and $E_p = 7\,\mathrm{TeV}$, where clean signatures are provided without the challenges posed by pile-up. As a result, the cross-section of the SM in association with a single top in e^-p collisions is large enough to perform competitive measurements. This includes the measurement of the absolute value of the Top Yukawa coupling and, most prominently, its CP-phase [476].

In the SM, the Yukawa coupling of the third generation of quarks can be written down as:

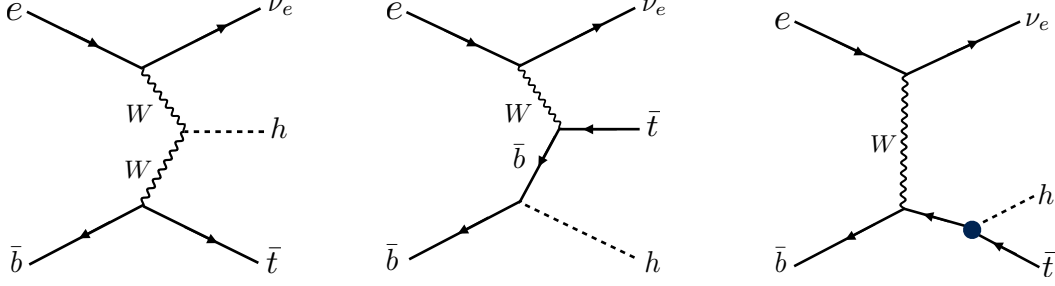$$\mathcal{L}_\mathrm{Y} = -\frac{m_t}{v}\bar{t}th - \frac{m_b}{v}\bar{b}bh, \tag{7.12}$$

Figure 7.14: Leading order Feynman diagrams contributing to the process $p\,e^- \to \bar{t}\,h\,\nu_e$ in high energy e^-p collisions. The black dot in the Feynman diagram on the right denotes the top-quark–Higgs coupling of interest in this section.

where $v \equiv \left(\sqrt{2}G_F\right)^{-1/2} = 2m_W/g \simeq 246$ GeV, and m_t (m_b) is the mass of the top (bottom) quark. Due to the pure scalar nature of the Higgs boson in the SM, the top- and bottom-Higgs couplings are completely CP-even. To investigate any BSM contributions in terms of mixtures of CP-even and CP-odd states, we write a CP-phase dependent generalised Lagrangian as follows [606]:

$$
\begin{aligned}
\mathcal{L} = &-\frac{m_t}{v}\bar{t}\left[\kappa\cos\zeta_t + i\gamma_5\sin\zeta_t\right]t\,h \\
&-\frac{m_b}{v}\bar{b}\left[\cos\zeta_b + i\gamma_5\sin\zeta_b\right]b\,h.
\end{aligned}
\tag{7.13}
$$

Here, ζ_t and ζ_b are the phases of the top-Higgs and bottom-Higgs couplings, respectively. It is clear from the Lagrangian in Eq. (7.13) that $\zeta_{t,b} = 0$ or $\zeta_{t,b} = \pi$ correspond to a pure scalar state while $\zeta_{t,b} = \frac{\pi}{2}$ to a pure pseudo scalar state. Thus, the ranges $0 < \zeta_{t,b} < \pi/2$ or $\pi/2 < \zeta_{t,b} < \pi$ represent a mixture of the different CP-states. The case $\kappa = 1$, $\zeta_t = 0$ corresponds to the SM.

In e^-p collisions, the top-Higgs couplings can be probed via associated production of the Higgs boson with an anti-top quark $e^-p \to \bar{t}\,h\,\nu_e$ It is necessary to consider a 5-flavour proton including the b-quark parton distribution. The Feynman diagrams for the process under investigation are shown in Fig. 7.14. It is important to note that three important couplings are involved, namely hWW, Wtb and the top-Higgs (tth). A detailed study of hWW and Wtb couplings at the e^-p collider have been performed in Refs. [465,607], respectively. For our studies we do not consider the BSM bottom-Higgs coupling since the effect of the phase ζ_b on the total production cross section or kinematics of top-Higgs production at the LHeC are negligible. Thus in what follows, we simply set $\zeta_b = 0$.

In the context of the LHC, quantitatively an interesting feature can be observed: in the pure SM case there is constructive interference between the diagrams shown in Fig. 7.14, left and middle, for $\zeta_t > \pi/2$ resulting in an enhancement in the total production cross section of associated top-Higgs significantly. This is also true for $\zeta_t < \pi/2$ - however the degree of enhancement is much smaller owing to the flipped sign of the CP-even part of the coupling.

We probe the sensitivity of the top-Higgs couplings in terms of ζ_t by building a model file for the Lagrangian in Eq. (7.13) using FeynRules [608], and then simulating the charged current associated top-Higgs production channel $p\,e^- \to \bar{t}\,h\,\nu_e$ (see Fig. 7.14), with h further decaying into a $b\bar{b}$ pair and the $\bar{t}$ decaying leptonically in the LHeC set-up with centre of mass energy of $\sqrt{s} \approx 1.3$ TeV. Here we perform the analysis at parton level only where for signal and background event generation we use the Monte Carlo event generator package MadGraph5 [367]. We use `NNPDF23_lo_as_0130_qed` [609] parton distribution functions for all event generations.
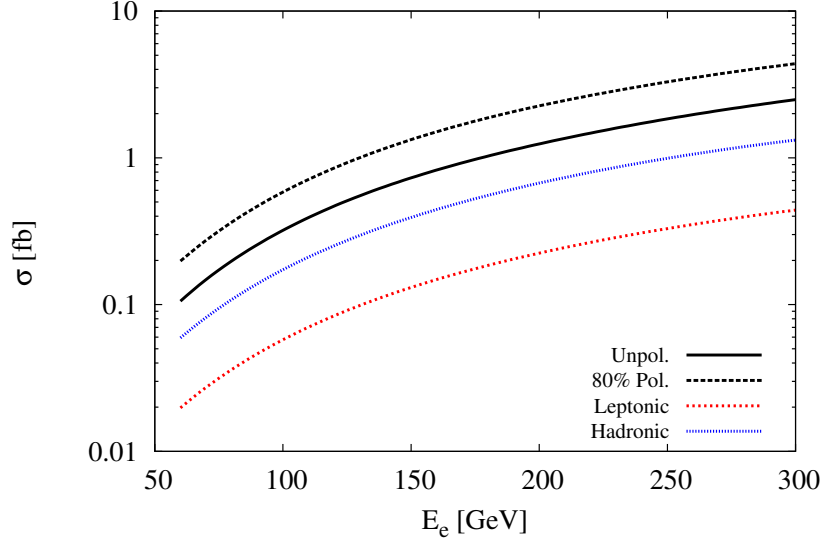
Figure 7.15: Cross-sections of the Higgs boson produced in association with a top quark in e^-p collisions with $E_p = 7$ TeV. for different electron beam energies The dotted and solid *black* lines correspond to $p\,e^- \to \bar{t}\,h\,\nu_e$ with and without longitudinal polarisation of the electron beam, respectively. The dotted *red* and *blue* lines correspond to $\sigma \times$BR for the leptonic and hadronic decay modes of $\bar{t}$ where for this estimation we use basic cuts (see text).

The factorisation and renormalisation scales for the signal simulation are fixed at $\mu_F = \mu_R = (m_t + m_h)/4$ while background simulations are done with the default MadGraph5 [367] dynamic scales. The e^- polarisation is assumed to be -80%. We now list and explain various kinematic observables that can serve as possible discriminants of a CP-odd $t\bar{t}h$ coupling.

In Fig. 7.15 we present the variation of the total cross section against the electron beam energy for the signal process $p\,e^- \to \bar{t}h\nu_e$, by considering un-polarised and polarised e^- beam. Also, the effect of branchings of $h \to b\bar{b}$ and the $\bar{t}$ decay for both leptonic and hadronic modes are shown. Possible background events typically arise from $W+$ multi-jet events, $Wb\bar{b}\bar{b}$ with missing energy which comes by considering only top-line, only Higgs-line, and without top- nor Higgs-line, in charged and neutral current deep-inelastic scattering and in photo-production by further decaying W into leptonic mode. We have estimated the cross sections for signal and all possible backgrounds imposing only basic cuts on rapidity $|\eta| \le 10$ for light-jets, leptons and b-jets, the transverse momentum cut $p_T \ge 10\,\text{GeV}$ and $\Delta R_{\min}=0.4$ for all particles.

We now estimate the sensitivity of the associated top-Higgs production cross-section, $\sigma(\zeta_t)$, as a function of the CP phase of the tth-coupling as shown in Fig. 7.16 by considering $E_e = 60$ and with fixed $E_p = 7$ TeV. The scale uncertainties are taken as $(m_t + m_h)/8 \le \mu_F = \mu_R \le (m_t+m_h)/2$. Here $\sigma(\zeta_t = 0)$ corresponds to the SM cross section. We notice that the cross section is very sensitive to ζ_t in the region $\zeta_t > \frac{\pi}{2}$ where the interference between the diagrams becomes constructive. Below $\zeta_t = \frac{\pi}{2}$ the interference is still constructive though its degree decreases with ζ_t, thus increasing the cross section by around 5 times at $\zeta_t = \frac{\pi}{2}$ which corresponds to the pure CP-odd case. On the other hand, for pure CP-even case $\zeta_t = \pi$ with opposite-sign of tth-coupling the cross section can be enhanced by up to 24 times for $E_e = 60$ GeV. The scale uncertainty on an average is approximately 7% for $E_e = 60$ GeV in the whole range of ζ_t.

In order to evaluate sensitivity to the measurement of the top Yukawa coupling and its P-phase, we implement the following criteria to select events, referred to as the fiducial selection:
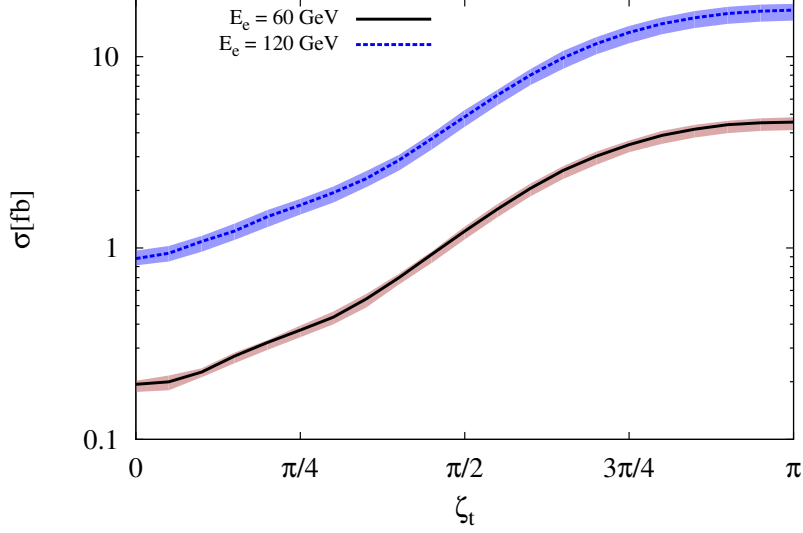
Figure 7.16: Total cross section of the Higgs boson produced in association with a single top as a function of ζ_t, including scale uncertainties. The *black* solid and *blue* dotted lines correspond to $E_e = 60$ and $120\,\text{GeV}$, respectively. These are obtained for fixed $E_p = 7\,\text{TeV}$ and scales $\mu_F = \mu_R = (m_t + m_h)/4$.

- $p_T \geq 20$ GeV for b-tagged jets and light-jets, and $p_T \geq 10$ GeV for leptons.

- Since the LHeC collider is asymmetric, event statistics of final state particles are mostly accumulated on the left or right sides of the transverse plane $\eta = 0$ (depending on the initial direction of p and e^-) - we select events within $-2 \leq \eta \leq 5$ for b-tagged jets while $2 \leq \eta \leq 5$ for leptons and light-jets,

- The separation distance of all final state particles are taken to be $\Delta R > 0.4$.

- Missing transverse energy $\not{E}_T > 10$ GeV to select the top events.

- Invariant mass windows for the Higgs through b-tagged jets and the top are required to be $115 < m_{bb} < 130$ GeV and $160 < m_t < 177$ GeV, respectively, which are important to reduce the background events substantially.

In these selections the b-tagging efficiency is assumed to be 70%, with fake rates from c-initiated jets and light jets to the b-jets to be 10% and 1%, respectively.

We estimated the exclusion regions of ζ_t as a function of L in fb^{-1}. The exclusion is based on significance using the Poisson formula, where S and B are the number of expected signal and background events at a particular luminosity, respectively. Here we used 10% systematic uncertainty for background yields only. In Fig. 7.17, we present exclusion contours at various confidence levels for $E_e = 60$ GeV – understandably, higher σ-contours demand larger luminosities. It is also seen that there is a kink around $\zeta_t = \pi/2$ such that for the region $0 < \zeta_t < \pi/2$, we need larger luminosities for exclusion. This is in keeping with the feature exhibited in Fig. 7.16 where the constructive interference between the signal diagrams enhances the cross-section over the SM value much more for $\zeta_t > \pi/2$ thus requiring less luminosity to probe that region. For $L = 100$ fb^{-1}, regions above $\pi/5 < \zeta_t \leq \pi$ and $3\pi/10 < \zeta_t \leq \pi$ are excluded at 2σ and 3σ C.L. While around $L = 400$ fb^{-1}, regions above $\pi/6 < \zeta_t \leq \pi$ and $\pi/4 < \zeta_t \leq \pi$ are excluded at 4σ and 5σ C.L., respectively.

As a measure of comparison, that asymmetry studies at the HL-LHC [606] help probe up to
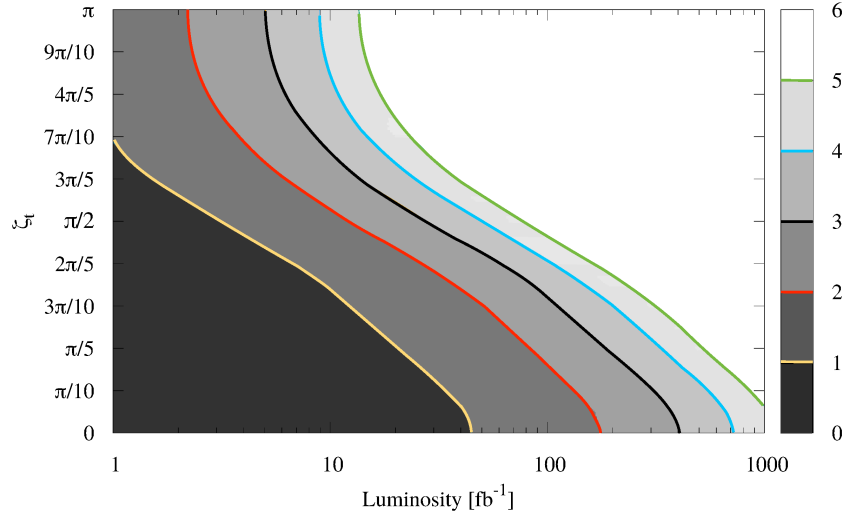
Figure 7.17: Exclusion contours for ζ_t as a function of integrated luminosity for $E_e = 60$ GeV and $E_p = 7$ TeV. The regions beyond each contours are excluded for the particular luminosity, *black* and *red* solid lines correspond to 3σ and 2σ regions. Results are obtained based on fiducial cross-sections (see text).

$\zeta_t = \pi/6$ for a total integrated luminosity of 3 ab^{-1}. Thus, it is clear that the LHeC provides a better environment to test the CP nature of Higgs boson couplings.

For the integrated luminosity $L = 1$ ab^{-1}, almost all values of ζ_t can be excluded up to 4σ C.L. While investigating the overall sensitivity of ζ_t by applying these two observables, it is also important to measure the accuracy of SM tth coupling κ at the LHeC energies. To measure the accuracy of κ by using signal and background yields we use the formula $\sqrt{(S+B)}/(2S)$ at a particular luminosity. And for $E_e = 60$ GeV, the measured accuracy at the design luminosity $L = 1$ ab^{-1} is given to be $\kappa = 1.00 \pm 0.17$ of its expected SM value, where a 10% systematic uncertainty is been taken in background yields only.

These results are obtained based on the evaluation of the fiducial cross-sections alone. As pointed out in Ref. [476], a number of other observables carry sensitivity to the structure of the top-Higgs Yukawa coupling, such as the rapidity difference between the top quark and the Higgs boson and a number of angular variables. While the fiducial rate studied here is the single most sensitive observable, it is evident that a multi-variate approach will significantly enhance the sensitivity reported here.

7.6 Higgs Decay into Invisible Particles

The Higgs decay into invisible particles could be a key to BSM physics. The SM branching ratio of $H \to ZZ \to 4\nu$ is only 0.1%. Any sizable decay rate into invisible particles would thus indicate an exotic decay, for example to dark matter particles. Its non-observation would give the SM cross section measurement, reconstructing more than 99% of the ordinary decays a higher meaning for constraining the total Higgs decay width.

For the LHeC at a luminosity of 1 ab^{-1}, initial parton-level studies of this decay were presented in Ref. [610], with the estimate of a two σ sensitivity to a branching fraction of 6%. For this study, NC production via ZZ fusion $eq \to eqZZ \to eqH$ was used, which has a cross section

185

of about 25 fb at the LHeC. The CC production via WW fusion has a larger cross section, but entails a missing energy signal by itself which requires further study of potentially quite some gain in precision. This channel, when employed for the invisible decay study, results in a mono-jet signature which is hard to separate from the SM DIS CC background.

The neutral current study has been repeated using the LHeC Higgs WG analysis tools, introduced above: MadGraph, Pythia and Delphes. Similar to [610], an electron beam of 60 GeV with a polarization of -80% is assumed. The basic event topology contains the scattered electron, jet and missing transverse energy. Its main background results from SM W and Z productions (followed by $W \to \ell\nu$ and $Z \to \nu\bar{\nu}$). In the study NC and CC W production and NC Z production are considered, while single-top, NC multijets and W photoproduction were all found to be negligible. Requiring missing transverse energy of 60 GeV, exactly one electron and one jet, and no other leptons (including τ), as well as imposing several selection criteria on the kinematics of electron, jet and missing transverse momentum, we get a two σ sensitivity to a branching ratio of 7.2 %, which is similar to the earlier result [610]. Fig. 7.18 shows the electron-jet invariant mass distribution after the selection for the signal (normalized to a 100 % branching ratio) and the background.
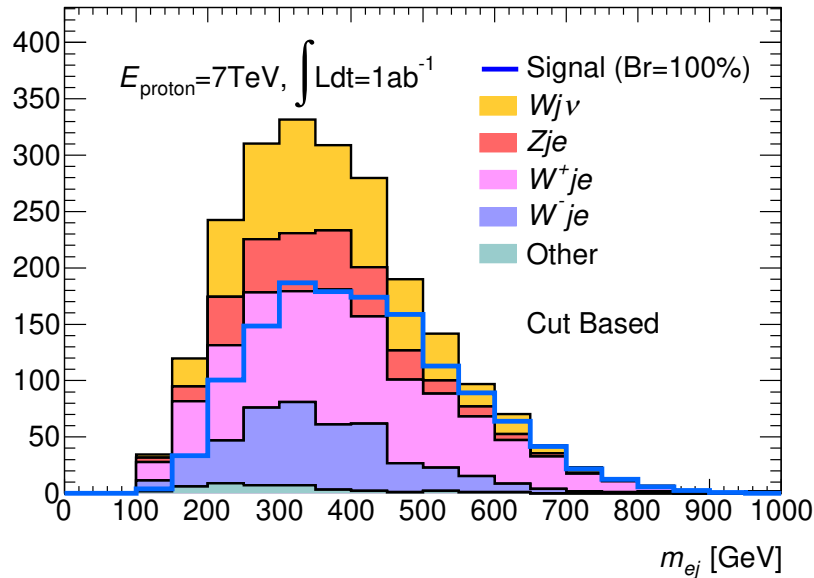

Figure 7.18: Electron-jet invariant mass distribution for the Higgs to invisible decay signal (normalized to 100% branching ratio) and the stacked backgrounds for an integrated luminosity of 1 ab^{-1} at the LHeC after all selection cuts.

The analysis has been further refined with a usage of multivariate analysis (Boosted Decision Tree in TVMA package). Basically the set of selection variables used in the cut-based analysis above was used as inputs to the multivariate analysis, tuned to yield the best output score to discriminate the signal from backgrounds. Fig. 7.19 shows the distribution of the discriminant variable for the signal and background (both area normalised). An optimization on the statistical significance is found at the BDT score > 0.25, and the resulting mass distribution is shown in Fig. 7.20. With 1 ab^{-1} of integrated luminosity, a two σ sensitivity of 5.5% is obtained consistent with the previous results. For a comparison, an estimate of 3.5 % is given for a HL-LHC sensitivity study on this channel [611]. The result on the LHeC may be further improved in the future with a refined BDT analysis when one introduces extra parameters, beyond those

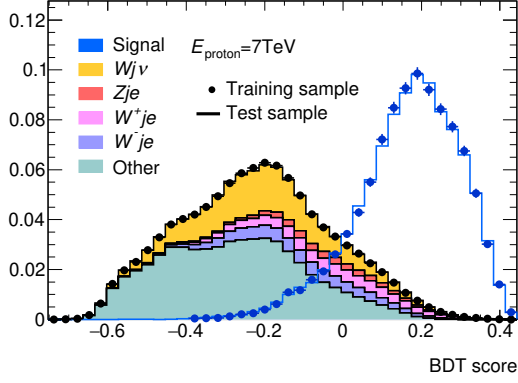initially introduced with the cut based analysis.

Figure 7.19: BDT output score distribution for the Higgs to invisible decay signal and the stacked backgrounds (both area normalized) at the LHeC.
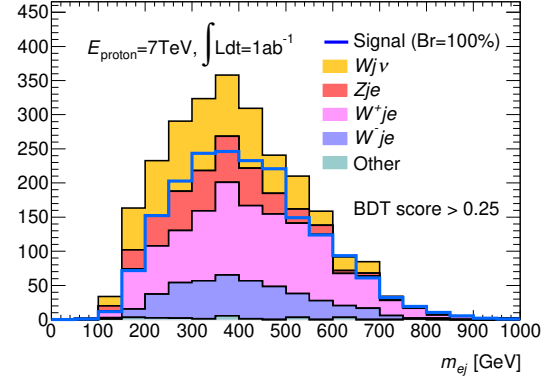
Figure 7.20: Electron-jet invariant mass distribution for the Higgs to invisible decay signal (normalized to 100% branching ratio) and the stacked backgrounds for an integrated luminosity of 1 ab^{-1} at the LHeC after the BDT score cut of 0.25.

In these initial studies no systematic uncertainties were considered. This may be justified with the very a clean environment of electron-hadron collider, in which precise measurements of W and Z production will be made, for example in their decays to muons, for accurately controlling the systematics in the background prediction to a negligible level.

The BDT analysis was repeated for higher proton energies. At the HE-LHeC (E_p=13.5 TeV) the NC production cross section increases to 45 fb and the branching ratio sensitivity improves to 3.4 % because the luminosity is doubled in the configurations here assumed. At the FCC-eh, the cross section rises to 120 fb and the sensitivity of the branching ratio reaches about 1.7 %.

Chapter 8

Searches for Physics Beyond the Standard Model

8.1 Introduction

The LHC was originally envisioned as the ultimate machine to search for physics beyond the Standard Model at the TeV scale. Since electrons and quarks share only electroweak interactions, an electron-proton collider could allow to measure the same phenomena in a different environment with generally higher precision. It could add complementary search channels or lead to the discovery of a weak signal. The possibility of undiscovered New Physics (NP) below the TeV scale could thus be also addressed by the LHeC, which is projected to operate when the LHC will be in its high luminosity phase, in spite of the lower centre-of-mass energy. Exotic phenomena that can be studied at ep colliders have been reviewed, for example, in [612]. More recently, but when the LHC was only beginning to yield data in Run I, an overview of the potential of the LHeC for probing physics beyond the Standard Model has been given in the Conceptual Design Report [1]. Since then, stringent constraints on NP phenomena have been obtained from the LHC and the absence of hints from NP to date is presently changing this paradigm to two alternative scenarios: NP may actually reside at an even larger energy scale; NP may be at or below the TeV scale, but more weakly coupled, and thus hidden in the SM backgrounds [613].

A similar pp-ep synergy could be envisaged with higher proton beam energies at the FCC 100 km tunnel. With an electron beam of 60 GeV, the expected centre-of-mass energies for ep could be 2.9 TeV for $E_p = 19$ TeV (Low-Energy FCC) and 3.5 TeV for $E_p = 50$ TeV (FCC). Below we list recent developments which discuss new physics opportunities at the LHeC and its potential future high-energy upgrades.

8.2 Extensions of the SM Higgs Sector

Presently, given the precision of measurements in the Higgs sector, it appears that the discovered 125 GeV scalar is indeed the SM Higgs boson. The question remains, however, if the scalar potential is truly that of the SM or if it should be extended, possibly with additional degrees of freedom. Several extensions of the Higgs sector have been proposed and can be studied at the ep colliders with results often complementary to those of pp colliders and other future facilities.

8.2.1 Modifications of the Top-Higgs interaction

In electron-proton collisions the heavy top-quarks can be produced in association with a Higgs boson, which allows us to study the sensitivity of the LHeC or the FCC-eh to the top-Higgs (tH) interaction. In Ref. [476] the sensitivity of the process $pe^- \to \bar{t}H\nu_e$ to the CP nature of the tH coupling is investigated by considering a CP phase ζ_t at the ttH and bbH vertices. The authors conclude, based on several observables and with appropriate error fitting methodology, that better limits on ζ_t are obtained at the LHeC than at the HL-LHC. At the design luminosity of $1\,\text{ab}^{-1}$, almost all values of ζ_t are excluded up to 4σ C.L. and the SM top-Higgs coupling could be measured relative to its SM value with a precision of $\kappa = 1.00 \pm 0.17$.

Flavour changing neutral currents (FCNC) are completely absent at tree-level in the SM and strongly constrained, especially by low energy experiments. Anomalous flavour changing neutral current Yukawa interactions between the top quark, the Higgs boson, and either an up or charm quark are documented in Chapter 3, Sec. 5.3.6. Among other studies, in Ref. [614] the authors consider the Higgs decay modes $H \to \gamma\gamma, bb$ and $\tau\tau$ and $E_e = 150\,\text{GeV}$. The results are updated in Ref. [484] for $E_e = 60\,\text{GeV}$, including estimates for lower electron beam energies, and the 2σ sensitivity on the branching ratio $\text{Br}(t \to uh)$ is found to be 0.15×10^{-2}. Making use of the polarisation of the electron beam and multivariate techniques, Ref. [615] shows that limits on the branching ratio $\text{Br}(t \to uh)$ of $\mathcal{O}(0.1)\,\%$ can be obtained, an improvement over present LHC limits of $0.19\,\%$ [616, 617]. These results vary with E_e and E_p.

8.2.2 Charged scalars

The prospects to observe a light charged Higgs boson through the decay $H^+ \to c\bar{b}$ are investigated within the framework of the Two Higgs Doublet Model (2HDM) Type III, assuming a four-zero texture in the Yukawa matrices and a general Higgs potential [618]. The charged current production processes $e^-p \to \nu H^+ q$ are considered. The analysed signature stems from the subsequent decay $H^+ \to c\bar{b}$. The parton level analysis accounts for irreducible SM backgrounds and considers scenarios up to a mass of $200\,\text{GeV}$, consistent with present limits from Higgs and flavour physics. The authors show that for $L = 100\,\text{fb}^{-1}$ a charged Higgs boson could be observed with about $3 - 4\sigma$ significance. This is to be compared with results from present LHC searches in which strong limits are set on the branching fraction $B(t \to H^+b)$, assuming $B(H^+ \to c\bar{b}) = 1.0$ or $B(H^+ \to c\bar{s}) = 1.0$ for the charged Higgs boson mass range $\sim 90 - 160\,\text{GeV}$ [619, 620].

A similar study, $H^\pm \to sc + su$, for the FCC-eh (with $\sqrt{s} \approx 3.5\,\text{TeV}$) is presented in Ref. [621], in the context of a next-to-minimal supersymmetric model (NMSSM). Using dedicated optimisation techniques, the authors show that a light charged boson $H^\pm$ can be observed with maximal significance of $4.4\ (2.2)\sigma$ provided its mass is at most $m_{H^\pm} = 114(121)\,\text{GeV}$, for the total luminosity of $1\,\text{ab}^{-1}$.

The Georgi-Machacek (GM) model extends the Higgs sector by including higher multiplet states while preserving custodial symmetry. The physical states include, besides the SM Higgs, a heavier singlet H, a triplet (H_3^+, H_3^0, H_3^-) and a quintuplet $(H_5^{++}, H_5^+, H_5^0, H_5^-, H_5^{--})$. The H_5 scalars do not couple to fermions and can therefore only be produced by vector boson fusion. An analysis for the prospects to discover the doubly charged Higgs bosons in the GM model at the LHeC and the FCC-eh is presented in Ref. [622]. Therein the production of a doubly-charged member of five-plet Higgs-bosons ($H_5^{\pm\pm}$), produced from $W^\pm W^\pm$ fusion is studied. The authors find that 2 to 3σ limits can be obtained for mixings $\sin(\theta_H)$ as low as 0.2, for $M(H_5) < 300$ GeV.
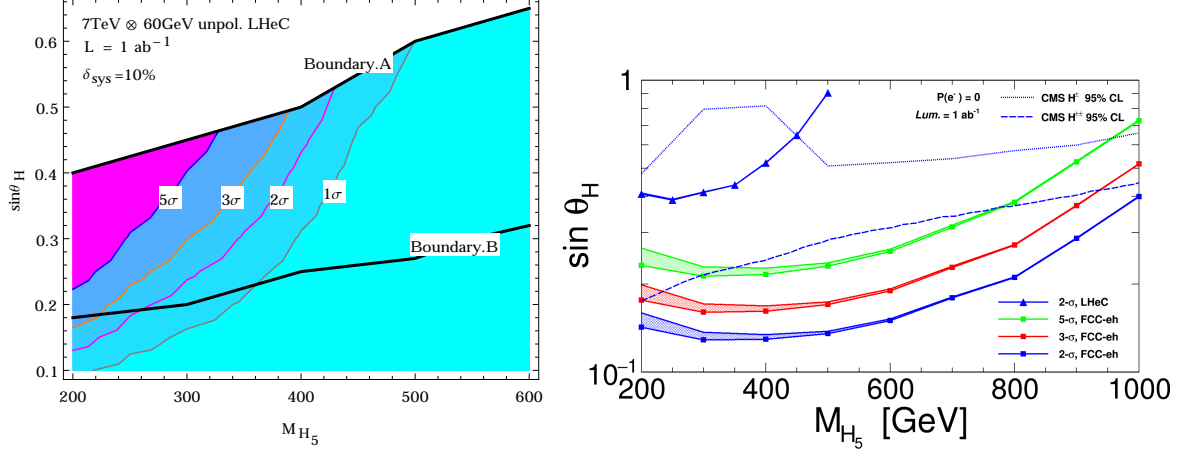
Figure 8.1: *Left:* Discovery contour with respect to $\sin\theta_H$ and $M(H_5^{++/--})$ at LHeC with unpolarized beam; *Right:* Limit Contours for the case of singly charged Higgs for FCC-eh and LHeC. The blue dotted curve and the blue dashed curves give the 95% CL limit from CMS for $H_5^{+/-}$ and for $H^{++/--}$ respectively [624, 625]. An unpolarized beam of integrated luminosity of 1 ab^{-1} and a 10% systematic uncertainty for background yields is assumed in both plots.

The prospects can be improved at the FCC-eh collider, where doubly charged Higgs bosons can be tested for masses $M_{H_5} < 400\,\mathrm{GeV}$, also for small scalar mixing angles (Fig. 8.1 (left)).

The discovery prospects for the singly charged Higgs, $H_5^{\pm}$ of the Georgi-Machacek model, produced in $W^{\pm}Z$ fusion, are evaluated in Ref. [623]. The authors perform a multivariate analysis, including a fast detector simulation, and consider the LHeC and the FCC-eh for a mass range from 200–1000 GeV. They find that the LHeC can improve over current LHC limits on $H_5^{\pm}$ for masses up to about 400 GeV and scalar mixing angles $\sin\theta_H \sim 0.5$ (Fig. 8.1 (right)).

8.2.3 Neutral scalars

Neutral scalar bosons generally appear in many extensions of the scalar sector. They can be added directly, as $SU(1)$ singlets, or be part of higher representation $SU(2)$ multiplets. They generally mix with the SM Higgs boson, from which they inherit a Higgs-like phenomenology.

The potential of testing the heavier CP-even scalar that is contained in the 2HDM Type-I is presented in Ref. [626]. Therein, the lighter scalar particle is considered to be a SM-like Higgs boson and the properties of a heavy scalar, assumed to have the specific mass 270 GeV, is discussed. The authors state that the final state $H \to Sh$, where S is a scalar singlet with a mass around 100 GeV, is of particular interest, as it connects to the findings in Ref. [613].

The prospects to search for a generic heavy neutral scalar particle are presented in detail Ref. [627]. The model is a minimal extension of the SM with one additional complex scalar singlet that mixes with the SM Higgs doublet, which governs its production and decay mode. The heavy scalar is produced via vector-boson fusion and decays into two vector bosons. A multivariate analysis is performed and detector simulation is taken into account. Masses between 200 and 800 GeV and scalar mixings as small as $\sin^2\alpha \sim 10^{-3}$ are considered. The resulting sensitivity for a total luminosity of 1 ab^{-1} is shown in Fig. 8.2, including existing bounds from the LHC and future HL-LHC projections. A significant improvement over existing LHC limits is found, with the LHeC probing scalar boson masses below $\sim 500\,\mathrm{GeV}$, a region which remains difficult at the HL-LHC.
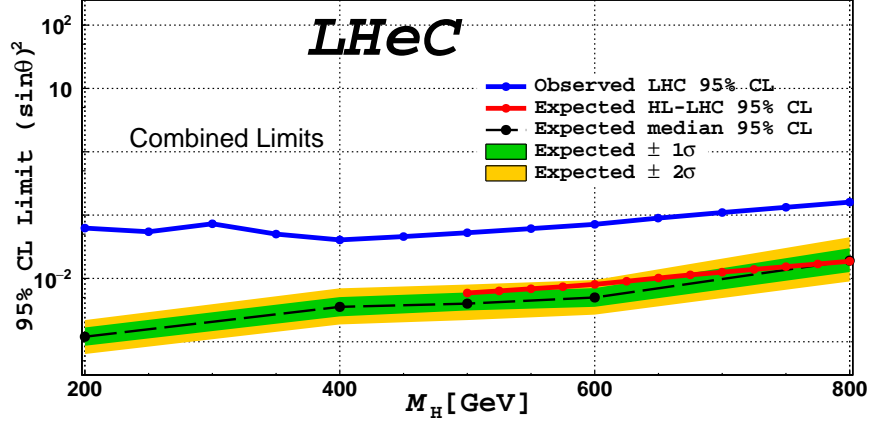
Figure 8.2: Expected exclusion limits (green and yellow bnds) for a heavy scalar search at the LHeC, assuming a systematic uncertainty on the SM background of 2% (from Ref. [627]). The blue line represents the current LHC limit at 95% CL as extracted from [628], the red line the forecast of the HL-LHC sensitivity via $h_2 \to ZZ$ searches from Ref. [629]. The LHeC results correspond to an integrated luminosity of $1\,\mathrm{ab}^{-1}$.

The scalar bosons from the 2HDM Type-III framework may give rise to flavour violating signatures, as discussed in Ref. [630]. The prospects to observe the light and heavy CP-even neutral Higgs bosons via their decays into flavour violating $b\bar{s}$ channels were studied with specific Yukawa textures and a general Higgs potential. The signature consists of one jet originating from b-hadron fragmentation (b-tagged jets) and one light-flavour jet in the central rapidity region, with a remaining jet in the forward region. Relevant SM backgrounds were considered and it is found that flavour violating decays of the SM-like Higgs boson would be accessible with $L = 100\,\mathrm{fb}^{-1}$ at ep colliders.

The prospects of observing the light CP-even neutral Higgs bosons of the NMSSM framework, the MSSM with an additional singlet superfield, via their decays into b-quarks and in the neutral and charged current production processes, are studied in Ref. [631]. In this work the following constraints are incorporated into the spectrum: neutralino relic density corresponding to the observed dark matter relic density; direct and indirect mass bounds from searches for specific sparticles; the SM-like Higgs boson has a mass around $126\,\mathrm{GeV}$ and an invisible branching ratio below 0.25. The signal is given by three jets plus an electron or missing transverse momentum (E_T^{miss}) arising from the neutral (charged) current interaction, where two jets are required to be originating from a b-quark and the remaining jet is required to be in the forward region. For the cut-based analysis a number of reducible and irreducible SM backgrounds, generated with a fast detector simulation with an adaptation of the LHeC detector, are considered. It is found that the boson h_1 could be observable for some of the NMSSM benchmark points, at up to 2.5σ level in the $e + 3j$ channel up to masses of $75\,\mathrm{GeV}$; in the $3j + E_T^{miss}$ channel h_1 could be discovered at 2.4σ level up to masses of $88\,\mathrm{GeV}$ with $L = 100\,\mathrm{fb}^{-1}$, and a 5σ observation is possible with $\mathcal{L} = 1\,\mathrm{ab}^{-1}$ for masses up to $90\,\mathrm{GeV}$.

8.2.4 Modifications of Higgs self-couplings

As in the chapter on Higgs physics above, the e^-p collisions are a very convenient environment to study the property of the SM Higgs boson itself. The latter is produced through vector-boson fusion processes and the precise measurement of its properties provides a unique opportunity

to probe the interaction HVV, $(V = W^{\pm}, Z)$. These interactions are in general sensitive to certain classes of beyond the SM physics, which can be parameterized, for instance, via higher dimensional operators and their coefficients, cf. Refs. [578, 607, 632–634].

The prospects of inferring the strengths of the two couplings HWW and HZZ were studied in Refs. [607, 633] in the context of electron-proton collisions. The authors find that the higher-dimensional operator coefficients can be tested for values around $\mathcal{O}(10^{-1})$ at the LHeC. This sensitivity is improved at the FCC-eh due to larger centre-of-mass energies, which in general enhance the vector-boson fusion cross sections.

The Higgs self-coupling itself HHH can be tested through the measurement of the di-Higgs production cross section as was shown in Ref. [578]. With appropriate error fitting methodology this study illustrates that the Higgs boson self-coupling could be measured with an accuracy of $g_{HHH}^{(1)} = 1.00^{+0.24(0.14)}_{-0.17(0.12)}$ of its expected SM value at $\sqrt{s} = 3.5(5.0)\,\mathrm{TeV}$, considering an ultimate $10\,\mathrm{ab}^{-1}$ of integrated luminosity.

An analysis presented in Ref. [634] evaluates the LHeC sensitivity to dimension-six operators. The authors employ jet substructure techniques to reconstruct the boosted Higgs boson in the final state. A shape analysis on the differential cross sections shows in some cases improvements with respect to the high-luminosity LHC forecasts.

8.2.5 Exotic Higgs boson decays

The LHeC sensitivity to an invisibly decaying Higgs boson was investigated in Ref. [610]. Therein the focus is on the neutral current production channel due to the enhanced number of observables compared to the charged current counterpart. The signal contains one electron, one jet and large missing energy. A cut-based parton level analysis yields the estimated sensitivity of $\mathrm{Br}(h \rightarrow \mathrm{invisible}) = 6\,\%$ at 2σ level. Exotic decays of the Higgs boson into a pair of light spin-0 particles referred to as Φ was discussed in Ref. [635]. The studied signature is a final state with 4 b-quarks, which is well motivated in models where the scalars can mix with the Higgs doublet, and suffers from multiple backgrounds at the LHC. The analysis is carried out at the parton level, where simple selection requirements render the signature nearly free of SM background and makes Φ with masses in the range $[20, 60]\,\mathrm{GeV}$ testable for a hVV $(V = W, Z)$ coupling strength relative to the SM at a few per-mille level and at $95\,\%$ confidence level.

The prospects of testing exotic Higgs decays into pairs of light long-lived particles at the LHeC were studied in Ref. [636] where it was shown that proper lifetimes as small as μm could be tested, which is significantly better compared to the LHC. This is shown in Fig. 8.3 (left). This information can be interpreted in a model where the long-lived particles are light scalars that mix with the Higgs doublet, where both, production and decay, are governed by this scalar mixing angle. The area in the mass-mixing parameter space that give rise to at least 3 observable events with a displaced vertex are shown in Fig. 8.3. It is apparent that mixings as small as $\sin^2 \alpha \sim 10^{-7}$ can be tested at the LHeC for scalar masses between 5 and $15\,\mathrm{GeV}$ [636].

8.3 Searches for supersymmetry

Several SUSY scenarios might remain still elusive in searches performed at pp colliders. While the null results from current searches by the LHC experiments have produced impressive constraints on the SUSY coloured sector (squarks and gluinos) because of their large production
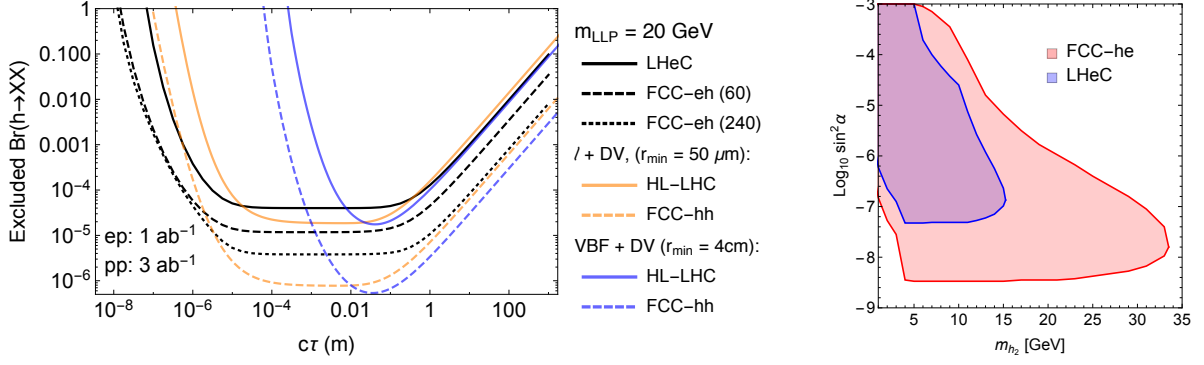
Figure 8.3: Sensitivity contours for displaced vertex searches for Higgs decays into long-lived scalar particles (LLP), which are pair produced from decays of the Higgs boson, and which themselves decay via scalar mixing into fully visible final states. Left: As a function of the LLP lifetime for a fixed mass from Ref. [636]. Right: For a specific model, where lifetime and production rate of the LLP are governed by the scalar mixing angle. The contours are for 3 events and consider displacements larger than $50\,\mu$m to be free of background.

cross sections in strong interactions, less stringent constraints have been placed on weakly-produced SUSY particles, namely neutralinos $\tilde{\chi}^0$, charginos $\tilde{\chi}^\pm$, and sleptons $\tilde{\ell}^\pm$. Some of these scenarios where *ep* colliders might have discovery potential complementary to that of the HL-LHC are discussed below. These include R-parity conserving SUSY models, e.g. motivated by dark matter, or R-parity violating SUSY models, e.g. including single production of bottom and top squarks and low mass gluinos.

8.3.1 Search for the SUSY Electroweak Sector: prompt signatures

Electroweakino scenarios where charginos, neutralinos, and sleptons are close in mass can be characterised by the neutralino mass m and the mass splitting between charginos and neutralinos Δm. We here refer to scenarios with $\Delta m < 50$GeV as *compressed*. A subtlety arises for $\Delta m \leq 1\,\text{GeV}$, when the $\tilde{\chi}_1^\pm/\tilde{\chi}_2^0$ becomes long lived and its decays are displaced. For $\Delta m > 1\,\text{GeV}$ the decays are prompt, the visible decay products from $\tilde{\ell}$ and $\tilde{\chi}_1^\pm/\tilde{\chi}_2^0$ have very soft transverse momenta (p_T) and the SM backgrounds are kinematically similar to the signal. The analyses therefore become challenging and sensitivities decrease substantially. Two SUSY scenarios are considered in Ref. [637] and depicted in Fig. 8.4 where the LSP $\tilde{\chi}_1^0$ is Bino-like, $\tilde{\chi}_1^\pm$ and $\tilde{\chi}_2^0$ are Wino-like with almost degenerate masses, and the mass difference between $\tilde{\chi}_1^0$ and $\tilde{\chi}_1^\pm$ is small. The signal is produced via the process "$p\,e^- \rightarrow j\,e^-\,\tilde{\chi}\tilde{\chi}$", where $\tilde{\chi} = \tilde{\chi}_1^0$, $\tilde{\chi}_1^\pm$ or $\tilde{\chi}_2^0$.
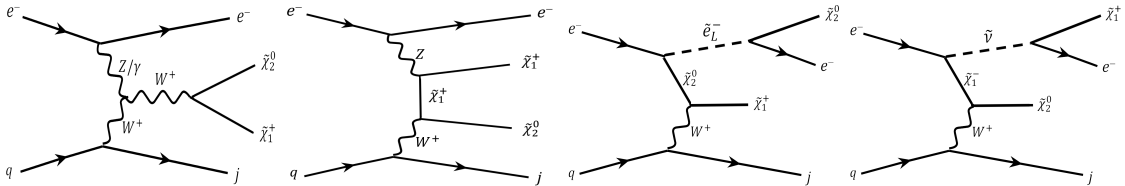

Figure 8.4: Representative production diagrams for the signal processes considered in Ref. [637]. The *decoupled-slepton* scenario includes only the first two diagrams, while the *compressed-slepton* scenario includes all four diagrams.

Conservative leading order cross sections are considered for the SUSY signal models. The kinematic observables are input to the TMVA package to perform a multivariate analysis at the
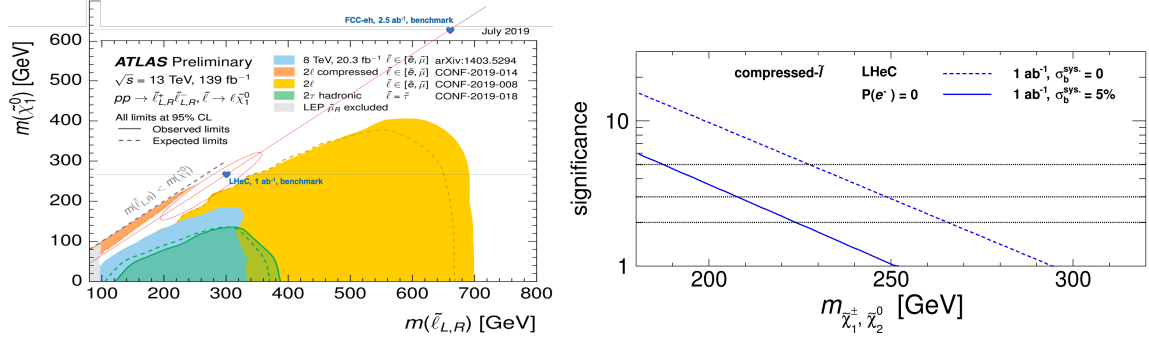
Figure 8.5: *Left:* Benchmark assumption on slepton masses and 2019 reach of current ATLAS searches for sleptons (Ref. ATLAS public twiki). *Right:* Significances as varying the masses of $\tilde{\chi}_1^\pm$ and $\tilde{\chi}_2^0$ for the compressed-slepton scenario at the LHeC with unpolarised beams and 1 ab^{-1} luminosity. For dashed (solid) curve, a systematic uncertainty of 0 % (5 %) on the background is considered. The figure is from Ref. [637].

detector level.

In the compressed-slepton scenario, the case where the left-handed slepton $\tilde{\ell}_L$ and sneutrino $\tilde{\nu}$ are slightly heavier than $\tilde{\chi}_1^\pm$ or $\tilde{\chi}_2^0$ is considered. When fixing the mass difference $\Delta m = m_{\tilde{\ell}} - m_{\tilde{\chi}_1^\pm,\tilde{\chi}_2^0} = 35$ GeV and ignoring the systematic uncertainty on the background, the analysis indicates that the 2 (5)σ limits on the $\tilde{\chi}_1^\pm$, $\tilde{\chi}_2^0$ mass are 616 (517) GeV for 2.5 ab^{-1} luminosity at the FCC-eh, and 266 (227) GeV for 1 ab^{-1} luminosity at the LHeC, respectively. An illustration of the model assumptions in terms of sleptons and neutralino masses and the current constraints at the LHC is presented in Fig. 8.5 (left). Results are illustrated in Fig. 8.5 (right). The effects of varying Δm are investigated: fixing $m_{\tilde{\chi}_1^\pm,\tilde{\chi}_2^0}$ to be 400 GeV, it is found that at the FCC-eh the significance is maximal when Δm is around 20 GeV.

In the decoupled-slepton scenarios where only $\tilde{\chi}_1^0$, $\tilde{\chi}_1^\pm$ and $\tilde{\chi}_2^0$ are light and other SUSY particles are heavy and decoupled, the 2σ limits obtained on the $\tilde{\chi}_1^\pm$, $\tilde{\chi}_2^0$ mass are 230 GeV for 2.5 ab^{-1} luminosity at the FCC-eh when neglecting the systematic uncertainty on the background. Large systematic uncertainties on the SM background processes can substantially affect the sensitivity, hence good control of experimental and theoretical sources of uncertainties is very important.

Finally, it is also found that the possibility of having a negatively polarised electron beam ($P_e = 80\%$) could potentially extend the sensitivity to electroweakinos by up to 40 %.

Overall, since the sensitivity to the electroweak SUSY sector depends on the mass hierarchy of $\tilde{\chi}_1^\pm$, $\tilde{\chi}_1^0$, $\tilde{\chi}_2^0$ and sleptons, and given the difficulty to probe efficiently small Δm regions at the current LHC and possibly at the HL-LHC, measurements at *ep* colliders may prove to offer complementary or additional reaches, in particular for the compressed scenarios.

8.3.2 Search for the SUSY Electroweak Sector: long-lived particles

Studies on Higgsinos (χ) with masses $\mathcal{O}(100)$ GeV are motivated by natural SUSY theories and help to avoid large fine-tuning on the Higgs boson mass. In these scenarios the low energy charginos (χ^+)/neutralinos(χ^0) are all Higgsino-like and their masses are nearly degenerate, only slightly above the neutralino.

As mentioned above, a compressed spectrum with nearly degenerate masses results in a kinematic suppression of the heavier χ^+ decays into $W^\pm\chi^0$, which has twofold consequences: it yields final
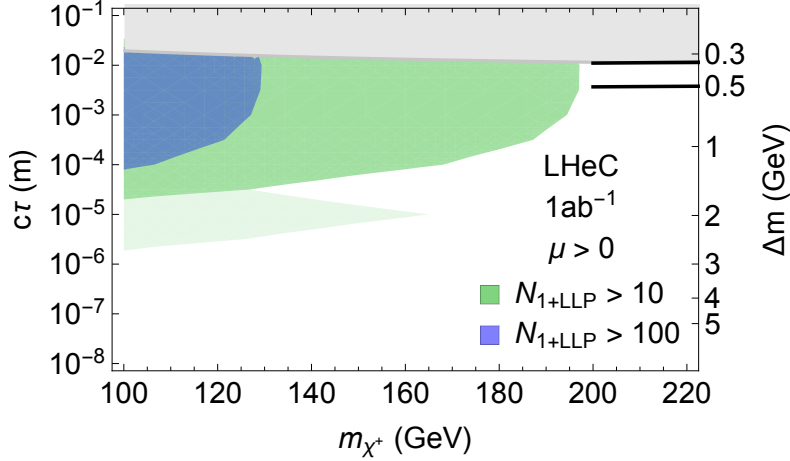
Figure 8.6: Exclusion limits on Higgsino masses as a function of their lifetime from Ref. [636]. Coloured regions denote where 10 or 100 events with at least one LLP decay are observed. Light shading indicates the uncertainty in the predicted number of events due to different hadronisation and LLP reconstruction assumptions. The black curves are the optimistic and pessimistic projected bounds from HL-LHC disappearing track searches.

states without hard leptons; it enhances the χ^+ lifetime up to $\mathcal{O}(1)$ mm. At the LHC the absence of hard leptons with sizable transverse momentum makes this signature difficult to investigate. One possibility is to search for the tracks from χ^+, which effectively disappear once it decays and are thus called *disappearing tracks*.

The discovery prospects for prompt signatures of electroweakino decays in electron-proton collisions are presented in Ref. [638]. The light χ^+ (and χ^0) can be produced in pairs via in vector boson fusion of the charged or neutral currents. A cut-based analysis of these processes at the LHeC, assuming prompt χ^+ decays, yields 2σ discovery prospects for masses up to 120 GeV.

Taking into account the finite lifetime of the charginos, two comments are in order: first, the lifetimes and boosts of the χ^+ are in general too small to resolve a disappearing track; second, the soft final state is not a problem per se and can in principle be observed.

Instead of searching for a disappearing track, the long lifetimes of the χ^+ can be exploited via the measurement of the impact parameter of the soft hadronic final, as is discussed in Ref. [636]. The crucial machine performance parameters are the tracking resolution, which is as good as $\mathcal{O}(10)\,\mu$m, and the absence of pile up, which allows to identify and measure a single soft pion's impact parameter. In this way the LHeC can test χ with masses up to 200 GeV. The corresponding sensitivity is shown in Fig. 8.6, and the bounds on disappearing track searches at the HL-LHC are shown as black lines in the figure. By considering non-prompt decays of Higgsinos, the discovery prospects compared to the prompt analysis is thus significantly improved. Further means of improving the prospects is an increased centre-of-mass energy, which enhances the production rate of the Higgsinos.

8.3.3 R-parity violating signatures

Supersymmetry typically evokes the so-called R-parity, which implies that each fundamental vertex contains an even number of sparticles and helps preventing rapid proton decays. In general, R-parity need not be an exact symmetry of the theory, such that interactions can be

present that allow for sparticles to decay into SM particles and include the possibility to violate lepton and/or baryon number.

R-partiy violating interactions are particularly interesting in electron-proton collisions, where single superpartners might be produced resonantly, and detected via the corresponding $2 \to 2$ process. This is discussed in Refs. [639, 640] for the case of the *sbottom*, showing that a good level of precision could be achieved at LHeC compared with all the knowledge derived from indirect measurements.

Single (anti-)top quark production associated with a lightest neutralino in the MSSM with R-parity breaking coupling is investigated in Ref. [641] for the LHeC. The study, which includes calculations of QCD contributions at NLO, concludes that the available constraints would allow a notable production rate.

Certain SUSY scenarios might produce prompt signals of multiple soft jets, which generally resemble QCD backgrounds at the LHC and are thus notoriously difficult to test. The largely QCD-free environment of electron-proton collisions allows to test this class of signatures. One example of this signal can come from gluinos, which are tested at the LHC via signatures that involve large amounts of missing energy. If the gluino has an all-hadronic decay – as in R-parity violating scenarios or Stealth SUSY models – the current experimental searches have a gap in sensitivity for masses between about 50 to 70 GeV [642]. Gluinos within this gap can be tested at the LHeC [643], where a three sigma exclusion sensitivity was demonstrated with simple signal selection cuts.

8.4 Feebly Interacting Particles

New physics may interact with the SM via the so-called portal operators, including the vector, scalar, pseudoscalar, or neutrino portal. In these scenarios, the SM is often extended by an entire sector of new physics, comprising new forces and several particle species, which may be connected to the big open questions of Dark Matter or the origin of neutrino mass.

These hypothetical new sectors derive their typically very feeble interaction strength with the known particles from mass mixing with a SM particle that shares their quantum numbers. Some examples are being discussed below.

8.4.1 Searches for heavy neutrinos

The observation of neutrino oscillations requires physics beyond the SM that gives rise to the light neutrino masses. One well-motivated class of models for this purpose is the so-called symmetry protected type I seesaw scenario, which features heavy neutrinos with signatures that are in principle observable at colliders, cf. Ref. [644] and references therein. A comprehensive overview over collider searches for the heavy and mostly sterile neutrinos can be found in Ref. [645], where the promising signatures for such searches at electron-proton colliders have been identified.

In electron-proton collisions heavy neutrinos can be produced via the charged current (see the left panel of Fig. 8.7). The heavy neutrino production cross section is dependent on the active-sterile neutrino mixing with the electron flavour called $|\theta_e|^2$. The most promising searches at the LHeC are given by processes with lepton flavour violating final states and displaced vertices, the prospects of which are evaluated in Ref. [646] and are shown in the right panel of Fig. 8.7. It is remarkable, that the prospects to detect heavy neutrinos with masses above about 100 GeV
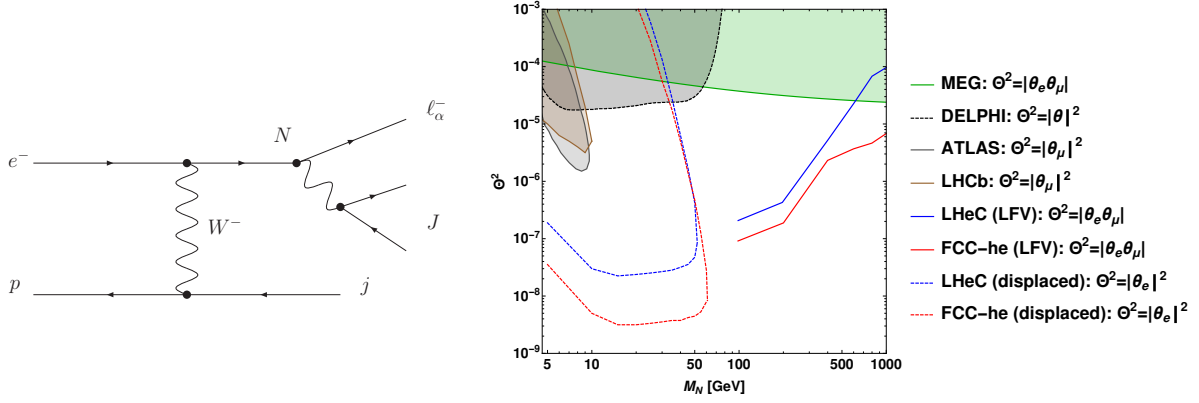
Figure 8.7: Left: Dominant tree-level production mechanism for sterile neutrinos at the LHeC. The sterile neutrino decay via the charged current gives rise to the so-called lepton flavor violating lepton-trijet signature. Right: Sensitivity of the LFV lepton-trijet searches (at $95\,\%$ C.L.) and the displaced vertex searches (at $95\,\%$ C.L.) from Ref. [646] compared to the current exclusion limits from ATLAS [648], LHCb [649], LEP [650], and MEG [651].

are much better in electron-proton collisions compared to proton-proton or electron-positron, due to the much smaller reducible backgrounds.

The prospects of heavy neutrino detection can be further enhanced with jet substructure techniques when the W boson in the decay $N \to eW$, $W \to jj$ is highly boosted. Ref. [647] shows that these techniques can help to distinguish the heavy neutrino signal from the few SM backgrounds. A considerable improvement in the bounds of $|V_{eN}|^2$ over present limits from LHC, $0\nu2\beta$ experiments and from electroweak precision data is obtained with $1\,\mathrm{ab}^{-1}$ of integrated luminosity at the LHeC.

An alternative approach is employed in Ref. [652] where the dominant sterile neutrino interactions with the SM are taken to be higher dimension effective operators (parameterizing a wide variety of UV-complete new physics models) while contributions from neutrino mixing is neglected. The study shows prospects of Majorana neutrino detection for masses lower than 700 and 1300 GeV can be discovered at the LHeC with $E_e = 50$ and $150\,\mathrm{GeV}$, respectively, for $E_p = 7\,\mathrm{TeV}$. Recently the influence of vector and scalar operators on the angular distribution of the final anti-lepton was investigated. The forward-backward asymmetry is studied in Ref. [653], wherein, in particular, the feasibility of initial electron polarisation as a discriminator between different effective operators is studied.

Prospects of testing left-right symmetric models, featuring additional charged and neutral gauge bosons and heavy neutrinos, were studied in the context of electron-proton collisions in Refs. [654, 655]. The authors show that the production of heavy right-handed neutrinos of mass $\mathcal{O}(10^2$-$10^3)\,\mathrm{GeV}$ at the LHeC, with a lepton number violating final state, can yield information on the parity breaking scale in left-right symmetric theories. Heavy neutrinos of sub-TeV mass in inverse see-saw model with Yukawa coupling of $\mathcal{O}(0.1)$ are investigated for the LHeC in Ref. [656].

8.4.2 Fermion triplets in type III seesaw

Another technically natural way of generating the light neutrino masses is the so-called Type III seesaw mechanism, which extends the SM with a fermion $SU(2)$ triplet. In minimal versions of these models the neutral and charged triplet fermions have almost degenerate masses around the TeV scale.
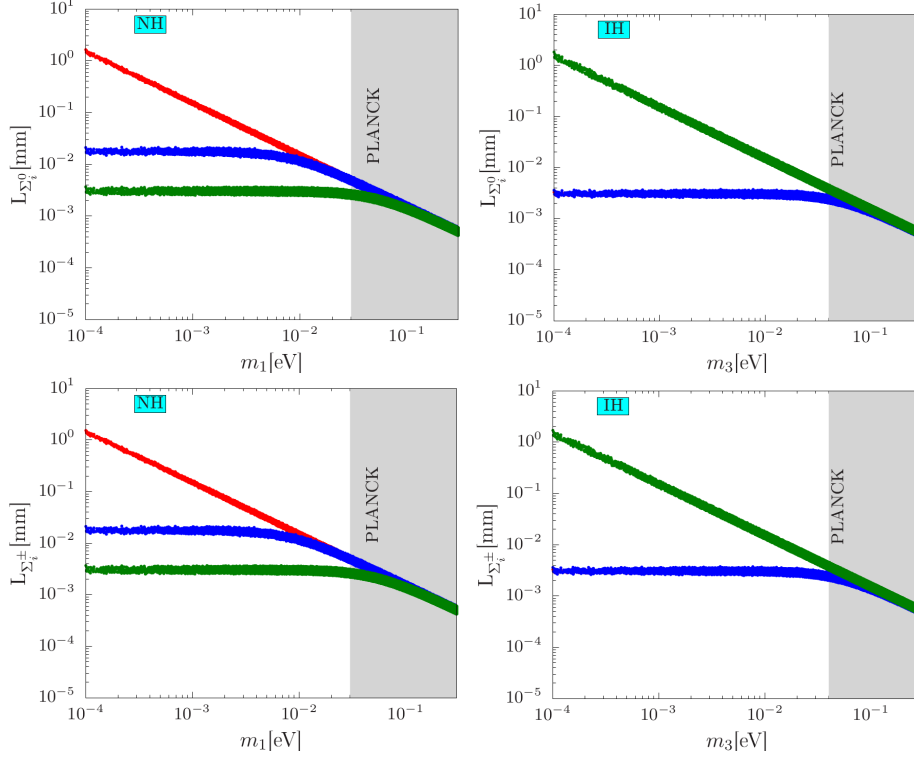
Figure 8.8: Proper decay length of $\Sigma_i^0(\Sigma_i^\pm)$ with respect to the lightest light neutrino mass in the upper (lower) panel for 1 TeV triplet. The Normal (Inverted) hierarchy case is shown in the left (right) panel. The first generation triplet is represented by the red band, the second generation is represented by the blue band and the third generation is represented by the green band respectively. The shaded region is excluded by the PLANCK data [658].

In the three generation triplet extension of the type-III seesaw, the role of mixings between active neutrinos and neutral triplet fermions has been investigated in Ref. [657]. Depending upon the choices of Dirac Yukawa coupling, the mixing angles can take many possible values, from very small to large. With very small mixings, decay length of the triplet fermion can be very large. It can show a displaced decay inside the detector or outside the detector of the high energy colliders. The proper decay length as a function of the lightest light neutrino mass $m_1(m_3)$ for the Normal (Inverted) hierarchy case are shown in Fig. 8.8.

The prospects of probing this mechanism via searches for the new fermions are evaluated in Ref. [659], wherein signatures from long-lived particles at various experiments were considered. The triplet fermions are primarily produced through their gauge interactions, as shown in the left panel of Fig. 8.9, and can be observed via displaced vertices and disappearing track searches for masses of a few hundred GeV. The authors find that the LHeC can observe displaced vertices from the decays of the charged fermion triplet components via the soft pion impact parameters for triplet masses up to about 220 GeV and has a complementary sensitivity to the light neutrino mass scale, which governs the lifetime of the neutral fermion, compared the LHC and MATHUSLA. The final results from Ref. [659] for the LHeC are shown in the right panel of Fig. 8.9.

If the mixing becomes sufficiently large, and/or if the masses are $\mathcal{O}(100)$ GeV, the triplet fermions decay promptly. Also in this case, the heavy triplets can show a variety of interesting collider signatures including fat jets. The latter have been studied for FCC-he in Ref. [660].
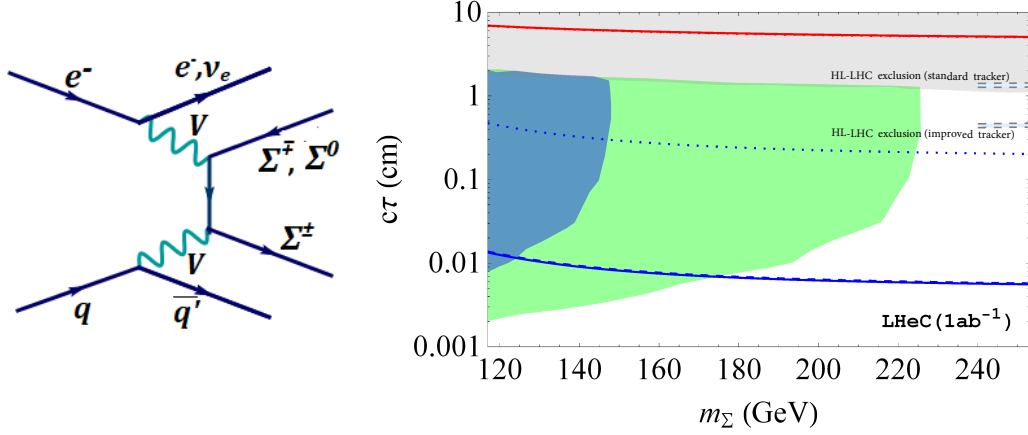
Figure 8.9: Left: Dominant production diagram of triplet fermion pairs via their gauge interactions. Right: Prospects of displaced vertex searches from charged fermion triplet $\Sigma^\pm$. The blue and green shaded regions denote the expected observability of 10 (100) events, dashed lines denote HL-LHC exclusion sensitivity, and the red line is connected to the light neutrino properties. For details, see text and Ref. [659].
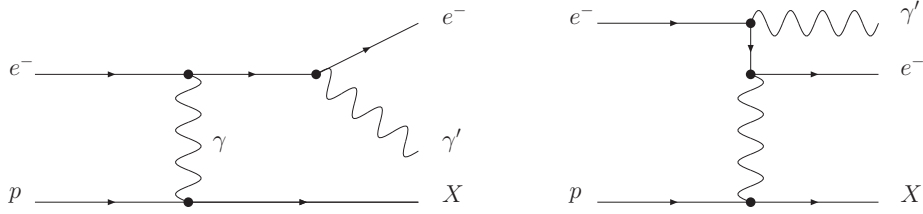

Figure 8.10: Feynman diagrams for the dark photon production processes in electron-proton collisions. Here X denotes the final state hadrons after the scattering process.

8.4.3 Dark photons

Minimal extensions of the SM often involve additional gauge factors. In particular the $U(1)_X$ extensions are interesting, because they are often connected to a dark charge that can be associated with the dark matter.

An SM-extending $U(1)_X$ predicts an additional gauge boson that naturally mixes with the $U(1)_Y$ factor of the SM kinetically [661]. This kinetic mixing lets the SM photon couple to fermions that carry the dark charge X, and the other gauge boson to the electric charge. Both interactions are suppressed by the mixing parameter ϵ. In most models the additional gauge boson also receives a mass, possibly from spontaneous breaking of the $U(1)_X$, and the corresponding mass eigenstate is called a dark photon. Dark photons typically have masses around the GeV scale and their interactions are QED-like, scaled with the small mixing parameter ϵ. It can decay to pairs of leptons, hadrons, or quarks, which can give rise to a displaced vertex signal due to its long lifetime.

The prospects for the dark photon searches via their displaced decays in ep collisions are presented in Ref. [662]. The dark photon production process targeted in this search is depicted in Fig. 8.10. The signal is given by the process $e^- p \to e^- X \gamma'$, where X denotes the final state hadrons, and the dark photon γ' decays into two charged fermions or mesons.

The most relevant performance characteristics of the LHeC are the very good tracking resolution
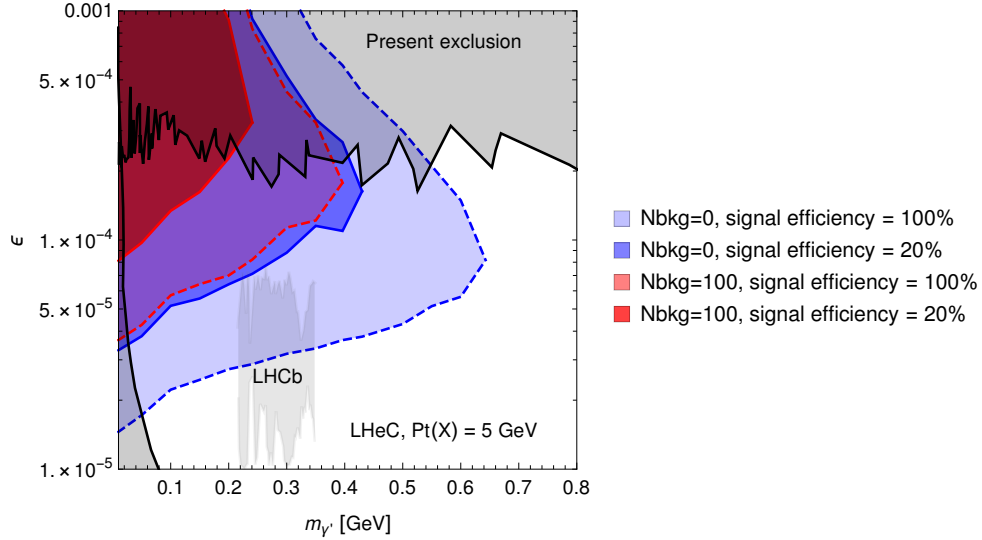
Figure 8.11: Projected sensitivity of dark photon searches at the LHeC via displaced dark photon decays from Ref. [662]. The sensitivity contour lines are at the 90 % confidence level after a transverse momentum cut on the final state hadrons of 5 GeV. The blue and red areas denote the assumption of zero and 100 background events, respectively, the solid and dashed lines correspond to a reconstruction efficiency of 100 % and 20 %, respectively. See Ref. [662] for details.

and the very low level of background, which allow the detection of a secondary vertex with a displacement of $\mathcal{O}(0.1)$ mm.

The resulting sensitivity contours in the mass-mixing parameter space are shown in Fig. 8.11, where the different colours correspond to different assumptions on the irreducible background and the solid and dashed lines consider different signal reconstruction efficiencies. Also shown for comparison are existing exclusion limits from different experiments, and the region that is currently investigated by the LHCb collaboration [663].

The domain in parameter space tested in electron-proton collisions is complementary to other present and planned experiments. In particular for masses below the di-muon threshold, searches at the LHC are practically impossible. It is remarkable that dark photons in this mass range can be part of a dark sector that explains the observed Dark Matter in the Universe via a freeze-in mechanism, cf. e.g. Ref. [664].

8.4.4 Axion-like particles

The axion is the Goldstone boson related to a global $U(1)$ symmetry, which is spontaneously broken at the so-called Peccei-Quinn scale, assumed to be around the GUT scale. Its mass, being inversely proportional to the Peccei-Quinn scale, is therefore usually in the sub-eV regime and the axion provides a dynamical solution to the strong CP problem of the standard model. Axions are a very attractive candidate for *cold* dark matter, despite their tiny mass.

Axion-like particles (ALP) are motivated by the original idea of the QCD axion and similarly, they are good dark matter candidates. ALPs are pseudoscalar particles that are usually assumed to be relatively light (i.e. with masses around and below one GeV) and couple to the QCD field strength. In addition, they may have a number of further interactions, for instance they can interact with the other fields of the SM and also mix with the pion. Particularly interesting is
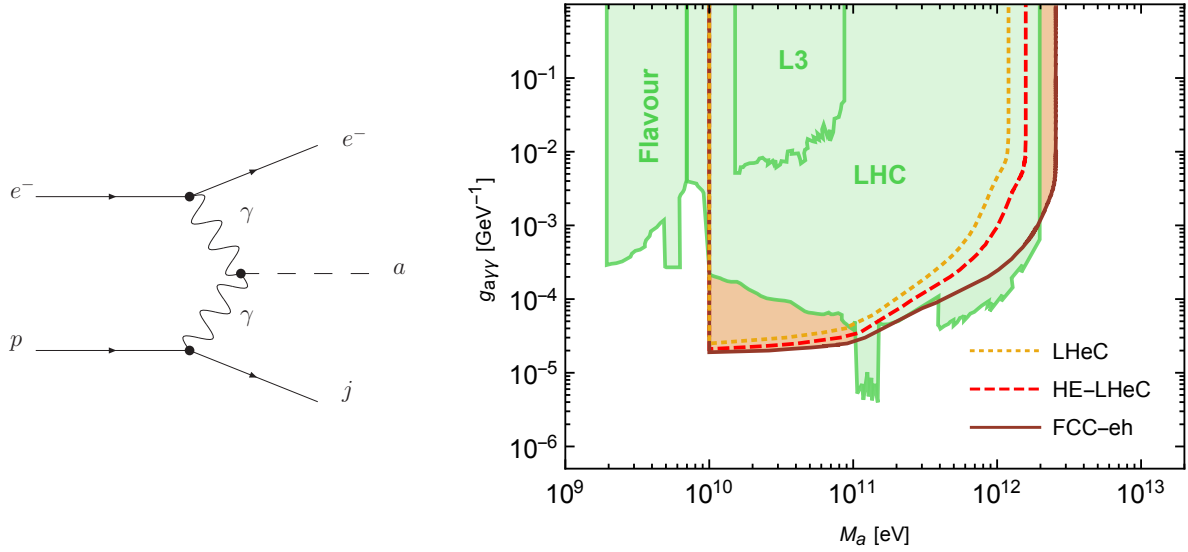
Figure 8.12: Left: Production of axion-like particles (ALPs) via photon fusion. Right: Projected sensitivity of the LHeC to ALPs coupling with photons at 95% CL. The existing exclusion limits are shown with the green regions. See Ref. [665] for details.

the possibility to produce ALPs via vector boson fusion processes.

A recent study [665] has evaluated the prospects of detecting ALPs at the LHeC via the process $e^-\gamma \rightarrow e^- a$, as shown in the left panel of Fig. 8.12, in a model independent fashion. The investigated signature is the decay $a \rightarrow \gamma\gamma$, which allows to test the effective ALP-photon coupling for ALPs with masses in the range of $10\,\text{GeV} < m_a < 3\,\text{TeV}$. It was found that sensitivities can improve current LHC bounds considerably, especially for ALP masses below $100\,\text{GeV}$, as shown in the right panel of Fig. 8.12. The authors state that ALP searches at ep colliders might become an important handle on this class of new physics scenarios [665].

8.5 Anomalous Gauge Couplings

New physics beyond the SM can modify SM interactions, for instance at the loop level. Such contributions could either modify the interaction strength of SM particles or introduce additional interactions that are not present in the SM, like flavour changing neutral couplings.

Searches for anomalous couplings of top quarks are summarised in Section 5.3. They are parametrised via an effective Lagrangian and are studied by analysing specific processes. For example, anomalous Wtb couplings are studied in $e^-p \rightarrow \nu_e \bar{t}$, and anomalous $t\bar{t}\gamma$ and $t\bar{t}Z$ couplings are studied in top quark pair production. In addition FCNC $tu\gamma$ and tuZ couplings are analysed in NC DIS single top quark production, and FCNC tHu couplings are investigated in CC DIS single top quark production. Limits on the corresponding FCNC branching ratios are discussed in Section 5.3.6 and summarised and compared to different colliders in Fig. 5.19.

Triple gauge boson couplings (TGC) W^+W^-V, $V = \gamma, Z$ are precisely defined in the SM and any significant deviation from the predicted values could indicate new physics. Present constraints on anomalous triple vector boson couplings are dominated by LEP (but they are not free of assumptions) and the WWZ and $WW\gamma$ vertices can be tested at LHeC in great detail.

The search for anomalous $WW\gamma$ and WWZ couplings with polarised electron beam were studied in Ref. [458] via the processes $ep \rightarrow \nu q\gamma X$ and $ep \rightarrow \nu qZX$. It was found that the LHeC sensitivity with $E_e = 60\,\text{GeV}$ and $L = 100/\text{fb}$ is comparable with existing experimental limits from lepton and hadron colliders, and that the sensitivity to anomalous Z couplings might be better, reaching $(\Delta\kappa_{\gamma,Z}, \lambda_{\gamma,Z})$ as small as $\mathcal{O}(10^{-1}, 10^{-2})$. In general, beam polarisation and larger electron beam energies improve the sensitivity, and the LHeC was found to give complementary information on the anomalous couplings compared to the LHC.

The prospects of testing anomalous triple gauge couplings are also investigated in Ref. [457]. Therein the authors study the kinematics of an isolated hard photon and a single jet with a substantial amount of missing transverse momentum. They show that the LHeC is sensitive to anomalous triple gauge couplings via the azimuthal angle differences in the considered final state. It is pointed out that, in such an analysis, it is possible to probe the $WW\gamma$ vertex separately with no contamination from possible BSM contributions to the WWZ coupling. The estimations consider $E_e = 100, 140, 200\,\text{GeV}$ and it is claimed that, while higher energies yield better sensitivities, the differences are not very large. For an integrated luminosity of $200\ \text{fb}^{-1}$ and $E_e = 140\,\text{GeV}$ the exclusion power of the LHeC is superior to all existing bounds, including those from LEP.

The process $e^- p \rightarrow e^- \mu^+ \nu j$ is investigated in Ref. [459]. The analysis is carried out at the parton level and includes the cross section measurement and a shape analysis of angular variables, in particular of the distribution of the azimuthal angle between the final state forward electron and jet. It is shown that the full reconstruction of leptonic W decay can be used for W polarization which is another probe of anomalous triple gauge couplings. The results show that the LHeC could reach a sensitivity to λ_γ and Δk_γ as small as $\mathcal{O}(10^{-3})$ for $L = 2 - 3/\text{ab}$.

8.5.1 Radiation Amplitude Zero

The LHeC is ideal for testing a novel feature of the Standard Model: the *radiation amplitude zero* [666–669] of the amplitude $\gamma W^- \rightarrow c\bar{b}$ and related amplitudes, see Fig. 8.13. The Born amplitude is predicted to vanish and change sign at $\cos\theta_{CM} = \frac{e_{\bar{b}}}{e_W^-} = -1/3$. This LHeC measurement tests the compositeness of the W boson and its zero anomalous magnetic moment at leading order, where one has $g_W = 2$, $\kappa_W = 1$, as well as $g_q = 2$ for the quarks. More generally, one can also test the radiation amplitude zero for the top quark from measurements of the process $\gamma b \rightarrow W^- t$.

8.6 Theories with heavy resonances and contact interaction

In many other BSM scenarios, new physics will manifest itself by the presence of new resonances. Although the high centre-of-mass energy of pp colliders allow for a better reach in most of these scenarios, the LHeC and FCC-eh, thanks to the clean collision environment and the virtual absence of pileup, can complement the LHC in the search for these new phenomena. Deviations from Standard Model predictions could signal new physics even if it is at an energy scale beyond the centre-of-mass energy of the collider. In this case, the effective four-fermion contact interaction could be explained by the exchange of a virtual heavy particle, such as a leptoquark, a heavy boson or elementary constituents of quarks and leptons in composite models. The effective contact interaction scale then represents the typical mass scale of the new
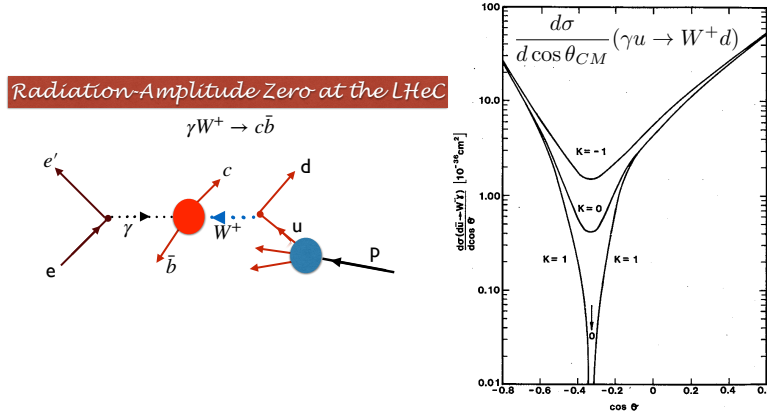
Figure 8.13: The radiation amplitude zero of the Standard Model in $\gamma W^+ \to c\bar{b}$ and $\gamma u \to W^+ d$. The prediction for the angular distribution $\frac{d\sigma}{d\cos(\theta_{CM})}(\gamma u \to W^+ d)$ is from Ref. [669].

particles. Relevant studies on various topics including scalar and vector leptoquarks and excited leptons, are collected in this section.

8.6.1 Leptoquarks

In recent years the experiments that study heavy flavoured mesons have revealed intriguing hints for new physics in semileptonic decays of B mesons. A violation of lepton flavour universality at the level of 3 to 5σ is apparent in both the charged current and neutral current mediated processes [670]. In this context BSM theories involving leptoquarks (LQs) have gained renewed interest as they can give rise to lepton universality violating decays of heavy mesons at tree level, provided they couple to the second and third generation of quarks. Leptoquarks first appeared in Ref. [671] in Pati and Salam's $SU(4)$ model, where lepton number was considered to be the fourth colour. They also appear in Grand Unified theories, extended technicolor models and compositeness models. The nomenclature and classification are based on their transformation properties under the SM gauge groups [672, 673].

In ep collisions LQs can be produced in an s-channel resonance via their coupling to the first generation of quarks, the signature being a peak in the invariant mass of the outgoing ℓq system. Contrary to what is achievable in the LHC environment, it has been shown that at the LHeC many properties of the LQs can be measured with high precision [1].

The search for LQs at the LHC is essentially insensitive to the coupling LQ-e-q, characterized by the parameter λ, since the dominant process is pair production via the strong interaction. Recent searches have therefore been able to exclude LQs of the first generation of mass up to 1.4 TeV, assuming a branching ratio to charged leptons = 1.0. For other generations, the bounds are ~ 1 TeV. (for the latest results, see, for example Ref. [674, 675]). Under the assumption that the LQ has O(0.1) branching ratios to a number of tested final states, there remains some parameter space where the LHeC can make a significant contribution in the search for LQs.

For LQs with masses below the centre-of-mass energy of the collider, suitable searches promise a sensitivity to λ as small as $\mathcal{O}(10^{-3})$. As shown in [676], production of the first generation scalar leptoquarks at LHeC can have a much higher cross section than at the LHC. The authors also show that a sensitivity to the Yukawa coupling, for the LQs called $R_2^{5/3} \sim (\mathbf{3}, \mathbf{2}, 7/6)$ and
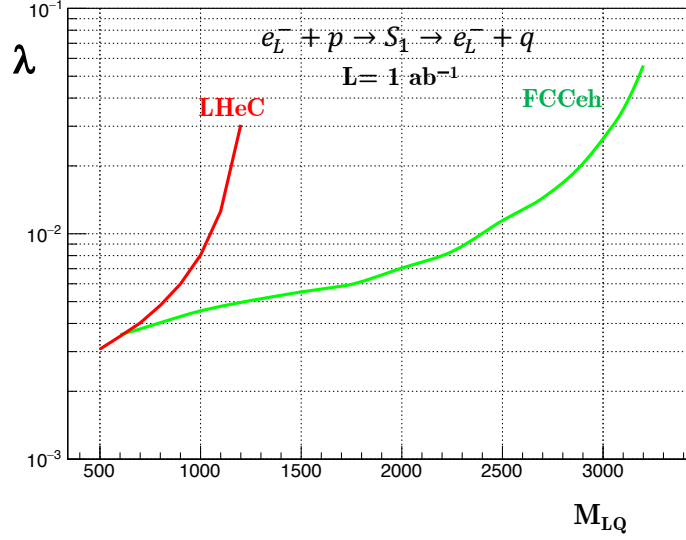
Figure 8.14: Estimated 2σ significance for the coupling λ at LHeC and FCC-eh for the scalar lepto-quark S_1 as a function of its mass, assuming $1\,\mathrm{ab}^{-1}$ luminosity and no systematic uncertainty.

$\tilde{R}_2^{2/3} \sim (\mathbf{3},\mathbf{2},1/6)$, better than the electromagnetic strength (~ 0.3) of 5σ can be reached up to a mass of $1.2\,\mathrm{TeV}$.

For the S_1 scalar leptoquark $(\bar{\mathbf{3}},\mathbf{1},1/3)$, an estimate of the sensitivity of the LHeC and the FCC-eh as a function of the LQ mass and LL Yukawa coupling is shown in Fig. 8.14, assuming $1\,\mathrm{ab}^{-1}$ of integrated luminosity. Here, the signal was generated at leading order using MadGraph with the model files from Ref. [677], with hadronisation performed by Herwig7 [368,678] and detector simulation with Delphes [467]. The SM background $e^- p \to e^- j$ was also generated at leading order. A simple set of cuts on the p_T of the leading electron and jet and a window on the invariant mass of the e-jet system was applied.

The $\tilde{R}_2^{2/3}$ scalar LQ allows for coupling to right-handed neutrinos, providing interesting search channels. Its signatures at ep colliders have been investigated recently [679,680]. In the lepton + jet final state, it is found that LHeC can probe up to $1.2\,\mathrm{TeV}$ at 3σ significance with an e^- beam, and at 5σ discovery with an e^+ beam and $1\,\mathrm{ab}^{-1}$ of integrated luminosity. At FCC-eh, a 5σ discovery can be reached with an e^- beam up to $\sim 2.3\,\mathrm{TeV}$ and $1\,\mathrm{ab}^{-1}$ of integrated luminosity.

8.6.2 Z' mediated charged lepton flavour violation

Charged lepton flavour violating signatures are well tested involving electrons and muons, but less so when they involve tau leptons. Interestingly, in many extensions of the SM lepton flavour is much more strongly violated in the tau sector whilst weaker experimental constraints at low energy exist. In Ref. [681] the Z' mediated $e - \tau$ (and $e - \mu$) conversion processes are studied at the LHeC, considering the lepton flavour violating processes $pe^- \to \tau^- j$ (and $pe^- \to \mu^- j$).

For this LHeC study, a 60-GeV electron beam with up to 80% polarization is considered, to achieve a centre-of-mass energy close to $1.3\,\mathrm{TeV}$ with a total of $1\,\mathrm{ab}^{-1}$ integrated luminosity. Several backgrounds featuring tau leptons are considered, a parameterised reconstruction efficiency and mis-identification for tau jets is included in the analysis. To distinguish between the signal events and all relevant backgrounds, 31 kinematic variables (at the reconstruction level after the detector simulation) are used as input to a tool for Multi-Variate Analysis (TMVA).
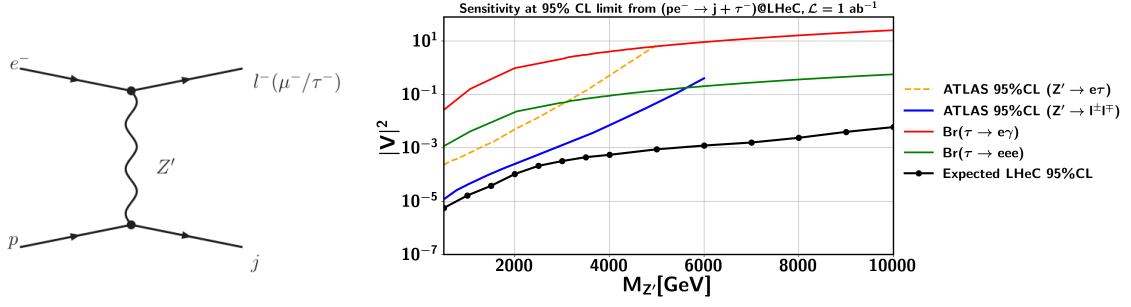
Figure 8.15: Left: Feynman diagram for the e-τ (and e-μ) conversion processes $pe^- \to \tau^- + j$ (and $pe^- \to \mu^- + j$) mediated by a Z' with flavour-violating couplings to charged leptons at the LHeC. Right: Limits on the coupling parameter $|V|^2$ for signal hypothesis compared with the existing limits from experimental constraints on the relevant flavour conserving and flavour violating processes. The black line is the LHeC sensitivity for the process $pe^- \to \tau j$. For the other limits, see text.

A BDT algorithm is used to separate the signal events from the background events. Systematic uncertainties are evaluated and are found to be around 2%.

Asuming equal couplings $|V_R^{ij}| = |V_L^{ij}| \equiv |V|$ of the Z' to quark-quark or lepton-lepton flavours i, j, the LHeC is found to be sensitive to Z' masses up to $\mathcal{O}(10)$ TeV, as depicted in Fig. 8.15 by the black line. Included in the Figure are also the existing limits from ATLAS searches for Z' decays into $e\tau$ [682] and the search for same flavour final states [683]. The experimental limits based on the branching ratio $\mathrm{BR}(\tau \to e\gamma)$ [684] and $\mathrm{BR}(\tau \to eee)$ [685] are also reported.

Overall, lepton flavour violation in the tau sector can be tested extremely well at the LHeC, surpassing the sensitivity of the LHC and low energy experiments in the whole considered mass range by more than two orders of magnitude. This is particularly interesting for very heavy Z' that are not accessible for direct production, where the LHeC provides an exciting new discovery channel for this kind of lepton flavour violating processes.

8.6.3 Vector-like quarks

In composite Higgs models, new vector-like quarks are introduced. The third generation is favored, in particular the top-partner (T) with charge 2/3. The prospects of detecting T at the LHeC are discussed in Ref. [686]. For this search a simplified model is considered where T is produced from positron proton scattering via intergenerational mixing and decays as $T \to tZ$, with the final state $\nu_e \ell^+ \ell^- bjj'$, considering $E_e = 140$ GeV. The authors find that for $L = 1/\mathrm{ab}$ masses for the top partner T around 800 GeV can be tested when the model-related coupling constants are $\mathcal{O}(0.1)$ and that mixing between T and the first generation quarks can significantly enhance the LHeC sensitivity.

Another search strategy for singly produced top partners is given by their decays $T \to Wb$ and $T \to th$, which is presented in Ref. [687]. The analysis is based on a simplified model where the top partner is an $SU_L(2)$ singlet and interacts only with the third generation of quarks. It considers collisions of positrons and protons with $E_e = 140$ GeV. The analysis, carried out at the parton level, investigates the kinematic distributions of the final states. Useful kinematic variables for the bW final state were found to be the transverse momentum of the lepton, b-jet missing energy, while for the th final state the most useful observable is the transverse hadronic energy. For masses of $\mathcal{O}(1)$ TeV the LHeC is found to be sensitive to the new interactions when they are $\mathcal{O}(0.1)$ for $L = 1/\mathrm{ab}$, in agreement with [686]. A very similar analysis was performed

for the $T \to Wb$ signal channel with comparable results [688].

8.6.4 Excited fermions (ν^*, e^*, u^*)

The potential of searches for excited spin-1/2 and spin-3/2 neutrinos are discussed in Ref. [689]. For the analysis the authors consider effective currents that describe the interactions between excited fermions, gauge bosons, and SM leptons. For the signature, the production of the excited electron neutrino ν^* and its subsequent decay $\nu^* \to We$ with $W \to jj$ was chosen. The analysis, carried out at the parton level, considers $E_e = 60\,\mathrm{GeV}$, and consists in a study of the kinematic distributions of the final states. It is concluded that the signature can be well distinguished from backgrounds, and that other lepton-hadron colliders would be required to test the excited neutrinos of different flavours.

Analyses in similar models, considering electron-proton collisions at energies of the FCC-eh and beyond, were carried out for excited electron neutrinos and are presented in Ref. [690]. An analysis for the reach for testing excited electrons is discussed in Ref. [691], and for excited quarks in a composite model framework in Ref. [692].

8.6.5 Colour octet leptons

Unresolved issues of the SM, like family replication and quark-lepton symmetry, can be addressed by composite models, where quarks, leptons, and gauge bosons are composite particles made up of more basic constituents. One general class of particles, predicted in most composite models, are colour octet leptons, which are bound states of a heavy fermion and a heavy scalar particle that is assumed to be colour-charged. In this scenario each SM lepton is accompanied by a colour octet lepton, which may have spin 1/2 or 3/2. Since they are unobserved, the compositeness scale is expected to be at least $\mathcal{O}(1)\,\mathrm{TeV}$.

At the LHeC, the colour octet partner of the electron e_8 can be produced through the process $e^-p \to e_8 g + X$ and studied via its decays products. An analysis including the study of kinematic distributions that were obtained at the parton level is presented in Ref. [693]. It was shown that discovery prospects exist for masses of $\mathcal{O}(\mathrm{TeV})$. A similar analysis is performed for the FCC-eh at much higher energies in Ref. [694].

8.6.6 Quark substructure and Contact interactions

Several long-standing questions arise in the SM, such as those enumerated in Section 1.1. Perhaps most seriously, the SM does not appear to provide a clear, dynamical raison d'être for the existence of quarks. Leptons and quarks appear in the Standard Model in a symmetric way, sharing electromagnetic interaction with the same charge quantization and with a cancellation of anomaly in the family structure. This strongly suggests that they may be composed of the same fundamental constituents, or that they form a representation of an extended gauge symmetry group of a Grand Unified Theory.

Assuming that the electron is a point-like particle, the quark substructure can be investigated
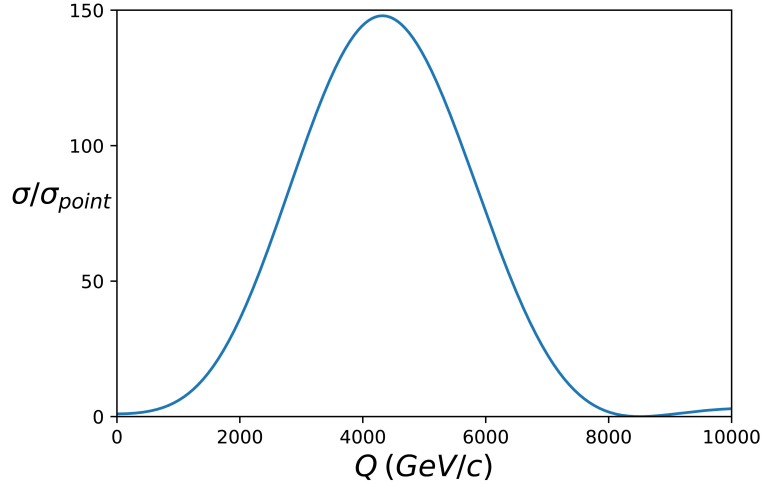
Figure 8.16: Form factor effect in the e-p interaction produced by substructure according to Model II of Hofstadter [700] with the model parameters given in the text.

by introducing a form factor $f_q(Q^2)$ to describe deviations of the *ep* scattering cross section:

$$\frac{d\sigma}{dQ^2} = \frac{d\sigma^{SM}}{dQ^2} f_q^2(Q^2) \tag{8.1}$$

$$f_q^2(Q^2) \simeq 1 - \frac{R^2}{6}Q^2 \tag{8.2}$$

Here, R is the rms electric charge quark radius. The present limit from HERA is 4.3×10^{-19} m [695] while it is estimated that LHeC will be sensitive up to $\sim 10^{-19}$ m [696].

An electric precursor to QCD was formulated in 1969 that assumed that hadron constituents are highly electrically charged and where the strong attraction between positive and negative constituents was assumed to bind them together [697]. Neither the electric model nor Schwinger's comparable model of monopoles [698] reproduce the observed particle spectrum of hadrons, or the observed pattern of weak interactions. The ATLAS Collaboration has recently reported searches for free magnetic monopoles and free highly electrically charged particles produced in *pp* collisions at 13 TeV [699]. No candidates were detected with one or two Dirac magnetic charges or with electric charges $20e < |z| < 100e$. This extends the results of previous searches made at lower energies and in cosmic rays or bulk matter. A simple picture of what might emerge with highly electrically charged constituents is obtained by modeling the proton's substructure by a charge of (say) $21|e|$ smeared uniformly over a region of radius 10^{-19} m, and two charges of $-10|e|$ smeared over a larger region of radius 2×10^{-19} m. The model II by Hofstadter [700] predicts the form factor results shown in Fig. 8.16, consistent the HERA upper limit.

More generally [701], contact interactions can be parameterized in the Lagrangian by coupling coefficients η_{ij}^q where the indices i, j indicate the left-handed or right-handed fermion helicities and q the quark flavor. The interaction can be of a scalar, vector or tensor nature and the interference with SM currents can be constructive or destructive. It has been estimated that the LHeC can be sensitive to a scale of contact interaction of $\sim 40 - 60$ TeV with 100 fb^{-1} of integrated luminosity [696] while the present LHC limits are between 20 and 40 TeV, depending on the sign of the interference [702, 703].

8.7 Summary and conclusion

The lack of new physics at the LHC to date forces the community to develop new theoretical ideas as well as to explore the complementarities of pp machines with other possible future facilities. In the context of ep colliders, several studies are being carried out to understand the potential to search for new physics, considering that many interactions can be tested at high precision that are otherwise not easily accessible.

At ep colliders, most BSM physics is accessed via vector-boson fusion, which suppresses the production cross section quickly with increasing mass. Nonetheless, scalar extensions of the SM as well as neutrino-mass related BSM physics can be well tested at ep due to the smallness and reducibility of the SM backgrounds. The absence of pile up and complicated triggering makes searches for soft-momenta final state particles feasible, so that results for BSM theories for example characterised by the presence of non-prompt, long-lived particles are complementary to those at the LHC. Additionally, the excellent angular acceptance and resolution of the detector also renders the LHeC a very suitable environment for displaced vertex searches. An increase in the centre-of-mass energy as high as the one foreseen at the FCC would naturally boost the reach in most scenarios considerably.

Finally, it is worth noting that the LHeC can offer different or indirect ways to search for new physics. It was shown recently that Lorentz invariance violation in the weak vector-boson sector can be studied in electron-proton scattering [704] via a Fourier-analysis of the parity violating asymmetry in deep inelastic scattering. Moreover, New Physics could be related to nucleon, nuclear, and top structure functions as discussed in Refs. [40, 705, 706]. Investigating of the $B_c^{(*)}$ meson and doubly heavy baryon also was shown to have discovery potential for New Physics [707–709].

Chapter 9

Influence of the LHeC on Physics at the HL-LHC

After almost 10 years of scientific exploitation of the LHC and about $175\,\mathrm{fb}^{-1}$ of proton-proton collision data delivered to each of the ATLAS and CMS experiments, the sensitivity of a significant fraction of leading measurements and searches becomes limited by systematic uncertainties. Uncertainties induced by the strong interaction, in particular related to the proton structure, play a prominent role and tend to saturate the physics reach of the experiments. This context will only become more evident when the LHC enters its high-luminosity era.

With high precision PDFs measured independently from the other LHC experiments, the LHeC project can resolve this situation. It allows a clean study of the pure QCD effects it aims at measuring, resolving the ambiguity between new physics effects at high mass and PDF uncertainties that intrinsically affects the interpretation of proton-proton data alone. At the weak scale, improved PDFs provide a significant boost to the achievable precision of measurements of the Higgs boson properties and of fundamental electroweak parameters. The LHeC is thus a perfect companion machine for the HL-LHC, allowing a full exploitation of the data and significantly extending its reach.

The present chapter illustrates this with a few selected examples in the domain of precision measurements of the W-, Z- and Higgs boson properties. The impact of precise PDFs on searches for TeV-scale new physics is also illustrated. Besides, the complementarity of PDF studies at the LHeC and the HL-LHC and the impact of new QCD dynamics at small x on measurements at hadronic colliders, as well as the impact of electron-nucleus scattering data on heavy-ion physics at the LHC, are presented.

9.1 Precision Electroweak Measurements at the HL-LHC

9.1.1 The effective weak mixing angle

Prospective studies for the measurement of the effective weak mixing angle using the forward-backward asymmetry, A_{FB}, in Drell-Yan di-lepton events at the HL-LHC were performed at ATLAS [710], CMS [711] and LHCb [712] and reported in the CERN report on Standard Model physics at the HL-LHC [185]. A brief summary is given here, focusing on the impact of the LHeC on this measurement.

At leading order, lepton pairs are produced through the annihilation of a quark and antiquark via the exchange of a Z boson or a virtual photon. The definition of A_{FB} is based on the angle θ^* between the initial- and final-state fermions:

$$A_{\mathrm{FB}} = \frac{\sigma_{\mathrm{F}} - \sigma_{\mathrm{B}}}{\sigma_{\mathrm{F}} + \sigma_{\mathrm{B}}}, \tag{9.1}$$

where σ_{F} and σ_{B} are the cross sections in the forward ($\cos\theta^* > 0$) and backward ($\cos\theta^* < 0$) hemispheres, respectively.

A non-zero A_{FB} in dilepton events arises from the vector and axial-vector couplings of electroweak bosons to fermions. At tree level, the vector and axial-vector couplings of the Z boson to a fermion f are

$$g_V^f = T_3^f - 2Q_f \sin^2\theta_W, \qquad g_A^f = T_3^f. \tag{9.2}$$

The coupling ratio, $g_V^f/g_A^f = 1 - 4|Q_f|\sin^2\theta_W$, generates the asymmetry. Defining

$$\mathcal{A}_f = 2\frac{g_V^f/g_A^f}{1 + (g_V^f/g_A^f)^2} \tag{9.3}$$

one finds, for a given sub-process $q\bar{q} \to Z \to \ell^+\ell^-$,

$$A_{\mathrm{FB}} = \frac{3}{4}\mathcal{A}_q\mathcal{A}_\ell. \tag{9.4}$$

As discussed in Sects. 5.1 and 9.1.3 below, Eq. (9.2) is subject to radiative corrections introducing the effective weak mixing angle $\sin^2\theta_{\mathrm{eff}}^\ell$ in replacement of the leading order observable $\sin^2\theta_W$. The asymmetry definitions downstream are however unchanged.

The angle θ^* is uniquely defined in e^+e^- collisions, where the directions of the e^+ and e^- beams are known. In proton-antiproton collisions, at the Tevatron, the incoming quarks and anti-quarks also have preferred directions, and a non-zero asymmetry exists for all lepton-pair rapidities. At the LHC the beams are symmetric, and a non-zero asymmetry only appears for high-rapidity events, as the direction of the longitudinal boost reflects, on average, the direction of the incoming valence quark. While the expected Z-boson statistics are very large, with $\mathcal{O}(3 \times 10^9)$ events expected in ATLAS and CMS, the measuremend is thus highly affected by PDF uncertainties, and in particular by the u and d valence and sea distributions.

Prospective studies were performed by ATLAS, CMS and LHCb, including a discussion of expected PDF uncertainties. The impact of LHeC PDFs was evaluated by ATLAS and is discussed further. Tab. 9.1 compares the published ATLAS result [440] with the prospects for $3\,\mathrm{ab}^{-1}$, for a variety of PDF sets. The statistical uncertainty is at the level of 3×10^{-5} with this sample, and the experimental systematic uncertainties are improved by $10-25\,\%$ depending on the PDF scenario considered. While MMHT2014 [713] and CT14 [714] claim comparable PDF uncertainties, the size of the PDF uncertainty is reduced at the HL-LHC thanks to the increased sample size, which helps constraining this component *in situ*. The HL-LHC PDF set [256], which incorporates the expected constraints from present and future LHC data, further decreases the associated uncertainty by about 20%. The LHeC projection [54] results from a QCD fit to $1\,\mathrm{ab}^{-1}$ of *ep* scattering pseudodata, with $E_e = 60\,\mathrm{GeV}$ and $E_p = 7\,\mathrm{TeV}$; in this case, the PDF uncertainty is subleading compared to the experimental systematics.

Fig. 9.1 compares the ATLAS sensitivity studies of $\sin^2\theta_{\mathrm{eff}}^\ell$ to previous measurements from the LHC experiments [439–441, 715], and to the legacy measurements by the experiments at LEP and SLC [436] and the Tevatron [438]. The precision of the measurement of the weak mixing

Parameter	Unit	ATLAS (Ref. [440])	HL-LHC projection		
		MMHT2014	CT14	HL-LHC PDF	LHeC PDF
Centre-of-mass energy, $\sqrt{s}$	TeV	8	14	14	14
Int. luminosity, $\mathcal{L}$	fb^{-1}	20	3000	3000	3000
Experimental uncert.	10^{-5}	$\pm\,23$	$\pm\,9$	$\pm\,7$	$\pm\,7$
PDF uncert.	10^{-5}	$\pm\,24$	$\pm\,16$	$\pm\,13$	$\pm\,3$
Other syst. uncert.	10^{-5}	$\pm\,13$	–	–	–
Total uncert., $\Delta\sin^2\theta_W$	10^{-5}	$\pm\,36$	$\pm\,18$	$\pm\,15$	$\pm\,8$

Table 9.1: The breakdown of uncertainties of $\sin^2\theta_W$ from the ATLAS preliminary results at $\sqrt{s} = 8$ TeV with $20\,\text{fb}^{-1}$ [440] is compared to the projected measurements with $3000\,\text{fb}^{-1}$ of data at $\sqrt{s} = 14$ TeV for two PDF sets considered in this note. All uncertainties are given in units of 10^{-5}. Other sources of systematic uncertainties, such as the impact of the MC statistical uncertainty, evaluated in Ref. [440] are not considered in the HL-LHC prospect analysis.

angle in Z-boson events, using 3000 fb^{-1} of pp collision data at $\sqrt{s} = 14$ TeV, exceeds the precision achieved in all previous single-experiments to date. The LHeC is thus essential in exploiting the full potential of the HL-LHC data for this measurement.
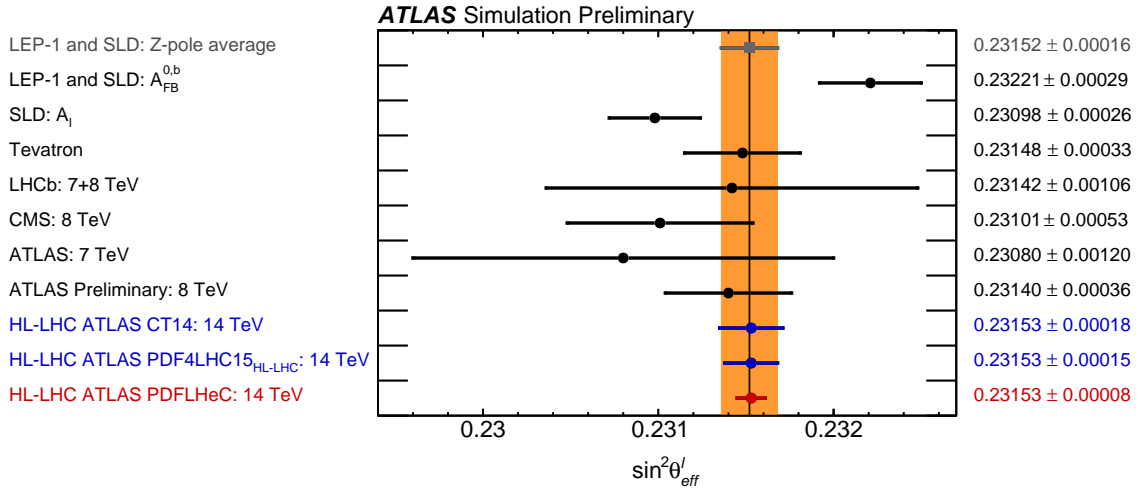

Figure 9.1: Comparison of measurements or combinations of $\sin^2\theta^\ell_{\text{eff}}$ with the world average value (orange band) and the projected uncertainties of measurements at the HL-LHC. For the HL-LHC the central values are set to the world average value and uncertainties are displayed for different assumptions of the available PDF sets, similar to Tab. 9.1.

9.1.2 The W-boson mass

This section summarises a study describing prospects for the measurement of m_W with the upgraded ATLAS detector, using low pile-up data collected during the HL-LHC period [716]. Similar features and performance are expected for CMS.

Proton-proton collision data at low pile-up are of large interest for W boson physics, as the low detector occupancy allows an optimal reconstruction of missing transverse momentum, and the W production cross section is large enough to achieve small statistical uncertainties in a moderate running time. At $\sqrt{s} = 14$ TeV and for an instantaneous luminosity of $\mathcal{L} \sim 5 \times 10^{32}\,\text{cm}^{-2}\text{s}^{-1}$,

corresponding to two collisions per bunch crossing on average at the LHC, about $\times 10^7$ W boson events can be collected in one month. Such a sample provides a statistical sensitivity at the permille level for cross section measurements, at the percent level for measurements of the W boson transverse momentum distribution, and below $4\,\mathrm{MeV}$ for a measurement of m_W.

Additional potential is provided by the upgraded tracking detector, the ITk, which extends the coverage in pseudorapidity beyond $|\eta| < 2.5$ to $|\eta| < 4$. The increased acceptance allows W-boson measurements to probe a new region in Bjorken x at $Q^2 \sim m_W^2$. This will in turn allow further constraints on the parton density functions (PDFs) from cross section measurements, and reduce PDF uncertainties in the measurement of m_W. A possible increase of the LHC centre-of-mass energy, such as the HE-LHC program with $\sqrt{s} = 27\,\mathrm{TeV}$ [717], could play a similar role on a longer timescale.

Leptonic W boson decays are characterised by an energetic, isolated electron or muon, and significant missing transverse momentum reflecting the decay neutrino. The hadronic recoil, u_T, is defined from the vector sum of the transverse momenta of all reconstructed particles in the event excluding the charged lepton, and provides a measure of the W boson transverse momentum. Lepton transverse momentum, p_T^ℓ, missing transverse momentum, $E_\mathrm{T}^\mathrm{miss}$, and the hadronic recoil are related through $\vec{E}_\mathrm{T}^\mathrm{miss} = -(\vec{p}_\mathrm{T}^\ell + \vec{u}_\mathrm{T})$. The p_T^ℓ and $E_\mathrm{T}^\mathrm{miss}$ distributions have sharp peaks at $p_\mathrm{T}^\ell \sim E_\mathrm{T}^\mathrm{miss} \sim m_W/2$. The transverse mass m_T, defined as $m_\mathrm{T} = \sqrt{2 p_\mathrm{T}^\ell E_\mathrm{T}^\mathrm{miss} \cos(\phi_\ell - \phi_\mathrm{miss})}$, peaks at $m_\mathrm{T} \sim m_W$.

Events are selected applying the following cuts to the object kinematics, after resolution corrections:

- $p_\mathrm{T}^\ell > 25\,\mathrm{GeV}$, $E_\mathrm{T}^\mathrm{miss} > 25\,\mathrm{GeV}$, $m_\mathrm{T} > 50\,\mathrm{GeV}$ and $u_\mathrm{T} < 15\,\mathrm{GeV}$;

- $|\eta_\ell| < 2.4$ or $2.4 < |\eta_\ell| < 4$.

The first set of cuts select the range of the kinematic peaks of the W boson decay products, restricting to the region of small p_T^W to maximise the sensitivity of the distributions to m_W. Two pseudorapidity ranges are considered, corresponding to the central region accessible with the current ATLAS detector, and to the forward region accessible in the electron channel with the ITk.

The W-boson mass is determined comparing the final state kinematic peaks in the simulation to those observed in the data, and adjusting the value of m_W assumed in the former to optimise the agreement. The shift in the measured value of m_W resulting from a change in the assumed PDF set is estimated using a set of template distributions obtained for different values of m_W and a given reference PDF set, and "pseudo-data" distributions obtained for an alternate set representing, for example, uncertainty variations with respect to the reference set. The PDF uncertainty for a given set is calculated by summing the shifts obtained for all uncertainty variations in quadrature.

The PDF uncertainty is calculated for the CT14 [714], MMHT2014 [713], HL-LHC [256] and LHeC [54] PDF sets and their associated uncertainties. Compared to current sets such as CT14 and MMHT2014, the HL-LHC set incorporates the expected constraints from present and future LHC data; it starts from the PDF4LHC convention [252] and comes in three scenarios corresponding to more or less optimistic projections of the experimental uncertainties.

The expected statistical and PDF uncertainties are illustrated in Tab. 9.2 and Fig. 9.2. The CT10 and CT14 sets yield comparable uncertainties. The MMHT2014 uncertainties are about $30\,\%$ lower. The three projected HL-LHC PDF sets give very similar uncertainties; scenario 2

is the most conservative and shown here. Compared to CT10 and CT14, a reduction in PDF uncertainty of about a factor of two is obtained in this case.

The LHeC sample can be collected in about three years, synchronously with the HL-LHC operation. In this configuration, the neutral- and charged-current DIS samples are sufficient to disentangle the first (d, u) and second (s, c) generation parton densities without ambiguity, and reduce the PDF uncertainty below $2\,\mathrm{MeV}$, a factor 5–6 compared to present knowledge. Also in this case the m_W measurement will benefit from the large W boson samples collected at the LHC, and from the combination of the central and forward categories. In this context, PDF uncertainties would be sub-leading even with $1\,\mathrm{fb}^{-1}$ of low pile-up LHC data.

Parameter	Unit	ATLAS (Ref. [431])	HL-LHC projection			
		CT10	CT14	HL-LHC	LHeC	LHeC
Centre-of-mass energy, $\sqrt{s}$	TeV	7	14	14	14	14
Int. luminosity, $\mathcal{L}$	fb^{-1}	5	1	1	1	1
Acceptance		$\|\eta\| < 2.4$	$\|\eta\| < 2.4$	$\|\eta\| < 2.4$	$\|\eta\| < 2.4$	$\|\eta\| < 4$
Statistical uncert.	MeV	± 7	± 5	± 4.5	± 4.5	± 3.7
PDF uncert.	MeV	± 9	± 12	± 5.8	± 2.2	± 1.6
Other syst. uncert.	MeV	± 13	-	-	-	
Total uncert. Δm_W	MeV	± 19	13	7.3	5.0	4.1

Table 9.2: Measurement uncertainty of the W-boson mass at the HL-LHC for different PDF sets (CT14, HL-LHC PDF and LHeC PDF) and lepton acceptance regions in comparison with a measurement by ATLAS [431]. The HL-LHC projections are obtained from a combined fit to the simulated p_T^ℓ and m_T distributions.
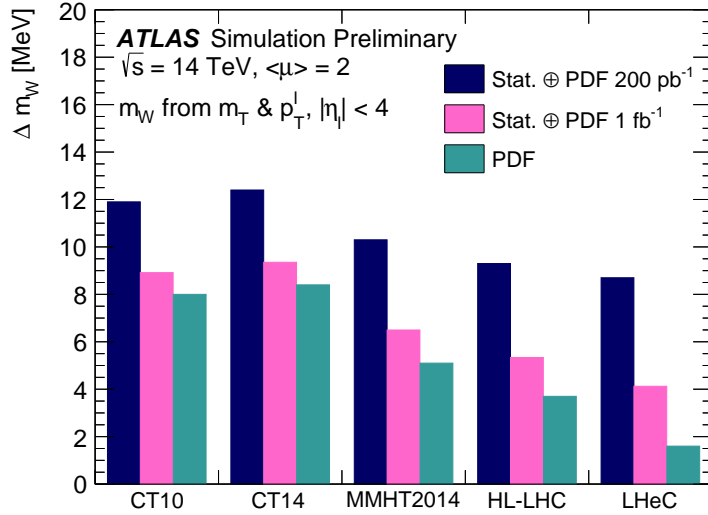

Figure 9.2: Measurement uncertainty of m_W at the HL-LHC with $200\,\mathrm{pb}^{-1}$ (dark blue) and $1\,\mathrm{fb}^{-1}$ (pink) of collected low pile-up data for different present and future PDF sets. The green area indicates the PDF uncertainty from those sets alone. The projections are obtained from a combined fit to the simulated p_T^ℓ and m_T distributions in the acceptance $|\eta| < 4$.

.

9.1.3   Impact on electroweak precision tests

The theoretical expressions for the electroweak parameters discussed above are functions of the other fundamental constants of the theory. In the Standard Model, an approximate expression for m_W, valid at one loop for $m_H > m_W$, is [436]

$$m_W^2 = \frac{m_Z^2}{2}\left(1 + \sqrt{1 - \frac{\sqrt{8}\pi\alpha_{em}}{G_{\mathrm{F}}m_Z^2}\frac{1}{1-\Delta r}}\right), \tag{9.5}$$

$$\Delta r = \Delta\alpha_{em} - \frac{\cos^2\theta_W}{\sin^2\theta_W}\Delta\rho, \tag{9.6}$$

$$\Delta\rho = \frac{3G_{\mathrm{F}}m_W^2}{8\sqrt{2}\pi^2}\left[\frac{m_{\mathrm{top}}^2}{m_W^2} - \frac{\sin^2\theta_W}{\cos^2\theta_W}\left(\ln\frac{m_H^2}{m_W^2} - \frac{5}{6}\right) + \cdots\right]. \tag{9.7}$$

Δr includes all radiative corrections to m_W, $\Delta\alpha_{em}$ is the difference between the electromagnetic coupling constant evaluated at $q^2 = 0$ and $q^2 = m_Z^2$, and $\Delta\rho$ is the quantum correction to the tree-level relation $\rho \equiv m_W^2/(m_Z^2\cos^2\theta_W) = 1$, defined as $\rho = 1 + \Delta\rho$.

Similarly, approximate one-loop expressions for the vector and axial-vector couplings between the Z boson and the fermions, g_V and g_A, are

$$g_V = \sqrt{1 + \Delta\rho}\left(T_3 - 2Q(1 + \Delta\kappa)\sin^2\theta_W\right), \tag{9.8}$$

$$g_A = \sqrt{1 + \Delta\rho}\,T_3\,, \tag{9.9}$$

where

$$\Delta\kappa = \frac{3G_{\mathrm{F}}m_W^2}{8\sqrt{2}\pi^2}\left[\frac{\cos^2\theta_W}{\sin^2\theta_W}\frac{m_{\mathrm{top}}^2}{m_W^2} - \frac{10}{9}\left(\ln\frac{m_H^2}{m_W^2} - \frac{5}{6}\right) + \cdots\right]. \tag{9.10}$$

At two loops, also the strong coupling constant enters.

A large class of theories beyond the SM predict particles that contribute to the W- and Z-boson self-energies, modifying the above expressions. From the point of view of on-shell observables of the W and Z, these modifications are usually parameterized using the so-called *oblique* parameters, called S, T and U [718]. Their values are by definition 0 in the SM and, for example, a significant violation of the relation between m_W, m_H and m_{top} would translate into non-zero values for S and T.

A typical application of this formalism consists in using the measured properties of the W and Z bosons, the top quark mass, and the values of coupling constants, to derive an indirect determination of the Higgs boson mass in the SM and compare the latter to the measured value. Beyond the SM, the measured values can be used to derive allowed contours in the (S, T) plane.

Present and future measurement uncertainties for the most relevant electroweak parameters are summarised in Tab. 9.3, and are used to evaluate the impact of the improved measurements on electroweak precision tests. Specifically, we consider the effect of improved measurements of m_W and $\sin^2\theta_{\mathrm{eff}}^\ell$ discussed in this chapter, and of the improved precision of α_{s} discussed in Chapter 4. In addition, we consider an ultimate precision of $300\,\mathrm{MeV}$ for the top quark mass measured at the LHC.

The results are illustrated in Figs. 9.3 and 9.4. The former results from a fit performed using the GFitter framework [433], and compares the indirect determinations of the Higgs boson mass

Parameter	Unit	Value	Uncertainty	
			Present	Expected
m_Z	MeV	91187.6	2.1	2.1
m_W	MeV	80385	15	5
$\sin^2\theta^\ell_{\text{eff}}$		0.23152	0.00016	0.00008
m_{top}	GeV	173.1	0.7	0.3
$\alpha_{\text{s}}(M_{\text{Z}})$		0.1179	0.0010	0.0001

Table 9.3: Present uncertainties for the relevant EW precision observables [134, 181, 436], and their expected precision in the LHeC and HL-LHC era.
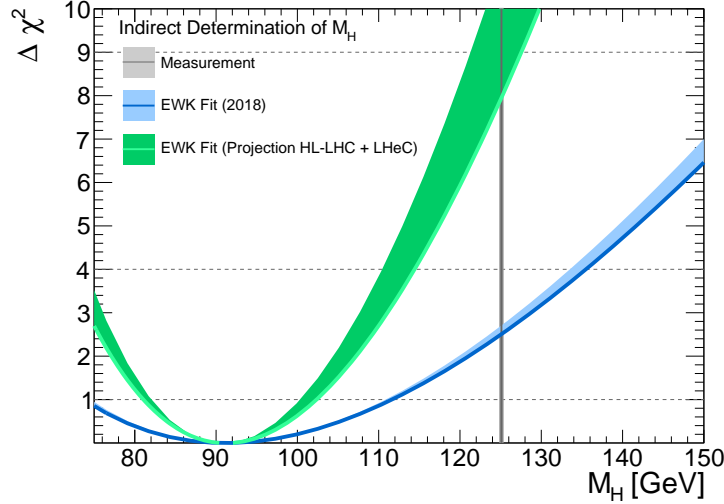
Figure 9.3: Comparisons of χ^2 distributions for different Higgs boson mass values, using present and future experimental uncertainties. The theoretical uncertainties are indicated by the filled areas. The Gfitter program [433] was used for this analysis.

for the present and expected measurement precisions. The indirect uncertainty in m_H reduces from about 20 % to 10 %.

Fig. 9.4 was performed using HEPfit [719], and compares allowed contours for the S and T parameters. Here also, the allowed region is reduced by a factor of about two from the improved measurements of m_W, $\sin^2\theta^\ell_{\text{eff}}$, m_{top} and α_{s}. Improved theoretical calculations in the SM will provide an additional reduction of 10-15 %.

In summary, the LHeC data promises significant improvements in the measurement precision of fundamental electroweak parameters such as m_W and $\sin^2\theta^\ell_{\text{eff}}$. The improved measurements enhance the sensitivity of electroweak tests by a factor of two or more.

9.2 Higgs Physics

9.2.1 Impact of LHeC data on Higgs cross section predictions at the LHC

A detailed analysis of Higgs boson production cross sections was given in the report on Higgs Physics at the HL-LHC and HE-LHC [720]. Central values at $\sqrt{s} = 14\,\text{TeV}$ and the corresponding uncertainties are reported in Tab. 9.4. Perturbative uncertainties (labelled $\Delta\sigma_{\text{scales}}$ in

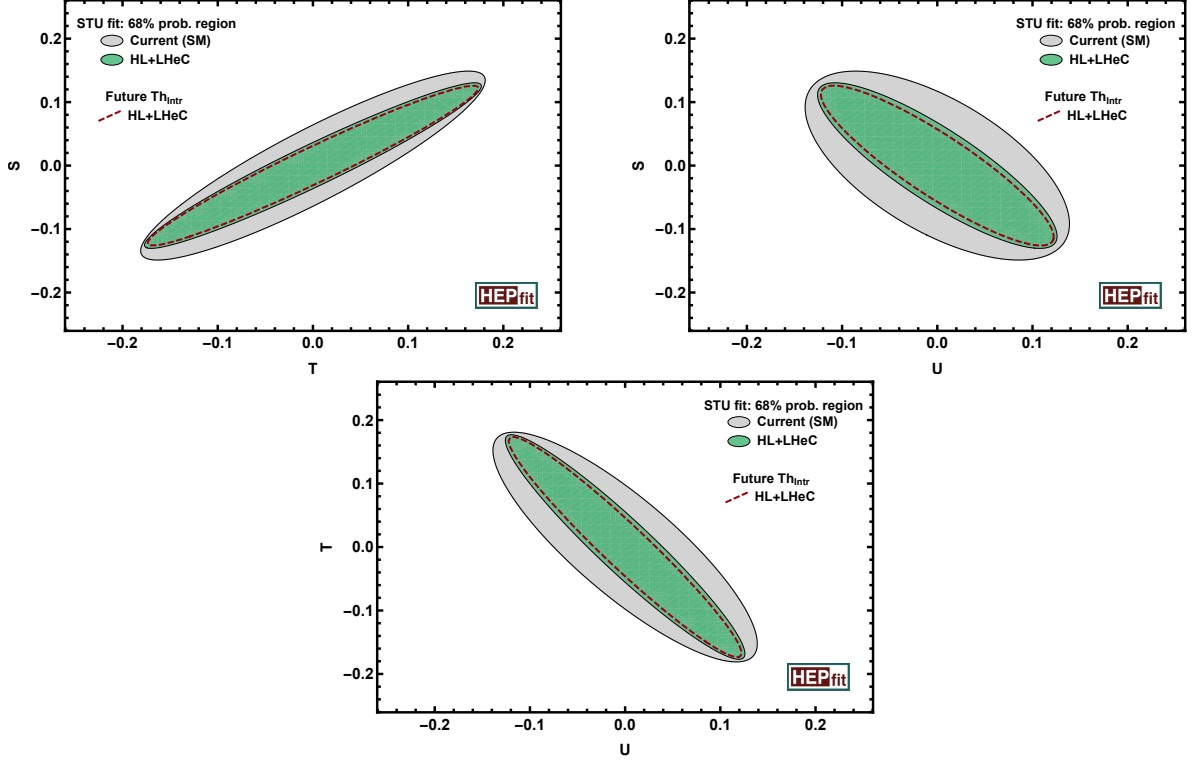**Figure 9.4:** Allowed regions in the (S,T,U) plane showing all three combinations: S vs T (top-left), S vs U (top-right), T vs U (bottom). The grey and green areas indicate the currently allowed region and the LHeC projection, respectively. The dashed line indicates the effect of expected theoretical improvements. The HEPfit program [719] was used for this analysis.

Tab. 9.4) generally dominate compared to the contributions of α_s and the PDFs. This is especially true for gluon fusion, where the residual theoretical uncertainties correspond to missing corrections beyond N³LO in QCD, and for $t\bar{t}H$ production which is known to NLO QCD+EW accuracy. The weak boson fusion, WH and ZH cross sections are known to NNLO QCD + NLO EW accuracy; residual theoretical uncertainties are smaller for these weak interaction processes.

In Ref. [720], α_s-related uncertainties are propagated assuming $\alpha_s = 0.118 \pm 0.0015$, and the assumed PDF uncertainties reflect the HL-LHC prospects [256]. They are in excess of 3 % for gluon fusion and $t\bar{t}H$, below 2 % for WH and ZH, and 0.4% for weak boson fusion. The LHeC uncertainties in Tab. 9.4 are calculated using MCFM [721], interfaced to PDFs determined from LHeC pseudodata as described in Chapter 3. Assuming the prospects for α_s and PDFs described in Chapters 3 and 4, and with the exception of weak-boson fusion production, the corresponding uncertainties decrease by a factor 5 to 10.

The important, beneficial role of ep PDF information for LHC Higgs physics can also be illustrated using the predictions for the total cross section, $pp \rightarrow HX$ at the LHC. This has recently been calculated [722] to N³LO pQCD. In Fig. 9.5 calculations of this cross section are shown for several recent sets of parton distributions, calculated with the iHix code [723], including the LHeC set.

The effect of these improvements on Higgs boson coupling determination at the HL-LHC is at present modest, due to the combined effect of still significant perturbative uncertainties and of the expected experimental systematic uncertainties. The influence of the LHeC on these measurements is further discussed in the next section.

Process	σ_H [pb]	$\Delta\sigma_{\text{scales}}$	$\Delta\sigma_{\text{PDF}+\alpha_{\text{s}}}$	
			HL-LHC PDF	LHeC PDF
Gluon-fusion	54.7	5.4 %	3.1 %	0.4 %
Vector-boson-fusion	4.3	2.1 %	0.4 %	0.3 %
$pp \to WH$	1.5	0.5 %	1.4 %	0.2 %
$pp \to ZH$	1.0	3.5 %	1.9 %	0.3 %
$pp \to t\bar{t}H$	0.6	7.5 %	3.5 %	0.4 %

Table 9.4: Predictions for Higgs boson production cross sections at the HL-LHC at $\sqrt{s} = 14\,\text{TeV}$ and its associated relative uncertainties from scale variations and two PDF projections, HL-LHC and LHeC PDFs, $\Delta\sigma$. The PDF uncertainties include uncertainties of α_{s}.
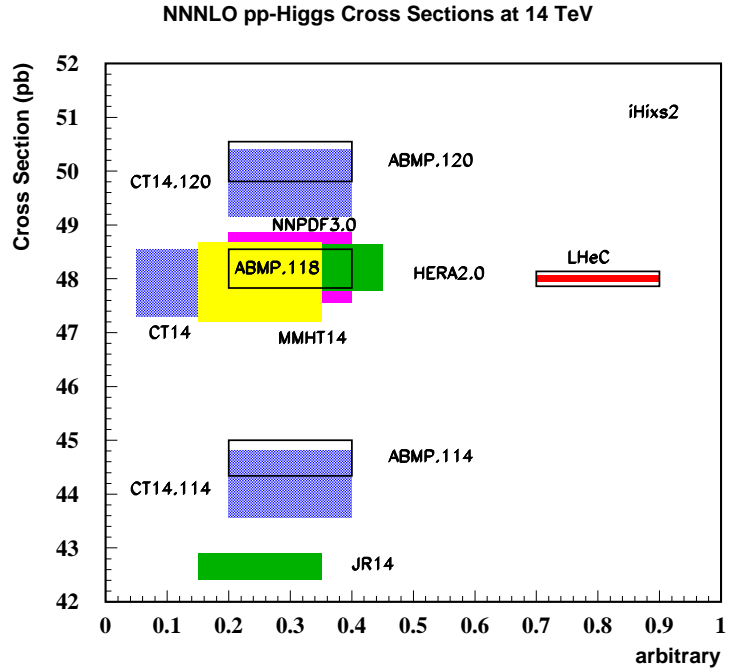
Figure 9.5: Cross sections of Higgs production calculated to N³LO using the iHix program [723] for existing PDF parameterisation sets (left side) and for the LHeC PDFs (right side). The widths of the areas correspond to the uncertainties as quoted by the various sets, having rescaled the CT14 uncertainties from 90 to 68 % C.L. Results (left) are included also for different values of the strong coupling constant $\alpha_{\text{s}}(M_Z^2)$, from 0.114 to 0.120. The inner LHeC uncertainty band (red) includes the expected systematic uncertainty due to the PDFs while the outer box illustrates the expected uncertainty resulting from the determination of α_{s} with the LHeC.

9.2.2 Higgs Couplings from a simultaneous analysis of *pp* and *ep* collision data

The LHC data collected during the Runs I and II have provided a first exploration of the properties of the Higgs boson. The so-called κ framework [724] – which allows modifications of the SM-like couplings of the Higgs boson to each SM particle i, parameterised by coupling

modifiers κ_i – has been widely used for the interpretation of these measurements. With current data, the κ parameters associated to the main couplings of the Higgs can be determined to a precision of roughly 10-20 %, see e.g. [725].[1] This knowledge will be further improved at the high-luminosity phase of the LHC, reaching a precision in many cases well below the 10 % level [720]. Even at the HL-LHC it will however, be difficult to obtain sensible measurements of certain Higgs interactions, especially the coupling to charm quarks. Such gap would be covered by the precise measurements of that channel at the LHeC, as described in Sect. 7. Channels measured to a few percent accuracy at both HL-LHC and LHeC would provide important cross checks and additional physics information because of the different dominant Higgs production mechanisms, $gg \to H$ in pp and $WW \to H$ in ep. There follows a remarkable complementarity between the measurements from both machines and a joint precision that is comparable to that at ILC or CLIC [726], which yet have the important possibility to determine the total cross section through the $e^+e^- \to Z^* \to ZH$ reaction. Furthermore, as also explained in Sect. 7, the LHeC environment allows very precise determinations of certain interactions, well beyond of what will be possible at the high-luminosity pp collider. In this subsection we briefly describe the complementarity between the Higgs measurements at the pp and ep colliders, illustrated via a combined fit to the HL-LHC and LHeC projections in the κ framework.

For a detailed description of the Higgs physics program at the LHeC we refer to Chapter 7. The only information not included in the fit presented in this section is that of the determination of the top Yukawa coupling, since projections from that study are performed assuming any coupling other than κ_t to be SM like. Comments in this regard will be made, when necessary, below.

For the HL-LHC inputs of the combined fit we rely on the projections presented in Ref. [720], as used in the comparative study in Ref. [726]. These HL-LHC inputs include projections for the total rates in the main production (ggF, VBF, VH and ttH) and decay channels ($H \to bb$, $\tau\tau$, $\mu\mu$, ZZ^*, WW^*, $\gamma\gamma$, $Z\gamma$). They are available both for ATLAS and CMS. Regarding the theory systematics in these projections, we assume the scenario S2 described in [720], where the SM theory uncertainties are reduced by roughly a factor of two with respect to their current values, a reduction to which LHeC would contribute by eliminating the PDF and α_s parts of the uncertainty, see Fig. 9.5. Theory systematics are assumed to be fully correlated between ATLAS and CMS. These projections are combined with LHeC ones, where, as in Ref. [726], we use the future projections for the SM theory uncertainties in the different production cross sections and decay widths. In the κ fit performed here we assume: (1) no Higgs decays into particles other than the SM ones; (2) heavy particles are allowed to modify the SM loops, so we use effective κ parameters to describe the SM loop-induced processes, i.e. we use κ_g, κ_γ, $\kappa_{Z\gamma}$ as free parameters. The total list of free parameters considered for this combined HL-LHC+LHeC κ fit is, therefore,

$$\{\kappa_b,\ \kappa_t,\ \kappa_\tau,\ \kappa_c,\ \kappa_\mu,\ ,\kappa_Z,\ \kappa_W,\ \kappa_g,\ \kappa_\gamma,\ \kappa_{Z\gamma}\}, \tag{9.11}$$

for a total of 10 degrees of freedom. Coupling modifiers associated to any other SM particles are assumed to be SM-like, $\kappa_i = 1$.

The results of the HL-LHC+LHeC fit, which has been performed using the HEPfit code [719], are shown in Tab. 9.5, and Fig. 9.6 and its zoomed version Fig. 9.7 [2]. The increment in constraining power after adding the LHeC measurements is especially apparent for the couplings to W bosons and b quarks, bringing an improvement with respect to the HL-LHC result of a factor $\simeq 3$. As

---

[1]Note that at the LHC one can only determine coupling ratios.

[2]The κ analysis of the LHeC has been performed independently using a MINUIT based fit program leading to perfect agreement with the HEPfit result.

Parameter	Uncertainty		
	HL-LHC	LHeC	HL-LHC+LHeC
κ_W	1.7	0.75	0.50
κ_Z	1.5	1.2	0.82
κ_g	2.3	3.6	1.6
κ_γ	1.9	7.6	1.4
$\kappa_{Z\gamma}$	10	–	10
κ_c	–	4.1	3.6
κ_t	3.3	–	3.1
κ_b	3.6	2.1	1.1
κ_μ	4.6	–	4.4
κ_τ	1.9	3.3	1.3

Table 9.5: Results of the combined HL-LHC + LHeC κ fit. The output of the fit is compared with the results of the HL-LHC and LHeC stand-alone fits. The uncertainties of the κ values are given in per cent.
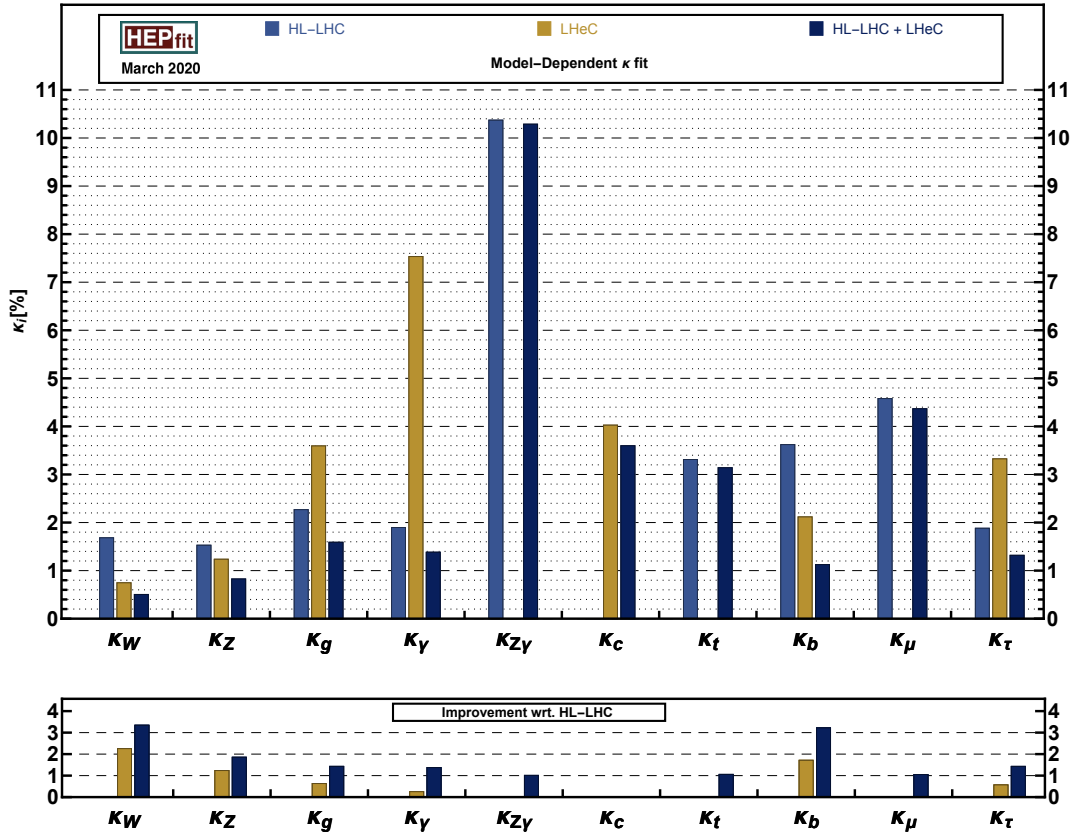
Figure 9.6: Top: Uncertainty of the determination of the scale factor κ in the determination of the Higgs couplings, in per cent. Results are given of the combined HL-LHC + LHeC κ fit (dark blue) and of the HL-LHC (blue) and LHeC (gold) stand-alone fits. There is no accurate measurement expected of κ_c at the LHC. Likewise the precision of the rare channels $Z\gamma$, $t\bar{t}$ and $\mu\mu$ will be very limited at the LHeC. Bottom: Improvement of the κ determinations through the addition of the ep information (gold) and by the combined $ep + pp$ analysis (dark blue), calculated with respect to the HL-LHC prospects. Strong improvements are seen for the W, Z and b couplings, while that for charm cannot be illustrated here as κ_c is considered to be not measurable at the HL-LHC.
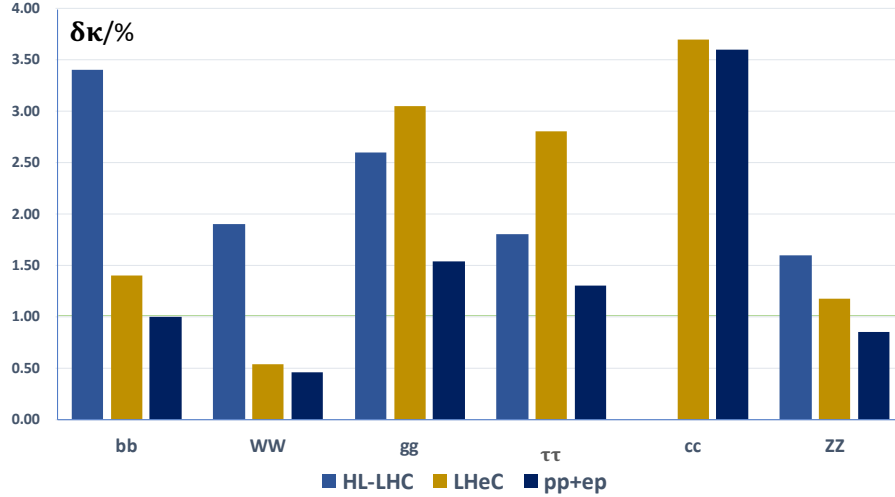
Figure 9.7: Uncertainty of the determination of the scale factor κ in the determination of the Higgs couplings, in per cent. Zoom of Fig. 9.6 into the six most frequent H decay channels. Results are given of the combined HL-LHC + LHeC κ fit (dark blue) and of the HL-LHC (blue) and LHeC (gold) stand-alone fits. There is no accurate measurement expected of κ_c at the LHC.

explained at the beginning of this section, the LHeC measurements also bring the possibility of setting sensible constraints on the Higgs interactions with charm quarks, with a precision of roughly 4%. The HL-LHC measurements, in turn, fill some of the *gaps* in the fit at the LHeC, where there is little sensitivity to the couplings involved in rare Higgs decays, e.g. $H \to \mu\mu$ and $H \to Z\gamma$. This makes apparent the complementarity between the measurements at ep and pp machines, with the former leading in terms of precision in the largest Higgs couplings, while the high-luminosity of the latter brings sensitivity to the smaller interactions.

Finally, as mentioned at the beginning, we did not include in this combined $ep+pp$ fit the projections for top Yukawa interactions at the LHeC from Section 7.5, as these were not derived in a global setup, but rather setting all other interactions involved in $\bar{t}H\nu_e$ product to their SM values. However, the main uncertainty from the other κ parameters is expected to come from the W and b couplings, κ_W and κ_b, which are determined with an overall precision of $\sim 0.8\%$ and 2%. Therefore one expects the LHeC result, $\delta\kappa_t \sim 17\%$ for $L = 1\,\mathrm{ab}^{-1}$, to be minimally affected. This number is to be compared with the HL-LHC projection of $\sim 4\%$, which is expected to dominate in a combined result.

9.3   Further precision SM measurements at the HL-LHC

The LHeC measurements and the results from their phenomenological interpretations will have an important impact on many areas of the HL-LHC physics programme. This goes far beyond the precision electroweak and the Higgs physics, as discussed at hand of dedicated analyses in the previous sections, and BSM or eA physics as discussed in the subsequent sections. In this section a few further selected topics of the Standard Model (SM) physics programme at the LHC and HL-LHC are discussed, where substantial improvements due to the LHeC can be expected.

In general, two distinct aspects can be considered for any SM measurement in that respect [3]:

---

[3]In some cases, a model- or physics parameter is directly extracted from the experiment data and the two

- improvements of the analysis of the recorded event data, and
- improvements of the phenomenological interpretation of the measurements.

In order to assess the impact of the LHeC for the first bullet, one must recollect that an essential key ingredient of the analysis of any hadron collider data is the utilisation of phenomenological models, and commonly QCD inspired Monte Carlo (MC) event generators are employed. These are used for calibration, corrections of limited acceptance and resolution effects (*unfolding*), training of machine learning algorithms for event or object classification, extrapolations from the *fiducial* to the *full* phase space, estimates of different background sources and also signal extraction. Although the implemented models are derived from more fundamental equations like the QCD Lagrangian, a number of model parameters remain poorly known and have to be *tuned* with data. Also, since most models involve approximations and may be numerically limited, any model needs to be validated, or invalidated, with independent measurements prior to its usage, of course. With more and more data being recorded at the (HL-)LHC, statistical uncertainties become very small and systematic uncertainties are reduced due to improved calibration and analysis algorithms, so that uncertainties associated to the MC event models become important and are limiting the accuracy of the HL-LHC measurements. It must be noted, that the MC parameters should be tuned with data from another experiment in order to avoid a potential bias of the actual measurement due to experimental correlations.

For the second bullet, the phenomenological interpretation of hadron collider measurements, like for instance tests of pQCD or the determination of SM parameters (e.g. $\alpha_{\rm s}(M_{\rm Z})$, $\sin^2\theta^{\ell}_{\rm eff}$, m_W, the κ parameters, ...), the proton PDFs and SM parameter which are input to the prediction must be known with high accuracy, most noteworthy the value of $\alpha_{\rm s}(M_{\rm Z})$.

The most important inputs of the LHeC to the HL-LHC measurements are of course the precise determination of the PDFs and $\alpha_{\rm s}(M_{\rm Z})$, see Chapter 3. These will improve both, the data analysis and its interpretation. Beyond that, the measurements of charged particle spectra, jet shape and jet substructure observables, jet cross sections and event shape observables or heavy flavor cross sections will help to improve MC models further, for instance with the determination of charm and bottom-quark masses, heavy quark (c, b) fragmentation functions and fragmentation fractions, finding optimal choices for all scales involved in a MC model, or determining the optimal parameters for the parton shower. Such measurements can be performed with high precision at the LHeC, since DIS represents a superior QCD laboratory. This is because in the final state there is always a lepton, which is used for trigger and vertexing, and simultaneously a hadronic system which is then subject of interest. In addition, the overconstrained kinematic system allows for the precise calibration of hadronic final state objects, and furthermore limiting effects like minimum bias definition or pile-up are absent.

In the following, a few selected subjects are discussed at hand of LHC analyses performed with Run-I data at $\sqrt{s} = 8$ or $13\,{\rm TeV}$, and thus giving a tangible indication about challenges at future HL-LHC measurements:

- The measurement of the integrated top-quark pair cross section represents an outstanding benchmark quantity for the entire field of top-quark physics. Its measurement for top-transverse momenta $p^t_{\rm T} > 400\,{\rm GeV}$ in the *lepton+jets* decay channel yields a high experimental precision with both, small statistical and systematic uncertainties. However, its measurement precision is limited by theoretical uncertainties (also called *modelling* uncertainties), and the largest individual source stems from the PDFs [181, 728]. A related

---

applications are merged into a single analysis workflow, for instance in many LHC top-quark mass analyses. Additionally to these two aspects, of course, the complementary of the physics case of *ep* collisions enhances our understanding of the fundamental laws of physics.
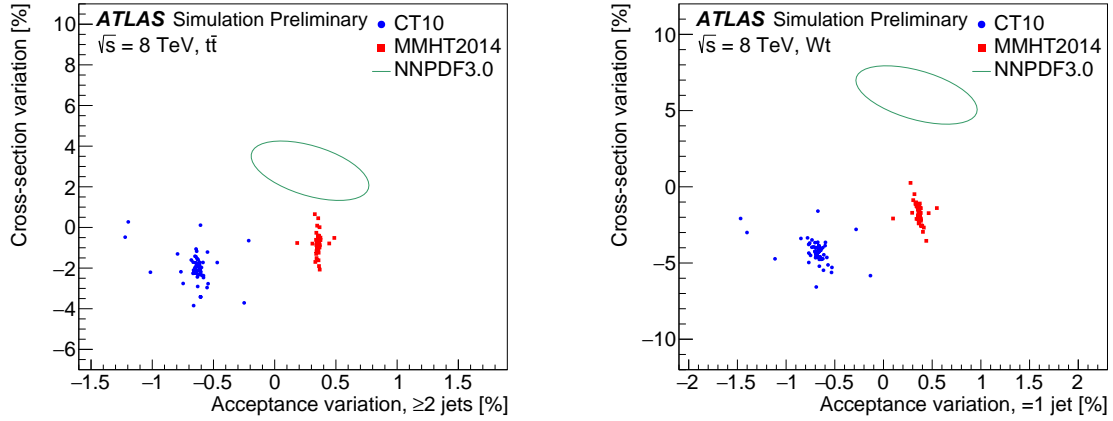
Figure 9.8: Impact of PDF uncertainty from CT10 and MMHT2014 eigenvectors or NNPDF3.0 replicas, on the cross section and the acceptance correction for top pair production $t\bar{t}$ (left) and single top production Wt (right) (taken from Ref. [727]). Events are selected with at least two jets or with exactly one jet, respectively. Depending on the PDF set and eigenvector employed, the cross sections varies by up to 5–7 % for top-pair and more than 10 % for single-top production. Also the acceptance correction varies by about 0.5–1 % for different PDF sets, and can become as large as 2.5 % for different PDF sets and eigenvectors. Since the acceptance correction has to be imposed for the measurement, the limited knowledge of the PDFs introduces a sizeable modelling uncertainty on the measurement.

study of PDF effects on the acceptance correction for the integrated top-pair production cross section and single-top production Wt is displayed in Fig. 9.8. The acceptance correction changes by up to 0.5–1 % for different PDF sets, and can become as large as 2.5 % for different PDF sets and eigenvectors. Another very important uncertainty for top-quark measurements is from the modelling of the parton shower. Both uncertainties from the PDFs and from parton shower modelling, are expected to be significantly reduced with LHeC data.

- The determination of the top-quark mass m_t from LHC data requires the precise modelling of the physics and all background processes with suitable MC models. Today, the value of m_t is determined most precisely from a combination of such individual analyses, and uncertainties of 0.4–0.8 GeV are reported [181, 729–733]. Any of these individual precision determinations are limited by model uncertainties, and therefore improvements at the HL-LHC cannot be obtained with more data, but only with improved models. Some of the model uncertainties, e.g. PDF, parton shower, hadronisation or fragmentation related uncertainties can expected to be reduced with LHeC data.

- At the HL-LHC also rare decay channels can be exploited for precision measurements. For example, the top-quark mass can be determined from top-quark pair production with a subsequent decay, where one b-quark hadronises into a B-hadron which then decays through a J/ψ-meson into a pair of muons, $t\bar{t} \rightarrow W^+bW^-b \rightarrow \ell\nu_\ell J/\psi(\rightarrow \mu^+\mu^-)Xqq'b$ [734]. Such a measurement requires the precise knowledge of b-quark fragmentation, which can be well measured at the LHeC, and will thus improve the HL-LHC measurement.

- The value of the strong coupling constant $\alpha_s(M_Z)$ is one of the least known fundamental parameters in physics and an improved determination with new measurement constitutes a real challenge for LHC an HL-LHC experiments. A large number of observables at the LHC are *per-se* sensitive to $\alpha_s(M_Z)$, and its value was determined in the past from various definitions of jet cross section observables (see e.g. [156, 157, 735, 736]) or transverse
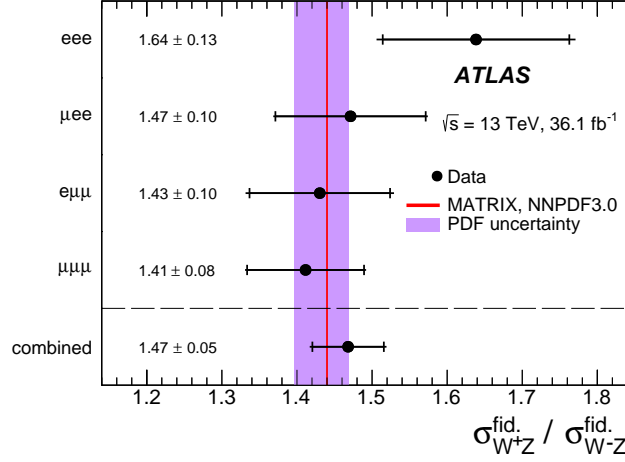
Figure 9.9: Measurement of the ratio of di-boson $\sigma(W^+Z)/\sigma(W^-Z)$ integrated cross sections in a fiducial phase space for four different decay channels and their combination at $\sqrt{s} = 13\,\text{TeV}$ in comparison with NNLO predictions [744, 745] (taken from Ref. [746]). The total uncertainties of the data points are dominated by statistical uncertainties and will be reduced in the future. The shaded violet band indicates the size of the PDF uncertainties that limits the overall interpretation of the measurement.

energy-energy correlations [737], Z+jet cross sections [738], integrated [739] or differential top-quark cross sections [740], inclusive W or Z production [741, 742], prompt photon data [743], and many other observables (see Ref. [181] for a review). Although the harsh environment in high-luminosity hadron-hadron collisions requires sophisticated analysis techniques and dedicated measurements, small experimental uncertainties for $\alpha_{\text{s}}(M_{\text{Z}})$ could be achieved. Hence, α_{s} determinations are nowadays limited due to theoretical uncertainties and the dominant uncertainties are most commonly PDF related [738, 739, 741, 742] (only for observables where NNLO predictions are not yet applicable, the scale uncertainties may overshoot the PDF uncertainties). Therefore, already today the knowledge of the PDFs represent the limiting factor, and a significant reduction of the total uncertainty for $\alpha_{\text{s}}(M_{\text{Z}})$ can (only) be achieved with PDFs determined at the LHeC.

- The production of $W^{\pm}Z$ pairs in pp collisions provides a crucial test of the electroweak sector of the SM, since di-boson production is sensitive to the gauge-boson self-interactions. Already small deviations in the observed distributions could provide indications for new physics. The process can be well measured in a high-pile up environment and can be well separated from its huge QCD background. However, due to the relatively small $W^{\pm}Z$ cross sections high statistical precision can only be achieved with high luminosity. Recent measurement of $W^{\pm}Z$ pairs at $\sqrt{s} = 13\,\text{TeV}$ based on $36\,\text{fb}^{-1}$ of integrated luminosity have been performed by ATLAS and CMS [746, 747]. In Fig. 9.9 the ratio of fiducial cross sections $\sigma_{W^+Z}/\sigma_{W^-Z}$ is displayed. The largest individual uncertainty is the statistical uncertainty and therefore future measurements at the LHC and HL-LHC are of great importance in order to reach higher precision. Nontheless, already today, the overall phenomenological interpretation is limited by PDF uncertainties, as visible from Fig. 9.9, and these can be improved best with PDFs from LHeC.

In the situation of the absence of indications for new physics, an important goal of the future LHC and HL-LHC physics programme has to be devoted to precision measurements. From the examples discussed above (W-boson mass and Higgs measurements are discussed in previous sections), it becomes obvious that limiting factors of such measurements arise from the signal

and MC modelling, where PDF uncertainties constitute a limiting factor, and also improved understandings of parton shower, hadronisation and fragmentation processes are of importance. These aspects can all be ameliorated with independent precision measurements at the LHeC.

Similarly, the phenomenological interpretation of many processes is already today limited by PDF uncertainties, and as outlined, α_s determinations, di-boson processes, top-mass or top-cross section measurements, and many other topics, require a higher precision for PDFs. In the HL-LHC era, where data and predictions are more precise, the detailed knowledge of the PDFs will become of even greater importance.

9.4 High Mass Searches at the LHC

9.4.1 Strongly-produced supersymmetric particles

The potential of the HL- and HE-LHC to discover supersymmetry was extensively discussed in Ref. [748]. Here we focus on searches for gluinos within MSSM scenarios. Gluino pairs are produced through the strong interaction, and their production cross section is relatively large; naturalness considerations indicate that gluino masses should not exceed a few TeV and lie not too far above the EW scale. Hence, they are certainly among the first particles that could be discovered at the HL-LHC.

In the following we assume that a simplified topology dominates the gluino decay chain, culminating in jets plus missing energy originating from a massless LSP, $\tilde{\chi}_0$. Ref. [748] evaluated the sensitivity of the HL- and HE-LHC to gluino pair production with gluinos decaying exclusively to $q\bar{q}\tilde{\chi}_0$, through off-shell first and second generation squarks, using a standard search for events with jets and missing transverse energy. Currently, the reach for this simplified model with $36\,\mathrm{fb}^{-1}$ of $13\,\mathrm{TeV}$ data is roughly $2\,\mathrm{TeV}$ gluinos, for a massless LSP [749, 750]. Extrapolating to $3\,\mathrm{ab}^{-1}$ at $14\,\mathrm{TeV}$, the limit grows to $3.2\,\mathrm{TeV}$. For $15\,\mathrm{ab}^{-1}$ at $27\,\mathrm{TeV}$, a limit of $5.7\,\mathrm{TeV}$ was found.

When deriving limits, an overall systematic uncertainty of 20% was assumed on the SM background contributions, and a generic 10% uncertainty was assumed on the signal normalisation, not taking into account PDF-related uncertainties which are as large as 50% for gluinos around $3\,\mathrm{TeV}$. The effect of this additional source of uncertainty was found to induce a variation in the mass limit by $\pm 200\,\mathrm{GeV}$ at the HL-LHC, and as much as $\pm 500\,\mathrm{GeV}$ at the HE-LHC.

We can revert this argument, and claim that with present PDF knowledge, mass limits could be as low as $3.0\,\mathrm{TeV}$ and $5.3\,\mathrm{TeV}$ at the HL- and HE-LHC, respectively. Data from the LHeC would make this contribution negligible compared to other sources of uncertainty. Compared to the most conservative scenario, the increase in sensitivity would correspond to an increase in centre-of-mass energy by approximately 5 to 10%.

9.4.2 Contact interactions

New, high-mass gauge bosons are most often searched for in resonant final states. Peaks in the invariant-mass distributions of electron, muon or jet pairs directly reflect the presence of such new particles; the accessible mass range is limited by the available centre-of-mass energy.

Particles with a mass beyond the kinematic limit generally interfere with the Z boson and the photon, generating non-resonant deviations in the invariant mass distributions. Such models

can be parameterised as contact interactions (CI) between two initial-state quarks and two final-state leptons of given chirality:

$$\mathcal{L}_{\text{CI}} = \frac{g^2}{\Lambda^2}\eta_{ij}(\bar{q}_i\gamma_\mu q_i)(\bar{\ell}_i\gamma^\mu\ell_i), \tag{9.12}$$

where $i, j = \text{L}$ or R (for left- or right-handed chirality), g is a coupling constant set to be 4π by convention, and Λ is the CI scale. The sign of η_{ij} determines whether the interference between the SM Drell–Yan (DY) process, $q\bar{q} \to Z/\gamma^* \to \ell^+\ell^-$, is constructive or destructive.

The size and sign of the observed deviation with respect to the SM probes the scale and interference pattern of the interaction. The sensitivity of the search is limited by experimental uncertainties (finite statistics and experimental systematic uncertainties) and by uncertainties in the theoretical modelling of the DY background.

The most recent results of the ATLAS and CMS Collaborations [702, 703] are based on e^+e^- and $\mu^+\mu^-$ final states in $36\,\text{fb}^{-1}$ of data, and probe CI's up to a typical scale of $25\,\text{TeV}$, depending on the chirality and sign of the interaction coupling parameter. The limits derived by ATLAS, summarised in Tab. 9.6, accounted for theoretical uncertainties induced by the PDFs and by α_{s}. The dominant PDF uncertainty was estimated from the 90% CL uncertainty in the CT14nnlo PDF set, adding an envelope from the comparison of the CT14nnlo, MMHT2014 and NNPDF3.0 [751] central sets. The strong coupling constant uncertainty was propagated assuming $\alpha_{\text{s}} = 0.118 \pm 0.003$, with a subleading effect.

The present study evaluates the sensitivity of this search at the HL-LHC. The increase in sensitivity is estimated using samples of Standard-Model like pseudo data, corresponding to the integrated luminosity of $3\,\text{ab}^{-1}$. In a first step, both the experimental and theoretical systematic uncertainties are kept in the publication. In this regime, the extrapolated statistical uncertainty is typically a factor 5 to 10 smaller than the theoretical uncertainty. Improvements from the LHeC in α_{s} and in the proton PDFs are incorporated in a second step. Assuming the prospects described in Chapter 3, α_{s} and PDF uncertainties are smaller than the statistical fluctuations and can be neglected in a first approximation.

The results are summarised in Tab. 9.6. Everything else equal, increasing the sample size from $36\,\text{fb}^{-1}$ to $3\,\text{ab}^{-1}$ enhances the CI reach by a typical factor of two. Accounting for the improvement in the theoretical modelling of the DY process brought by the LHeC brings another factor of 1.5–1.8 in the limits. In the last case, the limits reach well into range directly accessible with proton-proton collisions at $\sqrt{s} = 100\,\text{TeV}$, as envisioned at the FCC-hh.

| Model | ATLAS (Ref. [702]) | HL-LHC | |
	$\mathcal{L} = 36\,\text{fb}^{-1}$ (CT14nnlo)	$\mathcal{L} = 3\,\text{ab}^{-1}$ (CT14nnlo)	$\mathcal{L} = 3\,\text{ab}^{-1}$ (LHeC)
LL (constr.)	28 TeV	58 TeV	96 TeV
LL (destr.)	21 TeV	49 TeV	77 TeV
RR (constr.)	26 TeV	58 TeV	84 TeV
RR (destr.)	22 TeV	61 TeV	75 TeV
LR (constr.)	26 TeV	49 TeV	81 TeV
LR (destr.)	22 TeV	45 TeV	62 TeV

Table 9.6: Contact interaction limits from ATLAS based on $36\,\text{fb}^{-1}$ of data [702], and extrapolated to the full HL-LHC dataset ($3\,\text{ab}^{-1}$). The extrapolation is performed assuming the same PDF and α_{s} uncertainties as in Ref. [702], and assuming the improved uncertainties as obtained from the LHeC.

9.5 PDFs and the HL-LHC and the LHeC

As discussed in the previous Sections, a precise determination of PDFs is an essential ingredient for the success of the HL-LHC. Conversely, the HL-LHC itself offers a significant opportunity to improve our understanding of proton structure. In this Section we will discuss the possibilities that the combination of HL-LHC ad LHeC measurements offer for the determination of PDFs in the proton.

9.5.1 PDF Prospects with the HL-LHC and the LHeC

In Ref. [256] the HL-LHC potential to constrain PDFs was analysed in detail, focussing on SM processes that are expected to have the most impact at higher x. In particular, projections for the production of top quark pairs, inclusive jets, forward W + charm quark and direct photons, as well as forward and high–mass Drell-Yan and the Z boson $p_\perp$ distribution were included. It was found that PDF uncertainties on LHC processes can be reduced by a factor between two and five, depending on the specific flavour combination and on the optimistic assumptions about the reduction of the (experimental) systematic uncertainties.

It is of interest to compare these constraints with those expected to come from the LHeC itself, as well as potential improvements from a combined PDF fit to the HL-LHC and LHeC datasets; this was studied in [59]. The basic procedure consists in generating HL-LHC and LHeC pseudodata with the PDF4LHC15 set [252] and then applying Hessian PDF profiling [254, 752], in other words a simplified version of a full refit, to this baseline to assess the expected impact of the data. While the HL-LHC datasets are described above, the LHeC pseudodata correspond to the most recent publicly available official LHeC projections, see Section 3.2, for electron and positron neutral-current (NC) and charged-current (CC) scattering. As well as inclusive data at different beam energies ($E_p = 1, 7\,\mathrm{TeV}$), charm and bottom heavy quark NC and charm production in e^-p CC scattering are included.

The expected impact of the HL-LHC, LHeC and their combination on the PDF uncertainties of the gluon, down quark, anti–up quark and strangeness distributions are shown in Fig. 9.10. One observes that at low x the LHeC data place in general by far the strongest constraint, in particular for the gluon, as expected from its greatly extended coverage at small x. At intermediate x the impact of the HL-LHC and LHeC are more comparable in size, but nonetheless the LHeC is generally expected to have a larger impact. At higher x the constraints are again comparable in size, with the HL-LHC resulting in a somewhat larger reduction in the gluon and strangeness uncertainty, while the LHeC has a somewhat larger impact for the down and anti–up quark distributions. Thus, the combination of both HL-LHC and LHeC pseudodata nicely illustrate a clear and significant reduction in PDF uncertainties over a very wide range of x, improving upon the constraints from the individual datasets in a non-negligible way.

9.5.2 Parton luminosities at the HL-LHC

In Fig. 9.11 we show the impact on the gluon-gluon, quark-gluon, quark-antiquark and quark-quark partonic luminosities for a centre-of-mass energy $\sqrt{s} = 14\,\mathrm{TeV}$. Some clear trends are evident from this comparison, consistent with the results from the individual PDFs. We can in particular observe that at low mass the LHeC places the dominant constraint, while at intermediate masses the LHeC and HL-LHC constraints are comparable in size, and at high mass the stronger constraint on the gluon-gluon and quark-gluon luminosities comes from the
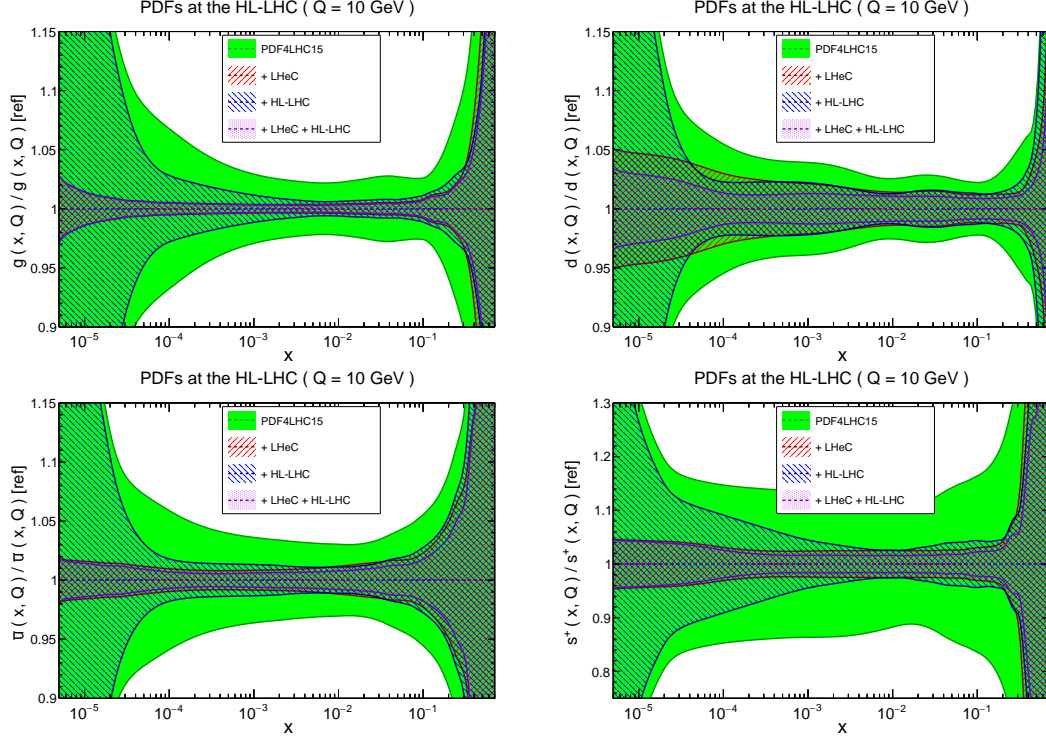
Figure 9.10: Impact of LHeC on the 1-σ relative PDF uncertainties of the gluon, down quark, anti–up quark and strangeness distributions, with respect to the PDF4LHC15 baseline set (green band). Results for the LHeC (red), the HL-LHC (blue) and their combination (violet) are shown.

HL-LHC, with the LHeC dominating for the quark-quark and quark-antiquark luminosities. As in the case of the PDFs, for the partonic luminosities the combination of the HL-LHC and LHeC constraints leads to a clear reduction in the PDF uncertainties in comparison to the individual cases, by up to an order of magnitude over a wide range of invariant masses, M_X, of the produced final state.

In summary, these results demonstrate that while the HL-LHC alone is expected to have a sizeable impact on PDF constraints, the LHeC can improve our current precision on PDFs significantly in comparison to this, in particular at low to intermediate x. Moreover, the combination of both the LHeC and HL-LHC pseudodata leads to a significantly superior PDF error reduction in comparison to the two facilities individually. Further details, including LHeC-only studies as well as an investigation of the impact of the PDF baseline on the uncertainty projections, can be found in Ref. [59].

9.5.3 PDF Sensitivity: Comparing HL-LHC and LHeC

While the experimental reach of each facility in the $\{x, Q^2\}$ kinematic plane provides a useful comparison, there are more factors to consider – especially when we are striving for ultra-high precision measurements. One measure that provides a dimension beyond the $\{x, Q^2\}$ plane is the *sensitivity*; this is a combination of the correlation coefficient times a scaled residual [753, 754]. This provides an extra dimension of information in comparison to a simple $\{x, Q^2\}$ map and represents a measure of the impact of the data.

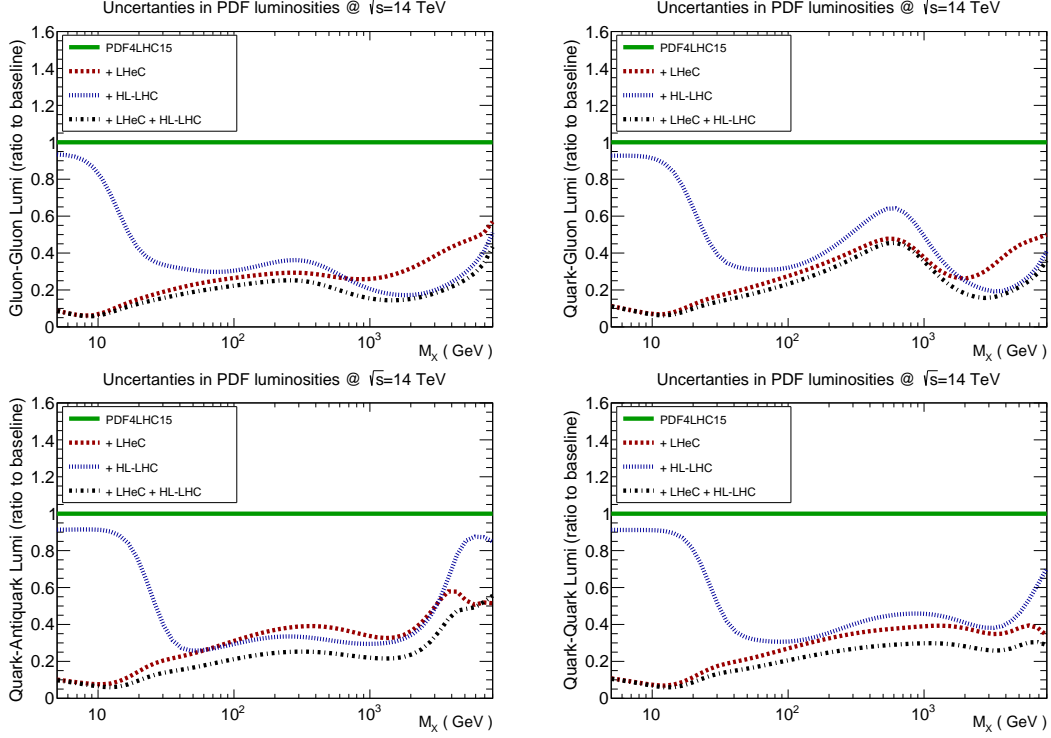In Fig. 9.12 this PDF sensitivity for a sample PDF flavour is displayed for the LHeC and the

Figure 9.11: Impact of LHeC, HL-LHC and combined LHeC + HL-LHC pseudodata on the uncertainties of the gluon-gluon, quark-gluon, quark-antiquark and quark-quark luminosities, with respect to the PDF4LHC15 baseline set. In this comparison we display the relative reduction of the PDF uncertainty in the luminosities compared to the baseline.
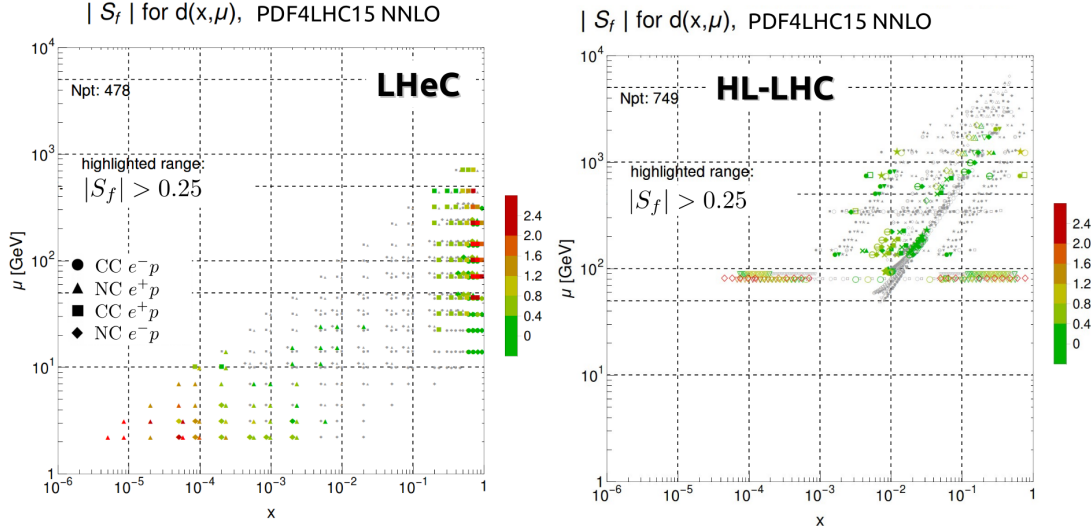

Figure 9.12: Sensitivity for a sample flavour $\{d(x, Q)\}$ in the $\{x, Q^2\}$ kinematic plane for the LHeC (left) and the HL-LHC (right) calculated with pseudodata [754]. We observe the LHeC is particularly sensitive in both the high and low x regions, and the HL-LHC covers the intermediate x region out to large Q scales.

HL-LHC pseudo-data. In particular, one observe that the LHeC provides strong sensitivity in the high-x region, which is of great importance for BSM searches, and also in the low-x region, which is relevant for QCD phenomena such as saturation. The HL-LHC provides constraints

coming from W/Z production ($Q \sim M_{W/Z}$) as well as from jets at high scales. The combination of these measurements will provide strongest constraints on the various PDF flavours across the broad $\{x, Q^2\}$ kinematic plane.

9.6   Impact of New Small-x Dynamics on Hadron Collider Physics

As discussed in Subsections 4.2.1 and 4.2.3, the presence of new dynamics at small x as claimed in Refs. [246, 250, 251] will have impact on hadronic observables. The impact is stronger for larger energies, therefore more important for the FCC-hh than for the LHC. But it may compete with other uncertainties and thus become crucial for precision studies even at LHC energies. Studies on the impact of non-linear dynamics at hadron colliders have been devoted mainly to photoproduction in UPCs, see e.g. [755–757] and Refs. therein for the case of gauge boson production. In this section we focus on the effect of resummation at small x.

While hadronic data like jet, Drell-Yan or top production at existing energies do not have much constraining power at low x [246] and thus need not be included in the extraction of PDFs using resummed theoretical predictions, this fact does not automatically mean that the impact of resummation is not visible at large scales for large energies. Indeed the PDFs obtained with small-x resummation may change at low energies in the region of x relevant for hadronic data, thereby giving an effect also at higher energies after evolving to those scales. A consistent inclusion of resummation effects on hadronic observables is thus crucial for achieving precision. The difficulty for implementing resummation on different observables lies in the fact that not only evolution equations should include it but also the computation of the relevant matrix elements for the observable must be performed with matching accuracy.

Until present, the only observable that has been examined in detail is Higgs production cross section through gluon fusion [758]. Other observables like Drell-Yan [759] or heavy quark [760] production are under study and they will become available in the near future.

For $gg \to H$, the LL resummation of the matrix elements matched to fixed order at N^{3}LO was done in Refs. [271, 758] and the results are shown in Figs. 9.13 and 9.14. Fig. 9.13 shows the increasing impact of resummation on the cross section with increasing energy. It also illustrates the fact that the main effect of resummation comes through the modification of the extraction of parton densities and their extrapolation, not through the modification of the matrix elements or the details of the matching.

Fig. 9.14 indicates the size of the different uncertainties on the absolute values of the cross section with increasing accuracy of the perturbative expansion, at HL-LHC and FCC-hh energies. For N^{3}LO(+LL) it can be seen that while at the HL-LHC, the effect of resummation is of the same order as other uncertainties like those coming scale variations, PDFs and subleading logarithms, this is not the case for the FCC where it can be clearly seen that it will be the dominant one. Resummation should also strongly affect the rapidity distributions, a key need for extrapolation of observed to total cross sections. In particular, rapidity distributions are more directly sensitive to PDFs at given values of momentum fraction x, and therefore in regions where this momentum fraction is small (large rapidities) the effect of resummation may be sizeable also at lower collider energies. These facts underline the need of understanding the dynamics at small x for any kind of precision physics measurements at future hadronic colliders, with increasing importance for increasing energies.

Finally, it should be mentioned that a different kind of factorisation, called transverse momentum (TMD) factorisation [38, 503, 761–764], may have an effect on large scale observables in hadronic
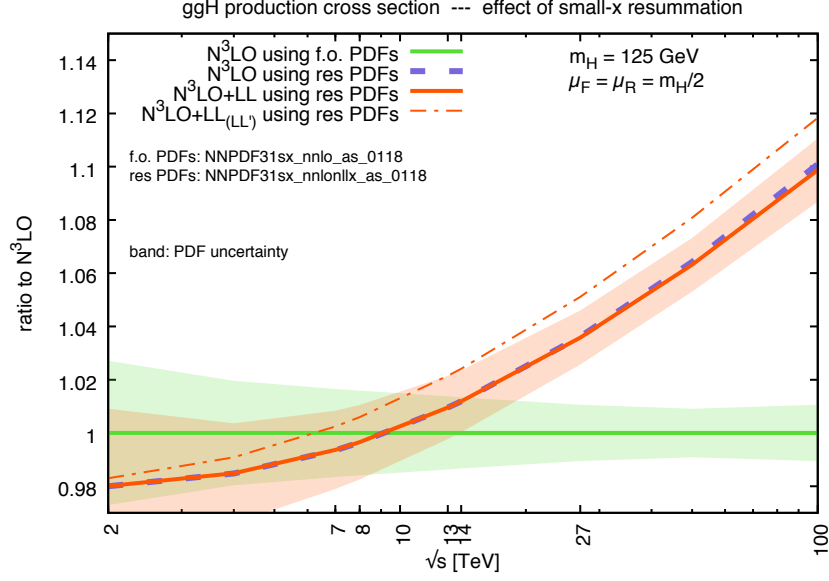
Figure 9.13: Ratio of the N³LO Higgs cross section with and without resummation to the N³LO fixed-order cross section, as a function of the collider centre-of-mass energy. "f.o." denotes fixed order, "res" denotes resummed and "LL′" a different anomalous dimension matching at leading logarithmic accuracy, see the legend on the plot and Ref. [758] for details. The PDFs used are from the global dataset of Ref. [250]. Figure taken from Ref. [758].
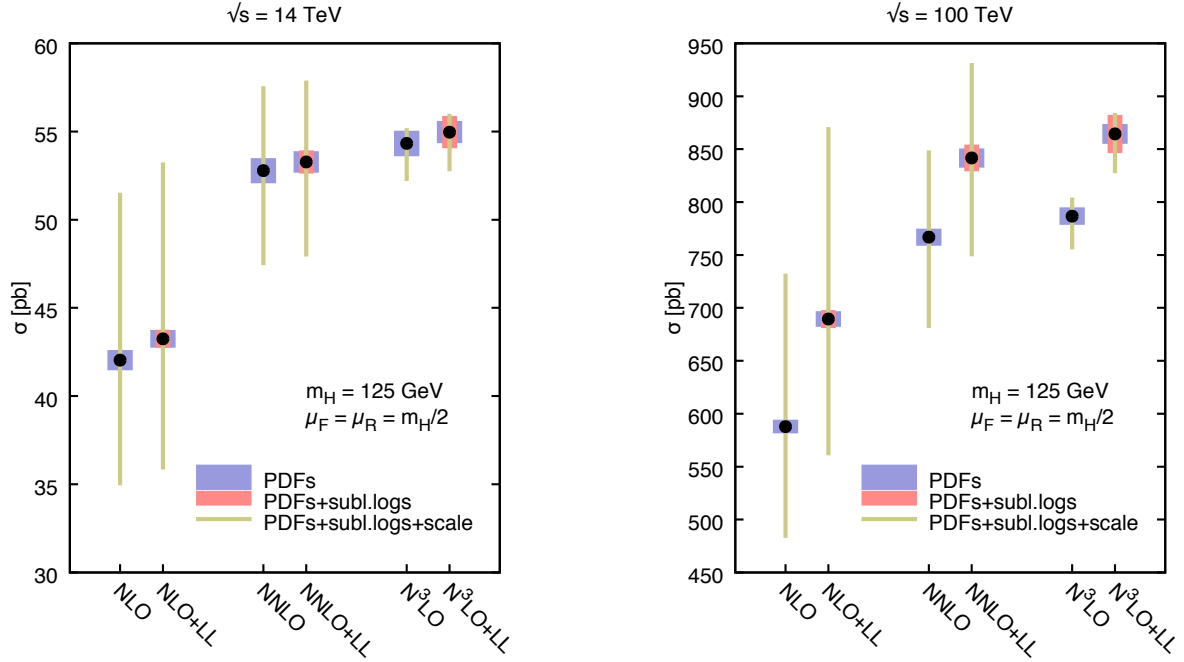

Figure 9.14: Perturbative progression of the Higgs cross section for two collider energies $\sqrt{s} = \{14, 100\}$ TeV. In each plot the NLO, NLO+LL, NNLO, NNLO+LL, N³LO and N³LO+LL results are shown. The results are supplemented by uncertainty bands from PDF, subleading logarithms and scale uncertainties. Figure taken from Ref. [758].

colliders. The extension of the TMD evolution equations towards small x [765] and the relation of such factorisation with new dynamics at small x, either through high-energy factorisation [766–

769] or with the CGC [499, 500], is under development [770].

9.7 Heavy Ion Physics with eA Input

The study of hadronic collisions at RHIC and the LHC, proton-proton, proton-nucleus and nucleus-nucleus, has produced several observations of crucial importance for our understanding of QCD in complex systems where a large number of partons is involved [771, 772]. The different stages of a heavy ion collision, as we presently picture it, are schematically drawn in Fig 9.15.
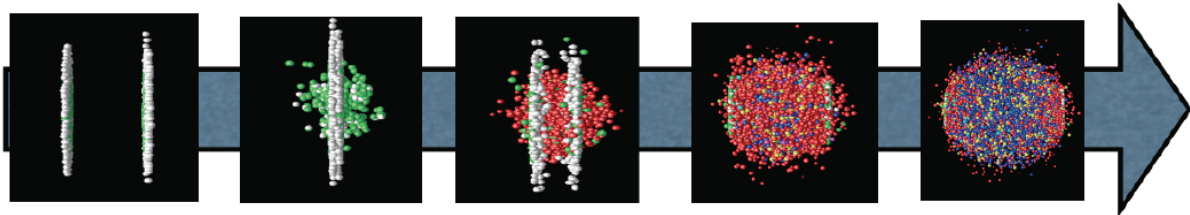

Figure 9.15: Sketch of a heavy ion collision with time running left to right, going from the approach of two ultrarelativistic Lorentz-contracted nuclei, the collision and parton creation in the central rapidity region, the beginning of expansion and formation of the QGP, the expansion of the QGP until hadronisation, and, finally, the expansion of the hadronic gas.

First, the hot and dense partonic medium created in heavy ion collisions, the quark-gluon plasma (QGP), experiences a collective behaviour of which azimuthal asymmetries and transverse spectra with a specific ordering in particle masses are the most prominent observables. This collectivity can be very well described by relativistic hydrodynamics [773]. For this description, the system has to undergo some dynamics leading to rough isotropisation in a short time, $\lesssim 1$ fm/c, for which both strong and weak coupling explanations have been proposed [552].

Second, collisions between smaller systems, pp and pA, show many of the features [549–551] that in heavy ion collisions are taken as indicative of the production of a dense hot partonic medium. The most celebrated of such features, the long rapidity range particle correlations collimated in azimuth, named the ridge (see Sect. 6.5), has been found in all collisions systems. The dynamics underlying this phenomena, either the formation of QGP and the existence of strong final state interactions, or some initial state dynamics that leaves imprint on the final observables, is under discussion [552].

Finally, the QGP is extremely opaque to both highly energetic partons [774] and quarkonia [775] traversing it. These observables, whose production in pp can be addressed through perturbative methods, are called hard probes [776]. The quantification of the properties of the QGP extracted through hard probes is done by a comparison with predictions based on assuming a nuclear collision to be a superposition of collisions among free nucleons. Such predictions contain uncertainties coming both from nuclear effects other than those in QGP (named cold nuclear matter effects), and from uncertainties in the dynamics determining the interaction between the energetic parton or bound state and the medium. In the case of partons, this has motivated the development of sophisticated jet studies in heavy ion collisions [777].

eA collisions studied in the energy range relevant for the corresponding hadronic accelerator – the LHeC for the LHC – would substantially improve our knowledge on all these aspects and, indeed, on all stages of a heavy ion collisions depicted in Fig. 9.15. Besides, they can reduce sizeably the uncertainties in the extracted QGP parameters, the central goal of the heavy program for the understanding of the different phases of QCD. Here we provide three examples of such synergies:

- Nuclear parton densities: The large lack of precision presently existing in the determination of parton densities induce large uncertainties in the understanding of several signatures of the QGP. For example, for J/ψ suppression, its magnitude at midrapidity at the LHC is compatible with the sole effect of nuclear shadowing on nPDFs [775], see Fig. 9.16. While from data at lower energies and at forward and backward rapidities it is clear that this is not the only effect at work, only a reduction on the nPDF uncertainty as feasible at the LHeC , see Sect. 6.2, will make possible a precise quantification of the different mechanisms producing either suppression (screening, gluon dissociation, energy loss) or enhancement (recombination or coalescence), that play a role for this observable.
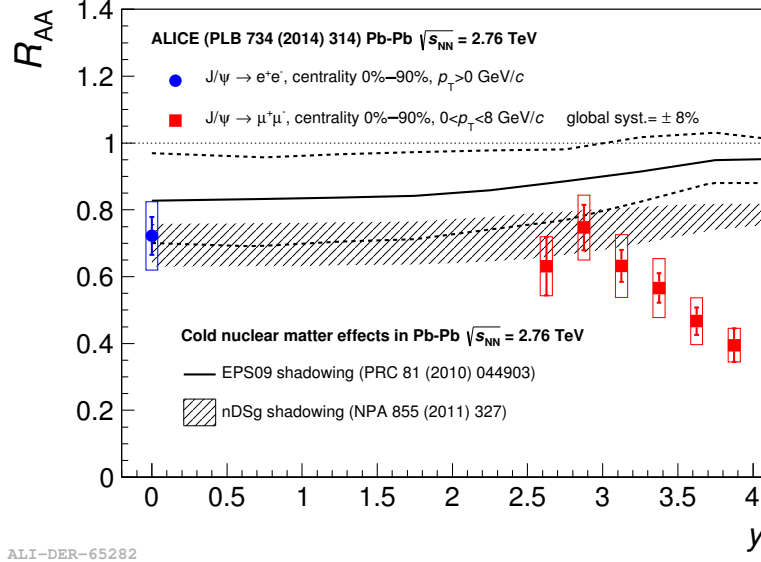
Figure 9.16: ALICE inclusive J/ψ nuclear modification factor versus rapidity [778], compared to nPDF calculations. Taken from [775].

- Initial conditions for the collective expansion and the small system problem: At present, the largest uncertainty in the determination of the transport coefficients of the partonic matter created in heavy ion collisions [779, 780] (see Fig. 9.17), required in hydrodynamic calculations, and in our understanding of the speed of the approach to isotropisation and of the dynamics prior to it [781], comes from our lack of knowledge of the nuclear wave function and of the mechanism of particle production at small to moderate scales – i.e. the soft and semihard regimes. Both aspects determine the initial conditions for the application of relativistic hydrodynamics. This is even more crucial in the discussion of small systems, where details of the transverse structure of protons are key [782] not only to provide such initial conditions but also to establish the relative role of initial versus final state dynamics. For example, the description of azimuthal asymmetries in pp and pPb collisions at the LHC demands that the proton is modelled as a collection of constituent quarks or hot spots [773, 782]. ep and eA collisions at the LHeC can constrain both aspects in the pertinent kinematic region, see Sects. 3.4 and 6.3. Besides, they can clarify the mechanisms of particle production and the possible relevance of initial state correlations on the final state observables as suggested e.g. by CGC calculations, see Sects. 4.2.1 and 6.4, whose importance for LHC energies can be established at the LHeC.

- Impact on hard probes: Besides the improvement in the determination of nPDFs that affects the quantification of hard probes, commented above, eA collisions can help to understand the dynamics of the probes by analysing the effects of the nuclear medium on
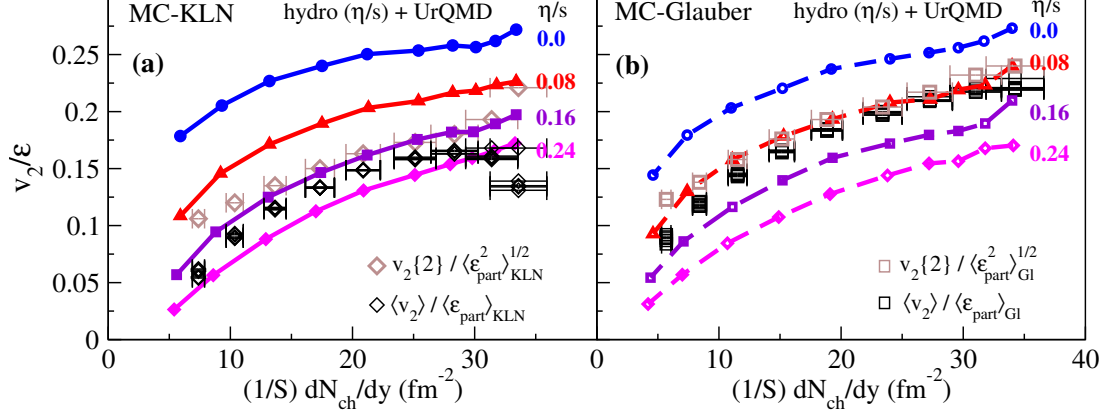
Figure 9.17: Comparison of the universal $v_2(\eta/s)/\varepsilon$ vs. $(1/S)(dN_{ch}/dy)$ curves with experimental data for $\langle v_2 \rangle$ [783], $v_2\{2\}$ [784], and dN_{ch}/dy [785] from the STAR Collaboration. The experimental data used in (a) and (b) are identical, but the normalisation factors $\langle \varepsilon_{part} \rangle$ and S used on the vertical and horizontal axes, as well as the factor $\langle \varepsilon_{part}^2 \rangle^{1/2}$ used to normalize the $v_2\{2\}$ data, are taken from the MC-KLN model in (a) and from the MC-Glauber model in (b). Theoretical curves are from simulations with MC-KLN initial conditions in (a) and with MC-Glauber initial conditions in (b). Taken from [779].

them. As two examples, the abundant yields of jets and large transverse momentum particles at the LHeC [1] will allow precise studies of the nuclear effects on jet observables and of hadronisation inside the nuclear medium. These two aspects are of capital importance not only in heavy ion collisions but also in small systems where the lack of jet modification is the only QGP-like characteristics not observed in pPb. On the other hand, measurements of exclusive quarkonium production at the LHeC [1] will provide a better understanding of the cold nuclear matter effects on this probe, on top of which the effects of the QGP will provide a quantitative characterisation of this new form of QCD matter.

As discussed in Sect. 6.2, pPb and PbPb collisions at the LHC offer possibilities for constraning nPDFs, through the measurement of EW vector boson production [786], dijets [515], D mesons at forward rapidities [527] and exclusive charmonium and dijet photoproduction in ultraperipheral collisions [787–789]. Specifically, dijets in UPCs could constrain nPDFs in the region $10^{-3} \lesssim x \lesssim 0.7$ and $200 \lesssim Q^2 \lesssim 10^4 \, \text{GeV}^2$. eA collisions would provide more precise nPDFs, whose compatibility with these mentioned observables would clearly establish the validity of collinear factorisation and the mechanisms of particle production in collisions involving nuclei.

Furthermore, eA offers another system where photon-photon collisions, recently measured in UPCs at the LHC [790], can be studied. For example, the observed acoplanarity of the produced muon pairs can be analysed in eA in order to clarify its possible origin and constrain the parton densities in the photon.

Finally, the possible existence of a new non-linear regime of QCD - saturation - at small x is also under study at the LHC, for example using dijets in the forward rapidity region in pPb collisions [791]. As discussed in Sect. 6.5, the ridge phenomenon (two particle correlations peaked at zero and π azimuthal angles and stretched along the full rapidity of the detector) observed in all collision systems, pp, pPb and PbPb at the LHC, has been measured in photoproduction on Pb in UPCs at the LHC [553]. For the time being, its existence in smaller systems like e^+e^- [554] at LEP and ep at HERA [555] has been scrutinised but the results are not conclusive. These studies are fully complementary to those in ep and eA, where its search at the smallest possible values of x at the LHeC would be most interesting. For example, the collision of the virtual

photon with the proton at the LHeC can be considered as a high energy collision of two jets or "flux tubes".

In conclusion, ep and eA collisions as studied at the LHeC will have a large impact on the heavy ion programme, as the comparison of the kinematic reach of DIS and hadronic machines shown in Fig. 9.18 makes evident. It should be noted that there exist proposals for extending such programme into Run 5 and 6 of the LHC [501], by running lighter ions and with detector upgrades in ATLAS and CMS (starting in Run 4) and LHCb (Upgrade II [792]).
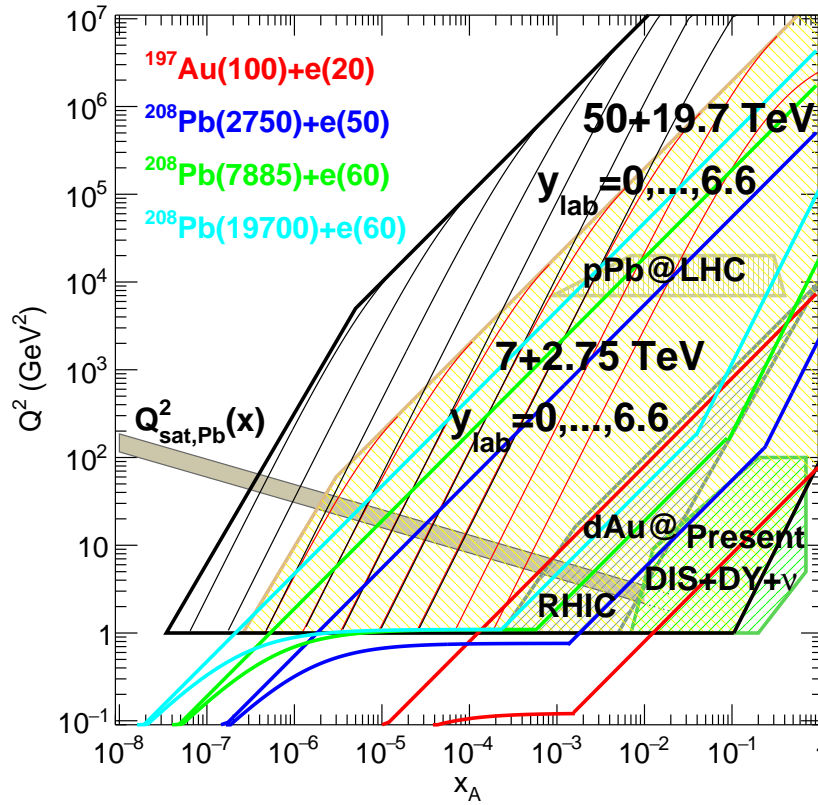
Figure 9.18: Kinematic regions in the $x - Q^2$ plane explored by data sets (charged lepton and neutrino DIS, DY, dAu at RHIC and pPb at the LHC) used in present nPDF analyses [495], compared to the ones achievable at the EIC (red), the LHeC (ERL against the HL-LHC beams, dark blue) and two FCC-eh versions (with Pb beams corresponding to proton energies of 20 TeV - green and 50 TeV - light blue). Acceptance is taken to be $1° < \theta < 179°$, and $0.01(0.001) < y < 1$ for the EIC (all other colliders). The areas delimited by thick brown and black lines show the regions accessible in pPb collisions at the LHC and the FCC-hh (50 TeV) respectively, while the thin lines represent constant rapidities from 0 (right) to 6.6 (left) for each case. The saturation scale Q_{sat} shown here for indicative purposes only, see also [496], has been drawn for a Pb nucleus considering an uncertainty ~ 2 and a behaviour with energy following the model in [497]. Note that it only indicates a region where saturation effects are expected to be important but there is no sharp transition between the linear and non-linear regimes.

Chapter 10

The Electron Energy Recovery Linac

We studied different options for the electron accelerator for LHeC in Ref. [1], of which the Energy Recovery Linac (ERL) option is retained in this update of the CDR. This is due to the higher achievable luminosity of the Linac-Ring option, as compared to the Ring-Ring option, as well as the interference of the installation of an electron ring in the LHC tunnel with its operation [793]. The clear advantage of the ERL compared to its contenders in 2012 is the possibility to keep the overall energy consumption at bay, albeit, in its baseline configuration and size of the return arcs, operation is still limited to lepton energies below 70 GeV to avoid excessive synchrotron radiation losses. Since there is no fundamental beam loading in an ERL by its principle, higher average currents and thus higher luminosities would not lead to larger power consumption.

10.1   Introduction – Design Goals

The main guidelines for the design of the Electron ERL and the Interaction Region (IR) with the LHC are:

- electron-hadron operation in parallel with high luminosity hadron-hadron collisions in LHC/HL-LHC;

- centre-of-mass collision energy in the TeV scale;

- power consumption of the electron accelerator smaller than 100 MW;

- peak luminosity approaching $10^{34}\,\mathrm{cm}^{-2}\mathrm{s}^{-1}$;

- integrated luminosity exceeding by at least two orders of magnitude that achieved by HERA at DESY.

The electron energy E_e chosen in the previous version of the CDR [1] was 60 GeV. This could be achieved with an ERL circumference of 1/3 of that of the LHC. Cost considerations and machine–detector performance aspects, in particular the amount of synchrotron radiation losses in the IR, have led to define a new reference configuration with $E_e = 49.2\,\mathrm{GeV}$ and a circumference of $\approx 5.4\,\mathrm{km}$, 1/5 of that of the LHC.

The ERL consists of two superconducting (SC) linacs operated in CW connected by at least three pairs of arcs to allow three accelerating and three decelerating passes (see Fig. 10.1). The length of the high energy return arc following the interaction point should be such as to provide a half RF period wavelength shift to allow the deceleration of the beam in the linac structures

in three passes down to the injection energy and its safe disposal. SC Cavities with an unloaded quality factor Q_0 exceeding 10^{10} are required to minimise the requirements on the cryogenic cooling power and to allow an efficient ERL operation. The choice of having three accelerating and three decelerating passes implies that the circulating current in the linacs is six times the current colliding at the Interaction Point (IP) with the hadron beam.
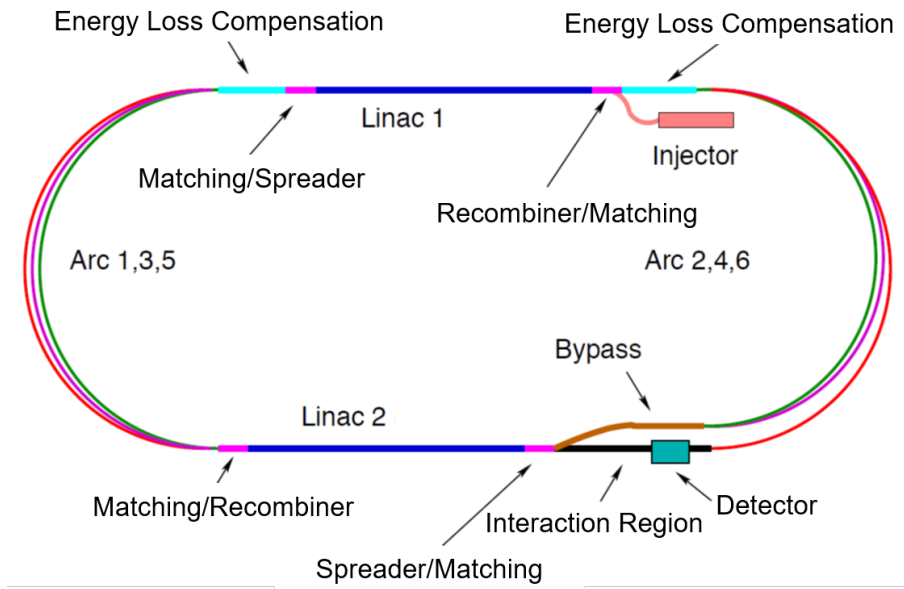

Figure 10.1: Schematic layout of the LHeC design based on an Energy Recovery Linac.

The choice of an Energy Recovery Linac offers the advantage of a high brightness beam and it avoids performance limitations due to the beam-beam effect seen by the electron beam [794], which was a major performance limitation in many circular lepton colliders (e.g. LEP) and for the LHeC Ring-Ring option. The current of the ERL is limited by its source and an operational goal of $I_e = 20\,\mathrm{mA}$ has been set, corresponding to a bunch charge of $500\,\mathrm{pC}$ at a bunch frequency of $40\,\mathrm{MHz}$. This implies operating the SRF cavities with the very high current of $120\,\mathrm{mA}$ for a virtual beam power (product of the beam current at the IP times the maximum beam energy) of $1\,\mathrm{GW}$. The validation of such performance in terms of source brightness and ERL 3-turn stable and efficient operation in the PERLE facility [11] is a key milestone for the LHeC design.

A small beam size at the IP is required to maximize luminosity and approach peak luminosities of $10^{34}\,\mathrm{cm^{-2}s^{-1}}$ and integrated luminosities of $1\,\mathrm{ab^{-1}}$ in the LHeC lifetime. In particular $\beta^* < 10\,\mathrm{cm}$ needs to be achieved for the colliding proton beam compatibly with the optics constraints imposed by the operation in parallel to proton-proton physics in the other IPs during the HL-LHC era [3]. The peak luminosity values quoted above exceed those at HERA by 2-3 orders of magnitude. The operation of HERA in its first, extended running period 1992–2000, provided and integrated luminosity of about $0.1\,\mathrm{fb^{-1}}$ for the H1 and ZEUS experiments, corresponding to the expected integrated luminosity collected over 1 day of LHeC operation.

10.2 The ERL Configuration of the LHeC

The main parameters of the LHeC ERL are listed in Tab. 10.1; their choices and optimisation criteria will be discussed in the following sections.

Parameter	Unit	Value
Injector energy	GeV	0.5
Total number of linacs		2
Number of acceleration passes		3
Maximum electron energy	GeV	49.19
Bunch charge	pC	499
Bunch spacing	ns	24.95
Electron current	mA	20
Transverse normalized emittance	µm	30
Total energy gain per linac	GeV	8.114
Frequency	MHz	801.58
Acceleration gradient	MV/m	19.73
Cavity iris diameter	mm	130
Number of cells per cavity		5
Cavity length (active/real estate)	m	0.918/1.5
Cavities per cryomodule		4
Cryomodule length	m	7
Length of 4-CM unit	m	29.6
Acceleration per cryomodule (4-CM unit)	MeV	289.8
Total number of cryomodules (4-CM units) per linac		112 (28)
Total linac length (with with spr/rec matching)	m	828.8 (980.8)
Return arc radius (length)	m	536.4 (1685.1)
Total ERL length	km	5.332

Table 10.1: Parameters of LHeC Energy Recovery Linac (ERL).

10.2.1 Baseline Design – Lattice Architecture

The ERL, as sketched in Fig. 10.1, is arranged in a racetrack configuration; hosting two superconducting linacs in the parallel straights and three recirculating arcs on each side. The linacs are 828.8 m long and the arcs have 536.4 m radius, additional space of 76 m is taken up by utilities like Spreader/Recombiner (Spr/Rec), matching and energy loss compensating sections adjacent to both ends of each linac (total of 4 sections) [795]. The total length of the racetrack is 5.332 km: 1/5 of the LHC circumference $2 \cdot (828.8 + 2 \cdot 76 + 536.4\pi)$ m. Each of the two linacs provides 8.114 GV accelerating voltage, therefore a 49.19 GeV energy is achieved in three turns. After the collision with the protons in the LHC, the beam is decelerated in the three subsequent turns. The injection and dump energy has been chosen at 0.5 GeV.

Injection into the first linac is done through a fixed field injection chicane, with its last magnet (closing the chicane) being placed at the beginning of the linac. It closes the orbit *bump* at the lowest energy, injection pass, but the magnet (physically located in the linac) will deflect the beam on all subsequent linac passes. In order to close the resulting higher pass *bumps*, the so-called re-injection chicane is instrumented, by placing two additional opposing bends in front of the last chicane magnet. The chosen arrangement is such that, the re-injection chicane magnets are only *visible* by the higher pass beams. The second linac in the racetrack is configured exactly as a mirror image of the first one, with a replica of the re-injection chicane at its end, which facilitates a fixed-field extraction of energy recovered beam to the dump.
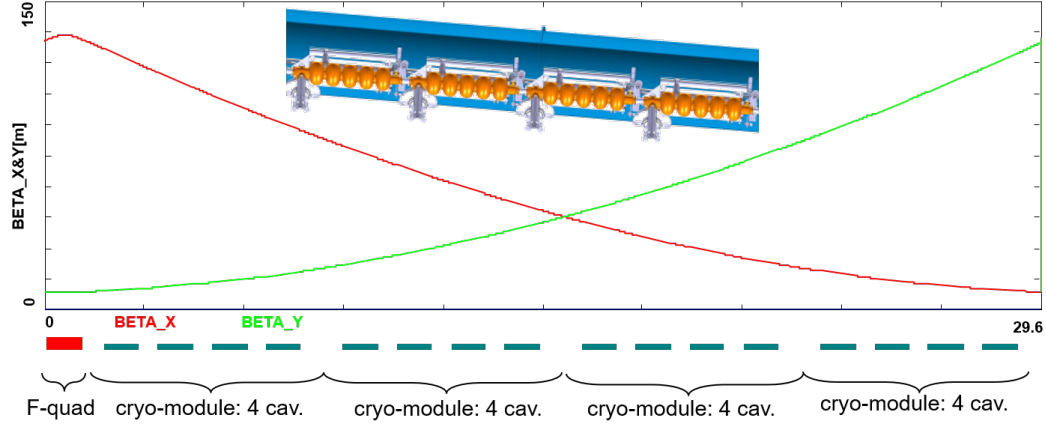
Figure 10.2: Layout of a half-cell composed out of four cryomodules (each hosting four, 5-cell cavities: top insert) and a focusing quad. Beta functions reflect 130° FODO optics.

Linac Configuration and Multi-pass Optics

Appropriate choice of the linac optics is of paramount importance for the transverse beam dynamics in a multi-pass ERL. The focusing profile along the linac (quadrupole gradients) need to be set (and they stay constant), so that multiple pass beams within a vast energy range may be transported efficiently. The chosen arrangement is such that adequate transverse focusing is provided for a given linac aperture. The linac optics is configured as a strongly focusing, 130° FODO. In a basic FODO cell a quadrupole is placed every four cryomodules, so that the full cell contains two groups of 16 RF cavities and a pair of quads (F, D) as illustrated in Fig. 10.2. The entire linac is built out of 14 such cells. Energy recovery in a racetrack topology explicitly requires that both the accelerating and decelerating beams share the individual return arcs [796]. This in turn, imposes specific requirements for TWISS function at the linacs ends: TWISS functions have to be identical for both the accelerating and decelerating linac passes converging to the same energy and therefore entering the same arc. There is an alternative scheme, proposed by Peter Williams [797], who has argued that it would be beneficial to separate the accelerating and decelerating arcs. This would simplify energy compensation systems and linac-to-arc matching, but at an higher cost of the magnetic system of the arcs. However, doubling number of arcs is a very costly proposition. On the other hand, C-BETA experiment is pioneering a multi-pass arcs to transport a vast energy range through the same beam-line and it still intends to use them for energy recovery. Our approach, based on proven, CEBAF-like, RLA technology [798] is somewhere in the 'middle'.

To visualize beta functions for multiple accelerating and decelerating passes through a given linac, it is convenient to reverse the linac direction for all decelerating passes and string them together with the interleaved accelerating passes, as illustrated in Fig. 10.3. This way, the corresponding accelerating and decelerating passes are joined together at the arc's entrance/exit. Therefore, the matching conditions are automatically built into the resulting multi-pass linac beamline. One can see that both linacs uniquely define the TWISS functions for the arcs: Linac 1 fixes input to all odd arcs and output to all even arcs, while Linac 2 fixes input to all even arcs and output to all odd arcs. The optics of the two linacs are mirror-symmetric; They were optimised so that, Linac 1 is periodic for the first accelerating pass and Linac 2 has this feature for last decelerating one. In order to maximize the BBU threshold current [799], the optics is tuned so that the integral of β/E along the linac is minimised. The resulting phase advance per
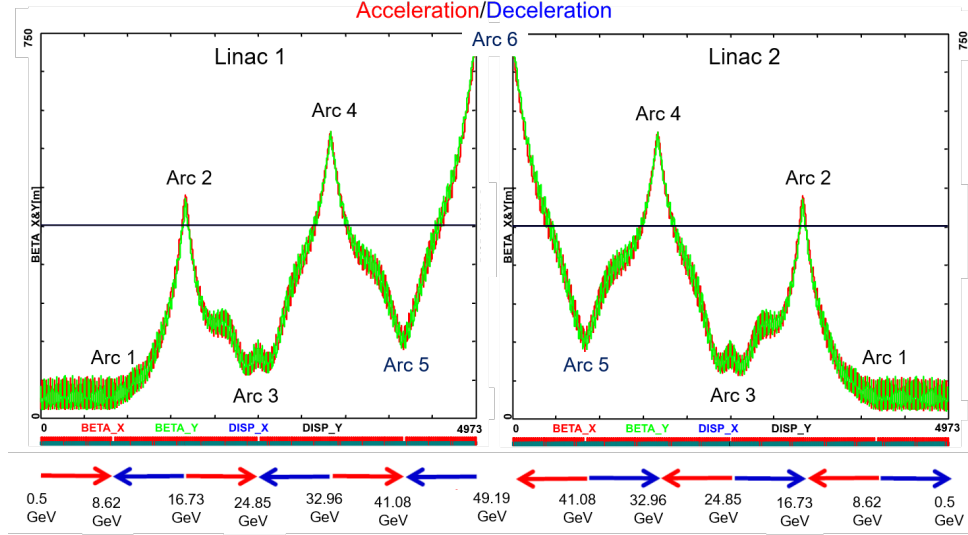
Figure 10.3: Beta function in the optimised multi-pass linacs (3 accelerating passes and 3 decelerating passes in each of two linacs). The matching conditions are automatically built into the resulting multi-pass linac beamline.

cell is close to 130°. Non-linear strength profiles and more refined merit functions were tested, but they only brought negligible improvements.

Recirculating Arcs – Emittance Preserving Optics

Synchrotron radiation effects on beam dynamics, such as the transverse emittance dilution induced by quantum excitations have a paramount impact on the collider luminosity. All six horizontal arcs are accommodated in a tunnel of 536.4 m radius. The transverse emittance dilution accrued through a given arc is proportional to the emittance dispersion function, H, averaged over all arc's bends [800]:

$$\Delta \epsilon = \frac{2\pi}{3} C_q r_0 < H > \frac{\gamma^5}{\rho^2} \, , \tag{10.1}$$

where

$$C_q = \frac{55}{32\sqrt{3}} \frac{\hbar}{mc} \tag{10.2}$$

and r_0 is the classical electron radius and γ is the Lorentz boost. Here, $H = (1 + \alpha^2)/\beta \cdot D^2 + 2\alpha \, DD' + \beta \cdot D'^2$ where D, D' are the bending plane dispersion and its derivative, with $< ... > = \frac{1}{\pi} \int_{\text{bends}} ... \, d\theta$.

Therefore, emittance dilution can be mitigated through appropriate choice of arc optics (values of α, β, D, D' at the bends). In the presented design, the arcs are configured with a FMC (Flexible Momentum Compaction) optics to ease individual adjustment of, $< H >$, in various energy arcs.

Optics design of each arc takes into account the impact of synchrotron radiation at different energies. At the highest energy, it is crucial to minimise the emittance dilution due to quantum excitations; therefore, the cells are tuned to minimise the emittance dispersion, H, in the bending sections, as in the TME (Theoretical Minimum Emittance) lattice. On the other hand, at the
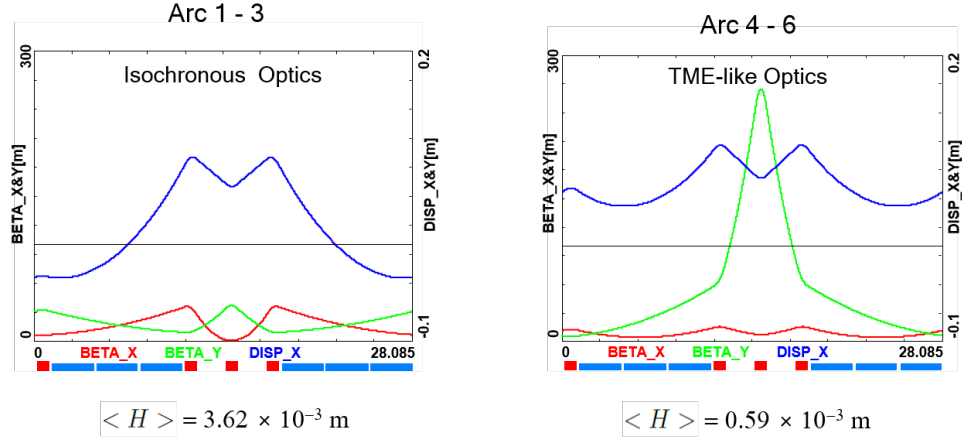
Figure 10.4: Two styles of FMC cells appropriate for different energy ranges. Left: lower energy arcs (Arc 1–3) configured with *Isochronous* cells, Right: higher energy arcs configured with *TME-like* cells. Corresponding values of the emittance dispersion averages, $< H >$, are listed for both style cells.

lowest energy, it is beneficial to compensate for the bunch elongation with isochronous optics. The higher energy arcs (4,5 and 6) configured with the TME cells are still quasi-isochronous. To fully compensate remnant bunch elongation one could set higher pass linacs slightly off-crest to compress the bunches, since one has full control of gang-phases for individual linac passes. All styles of FMC lattice cells, as illustrated in Fig. 10.4, share the same footprint for each arc. This allows us to stack magnets on top of each other or to combine them in a single design. Here, we use substantially shorter then in the 60 GeV design, 28.1 m, FMC cell configured with six 3 m bends, in groups of flanked by a quadrupole singlet and a triplet, as illustrated in Fig. 10.4. The dipole filling factor of each cell is 63 %; therefore, the effective bending radius ρ is 336.1 m. Each arc is followed by a matching section and a recombiner (mirror symmetric to spreader and matching section). Since the linacs are mirror-symmetric, the matching conditions described in the previous section, impose mirror-symmetric arc optics (identical betas and sign reversed alphas at the arc ends).

Path-length adjusting chicanes were also foreseen to tune the beam time of flight in order to hit the proper phase at each linac injection. Later investigations proved them to be effective only with lower energy beams, as these chicanes trigger unbearable energy losses, if applied to the highest energy beams. A possible solution may consist in distributing the perturbation along the whole arc with small orbit excitations. This issue will be fully addressed in a subsequent section on 'Synchrotron Radiation Effects - Emittance Dilution'.

Spreaders and Recombiners

The spreaders are placed directly after each linac to separate beams of different energies and to route them to the corresponding arcs. The recombiners facilitate just the opposite: merging the beams of different energies into the same trajectory before entering the next linac. As illustrated in Fig. 10.5, each spreader starts with a vertical bending magnet, common for all three beams, that initiates the separation. The highest energy, at the bottom, is brought back to the horizontal plane with a chicane. The lower energies are captured with a two-step vertical bending adapted from the CEBAF design [798].

Functional modularity of the lattice requires spreaders and recombiners to be achromats (both
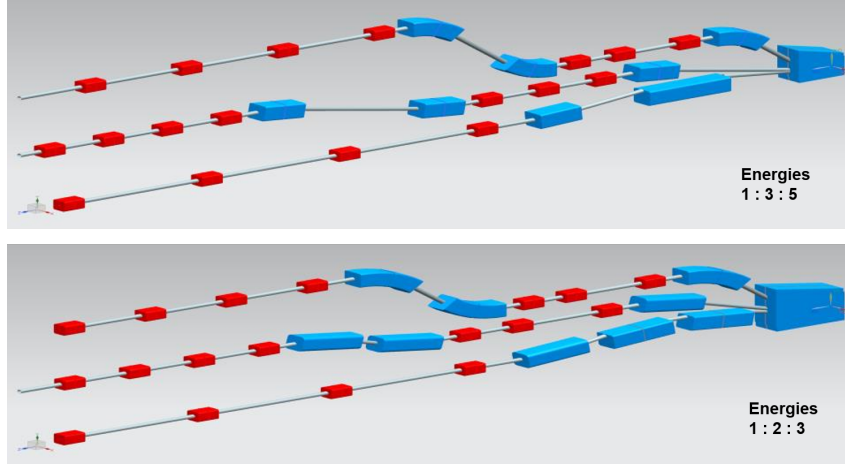
Figure 10.5: Layout of a three-beam switch-yard for different energy ratios: $1:3:5$ and $1:2:3$ corresponding to specific switch-yard geometries implemented on both sides of the racetrack
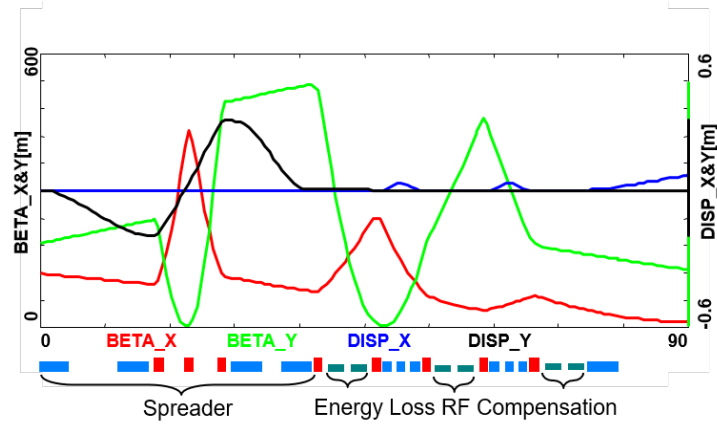

Figure 10.6: Spreader 3 (24.8 GeV) optics; featuring a vertical achromat with three dispersion suppressing quads in-between the two steps, a pair of path-length adjusting dogleg chicanes and four betatron matching quads, interleaved with three energy loss compensating sections (2-nd harmonic RF cavities marked in green).

in the horizontal and vertical plane). To facilitate that, the vertical dispersion is suppressed by a pair of quadrupoles located in-between vertical steps; they naturally introduce strong vertical focusing, which needs to be compensated by the middle horizontally focusing quad. The overall spreader optics is illustrated in Fig. 10.6. Complete layout of two styles of switch-yard with different energy ratios is depicted in Fig. 10.5. Following the spreader, there are four matching quads to *bridge* the Twiss function between the spreader and the following 180° arc (two betas and two alphas). Combined spreader-arc-recombiner optics, features a high degree of modular functionality to facilitate momentum compaction management, as well as orthogonal tunability for both the beta functions and dispersion, as illustrated in Fig. 10.7.

Alternative design of the spreader/recombiner

The desire to reduce the number of elements included in the spreader led to the reduction of the number of steps required to separate vertically the different beams and route them into their specific arcs. In particular, this alternative spreader design uses a single vertical step
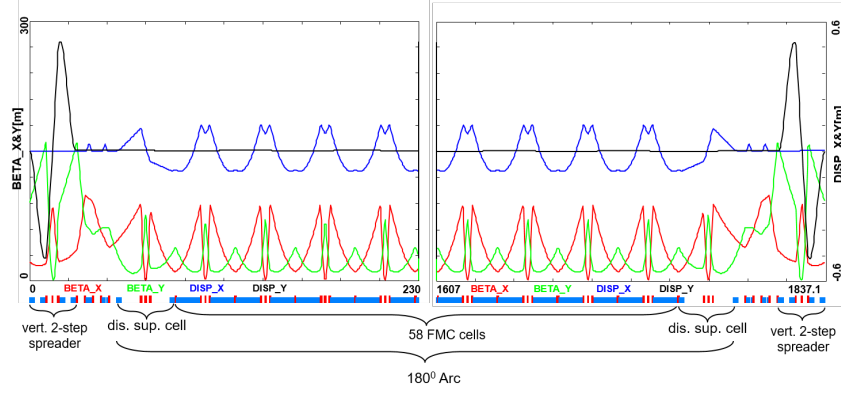
Figure 10.7: Complete Optics for Arc 3 (including switch-yard); featuring: low emittance 180° arc based on isochronous cells (30 cells flanked by dispersion suppression cell with missing dipoles on each side), spreaders and recombiners with matching sections and doglegs symmetrically placed on each side of the arc proper.
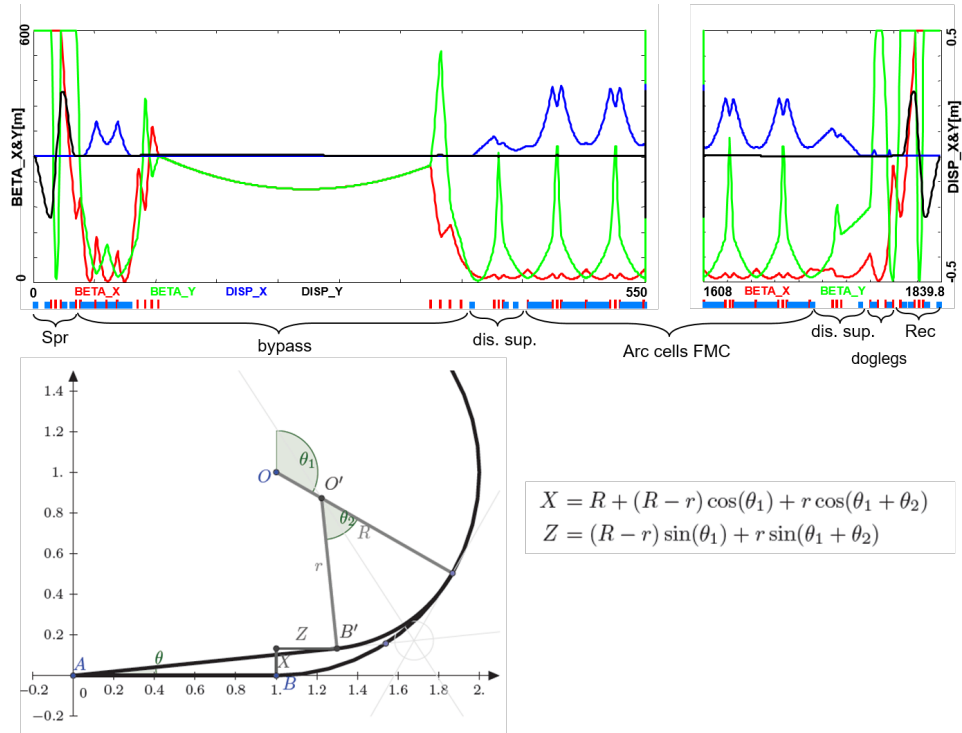

Figure 10.8: Optics and layout of Arc 4 including the detector bypass. The lattice (top insert) features a vertical spreader, an initial horizontal bending, a straight section, a modified dispersion suppressor, seven junction cells, and four regular cells. The bypass geometry (bottom insert), features a long IP line, AB, which for visual reasons has been purposely stretched, being actually about 1/5 of the arc radius. All geometric dependencies of the bypass parameters are summarized in the inserted formulae.

instead of two. Although the concept has been briefly discussed in [1] it was not retained due to the superconducting technology needed for the quadrupoles that must be avoided in this highly radiative section. Nevertheless, recent studies have been pursuing a one step spreader version, based on normal conducting magnet technology. It assumes a pole tip field of less than 1 T for an aperture radius of 30 mm, allowing the use of thin quadrupoles and thus minimise potential overlap with the other beamlines. With respect to the previous study, the use of normal conductors was made possible by increasing the overall spreader length and reducing the number of quadrupoles. In particular, the focusing magnets are limited to two outer quadrupoles for the achromatic function and one quadrupole in the middle, where the dispersion is zero, to control the beta function in the defocusing plane. Two visualisations are given Fig 10.9 and 10.10.
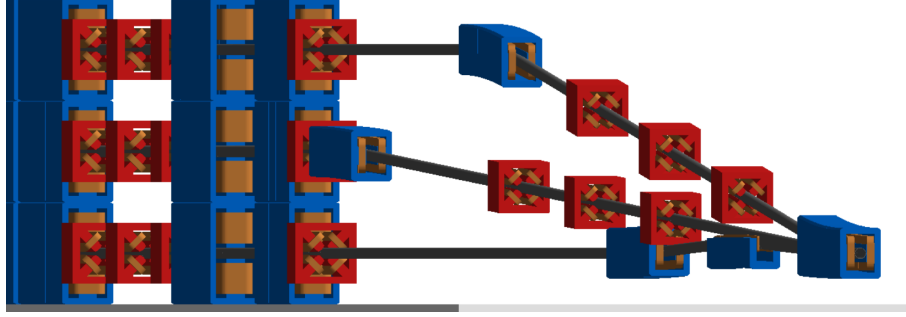

Figure 10.9: 3D visualisation of the spreader 1,3,5 inserted between the end of the linac and routing the different beamlines into their respective dispersion suppresors.

Both spreader types start with a first dipole that separates vertically the different beamlines in a 1-3-5 ratio for the odd number spreaders and in a 1-2-3 ratio for the even number spreaders. Theses ratios are defined by the beam energies of the corresponding turn. Therefore by fixing the length of the longest beamline for each spreaders (odd and even numbers) one obtains the required angle to get a 50 cm vertical offset between each beamlines. The equations below represent the required bending angle in the dipole and beamline lengths in order to meet the requirements,

$$\theta_3 = \frac{0.5}{l_3 - L} \qquad\qquad l_1 = \frac{2E_1}{E_3}(l_3 - L) + L \qquad\qquad (10.3)$$

$$\theta_2 = \frac{1}{l_2 - L} \qquad\qquad l_4 = \frac{1}{2}\frac{E_4}{E_2}(l_2 - L) + L \qquad\qquad (10.4)$$

where the index i corresponds to the beamline number associated to an energy E_i. L is the dipole length and l is the whole spreader beamline length.

For the beam line 2 and 4 we obtain $l_4 \approx l_2$ according to the energy ratio of 1.97. On the other hand, l_3 will be longer than l_1 because the energy ratio is 2.88. One can therefore tune the angle of the even number spreaders by defining l_2 as it will be the longest. However the angle of the odd number spreaders will be determined by the length of l_3. Regarding the chicane used for the highest energy only a minimum separation between the highest energy and the intermediate energy allows the introduction of the opposite bending dipole. It constraints in return the placement of the quadrupoles of the intermediate energy. The location of the magnets is the main limitation towards a minimization of the spreader length: the shorter the lattice gets, the stronger the quadrupoles need to be in order to preserve the achromatic function.

As a result, a one step spreader halves the number of dipoles present in the lattice and relaxes the constraint on magnets interference and overlap favorable for compactness. Dividing by two

the number of dipoles has a noticeable effect on the synchrotron power radiated in the spreader which is, in addition, beneficial for the emittance growth. The dipole fields required, for a maximal length of 50 m, are 226 mT for the odd number spreaders and 326 mT for the even number spreaders. The multipass linac optics Fig. 10.3 shows that the even number spreaders ,*i.e.* 2, 4 and 6, have the highest beta functions at their entrance which is detrimental from the perspective of minimizing the emittance growth within the spreader lattice. A solution to solve this issue is to insert a doublet of quadrupoles at the exit of the linac. All three energies will go through the doublet and, therefore, a compromise has to be found for the gradients. Finally, the reduction of the $\mathcal{H}$ function over the length of the spreader and specifically in the dipoles contributes to a further reduction of the emittance growth.

The energy loss for spreader 1 is low due to the low beam energy; spreader 2 and 3 have similar values that are acceptable as well as the one of spreader 4. Spreader 5 and 6 have the highest beam energies and therefore the largest energy loss. In addition, the dipoles used to produce the chicane need double the field strength compared to the other dipoles for the same length, *i.e.* half the bending radius, in order to save space for the other elements in the other beamlines. The vertical emittance growth is well controlled just as in the even number spreaders. Only spreader 6 has an order of magnitude higher contribution but one has to keep in mind that the even number spreaders will only act as recombiner since there will be the horizontal bypass doing the separation with the detector and a vertical separation will only occur for arc 2 and 4. Consequently spreader 6 should not be taken into account for the emittance growth contribution until the interaction point.
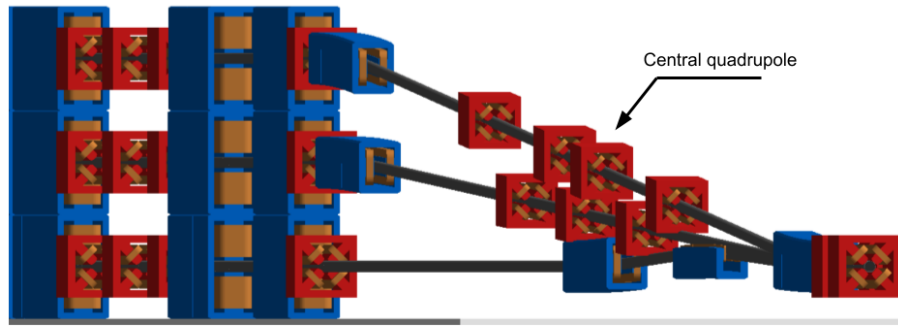

Figure 10.10: 3D visualisation of the spreader 2,4,6 inserted between the end of the linac and routing the different beamlines into their respective dispersion suppressors.

The optics for the Spreader/Recombiner of arc 2 and 4 are presented Fig. 10.11, it shows the achromatic function supported by the outer quadrupoles while the control of the horizontal beta function is provided by the "middle" quadrupole. One sees that the lattice of the arc 2 requires to split the "middle" quadrupole in two, in order to avoid overlap with the other beamline (arc 4), see Fig.10.10. These two optics are the most challenging as they have high beta functions at the entrance of their lattices, due to the multi pass linac optics as previously explained.

IR Bypasses

After the last spreader the 49.19 GeV beam goes straight to the interaction region. However the lower energy beams; at 16.7 and 33.0 GeV, need to be further separated horizontally in order to avoid interference with the detector. Different design options for the bypass section were explored [801] and the one that minimises the extra bending has been chosen and implemented in the lattice.
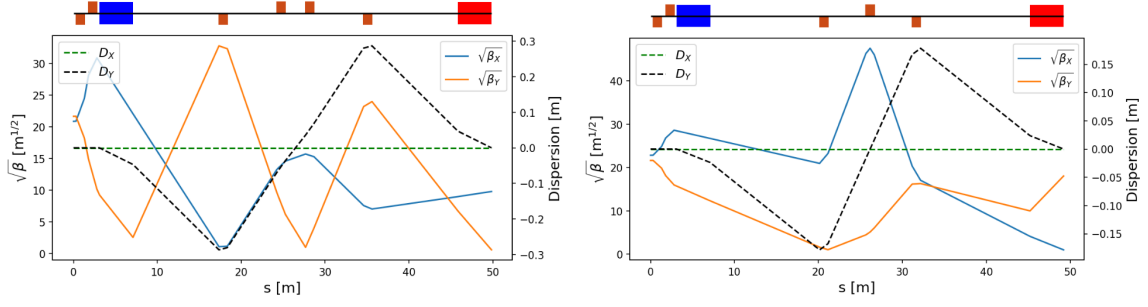
Figure 10.11: Left : Spreader/Recombiner optics of the arc 2 for the 16.73 GeV electron beam. Right : Spreader/Recombiner optics of the arc 4 for the 32.96 GeV electron beam.

Ten arc-like dipoles are placed very close to the spreader, to provide an initial bending, θ, which results in $X = 10$ m separation from the detector located 120 m downstream. The straight section of the bypass is approximately 240 m long. After the bypass, in order to reconnect to the footprint of Arc 6, 7 of 30 standard cells in Arc 2 and Arc 4 are replaced with 7 higher field, junction cells. The number of junction cells is a compromise between the field strength increase and the length of additional bypass tunnel, as can be inferred from the scheme summarised in Fig. 10.8. The stronger bending in the junction cells creates a small mismatch, which is corrected by adjusting the strengths of the quadrupoles in the last junction cell and in the first regular cell.

Synchrotron Radiation Effects – Emittance Dilution

ERL efficiency as a source of multi-GeV electrons for a high luminosity collider is limited by the incoherent synchrotron radiation effects on beam dynamics; namely the transverse emittance dilution and the longitudinal momentum spread (induced by quantum excitations). The first effect, the transverse emittance increase, will have a paramount impact on the collider luminosity, due to stringent limits on the allowed emittance increase. The second one, accrued momentum spread, governs asymmetries of accelerated and decelerated beam profiles. These asymmetries substantially complicate multi-pass energy recovery and matching, and ultimately they limit the energy reach of the ERLs due to recirculating arc momentum acceptance.

Arc optics was designed to ease individual adjustment of momentum compaction (needed for the longitudinal phase-space control, essential for operation with energy recovery) and the horizontal emittance dispersion, H, in each arc. Tab. 10.2 lists arc-by-arc dilution of the transverse, $\Delta\epsilon$, and longitudinal, $\Delta\sigma_{\frac{\Delta E}{E}}$, emittance due to quantum excitations calculated using analytic formulas, Eqs. (10.5), (10.6) and (10.7), introduced by M. Sands [800]:

$$\Delta E = \frac{2\pi}{3} r_0 \ mc^2 \ \frac{\gamma^4}{\rho} \tag{10.5}$$

$$\Delta\epsilon_N = \frac{2\pi}{3} C_q r_0 < H > \frac{\gamma^6}{\rho^2} \, , \tag{10.6}$$

$$\frac{\Delta\epsilon_E^2}{E^2} = \frac{2\pi}{3} C_q r_0 \ \frac{\gamma^5}{\rho^2} \, , \tag{10.7}$$

where C_q is given by Eq. (10.2). Here, $\Delta\epsilon_E^2$ is an increment of energy square variance, r_0 is the classical electron radius, γ is the Lorentz boost and $C_q \approx 3.832 \cdot 10^{-13}$ m for electrons (or positrons).

Beamline	Beam energy [GeV]	ΔE [MeV]	$\Delta\epsilon_N^x$ [mm mrad]	$\Delta\sigma_{\frac{\Delta E}{E}}$ [%]
arc 1	8.62	0.7	0.0016	0.0005
arc 2	16.73	10	0.085	0.0027
arc 3	24.85	49	0.91	0.0072
arc 4	32.96	152	0.81	0.015
arc 5	41.08	368	3.03	0.026
arc 6	49.19	758	8.93	0.040

Table 10.2: Energy loss and emittance dilution (horizontal and longitudinal) due to synchroton radiation generated by all six 180° arcs (not including Spreaders, Recombiners and Doglegs). Here, $\Delta\sigma_{\frac{\Delta E}{E}} = \sqrt{\frac{\Delta\epsilon_E^2}{E^2}}$.

Beamline	Beam energy [GeV]	ΔE [MeV]	$\Delta\epsilon_N^y$ [mm mrad]	$\Delta\sigma_{\frac{\Delta E}{E}}$ [%]
Spr/Rec 1	8.62	0.2	0.035	0.0008
Spr/Rec 2	16.73	3.0	0.540	0.0044
Spr/Rec 3	24.85	6.0	0.871	0.0066
Spr/Rec 4	32.96	21.6	5.549	0.0143
Spr/Rec 5	41.08	7.1	0.402	0.0062
Spr/Rec 6	49.19	39.2	3.92	0.0205

Table 10.3: Energy loss and emittance dilution (vertical and longitudinal) due to synchroton radiation generated by the two step Spreader, or Recombiner design of a given arc. Here, $\Delta\sigma_{\frac{\Delta E}{E}} = \sqrt{\frac{\Delta\epsilon_E^2}{E^2}}$.

Apart from the horizontal 180° arcs, there are other sources of emittance dilution due to synchrotron radiation, namely vertical Spreaders and Recombiners, as well as horizontal 'Doglegs' used to compensate seasonal variation of path-length. To minimise their contribution to the vertical emittance dilution, special optics with small vertical $< H >$ has been introduced in Spr/Rec sections. The effects on vertical emittance dilution coming from these beamlines (Spr/Rec) are summarized in Tab. 10.3 for the two-step spreaders and in Tab. 10.4 for the alternative version of a one-step spreader.

	Beam Energy [GeV]	ΔE [MeV]	$\Delta\epsilon_N^y$ [mm.mrad]	$\Delta\sigma_{\frac{\Delta E}{E}}$ [%]
Spreader 1	8.62	0.04	0.004	0.0002
Spreader 2	16.73	0.31	0.004	0.0007
Spreader 3	24.85	0.32	0.012	0.0006
Spreader 4	32.96	1.18	0.112	0.0013
Spreader 5	41.08	2.64	0.083	0.0019
Spreader 6	49.19	7.92	1.060	0.0040

Table 10.4: Energy loss and emittance dilution (vertical and longitudinal) due to synchroton radiation generated by a one-step Spreader, or Recombiner design of a given arc. Here, $\Delta\sigma_{\frac{\Delta E}{E}} = \sqrt{\frac{\Delta\epsilon_E^2}{E^2}}$

Similarly, the horizontal emittance dilution induced by the Doglegs (four dogleg chicanes per arc) in various arcs is summarized in Tab. 10.5. Each dogleg chicane is configured with four 1 meter bends (1 Tesla each), so that they bend the lowest energy beam at 8.6 GeV by 2 degrees.

The corresponding path-lengths gained in the Doglegs of different arcs are also indicated.

Beamline	Beam energy [GeV]	ΔE [MeV]	$\Delta \epsilon_N^x$ [mm mrad]	$\Delta \sigma_{\frac{\Delta E}{E}}$ [%]	path-length [mm]
Doglegs 1	8.62	2	0.201	0.007	7.32
Doglegs 2	16.73	9	0.667	0.009	1.96
Doglegs 3	24.85	19	5.476	0.014	0.84
Doglegs 4	32.96	33	5.067	0.014	0.52
Doglegs 5	41.08	52	12.067	0.028	0.36
Doglegs 6	49.19	74	2.836	0.011	0.28

Table 10.5: Energy loss and emittance dilution (horizontal and longitudinal) due to synchroton radiation generated by the Doglegs (four dogleg chicanes) of a given arc. Here, $\Delta \sigma_{\frac{\Delta E}{E}} = \sqrt{\frac{\Delta \epsilon_E^2}{E^2}}$.

As indicated in Tab. 10.5, the Doglegs in the highest energy arcs, Arc 5 and Arc 6, provide only sub mm path-length gain with large synchrotron radiation effects. They are not very effective and generate strong, undesired emittance dilution. Therefore, it is reasonable to eliminate them from both Arc 5 and 6. Instead, one could resort to an alternative path-length control via appropriate orbit steering with both horizontal and vertical correctors present at every girder and distributed evenly throughout the arc.

Combining all three contributions: (180° arc, Spreader, Recombiner and Doglegs (no Doglegs in Arcs 5 and 6), the net cumulative emittance dilution is summarized in Tab. 10.6 for the case of the two-step spreader.

Beamline	Beam energy [GeV]	ΔE [MeV]	$\Delta^{\text{cum}} \epsilon_N^x$ [mm mrad]	$\Delta^{\text{cum}} \epsilon_N^y$ [mm mrad]	$\Delta^{\text{cum}} \sigma_{\frac{\Delta E}{E}}$ [%]
Arc 1	8.62	3	0.2	0.1	0.01
Arc 2	16.73	25	1.0	1.2	0.03
Arc 3	24.85	80	7.3	2.9	0.06
Arc 4	32.96	229	13.2	14.0	0.12
Arc 5	41.08	383	16.2	14.8	0.16
IR	49.19	39	**16.2**	**18.7**	**0.18**
Arc 6	49.19	797	25.2	22.6	0.24
Arc 5	41.08	383	28.2	23.4	0.28
Arc 4	32.96	229	34.1	34.5	0.33
Arc 3	24.85	80	40.5	36.3	0.37
Arc 2	16.73	25	41.2	37.4	0.39
Arc 1	8.62	3	41.4	37.4	0.40
Dump	0.5		41.4	37.4	0.40

Table 10.6: Energy loss and cumulative emittance dilution (transverse and longitudinal) due to synchroton radiation at the end of a given beam-line (complete Arc including: 180° arc, Spreader, Recombiner and Doglegs in arcs 1-4). The table covers the entire ER cycle: 3 passes 'up' + 3 passes 'down'. Cumulative emittance dilution values just before the IP (past Arc 5 and Spr 6), which are critical for the luminosity consideration are highlighted in 'bold'. That row accounts for contributions from Spr 6 (the last bending section before the IR) to energy loss, as well as the vertical and longitudinal emittance dilutions. Here, $\Delta \sigma_{\frac{\Delta E}{E}} = \sqrt{\frac{\Delta \epsilon_E^2}{E^2}}$.

Tab. 10.6 shows, the LHeC luminosity requirement of total transverse emittance dilution in either plane (normalized) at the IP (at the end of Arc 5), not to exceed 20 mm mrad (hor:

16.2 mm mrad and ver: 18.7 mm mrad) is met by-design, employing presented low emittance lattices in both the arcs and switch-yards. In the case of the optimised one-step spreader design, another reduction - mainly of the vertical emittance budget - is obtained, providing a comfortable safety margin of the design.

Finally, one can see from Eqs. (10.6) and (10.7) an underlying universal scaling of the transverse (unnormalized) and longitudinal emittance dilution with energy and arc radius; they are both proportional to γ^5/ρ^2. This in turn, has a profound impact on arc size scalability with energy; namely the arc radius should scale as $\gamma^{5/2}$ in order to preserve both the transverse and longitudinal emittance dilutions, which is a figure of merit for a synchrotron radiation dominated ERL.

10.2.2   30 GeV ERL Options

One may think of an upgrade path from 30 to 50 GeV ERL, using the same 1/5 of the LHC circumference (5.4 km), footprint. In this scenario, each linac straight (front end) would initially be loaded with 18 cryomodules, forming two 5.21 GV linacs. One would also need to decrease the injector energy by a factor of 5.21/8.11. The top ERL energy, after three passes, would reach 31.3 GeV. Then for the upgrade to 50 GeV, one would fill the remaining space in the linacs with additional 10 cryomodules each; 2.9 GV worth of RF in each linac. This way the energy ratios would be preserved for both 30 and 50 GeV ERL options, so that the same switch-yard geometry could be used. Finally, one would scale up the entire lattice; all magnets (dipoles and quads) by 8.11/5.21 ratio.

If one wanted to stop at the 30 GeV option with no upgrade path, then a 1/14 of the LHC circumference (1.9 km) would be a viable footprint for the racetrack, featuring: two linacs, 503 m each, (17 cryomodules) and arcs of 94.5 m radius. Again, assuming 0.32 GeV injection energy, the top ERL energy would reach 30.2 GeV. Such a configuration may become of interest if time and funds may permit a small version of the LHeC or none. This version of the LHeC would have a reduced Higgs, top and BSM physics potential. Yet, owing to the high proton beam energy, this configuration would still have a TeV in the centre-of-mass such that the core QCD, PDF and electroweak programme would still be striking.

10.2.3   Component Summary

This closing section will summarise active accelerator components: magnets (bends and quads) and RF cavities for the 50 GeV baseline ERL. The bends (both horizontal and vertical) are captured in Tab. 10.7, while the quadrupole magnets and RF cavities are collected in Tab. 10.8.

One would like to use a combined aperture (3-in-one) arc magnet design with 50 cm vertical separation between the three apertures, proposed by Attilo Milanese [802]. That would reduce net arc bend count from 2112 to 704. As far as the Spr/Rec vertical bends are concerned, the design was optimised to include an additional common bend separating the two highest passes. So, there are a total of 8 trapezoid B-com magnets, with second face tilted by 3° and large 10 cm vertical aperture, the rest are simple rectangular bends with specs from the summary Tab. 10.7.

	Arc dipoles (horiz.)				Spr/Rec dipoles (vert.)				Dogleg dipoles (horiz.)			
Section	N	B[T]	$g/2$[cm]	L[m]	N	B[T]	$g/2$[cm]	L[m]	N	B[T]	$g/2$[cm]	L[m]
Arc 1	352	0.087	1.5	3	8	0.678	2	3	16	1	1.5	1
Arc 2	352	0.174	1.5	3	8	0.989	2	3	16	1	1.5	1
Arc 3	352	0.261	1.5	3	6	1.222	2	3	16	1	1.5	1
Arc 4	352	0.348	1.5	3	6	1.633	2	3	16	1	1.5	1
Arc 5	352	0.435	1.5	3	4	1.022	2	3				
Arc 6	352	0.522	1.5	3	4	1.389	2	3				
Total	2112				36				64			

Table 10.7: 50 GeV ERL – Dipole magnet count along with basic magnet parameters: Magnetic field (B), Half-Gap ($g/2$), and Magnetic length (L).

	Quadrupoles				RF cavities			
Section	N	G[T/m]	a[cm]	L[m]	N	f[MHz]	cell	G_{RF}[T/m]
Linac 1	29	1.93	3	1	448	802	5	20
Linac 2	29	1.93	3	1	448	802	5	20
Arc 1	255	9.25	2.5	1				
Arc 2	255	17.67	2.5	1				
Arc 3	255	24.25	2.5	1	6	1604	9	30
Arc 4	255	27.17	2.5	1	12	1604	9	30
Arc 5	249	33.92	2.5	1	18	1604	9	30
Arc 6	249	40.75	2.5	1	36	1604	9	30
Total	1576				968			

Table 10.8: 50 GeV ERL – Quadrupole magnet and RF cavities count along with basic magnet/RF parameters: Magnetic field gradient (G), Aperture radius (a), Magnetic length (L), Frequency (f), Number of cells in RF cavity (cell), and RF Gradient (G_{RF}).

10.3 Electron-Ion Collisions

Besides colliding proton beams, the LHC also provides collisions of nuclear (fully-stripped ion) beams with each other (AA collisions) or with protons (pA). Either of these operating modes offers the possibility of electron-ion (eA) collisions in the LHeC configuration[1]

Here we summarise the considerations leading to the luminosity estimates given in Tab. 2.4 for collisions of electrons with ^{208}Pb^{82+} nuclei, the nominal heavy ion species collided in the LHC. Other, lighter, nuclei are under consideration for future LHC operation [501] and could also be considered for electron-ion collisions.

The heavy ion beams that the CERN injector complex can provide to the LHC, the HE-LHC and the FCC provide a unique basis for high energy, high luminosity deep inelastic electron-ion scattering physics. Since HERA was restricted to protons only, the LHeC or FCC-eh would extend the kinematic range in Q^2 and $1/x$ by 4 or 5 orders of magnitude. This is a huge increase in coverage and would be set to radically change the understanding of parton dynamics in nuclei and of the formation of the quark gluon plasma.

---

[1] In pA operation of the LHC the beams may be reversed (Ap) for some part of the operating time. Only one direction (ions in Beam 2) would provide eA collisions while the other would provide ep collisions at significantly reduced luminosity compared to the pp mode, since there would be fewer proton bunches of lower intensity.

An initial set of parameters in the maximum energy configurations was given in [35]. The Pb beam parameters are essentially those foreseen for operation of the LHC (or HL-LHC) in Run 3 and Run 4 (planned for the 2020s). These parameters have already been largely demonstrated [803] except for the major remaining step of implementing slip-stacking injection in the SPS which would reduce the basic bunch spacing from 100 to 50 ns [804]. With respect to the proton spacing of 25 ns, this allows the electron bunch intensity to be doubled while still respecting the limit on total electron current. In fact, without the slip-stacking in the SPS, the initial luminosity would be the same with a 100 ns Pb spacing (and quadrupled electron bunch intensity). However one must remember that the evolution of the Pb beam intensity will be dominated by luminosity burn-off by the concurrent PbPb collisions at the other interaction points and integrated luminosity for both PbPb and ePb collisions will be higher with the higher total Pb intensity. The details of this will depend on the operating scenarios, number of active experiments, etc, and are not considered further here. The time-evolution of eA luminosity will be determined by that of PbPb and pPb collisions, as discussed, for example, in Ref. [16,501,805].

Combining these assumptions with the default 50 GeV electron ERL for LHeC and 60 GeV for FCC-eh, yields the updated parameter sets and initial luminosities given in Tab. 2.4, earlier in the present report.

Radiation damping of Pb beams in the hadron rings is about twice as fast as for protons and can be fully exploited since it takes longer to approach the beam-beam limit at the PbPb collisions points. For the case of the FCC-hh [16], one can expect the emittance values in Tab. 2.4 to be reduced during fills [16,501,805].

The Pb beam will be affected by ultraperipheral collision effects, mainly bound-free pair production and Coulomb dissociation of the nuclei, induced by the electromagnetic fields of the electrons, seen as pulses of virtual photons. The relevant cross-sections will be similar to those in pPb collisions which are down by a factor of Z^2 compared to those in PbPb collisions and can be neglected in practice.

10.4 Beam-Beam Interactions

In the framework of the Large Hadron electron Collider, the concept of an Energy Recirculating Linac (ERL) allows to overcome the beam-beam limit that one would face in a storage ring. The electron beam can be heavily disturbed by the beam collision process, while the large acceptance of the ERL will still allow for a successful energy recovery during the deceleration of the beam so that the power consumption is minimised. In order to compare the relevant beam-beam parameters and put them into the context of other colliders, two tables are shown highlighting, on the one hand, the parameters from LEP and LHC runs in Tab. 10.9, and on the other hand, the parameters planned for LHeC at HL-LHC in Tab. 10.10.

In the case of LHeC, the β-functions at the interaction point are chosen such that the transverse beam sizes of the e- and p- beams are equal in both transverse planes. Although the proton and electron emittances are different, the beta functions at the interaction point are set accordingly so that the two beams conserve $\sigma_x^e = \sigma_x^p$ and $\sigma_y^e = \sigma_y^p$.

Parameter	Unit	LEP	LHC
Beam sizes σ_x / σ_y	µm	180 / 7	16.6 / 16.6
Intensity	10^{11} particles/bunch	4.00	1.15
Energy	GeV	100	7000
β_x^*/β_y^*	cm	125/5	55/55
Crossing angle	µrad	0	0/285
Beam-beam tune shift $\Delta Q_x/\Delta Q_y$		0.0400/0.0400	0.0037/0.0034
Beam-beam parameter ξ		0.0700	0.0037

Table 10.9: Comparison of parameters for the LEP collider and LHC. Taken from CDR 2012, p.286.

Beam parameter	Unit	LHeC at HL-LHC	
		Proton beam	Electron beam
Energy	GeV	7000	49.19
Normalized emittance	mm·mrad	2.5	50
Beam sizes $\sigma_{x,y}$	µm	5.8	5.8
Intensity	10^9 particles/bunch	220.00	3.12
Bunch length σ_s	mm	75.5	0.6
$\beta_{x,y}^*$	cm	10.00	6.45
Disruption factor		1.2×10^{-5}	14.5
Beam-beam parameter ξ		1.52×10^{-4}	0.99

Table 10.10: Comparison of parameters for the LHeC at HL-LHC. The parameters presented correspond to the default design.

10.4.1 Effect on the electron beam

The disruption parameter for the electron beam is of the order of 14.5 which corresponds, in linear approximation, to almost 2 oscillations of the beam envelope within the proton bunch. The non linearity of the interaction creates a distortion of the phase space and a mismatch from the design optics (see Fig. 10.12). The mismatch and distortion can be minimized by tuning the Twiss parameters (α^*, β^*) at the interaction point.

In a series of studies the optics parameters of the electron beam were tracked back to the interaction point in presence of the beam-beam forces in order to show the impact of the beam-beam effect for different values of the electron Twiss parameters at the IP. In addition, the influence of a waist shift from the IP (proportional to α^*), similar to changing the foci of the interacting beams, has been studied and allows to keep the electron beam for a longer time within the proton bunch, thus optimizing the luminosity. The modification of the electron beta function (β^*) leads to more freedom and gives access, among all the possibilities, to two different optima regarding the luminosity and the mismatch from the design optics. The results are summarized in the contour plots of Fig. 10.13.

As a consequence, the Twiss parameters at the interaction point can be set in a way, to minimize the mismatch of the optics (i.e. the effective emittance) or to maximize the luminosity. In case the optimization of the luminosity is chosen (see the circle marker in Fig. 10.13), a modified capture optics in the beam transfer to the arc structure will be needed to re-match the modified Twiss functions perturbed by the non-linear beam-beam effects.

The effect of possible offsets between the two colliding beams has been characterized in previous beam-beam studies [806], and – if uncorrected – might lead to an electron beam emittance
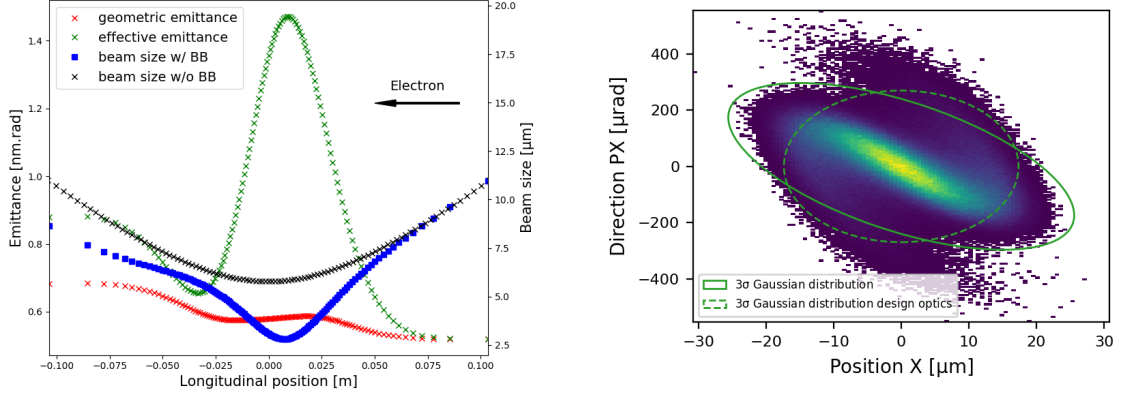
Figure 10.12: Left: Electron beam sizes with (blue) and without (black) the beam-beam forces exerted on the electron beam. The geometric emittance is represented in red and the effective emittance that takes into account the mismatch from the original optics is illustrated in green. Right: The horizontal phase space of the spent electron distribution backtracked to the interaction point. 3σ Gaussian distribution are highlighted for the post-collided distribution (solid line) and the design optics (dashed line).
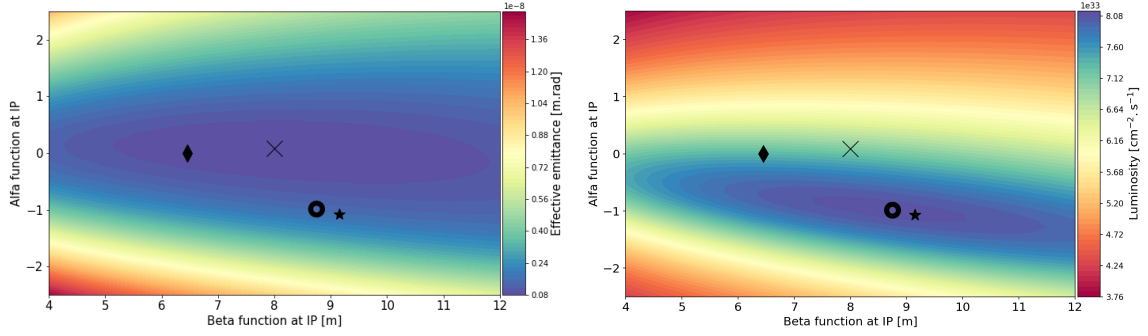
Figure 10.13: Left : Contour plot describing the effective emittance post collision as a function of the alfa and beta functions at IP. Right : Contour plot describing the luminosity as a function of the alfa and beta functions at the IP. The diamond marker represents the initial Twiss parameters, the circle shows the luminosity optimum, the cross symbolizes the smallest mismatch from the original optics and the star illustrates the minimal geometric emittance growth.

growth. The parameters for these studies have been updated and the results are presented in Fig. 10.14. As any offset between the two beams is amplified, it results in a larger increase of the beam envelope. As a solution, a fast feed-forward system is proposed, across the Arc 6, which would aim at damping the transverse motion so that the beam emittance can be recovered. Using two sets of kickers placed at the center and at the end of the arc, an offset of 0.16σ can be damped. A single set cutting across the whole arc can correct a 1σ offset with approximately $4.4\,\mathrm{kV}$.

Additionally, the coupling of the beam-beam effect with long range wakefields has been addressed [806]. Assuming a misaligned bunch injected among a train of nominal bunches, the coupling of the beam-beam effect with the wakefields leads to a reduction of the damping of the excitation created by the misaligned bunch. Nevertheless it can be shown that the beam stability is conserved and the total amplification remains acceptable with respect to the study that was not considering the coupling.
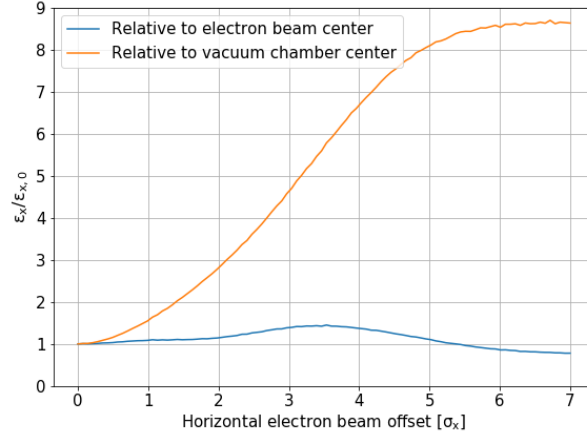
Figure 10.14: Electron bean emittance relative change with respect to its centroid (blue) and with respect to the vacuum chamber center (orange).

10.4.2 Effect on the proton beam

The beam-beam interaction between the electron and proton beams is asymmetric in terms of beam rigidities. Although the less energetic 49.19 GeV electron beam is heavily distorted by the strong 7 TeV proton beam, the proton beam will suffer from an emittance growth adding up turn by turn [806] due to the build up of the tiny disruption created by the offset between the beams. In fact, the previous studies gave a growth rate of around 0.01 %/s for a jitter of 0.2 σ_x. As long as an adequate control of the bunches is preserved, this effect should lie in the shadow of other effects leading to emittance blow-up in the LHC (e.g. IBS). Since the electron beam energy decreased from 60 GeV to 49.19 GeV this study needs to be updated and the results should remain in agreement with the previous statement.

10.5 Arc Magnets

In this section, a conceptual design of the main magnets needed for the Linac-Ring (LR) accelerator at 50 GeV is described. The number and types of magnets is listed in Tabs. 10.7 and 10.8.

10.5.1 Dipole magnets

The bending magnets are used in the arcs of the recirculator. Each of the six arcs needs 352 horizontal bending dipoles. Additional dipoles are needed in the straight sections: 36 vertical bending dipoles in the spreader/recombiner and 64 horizontal bending dipoles for the "dogleg". These magnets are not considered at the moment.

In the CDR issued in 2012 for a 60 GeV lepton ring (LR) , a design based on three independent dipoles stacked on top of each other was proposed. A post-CDR design with three apertures dipoles was introduced in 2014 [802]. This solution allows reducing the Ampere-turns and the production cost of the dipoles. For a 50 GeV LR, the three apertures dipole design is adapted to fulfil new magnetic field requirements.

The 352 horizontal bending dipoles needed for each arc, combined in three apertures dipoles result in a total of 704 units. These magnets are 3 m long and provide a field in the 30 mm aperture ranging from 0.087 T to 0.522 T depending on the arc energy, from 8.62 GeV to 49.19 GeV.

Parameter	Unit	Value
Beam energy	GeV	8.62 to 49.19
Magnetic field	T	0.087 to 0.522
Magnetic length	m	3
Vertical aperture	mm	30
Pole width	mm	90
Number of apertures		3
Distance between apertures	mm	500
Mass	8000	kg
Number of magnets		704
Current	A	4250
Number of turns per magnet		4
Current density	A/mm^2	1
Conductor material		aluminum
Magnet resistance	mΩ	0.17
Power	kW	3
Total power consumption six arcs	MW	2.1
Cooling		air

Table 10.11: 50 GeV ERL – Main parameters of the three apertures bending magnets.
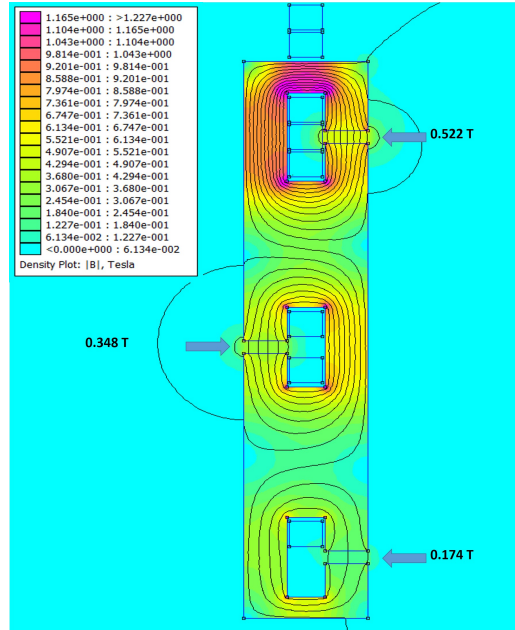
Figure 10.15: 50 GeV ERL - Cross section of the three apertures bending magnet, arc 2, 4 and 6 with 500 mm between consecutive arcs - Finite Element Method (FEM).

In the proposed design, the three apertures are stacked vertically but offset transversely. This allows recycling the Ampere-turns from one aperture to the other. The coils are centrally located on the yoke and are made of simple aluminium bus-bars all powered in series. A current density of 1 A/mm^2 in the coils is sufficiently low to not have water-cooling but in order to limit the temperature in the tunnel it may be required. Trim coils can be added on two of the apertures to provide some tuning. Alternatively, each stage could be powered separately. The dipole yokes

are made of low carbon steel plates. The relevant parameters are summarised in Tab. 10.11 and the cross section is illustrated in Fig. 10.15 for 500 mm between consecutive arcs.

10.5.2   Quadrupole magnets

Quadrupoles for recirculator arcs

In total 1518 quadrupoles are needed for the recirculator arcs: 255 for each of the arcs one to four and 249 for each of the arcs five and six. The required integrated gradients, comprised between 9.25 T and 40.75 T, can be achieved using one type of quadrupole one meter long. However, instead of operating the magnets at low current for lower arcs energy, it can be considered to have a shorter model 0.6 meter long for arcs one to three. These quadrupoles require water-cooling for the coils. The relevant parameters are summarised in Tab. 10.12 and the cross section is illustrated in Fig. 10.16 (left).

In order to reduce the power consumption, it could be envisaged to use a hybrid configuration for the quadrupoles, with most of the excitation given by permanent magnets. The gradient strength could be varied by trim coils or by mechanical methods.

Parameter	Unit	Value
Beam energy	GeV	8.62 to 49.19
Field gradient	T/m	9.25 to 40.75
Magnetic length	m	1
Aperture radius	mm	25
Mass	kg	550
Number of magnets		1518
Current at 40.75 T/m	A	560
Number of turns per pole		17
Current density at 40.75 T/m	A/mm^2	6.7
Conductor material		copper
Magnet resistance	mΩ	33
Power at 8.62 GeV	kW	0.5
Power at 16.73 GeV	kW	1.9
Power at 24.85 GeV	kW	3.7
Power at 32.96 GeV	kW	4.6
Power at 41.08 GeV	kW	7.2
Power at 49.19 GeV	kW	10.3
Total power consumption six arcs	MW	7.1
Cooling		water

Table 10.12: 50 GeV ERL – Main parameters of the arc quadrupoles.

Quadrupoles for the two 8.1 GeV linacs

In the two 8.1 GeV linacs, 29 + 29 quadrupoles, each providing 1.93 T integrated strength are required. The present design solution considers 30 mm aperture radius magnets. The relevant parameters are summarised in Tab. 10.13 and the cross section is illustrated in Fig. 10.16 (right).
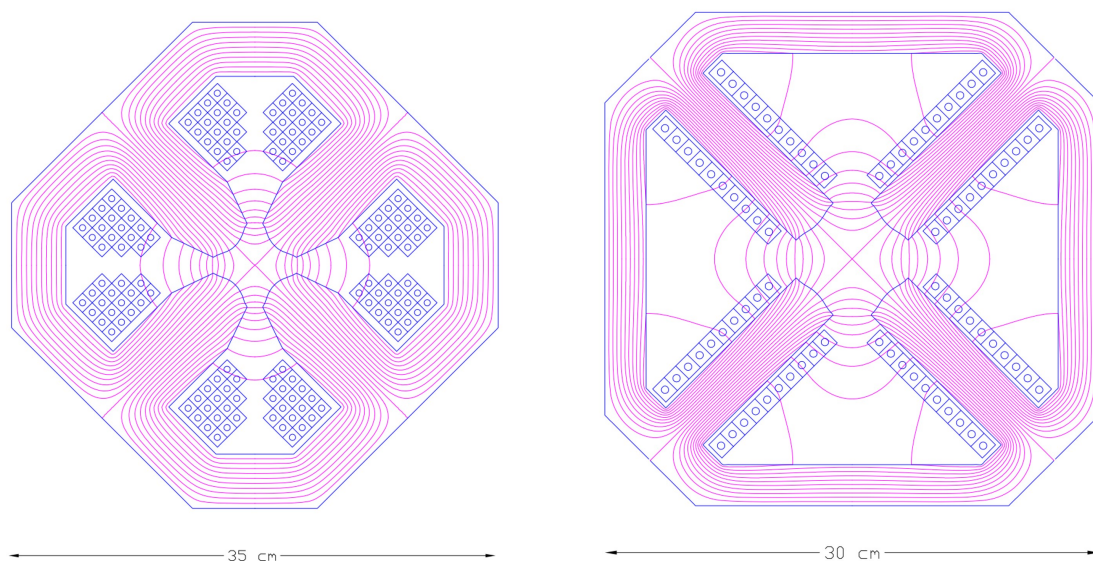
Figure 10.16: 50 GeV ERL. Left: Cross section of the arc quadrupole magnets. Right: Cross section of the linac quadrupole magnets.

Parameter	Unit	Value
Beam energy	GeV	8.62 to 49.19
Field gradient	T/m	7.7
Magnetic length	m	0.25
Aperture radius	mm	30
Mass	kg	110
Number of magnets		56
Current at 7.7 T/m	A	285
Number of turns per pole		10
Current density at 7.7 T/m	A/mm^2	3
Conductor material		copper
Magnet resistance	mΩ	6
Power at 8.1 GeV	kW	0.5
Total power consumption 2 linacs	MW	0.03
Cooling		water

Table 10.13: 50 GeV ERL – Main parameters of the linac quadrupoles.

10.6   LINAC and SRF

Each of the two main linacs has an overall length of 828.8 m and provides an acceleration of 8.114 GV. Each linac consists of 112 cryomodules, arranged in 28 units of 4 cryomodules with their focussing elements – each cryomodule contains four 5-cell cavities, optimised to operate with large beam current (up to 120 mA at the High Order Mode – HOM – frequencies). The operating temperature is 2 K; the cavities are based on modern SRF technology and are fabricated from bulk Nb sheets; they are described in detail in section 10.6.2 below. The nominal acceleration gradient is 19.73 MV/m.

In addition to the main linacs, the synchrotron losses in the arcs will make additional linacs necessary, referred to here as the *loss compensation linacs.* These will have to provide different accelerations in the different arcs, depending on the energy of the beams as shown in Tab. 10.14.

The quoted beam energies are at entry into the arc. Their natural placement would be at the end of the arcs just before the combiner, where the different energy beams are still separate. The largest of these linacs would have to compensate the SR losses at the highest energy, requiring a total acceleration of about 700 MV. The loss compensation linacs will be detailed in section 10.6.6 below.

Section	Beam energy [GeV]	ΔE [MeV]
Arc 1	8.62	3
Arc 2	16.73	25
Arc 3	24.85	80
Arc 4	32.96	229
Arc 5	41.08	383
Arc 6	49.19	836

Table 10.14: Synchroton radiation losses for the different arc energies

Through all arcs but Arc 6, the beam passes twice, once while accelerated and once while decelerated. It is planned to operate these additional *loss compensation linacs* at 1603.2 MHz, which allows energy compensation of both the accelerated and the decelerated beam simultaneously. This subject will be discussed in detail in a subsequent section 10.6.6.

10.6.1 Choice of Frequency

The RF frequency choice primarily takes into account the constraints of the LHC bunch repetition frequency, f_0, of 40.079 MHz, while allowing for a sufficiently high harmonic, h, for a flexible system. For an ERL with $n_{pass} = 3$ recirculating passes and in order to enable equal bunch spacing for the 3 bunches – though not mandatory – it was originally considered to suppress all harmonics that are not a multiple of $n_{pass} \cdot f_0 = 120.237$ MHz. Initial choices for instance were 721.42 MHz ($h = 18$) and 1322.61 MHz ($h = 33$) in consideration of the proximity to the frequencies used for state-of-the-art SRF system developments worldwide [807]. In synergy with other RF system developments at CERN though, the final choice was 801.58 MHz ($h = 20$), where the bunching between the 3 recirculating bunches can be made similar but not exactly equal. Note that this frequency is also very close to the 805 MHz SRF proton cavities operating at the Spallation Neutron Source (SNS) at ORNL, so that one could leverage from the experience in regard to cryomodule and component design at this frequency.

Furthermore, in the frame of an independent study for a 1 GeV CW proton linac, a capital plus operational cost optimisation was conducted [808]. This optimisation took into account the expenditures for cavities, cryomodules, the linac tunnel as well as the helium refrigerator expenses as a function of frequency and thus component sizes. Labor costs were included based on the existing SNS linac facility work breakdown structure. It was shown that capital plus operating costs could be minimised with a cavity frequency between 800 MHz and 850 MHz, depending also on the choice of the operating He bath temperature (1.8 K to 2.1 K). Clear benefit of operating in this frequency regime are the comparably small dynamic RF losses per installation length due to a relatively small BCS surface resistance as well as low residual resistance of the niobium at the operating temperature. This could be principally verified as part of the prototyping effort detailed in the next sub-section. Note that the cost optimum also favors cavities operating at rather moderate field levels (< 20 MV/m). This comes as a benefit in concern of field emission and associated potential performance degradations.

10.6.2 Cavity Prototype

Given the RF frequency of 801.58 MHz, JLab has collaborated with CERN, and consequently proposed a five-cell cavity design that was accepted for prototyping, see Fig. 10.17. The cavity shape has also been adopted for PERLE. Tab. 10.15 summarises the relevant cavity parameters.
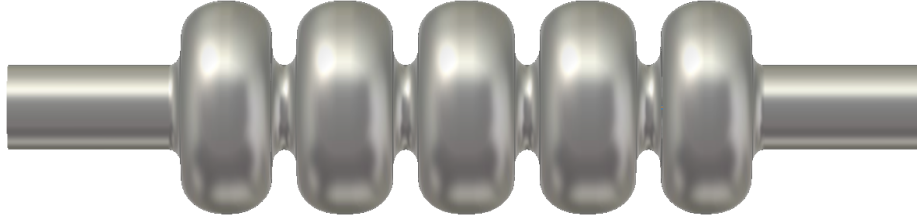

Figure 10.17: Bare 802 MHz five-cell cavity design (RF vacuum) with a 130 mm iris and beam tube aperture.

Paramater	Unit	Value
Frequency	MHz	801.58
Number of cells		5
active length l_{act}	mm	917.9
loss factor	$V\,pC^{-1}$	2.742
R/Q (linac convention)	Ω	523.9
$R/Q \cdot G$ per cell	Ω^2	28788
Cavity equator diameter	mm	327.95
Cavity iris diameter	mm	130
Beam tube inner diameter	mm	130
diameter ratio equator/iris		2.52
E_{peak}/E_{acc}		2.26
B_{peak}/E_{acc}	mT/(MV/m)	4.2
cell-to-cell coupling factor k_{cc}	%	3.21
TE_{11} cutoff frequency	GHz	1.35
TM_{01} cutoff frequency	GHz	1.77

Table 10.15: Parameter table of the 802 MHz prototype five-cell cavity.

The cavity exhibits a rather large iris and beam tube aperture (130 mm) to consider beam-dynamical aspects such as HOM-driven multi-bunch instabilities. Despite the comparably large aperture, the ratio of the peak surface electric field, E_{pk}, respectively the peak surface magnetic field, B_{pk}, and the accelerating field, E_{acc}, are reasonably low, while the factor $R/Q \cdot G$ is kept reasonably high, concurrently to limit cryogenic losses. This is considered as a generically well *balanced* cavity design [809]. The cavity cell shape also avoids that crucial HOMs will coincide with the main spectral lines (multiples of 801.58 MHz), while the specific HOM coupler development is pending.

Furthermore, as shown in Fig. 10.18 for the case of the bunch recombination pattern considered for PERLE originally, the much denser intermediate beam current lines (green) are not coinciding with cavity HOMs. Here the figure plots the real part of the beam-excited cavity monopole impedance spectrum up to 6 GHz, and denotes the power deposited at each spectral line (in Watt) for an injected beam current of 25 mA. For instance, the summation of the power in this spectral range results in a moderate 30 W. This covers the monopole modes with the highest impedances residing below the beam tube cutoff frequency. The HOM-induced heat has
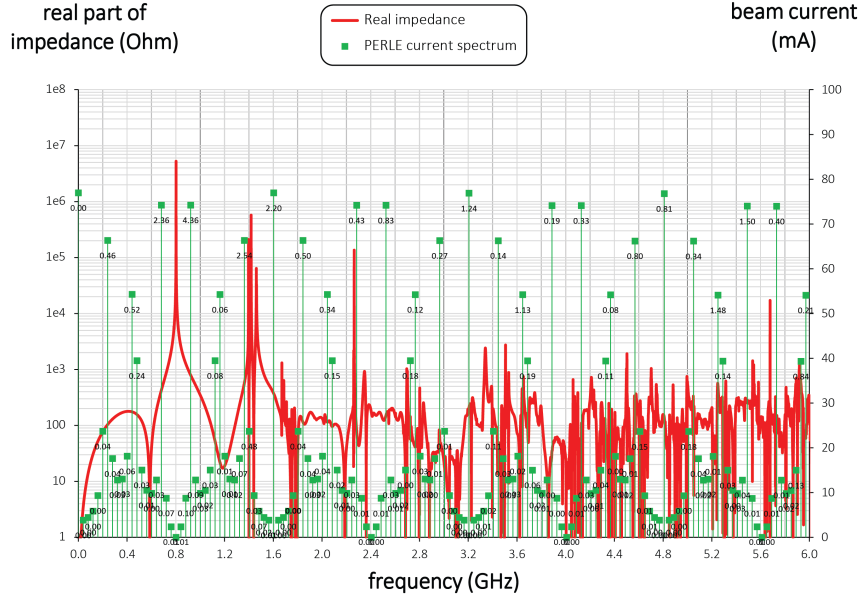
Figure 10.18: Real monopole impedance spectrum of the five-cell 802 MHz cavity prototype (red) together with the considered beam current lines (green) for the 3-pass PERLE machine (25 mA injected current). The numbers associated with the spectral lines denote the power dissipation (in Watt).

to be extracted from the cavity and shared among the HOM couplers attached to the cavity beam tubes. The fraction of the power escaping through the beam tubes above cutoff can be intercepted by beam line absorbers.

Note that for Fig. 10.18 a single HOM-coupler end-group consisting of three scaled TESLA-type coaxial couplers was assumed to provide damping. Instead of coaxial couplers, waveguide couplers could be utilized, which for instance have been developed at JLab in the past for high current machines. These are naturally broadband and designed for high power capability, though some penalty is introduced as this will increase the complexity of the cryomodule. Ultimately, the aim is to efficiently damp the most parasitic longitudinal and transverse modes (each polarization). The evaluation of the total power deposition is important for LHeC to decide which HOM coupler technology is most appropriate to cope with the dissipated heat and whether active cooling of the couplers is a requirement.

Though the prototype efforts focused on the five-cell cavity development, JLab also produced single-cell cavities, i.e. one further Nb cavity and two OFE copper cavities. The former has been shipped to FNAL for N-doping/infusion studies, whereas the latter were delivered to CERN for Nb thin-film coating as a possible alternative to bulk Nb cavities. In addition, a copper cavity was built for low power bench measurements, for which multiple half-cells can be mechanically clamped together. Presently, a mock-up can be created with up to two full cells. This cavity has been produced in support of the pending HOM coupler development. The ensemble of manufactured cavities resonating at 802 MHz is shwon in Fig. 10.19.

Results for the Nb cavities - made from fine grain high-RRR Nb - were encouraging since both cavities reached accelerating fields, E_{acc}, slightly above 30 MV/m ultimately limited by thermal breakdown (quench). Moreover, the RF losses were rather small as a benefit of the relatively low RF frequency as anticipated. The residual resistance extracted from the measurement data upon cooldown of the cavity was $3.2\,\Omega \pm 0.8\,\Omega$. This resulted in unloaded quality factors, Q_0, well above 4×10^{10} at 2 K at low field levels, while Q_0-values beyond 3×10^{10} could be
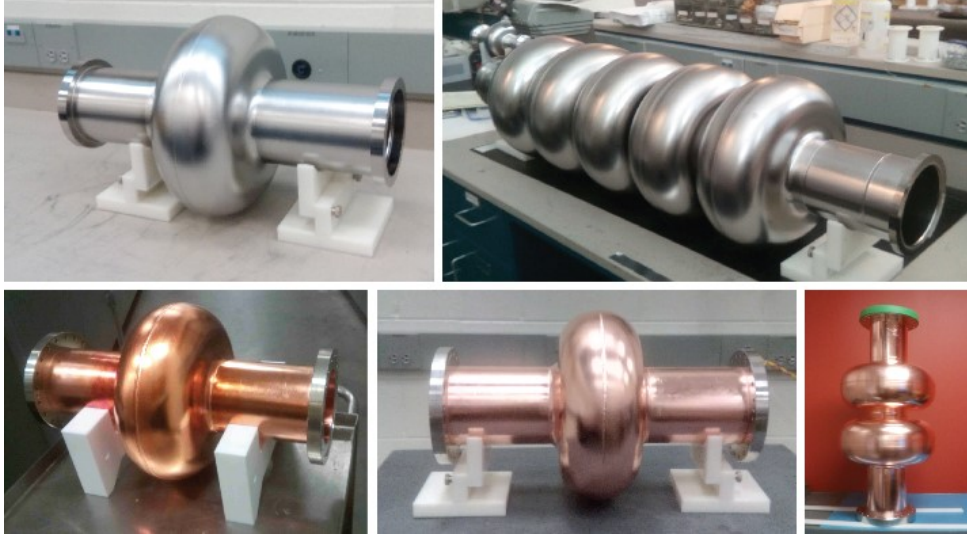
Figure 10.19: Ensemble of 802 MHz cavities designed and built at JLab for CERN. The Nb cavities have been tested vertically at 2 Kelvin in JLab's vertical test area.

maintained for the five-cell cavity up to $\sim$27 MV/m (see Fig. 10.20). Only standard interior surface post-processing methods were applied including bulk buffered chemical polishing, high temperature vacuum annealing, light electropolishing, ultrapure high-pressure water rinsing, and a low temperature bake-out. While the vertical test results indicate generous headroom for a potential performance reduction once a cavity is equipped with all the ancillary components and installed in a cryomodule, clean cavity assembly procedure protocols must be established for the cryomodules to minimise the chance of introducing field-emitting particulates.
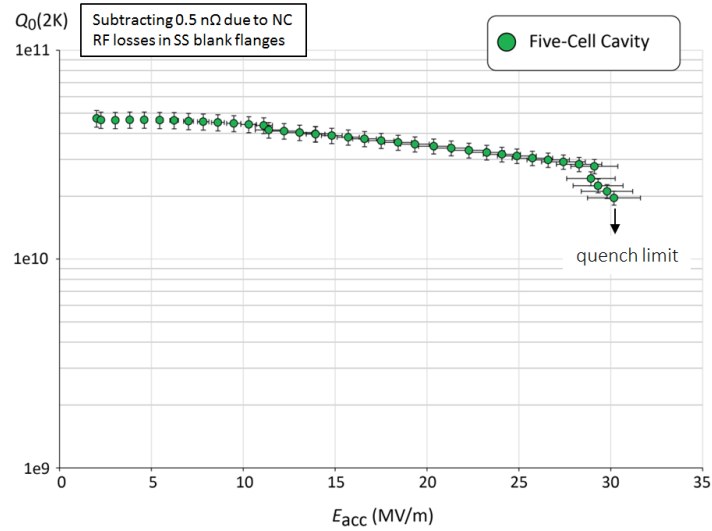
Figure 10.20: Vertical test result of the five-cell 802 MHz niobium cavity prototype.

10.6.3 Cavity-Cryomodule

The ERL cryomodules hosting the superconducting RF cavities are a key component of the accelerator. They should provide the proper mechanical, vacuum and cryogenic environment to

the SRF cavities equipped with their ancillaries systems: helium tank, power coupler and HOM couplers. Each cryomodule is containing 4 superconducting 801.58 MHz 5-cells elliptical cavities described in the previous chapters.

Recently, several projects worldwide have designed cryomodules for elliptical cavities with a cavity configuration (number, length and diameter) quite close to the one required by LHeC ERL:

- SNS [810]: two different sized cryomodules host either 4 elliptical 6-cells 805 MHz cavities of $\beta = 0.81$ or 4 elliptical 6-cells 805 MHz of $\beta = 0.61$;

- SPL [811]: the cryomodule is designed to integrate 4 elliptical 5-cells 704 MHz cavities of $\beta = 1$;

- ESS [812]: two cryomodules of the same length can host either 4 elliptical 6-cells 704 MHz cavities of $\beta = 0.67$ or 4 elliptical 5-cells 704 MHz cavities of $\beta = 0.85$.

These three cryomodule designs are based on two completely different concepts for the cavity string support structure. SNS and ESS cryomodules are based on an intermediate support system, called the spaceframe, which is horizontally translated inside the cryomodule vacuum vessel. The low pressure cryogenic line is located above the cavities string and connected to the cryogenic transfer line by a double angled connection, the jumper. RF waveguides are connected underneath the cryomodule, using door-knob transition to the couplers. All the hanging and alignment operations of the cavities string and shielding are implemented outside the vacuum tank, using the spaceframe. In the ESS case, each cavity is hanged by 2 sets of 4 cross rods. The thermal shield is also hanged to these rods by the mean of an aluminium "elastic boxes" that allow the thermal shrinkage while maintaining the transverse stability. The thermal shield is made of 2.5 mm thick aluminium and wrapped with multi-layer insulation. It is fastened directly to the support rods of the cavities string.
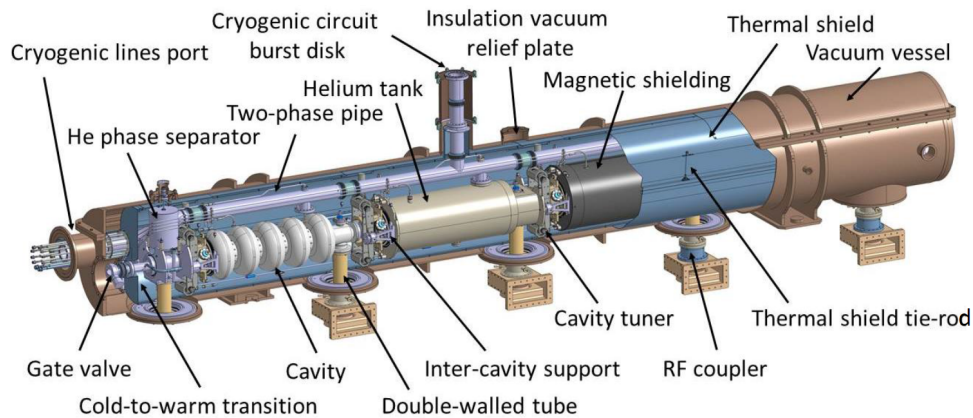
Figure 10.21: SPL cryomodule general assembly view

In the SPL cryomodule, the cavity string is directly supported by the power coupler and with dedicated inter-cavity support features. Moreover, the SPL cryomodule integrates a full length demountable top lid, enabling the cavity string assembly from the cryomodule top (Fig. 10.21). The thermal shield is made of rolled aluminium sheets, and is composed of four main parts assembled before the vertical insertion of the string of cavities. The shield, wrapped with multi-layer insulation, is suspended to the vacuum vessel via adjustable tie rods in titanium alloy which also cope, by angular movements, with its thermal contractions. The cavity stainless steel helium tanks are connected by a 100-mm-diameter two-phase pipe placed above the cavities. This pipe

ensures liquid feeding to the cavities by gravity, and is also used as a pumping line for gaseous helium.
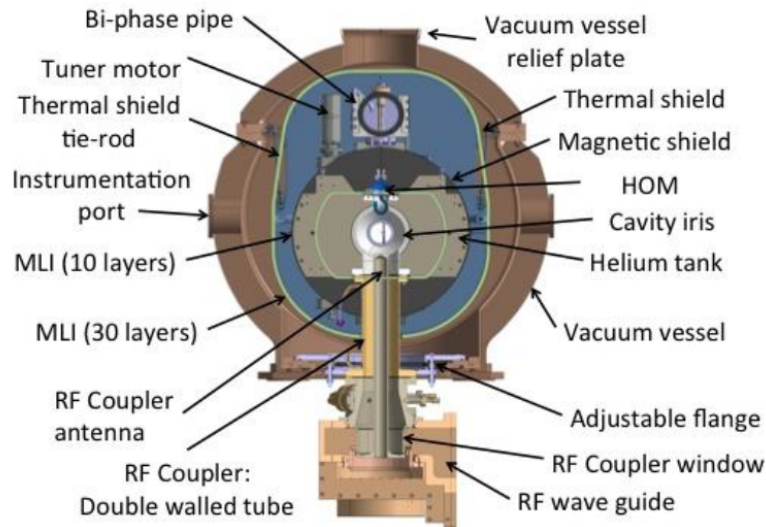

Figure 10.22: Cross-view of the SPL cryomodule

With the aim of minimizing static heat loads from room temperature to 2 K by solid thermal conduction, the number of mechanical elements between the two extreme temperatures is reduced to the strict minimum: the cavities are supported directly via the external conductor of the RF coupler (Fig. 10.22), the double-walled tube (DWT). The latter is made out of a stainless steel tube with an internal diameter of 100 mm, which is actively cooled by gaseous helium circulating inside a double-walled envelope in order to improve its thermal efficiency.

An additional supporting point to keep cavity straightness and alignment stability within requirements is obtained by supporting each cavity on the adjacent one via the inter-cavity support, which is composed of a stem sliding inside a spherical bearing. As a result, a pure vertical supporting force is exchanged by adjacent cavities whereas all other degrees of freedom remain unrestrained allowing thermal contraction movements to occur unhindered. The thermo-mechanical behaviour of this supporting system has been extensively studied on a dedicated test bench at CERN, proving its efficiency and reliability.

There are some specific additional constraints or requirements for a cryomodule to be used in an ERL, and some of them are quite challenging, The first set of constraints is linked to the CW operation of the cryomodules (contrary to SNS, SPL and ESS which are pulsed accelerators), where dynamic heat loads are much larger than the static ones. Thus, reaching high Q_0 (low cryogenic losses) is a main objective in these machines and beside specific optimization on cavity design and preparation (such as N-doping), magnetic shielding should be carefully studied: material, operating temperature, numbers of layers, active and/or passive shielding. Another important constraint is linked to relative high power to be extracted by the HOM couplers: thermal analysis should be carefully performed to have an optimized evacuation of the HOM thermal load not to degrade the cryogenic performances of the cryomodule.

We recently decided to push further away the analysis to use the SPL cryomodule for the LHeC ERL, thanks to its geometrical compatibility with the LHeC ERL superconducting cavities, but also because it fits quite well the overall ERL requirements. One of the clear advantages of the SPL configuration is a much simplified assembly procedure (Fig. 10.23), with its top-lid configuration which also allows an easier maintenance.
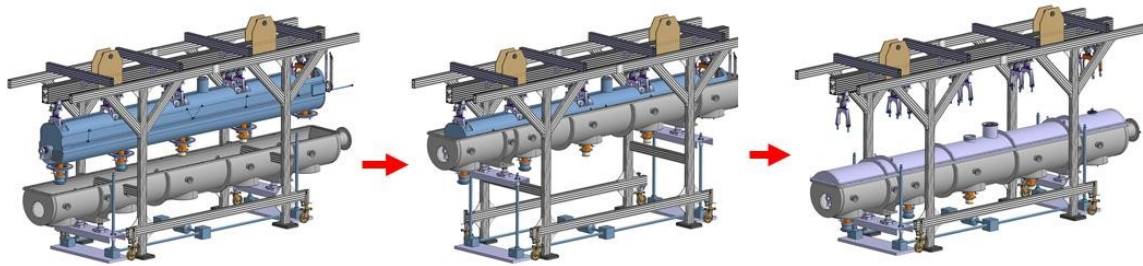
Figure 10.23: Cryomodule assembly procedure main steps

The first study performed was to analyse the possibility to integrate the ERL cavities instead of the SPL ones. The 802 MHz cavities are a little bit shorter than the SPL ones and the cells are also smaller in diameter. The beam port internal diameter is about the same, as well as the power coupler port. As a result, the SPL cryomodule is well fitted to the ERL 802 MHz superconducting cavities from the geometrical point of view, and they could be easily integrated providing minor mechanical features adaptations.

The second analysed point is the beam vacuum. As the SPL cryomodule existing design was done for a prototype, intended for RF and cryogenic test only, without beam, the vacuum valve is a VAT CF63 "vatterfly" valve with viton seal and manual actuator, which is not adapted for a real operating cryomodule. Integration of an all-metal gate valve instead is not an issue and we also designed a specific solution based on a two stages valves (Fig. 10.24) to adapt the already fabricated SPL prototype cryomodule in order to be able to integrate the 802 MHz cavities.
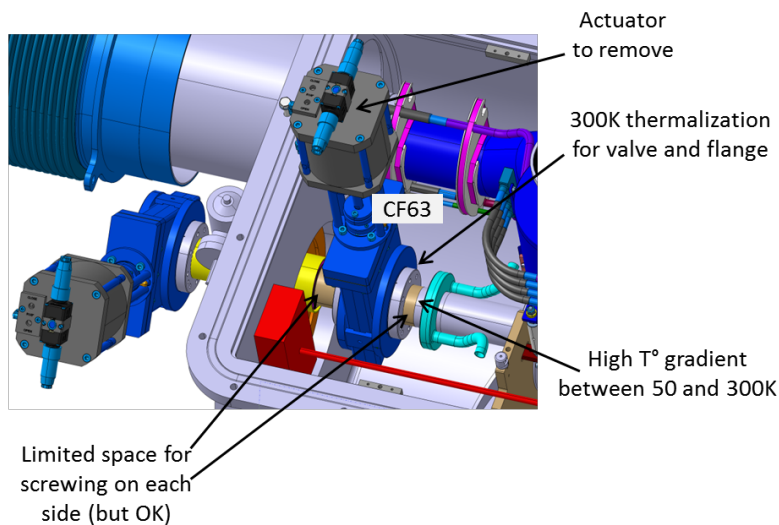
Figure 10.24: The two stages vacuum valve solution for adapting the SPL cryomodule prototype to the 802 MHz cavities of the LHeC ERL.

The third study performed is the compatibility of the SPL cryogenic features with the ERL requirements. SPL was designed to operate 702 MHz cavities at 25 MV/m with a Q_0 of 5×10^9 with a 8.2 % duty cycle. The LHeC ERL will operate SRF cavities in CW regime, but at a lower field (20 MV/m) and with a higher expected Q_0 at the nominal gradient (about 1.5×10^{10}). As a result, and despite the different duty cycle, the dynamic cryogenic losses are estimated to be only about 30 % more in the ERL case. The overall cryogenic dimensioning is then fully compatible, providing some unavoidable adaptation of a few internal cryogenic piping. The

main issue still to address is the need and consequences of the HOM coupler cooling. Even if the present engineering analysis showed that this point will not be a showstopper, it might have an impact on some cryogenic piping and cooling circuit.

Detailed engineering studies are being pursued to transform the SPL cryomodule prototype into an ERL LHeC cryomodule prototype. We are taking benefit of all the design and fabrication work previously performed on the SPL, and also on the fact some parts, such as the thermal and magnetic shielding, are not yet fabricated and could be exactly adapted to the ERL requirements. This will give the possibility to have an earlier full prototype cryomodule RF and cryogenic test as compared to a standard experimental plan where the complete study and fabrication is starting from scratch.

10.6.4 Electron sources and injectors

Specification of electron sources

Operation of the LHeC with an electron beam, delivered by a full energy ERL imposes specific requirements on the electron source. It should deliver a beam with the charge and temporal structure required at the Interaction Point. Additionally as during acceleration in a high energy ERL both longitudinal and transverse emittances of the beam are increased due to Synchrotron Radiation (SR), the 6D emittance of the beam delivered by electron source should be small enough to mitigate this effect. The general specification of the electron source are shown in Tab. 10.16. Some parameters in this table such as RMS bunch length, uncorrelated energy spread and normalised transverse emittance are given on the basis of the requirements for the acceleration in ERL and to pre-compensate the effects of SR. The most difficult of the parameters to specify is injector energy. It should be as low as possible to reduce the unrecoverable power used to accelerate the beam before injection into the ERL while still being high enough to deliver short electron bunches with high peak current. Another constraint on the injection energy is the average energy and energy spread of the returned beam. The average energy cannot be less than the energy of electron source, but the maximum energy in the spectrum should not exceed 10 MeV the neutron activation threshold. An injection energy of 7 MeV is a reasonable compromise to meet this constraint.

Parameter	Unit	Value
Booster energy	MeV	7*
Bunch repetition rate	MHz	40.1
Average beam current	mA	20
Bunch charge	pC	500
RMS bunch length	mm	3
Normalised transverse emittance	π·mm·mrad	<6
Uncorrelated energy spread	keV	10
Beam polarisation		Unpolarised/Polarised

Table 10.16: General specification of the LHeC ERL electron source.

The required temporal structure of the beam and the stringent requirements for beam emittance do not allow the use of conventional thermionic electron sources for the LHeC ERL without using a bunching process involving beam losses. While this option cannot completely be excluded as a source of unpolarised electrons. The additional requirement to deliver polarised beam can only be met with photoemission based electron sources.

There are now four possible designs of electron sources for delivering unpolarised beams and (potentially) three for delivering polarised beams:

1. A thermionic electron source with RF modulated grid or gate electrode with following (multi)stage compression and acceleration. The electron source could be either a DC electron gun or an RF electron source in this case. Although these sources are widely used in the injectors of Infra-Red FELs [813] their emittance is not good enough to meet the specification of the LHeC injector. Moreover, thermionic sources cannot deliver polarised electrons.

2. A VHF photoemission source. This is a type of normal conducting RF source which operates in the frequency range 160 MHz – 200 MHz. The relatively low frequency of these sources means that they are large enough that sufficient cooling should be provided to permit CW operation. This type of source has been developed for the new generation of CW FELs such as LCLS-II [814], SHINE [815] and a back-up option of the European XFEL upgrade [816], but they have not yet demonstrated the average current required for the LHeC injector. The possibility of generating polarised electrons with this type of source has not investigated yet.

3. A superconducting RF photoemission source. This type of sources are under development for different applications such as CW FEL's (ELBE FEL [817], SRF option of LCLS-II injector [818], European XFEL upgrade [819]), as a basis of injectors for ERL's (bERLin-Pro [820]) and for electron cooling (BNL [821]). Though this type of sources has already demonstrated the possibility of delivering the average current, required for the LHeC with unpolarised beams (BNL), and has the potential for operation with GaAs type photocathodes (HZDR) which are required for delivery of polarised beams, the current technology of SRF photoelectron source cannot be considered as mature enough for use in the LHeC.

4. A DC photoemission source. In this type of source the electrons are accelerated immediately after emission by a potential difference between the source cathode and anode. This type of source is the most common for use in ERL injectors. It has been used in the projects which are already completed (JLAB [822], DL [823]), is being used for ongoing projects (KEK [824], Cornell/CBeta [825]) and is planned to be used in new projects such as the LHeC prototype PERLE [826]. The technology of DC photoemission sources is well-developed and has demonstrated the average current and beam emittance required for the LHeC ERL (Cornell). Another advantage of the photoelectron source with DC acceleration is the possibility of operation with GaAs based photocathodes for delivering of polarised beam. Currently it's the only source, which can deliver highly polarised electron beams with the current of several mA's which is already in the range of LHeC specifications (JLab [827]).

Based on this analysis at CDR stage we consider the use of DC photoemission source as a basic option, keeping in mind that in the course of the injector development other types of electron sources may be considered, especially for providing of unpolarised beam.

The LHeC unpolarised injector

The injector layout follows the scheme depicted in Fig. 10.25. Its design will be similar to the unpolarised variant of the PERLE injector [826]. The electron source with DC acceleration delivers a CW beam with the required bunch charge and temporal structure. Immediately after the source is a focusing and bunching section consisting of two solenoids with a normal
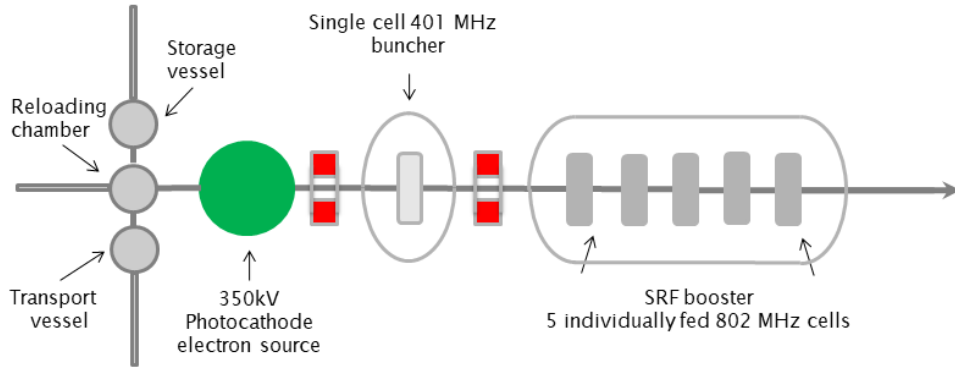
Figure 10.25: The layout of the unpolarised injector.

conducting buncher placed between them. The solenoids have two purposes. Firstly to control the transverse size of the space charge dominated beam which will otherwise rapidly expand transversely. This ensures that the beam will fit through all of the apertures in the injector beamline. Secondly the solenoids are used for emittance compensation to counter the space charge induced growth in the projected emittance. This is then followed by a superconducting booster linac. This accelerates the beam up to its injection energy, provides further longitudinal bunch compression and continues the emittance compensation process.

The DC electron source will have an accelerating voltage of 350 kV using a high quantum efficiency antimonide based photocathode such as Cs_2KSb. The photoinjector laser required for this cathode type will be a 532 nm green laser. There will be a load lock system to allow photocathodes to be replaced without breaking the source vacuum. This significantly reduces the down time required for each replacement which is a major advantage in a user facility such as the LHeC where maximising uptime is very important. The cathode electrode will be mounted from above similar to the Cornell [828] and KEK [829] sources. This electrode geometry makes the addition of a photocathode exchange mechanism much easier as the photocathode can be exchanged through the back of the cathode electrode. In addition the cathode electrode will be shaped to provide beam focusing. The operational voltage of 350 kV for the source was chosen as practical estimate of what is achievable. A higher voltage would produce better performance but would be challenging to achieve in practice. The highest operational voltage successfully achieved is 500 kV by the DC electron source that is used for the cERL injector [830]. However 350 kV is sufficient to achieve the required beam quality [826].

Polarised electron source for ERL

Providing polarised electrons has always been a challenging process, especially at relatively high average current as required for the LHeC. The only practically usable production mechanism of polarised electrons is the illumination of activated to Negative Electron Affinity (NEA) state GaAs based photocathodes with circularly polarised laser light. The vacuum requirements for these cathodes mean that this must be done in a DC electron source only. In the course of the last 30 years significant progress has been achieved in improving the performance of polarised electron sources. The maximum achievable polarisation has reached 90 % and the maximum Quantum Efficiency (QE) of the photocathode at the laser wavelength of maximum polarisation has reached 6 %. Meanwhile the implementation of a polarised electron source into the LHeC remains a challenge as the practical operational charge lifetime of the GaAs based photocathode does not exceed hundreds Coulombs (JLAB [831]) at an operational current in mA range.

In Fig. 10.26 a preliminary design of the LHeC polarised injector is shown. In general, the design
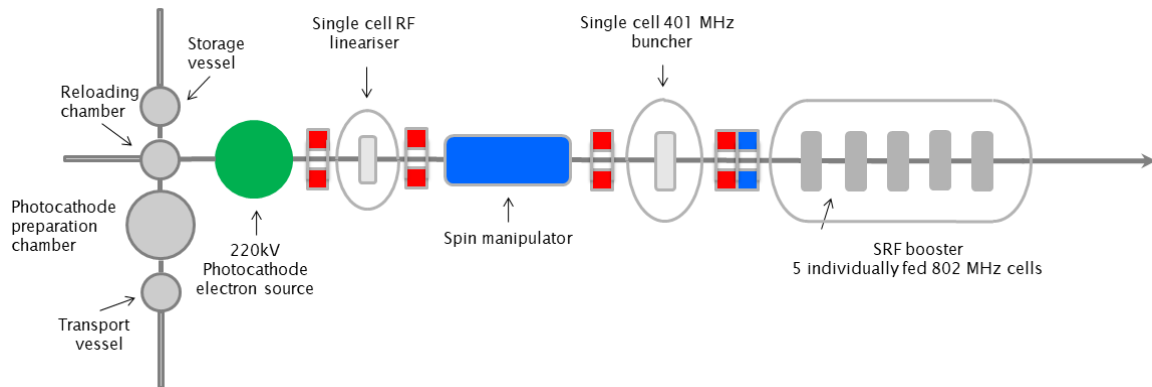

Figure 10.26: The layout of the polarised injector.

of the polarised electrons injector is close to that of the unpolarised injector and is based on a DC electron source where a photocathode is illuminated by a pulsed laser beam. The choice of a DC source is dictated by the necessity of achieving extra high vacuum, with a pressure at a level of 10^{-12} mbar, in the photocathode area. This level of vacuum is neccesary for providing long lifetime of the photocathode. In order to reduce photocathode degradation caused by electron stimulated gas desorption, the accelerating voltage in the source is reduced to 220 kV. The main differences with unpolarised injector are the presence of a photocathode preparation system, permanently attached to the source, and a Wien filter based spin manipulator between the source and the buncher. In order to reduce depolarisation of the beam in the spin manipulator, caused by the space charge induced energy spread of the beam, an RF dechirper is installed between the source and the spin manipulator. The injector is also equipped with a Mott polarimeter to characterise the polarisation of the beam delivered by the source.

An important consideration of the operation with interchangeable photocathodes is minimisation of the down time required for the photocathode exchange. It typically takes few hours to replace the photocathode and to characterise polarisation of the beam. For large facility like LHeC this is unacceptable. A practical solution could be operation with 2 or more electron sources which operate in rotation similar to the way which was proposed at BNL [832]. Another motivation for using multi-source injector is the nonlinear dependence of photocathode charge lifetime on average beam current (JLAB [827]), which reduces with increasing of the average current. For example in case of 3 electron sources 2 of them can be operated with half operation frequency 20.05 MHz in opposite phase delivering average current of 10 mA each, while the third is in stand by regime with freshly activated photocathode. The only time which is necessary to switch it on is the time required for rising the high voltage. Another advantage of using a multi-source scheme is the reduction of the average laser power deposited on the photocathode and as result relaxing requirements for the photocathode cooling. In order to implement the multi-source polarised electron injector, development of a deflection system which is able to merge the beams from different sources before the spin rotator is required.

Lasers for electron sources

In the proposed design of the LHeC injection system at least 2 lasers must be used. In the unpolarised electron injector, which is going to operate with antimionide-based photocathode, a laser with a wavelength of 532 nm is required. Typical initial QE of these photocathodes is

10% and for practical application reduction of QE up to 1% may be expected. For polarised electron source typical QE varies from 1% down to 0.1% and laser with a wavelength of 780 nm is required. The optimised parameters of the required lasers are summarised in Tab. 10.17. Laser temporal profile and spot size on the photocathode are given on the basis of source optimisation for operation at 350 kV for unpolarised regime and 220 kV for polarised.

Laser beam parameter	Unit	Unpolarised mode	Polarised mode
Laser wavelength	nm	532	780
Laser pulse repetition rate	MHz	40.1	40.1
Energy in the single pulse at photocathode QE=1%	μJ	0.12	
Average laser power at photocathode QE=1%	W	4.7*	
Energy in the single pulse at photocathode QE=0.1%	μJ		0.79
Average laser power at photocathode Qe=0.1%	W		32*
Laser pulse duration	ps FWHM	118	80
Laser pulse rise time	ps	3.2	3.2
Laser pulse fall time	ps	3.2	3.2
Spot diameter on the photocathode surface	mm	6.4	8
Laser spot shape on the photocathode surface		Flat top	

Table 10.17: Parameters of the electron source drive laser.

10.6.5 Positrons

Physics and Intensity Considerations

Variation of the beam conditions (energies, lepton charge and polarisation, hadron types) provides a considerable extension of the physics programme of the LHeC. The LHC permits a variation of the proton beam energy between about 1 and 7 TeV. It is a proton collider with options for heavy ions, primarily Pb and possibly lighter ones. The electron beam energy may be varied between about 10 and the maximum of 50 (or eventually 60) GeV. Highly intense polarised electron beam sources are under development which shall allow detailed investigations of weak interactions and searches for new physics to be performed through variations of the electron beam helicity, P. It is an advantage of the linac to achieve very high values of P, as compared to a ring electron accelerator where the polarisation build up due to the Sokolov-Ternov effect [833] runs into serious difficulties at higher energies. The electron beam polarisation at HERA was limited to about 40%. Positrons are the genuine challenge for the LHeC and as well for future e^+e^- linear colliders. The reason is the difficulty to generate intense beams as was discussed for the LHeC in quite some detail already in the 2012 CDR [1].

The physics reasons for positrons at the LHeC are somehow obvious: positrons permit to establish, exploit and question the existence of charge symmetry which may lead to discovery. For example, the charm tagging process in electron initiated charged current scattering measures the anti-strange quark density $x\bar{s}(x, Q^2)$ in the proton. There are expectations that the difference $x(s - \bar{s})$ may be different from zero, i.e. that there existed a strange-quark valence component. That requires a precision measurement of also $xs(x, Q^2)$ for which one needs about $1\,\mathrm{fb}^{-1}$ of integrated e^+p luminosity, desirably of course more. Further reasons, presented in the CDR [1] regard the nature of excited leptons, the origin of contact interactions, the spectroscopy of lepto-quarks, the understanding of DIS, as for the measurement of F_L where the signal is charge sensitive but background at high inelasticity dominantly charge symmetric, the

thorough resolution of the parton contents of hadrons etc. Thus, yes, one has many reasons to operate LHeC as a positron-hadron collider also.

However, from today's perspective, one has to be realistic in one's assumptions about what intensity may be realistically achievable and required in the positron linac - proton ring configuration. The current luminosity goal of the LHeC had been set with the observation that the Higgs production cross section in ep is about 200 fb, comparable to that of the e^+e^- colliders, and the LHeC could become a Higgs factory [834]. Higgs production at the LHeC is dominantly due to $e^-p \rightarrow \nu HX$ scattering, i.e. the LHeC has a competitive Higgs physics potential which is complementary to e^+e^- and pp as the dominant production mechanisms are $WW - H$, $Z^* - HZ$ and $gg - H$, respectively. The electron-proton CC Higgs cross section is much larger than the one in positron-proton scattering which is related to the dominance of up quarks as compared to down quarks in the proton. Much of the running optimisation used in this paper has targeted to maximise the number of Higgs events and preferred electron over positron operation.

The target electron current to achieve $10^{34}\,\mathrm{cm}^{-2}\mathrm{s}^{-1}$ luminosity has been set to 20 mA. This origins from a 500 pC gun which for 40 MHz LHC operation frequency leads to a charge of $3 \cdot 10^9$ electrons per bunch corresponding to $1.2 \cdot 10^{17}\,e^-/\mathrm{s}$. Given the current and near future status of positron intensity requirements, one may set an LHeC target of order $10^{15-16}\,e^+/\mathrm{s}$. Note that the normalised transverse emittance of of the electron beam is 50 mm mrad and the longitudinal emittance 5 MeV mm.

The intensity above would potentially provide a luminosity of order of $1-10\,\mathrm{fb}^{-1}$ within one year. With a drastic difference in the electron and positron intensities, later operation would favour e^-p over e^+p running to maximise the statistics. We thus assumed e^+p would operate for about one year, somehow comparable to the heavy ion operation of the LHC. In the physics studies, as on PDF and electroweak measurements, we have used values of integrated e^+p luminosities corresponding to these assumptions. It was also assumed the positrons were not polarised. The linac-ring ep configuration thus has a highly polarised, intense electron beam and a less intense unpolarised positron beam. The ring-ring configuration, a still possible back-up for the LHeC at HE-LHC, has intense electron and positron beams but with rather lower polarisations.

Positron Sources

One can compare the LHeC e^+ intensity target with the goals for CLIC and ILC as listed in Tab. 10.18. One finds that the chosen LHeC value is more demanding than that of CLIC and ILC. Recently the interest in very intense e^+ production has been renewed with the revival of the

Parameter	CLIC	ILC	LHeC
Energy [GeV]	1500	250	50
e^+/bunch [10^9]	3.7	20	2
Norm. emittance [mm.mrad]	0.66 (H)	10 (H)	50
	0.02 (V)	0.04 (V)	50
Norm. emittance [eV.m]	5000	60000	5000
Repetition rate [Hz]	50	10	CW
Bunches / s	15600	26250	$2 \cdot 10^7$
e^+ flux [$10^{15}\,e^+/\mathrm{s}$]	0.1	0.4	1-10

Table 10.18: Characteristics of positron beams for CLIC, ILC and LHeC. Note that the muon collider target value in the LEMMA scheme is about $4 \cdot 10^{16}\,e^+/\mathrm{s}$.

muon collider studies and the so-called LEMMA proposal [835] to generate muons from e^+e^- pairs, i.e. not from pion decays to achieve small emittance beams. This requires to generate an intense, 45 GeV energy positron beam annihilating with electrons from a target for muon pair production near threshold. In a study following the LEMMA idea, a target positron intensity of $3.9 \, 10^{16} \, e^+$/s was set [836] which requires considerable R+D efforts.

A conventional positron source uses only a single amorphous target. An electron beam hits the target where Bremstrahlung and pair-production take place. Downstream the target, particular devices (Quarter Wave Transformer QWT or Adiabatic Matching Device AMD) allow capturing as many positrons as possible, with a large emittance. The CLIC e^+ source [837] takes advantage of a hybrid target design. A thin crystal target allows reducing the peak power deposition and enhances photon production via a channelling process. An amorphous target converting the photons into positrons follows it. In between, a magnet sweeps out charged particles.

The ILC e^+ source [838] takes advantage of a long helical undulator using the high-energy electron beam of the collider. The electron beam passing through the undulator produces polarised photons by impinging on a moving target the design of which is still to be finalised. This target converts photons into positrons. The ILC-type positron source is not an option for the LHeC since it requires an electron beam energy above 100 GeV

One option considered for the initial LHeC e^+ source [1] was using ten hybrid targets in parallel. Bunch intensity and density could be enhanced by a tri-ring transformer system converting from CW to pulsed mode for accumulation, and again back to CW.

To evaluate the performance of e^+ sources, one defines a *positron yield* parameter. This parameter is the number of positrons, at a given place along the production channel, per electron impinging onto the target. It is crucial to improve the positron yield while keeping the peak energy density deposition PEDD and the shockwave inside the target within acceptable limits. The target lifetime suffers from the cyclic thermal loads and stresses due to the beam pulses. The evacuation of the average power (kW to MW) from the target is challenging and should be investigated for the reliability of the target. Heat dissipation in the amorphous target may be improved by replacing it with a granular target (experiment at KEK). The capture and accelerating sections should also be optimised. Peak magnetic field and its shape, aperture and accelerating gradient of the RF structures are important parameters. Given the large emittance of the e^+ beam, a damping ring is mandatory. Due to the high requested e^+ flux, an accumulation process should be considered. The e^+ flux is

$$\frac{dN^+}{dt} = a \cdot y \cdot N^- \cdot f \,, \tag{10.8}$$

where a is the accumulation efficiency and is a function of the damping time, y is the yield as defined above depending on the electron beam energy E^-, further N^- is the number of electron impinging on the target, and f the linac repetition rate. This accumulation could be realised by means of a tri-ring system as presented in the CDR.

Approaches towards LHeC Positrons

It is to be mentioned that positrons have not been in the focus of our recent LHeC design activity such that basic discussions as presented in the CDR [1] still hold.

The CLIC positron source was studied in great detail and many pertinent simulations were performed. Based on the expected flux of the CLIC e^+ source, we have identified three possibilities for the LHeC:

- Option 1: Keep the CW mode and the bunch spacing of 25 ns. This implies a bunch charge of $2.5 \times 10^6 \, e^+$/bunch and a current of $16 \, \mu$A;

- Option 2: Keep the CW mode with a bunch charge of $2.5 \times 10^9 \, e^+$/bunch. This implies a bunch spacing of $25 \, \mu$s and a current of $16 \, \mu$A;

- Option 3: Keep the bunch spacing of 25 ns with a bunch charge of $1 \times 10^9 \, e^+$/bunch. This implies a pulsed mode with a repetition rate of 50 Hz. The beam current is now 6.4 mA.

The CLIC source, however, just provides $O(10^{14}) \, e^+$/s which would provide maximally $100 \, \text{pb}^{-1}$ ep luminosity in an efficient year.

One notes that the ILC luminosity upgrade foresees a positron rate up to eight times higher than the CLIC rate. A recent ILC status report cites novel concepts for high intense and polarised positron beams, obtained in an electron beam driven configuration [839].

Two alternative options, not yet studied in greater detail, promise to deliver a still much higher positron rate, indeed close to that of the electrons, providing 1000 times more positron per second than a CLIC-based source: One possibly may i) convert high-energy photons from the LHC-based gamma factory [840] for producing a positron rate of up to $10^{17} \, e^+$/s [841] or ii) using the photons from an LHeC based FEL [842] to generate a similarly high rate of positrons, which in both cases would already be at the correct bunch spacing. These two options rely on either the LHC hadron or the LHeC lepton-beam infrastructure, and thus do not need other, possibly additional investments.

Depending on how challenging the parameter requirements are, a more or less radical change of paradigm is necessary. There is no easy path even to $10^{14} \, e^+$/s. As to LHeC, it may profit from recent and forthcoming developments for lepton colliders for which higher intense positron sources and beams are a matter of existence. When approved, however, serious R+D efforts will be inevitable also for LHeC, and later FCC-he, for which positron beams may even be more important, if, for example, lepto-quarks or SUSY particles in the few TeV range were found and to be examined in $e^{\pm}p$ scattering at the FCC.

10.6.6 Compensation of Synchrotron Radiation Losses

Depending on energy, each arc exhibits fractional energy loss due to the synchrotron radiation, which scales as γ^4/ρ (see Eq. (10.5)). Arc-by-arc energy loss was previously summarised in Tab. 10.14. That energy loss has to be replenished back to the beam, so that at the entrance of each arc the accelerated and decelerated beams have the same energy, unless separate arcs are used for the accelerated and decelerated beams. Before or after each arc, a matching section adjusts the optics from and to the linac. Adjacent to these, additional cells are placed, hosting the RF compensating sections. The compensation makes use of a second harmonic RF at 1603.2 MHz to replenish the energy loss for both the accelerated and the decelerated beams, therefore allowing them to have the same energy at the entrance of each arc, as shown in Fig. 10.27.

Parameters of the RF compensation cryomodules, shown in Table 10.19, have been extrapolated from the ILC cavity design, expecting that the higher frequency and lower gradient would support continuous operation.

As illustrated schematically in Fig. 10.27, there are two beams in each arcs (with exception of Arc 6) one needs to replenish energy loss for: the accelerated and the decelerated beams. Assuming nominal beam current of 20 mA, the net current for two beams doubles. Therefore,
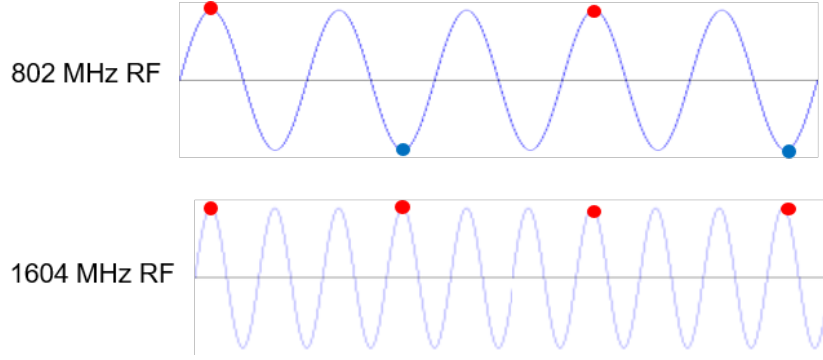
Figure 10.27: The second-harmonic RF restores the energy loss in both the accelerating and decelerating passes.

Parameter	Unit	Value
Frequency	MHz	1603.2
Gradient	MV/m	30
Design		Nine cells
Cells length	mm	841
Structure length	m	1
Cavity per cryomodule		6
Cryomodule length	m	6
Cryomodule voltage	MV	150

Table 10.19: A tentative list of parameter for the compensating RF cryomodules extrapolated from the ILC design.

40 mA current in Arcs 1-5, was used to evaluated power required to compensate energy loss by 2-nd harmonic RF system, as summarized in Table 10.20.

Section	ΔE [MeV]	P [MW]	Cryomodules
Arc 1	3	0.12	0
Arc 2	25	1.0	0
Arc 3	80	3.2	1
Arc 4	229	9.16	2
Arc 5	383	15.32	3
Arc 6	836	16.7	6

Table 10.20: Arc-by-arc synchrotron radiated power for both the accelerated and decelerated beams (only one beam in Arc 6) along with a number of 2-nd harmonic RF cryomodules required to compensate energy loss.

The compensating cryomodules are placed into Linac 1 side of the racetrack, before the bending section of Arc 1, Arc 3, and Arc 5 and after the bending section of Arc 2, Arc 4, and Arc 6. This saves space on Linac 2 side to better fit the IP line and the bypasses. Note that with the current vertical separation of 0.5 m it will not be possible to stack the cryomodules on top of each other; therefore, they will occupy 36 m on the Arc 4 and Arc 6 side and 18 m on the Arc 3 and Arc 5 side of the racetrack. Each of the compensating cavities in Arc 5 needs to transfer up to 1 MW to the beam. Although a 1 MW continuous wave klystron are available [843], the cryomodule integration and protection system will require a careful design. Tab. 10.20 shows the energy loss for each arc and the corresponding synchrotron radiated power, along with number

of cryomodules at 1603.2 MHz RF frequency required to replenish the energy loss.

10.6.7   LINAC Configuration and Infrastructure

Since the power supplied to the beam in the main linacs will be recovered, the average RF power requirements at 802 MHz are relatively small and determined by the needs to handle transients and microphonics.

The RF power required for the second-harmonic RF system however is substantial – it can be estimated from Tab. 10.14 with the nominal current of 20 mA. Tab. 10.20 above summarizes the estimated power lost in each arc depending on beam energy; these power values must be supplied by the 6 2-nd harmonic RF systems.

The RF infrastructure required at 802 MHz

10.7   Interaction Region

The design of the LHeC Interaction region has been revised with respect to the LHeC CDR to take into account the reduction of the electron energy from 60 GeV to 50 GeV and the latest design of the HL-LHC optics and it has been optimized to minimize synchrotron radiation power and critical energy at the IP.

10.7.1   Layout

The basic principle of the Linac-Ring IR design remains unchanged and it is shown in Fig. 10.28: the two proton beams are brought onto intersecting orbits by strong separation and recombination dipoles. A collision of the proton beams at the IP is avoided by selecting appropriately its location, i.e. by displacing it longitudinally with respect to the point where the two counter-rotating proton beams would collide. The large crossing angle keeps the long range beam-beam effect small and separates the beams enough to allow septum quadrupoles to focus only the colliding beam (the anti-clockwise rotating LHC beam – Beam 2). The non-colliding beam (the clockwise rotating LHC beam – Beam 1) is unfocused and passes the septum quadrupoles in a field free aperture. The electron beam is brought in with an even larger angle, partly sharing the field free aperture of the septum quadrupoles with the non-colliding beam. A weak dipole in the detector region bends the electron beam into head-on collisions with the colliding proton beam. The two proton beams are also exposed to the dipole field but, due to the large beam rigidity, they are barely affected. After the interaction point a dipole with opposite polarity separates the orbits of the electron and proton beam.

The high electron current (cf. Tab. 10.1) required to approach the goal peak luminosity of $10^{34}\mathrm{cm}^{-2}\mathrm{s}^{-1}$ poses a potential problem for the interaction region (IR) as it increases the already high synchrotron radiation.

The ERL parameters are not the only major change the new IR design has to account for. The first design of the quadrupole septa featured a separation of 68 mm for the two proton beams. However, this design focused strongly on providing a field free region for the non-colliding beam. Unfortunately, this lead to a poor field quality for the strongly focused colliding beam. The first quadrupole Q1 was a half quadrupole design effectively acting as a combined function magnet with a dipole component of 4.45 T [844]. The sextupole field component was
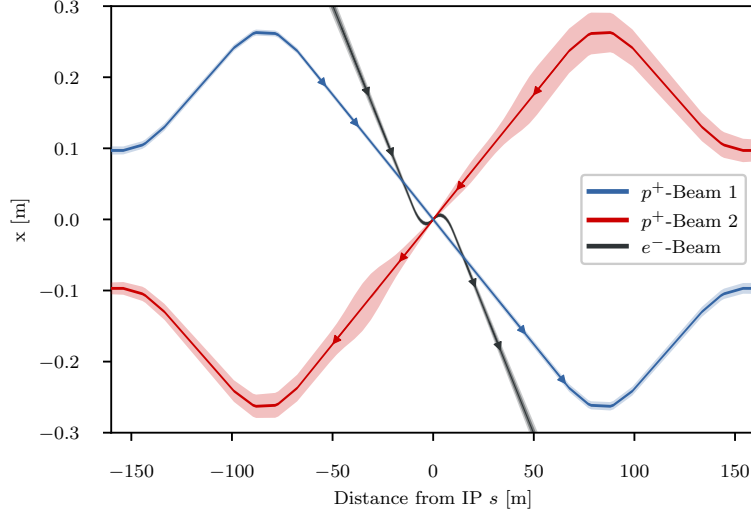
Figure 10.28: Geometry of the interaction region with $10\,\sigma$ envelopes. The electron beam is colliding with the focussed anti-clockwise rotating LHC beam (Beam 2) while the clockwise rotating LHC beam is unfocussed and passes the Interaction Region without interacting with the other two beams

Magnet	Gradient [T/m]	Length [m]	Free aperture radius [mm]
Q1A	252	3.5	20
Q1B	164	3.0	32
Q2 type	186	3.7	40
Q3 type	175	3.5	45

Table 10.21: Parameters of the final focus quadrupole septa. The parameters of Q1A/B and Q2 are compatible with the Nb$_3$Sn based designs from [845] assuming the inner protective layer of Q2 can be reduced to 5 mm thickness.

also prohibitively high. Consequently, a new design approach focusing on the field quality in the quadrupole aperture was necessary. The parameters relevant for the interaction region design are summarised in Tab. 10.21.

It is noteworthy that the minimum separation of the two beams at the entrance of the first quadrupole Q1A increased from 68 mm to 106 mm requiring a stronger bending of the electron beam. This would increase the already high synchrotron radiation in the detector region even more. In order to compensate this increase, it was decided to increase L^* (i.e. the distance from the IP to the first superconducting septum quadrupole focussing Beam 2) to 15 m, an approach that was shown to have a strong leverage on the emitted power [846].

The increased separation of the two proton beams, the longer L^* and the overall longer final focus triplet make longer and stronger separation and recombination dipoles necessary. The dipoles differ from the arc dipoles in that the magnetic field in both apertures has the same direction. Consequently the cross talk between both apertures is significant and the maximum reachable field is lower. The new geometry keeps the required field below 5.6 T. The required lengths and strength of these dipoles are listed in Tab. 10.22. It should be noted that the inter–beam distance is different for each of the five magnets per side, so each magnet will likely require an individual design. The design of the D1 dipoles is further complicated by the fact that an escape line for neutral collision debris traveling down the beam pipe will be necessary [1], as well as a small angle electron tagger. These issues have not been addressed so far, further studies

Magnet	Field strength [T]	Interbeam distance [mm]	Length [m]	Number
D1	5.6	$\geq 496\,\mathrm{mm}$	9.45	6
D2	4.0	$\geq 194\,\mathrm{mm}$	9.45	4
IP Dipole	0.21	-	10	-

Table 10.22: Parameters of the separation and recombination dipoles. The respective interbeam distances are given for the magnet with the lowest value.

will require detailed dipole designs.

The first design of the LHeC interaction region featured detector dipoles occupying almost the entire drift space between the interaction point and first quadrupole. The approach was to have the softest synchrotron radiation possible to minimise the power. However, since the purpose of the dipoles is to create a spacial separation at the entrance of the first quadrupole, it is possible to make use of a short drift between dipole and quadrupole to increase the separation without increasing the synchrotron radiation power. A dipole length of $\frac{2}{3}L^*$ is the optimum in terms of synchrotron radiation power [847]. Compared to the full length dipole it reduces the power by 15.6 % at the cost of a 12.5 % higher critical energy. With an L^* of 15 m the optimum length of the detector dipoles is 10 m. A magnetic field of 0.21 T is sufficient to separate the electron and proton beams by 106 mm at the entrance of the first quadrupole. With these dipoles and an electron beam current of 20 mA at 49.19 GeV the total synchrotron radiation power is 38 kW with a critical energy of 283 keV to be compared with a power of 83 kW and a critical energy of 513 keV for the electron beam energy of 60 GeV. More detailed studies on the synchrotron radiation for different options and including a beam envelope for the electron beam are summarised in Tab. 10.25 below.

A schematic layout of the LHeC interaction region with the dipoles discussed above is shown in Fig. 10.29. The corresponding beam optics will be discussed in the following sections.
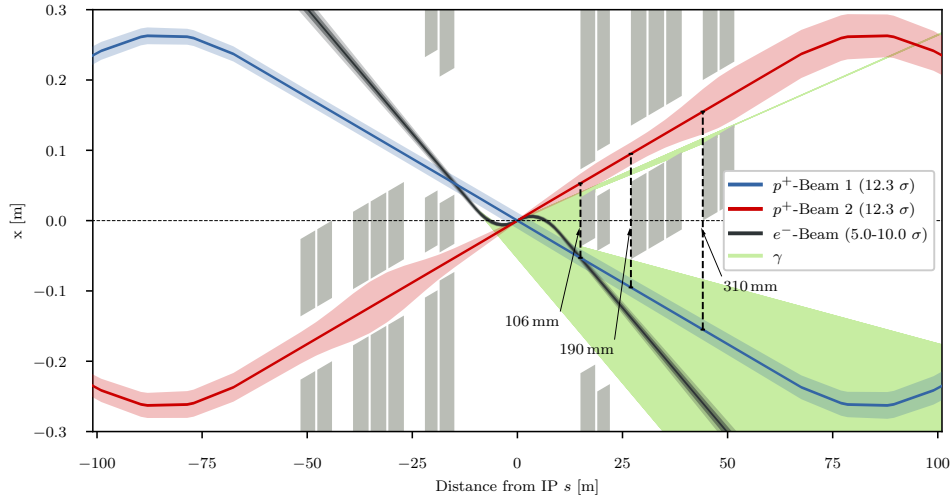
Figure 10.29: Schematic layout of the LHeC interaction region. The colliding proton beam and the electron beam are shown at collision energy while the non-colliding beam is shown at injection energy when its emittance is the largest.

10.7.2 Proton Optics

As discussed above, the L^* was increased to 15 m in order to compensate the increased synchrotron radiation due to the larger separation. The final focus system is a triplet consisting of the quadrupoles Q1A and Q1B (see Tab. 10.21), three elements of the Q2 type and two of the Q3 type. Between the elements a drift space of 0.5 m was left to account for the magnet interconnects in a single cryostat. Between Q1 and Q2 as well as Q2 and Q3 a longer drift of 5 m is left for cold-warm transitions, Beam Position Monitors (BPMs) and vacuum equipment. Behind Q3, but before the first element of the recombination dipole D1, another 16 m of drift space are left to allow for the installation of non-linear correctors in case the need arises, as well as a local protection of the triplet magnets from asynchronous beam dumps caused by failures of the beam dump kickers (MKD) as discussed below.

As the recombination dipoles D1 and D2 for the LHeC interaction region require more space than the current ALICE interaction region, the quadrupoles Q4 and Q5 had to be moved further away from the IP. The position of Q6 is mostly unchanged but due to a need for more focusing the length was increased by replacing it with two elements of the MQM magnet class of LHC.

With the triplet quadrupole parameters provided in Tab. 10.21 we were able to match optics with a minimum β^* of 10 cm. The corresponding optics are shown in Fig. 10.30 and feature maximum β functions in the triplet in the order of 20 km. With these large β functions, the free apertures
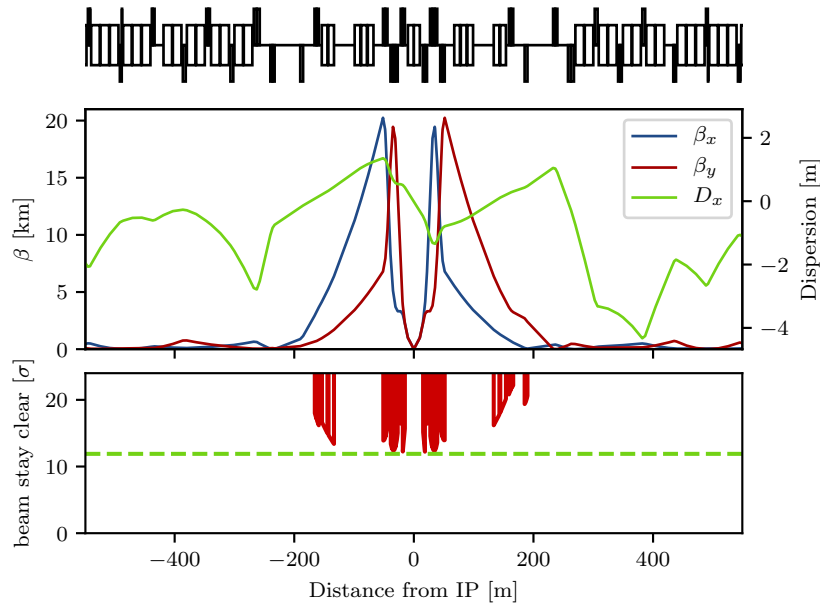
Figure 10.30: Optics (top) and beam stay clear (bottom) of the colliding beam with $\beta^* = 10$ cm.

of the quadrupoles leave just enough space for a beam stay clear of 12.3 σ, the specification of the LHC. This is illustrated in Fig 10.30. However, since the LHeC is supposed to be incorporated in the HL-LHC lattice, this minimum beam stay clear requires specific phase advances from the MKD kicker to the protected aperture as detailed later. The large β functions not only drive the aperture need in the final focus system, but also the required chromaticity correction in the adjacent arcs. To increase the leverage of the arc sextupoles, the Achromatic Telescopic Squeezing scheme (ATS) developed for HL-LHC [848] was extended to the arc upstream of IP2 for the colliding beam (Beam 2) (see Fig. 10.31). This limited the optical flexibility in

the matching sections of IR2, specifically of the phase advances between arc and IP2. As a consequence, the optical solution that has been found (Fig. 10.30) still has a residual dispersion of 15 cm at the IP and the polarities of the quadrupoles Q4 and Q5 on the left side of the IP break up the usual sequence of focusing and defocusing magnets. It needs to be studied whether this is compatible with the injection optics. The latest optics designs can be found at the webpage [849].
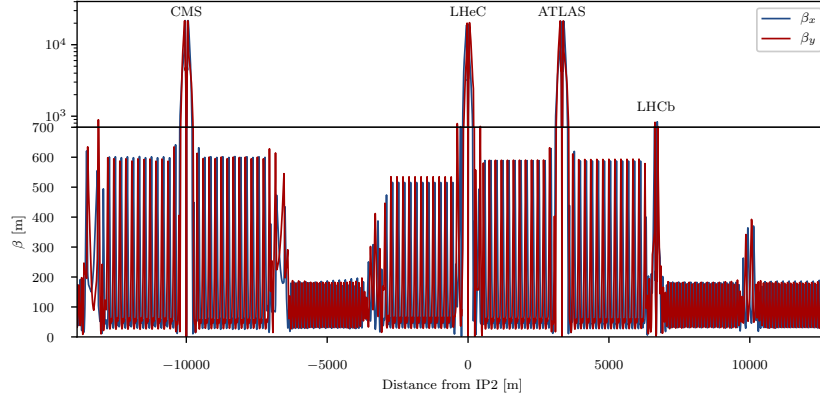
Figure 10.31: Optics of full ring of the colliding LHC proton beam (Beam 2).

The free apertures given in Tab. 10.21 include a 10 mm thick shielding layer in Q1 and 5 mm in Q2 and Q3. This is necessary to protect the superconducting coils from synchrotron radiation entering the magnets as can be seen in Fig. 10.29. The absorber must also protect the magnets from collision debris. Simulations of both synchrotron radiation and collision debris are yet to be conducted in order to confirm the feasibility of this design.

A separation between the two proton beams in time is currently foreseen, i.e. while the orbits of the two proton beams do cross, the bunches do not pass through the IP at the same time. This approach is complicated by the fact that the timing of the bunches in the other three interaction points should not be affected. The easiest way to accomplish this is by shifting the interaction point of LHeC by a quarter of a bunch separation, i.e. $6.25\,\mathrm{ns} \times c \approx 1.87\,\mathrm{m}$ upstream or downstream of the current ALICE IP, similar to what has been done for the LHCb detector in Point 8 of the LHC. This will of course have an impact in the integration of the detector in the underground cavern [850], however it seems feasible [851].

The LHC protected aperture in the event of an asynchronous beam dump significantly depends on the phase advance between the MKD kicker and the local aperture protection [852]. This is due to the oscillation trajectory of bunches deflected during the kicker rise time. With a phase advance of $0°$ or $180°$ from the kicker to the protected aperture, a direct hit should be unlikely, so aperture bottlenecks should be close to that. For a beam stay clear of $12.3\,\sigma$ a phase advance of less than $30°$ from either $0°$ or $180°$ was calculated to be acceptable [852]. The major complication comes from the fact that not only the final focus system of LHeC, but also of the two main experiments ATLAS and CMS need to have to correct phase advances and since the phase advances between IP2 (LHeC) and IP1 (ATLAS) are locked in the achromatic telescopic squeezing scheme there are few degrees of freedom to make adaptations.

The Achromatic Telescopic Squeezing (ATS) scheme [848] is a novel optical solution proposed for the HL-LHC to strongly reduce the β^* while controlling the chromatic aberrations induced, among other benefits.

The principles of the ATS as implemented for the HL-LHC are as follows: first, in the presqueeze stage, a standard matching procedure is performed in the interaction regions to obtain a value of β^* which is achievable in terms of quadrupole strengths and chromaticity correction efficiency, in the case of HL-LHC this corresponds to IR1 and IR5. A further constraint at this point is to match the arc cell phase advance on the regions adjacent to the low β^* interaction regions to exactly $\pi/2$. Later, at the collision stage, the low β^* insertions remain unchanged and instead the adjacent interaction regions contribute to the reduction of β^*, that is IR8 and IR2 for IR1, and IR4 and IR6 for IR5. The $\pi/2$ phase advance allows the propagation of β-waves in the arc. If phased correctly with the IP, these β-waves will reach their maximum at every other sextupoles, increasing the β function at their location at the same rate that the decrease in β^*. The increase of the β function at the location of the sextupoles will result in an increase of their efficiency, allowing the system to correct the high chromaticity produced by the high-β function in the inner triplet. This way, the ATS allows a further reduction of the β^* at the same time that correcting the chromaticity aberrations produced in the low β insertions.

Following the experience for HL-LHC, the ATS scheme was proposed for the LHeC project to overcome some of the challenges of this design in terms of limits in the quadrupole strengths of the interaction region and in the chromaticity correction.

A first integration of the LHeC IR into the HL-LHC lattice using the ATS scheme for the previous nominal case with $\beta^* = 10$ cm and $L^* = 10$ m was presented by extending the β wave into the arc 23 [846]. The flexibility of this design was later explored to study the feasibility of minimising β^*, to increase the luminosity, and increasing L^*, to minimise the synchrotron radiation. It was found that increasing L^* to 15 m provided a good compromise but keeping the β^* to 10 cm.

The changes made to the HLLHCV1.3 lattice [853] to obtain the LHeC lattice and the detailed matching procedure are described in Ref. [854]. At the end of this process a lattice for the required collision optics in all IRs (β^*=15 cm for IR1 and IR5 and β^*=10 cm for IR2) has been obtained, with the appropriate corrections (crossing, dispersion, tune and chromaticity). The phases between the MKD kicker in IR6 and the different low β^* triplets were also checked, resulting in 15° from the horizontal for IR1, 22° for IR2 and 26° for IR5, therefore fulfilling the $< 30°$ requirement for all three IRs.

Similarly the chromaticity correction for the LHeC lattice further develops from the HL-LHC chromaticity correction scheme [854] allowing to correct the chromaticity for the case with $\beta^* = 10$ cm in IP2 within the available main sextupole strength. Lattices with β^*= 7, 8 and 9 cm and $L^* = 15$ m were also successfully matched in terms of both the β^* and the chromaticity correction. It must be noted however that these cases require a larger aperture in the inner triplet.

Dynamic aperture (DA) studies were performed to analyze the stability of the lattice designs using SixTrack [855] on a thin-lens version of the LHeC lattice at collision ($\beta^* = 0.15$ m in IP1 and IP5, $\beta^* = 10$ cm in IP2) over 10^5 turns with crossing angles on, 30 particles pairs per amplitude step of $2\,\sigma$, 5 angles in the transverse plane and a momentum offset of 2.7×10^{-4}. The energy was set to 7 TeV and the normalised emittance of the proton beam to $\epsilon = 2.5\,\mu$m. No beam-beam effects were included in this study.

Previous DA studies had been performed for an earlier version of the LHeC lattice [846]. These studies did not include triplet errors of either of the low-β interaction regions, as these errors were not available at that stage. These studies were updated for the newer version of the LHeC lattice described in the previous sections and included errors on the triplets of IR1 and IR5. For

the case of IR2 errors tables for the new triplet are not yet available but it was estimated that the same field quality than the triplets for the HL-LHC IR can be achieved for these magnets, and therefore the same field errors were applied but adjusted to the LHeC triplet apertures.

The initial DA resulted in $7\,\sigma$ but following the example of HL-LHC and FCC studies [856] two further corrections were implemented: the use of non-linear correctors to compensate for the non linear errors in the LHeC IR, and the optimisation of the phase advance between IP1 and IP5. With these corrections the DA was increased to $10.2\,\sigma$, above the target of $10\,\sigma$. The case for lower β^*, particularly for the case of interest with $\beta^* = 7\,\mathrm{cm}$ proved to be more challenging, as expected, when adding errors on the LHeC IR; however with the use of the latest corrections a DA of $9.6\,\sigma$ was achieved, that is not far off from the target. The DA versus angle for both these cases are shown in Fig. 10.32. It is important to point out that the challenge for the $\beta^*{=}7\,\mathrm{cm}$ case comes instead from the quadrupole aperture and gradient requirements, particularly in the first magnet.
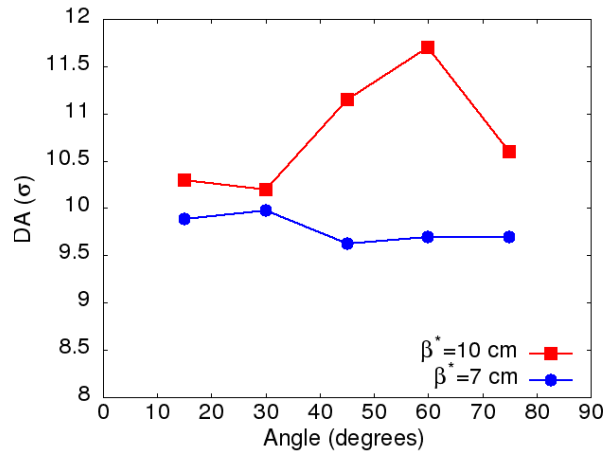
Figure 10.32: Dynamic aperture vs angle for 60 seeds for the LHeC lattice at collision for the cases $\beta^* = 10$ cm (red) and $\beta^* = 5$ cm in IP2.

β^* values lower than 10 cm require a completely different final focus system as the lower β^* means the beam size in the triplet will become larger. Larger apertures are required and consequently the gradients in the quadrupoles will decrease. However similar integrated focusing strengths will be required so the overall length of the triplet will increase. As this will in turn increase the β functions in the triplet further it is imperative to optimise the use of the available space. An example of available space is the drift between the detector region dipoles and the triplet magnets as shown in Fig. 10.33. The optimum dipole lengths in terms of synchrotron radiation power was determined to be $2/3 \cdot L^*$ so a drift of $5\,\mathrm{m}$ is left. Now it is immediately clear that this region cannot be occupied by a superconducting quadrupole septum as that would effectively decrease L^* and thus increase the synchrotron radiation power as a stronger separation is necessary. Instead it is thinkable that a normal conducting quadrupole septum can be built that either does not require a yoke or similar structure between the beams or has a very thin yoke, or a septum that has a very limited and controlled field in the region of the electron beam trajectory. In the later case it might even be used as part of the final focus system of the electron beam. Either way, it is clear that such a normal conducting septum must have a pole tip field way below the saturation limit of iron. The section on electron optics shows that a normal quadrupole of this kind can also have benefits in terms of synchrotron radiation, but studies remained to be done to make sure the parameters work for both cases. For our calculation a pole tip field of $1\,\mathrm{T}$ was assumed. For $\beta^* = 5\,\mathrm{cm}$ an aperture radius of $20\,\mathrm{mm}$ is required at a distance of $14\,\mathrm{m}$
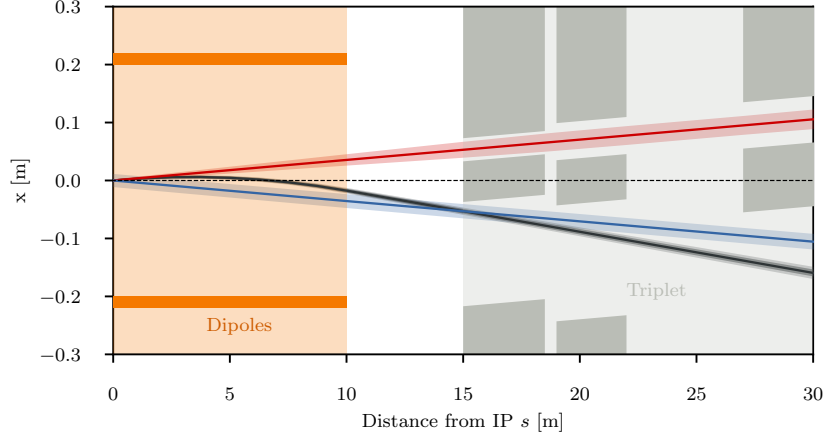
Figure 10.33: Empty space between the detector dipole and the superconducting quadrupoles of the final focus triplet.

from the IP, resulting in a pole tip field of 50 T/m for the normal conducting septum called Q0. Possible ratios of apertures and gradients for the remaining triplet magnets were approximately based on the quadrupole parameters shown in Tab. 10.21, however these parameters would require a magnet design for confirmation. With the quadrupole parameters shown in Tab. 10.23 we were able to obtain triplet optics that can accommodate a beam with a minimum β^* of 5 cm.

Magnet	Gradient [T/m]	Length [m]	Aperture radius [mm]
Q0 (nc)	50	3.0	20
Q1A	110	3.5	27
Q1B	162	5.0	37
Q2	123	5.0	62
Q3	123	4.5	62

Table 10.23: Parameters of the final focus quadrupole septa required to accommodate a β^* of 5 cm. The normal conducting quadrupole is called Q0 although it has the same polarity as Q1A/B.

The corresponding optics are shown in Fig. 10.34. So from the triplet point of view it appears possible to reach lower β^*, however many assumptions need verification: First the magnetic design for the normal conducting quadrupole septum must be shown to be possible. If there is a residual field in the space of the electron beam trajectory, the impact on the electron beam and the synchrotron radiation power must be evaluated. The parameters of the modified superconducting triplet quadrupole septa, although scaled conservatively, must be confirmed. Furthermore the larger aperture radius of Q1 might require a larger separation at the entrance of Q1, increasing the synchrotron power that is already critical. Thus a full design of such magnets is required. Lastly, the interaction region must be integrated into the full ring to verify that chromaticity correction is possible. Studies in Ref. [854] that were conducted on the normal triplet without regard for aperture constraints suggest that a chromaticity correction is only possible for a β^* down to around 7 cm.

So far, the optics of the final focus system featured asymmetrically powered triplets on the two sides of the IP. This is inherited from the ALICE final focus system where the aperture is shared and the antisymmetry guarantees the same optics for both beams and similar chromaticities in
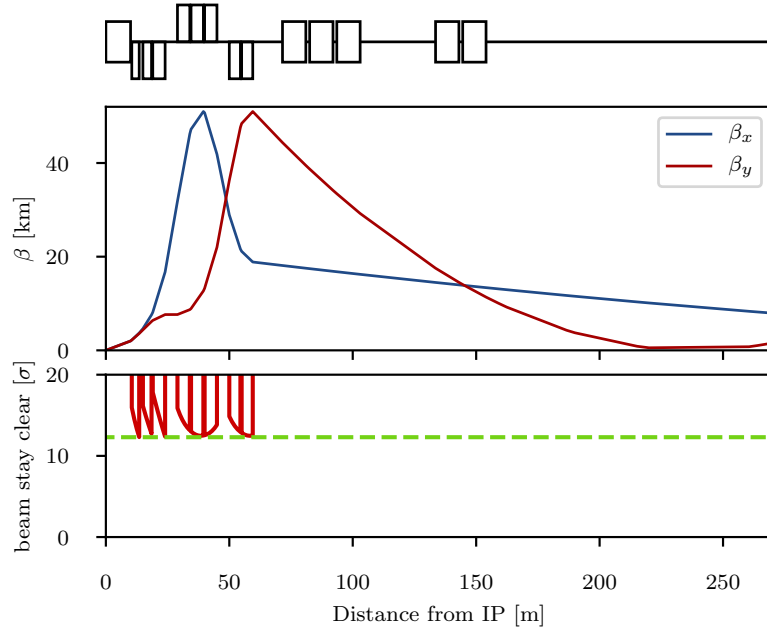
Figure 10.34: Optics (top) and beam stay clear (bottom) in the triplet region of colliding beam with $B^* = 5\,\text{cm}$.

both horizontal and vertical planes. In the LHeC final focus system however, the apertures of the quadrupoles are not shared between both beams, so the antisymmetry is not strictly necessary, although it eases the integration in the full ring. An alternative approach that is worth studying is a symmetric doublet. Doublets feature a large β function in one plane and a relatively low one in the other plane for equal β functions at the IP. Since the non-colliding proton beam is of no concern for LHeC it makes sense to create doublets on each side of the IP that have the peak β function in the horizontal plane as the chromaticity correction was limited in the vertical plane. Furthermore, in a doublet the integrated focusing strength needed is lower as fewer quadrupoles act against each other. This further reduces the chromaticity and should also reduce the overall length of the final focus system. With the space saved by the doublet it is possible to either shift the recombination dipoles D1 and D2 closer to the IP, reducing the needed integrated strengths, or even to increase L^* to further reduce the synchrotron radiation power and critical energy. In order to make best use of the available doublet quadrupole aperture, it is also thinkable to collide with flat beams. The main disadvantage of symmetric doublets is the breaking of the sequence of focusing and defocusing quadrupoles. As no changes should be made to the arcs, the left-right symmetry needs to be broken up again in one of the matching sections, either by introducing another quadrupole on one side of the IP, or by overfocusing the beam.

At collision energy the non-colliding beam has no optics specification within the straight section. Consequently the optics should transfer the beam from the left arc to the right arc without hitting the aperture and at a specific phase advance. The same is true at injection energy, but with a larger emittance, making the satisfaction of the aperture constraint more difficult. Thus it is sufficient to find working injection optics, as no squeeze will be required for this beam. This approach of course will require some tuning as at least one arc will apply the ATS scheme at collision, but as the aperture constraint is less tight at higher energy there should be enough degrees of freedom available.

Finding injection optics appears trivial at first but is complicated by the fact that the distance

between the IP and the first quadrupole magnet Q4 is larger than 159 m. A total distance of 318 m needs to be bridged without any focusing available. A solution has been found with $\beta^* = 92$ m and $\alpha^* = \pm 0.57$ with the required beam size in the quadrupole septa and Q4 [854]. The corresponding optics are shown in Fig. 10.35. For the magnets Q4 and Q5 LHC quadrupoles
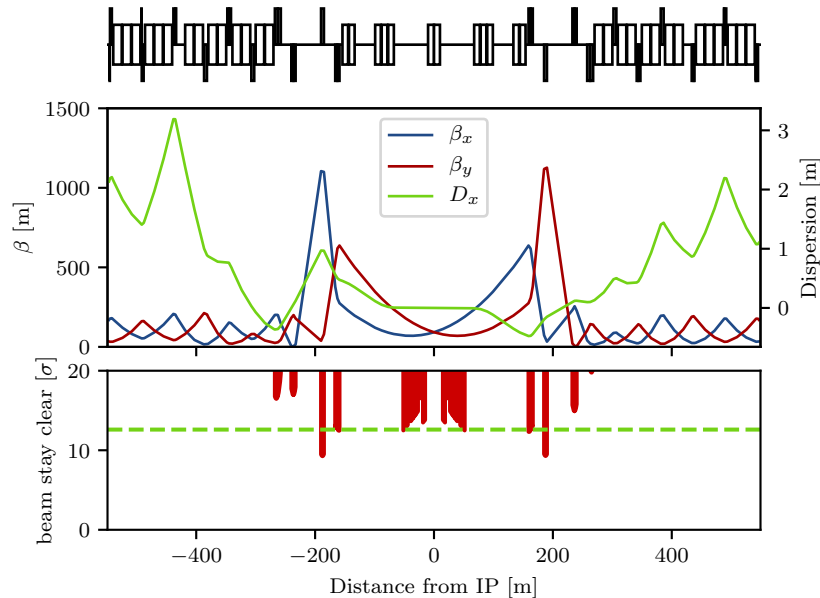
Figure 10.35: Optics (top) and beam stay clear of the non-colliding beam at injection energy. The Q5 quadrupole magnets on either side of the IP currently are aperture bottlenecks. It should be possible to mitigate this problem by replacing the magnets with longer, larger aperture magnets.

of the large aperture MQY type with 70 mm aperture diameter and a 160 T/m gradient were assumed. As can be seen in the aperture plot, the triplet quadrupole septa and Q4 are just below the minimum beam stay clear at injection of $12.6\,\sigma$ but it is expected that nominal aperture can be achieved With some minor optimisation. However the Q5 magnets only have a beam stay clear of about $9.2\,\sigma$ with little chance of decreasing the beam size without increasing it both in Q4 and in the quadrupole septa. Consequently it will be necessary to use quadrupoles with apertures larger than 106 mm and make up for the lower gradient by increasing the length or by using Nb$_3$Sn technology. At injection energy the remaining magnets in the IR have strengths according to the HL-LHC specification and thus do not pose any problems. However the injection optics shown in Fig. 10.35 will require some changes during the ramp as Q4, Q5 and Q6 would become too strong at collision energy. This is not considered a problem though, as the emittance shrinking will ease the aperture requirements.

The non-colliding proton beam does not need to be focused and consequently passes the quadrupole septa of the colliding beam in the field free region.

The large angle of 7200 μrad between the two beams (compared to 590 μrad in the high luminosity IPs) should suffice to mitigate long range beam-beam effects, considering that the shared aperture is only 30 m long as opposed to the main experiments where the shared aperture exceeds a length of 70 m.

10.7.3 Electron Optics

First ideas of a possible layout and design of the LHeC IR have already been presented in Ref. [1]. Based on the principles explained there, a further optimisation of the beam separation scheme has been established, with the ultimate goal of lowest synchrotron radiation power and critical energy in the direct environment of the particle detector. Depending on the requests from the actual detector geometry and shielding, the flexibility of the new IR layout allows to optimise for either side.

The basic principle is – as before – based on the large ratio (approximately 140) of the proton to electron beam momentum (or beam rigidity, $B\rho = p/e$) that makes a magnetic field based separation scheme the straightforward solution to the problem, using effective dipole fields.

Boundary conditions are set however due to the limited longitudinal space, resulting from the distance of the first focusing elements of the proton lattice, located at $L* = 15$ m, and the need for sufficient transverse separation, defined by the technical design of this first proton quadrupole. The size of the two beams and – clear enough – the power of the emitted synchrotron radiation P_{syn} and the critical energy E_{crit} have to be taken into account in addition. The well known dependencies of these two parameters on the beam energy $E_e = m_e c^2 \gamma$ and bending radius ρ are given by

$$P_{\mathrm{syn}} = \frac{e^2 c}{6\pi\varepsilon_0} \frac{\gamma^4}{\rho^2} \quad \text{and} \quad E_{\mathrm{crit}} = \frac{3}{2} \frac{\hbar c \gamma^3}{\rho} \,. \tag{10.9}$$

The schematic layout of the original design of the electron interaction region shown in Fig. 10.29 is reproduced in Fig. 10.36 (a). The long dipole magnet B, used to deflect the electron beam, is
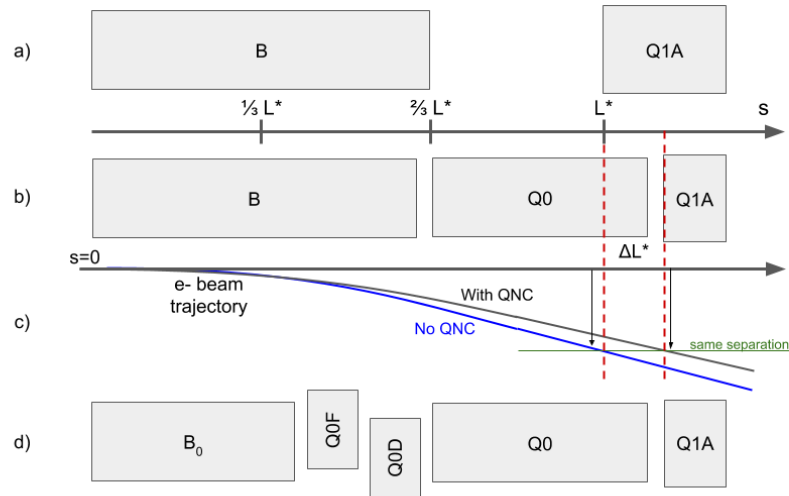
Figure 10.36: Separation scheme based on a long dipole magnet B (a) and improved layout using Q0, a normal conducting half-quadrupole as first focusing element of the proton beam (b). The last design features a doublet of off-centered quadrupoles to minimise the electron beam size at the entrance of Q1A (d).

embedded inside the detector structure which is ranging from -6 m to 4 m around the interaction point, extended by ± 1.65 m of muon chamber. Basic interaction region designs with and without chromaticity correction were presented [857, 858] but were not fully integrated in the ERL. The electron final quadrupoles were placed at 30 m from the IP [859], compatible with the proton layout described above. While this approach is straightforward, the only parameter that can be

used to minimise the power of the emitted synchrotron radiaton is the length of the separator-dipole field [847]. In addition, the installation of the first focusing elements of the electron beam downstream of the triplet focussing the colliding proton beam leads to a considerable increase of the electron beam size in the separation plane.

Lattices including chromaticity correction had a significant length of 150 m. However, the whole straight section between Linac and arc is only 290 m long [1] and the IR design did not include a matching and splitting section or a focus system for the spent, outgoing electron beam. Without chromaticity correction in the electron final focus, aberrations at the IP decrease luminosity by about 20 % [860].

Investigations have been launched to minimise critical energy and emitted synchrotron radiation power by reducing the separation in two main steps:

- introduce a compact mirror-plate half quadrupole (QNC) in front of Q1A (on the IP side) to focus the colliding proton beam and provide a field free region for the electron and non-interacting proton beam. This reduces the required bending field of the separation dipole B for the same separation at Q1A. In addition, the normal conducting magnet QNC will act as shielding of the superconducting triplet magnets that would otherwise be subject to direct synchrotron radiation. Additional shielding is foreseen, to protect the SC magnets and avoid as much as possible backshining to the detector. In addition, sufficient space will be provided to correct the vertical orbit and coupling of the electrons coming from the solenoid.

- reduce the beam size of the electron beam by a very early focusing of the beam. As positive side effect this leads to a considerable reduction of the chromaticity of the electron lattice.

The first step is sketched in Fig. 10.36 (b) and the corresponding electron beam trajectory is shown in Fig. 10.36 (c).

The introduction of the mirror plate half quadrupole QNC allows to reduce the length of the Q1A quadrupole while conserving the total integrated gradient, therefore leaving the overall focusing properties of the proton lattice quasi untouched. The entry of Q1A is therefore moved away from the IP to relax the separation fields.

Scanning the Q1A entry position leads to either an optimum of the critical energy or to a minimum of the emitted synchrotron power. Both cases are shown in Fig. 10.37 and for each of them the new Q1A entry position has been determined. The power of the emitted radiation is reduced by up to 28 %. The colliding proton beam, passing through this half quadrupole with a certain offset to guarantee sufficient beam stay clear, will receive a deflecting kick in the horizontal plane of about 90 µrad. It supports the dipole based beam separation, provided by the so-called D1 / D2 magnets in LHC, and will be integral part of the LHC design orbit.

The resulting beam optics of the protons differs only marginally from the original version and only a slight re-match is needed. However by carefully choosing the gradient of the new magnet the parameters of the superconducting proton quadrupoles are untouched and the phase advance at the end of the interaction region lattice is conserved in both planes.

Improved Electron lattice

A further improvement of the emitted synchrotron power and critical energy is obtained by introducing an early focusing scheme of the electrons, which leads to a reduced electron beam size and thus to softer separation requirements.
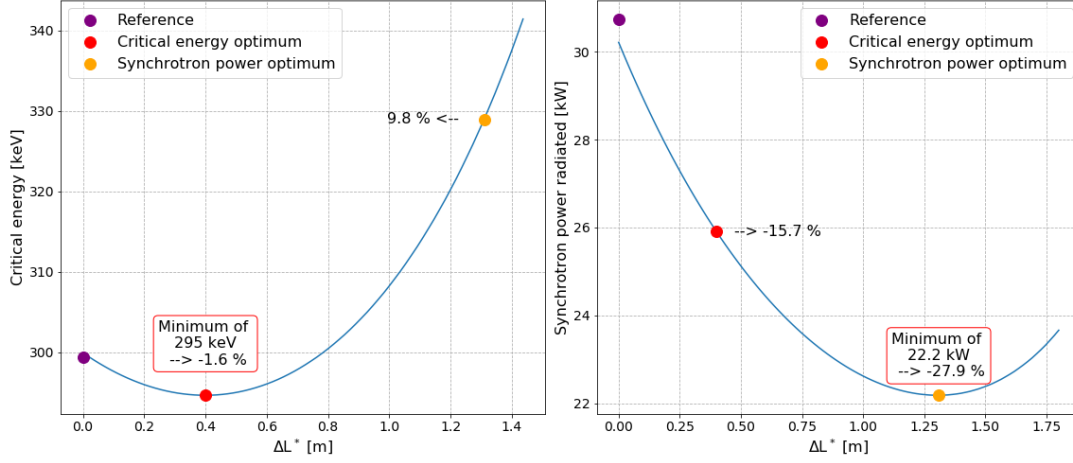
Figure 10.37: Improved critical energy and power of the synchrotron radiation for the half quadrupole based proton lattice. Left side: critical energy, right side: synchrotron radiation power. The horizontal axis refers to the shift ΔL^* of the position of the first proton superconducting magnet Q1A.

The reduction of the electron beam size is obtained by installing a quadrupole doublet in the electron lattice between the separation dipole and the QNC (half-) quadrupole. A carefully matched focusing strength of this doublet will minimise the β function of the electrons at the location of Q1A. At the same time an effective dipole field, that is needed to maintain the separation of proton and electron beams, is provided by shifting the magnet centres of the doublet lenses off axis. The horizontal offset of these quadrupoles has been chosen to provide the same bending radius as the separation dipole, thus leading in first order to the same critical energy of the emitted light in all separation fields. A detailed calculation of the divergence of the photons, the geometry of the radiation fan and the position of the absorbers and collimators will be one of the essential next steps within the so-called machine-detector-interface considerations.

Fig. 10.36 (d) shows the new layout – compared to the previous version. The doublet providing the early focusing of the electron beam is embedded in the separator dipole, i.e. it is positioned at $s = 6.3$ m and acts in combination with the separation dipole. The quadrupole gradients have been chosen for optimum matching conditions of the electron beam and the transverse shift of the field centres provide the same separation dipole effect as used in the long dipole.

The early focusing of the electron beam allows for a softer separation of the beams, and leads therefore directly to a reduced critical energy E_{crit} and power P_{syn} of the emitted radiation. Fig. 10.38 shows the dependence of E_{crit} and P_{syn} on the β-function at $s = L^*$ for the electron optics for different values of the required electron beam stay-clear expressed in units of the electron beam size σ. The beam separation has been re-calculated and the critical energy and radiation power are plotted. The graphs include different assumptions for the beam size considered. Including orbit tolerances, a beam stay-clear of 20 σ is considered as the most relevant case, which refers to the red curve in the graph.

In order to provide a complete study with the lattice featuring the off-centered quadrupoles, the new interaction region has been embedded in between the high energy end of the acceleration part of the linac and the *Arc 6* of the ERL, which marks the start of the energy recovery lattice. An optimum has been found for a beam optics with a beta function in the plane of the beam separation (i.e. horizontal) of $\beta_x = 90$ m at $L^* \approx 15$ m

An improvement of about 9 % for the critical energy and close to 25 % of the radiated power is
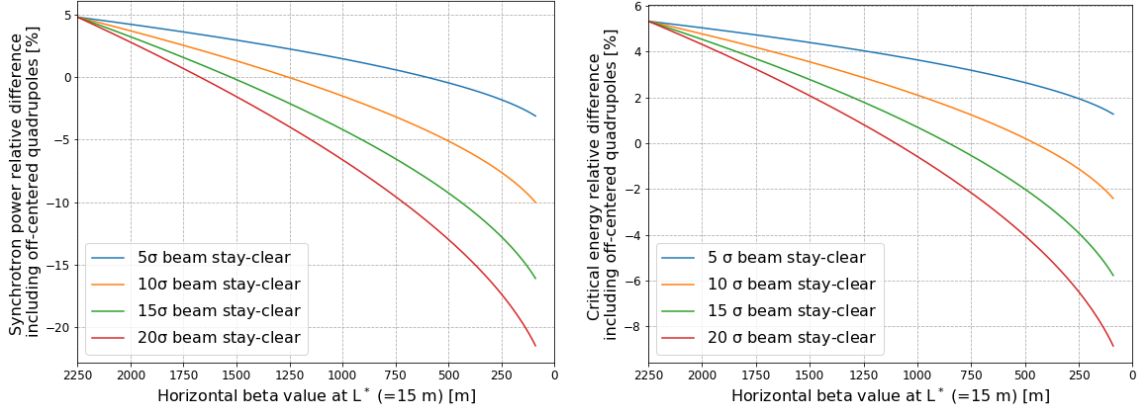
Figure 10.38: Relative difference with respect to the single dipole separation scheme for different values of the required beam stay-clear expressed in σ. Left : for the power of the emitted radiation, as function of the β-function of the electron beam at position s=15m. Left: for the critical energy of the emitted radiation, as function of the β-function of the electron beam at position s=15m. The early focusing of the electron beam allows for a much reduced separation field and thus to a reduced critical energy and power of the emitted radiation. The initial beta value is $2250\,\text{m}$.

obtained, if an electron beam optics with $\beta_x = 90\,\text{m}$ at the entrance of Q1A is used. For this most promising case the matched beam optics is shown in Fig. 10.39.

The lower β-function of the electron beam at the focusing elements has the additional positive feature of reducing considerably the chromaticity of the new lattice, which is a crucial parameter for the performance of the energy recovery process (details are described below in the chapter on tracking calculations). Compared to the dipole based separation and a late focusing, Q' is reduced to a level of 13 % horizontally and to a level of 11 % in the vertical plane. The details are listed in Tab. 10.24. Further studies will investigate the orbit correction scheme of the new IR, and an eventual interplay of the solenoid fringe field and the quadrupoles.

	Dipole based separation	Early focusing scheme
ξ_x	-116	-15
ξ_y	-294	-32

Table 10.24: Chromaticity of the dipole based separation scheme and the new lattice based on early focusing, off-axis quadrupole lenses.

The influence of the electron doublet magnets on the proton optics is marginal – as can be expected due to the large difference in beam rigidity: If uncorrected, the electron doublet creates a distortion (a so-called *beta-beat*) of the proton optics of roughly 1 %. Still it has been calculated and taken into account in the context of a re-match of the proton beam optics.

Combining the two improvement factors, namely the effective lengthening of L^* due to the use of a half quadrupole in front of the superconducting triplet, and the early focusing scheme in the lattice of the electrons, leads to an overall improvement of the interaction region with respect to synchrotron radiation power and critical energy that is shown in Fig. 10.40. The overall improvement factor is plotted with reference to the baseline dipole separation design with originally $\beta = 2250\,\text{m}$ at the separation point $s = L^*$. Using a normal conducting half quadrupole in combination with the early focusing scheme, the power of the emitted synchrotron radiation is reduced by 48 % for an electron beam stay-clear of $20\,\sigma$.
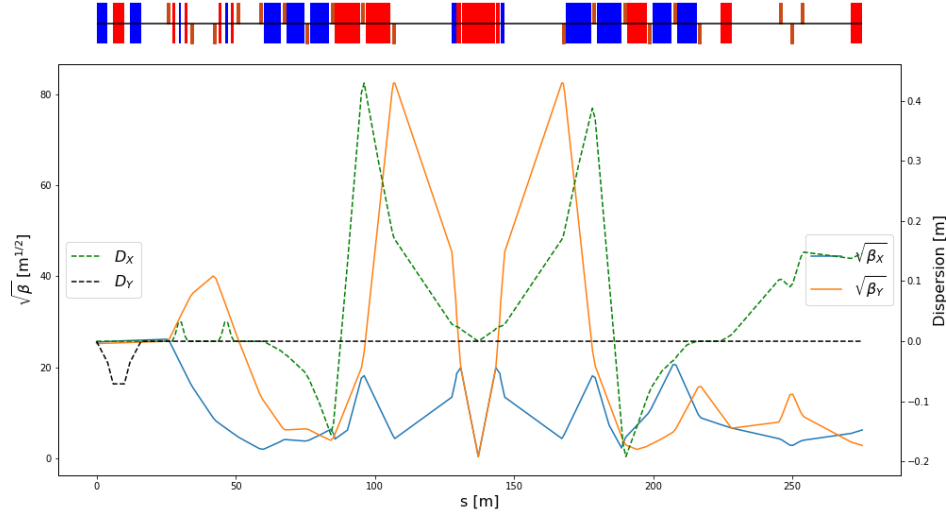
Figure 10.39: Electron beam optics for the new lattice including the early focusing scheme. The offset of the new doublet quadrupoles are chosen to provide the same separation field as in the dipole. The new optics is matched on the left side of the plot to the end of the acceleration linac. The right hand side is connected to Arc 6, the beginning of the decelerating ERL part. At the position of the first superconducting proton magnet the β-function in the (horizontal) separation plane of the electron beam is reduced to 90 m for lowest possible synchrotron radiation load.

The estimated synchrotron radiation power and critical energy for the different optimisations are plotted in Fig. 10.40 and the results are summarised in Tab. 10.25. Referring to a beam energy of 49.19 GeV and the design current of 20 mA an overall power of 16.2 kW is emitted within one half of the interaction region.

Optimised scheme	Synchrotron radiation		Critical energy	
	Radiation power [kW]	Critical energy [keV]	Radiation power [kW]	Critical energy [keV]
Reference design	30.8	300	30.8	300
Dipole length optimum	26.8	336	30.8	300
Half quadrupole optimum	22.2	331	26.1	295
Off-centered quadrupoles opti.	19.3	290	22.1	259
Half quad. + Off-centered quad. opti.	16.2	265	17.4	255

Table 10.25: Synchrotron radiation power and critical energy for the different optimised separation schemes.

Depending on the boundary conditions imposed by the integration of the particle detector, one of the two optimum layouts can be chosen – or a combination of both, i.e. an overall minimum defined by critical energy and radiated power.

The basic main parameters of the proton mirror plate half quadrupole are summarised in Tab. 10.26 for the two optimum scenarios explained above: the optimum found for smallest synchrotron radiation power and the optimum for smallest critical energy of the emitted radiation. The values result from the optics studies of the previous sections. The presented gradients lead to a pole tip field of $B_p \approx 1.3$ T.

In both cases, the proton aperture radius has been chosen to include an orbit tolerance of 2 mm, a 10 % tolerance on the beam size due to optics imperfections (beta-beating) and a beam size
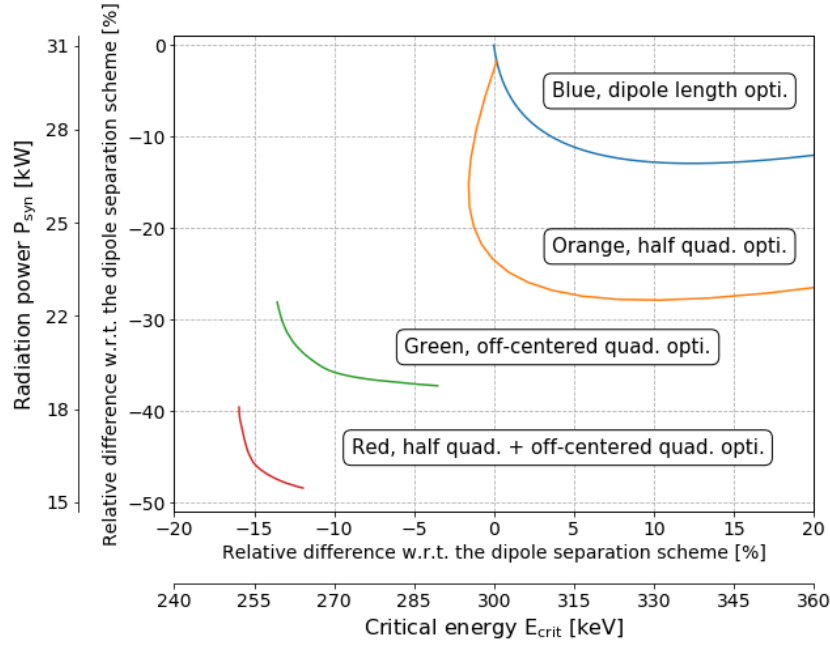
Figure 10.40: Relative differences with respect to the original single dipole separation scheme. The synchrotron radiated power is plotted as a function of the critical energy for different optimisation results: only optimising the dipole length (blue), only using a mirror quadrupole (orange), only using off-centered quadrupoles (green) and combining the mirror quadrupole with an earlier focusing (red).

Half quadrupole parameter	Unit	Minimum synchrotron radiation power	Minimum critical energy
$\gamma\varepsilon_p$	mm·mrad	2.50	2.50
Gradient	T/m	48.2	50.7
Aperture radius	mm	27.0	25.6
Length	m	6.84	2.08

Table 10.26: Magnet gradient of the proposed half quadrupole for lowest synchrotron radiaton power and lowest critical energy. An aperture of $15\,\sigma + 20\,\%$ beta-beating $+\,2\,$mm orbit tolerances has been assumed.

that corresponds to $n = 15\,\sigma$ for a proton beam normalised emittance $\varepsilon_p = 2.50\mu m$. A value that is comfortably larger than the requirements of the HL-LHC standard lattice. The injection proton optics has been taken into account and although it features a larger emittance it clearly fit in the aperture, see the red dashed line in Fig. 10.41. The electron beam and the non-colliding proton beam will pass through the field free region delimited by the mirror plate.

The aperture requirements inside the half quadrupole are determined on one side by the colliding proton beam optics in the main aperture of the magnet. The beam separation scheme and optics of electron and non-colliding proton beam on the other side have to fit into the field free region beyond the mid plane of the mirror plate. As described below, a crossing angle of $7\,$mrad is assumed for the non-colliding protons. These requirements are illustrated in Fig. 10.41. For the case of smallest synchrotron radiation power, the three beams are plotted at the entrance and exit of the quadrupole lens. For both proton beams the beam size shown in the graph corresponds to 15 sigma plus $2\,$mm orbit tolerance and $10\,\%$ beam size beating. Due to the mini-beta optics the colliding proton beam fills nearly the given aperture of the magnet. The
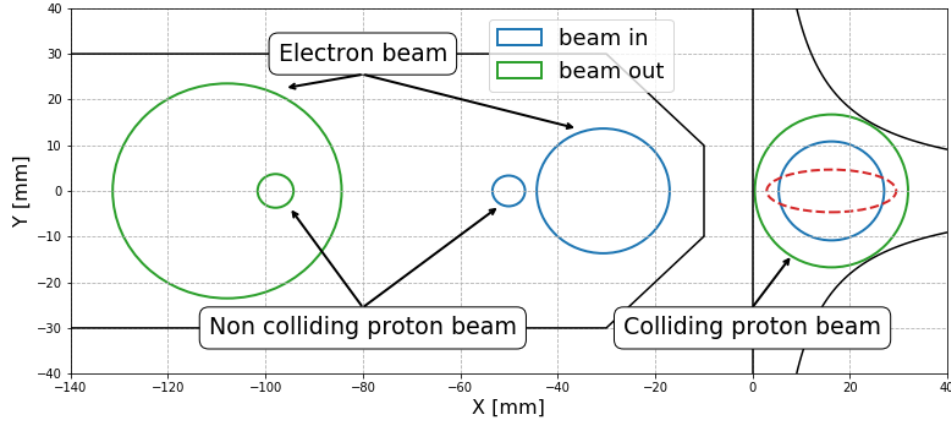
Figure 10.41: The position of the three beams at the entrance (blue) and exit (green) of the half quadrupole. The colliding proton beam is centered inside the main magnet aperture, while the second proton beam and the electrons are located in the field free region. The dashed red line represents the injection proton beam at the output of the half quadrupole.

non-colliding proton beam follows a relaxed optics with very limited aperture need. The envelope of the electron beam is shown for 20 σ beam size in both transverse planes.

In contrast to the proton half quadrupole, the doublet magnets of the early focusing scheme will house the three beams in one single aperture. In addition to the beam envelopes, the offset that has been chosen to provide the beam separation effect has to be taken into account and included in the aperture considerations.

In Fig. 10.42 the situation is visualised. On the left side the first off-center quadrupole (powered
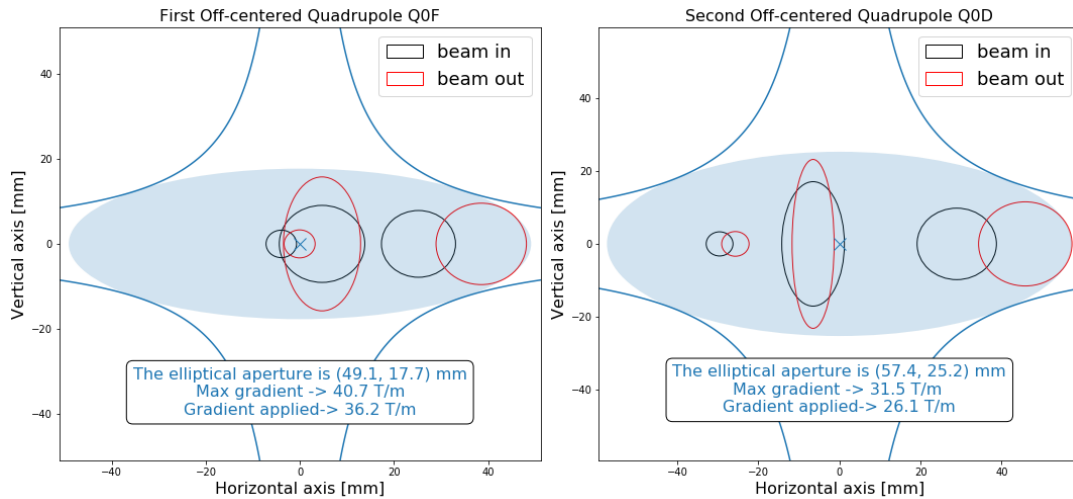
Figure 10.42: The position of the three beams at the entrance (black) and exit (red) of the electron doublet magnets. Following the internal convention, 15 σ plus 20 % beta beating plus 2 mm orbit tolerances beam envelopes are chosen for the proton beams. The beam size of the electrons refer to 20 σ. From left to right the three beams are respectively the non colliding proton beam (tiny circles), electron beam (squeezed ellipses) and the colliding proton beam.

as focusing lens) is presented. Following the field direction, the electron beam is offset towards the outer side of the ring (right side of the plot) as defined by the proton beam closed orbit. The right part of the figure shows the second quadrupole (powered as defocusing lens) with

the electron beam offset shifted to the other direction. In order to provide sufficient aperture for the three beams, an elliptical shape has been chosen for the vacuum chamber. It defines enough space for the beam envelopes and the off-centre design trajectories. The black ellipses correspond to the beams at the entrance of the magnet while the red shapes represent the beams at the exit. From left to right the three beams are respectively the non colliding proton beam (tiny circles), electron beam (squeezed ellipses) and the colliding proton beam. As defined before we refer to a beam size of $20\,\sigma$ in case of the electrons and 15 sigma plus beta-beating plus 2 mm orbit tolerance for the colliding and non-colliding proton beam.

In this context it should be pointed out that the non-colliding proton beam, travelling in the same direction as the electrons, is shifted in time by half the bunch spacing. While the projected beam envelopes in Figs. 10.42 and 10.41 seem to overlap in the transverse plane, they are well separated by 12.5 ns, corresponding to 3.75 m, in the longitudinal direction.

The minimum required gradients and pole tip radius of the quadrupoles of the doublet are listed in Tab. 10.27. Following the increasing beam size after the IP, the two quadrupoles are optimised

Parameter	Unit	Q0F	Q0D
$\gamma\varepsilon_e$	mm·mrad	50	50
$\gamma\varepsilon_p$	mm·mrad	2.50	2.50
Gradient	T/m	36.2	26.1
Min. pole-tip radius	mm	28.9	38.1
Length	m	1.86	1.86

Table 10.27: Magnet gradient and pole tip aperture of the quadrupoles of the doublet for the synchrotron power optimum.

for sufficient free aperture for the collidng beams and their design orbits. Accordingly a different layout has been chosen for the magnets, to provide the best conditions for the radiation power and critical energy. An alternative approach has been studied, based on a single quadrupole design for both lenses of the doublet. While an optics solution still is possible, it does however not allow for minimum radiation power and sets more stringent requirements on the shielding and absorption of the synchrotron light fan.
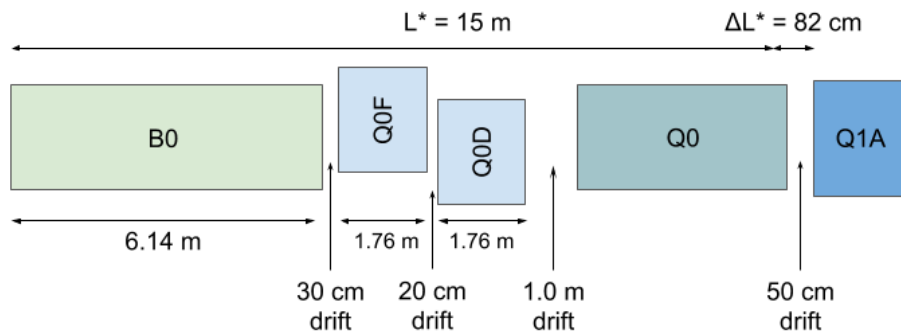
Figure 10.43: Possible optimised design featuring a 1.0 m drift between the off-centered quadrupoles and the half quadrupole in order to leave space for shielding material.

The chromatic effect of the two lattice versions as a function of the momentum spread is shown in Fig. 10.44. The lattice based on a single dipole magnet and late focusing of the electron beam shows an increase of the β function of up to 40% in the vertical plane for particles with a momentum deviation up to the design value of $\frac{\Delta p}{p} = 2.6 \cdot 10^{-4}$ (vertical cursor line in the graph)
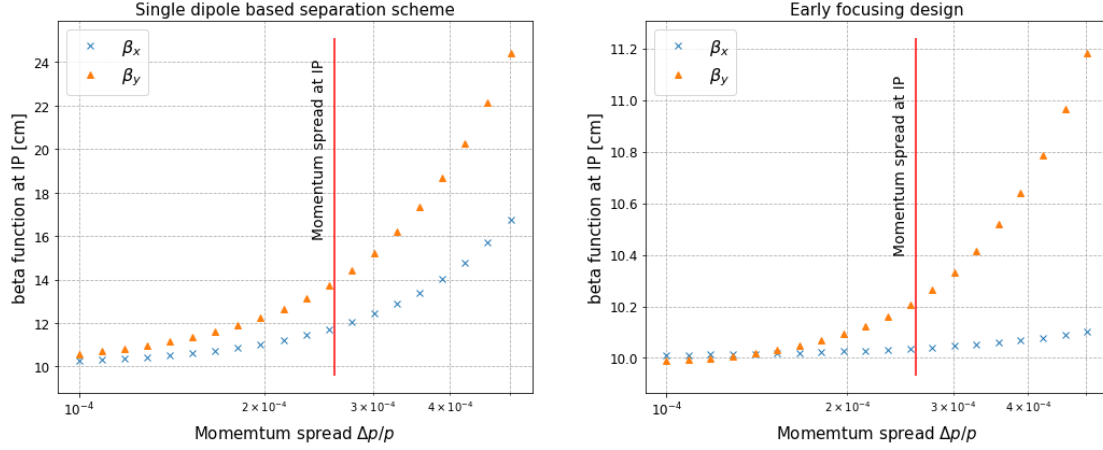
Figure 10.44: Beta function at the IP as a function of the momentum spread. Left : Situation for the single dipole based separation scheme. Right : With the design featuring an earlier focusing. The graphs show the increase of β^* due to the chromaticity of the lattice.

and a corresponding luminosity loss of 20% for those particles (see Fig. 10.45). The optimised design, based on the early focusing scheme, shows a much reduced chromatic effect and the resulting off-momentum beta-beating at the IP is limited to a few percent. As direct consequence the luminosity loss is well below the 1.5% level. A special local chromaticity correction scheme, therefore, dealing with the aberrations at IP, is thus not considered as necessary. Further studies will include the recirculation of the beam post-collision and the energy recovery performance and might nevertheless highlight the need of explicit sextupoles to mitigate the growing momentum spread through the deceleration process and to avoid beam losses.
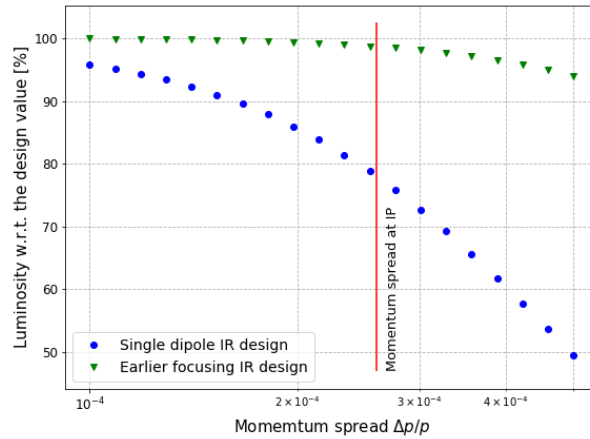
Figure 10.45: Luminosity as a function of the momentum spread for the single dipole based separation scheme (blue circles) and the design featuring an earlier focusing (green triangles).

10.7.4 Interaction Region Magnet Design

Triplet Magnet Design

While the Q1 magnets remain in the range achievable with the well proven Nb-Ti superconductors, operated at $1.8\,\mathrm{K}$, the Q2 magnets require Nb_3Sn technology at an operation temperature

of 4.2 K. The working points on the load-line are given for both superconducting technologies in Fig. 10.46.
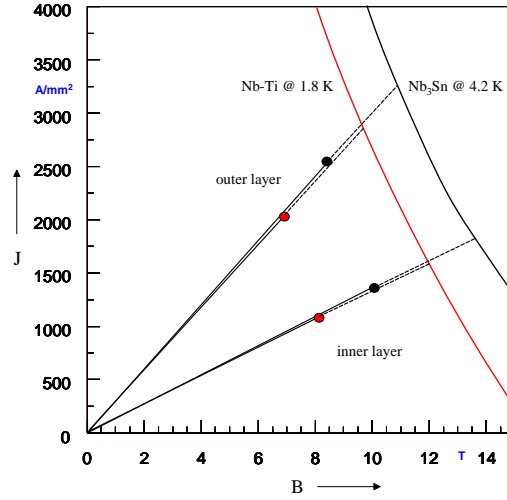
Figure 10.46: Working points on the load-line for both Nb-Ti and Nb$_3$Sn variants of Q1A.

The thickness of a coil layer is limited by the flexural rigidity of the cable, which will make the coil-end design difficult. Therefore multi-layer coils must be considered. However, a thicker, multi-layer coil will increase the beam separation between the proton and the electron beams. The results of the field computation are given in Tab. 10.28.

Magnet parameter	Unit	Magnet type			
		Q1A	Q1B	Q2 type	Q3 type
Superconductor type		Nb-Ti	Nb-Ti	Nb$_3$Sn	Nb$_3$Sn
Coil aperture radius R	mm	20	32	40	45
Nominal current I_{nom}	A	7080	6260	7890	9260
Nominal gradient g	T/m	252	164	186	175
Percentage on the load line	%	78	64	71	75
Beam separation distance S_{beam}	mm	106-143	148-180	233-272	414-452

Table 10.28: Main triplet magnet parameters

Unlike with the design proposed in the CDR of 2012 [1], the increased beam separation distance between the colliding proton beam and the electron beam makes it possible to neglect the fringe fields in the electron beam pipe. For the Q2 and Q3 magnets, the electron beam is outside of the quadrupole cold-mass and consequently, an HL-LHC inner-triplet magnet design can be adapted.

For the Nb$_3$Sn material we assume composite wire produced with the internal Sn process (Nb rod extrusions) [861]. The non-Cu critical current density is 2900 A/mm^2 at 12 T and 4.2 K. The filament size of 46 μm in Nb$_3$Sn strands give rise to higher persistent current effects in the magnet. The choice of Nb$_3$Sn would impose a considerable R&D and engineering design effort, which is however, not more challenging than other accelerator magnet projects, such as the HL-LHC.

The conceptual design of the mechanical structure of the Q1 magnets is shown in Fig. 10.47 (right). The necessary prestress in the coil-collar structure, which must be high enough to
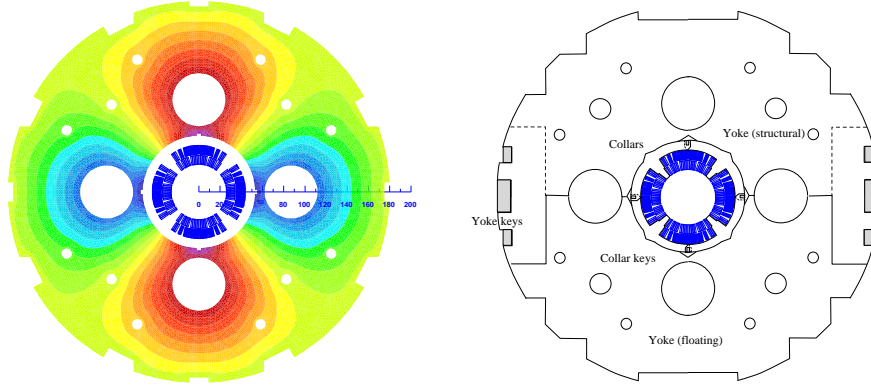
Figure 10.47: Conceptual design of the final focus septa Q1. Left: Magnetic vector potential (field lines). Right: Sketch of the mechanical structure.

avoid unloading at full excitation, cannot be exerted with the stainless-steel collars alone. Two interleaved sets of yoke laminations (a large one comprising the area of the yoke keys and a smaller, floating lamination with no structural function) provide the necessary mechanical stability of the magnet during cooldown and excitation. Preassembled yoke packs are mounted around the collars and put under a hydraulic press, so that the keys can be inserted. The sizing of these keys and the amount of prestress before the cooldown will have to be calculated using mechanical FEM programs. This also depends on the elastic modulus of the coil, which has to be measured with a short-model equipped with pressure gauges. Special care must be taken to avoid nonallowed multipole harmonics because the four-fold symmetry of the quadrupole will not entirely be maintained.

For the Q2 and Q3 magnets, a HL-LHC inner triplet desing using a bladder and key mechanical structure can be adapted.

Normal-Conducting Magnet Design

The proposed mini-beta doublet of the electron lattice, providing an early focusing of the beam, and the normal conducting proton-half quadrupole are new magnet concepts. These have been studied conceptually to determine their technical feasibility. The geometry of the QNC magnet is shwon in Fig. 10.48 (left). Left of the mirror plate, the field free region will provide space for the electron beam and the non-colliding proton beam. The thickness of the mirror plate at the magnet mid-plane is 20 mm, allowing for sufficient mechanical stability at the minimal beam separation between the electron and proton beams.

Field calculations, using the magnet design code ROXIE [862] are presented in Fig. 10.48 (right). The achieved field gradient is 50 T/m for a current of 400 A, assuming a current density of 21.14 A/mm^2. This is in line with conductor geometries used for normal conducting magnets installed in the CERN injector complex, for example, ID: PXMQNDD8WC, which is rated at 860 A corresponding to 45.45 A/mm^2. A more comprehensive design study must also include a further reduction of the multipole field components.

The geometry of the Q0F and Q0D quadrupoles are given in Fig. 10.42 and the main specifications are provided in Tab. 10.27. A maximum magnetic field of 1.2 T at the pole tip is well within reach for a normal conducting quadrupole.
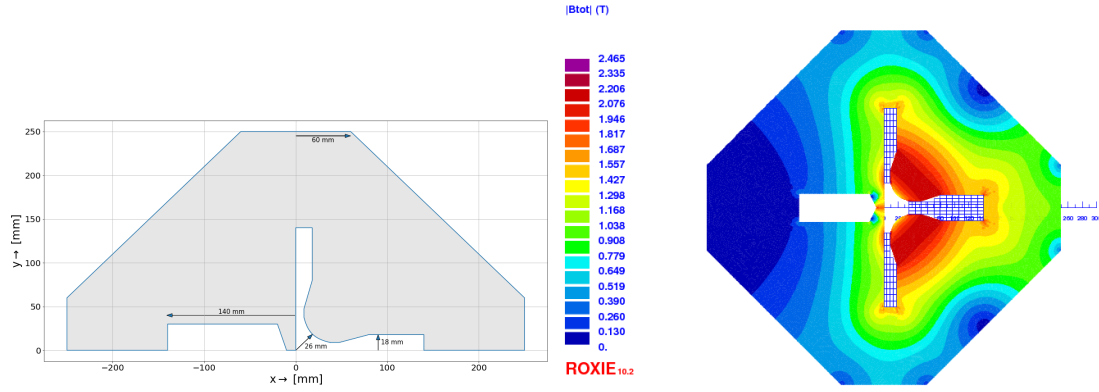
Figure 10.48: Left: Mechanical layout of the new half quadrupole for the proton beam. Right : Field distribution in the half quadrupole for the proton beam.

10.8 Civil Engineering

Since the beginning of the LHeC study which proposes a electron-hadron collider, various shapes and sizes of the *eh* collider were studied around CERN region. Two main options were initially considered, namely the Ring-Ring and the Linac-Ring. For civil engineering, these options were studied taking into account geology, construction risks, land features as well as technical constraints and operations of the LHC. The Linac-Ring configuration was selected, favouring a higher achievable luminosity. This chapter describes the civil engineering infrastructure required for an Energy Recovery Linac (ERL) injecting into the ALICE cavern at Point 2 LHC. Fig. 10.49 shows three options for the ERL of different sizes, represented as fractions of the LHC circumference, respectively 1/3, 1/4 and 1/5 of the LHC circumference.
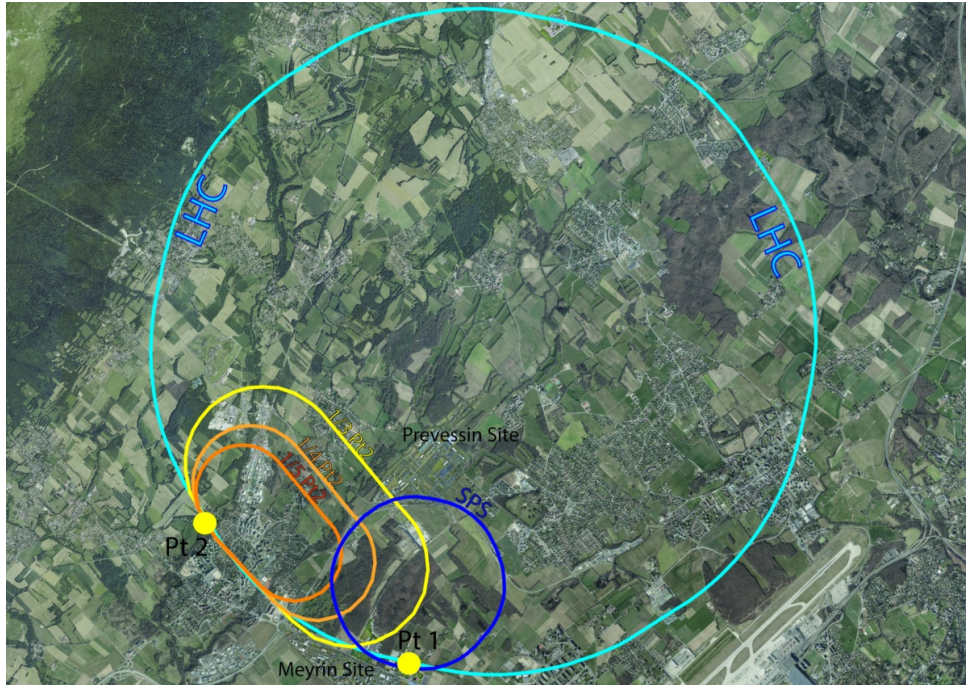
Figure 10.49: Racetrack options proposed for LHeC at Point 2 of the LHC. The color coding illustrated different options with 1/3, 1/4 and 1/5 of the LHC circumference, resulting in different electron beam energies.

Figure 10.50: Simplified map of Swiss geology.

10.8.1 Placement and Geology

The proposed siting for the LHeC is in the North-Western part of the Geneva region at the existing CERN laboratory. The proposed Interaction Region is fully located within existing CERN land at LHC Point 2, close to the village of St. Genis, in France. The CERN area is extremely well suited to housing such a large project, with well understood ground conditions having several particle accelerators in the region for over 50 years. Extensive geological records exist from previous projects such as LEP and LHC and more recently, further ground investigations have been undertaken for the High-Luminosity LHC project. Any new underground structures will be constructed in the stable molasse rock at a depth of 100–150 m in an area with low seismic activity.

The LHeC is situated within the Geneva basin, a sub-basin of the large molassic plateau (Fig. 10.50). The molasse is a weak sedimentary rock which formed from the erosion of the Alps. It comprises of alternating layers of marls and sandstones (and formations of intermediate compositions), which show a high variety of strength parameters [863]. The molasse is overlaid by the Quaternary glacial moraines. A simplified geological profile of the LHC is shown in Fig. 10.51. Although placed mainly within the molasse plateau, one sector of the LHC is situated in the Jura limestone.

The physical positioning of the LHeC has been developed based on the assumption that the maximum underground volume should be placed within the molasse rock and should avoid as much as possible any known geological faults or environmentally sensitive areas. Stable and dry, the molasse is considered a suitable rock type for Tunnel Boring Machines (TBM) excavation. In comparison, CERN has experienced significant issues with the underground construction of sector 3-4 in the Jura limestone. There were major issues with water ingress at and behind the tunnel face [864]. Another challenging factor for limestone is the presence of karsts. These are formed by chemical weathering of the rock and often they are filled with water and sediment, which can lead to water infiltration and instability of the excavation.

The ERL will be positioned inside the LHC layout, in order to ensure that new surface facilities are located on existing CERN land. The proposed underground structures for the LHeC with
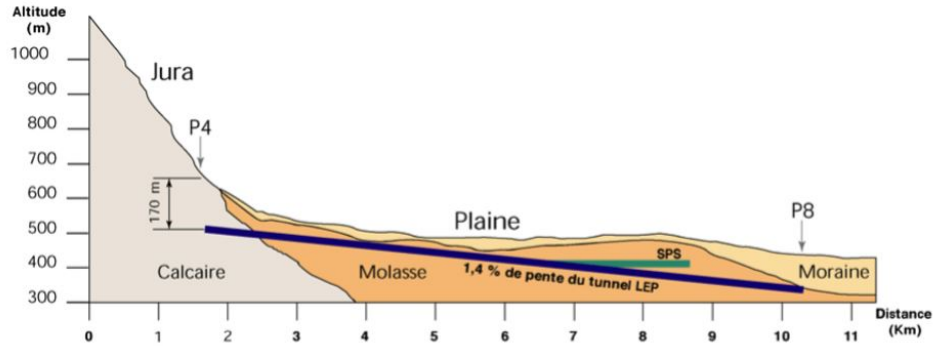
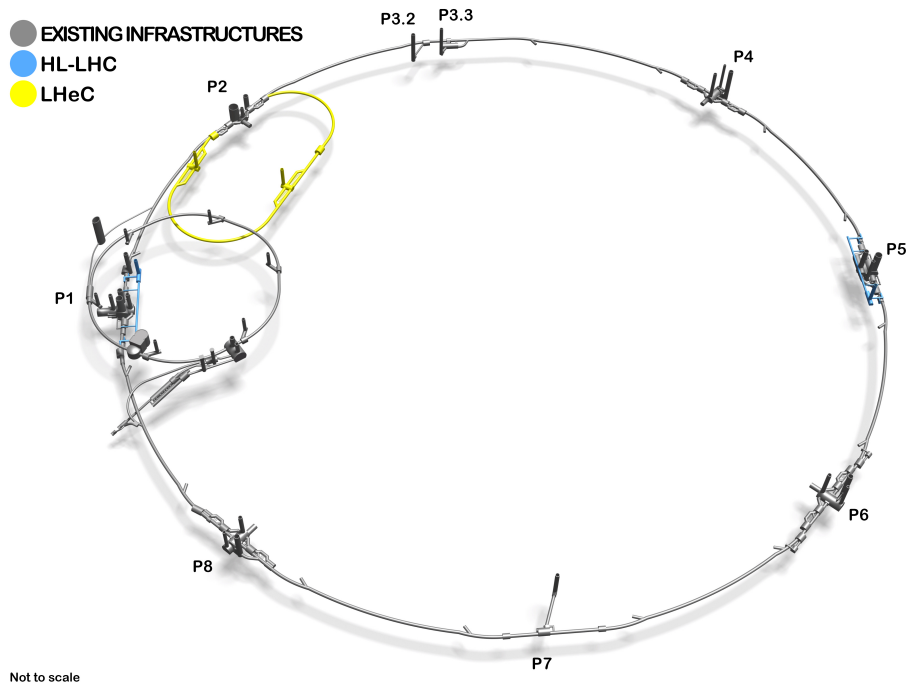**Figure 10.51:** Geological profile of the LHC tunnel.

Figure 10.52: 3D Schematic showing proposed underground structures of LHeC (shwon in yellow). The HL-LHC structures are highlighted in blue.

an electron beam energy of 60 GeV are shown in Fig. 10.52. The LHeC tunnel will be tilted similarly to the LHC at a slope of 1.4% to follow a suitable layer of molasse rock.

10.8.2 Underground infrastructure

The underground structures proposed for LHeC option 1/3 LHC require a 9 km long tunnel including two LINACs. The internal diameter of the tunnel is 5.5 m. Parallel to the LINACs, at 10m distance apart, there are the RF galleries, each 1070 m long. Waveguides of 1 m diameter and four connection tunnels are connecting the RF galleries and LINACs. These structures are listed in Tab. 10.29. Two additional caverns, 25 m wide and 50 m long are required for cryogenics and technical services. These are connected to the surface via two 9 m diameter shafts, provided with lifts to allow access for equipment and personnel. Additional caverns are needed to house injection facilities and a beam dump. As shown in Tab. 10.29, the underground structures

Structure	Quantities	Span [m]	1/3 LHC	1/5 LHC
			Length [m]	Length [m]
Machine tunnels	-	5.5	9000	5400
Service caverns	2	25	50	50
Service shafts	2	9	80	80
Injection caverns	1	25	50	50
Dump cavern	1	16.8	90	90
Junction caverns	3	16.8	20	20
RF galleries	2	5.5	1070	830
Waveguide connections	50	1	10	10
Connection tunnels	4	3	10	10

Table 10.29: List of underground structures for LHeC for two different options with 1/3 or 1/5 of the LHC circumference.
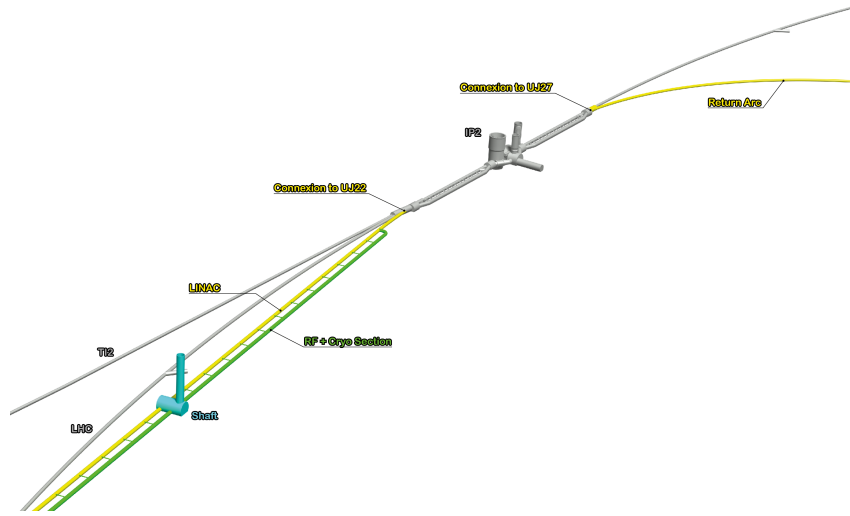
Figure 10.53: ERL injection area into IP2 and junction cavern

proposed for LHeC options 1/5 LHC and 1/3 LHC are similar with the exception of the main tunnel and the RF galleries which have different lengths.

Shaft locations were chosen such that the surface facilities are located on CERN land. The scope of work for surface sites is still to be defined. New facilities are envisaged for housing technical services such as cooling and ventilation, cryogenics and electrical distribution.

In addition to the new structures, the existing LHC infrastructure requires some modifications. To ensure connection between LHC and LHeC tunnels, the junction caverns UJ22 and UJ27 need to be enlarged. Fig. 10.53 shows the location of these caverns. Localised parts of the cavern and tunnel lining will be broken out to facilitate the excavation of the new spaces and the new connections, requiring temporary support.

Infrastructure works for LEP were completed in 1989, for which a design lifespan of 50 years was specified. If the LHC infrastructure is to be re-used, refurbishment and maintenance works are needed.
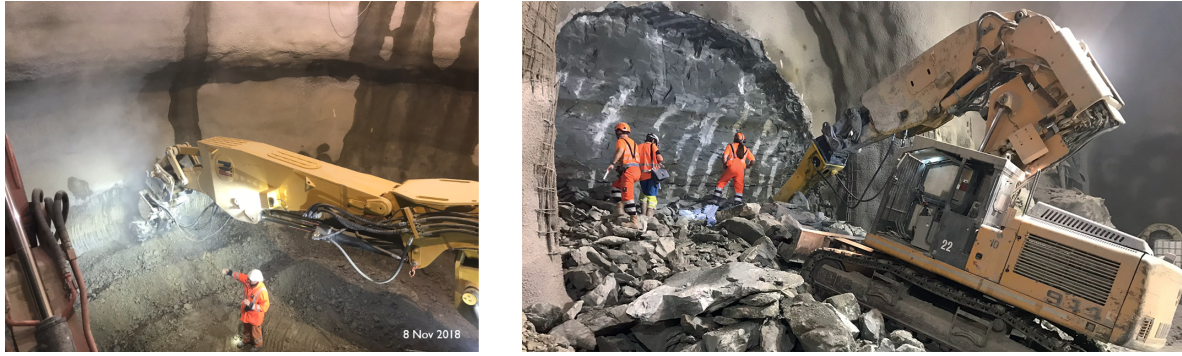
Figure 10.54: Left: Roadheader being used for shaft excavation at HL-LHC Point 1. Right: Rockbreaker used for new service tunnels excavation at HL-LHC Point 5 (Credit: Z. Arenas).

10.8.3 Construction Methods

A TBM would be utilised for the excavation of the main tunnel to achieve the fastest construction. When ground conditions are good and the geology is consistent, TBMs can be two to four times faster than conventional methods. A double shield TBM could be employed, installing pre-cast segments as primary lining, and injecting grouting behind the lining.

For the excavation of the shafts, caverns and connection tunnels, typical conventional techniques could be used. Similar construction methods used during HL-LHC construction can be adopted for LHeC, for example using roadheaders and rockbreakers. This machinery is illustrated in Fig. 10.54, showing the excavation works at Point 1. One main constraint that dictated what equipment to be used for the HL-LHC excavation, was the vibration limit. Considering the sensitivity of the beamline, diesel excavators have been modified and equipped with an electric motor in order to reduce vibrations that could disrupt LHC operation. Similar equipment could be required for LHeC, if construction works are carried out during operation of the LHC.

Existing boreholes data around IP2 shows that the moraines layer is approximately 25–35 m deep before reaching the molasse. Temporary support of the excavation, for example using diaphragm walls is recommended. Once reaching a stable ground in dry conditions, common excavation methods can be adopted. The shaft lining will consist of a primary layer of shortcrete with rockbolts and an in-situ reinforced concrete secondary lining, with a waterproofing membrane in between the two linings.

10.8.4 Civil Engineering for FCC-eh

A facility allowing collisions between protons and electrons was considered in the study for the Future Circular Collider (FCC). Fig. 10.55 shows the baseline position for FCC and the lepron ring located at Point L.

During FCC feasibility stage, a bespoke GIS based tool (the Tunnel Optimisation Tool – TOT) was used to optimise the placement and layout of the FCC ring. The current baseline location was chosen such that the FCC tunnel is placed in preferable geology (90 % of the tunnel is in molasse), the depth of the shafts and the overburden is minimised and tunnel under the Geneva Lake goes through the lake bed, passing though reasonably stable ground. More investigations are needed to determine the feasibility of tunnelling under the Geneva Lake. The baseline position also allows connections to the LHC. Fig. 10.56 shows the geological profile of the tunnel
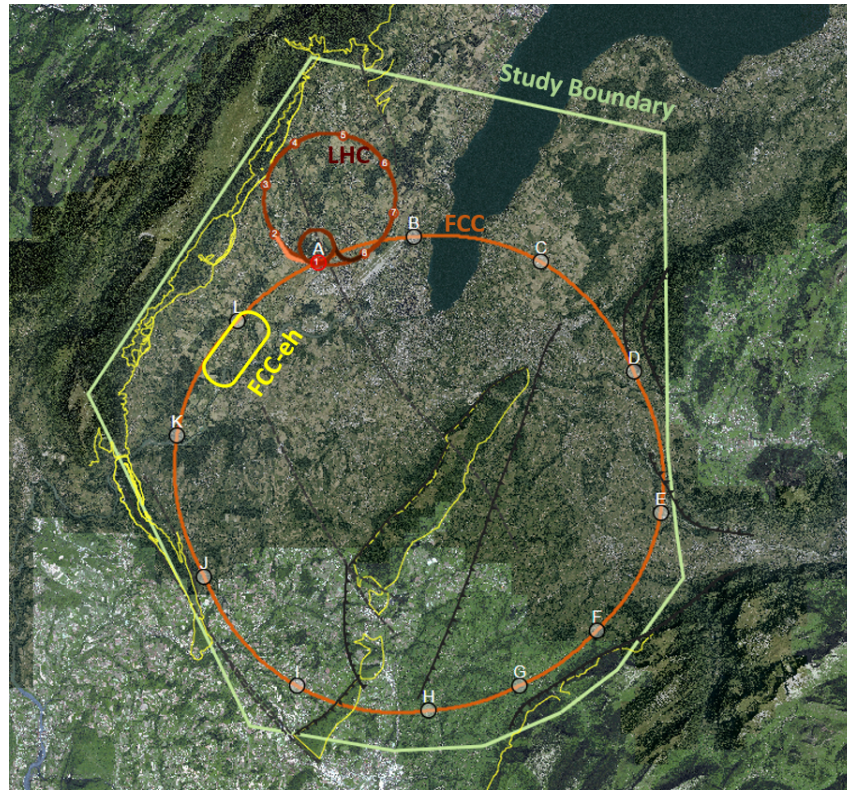
Figure 10.55: Baseline position and layout for FCC. The lepton ring location is shown at Point L.

in baseline position. TOT was used to evaluate different layouts and positions for the FCC ring and assess the impact on the location of the lepton ring. The candidate locations for the *eh* IR were the experimental points A, B, G and L. Point L was selected because it provides good geological conditions, being fully housed in the molasse layer at a depth of around 180 m. In comparison, Point G is much deeper, Point A is challenging due to proximity of the LHC and Point B is located in a congested urban area. Similarly to LHeC, the lepton ring will be located inside the FCC ring, in this instance to avoid the Jura limestone. The entire FCC-eh infrastructure is located in the molasse.

The geological data captured within the TOT tool was collected from various sources including previous underground projects at CERN, the French Bureau de Recherches Géologiques et Minières (BRGM), and existing geological maps and boreholes for geothermal and petroleum exploration. The data was processed to produce rock-head maps and to create the geological layers. No ground investigations have been conducted specifically for the FCC project [16]. In order to validate its baseline alignment and determine the geotechnical parameters required for the detailed design, site investigation campaigns will need to be carried out. Some boreholes exist in the region where the tunnel for the lepton ring will be built, reducing the uncertainty of the ground conditions. However, further ground investigations are needed in order to verify the boundary between geological layers. The geological features of interest in this region are the Allondon Fault and possible zones of poor rock and level of limestone, which should be avoided.

The IP will be in the experimental cavern at point L, defined as an experimental point for FCC-hh. The layout of the ERL and the underground infrastructure for the FCC-eh is similar to LHeC (see Table 10.29), with the exception of the shafts which are 180 m deep. The schematic layout and proposed civil engineering structures are shown in Fig. 10.57.
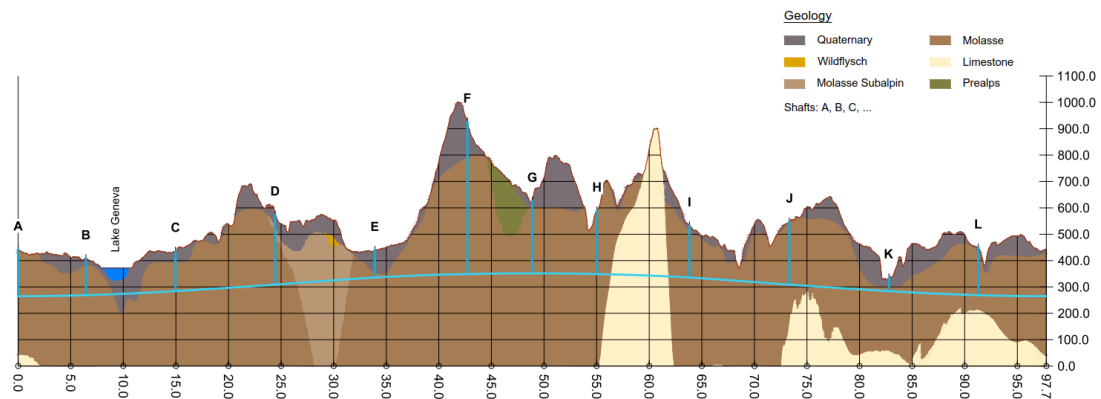
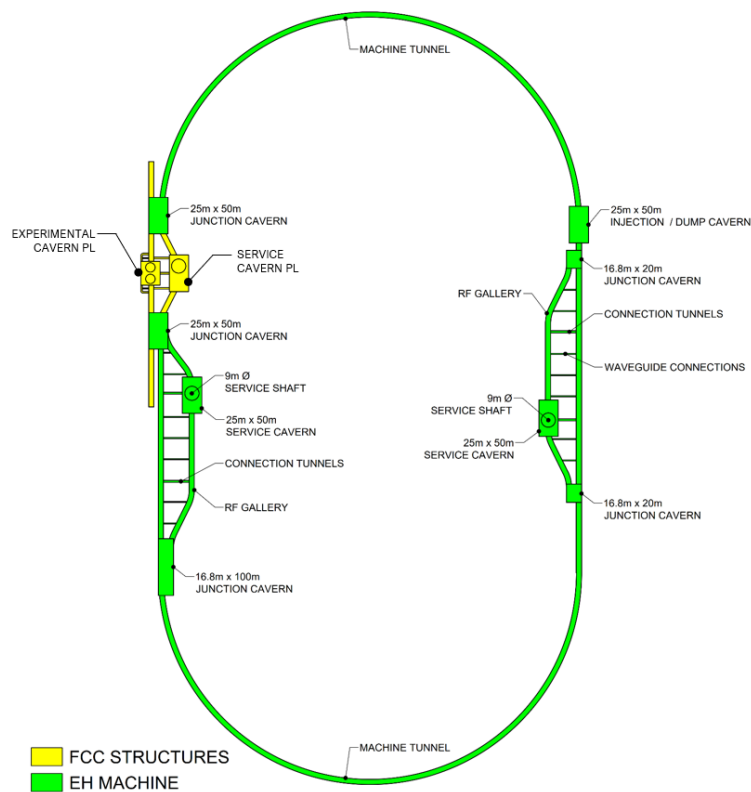**Figure 10.56:** Geological profile along FCC tunnel circumference

Figure 10.57: Schematic layout showing the proposed underground structures for FCC-eh

300

The upper excavation for each shaft will be through the moraines. Based on available geological data, the moraines layer should be approximately 30 m deep. Similar construction methods as described in Section 8.8.3 could be used. For FCC, the alternative technology that has been considered for deep shafts is using a Vertical Shaft Sinking Machine. The junction caverns connecting the ERL tunnel with the FCC tunnel must be designed such that they fit the requirements for the new collider and the lepton machine. The junction caverns near Point L will connect three tunnels, the FCC main tunnel, the ERL tunnel and the RF galleries. These caverns will have a 25 m span and 50 m length.

For the FCC TBM excavations, different lining designs have been developed corresponding to conditions of the rock [16]. Good ground conditions have been assumed based on available geological information in the area where the ERL tunnels are positioned and a single-pass pre-cast lining is proposed.

10.8.5   Cost estimates

The cost for underground civil engineering for FCC-eh facility was estimated to be approximately 430 MCHF. The construction programme for the lepton accelerator tunnels, caverns and shafts is currently integrated into the overall FCC construction schedule.

A detailed cost estimate was prepared for a 9 km ERL located at Point 2 of LHC, using the same unit prices as for FCC. More recently for LHeC, the cost figures were adapted to fit the smaller version, the 5.4 km racetrack at Point 2 (option 1/5 LHC). The civil engineering costs amount to about 25 % of the total project costs. For the 9 km ERL (1/3 LHC option) the civil engineering was estimated to 386 MCHF and for a 5.4 km configuration (1/5 LHC) the costs would be 289 MCHF. These costs do not include surface structures. Where possible, existing surface infrastructure will be re-used.

The cost estimates include the fees for preliminary design, approvals and tender documents (12 %), site investigations (2 %) and contractor's profit (3 %). The accuracy range of the cost estimates at feasibility stage is ± 30 %.

10.8.6   Spoil management

As with all construction projects, environmental aspects play an important role. A detailed study is being conducted at CERN to find a potential re-use for of the spoil that will be generated from the FCC underground excavations. The total amount of spoil calculated is approximately 10 million cubic meters, of which 778,000 cubic metres of spoil would be generated from the lepton ring tunnel construction.

Chapter 11

Technology of ERL and PERLE

Energy recovery has been proposed in 1965 [865] as a means for efficient colliding beam interactions. It has been demonstrated to indeed work at a number of laboratories, at BINP Novosibirsk, at Daresbury, at Jefferson Lab and very recently at Cornell. The striking technology developments of high quality superconducting cavities of the last decades and the need for high collider intensities at economic use of power have now lead to a wider recognition of ERL applications as one of the most promising and fundamental developments of energy frontier accelerator physics. For the LHeC, it had become clear already with and before the CDR, that ERL was the only way to achieve high luminosity in *ep* within the given power limit of 100 MW wall plug for the linac-ring *ep* collider configuration. For FCC-ee it has been promoted as an alternative to conventional synchrotron technology for extending the energy range and increasing the luminosity in the WW and top mass ranges [32]. A high current electron ERL is designed to reach high lumosities with proton beam cooling at the EIC [866]. High energy particle and nuclear physics colliders do await high current ERLs to become available.

Following the LHeC CDR it became increasingly clear, much emphasised by the IAC of the LHeC, that the basic concept, of high current, multi-turn ERL, needed a smaller size facility for gaining experience and developing the technology. This lead to the development of the PERLE concept as was described in a Conceptual Design Report published in 2017 [7]. PERLE imported the main characteristics of the LHeC, the 802 MHz frequency and the 3-turn racetrack configuration of two oppositely positioned linacs. With the 20 mA current goal and a 500 MeV beam it represents a first ERL facility in the 10 MW power range. Its intensity, exceeding that of ELI by 2-3 orders of magnitude, is the base for novel low energy experiments which are envisaged to follow the first years of dedicated accelerator design study and technology development. PERLE therefore has a physics and technical programme which reaches beyond supporting the LHeC design and possible future operation.

An international collaboration has recently been established with the aim to realise PERLE in a few stages at IJC Laboratory at Orsay near Paris within the next years. The following chapter has two parts, the first describing challenges and status of ERL developments and the second one briefly summarising PERLE. It has to be noted that crucial parts of PERLE are described above in the LHeC Linac part, such as the choice of frequency, the electron source, and the successful design, construction and test of the first 5-cell SC Niobium cavity, because all these characteristics are shared between the LHeC and its development facility.

11.1 Energy Recovery Linac Technology - Status and Prospects

In instances where high beam power is required, the concept of energy recovery presents an attractive solution. Energy recovering linacs (ERLs) are a class of novel accelerators which are uniquely qualified to meet the demands for a wide variety of applications by borrowing features from traditional architectures to generate linac quality beams with near storage ring efficiency [867]. After acceleration through a linac section, the electrons in an ERL are returned 180° out of phase with respect to the radio frequency (RF) accelerating field for energy recovery. The beam deposits energy into cavity fields, which can then accelerate newly injected bunches, thereby effectively canceling the beam loading effects of the accelerated beam. Therefore ERLs can accelerate very high average currents with only modest amounts of RF power. Because the beam is constantly being renewed, it never reaches an equilibrium state. Consequently this provides flexibility to manipulate the phase space and tailor the beam properties for a specific application. Further, since the energy of the decelerated beam is approximately equal to the injection energy, the dump design becomes considerably easier.

11.1.1 ERL Applications

Historically, nearly all ERLs built and operated were used to drive a free-electron laser (FEL). The requirement for high peak current bunches necessitated bunch compression and handling the attendant beam dynamical challenges. In recent years, ERLs have turned from being drivers of light sources toward applications for nuclear physics experiments, Compton backscattering sources and strong electron cooling. Unlike an FEL, these latter use cases require long, high charge bunches with small energy spread. Where once a short bunch length was the key performance metric, now there is a premium on maintaining a small correlated energy spread (with a commensurately long bunch).

11.1.2 Challenges

Energy recovery linacs are not without their own set of challenges. In the following sections a brief survey of some of the most relevant are given. These include collective effects, such as space charge, the multipass beam breakup (BBU) instability, coherent synchrotron radiation (CSR) and the microbunching instability (μBI), beam dynamic issues such as halo, the interaction of the beam with the RF system and other environmental impedances as well as issues related to common transport lines.

Space Charge

The role of space charge forces (both transverse and longitudinal) often dictate many operational aspects of the machine. Maintaining beam brightness during the low energy injection stage is vitally important. In addition to the low energy, ERL injectors must also preserve beam quality through the merger system that directs the beam to the linac axis. Once injected into the linac, the beam energy at the front end is often still low enough that space charge forces cannot be neglected. Just as important is the longitudinal space charge (LSC) force which manifests itself by an energy spread asymmetry about the linac on-crest phase [868]. The LSC wake acts to accelerate the head of the bunch while decelerating the tail. Operating on the rising part of the waveform leads to a decrease in the correlated energy spread, while accelerating on the

falling side leads to an increase. These observations inform where acceleration, and how the longitudinal match, is performed.

Beam Breakup Instability

The beam breakup instability is initiated when a beam bunch passes through an RF cavity off-axis, thereby exciting dipole higher-order modes (HOMs). The magnetic field of an excited mode deflects following bunches traveling through the cavity. Depending on the details of the machine optics, the deflection produced by the mode can translate into a transverse displacement at the cavity after recirculation. The recirculated beam induces, in turn, an HOM voltage which depends on the magnitude and direction of the beam displacement. Thus, the recirculated beam completes a feedback loop which can become unstable if the average beam current exceeds the threshold for stability [869]. Beam breakup is of particular concern in the design of high average current ERLs utilizing superconducting RF (SRF) technology. If not sufficiently damped by the HOM couplers, dipole modes with quality factors several orders of magnitude higher than in normal conducting cavities can exist, providing a threat for BBU to develop. For single pass ERLs, beam optical suppression techniques – namely, interchanging the horizontal and vertical phase spaces to break the feedback loop between the beam and the offending HOM – are effective at mitigating BBU [870].

Coherent Synchrotron Radiation

Coherent synchrotron radiation poses a significant challenge for accelerators utilizing high brightness beams. When a bunch travels along a curved orbit, fields radiated from the tail of the bunch can overtake and interact with the head. Rather than the more conventional class of head-tail instabilities where the tail is affected by the actions of the head, CSR is a tail-head instability. The net result is that the tail loses energy while the head gains energy leading to an undesirable redistribution of particles in the bunch. Because the interaction takes place in a region of dispersion, the energy redistribution is correlated with the transverse positions in the bend plane and can lead to projected emittance growth. While there has been much progress in recent years to undo the effects of CSR in the bend plane with an appropriate choice of beam optics [871], it is more difficult to undo the gross longitudinal distortion caused by the CSR wake. This is particularly true in applications where the intrinsic energy spread is small and/or where the effect can accumulate over multiple recirculations. One possible mitigation is shielding the CSR wake using an appropriately sized beam pipe [872].

Microbunching Instability

Microbunching develops when an initial density modulation, either from shot noise or from the drive laser, is converted to energy modulations through short-range wakefields such as space charge and CSR. The energy modulations are then transformed back to density modulations through the momentum compaction of the lattice. Danger arises when a positive feedback is formed and the initial modulations are enhanced. This phenomenon has been studied extensively, both theoretically and experimentally, in bunch compressor chicanes [873, 874]. Only recently has there been a concerted effort to study the microbunching instability in recirculating arcs [875–877]. Because the beam is subject to space charge and/or CSR throughout an ERL, density modulations can be converted to energy modulations. And because of the native momentum compaction of the lattice (in arcs, spreaders/recombiners, chicanes, etc.) those energy

modulations may be converted back to density modulations. Therefore, ERLs offer potentially favorable conditions for seeding the microbunching instability, which requires careful attention in the early design stages.

Halo

Halo is defined as the relatively diffuse and potentially irregularly distributed components of beam phase space that can reach large amplitudes. It is of concern because ERL beams are manifestly non-Gaussian and can have beam components of significant intensity beyond the beam core [878]. Though sampling large amplitudes, halo responds to the external focusing of the accelerator transport system in a predictable manner. It is therefore not always at large spatial amplitude, but will at some locations instead be small in size but strongly divergent. Halo can therefore present itself as *hot spots* in a beam distribution, and thus may be thought of as a lower-intensity, co-propagating beam that is mismatched to the core beam focusing, timing, and energy. Beam loss due to halo scraping is perhaps the major operational challenge for higher-power ERLs. Megawatt-class systems must control losses at unshielded locations to better than 100 parts-per-million to stay within facility radiation envelopes. Scaling to 100 MW suggests that control must be at the part-per-million level. This has been demonstrated – but only at specific locations within an ERL [879].

RF Transients

Dynamic loading due to incomplete energy recovery is an issue for all ERLs [880]. In some machines it is due to unintentional errors imposed on the energy recovered beam; for instance, path length errors in large-scale systems. In other machines, such as high power ERL-based FEL drivers, it is done intentionally. In cases where there is the potential for rapid changes in the relative phase of the energy recovered beam, dynamic loading would be difficult to completely control using fast tuners. In such cases adequate headroom in the RF power will have to be designed into the system. These transient beam-loading phenomena are widely unrecognized and/or neglected, however studies have been exploring these issues and the dependence on factors such as the bunch injection pattern [881]. RF drive requirements for an ERL are often viewed as *minimal*, because in steady-state operation the recovered beam notionally provides RF power for acceleration. It has however been operationally established that RF drive requirements for ERLs are defined not by the steady-state, but rather by beam transients and environmental/design factors such as microphonics [882]. As a result, the RF power required for stable ERL operation can differ dramatically from naïve expectations.

Wakefields and Interaction of Beam with Environment

As with other system architectures intended to handle high-brightness beams, ERLs can be performance-limited by wakefield effects. Not only can beam quality be compromised by interaction of the beam with environmental impedances, there is also significant potential for localized power deposition in beamline components. Resistive wall and RF heating have proven problematic during ERL operation in the past [883]. Extrapolation of this experience to higher bunch charges and beam powers leads to serious concern regarding heating effects. Careful analysis and management of system component impedances is required.

Multi-turn, Common Transport

Future systems must evolve to utilize multiple turns; it is a natural cost optimization method [884] and multi-turn systems can in principle provide performance equal to that of 1-pass up/down ERLs at significantly lower cost. In addition to the use of multiple turns, cost control motivates use of extended lengths of common transport, in which both accelerated and recovered passes are handled simultaneously using the same beam lines. This presents unique challenges for high energy ERLs, like LHeC in particular, where energy loss due to synchrotron radiation cannot be ignored and causes an energy mismatch for common transport lines. But addressing these challenges will open up exciting new opportunities for ERLs. In addition to PERLE and LHeC, a multi-turn ERL design from Daresbury illustrates the manner in which the cost/complexity optimum lies toward shorter linacs, more turns, and multiple beams in fewer beam lines [797]. This also drives the use of multiple turns in stacking rings for hadron cooling; the more turns the cooling beam can be utilized, the lower the current required from the driver ERL, which mitigates challenges associated with source lifetime [885].

11.1.3   ERL Landscape

One way to view the current state of ERLs globally is the so-called *ERL landscape* shown in Fig. 11.1 [886]. Every data point represents a machine that demonstrated energy recovery and is positioned in (maximum) energy and (average) current parameter space. For clarity, the plot is restricted to continuous-wave (CW), SRF-based ERLs only and includes legacy machines, those under construction and currently in operation as well as the LHeC and PERLE (proposed). The size of the marker is indicative of the charge per bunch while a black line around the marker indicates it was/is a *true ERL*. That is, where the beam power exceeds the installed RF power (they are represented in the plot by the three FEL drivers that were designed, built, commissioned and operated at Jefferson Laboratory).
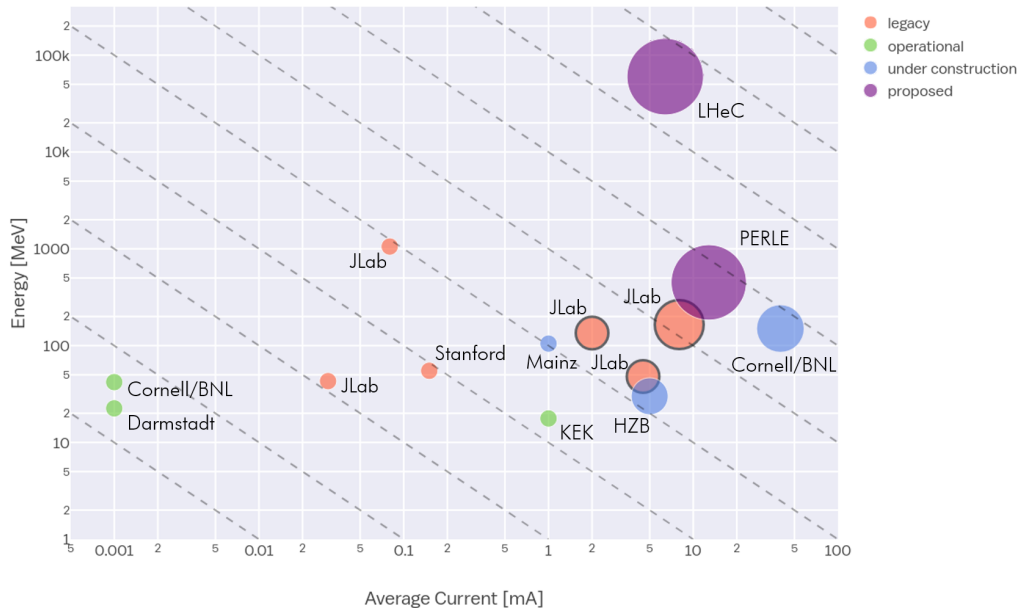
Figure 11.1: The *ERL landscape*, where data points are restricted to CW, SRF-based ERLs. The dashed lines represent lines of constant beam power – starting from 10 W in the lower left and going to 10 GW in the upper right. Note that both axes use a log scale.

A cursory look at Fig. 11.1 illustrates several of the challenges facing the next generation of ERLs. While getting from the current state-of-the-art to the LHeC requires only a modest increase in average current, it requires a significant increase in bunch charge and addressing the consequent collective effects [887]. Most significantly, however, is the leap in energy from systems that have operated in the 100 MeV range to several tens of GeV. Note that PERLE is strategically positioned to address incremental changes in both average current, bunch charge and energy. As such, it provides a convenient test bed facility to address the issues described previously [888]. Several ERLs are still in the nascent stages and as they ramp up beam power, will also be valuable in advancing the state-of-the-art. For instance, though it uses a Fixed Field Alternating Gradient (FFAG) arc, the Cornell/Brookhaven ERL Test Accelerator (CBETA) will address multi-turn energy recovery for the first time in an SRF system [5]. Note that with only minor modifications Jefferson Laboratory's Continuous Electron Beam Accelerator Facility (CEBAF) could be operated with multi-pass energy recovery at several GeV using common transport with the same topology as LHeC (i.e. bisected linacs of equal energy gain with arcs vertically separated by energy using spreaders and recombiners) [889].

11.2   The ERL Facility PERLE

PERLE is a compact three-pass ERL based on SRF technology, a new generation machine uniquely covering the 10 MW power regime of beam current and energy. Its Conceptual Design Report appeared recently [7]. Apart from low energy experiments it could host, thanks to its beam characteristics, PERLE will serve as a hub for the validation of a broad range of accelerator phenomena and the development of ERL technology for future colliders as introduced above. Particularly, the basic 3-turn configuration, design challenges and beam parameters (see Tab. 11.1) are chosen to enable PERLE as a testbed for the injection line and SRF technology development, as well as multi-turn and high current ERL operation techniques for the Large Hadron electron Collider. While the concept and promise of ERL's has been kick-started by demonstration machines based on existing accelerator technology, PERLE will be the first machine designed from the ground up to use fully optimised ERL-specific designs and hardware.

The PERLE collaboration involves today CERN, Jefferson Laboratory, STFC-Daresbury (AsTEC with Cockcroft), University of Liverpool, BINP-Novosibirsk and the newly formed Irène Joliot-Curie Lab (IJCLab) at Orsay. Four of these international partners have been pioneering the development of ERL technology, the other are leading laboratories on SRF technology and accelerator physics. The Orsay Lab, belonging to CNRS and IN2P3, is leading the effort to develop and host PERLE at the Orsay campus in close collaboration with the LHeC coordination.

The following PERLE summary focuses on the power challenge, the lattice, site and time schedule. PERLE uses a cryo-module with four 5-cell cavities like the LHeC. The prototype cavity production and test as well as the design status of the cryo-module are described in the LHeC linac chapter. Above one also finds a section on the source and injector and as well arc magnets, dipoles of a 3-in-1 design and quadrupoles, which are foreseen to also be used, *mutatis mutandis*, for PERLE.

11.2.1   Configuration

In the final PERLE configuration, a high current electron beam (20 mA) is accelerated through three passes to the maximum energy (500 MeV) in the superconducting RF CW linear accelerator

cryo-cavity units. The 3-passes up in energy do increase the energy spread and emittance while the major part of the beam power remains. The beam is then sent back through the accelerators again only this time roughly 180 degrees off the accelerating RF phase such that the beam is decelerated through the same number of passes and may be sent to a beam dump at the injection energy. Several benefits arise from this configuration: the required RF power (and its capital cost and required electricity) is significantly reduced to that required to establish the cavity field; the beam power that must be dissipated in the dump is reduced by a large factor, and often the electron beam dump energy can be reduced below the photo-neutron threshold so that activation of the dump region can be reduced or eliminated.

11.2.2 Importance of PERLE towards the LHeC

PERLE is an important and necessary step accompanying the LHeC realisation. Together with other ERL facilities, CBETA, hopefully bERLin-Pro and possibly others, it will bridge the gap of power level between the currently reached maximum (CEBAF-ER at 1 MW) and the targeted performances of LHeC (1 GW) by exploring a next higher operational power regime of around 10 MW. Moreover, sharing the same conceptual design with the LHeC, a racetrack configuration with 3 acceleration and 3 deceleration passes, identical injection line and the same SRF system, as well as the same beam current in the SRF cavities will allow to acquire with PERLE an enormous insight on multiple pass operation and common transport from full energy, before and possibly during LHeC operation.

Up to date, existing SRF systems have demonstrated stability at only a modest fraction ($\leq 20\,\%$) of the current envisaged for the LHeC. Though threshold currents have been indirectly measured at higher values, there is no direct evidence that multi-pass systems will be sufficiently resistant to BBU at the higher current, nor has the sensitivity of the instability threshold to linac length, dynamic range, and number of passes been directly or systematically measured as yet. PERLE will provide a single datum on linac length, and can directly measure the dependence on the number of passes and the turn-to-turn transfer matrix.

The dynamic range (which is the ratio of injected/extracted energy to full energy) is a critical design parameter, in as much as it defines the sensitivity of the overall system to magnetic field errors. Errors at full energy drive phase/energy errors that are magnified by adiabatic anti-damping during recovery, can exceed the dump acceptance should the errors be too large. Thus, the field quality needed is inversely proportional to the ratio of full energy to dump energy: that is, a very high energy machine (or one with very low dump energy) needs very high-quality magnets. For PERLE, the dynamic range is 70 : 1 (7 MeV injected and 490 MeV full energy). This implies a need of $\Delta B/B_{dipole} \simeq 0.001\,\%$ field flatness (extrapolated from JLAB ERL needs) to recover cleanly enough. This implies a tight constraint on magnet performances and also affects their cost, even when it is the SRF which drives the overall cost of the facility, for LHeC. PERLE has a very large dynamic range and a transport system with considerable symmetry and flexibility. It is therefore a suitable tool to explore this issue and evaluate the cost implications for larger scale systems.

Existing systems have operated at maximum 1 MW full beam power. This is too low for a precise understanding and control of beam halo. Extrapolation to 10 MW will demand suppression of localised losses to, or below, parts per million. Higher power requires a lower fractional loss. It is not yet well understood how to do this - in particular, collimation systems require a more optimised control of CW losses at rates observed in linacs. PERLE will provide a platform on which the next step in understanding can be taken. Other halo effects may become visible

at only the higher CW powers under consideration in PERLE (including Touschek and intra-beam scattering, beam-gas scattering, and ion trapping). These lead to scattering events that adiabatically anti-damp and result in intolerable loss in the back end of the machine, limiting dynamic range. There is no experience with these phenomena, although theoretical studies suggest they are problematic. PERLE will be the first system capable of directly exploring these issues.

There are many collective effects that have proven challenging at lower beam powers - including RF heating, resistive wall heating, THz emission heating... - that will have greater impact at both higher power and higher energy. There are at present no operating ERL systems that can study these. PERLE is the only system proposed or under construction that combines sufficient beam power with sufficient operational flexibility to study and test mitigation algorithms and methods. Without PERLE, higher energy/power machines will have very little insight regarding these problems and lack the ability to test solutions.

Beam quality preservation in the presence of collective effects is a significant challenge for modern machines. In particular, Longitudinal Space Charge (LCS), Coherent Synchrotron Radiation (CSR), and the micro-bunching instability have serious deleterious impact on performance, and can prevent a machine from producing beam consistent with user requirements - or, worse, from being able to operate at significant powers. PERLE probes the regions of parameter space where these effects are observable, and offers an opportunity to benchmark models and explore mitigation methods.

11.2.3 PERLE Layout and Beam Parameters

The PERLE accelerator complex is arranged in a racetrack configuration hosting two cryo-modules (containing 4 five-cell cavities operating at 801.6 MHz frequency), each located in one of two parallel straights completed with a vertical stack of three recirculating arcs on each side. The straights are 10 m long and the 180° arcs are 5.5 m across. Additional space is taken by 4 m long spreaders/recombiners, including matching sections. As illustrated in Fig. 11.2, the PERLE footprint, excluding shielding and experiments, is: $24 \times 5.5 \times 0.8\,\mathrm{m}^3$, accounting for 40 cm vertical separation between arcs. Each of the two cryo-modules provides up to 82 MeV energy boost per path. Therefore, in three turns, a 492 MeV energy beam is generated. Adding the initial injection energy of 7 MeV yields the total energy of approximately 500 MeV. The main beam parameters of PERLE facility are summarised in Tab. 11.1

Target parameter	Unit	Value
Injection energy	MeV	7
Electron beam energy	MeV	500
Norm. emittance $\gamma\epsilon_{x,y}$	mm·mrad	6
Average beam current	mA	20
Bunch charge	pC	500
Bunch length	mm	3
Bunch spacing	ns	25
RF frequency	MHz	801.6
Duty factor		CW

Table 11.1: Summary of main PERLE beam parameters.

As mentioned in the introduction, the essential PERLE parameters are the same as the LHeC.
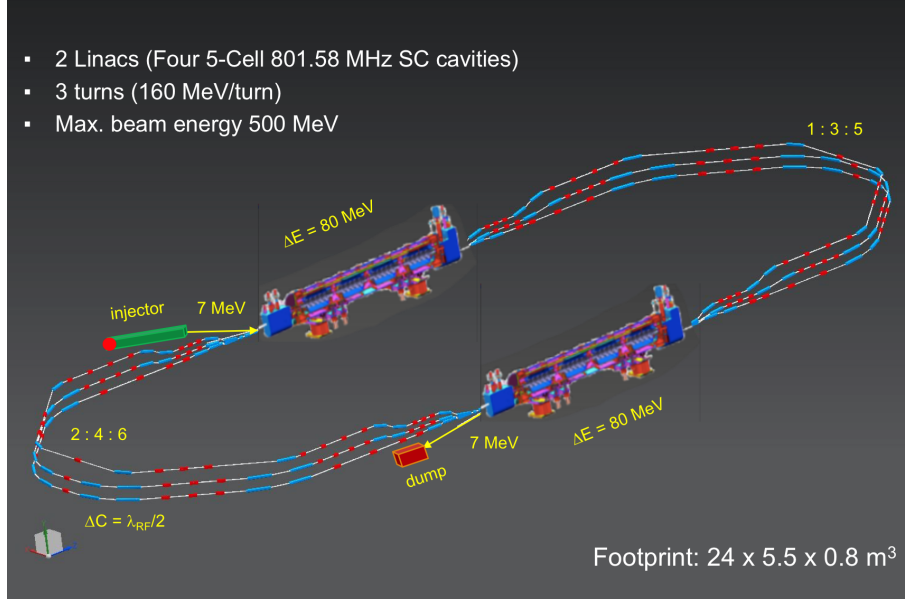
Figure 11.2: PERLE facility layout featuring two parallel linacs each hosting a cryomodule housing 4 five-cell SC cavities, achieving 500 MeV in three passes, see text.

The frequency choice, emittance, beam current and the time structure are chosen regarding the requirements of the electron-proton collisions in the LHeC.

11.2.4 PERLE Lattice

Multi-pass energy recovery in a racetrack topology explicitly requires that both the accelerating and decelerating beams share the individual return arcs (Fig. 11.2). Therefore, the TWISS functions at the linac ends have to be identical, for both the accelerating and decelerating linac passes converging to the same energy and therefore entering the same arc.

Injection at 7 MeV into the first linac is done through a fixed field injection chicane, with its last magnet (closing the chicane) being placed at the beginning of the linac. It closes the orbit bump at the lowest energy, injection pass, but the magnet (physically located in the linac) will deflect the beam on all subsequent linac passes. In order to close the resulting higher pass bumps, the so-called re-injection chicane is instrumented, by placing two additional bends in front of the last chicane magnet. This way, the re-injection chicane magnets are only visible by the higher pass beams. The spreaders are placed directly after each linac to separate beams of different energies and to route them to the corresponding arcs. The recombiners facilitate just the opposite: merging the beams of different energies into the same trajectory before entering the next linac. The current spreader design (Fig. 11.3) consists of a vertical bending magnet, common for all three beams, that initiates the separation. The highest energy, at the bottom, is brought back to the horizontal plane with a chicane. The lower energies are captured with a two-step vertical bending. The vertical dispersion introduced by the first step bends is suppressed by the three quadrupoles located appropriately between the two steps. The lowest energy spreader is configured with three curved bends following the common magnet, because of a large bending angle (45°) the spreader is configured with. This minimises adverse effects of strong edge focusing on dispersion suppression in the spreader. Following the spreader there are four matching quads to bridge the TWISS function between the spreader and the following 180° arc (two betas and two alphas). All six, 180° horizontal arcs are configured with Flexible Momentum Compaction
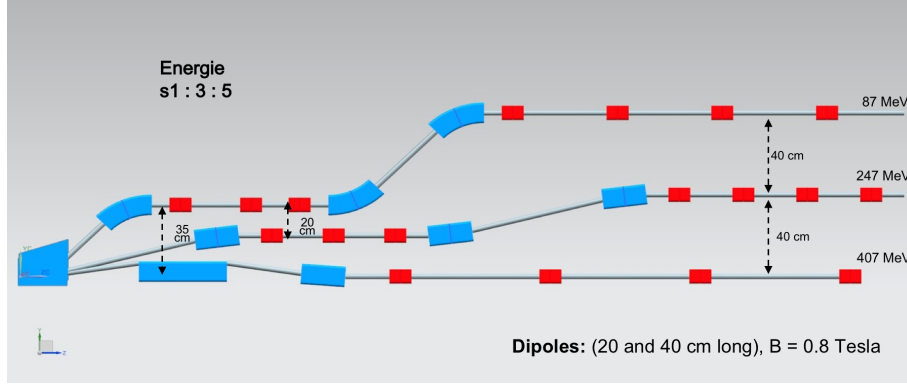
Figure 11.3: PERLE spreader design and matching to three circulating arcs.

(FMC) optics to ease individual adjustment of M56 in each arc (needed for the longitudinal phase-space reshaping, essential for operation with energy recovery). The lower energy arcs (1, 2, 3) are composed of four 45.6 cm long curved 45° bends and of a series of quadrupoles (two triplets and one singlet), while the higher arcs (4, 5, 6) use double length, 91.2 cm long, curved bends. The usage of curved bends is dictated by a large bending angle (45°). If rectangular bends were used, their edge focusing would have caused significant imbalance of focusing, which in turn, would have had adverse effect on the overall arc optics. Another reason for using curved bends is to eliminate the problem of magnet sagitta, which would be especially significant for longer, 91.2 cm, bends. Each arc is followed by a matching section and a recombiner (both mirror symmetric to previously described spreader and matching segments). As required in case of identical linacs, the resulting arc features a mirror symmetric optics (identical betas and sign reversed alphas at the arc ends).

The presented arc optics with modular functionality facilitates momentum compaction management (isochronicity), as well as orthogonal tunability for both beta functions and dispersion. The path-length of each arc is chosen to be an integer number of RF wavelengths except for the highest energy pass, arc 6, whose length is longer by half of the RF wavelength to shift the RF phase from accelerating to decelerating, switching to the energy recovery mode.

11.2.5 The Site

The IJCLab Orsay intends to host PERLE. The footprint of this facility occupies a rectangle of $24 \times 5.5 \, \text{m}^2$. This area should be enclosed by shielding at a sufficient distance to allow passage and maintenance operations. We estimate the required passage and half thickness of the accelerator component to 2 m. A concrete shielding is assumed here to stop photons and neutrons produced by halo electrons. A more detailed study of the radiation generated by the impinging electron will be necessary at a following stage. An increase of the shielding required could be alleviated by the use of denser materials.

The PERLE operation at the design beam parameters (Tab. 11.1) required an in-depth study of the machine failure scenario to estimate the power left in the machine during operation after beam losses and how to handle and control it. The study aimed at looking if the PERLE facility will be classified as INB (Infrastructure Nucleaire de Base) or not, with respect to the French radioprotection and nuclear safety rules. This conclusion is crucial for the decision of hosting PERLE at Orsay as such INB facilities require heavy regulation procedures and a very high investment to fulfil the requirements and ensure the safety provisions to be implemented. The

outcome of the study had concluded that PERLE shall not be considered as INB, even if the beam parameters are quite demanding, because for several failure scenarios the energy of the beam is brought back to the injection energy and safely dumped, in a few tenths of micro seconds thanks to the recovery mode. For other scenarios, hard interlocks and the machine safety system are fast enough to manage the situations. The complete report of this study has been delivered by the IRSD team at Orsay.

Besides the central area required for machine implementation, space needs to be allocated for the auxiliary systems (power converters for magnets, septa and kickers, RF power, Water cooling, Cryogenics, Electron source, Dump). One has also to consider sufficient space for experiments that may use the PERLE beam. These have been sketched in the PERLE CDR [7]. As a rough estimate one would need to triple the area of the accelerator itself to accommodate all services, with shielding included. The building that is foreseen to host this version of PERLE is a former experimental hall (Super ACO). It is equipped with cranes and electricity. The ground of the building is made of concrete slabs with variable ground resistance. More than half of the hall area has a sufficient resistance to allow the installation PERLE. Being next to the tunnel of the old Orsay Linac and close to the *Iglooo*, where new accelerators are being installed currently, the building is partially shielded and some equipment (water-cooling circuits, electrical transformer) can be shared with the other machines. The building gives the possibility to install the RF source and the power supplies at a different level than the accelerator. An existing control room that overlooks the experimental hall may be used for PERLE. Since all the accelerators installed nearby are based on warm technology, a cryogenic plant will be built. All the needed support for infrastructure could be assured by the CPER program. Altogether, this appears to be a well suitable place which has the great advantage to be available.

11.2.6   Building PERLE in Stages

The PERLE realisation starts with a design and prototyping phase that ends with the PERLE TDR. This phase will include the design, the simulations and the test of the main component prototypes allowing to define the technical choices and needs prior to the construction phases. The PERLE configuration (cf. Fig. 11.2) entails the possibility to construct PERLE in subsequent stages. Three phases of construction, commissioning and exploitation are foreseen to achieve the final configuration. Briefly these are characterised as follows:

- **Phase 0**: Installation of the injection line with a beam dump at its end: The injection line includes the DC gun, the load lock photocathode system, solenoids, buncher, booster, merger and required beam instrumentations to qualify the generated beam. The commissioning of the injection line will require the installation of cryogenics, RF power source, power supplies for the optics, photocathode laser, beam dump, control-command, vacuum systems, site shielding, safety control system, fluids, etc. Many of these installations must be already sized according to the final configuration of PERLE.

- **Phase 1**: 250 MeV Version of PERLE, see Fig. 11.4: Installation of a single linac in the first straight and installation of beam pipe and complete return arcs. The switchyards have to be chosen according to the beam energy at each end (energy acceptance ratio: 1:2:3 for the spreader and combiner). This version of the race track is connected to the injection line built in phase 0, via the merger. This particular staging is determined by the existence of the SPL cryomodule at CERN (see the discussion in Chapter 10) which will permit a rather rapid realisation of a 250 MeV machine likely still using the ALICE gun which resides already at IJCLab. This will permit first tests with beam of the various

SRF components, to explore the multi-turn ERL operation and to gain essential operation experience.

- **Phase 2**: 500 MeV version of PERLE: This phase is for the realisation of PERLE at its design parameters, as a 10 MW power machine which requires the nominal electron current, i.e. the upgraded electron gun and the completion of the production of a dedicated further cryomodule. Also, a second spreader and recombiner at the required acceptance ratio need to be installed on both sides of the second cryomodule.

The PERLE collaboration is currently developing a detailed time schedule for the project at its different phases, which depends on the suitability to use the SPL cryomodule adapted for PERLE and the availability of further essential components. In relation to the LHeC it may be noticed that PERLE offers to gain the experience one would have to gain with LHeC, years before it starts. LHeC cannot begin before early thirties while PERLE will operate in the twenties.
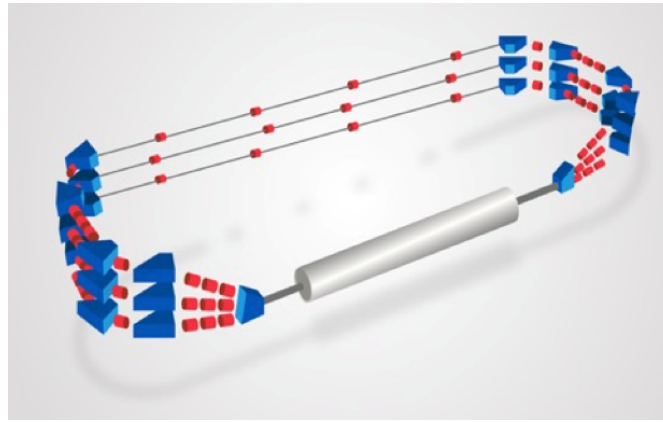
Figure 11.4: PERLE-Phase 1 layout featuring a single Linac in the first straight and beam line in the second straight, achieving 250 MeV in three passes.

11.2.7 Concluding Remark

Currently the focus of the planning for PERLE is on the development of ERL as a means for high power, large energy accelerator design, technology and realisation. PERLE has a considerable potential for low energy particle and nuclear physics too. Its intensity is orders of magnitude higher than that of ELI. This opens a huge field of physics and industrial applications for a user facility once the machine has been understood and operates close to its design in a reliable manner. With recent increased interest in energy recovery technology applications at LHeC, but also FCC and EIC, PERLE may become an important cornerstone for future high energy and nuclear physics. The re-use of power is a *per se* green technology which is an example as to how science may react to the low power requirements of our time.

Chapter 12

Experimentation at the LHeC

12.1 Introduction

The LHeC Conceptual Design Report [1] contained a very detailed description of a core detector concept for the LHeC. At the time of writing, the target luminosity was of order $10^{33}\,\mathrm{cm^{-2}s^{-1}}$ and, whilst evidence was building, the Higgs boson had yet to be discovered. A detector design based on established technologies either in use by the LHC General Purpose Detectors, ATLAS and CMS, or being developed for their upgrades was found to be adequate to realise the physics priorities of the project at the time and could comply with the *ep* machine constraints at an affordable cost, provided the angular acceptance was sufficient (nominally to within $1°$ of the beamline). A salient feature of experimentation at the LHeC, as compared to the LHC, is the complete absence of pile-up which can be estimated [1] to be around 0.1 in *ep* at the LHeC as compared to $\simeq 150$ in *pp* at HL-LHC. Similarly, there is a reduced level of radiation in *ep*, by orders of magnitude lower than in *pp*, which enables to also consider novel technologies that are less radiation hard than conventional ones, with HV CMOS Silicon detectors as an example.

This chapter provides a short overview of a partially revised LHeC detector design, with more detail on those aspects which have developed significantly since the 2012 version (notably the central tracking). To a large extent, the considerations in the CDR are still valid and are taken forward here. However, this update also profits from the evolution of the design in the subsequent years, the updated and long term physics priorities with the higher achievable luminosities. It also introduces new technologies where they are becoming available. In more detail, the major considerations which motivate an update of the detector with respect to the 2012 baseline are:

- The increased luminosity and the confirmation of a Higgs boson discovery at a mass of around $125\,\mathrm{GeV}$ opens the opportunity for the LHeC to provide a set of precision measurements of the Higgs properties, in particular, percent-level measurements of several of its couplings. The possibility of obtaining world-leading measurements of couplings

---

[1] The pile-up is given as the number of events per bunch crossing, which is obtained from the instantaneous luminosity, $L = 10^{34}\,\mathrm{cm^{-2}s^{-1}}$, the total cross section, $\sigma_{tot} \simeq \sigma(\gamma p)\cdot\Phi_\gamma$, and the bunch distance of 25 ns. The total photo-production cross section, with a minimum $Q^2 = (M_e\cdot y)^2/(1-y)$, is estimated as 220 (260) μb at the LHeC (FCC-he) using the parameterisation given in Ref. [890]. Here y is the inelasticity variable and M_e the electron mass. The photon flux factor in the Weizsäcker-Williams approximation is calculated as $\Phi_\gamma = 1.03$ (1.25) for $W = \sqrt{ys} > 1\,\mathrm{GeV}$. The hadronic final state at very small scattering angles, $\theta_h \leq 0.7°$ or $|\eta| \geq 5$, is not reaching the central detector acceptance such that at the LHeC W_{min} would be larger, about $10\,\mathrm{GeV}$, which reduces the flux to about 0.6. A conservative estimate is to use $W > 1\,\mathrm{GeV}$. This translates to an estimated pile-up of 0.06 at the LHeC and 0.09 at the FCC-eh which favourably compares with an estimated pile-up of 150 at HL-LHC.

to beauty and charm place a heavy emphasis on the inner tracking and vertexing. The tracking region has therefore been extended radially with an also increased segmentation. The requirement to maximise the acceptance for Higgs decays places an even heavier requirement on angular coverage than was the case in 2012, with forward tracking and vertexing being of particular importance.

- The fast development of detector technologies and related infrastructure in some areas necessitates a fresh look at the optimum choices. Most notably, silicon detector technologies have advanced rapidly in response to both commercial and particle physics requirements. The low material budget, potential high granularity, and cost-effectiveness offered by monolithic active pixel sensor (MAPS) solutions such as HV-CMOS are particularly attractive and can reasonably be assumed to be in wide use in future particle physics collider detector contexts.

- The long term, high energy hadron collider physics program, including FCC and possibilities in Asia, as well as the ultimate use of the LHC for two more decades, require the precise, independent, and comprehensive measurements to determine PDFs, over a wider range of x and Q^2 than has previously been possible. The implication for the LHeC is a need to further improve and extend the detector acceptance and overall performance.

- Options in which the ep centre-of-mass energy is increased, at HE LHC or FCC-eh, require a further reinforcement of the detector design in the forward (outgoing proton) direction, increasing the overall size of the detector. In particular, the calorimeter depth scales logarithmically with E_p so as to fully contain particles from very high energy forward-going hadronic showers and to allow for precise measurements of actual and missing energy. Using such scaling considerations, the LHeC design has been applied also to the post LHC hadron beam configurations.

The design described in the following addresses the points above. The updated detector requirements point in the tracking region to the need for higher spatial resolution, improved precision in momentum measurements and enhanced primary and secondary vertexing capabilities. The most significant change compared with 2012 is therefore a more ambitious tracking detector design. The detector must also provide accurate measurements of hadronic jets and missing transverse energy, as well as isolated electrons and photons. As an option compared to the CDR, the liquid argon (LAr) choice for the main electromagnetic barrel calorimeter sampling material is here changed to a scintillator-based solution. Both options are subsequently compared, and as expected the long term stability and resolution performance favour a LAr calorimeter while the modularity and installation aspects are easier solved with a warm crystal calorimeter.

Both the overall event kinematics (much larger proton than electron beam energy) and the specific acceptance requirements for the key Higgs production process imply an asymmetric design with enhanced hadronic final state detection capabilities in the forward direction where the deposited hadronic and electromagnetic energies are much higher than in the backward (the electron beam) direction, see Fig. 3.2 in Sect. 3.2.

A dipole magnet bends the electron beam into head-on collision with the colliding proton beam and after the interaction point a further dipole with opposite polarity separates the orbits of the electron and proton beam. These weak bending dipoles are placed outside of the tracker and electromagnetic calorimeter regions. The total length is $10\,\mathrm{m}$ or $2/3L*$ as explained in the IR section. The resulting synchrotron radiation fan has to be given free space and the beam pipe geometry is designed specifically to accommodate it. The residual synchrotron radiation background poses a constraint to the inner detector components.

The 2012 and 2020 versions of the LHeC detector design are both realisable in terms of technology readiness. It has been a goal of this conceptual design to study the feasibility, performance and integration of the detector, which will eventually be designed by a future ep/eA experiment collaboration. The two designs, albeit being still similar, can be considered as two example solutions to the LHeC requirements with differences in where the emphasis is placed in terms of performance and cost. The current design is performed using the DD4hep [891] software framework.

12.2 Overview of Main Detector Elements

A side projection overview of the current detector design is shown in Fig. 12.1, illustrating the main detector components. The overall size remains compact by recent standards, with overall dimensions of approximately $13\,\mathrm{m}$ in length and $9\,\mathrm{m}$ in diameter, small compared with ATLAS ($45 \times 25\,\mathrm{m}^2$) and even CMS ($21 \times 15\,\mathrm{m}^2$). The inner silicon tracker contains a central barrel component ('Tracker'), with additional disks in the forward and backward directions ('Tracker Fwd' and 'Tracker Bwd', respectively). It is surrounded at larger radii by the Electromagnetic Barrel ('EMC-Barrel') and in the forward and backward directions by the electromagnetic forward and backward plug calorimeters ('FEC-Plug-Fwd' and 'BEC-Plug-Bwd', respectively). The solenoid magnet is placed at radii immediately outside the EMC-Barrel, and is housed in a cryostat, which it shares with the weak dipole magnet that ensures head-on collisions. It is the dipole and cost considerations which suggest to place the solenoid there instead of surrounding the HCAL which in terms of performance surely would have been preferable.

The Hadronic-Barrel calorimeter (HCAL-Barrel) is located at radii beyond the solenoid and dipole, whilst the forward and backward hadronic plug detectors (FHC-Plug-Fwd and BHC-Plug-Bwd, respectively) lie beyond their electromagnetic counterparts in the longitudinal coordinate. The Muon Detector forms a near-hermetic envelope around all other parts of the main detector. It uses similar technologies to those employed by ATLAS, at much smaller surface, see below.

A magnified view of the inner part of the detector, including the magnet elements, is shown in Fig. 12.2. The solenoid and steering dipoles enclose the electromagnetic calorimeters and the tracker setup completely, the steering dipoles extending over the full $10\,\mathrm{m}$ length of the inner detector and forward and backward plugs. If liquid argon is chosen for the sensitive material in the EMC as in the 2012 design, the EMC will be mounted inside the cryostat, alongside the solenoid and dipoles. The hadronic calorimeter components remain outside the cryostat and magnet elements in all circumstances.

Exploiting the current state of the art, the beam pipe is constructed of berylium of 2.5–3 mm thickness. As in the 2012 CDR, the beam pipe has an asymmetric shape in order to accommodate the synchrotron radiation fan from the dipole magnets. It is thus $2.2\,\mathrm{cm}$ distant from the interaction region, comparable to the HL-LHC beam pipes of the GPDs, except in the direction of the synchrotron fan, where it is increased to $10.0\,\mathrm{cm}$, giving rise to an overall circular-elliptical profile (illustration of the profile at IP in Fig. 12.3). The beam pipe shape has implications for the design of the inner detector components, as illustrated in Fig. 12.4. The first layer of the barrel tracker follows the circular-elliptical beam pipe shape as closely as possible, with the profiles of subsequent layers reverting to a circular geometry.

Figure 12.1: Side view of the updated baseline LHeC detector concept, providing an overview of the main detector components and their locations. The detector dimensions are about 13 m length and 9 m diameter. The central detector is complemented with forward (p, n) and backward (e, γ) spectrometers mainly for diffractive physics and for photo-production and luminosity measurements, respectively. See text for details.

Figure 12.2: Side projection of the central part of the LHeC detector, illustrating also the solenoid and electron-beam-steering dipoles. See text for further details.

12.3 Inner Tracking

12.3.1 Overview and Performance

A schematic view of the updated tracking region is shown in Fig. 12.5. The layouts in the central, forward and backward directions have been separately optimised using the tkLayout performance estimation tool for silicon trackers [893]. The result is seven concentric barrel layers with the innermost layer approximately 3 cm from the beam line at its closest distance and with approximately equal radial spacing thereafter. The tracker barrel is supplemented by seven forward wheels and five backward wheels of which three in each direction comprise the central tracker end-cap and, respectively, four and two, respectively, are mounted beyond the central tracker enclosure.

317
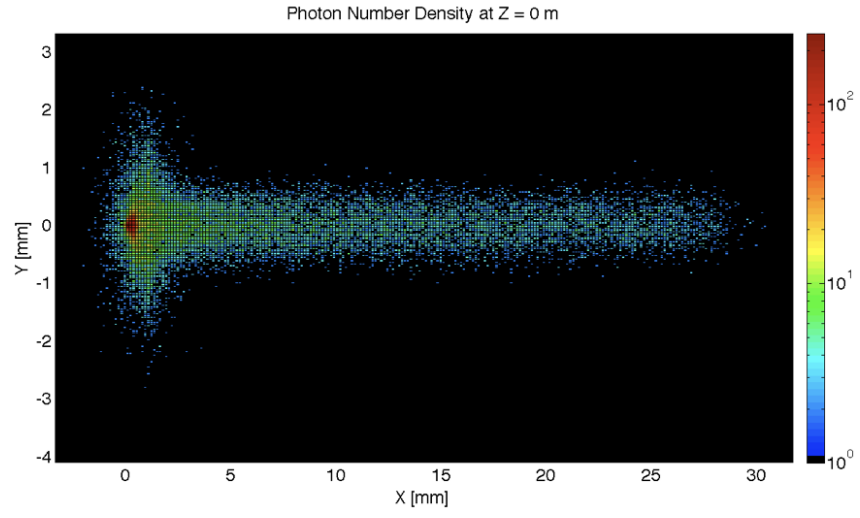
Figure 12.3: The simulation of synchrotron radiation profile at the IP using GEANT4 [1, 892].
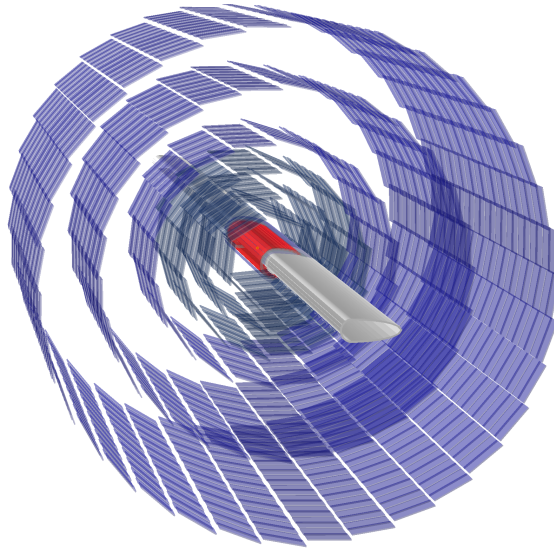
Figure 12.4: End-on view of the arrangement of the inner barrel tracker layers around the beam pipe.

For reasons described in Sect. 12.3.2, HV-CMOS MAPS sensors can be employed, restricting material associated with the pixel sensors to just 0.1 mm per layer. The strip detector sensors have a larger thickness of 0.2 mm. The preferred active silicon solutions vary with radial distance from the interaction point, so as to provide the highest spatial resolution in the layers closest to the the interaction point. The barrel is formed from one layer of pixel-wafers, with three layers of macro-pixels between 10 cm and 30 cm radius and a further three layers of strip-sensors beyond 30 cm. The end-cap wheels and the forward tracker also contain combinations of the three types of sensor, whilst the backward tracker consists of macro-pixels and strips only.
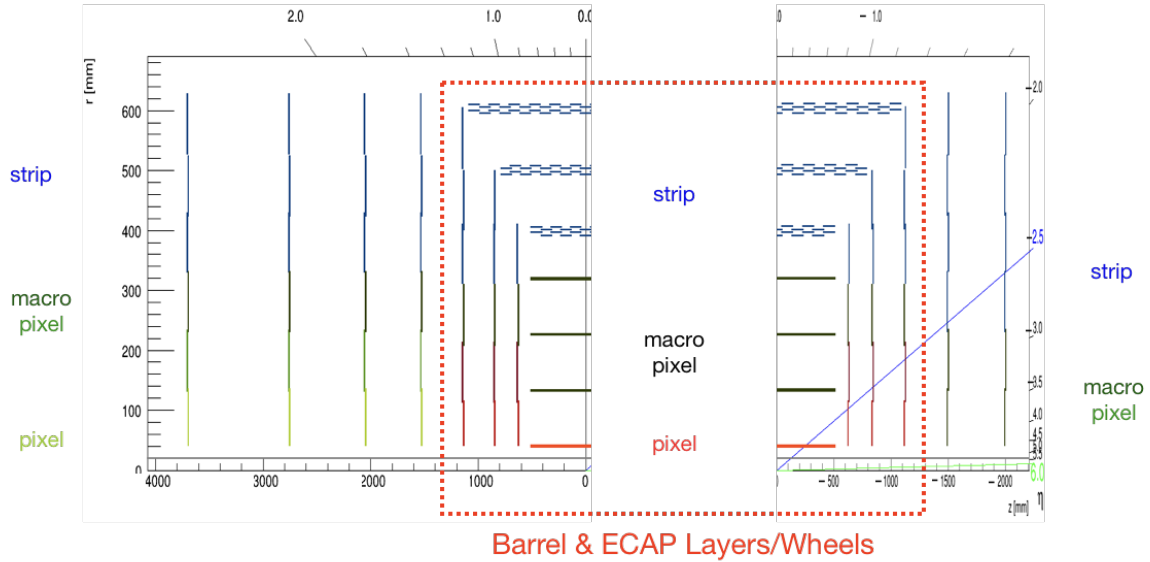
Figure 12.5: Schematic side-view of the tracker, subdivided into forward and backward parts and including disks as well as barrel components. The layers/wheels forming the barrel part are enclosed by the red-dotted box. The innermost pixel layers are coloured red, the macro-pixel layers are shown in black and the strip detectors in blue. For the forward and backward wheels, possibly formed with separate rings, (outside the dashed red box), the pixels, macro-pixels and strip detectors are shown in light green, dark green and blue, respectively.

Tabs. 12.1 and 12.2 summarise the overall basic properties of the tracker modules, including total numbers of channels and total area of silicon coverage, as well as spatial resolutions and material budgets. The inner barrel has a pseudorapidity coverage $|\eta| < 3.3$ for hits in at least one layer, increasing to $|\eta| < 4.1$ when the endcaps are also taken into account. The additional disks beyond the central tracker enclosure extend the coverage to $\eta = 5.3$ and $\eta = -4.6$ in the forward and backward directions, respectively. Fig. 12.6 illustrates the coverage in more detail, displaying the numbers of layers that provide acceptance as a function of pseudorapidity in both the forward and backward directions, also broken down into different sensor types. Charged particles are sampled in between 5 and 8 layers throughout the entire range $-3.5 < \eta < 4$, with sampling in at least two layers provided for $-4.2 < \eta < 5$.

Spatial resolutions in the $r - \phi$ plane, driven by the sensor pitches, reach 7.5 μm for the pixel layers. The resolutions are propagated using tkLayout to produce simulated charged particle transverse momentum resolutions, as shown in Fig. 12.7. Both active and passive material contributions are included, with a 2.5 mm Be beam pipe thickness. An excellent resolution $(\delta p_T/p_T)$ at the level of $1-2\%$ is achieved over a wide range of pseudorapidity and momentum. The precision degrades slowly in the forward direction, remaining at the sub 10 % level up to very forward pseudorapidities $\eta \sim 4.5$. Central tracks with transverse momenta up to 1 TeV are

319

Tracker (LHeC)		Inner Barrel			ECAP		
		pix	pix$_{\mathrm{macro}}$	strip	pix	pix$_{\mathrm{macro}}$	strip
$\eta_{\max},\eta_{\min}$		3.3, −3.3	2.1, −2.1	1.4, −1.4	±[4.1, 1.8]	±[2.4, 1.5]	±[2.0, 0.9]
Layers (Barrel)		1	3	3			
Wheels (ECAP)					2	1	1-3
Modules/Sensors		320	4420	3352	192	192	552
Total Si area	[m^2]	0.3	4.6	17.6	0.8	5.6	3.3
Read-out-Channels	[10^6]	224.5	1738	20.6	322.4	73.3	17.0
pitch$^{r-\phi}$	[μm]	25	100	100	25	100	100
pitch^z	[μm]	50	400	50k [2]	50	400	10k [1]
Average X_0/Λ_I	[%]	7.2 / 2.2			2.2 / 0.7		

[1] Reaching pitch$^{r-\phi}$ when using two wafer layers rotated by 20 mrad is achievable.

Table 12.1: Summary of the main properties of the Barrel and Endcap tracker modules based on calculations performed using tkLayout [893]. For each module, the rows correspond to the pseudorapidity coverage, numbers of barrel and disk layers, numbers of sensors, total area covered by silicon sensors, numbers of readout channels, the hardware pitches affecting the $(r-\phi)$ and the z resolution, respectively, and the average material budget in terms of radiation lengths and interaction lengths. Where appropriate, the numbers are broken down into separate contributions from pixels, macro-pixels and strips. See Tab. 12.2 for a sum of all tracker components.

Tracker (LHeC)		Fwd Tracker			Bwd Tracker		Total
		pix	pix$_{\mathrm{macro}}$	strip	pix$_{\mathrm{macro}}$	strip	(incl. Tab. 12.1)
$\eta_{\max},\eta_{\min}$		5.3,2.6	3.5,2.2	3.1,1.6	−4.6, −2.5	−2.9, −1.6	5.3, −4.6
Wheels		2	1	3	2	4	
Modules/Sensors		180	180	860	72	416	10736
Total Si area	[m^2]	0.8	0.9	4.6	0.4	1.8	40.7
Read-out-Channels	[10^6]	404.9	68.9	26.4	27.6	10.6	2934.2
pitch$^{r-\phi}$	[μm]	25	100	100	100	100	
pitch^z	[μm]	50	400	50k [2]	400	10k [1]	
Average X_0/Λ_I	[%]	6.7 / 2.1			6.1 / 1.9		
incl. beam pipe	[%]						40 / 25

[1] Reaching pitch$^{r-\phi}$ when using two wafer layers rotated by 20 mrad is achievable.

Table 12.2: Summary of the main properties of the forward and backward tracker modules in the revised LHeC detector configuration based on calculations performed using tkLayout [893]. For each module, the rows correspond to the pseudorapidity coverage, numbers of disk layers, numbers of sensors, total area covered by silicon sensors, numbers of readout channels, the hardware pitches affecting the $(r-\phi)$ and the z resolution, respectively, and the average material budget in terms of radiation lengths and interaction lengths. The polar angle dependence and decomposition of X_0 and Λ_I are shown in Fig. 12.9. Where appropriate, the numbers are broken down into separate contributions from pixels, macro-pixels and strips. The column *Total* contains the sum of corresponding values in tables 12.1 and 12.2.
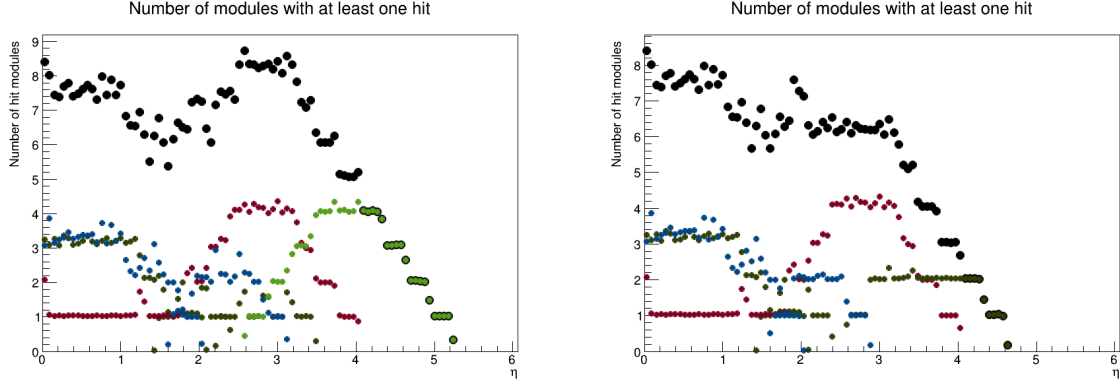
Figure 12.6: Numbers of silicon layers that provide acceptance for charged particles as a function of absolute value of pseudorapidity in the forward (left) and backward (right) directions, summed across the central, forward and backward trackers. The distributions are broken down according to sensor type, with colour coding of red for pixels, light or dark green for macro-pixels, blue for strips and black for the sum.

measured with $10-20\%$ precision. Similar results are achieved in the (negative η) backward direction (not shown).

A major requirement of the tracking detectors will be the precise determination of vertex coordinates and track impact parameters relative to the primary vertex in order to give the best possible sensitivity to secondary vertices from heavy flavour decays, for example for the study of the Higgs in its dominant $b\bar{b}$ decay mode. The simulated results for longitudinal and transverse track impact parameter resolutions using the full new tracking layout are shown in Fig. 12.8. The transverse spatial resolutions are at the level of $10-50\,\mu$m over a wide range of transverse momentum and pseudorapidity, extending well into the forward direction.

The material budget contributions from the sensors summed across all layers are given in Tabs. 12.1 and This is largest for the inner barrel, where it amounts to 7.2% of a radiation length. The sensors in the central tracker endcap and the forward and backward tracking rings contribute 2.2%, 6.7% and 6.1% of a radiation length, respectively. The material budget simulations, propagated for the full system and including passive contributions, are shown in Fig. 12.9. The use of thin sensors keeps the total material to the level of $0.2-0.4X_0$ throughout the entire tracking region up to $\eta \sim 4.5$. At the most forward (and backward) pseudorapidities, particles travel through a large effective thickness of material as they pass through the beam pipe; this becomes the dominant contribution for $\eta > 3.5$.

12.3.2 Silicon Technology Choice

Being developed for several High Luminosity-LHC (HL-LHC) upgrades and the proposed CLIC high-energy linear collider we envisage depleted CMOS sensor technology, also known as Depleted Monolithic Active Pixel Sensors (DMAPS), to be used as position sensitive detectors in industry standard CMOS processes or High Voltage-CMOS (HV-CMOS) processes [894]. These sensors are extremely attractive for experiments in particle physics as they integrate the sensing element and the readout ASIC in a single layer of silicon, which removes the need for interconnection with complex and expensive solder bump technology. Depleted CMOS sensors also benefit from faster turnaround times and lower production costs when compared to hybrid silicon sensors. To achieve fast charge collection and high radiation tolerance, DMAPS can be
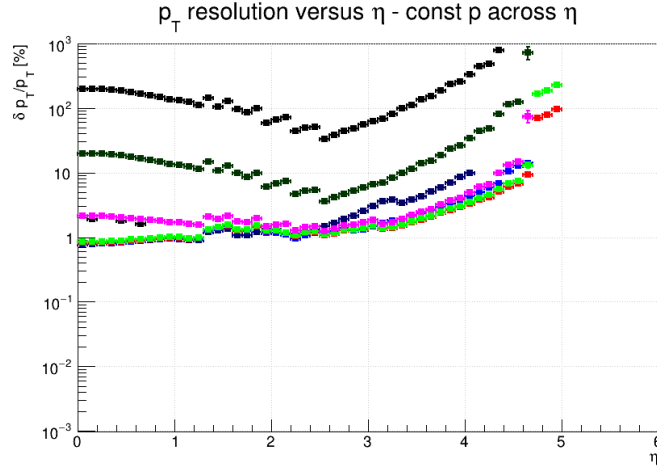
Figure 12.7: Simulated transverse momentum track resolution using all modules in the revised LHeC tracking system. Results are shown in terms of fractional p_T resolution as a function of pseudorapidity for several constant momenta, $p = 100\,\text{MeV}$ (Black, bottom, obscured), $1\,\text{GeV}$ (Dark Blue, obscured), $2\,\text{GeV}$ (Light Blue, obscured), $5\,\text{GeV}$ (Red), $10\,\text{GeV}$ (Light Green), $100\,\text{GeV}$ (Magenta), $1\,\text{TeV}$ (Dark Green) and $10\,\text{TeV}$ (Black, top).

implemented following two different approaches known as low fill-factor and large fill-factor. Low fill-factor DMAPS benefit from High Resistivity (HR) substrates and thick epitaxial layers accessible from large-scale CMOS imaging processes, while large fill-factor DMAPS exploit the High Voltage (HV) option developed by commercial CMOS foundries for power electronics. Recently, HR wafers have become available in the production line of foundries that manufacture HV-CMOS processes, thus DMAPS in HR/HV-CMOS are also possible to further improve the performance of the sensor. Today's most performant DMAPS detectors are 50μm thin and have 50μm x 50μm cell size with integrated mixed analogue and digital readout electronics, $6ns$ time resolution and $2\text{x}10^{15} 1\text{MeV}$ neq/cm^2 radiation tolerance. The typical cross-section of a large fill-factor DMAPS in a HV-CMOS process is shown in Fig. 12.10.

DMAPS in HR/HV-CMOS have been adopted as a world first as the sensor technology of choice for the **Mu3e** experiment at the Paul Scherrer Institute (PSI) in Switzerland [895]. MuPix, the DMAPS detector for Mu3e, implements active pixels that amplify the collected charge in the collecting electrode and peripheral readout electronics that discriminate and process the amplified signals. MuPix10, the first reticle size detector for Mu3e ($\simeq 2 \times 2\,\text{cm}^2$) and currently in production, features 250×256 pixels with an $80 \times 80\mu\text{m}^2$ pixel size, 11-bit time-stamp, 6-bit Time-over-Threshold (ToT) and continuous readout. Its peripheral readout electronics include readout buffers, a state machine, a Phase Locked Loop (PLL) and Voltage-Controlled Oscillator (VCO), 8/10-bit encoders and 3 serialisers for data transmission with a rate of up to 1.6 Gbit/s. Previous MuPix prototypes have been thinned to $50\,\mu$m successfully and tested to achieve a 6 ns time resolution after time-walk correction [896]. ATLASPix, the DMAPS development in HR/HV-CMOS that was originally aimed at providing an alternative sensor technology for the outermost pixel layer of the new ATLAS Inner Tracker (ITk) upgrade, has been tested to have an approximate 150 mW/cm^2 power consumption and be radiation tolerant up to $2 \cdot 10^{15}$ 1 MeV neq/cm^2 fluences [897] DMAPS in HR-CMOS, such as the MALTA development originally aimed at the new ATLAS ITk upgrade as well, have achieved full efficiency after $1 \cdot 10^{15}$ 1 MeV neq/cm^2 fluences [898]. However, further research is still needed to demonstrate reticle size DMAPS in HR-CMOS. Research to further develop DMAPS to meet the extreme requirements of future experiments in particle physics is on-going.
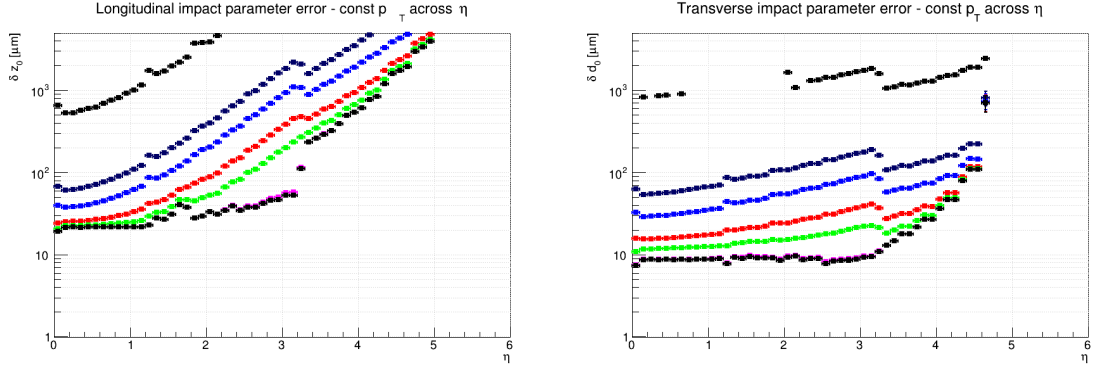
Figure 12.8: Simulated longitudinal (left) and transverse (right) impact parameter resolutions using all modules in the revised LHeC tracking system. Results are shown as a function of pseudorapidity for several constant momenta, $p = 100$ MeV (Black, top), 1 GeV (Dark Blue), 2 GeV (Light Blue), 5 GeV (Red), 10 GeV (Light Green), 100 GeV (Magenta, obscureed), 1 TeV (Dark Green, obscured) and 10 TeV (Black, bottom).
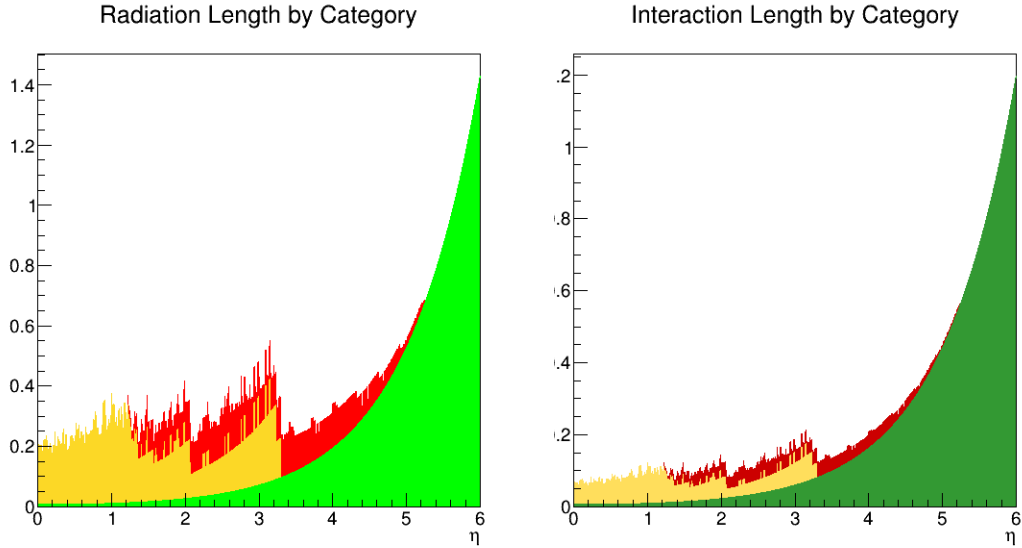

Figure 12.9: Material contributions from the tracking modules as a function of pseudorapidity. Results are given in terms of radiation lengths (left) and hadronic interaction lengths (right). The results are broken down into contributions from barrel modules (yellow) and endcap / additional disk modules (red) and are compared with the contribution from the 2.5 mm beam pipe (green).

323
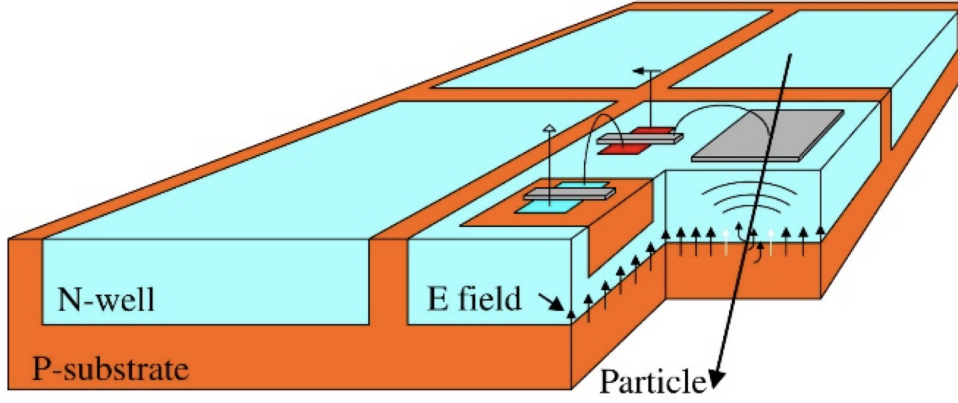
Figure 12.10: Typical sensor cross-section of a DMAPS detector in a HV-CMOS process [894].

The here presented tracker design of the LHeC utilises pixel detectors for high resolution tracking in the inner barrel and as well the barrel endcaps and the forward tracker. The number of readout channels is close to 10^9, with a high transverse and longitudinal segmentation provided by a pitch of $25 \times 50\,\mu m^2$. One can expect that such a fine segmentation is in reach for a detector which would be built in a decade hence. The radiation level in electron-proton scattering is by orders of magnitude lower than in proton-proton interactions at the LHC and is indeed in a range of $10^15\,\text{MeV}$ n_{eq}/cm^2 for which radiation hardness has been proven as indicated above. The monolithic CMOS detector technology leads to a significant simplification of the production of these detectors and a considerably reduced cost. We thus conclude that the LHeC pixel tracker represents a particularly suitable device for a large scale implementation of HV CMOS Silicon in a forthcoming collider detector.

12.4 Calorimetry

The 2012 CDR detector design leaned on technologies employed by ATLAS for calorimetry in the barrel region, adopting a lead / liquid argon sampling electromagnetic calorimeter with an accordion geometry and a steel / scintillating tile sampling hadronic component. For the version of the LHeC detector described here, an alternative solution of a lead / scintillator electromagnetic calorimeter has been investigated. This has the advantage of removing the need for cryogenics, whilst maintaining an acceptable performance level. Comparing the lead-scintintillator designs for the electromagnetic barrel calorimeter for the 2012 CDR with the updated setup, the **a**-term for shower fluctuations and transverse leakages and the **b**-term describing the back-leakages of the calorimeter the resolution performance of the updated design is better (**a**= 20% and **b**= 0.14% in the 2012 CDR and **a**= 12.4% and **b**= 1.9% in the new design). Although it is not discussed here, the liquid argon solution very much remains the favorable option due to its high level of performance and stability / radiation hardness. The fit-results in CDR 2012 the LAr calorimeter option show a slightly better resolution performance than the lead-scintillator variant. Due to the accordion shaped absorber it forces more energy deposit in the calorimeter volume. The CDR values for comparison: **a**= 8.47% and **b**= 0.318%. The hadronic calorimeter retains the steel and scintillating tile design, similar to ATLAS. As in the 2012 CDR, plug sampling calorimeters are also incorporated at large $|\eta|$, the forward and backward components using tungsten and lead absorber material, respectively, with both using silicon based sensitive readout layers. The steel structures in the central and plug calorimetry close the outer field of the central solenoid. The solenoid and the dipoles are placed between the Electromagnetic-
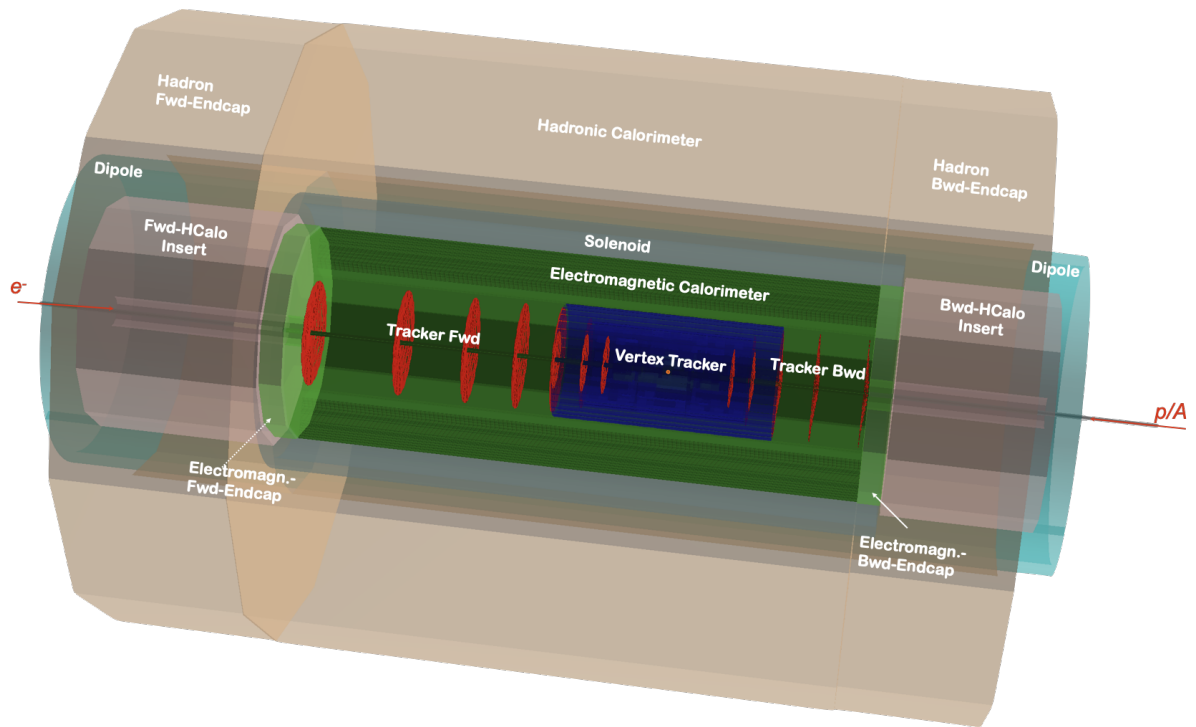
Figure 12.11: Three-dimensional view of the arrangement of Hadronic-Calorimeter, experimental magnets (solenoid and dipoles), the electromagnetic calorimeter and tracking detector layers.
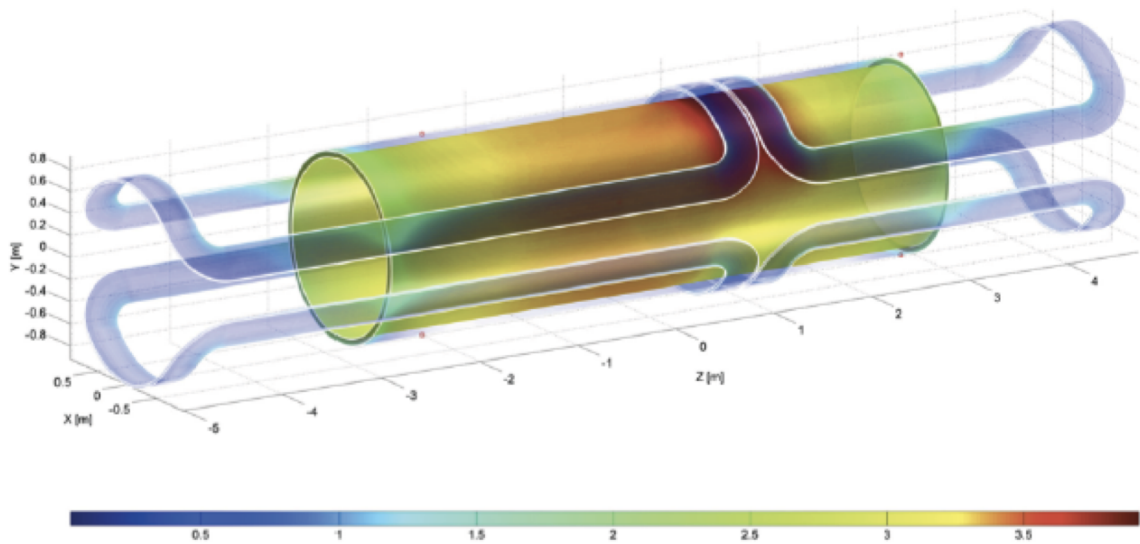

Figure 12.12: The coil arrangement of the solenoid and dipoles system housing in a common cryostat.

Barrel and the Hadronic-Calorimeter. The HCAL-Barrel sampling calorimeter using steel and scintillating tiles as absorber and active material, respectively, provides the mechanical stability for the Magnet/Dipole cryostat and the tracking system Fig. 12.11. How the solenoid/dipoles-system would look like has been discussed in more detail in [1] and is illustrated by Fig. 12.12. (and the LAr cryostat in a cold EMC version) along with the iron required for the return flux of the solenoidal field. The main features of the new calorimeter layout are summarised in Tab. 12.3 and 12.4. The pseudorapidity coverage of the electromagnetic barrel is $-1.4 < \eta < 2.4$, whilst the hadronic barrel and its end cap cover $-1.5 < \eta < 1.9$. Also including the forward and backward plug modules, the total coverage is very close to hermetic, spanning $-5.0 < \eta < 5.5$. The total depth of the electromagnetic section is 30 radiation lengths in the barrel and backward regions, increasing to almost $50 X_0$ in the forward direction where particle and energy densities are highest. The hadronic calorimeter has a depth of between 7.1 and 9.6 interaction lengths, with the largest values in the forward plug region.

Calo (LHeC)		EMC	HCAL		
		Barrel	Ecap Fwd	Barrel	Ecap Bwd
Readout, Absorber		Sci,Pb	Sci,Fe	Sci,Fe	Sci,Fe
Layers		38	58	45	50
Integral Absorber Thickness [cm]		16.7	134.0	119.0	115.5
$\eta_{\max}$, $\eta_{\min}$		2.4, −1.9	1.9, 1.0	1.6, −1.1	−1.5, −0.6
$\sigma_E/E = a/\sqrt{E} \oplus b$	[%]	12.4/1.9	46.5/3.8	48.23/5.6	51.7/4.3
Λ_I / X_0		$X_0 = 30.2$	$\Lambda_I = 8.2$	$\Lambda_I = 8.3$	$\Lambda_I = 7.1$
Total area Sci	[m^2]	1174	1403	3853	1209

Table 12.3: Basic properties and simulated resolutions of barrel calorimeter modules in the new LHeC detector configuration. For each of the modules, the rows indicate the absorber and sensitive materials, the number of layers and total absorber thickness, the pseudorapidity coverage, the contributions to the simulated resolution from the sampling (a) and material (b) terms in the form a/b, the depth in terms or radiation or interaction lengths and the total area covered by the sensitive material. GEANT4 [892] simulation based fits using crystal ball function [899–901].

Calo (LHeC)		FHC Plug Fwd	FEC Plug Fwd	BEC Plug Bwd	BHC Plug Bwd
Readout, Absorber		Si,W	Si,W	Si,Pb	Si,Cu
Layers		300	49	49	165
Integral Absorber Thickness [cm]		156.0	17.0	17.1	137.5
$\eta_{\max}$, $\eta_{\min}$		5.5, 1.9	5.1, 2.0	−1.4, −4.5	−1.4, −5.0
$\sigma_E/E = a/\sqrt{E} \oplus b$	[%]	51.8/5.4	17.8/1.4	14.4/2.8	49.5/7.9
Λ_I / X_0		$\Lambda_I = 9.6$	$X_0 = 48.8$	$X_0 = 30.9$	$\Lambda_I = 9.2$
Total area Si	[m^2]	1354	187	187	745

Table 12.4: Basic properties and simulated resolutions of forward and backward plug calorimeter modules in the new LHeC detector configuration. For each of the modules, the rows indicate the absorber and sensitive materials, the number of layers and total absorber thickness, the pseudorapidity coverage, the contributions to the simulated resolution from the sampling (a) and material (b) terms in the form a/b, the depth in terms or radiation or interaction lengths and the total area covered by the sensitive material. GEANT4 [892] simulation based fits using crystal ball function [899–901].

The performance of the new calorimeter layout has been simulated by evaluating the mean simulated response to electromagnetic (electron) and hadronic (pion) objects with various specific energies using GEANT4 [892] and interpreting the results as a function of energy in terms of sampling (a) and material / leakage (b) terms in the usual form $\sigma_E/E = a/\sqrt{E} \oplus b$. Example

results from fits are shown for the barrel electromagnetic and hadronic calorimeters in Fig. 12.13 and for the forward plug electromagnetic and hadronic calorimeters in Fig. 12.14. The results for the a and b parameters are summarised in Tabs. 12.3 and 12.4. The response of the barrel electromagnetic calorimeter to electrons in terms of both sampling ($a = 12.4\%$) and material ($b = 1.9\%$) terms is only slightly worse than that achieved with liquid argon sampling in the 2012 CDR. The resolutions of the forward and backward electromagnetic plug calorimeters are comparable to those achieved in the 2012 design. A similar pattern holds for the hadronic response, with sampling terms at the sub-50 % level and material terms of typically 5 % throughout the barrel end-caps and forward and backward plugs.
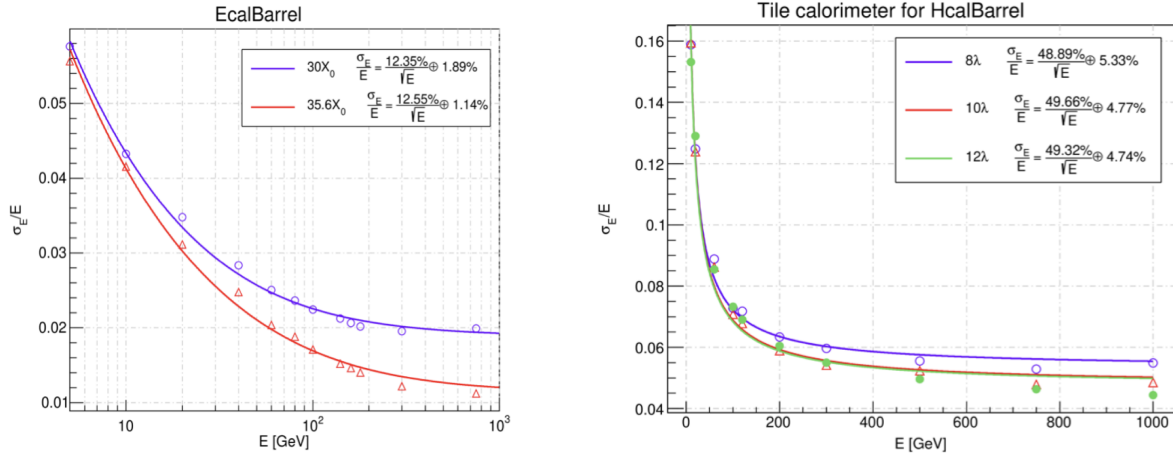
Figure 12.13: Crystal Ball fitted energy dependent resolution for the barrel electromagnetic (left) and barrel hadronic (right) calorimeters EMC and HCAL, respectively. The first (a) term includes shower fluctuations and transverse leakages and the second (b) term includes leakages from the calorimeter volume longitudinally.
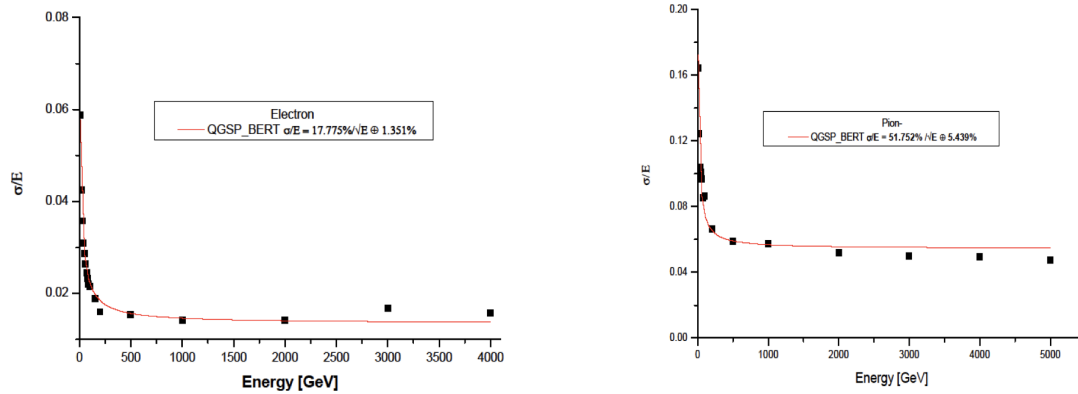
Figure 12.14: Crystal Ball fitted energy dependent resolution for the forward electromagnetic (left) and forward hadronic (right) plug calorimeters FEC and FHC, respectively. The first (a) term includes shower fluctuations and transverse leakages and the second (b) term includes leakages from the calorimeter volume longitudinally.

12.5 Muon Detector

Muon identification is an important aspect for any general purpose HEP experiment. At the LHeC the muon detector can widen the scope and the spectrum of many measurements, of which only a few are listed here:

- Higgs decay,

- Semi-leptonic decays of heavy flavoured hadrons,

- Vector meson production,

- Direct W and Z production,

- Di-muon production,

- Leptoquarks, lepton flavour violation, and other BSM phenomena.

The primary target of the muon detector at the LHeC is to provide a reliable muon tag signature which can be uniquely used in conjunction with the central detector for muon identification, triggering and precision measurements. This specification is appropriate to the constraints of limited space [2] and the lack of a dedicated magnetic field as in the baseline design. The muon chambers surround the central detector and cover the maximum possible solid angle. They have a compact multi-layer structure, providing a pointing trigger and a precise timing measurement which is used to separate muons coming from the interaction point from cosmics, beam halo and non prompt particles. This tagging feature does not include the muon momentum measurement which is performed only in conjunction with the central detector. A trigger candidate in the muon detector is characterised by a time coincidence over a majority of the layers in a range of η and ϕ, compatible with an ep interaction of interest in the main detector. The muon candidates are combined with the trigger information coming from the central detector (mainly the calorimetry at Level 1 trigger) to reduce the fake rate or more complex event topologies.

In terms of technology choices, the options in use in ATLAS and CMS and their planned upgrades are adequate for LHeC. Generally, muon and background rates in LHeC are expected to be lower than in pp. The option of an LHeC muon detector composed by layers of Resistive Plate Chambers (RPC), providing the Level 1 trigger and a two coordinate (η, ϕ) measurement possibly aided by Monitored Drift Tubes (MDT) for additional precision measurements, as chosen for the 2012 CDR, is still valid. Recent developments as presented in the LHC Phase 2 Upgrade Technical Design Reports [902, 903] further strengthen this choice. A new thin-RPC (1 mm gas gap) operated with lower HV, provides a sharper time response (few ns), a higher rate capability (tens of kHz/cm^2), and extends the already good aging perspective. Advances in low-noise, high-bandwidth front-end electronics can improve the performance of older detectors. Similar arguments also hold for smaller tube MDTs (15 mm diameter) which provide lower occupancy and higher rate capability.

Fig. 12.15 shows an adaptation for LHeC of an RPC-MDT assembly as will be implemented for the inner muon layer of ATLAS already during the Phase-1 upgrade as a pilot for Phase-2. A triplet of thin gap RPCs, each with 2 coordinate measurement, is combined with two superlayers of small MDTs. It is also important to note the reduced volume of this structure, in particular the RPC part which would provide the muon tag. For the LHeC a baseline would be to have one or two such stations forming a near-hermetic envelope around the central detector.

---

[2]As in the 2012 CDR, the baseline LHeC detector including the muon system and all of the services and supports is expected to fit into the octagonal shape envelope of the L3 magnet (11.6 m minimum diameter).

Finally, as already presented in the 2012 CDR, detector extensions, with a dedicated magnetic field in the muon detector, be this a second solenoid around the whole detector or extra dipole or toroid in the forward region are, at this stage, left open as possible developments only for upgrade scenarios.
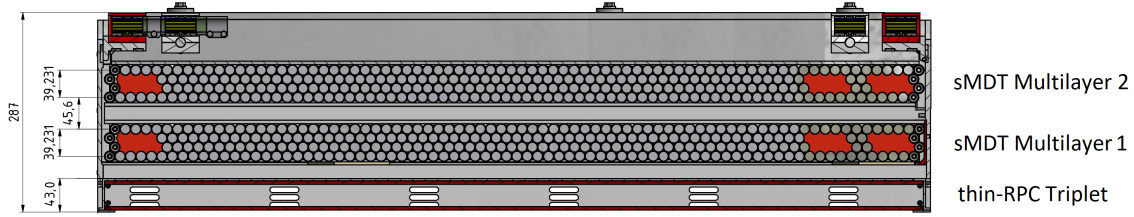

Figure 12.15: A transverse view of a RPC-MDT assembly as adapted from a drawing of the ATLAS Phase-1 muon upgrade [902]. In this case a station is composed of an RPC triplet for trigger and tw0-coordinate readout and two MDT superlayers for precise track measurements.

12.6 Forward and Backward Detectors

In the 2012 CDR, initial plans for beamline instrumentation were provided for the LHeC. In the backward direction, low angle electron and photon calorimeters were included with the primary intention of measuring luminosity via the Bethe-Heitler process $ep \rightarrow eXp$, also offering an electron tagger to identify photoproduction ($\gamma p \rightarrow X$) processes at intermediate y values. The current design carries forward the 2012 version of this backward instrumentation.

In the forward direction, Roman pot detectors were included in the region of $z \sim 420$ m, capable of detecting scattered protons over a range of fractional energy loss $10^{-3} < \xi < 3 \times 10^{-2}$ and wide transverse momentum acceptance, based on extensive previous work in the LHC context by the FP420 group [904]. This also forms the basis of forward proton tagging in the revised design. However, as is the case at ATLAS and CMS / TOTEM, further Roman pot detectors in the region of 200 m and (with HL-LHC optics) perhaps around 320 m would extend the acceptance towards higher ξ values up to around 0.2 allowing the study of diffractive processes $ep \rightarrow eXp$ where the dissociation system X has a mass extending into the TeV regime. It is worth noting that Roman pot technologies have come of age at the LHC, with the TOTEM collaboration operating 14 separate stations at its high point. Silicon sensor designs borrowed from the innermost regions of the ATLAS and CMS vertexing detectors have been used, providing high spatial resolution and radiation hardness well beyond the needs of LHeC. Very precise timing detectors based on fast silicon or Cherenkov radiation signals from traversing protons in quartz or diamond have also been deployed. It is natural that these advances and the lessons from their deployment at the LHC will be used to inform the next iteration of the LHeC design.

The forward beamline design also incorporates a zero angle calorimeter, designed primarily to detect high energy leading neutrons from semi-inclusive processes in ep scattering and to determine whether nuclei break up in eA events. This component of the detector was not considered in detail in 2012 and is therefore discussed here.

12.6.1 Zero-Degree (Neutron) Calorimeter

The Zero-Degree Calorimeter (ZDC) measures final state neutral particles produced at angles near the incoming hadron beam direction. They typically have large longitudinal momentum

$(x_F \gg 10^{-2})$, but with transverse momentum of order of Λ_{QCD}. Such a calorimeter has been instrumented in experiments for ep collisions (H1 and ZEUS) and for pp, pA and AA collisions at RHIC (STAR and PHENIX) and at the LHC (ATLAS, CMS, ALICE and LHCf at the ATLAS IP). The detector's main focus is to study the soft-hard interplay in the QCD description of ep and eA collisions by studying the dependence of forward-going particles with small transverse momentum on variables such as Q^2 and x that describe the hard scattering. The detector also allows the tagging of spectator neutrons to detect nuclear breakup in eA collisions and enables the precise study of the EMC effect by using neutron-tagged DIS on small systems, such as $e\,^3He \to ed + n \to eX + n$. For heavier ions, several tens of neutrons may enter within the aperture of the ZDC. Inclusive π^0 production has been measured by the LHCf experiments for pp collisions. It is of great interest to compare with DIS measurements at the same proton energies. Precise understanding of the inclusive spectrum of the forward-going particles is a key ingredient in simulating air showers from ultra-high energy cosmic rays.

Physics requirement for forward neutron and π^0 production measurement

It is known from various HERA measurements that the slope parameter b is about $8\,\text{GeV}^{-2}$ in the exponential parameterisation e^{bt} of the t distribution of leading neutrons. In order to precisely determine the slope parameter it is necessary to measure the transverse momentum of the neutrons up to or beyond $1\,\text{GeV}$. The aperture for forward neutral particles does not have to be very large, thanks to the large energy of the proton and heavy ion beam. For example, collisions with $E_p = 7\,\text{TeV}$ need $0.14\,\text{mrad}$ for $p_T = 1\,\text{GeV}$ neutrons at $E_{\text{particle}}/E_{\text{beam}} \equiv x_F = 1.0$, or $0.56\,\text{mrad}$ for $x_F = 0.25$.

The energy or x_F resolution for neutrons will not be a dominant factor thanks to the high energy of the produced particles. The energy resolution of a neutron with $x_F = 0.1$ is about 2% for cutting-edge hadron calorimeters with $\sigma_E/E = 50\,\%/\sqrt{E}$, where E is in GeV. Such a resolution can be achieved if non-unity e/h can be compensated either by construction of the calorimeter or by software weighting, and if the size of the calorimeter is large enough so that shower leakage is small.

On the other hand, the resolution requirement on the transverse momentum is rather stringent. For example, $1\,\text{mm}$ resolution on hadronic showers from the neutron measured at $100\,\text{m}$ downstream from the interaction point corresponds to $0.01\,\text{mrad}$ or $70\,\text{MeV}$, which is rather moderate ($\leq 10\,\%$ resolution for large p_T hadrons with $p_T > 700\,\text{MeV}$). For smaller p_T it is more appropriate to evaluate the resolution in terms of $t \simeq -(1 - x_F)p_T^2$ i.e. $\Delta t \simeq 2(\Delta p_T)p_T$ at $x_F = 1$. At $t = 0.1\,\text{GeV}^2$ or $p_T \simeq 300\,\text{MeV}$, Δt is about $50\,\%$. A shower measurement with significantly better than $1\,\text{mm}$ position resolution, therefore, would improve the t-distribution measurement significantly.

According to the current LHC operation conditions with $\beta^* = 5\,\text{cm}$, the beam spread is $8 \times 10^{-5}\,\text{rad}$ or $0.56\,\text{GeV}$. This is much larger than the required resolution in p_T. It is therefore neither possible to measure the particle flow nor to control the acceptance of the forward aperture. For precision measurement of forward particles, it is necessary to have runs with $\beta^* \geq 1\,\text{m}$, corresponding to $\sigma(p_T) < 70\,\text{MeV}$.

The calorimeter should be able to measure more than 30 neutrons of $5\,\text{TeV}$ to tag spectator neutrons from heavy-ion collisions. The dynamic range of the calorimeter should exceed $100\,\text{TeV}$ with good linearity.

As for π^0 measurements, the LHCf experiment has demonstrated that a position resolution of

200 μm on electromagnetic showers provides good performance for the inclusive photon spectrum measurements [905]. This also calls for fine segmentation sampling layers.

ZDC location

According to the IP design, a possible location for the ZDC is after the first bending of the outgoing colliding proton beam at around $Z = 110$ m, where no beam magnet is placed (see Fig. 12.16). It is anyhow planned to place a neutral particle dump around this location in order to protect accelerator components. A ZDC could serve as the first absorbing layer at zero degrees.
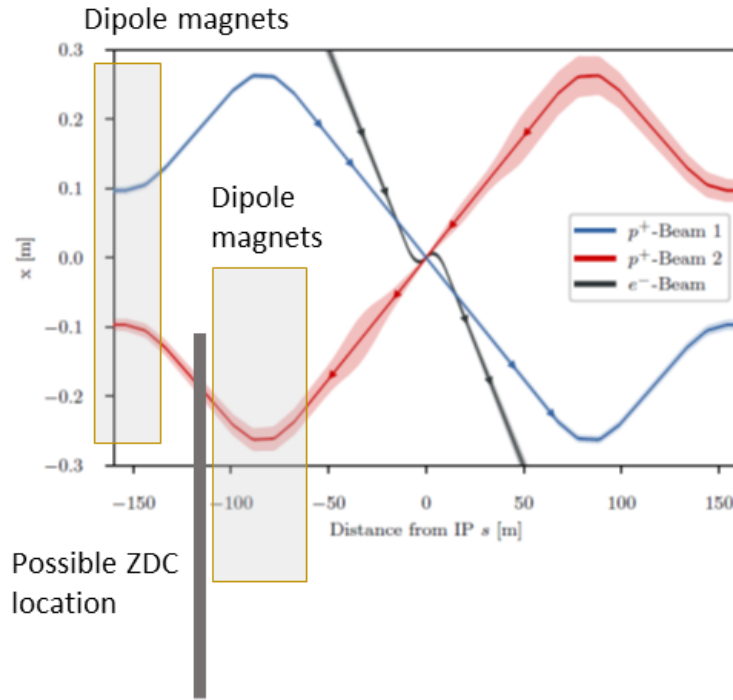
Figure 12.16: Possible location for a ZDC for the linac–ring design of LHeC. The solid rectangle represents the ZDC. The two boxes in front of and behind the ZDC indicate the locations of bending magnets.

The aperture to the ZDC would be determined by the last quadruple magnet at around $z = 50$ m. Assuming a typical aperture for the LHC magnets of 35 mm, the aperture could be as large as 0.7 mrad. The horizontal aperture of the dipole magnets between 75 and 100 m would be larger, since otherwise the magnets receive significant radiation from neutral particles produced from the collisions at the IP. Even if the aperture is limited by the vertical aperture of the last dipole at $z = 100$ m, the aperture is 0.35 mrad, corresponding to 2.4 GeV in p_T for 7 GeV particles. This fulfills the physics requirement.

The space for the ZDC location in the transverse direction should be at least $\pm 2\lambda_I$ to avoid large leakage of hadronic showers. This can be achieved if the proton beam passes inside the calorimeter, about 20 cm from the centre of the calorimeter. The total size of the calorimeter could then be $60 \times 60 \times 200$ cm^3 or larger according to the current layout of the beam and accelerator components. This would provide about $\pm 3\lambda_I$ in the transverse direction and about $10\lambda_I$ in depth.

Radiation requirement for the ZDC

It can safely be assumed that the energy spectrum of the forward neutral particles produced in ep and pp events are very similar. According to the LHCf simulation, their tungsten–scintillator sandwich calorimeter receives about $30\,\mathrm{Gy/nb}^{-1}$ or 10^8 events/nb^{-1} assuming $\sigma_{pp}^{\mathrm{tot}} = 100\,\mathrm{mb}$, i.e. 3×10^{-7} Joule/event. This means that about 1/4 of the total proton beam energy (7 TeV $\simeq$ 1.12×10^{-6} Joule/event) is deposited in 1 kg material in pp collisions. The ep total cross section is expected to be approximately $68\,\mu\mathrm{b}$ or $680\,\mathrm{kHz}$ at $10^{34}\,\mathrm{cm}^2\mathrm{s}^{-1}$. A 7 TeV beam or 1.12×10^{-6} Joule/event corresponds to 0.76 Joule/s at this instantaneous luminosity. A quarter of the total dose is then about $0.2\,\mathrm{Gy/sec}$ or $0.02\,\mathrm{Gy/nb}$. The contribution from beam-gas interactions is estimated to be much smaller ($\mathcal{O}(100\,\mathrm{kHz})$).

Assuming that the ZDC is always operational during LHeC running, one year of ep operation amounts to $2.5\,\mathrm{MGy/year}$ assuming 10^7 sec operation, or $\mathcal{O}(10\,\mathrm{MGy})$ throughout the lifetime of the LHeC operation. This approximately corresponds to $10^{14} - 10^{15}$ 1 MeV neutron equivalent.

Possible calorimeter design

The high dose of $\mathcal{O}(10\,\mathrm{MGy})$ requires calorimeters based on modern crystals (e.g. LYSO) or silicon as sampling layers, at least for the central part of the calorimeter where the dose is concentrated. Since we also need very fine segmentation for photons, it is desirable to use finely segmented silicon pads of order of 1 mm. As for the absorbers, tungsten should be used for good position resolution of photons and the initial part of hadronic showers.

In the area outside the core of the shower i.e. well outside the aperture, the dose may be much smaller and small scintillator tiles could be used for absorbers, which allows measurements with good e/h ratio. If we choose a uniform design using silicon across the detector, the segmentation of the outer towers could be order of a few cm, which still makes it possible to use software compensation technology, as developed for example for the calorimeters in the ILC design. It may also be possible to use lead instead of tungsten for outer towers to reduce the cost.

12.7 Detector Installation and Infrastructure

The usual constraints that apply to HEP detector integration and assembly studies also apply to the LHeC. In places, they are even tighter since the detector has to be installed in a relatively short time, as given by the duration of an LHC machine shutdown, which is typically two years. For the purposes of this report, it is assumed that the LHeC detector will be installed at IP2, see Fig. 12.17. The magnet formerly used by L3 and now in use by ALICE is already present at IP2 and its support structure will be used once again my LHeC. However, the time needed to remove the remainder of the existing detector and its services has to be included to the overall schedule. Thus the only realistic possibility to accomplish the timely dismantling of the old detector and the installation of the new one is to complete as much as possible of the assembly and testing of the LHeC detector on the surface, where the construction can proceed without impacting on the LHC physics runs. The condition for doing this is the availability of equipped free space at the LHC-P2 surface, namely a large assembly hall with one or two cranes. To save time, most of the detector components have been designed to match the handling means available on site, i.e. a bridge crane in the surface hall and experiment cavern. Nevertheless, a heavy lifting facility (about 300 tons capacity) will be rented for the time needed to lower the heaviest

detector components, such as the HCal barrel and plug modules. Large experience with this will be acquired during LHC Long Shutdown 3, when a significant part of the ATLAS and CMS detectors will be replaced by new elements. At CMS, for instance, a new Endcap Calorimeter weighting about 220 tons will be lowered into the experiment cavern, a scenario very close to what is envisaged for the LHeC detector assembly.

Figure 12.17: View of the surface infrastructure at Point 2, near St. Genis.

The detector has been split into the following main parts for assembly purposes:

- Coil cryostat, including the superconducting coil, the two integrated dipoles and eventually the EMCal.

- Five HCal tile calorimeter barrel modules, fully instrumented and cabled (5).

- Two HCal plugs modules, forward and backward (2).

- Two EMCal plugs, forward and backward (2).

- Innner Tracking detector (1).

- Beam-pipe (1).

- Central Muon detector (1 or 2).

- Endcaps Muon detector (2).

The full detector, including the Muon chambers, fits inside the former L3 detector Magnet Yoke, once the four large doors are taken away. The goal is to prevent losing time in dismantling the L3 Magnet barrel yoke and to make use of its sturdy structure to hold the detector central part on a platform supported by the magnet crown, whilst the Muon chambers are inserted into lightweight structures (space-frames) attached to the inner surface of the octagonal L3 magnet.

The assembly of the main detector elements on the surface can start at any time, without sensible impact on the LHC run, providing that the surface facilities are available. The Coil
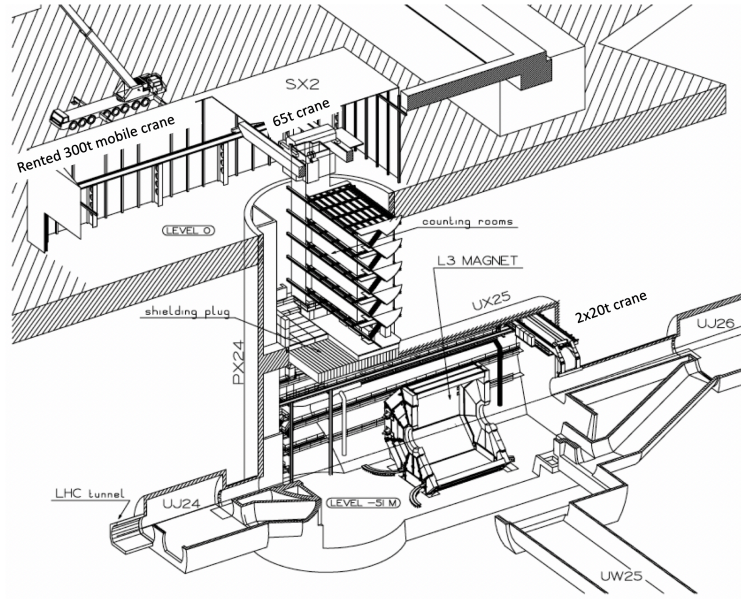
Figure 12.18: View of the cavern infrastructure at Point 2. The support structure of the magnet of the L3 experiment (at the centre) will house and support the LHeC detector.

system commissioning on site is estimated to require three months and preparation for lowering a further three months, including some contingency. In the same time window, the L3 Magnet will be freed up and prepared for the new detector [3]. Lowering of the main detector components into the cavern, illustrated in Fig. 12.18, is expected to take one week per piece (15 pieces in total). Underground integration of the central detector elements inside the L3 Magnet would require about 6 months, cabling and connection to services some 8 to 10 months, in parallel with the installation of the Muon chambers, the Tracker and the Calorimeter Plugs. Fig. 12.19 shows the installed complete detector housed in the L3 magnet support.

The total estimated time, from the starting of the testing of the Coil system on surface to the commissioning of the detector underground is thus 20 months. The beam-pipe bake out and vacuum pumping could take another 3 months and the final detector check-out one additional month. Some contingency (2–3 months in total) is foreseen at the beginning and the end of the installation period. A sketch of the installation schedule is provided in Fig. 12.20

Concerning the detector infrastructures, not much can be said at this stage. The LHeC detector superconducting coil will need cryogenic services and a choice has to be made between purchasing a dedicated liquid helium refrigeration plant or profiting from the existing LHC cryogenic infrastructure to feed the detector magnet. The electrical and water-cooling networks present at LHC-P2 are already well sized for the new detector and only minor interventions are expected there.

---

[3] The actual delay depends on the level of activation and the procedure adopted for dismantling the existing detector. Here again the experience acquired during the long shutdown LS2 with the upgrades of ALICE and LHCb and later with the ATLAS and CMS upgrades during LS3 will provide important insight for defining procedures and optimising the schedule.
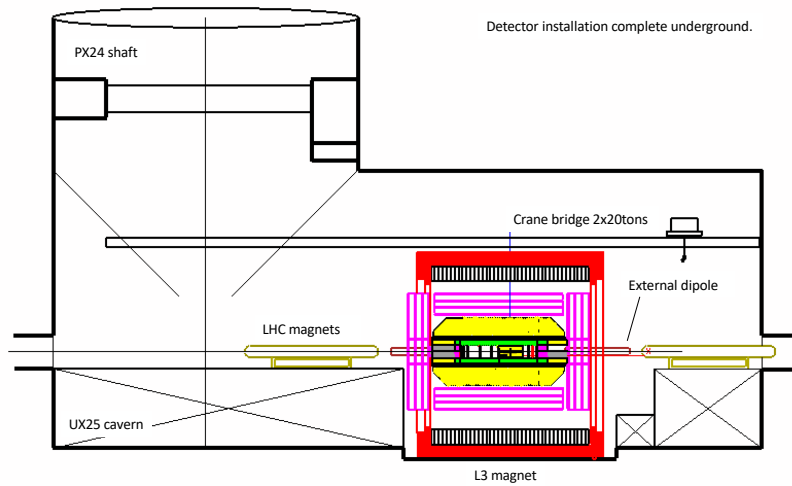
Figure 12.19: View of the LHeC detector, housed in the L3 magnet support structure, after installation at the interaction point.
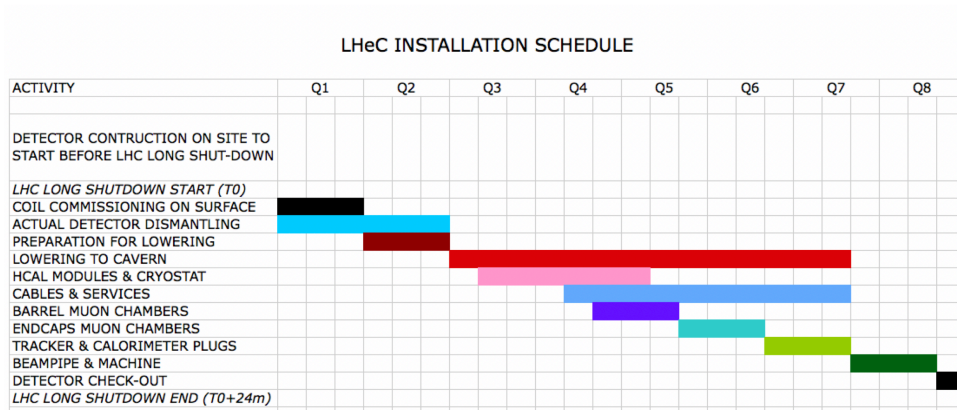
Figure 12.20: Time schedule of the sequential installation of the LHeC detector at point 2, as described in the text.

12.8 Detector Design for a Low Energy FCC-eh

Although not the primary focus of this report, a full detector design has also been carried out for an *ep* facility based on an FCC tunnel with proton-ring magnet strengths limited such that the proton energy is 20 TeV. For ease of comparison, the basic layout and the technology choices are currently similar to those of the LHeC detector. Similar or improved performance is obtained compared with the LHeC, provided that additional disks are included in the forward and backward trackers and the calorimeter depths are scaled logarithmically with the beam energies.
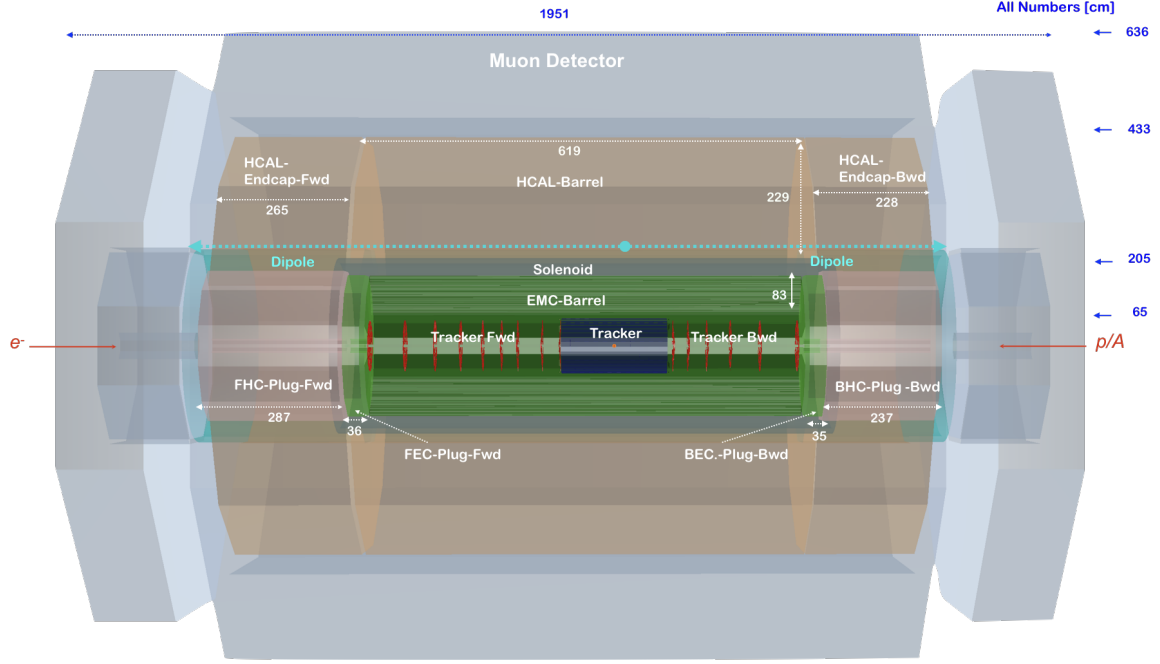
Figure 12.21: Side view of a low energy FCCeh ($E_p = 20\,\mathrm{TeV}$) concept detector, designed using the DD4hep framework [891], showing the essential features. The solenoid is again placed between the ECAL-Barrel and Hadronic-Barrel calorimeters and is housed in a cryostat in common with the beam steering dipoles extending over the full length of the barrel and plug hadronic calorimeters. The sizes have been chosen such that the solenoid/dipoles and ECAL-Barrel systems as well as the whole tracker are also suitable to operate after an upgrade of the beam energy to $E_p = 50\,\mathrm{TeV}$.

The basic layout is shown in Fig. 12.21. The barrel and end-caps of the central tracker are identical to those of the LHeC design, as given in table 12.1. The design parameters for the FCC-eh versions of the forward and backward trackers, the barrel calorimeters and the plug calorimeters are given in tables 12.5, 12.6 and 12.7, respectively. Comparing the performance of "warm" solution (Pb-Sctillator) with the "cold" variant (Pb-LAr) for the barrel electromagnetic calorimeter (EMC) the superior performance of the "cold" calorimeter setup again favorises the Pb-LAr option for the lowE-FCCeh detector (see figure 12.22 and table 12.6).

Tracker (lowE-FCCeh) [1]		Fwd Tracker			Bwd Tracker		Total
		pix	$\text{pix}_{\text{macro}}$	strip	$\text{pix}_{\text{macro}}$	strip	(incl. Tab. 12.1)
$\eta_{\text{max}}, \eta_{\text{min}}$		5.6,2.6	3.8,2.2	3.5,1.6	$-4.6, -2.6$	$-2.8, -1.6$	$5.3, -4.6$
Wheels		2	1	3	3	3	
Modules/Sensors		288	288	1376	216	1248	12444
Total Si area	[m^2]	1.35	1.45	7.35	1.0	6.5	49.85
Read-out-Channels	[10^6]	647.9	110.2	42.3	82.7	38.3	3317.2
pitch$^{r-\phi}$	[μm]	25	100	100	100	100	
pitch^z	[μm]	50	400	50k [2]	400	10k [2]	
Average X_0/Λ_I	[%]		6.7 / 2.1			6.1 / 1.9	
incl. beam pipe	[%]						40 / 25

[1] Based on tklayout calculations [893]

[2] Reaching pitch$^{r-\phi}$ when using two wafer layers rotated by 20 mrad is achievable.

Table 12.5: Summary of the main properties of the forward and backward tracker modules in the low energy FCC-eh detector configuration, based on calculations performed using tkLayout. For each module, the rows correspond to the pseudorapidity coverage, the numbers of disk layers and of sensors, the total area covered by silicon sensors, the numbers of readout channels, the hardware pitches affecting the $(r-\phi)$ and the z resolution, and the average material budget in terms of radiation lengths and interaction lengths. The numbers are broken down into separate contributions from pixels, macro-pixels and strips. The column *Total* contains the sum of corresponding values of barrel tracker modules (identical to the LHeC barrel layout, table 12.1)and the forward and backward trackers in this table, 12.5.

Calo (lowE-FCCeh)		EMC	HCAL		
		Barrel	Ecap Fwd	Barrel	Ecap Bwd
Readout, Absorber		Sci,Pb	Sci,Fe	Sci,Fe	Sci,Fe
Layers		49	91	68	78
Integral Absorber Thickness [cm]		36.6	206.0	184.0	178.0
$\eta_{\text{max}}, \eta_{\text{min}}$		2.8, -2.5	2.0, 0.8	1.6, -1.4	$-0.7, -1.8$
$\sigma_E/E = a/\sqrt{E} \oplus b$	[%]	12.6/1.1	38.9/3.3	42.4/4.2	40.6/3.5
Λ_I / X_0		$X_0 = 66.2$	$\Lambda_I = 12.7$	$\Lambda_I = 11.3$	$\Lambda_I = 11.0$
Total area Sci	[m^2]	2915	4554	12298	3903

Table 12.6: Basic properties and simulated resolutions of barrel calorimeter modules in a scaled configuration, suitable for a low energy FCC detector. For each of the modules, the rows indicate the absorber and sensitive materials, the numbers of layers and the total absorber thickness, the pseudorapidity coverage, the contributions to the simulated resolution from the sampling (a) and material (b) terms in the form a/b, the depth in terms or radiation or interaction lengths and the total area covered by the sensitive material. The resolutions are obtained from a GEANT4 [892] simulation, with fits using a crystal ball function [899–901].
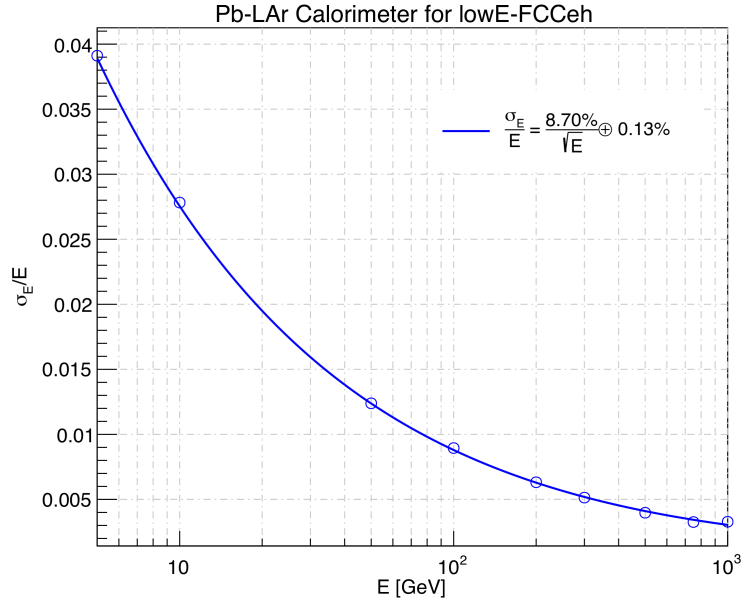
Calo (lowE-FCCeh)		FHC Plug Fwd	FEC Plug Fwd	BEC Plug Bwd	BHC Plug Bwd
Readout, Absorber		Si,W	Si,W	Si,Pb	Si,Cu
Layers		296	49	59	238
Integral Absorber Thickness [cm]		256.9	29.6	27.9	220.8
η_{max}, η_{min}		5.8, 1.8	5.4, 1.8	-1.5, -5.2	-1.5, -5.6
$\sigma_E/E = a/\sqrt{E} \oplus b$	[%]	61.9/0.5	26.5/0.4	24.7/0.4	46.7/4.4
Λ_I / X_0		$\Lambda_I = 15.5$	$X_0 = 84.7$	$X_0 = 50.2$	$\Lambda_I = 14.7$
Total area Si	[m^2]	2479	364	438	1994

Table 12.7: Basic properties and simulated resolutions of forward and backward plug calorimeter modules in a scaled configuration, suitablle for a low energy FCC detector. For each of the modules, the rows indicate the absorber and sensitive materials, the numbers of layers and the total absorber thickness, the pseudorapidity coverage, the contributions to the simulated resolution from the sampling (a) and material (b) terms in the form a/b, the depth in terms or radiation or interaction lengths and the total area covered by the sensitive material. The resolutions are obtained from a GEANT4 [892] simulation, with fits using a crystal ball function [899–901].

Figure 12.22: For comparison the achievable resolution of a cold version of an EM-calorimeter stack is shown. The sampling calorimeter setup (ATLAS type) is characterised by lead as absorber $2.2\,\mathrm{mm}$ thick and $3.8\,\mathrm{mm}$ gaps filled with liquid argon as detecting medium, a cartesian accordion geometry and stack folds having a length of $40.1\,\mathrm{mm}$ and an inclination angle of $\pm45°$ to each other. The radiation length for the setup described is estimated from geantino scans using **GEANT4** [892]. The simulated calorimeter stack has a depth of $83.7\,\mathrm{cm}$ (approximately $58\,\mathrm{X}_0$). The fits have been performed as for Fig. 12.13.

Chapter 13

Conclusion

The Large Hadron Collider determines the energy frontier of experimental collider physics for the next two decades. Following the current luminosity upgrade, the LHC can be further upgraded with a high energy, intense electron beam such that it becomes a twin-collider facility, in which ep collisions are registered concurrently with pp. A joint ECFA, CERN and NuPECC initiative led to a detailed conceptual design report (CDR) [1] for the Large Hadron Electron Collider published in 2012. The present paper represents an update of the original CDR in view of new physics and technology developments.

The LHeC uses a novel, energy recovery linear electron accelerator which enables TeV energy electron-proton collisions at high luminosity, of $\mathcal{O}(10^{34})\,\mathrm{cm^{-2}s^{-1}}$, exceeding that of HERA by nearly three orders of magnitude. The discovery of the Higgs boson and the surprising absence of BSM physics at the LHC demand to extend the experimental base of particle physics suitable to explore the energy frontier, beyond pp collisions at the LHC. The LHC infrastructure is the largest single investment the European and global particle physics community ever assembled, and the addition of an electron accelerator a seminal opportunity way to build on it, and to sustain the HL-LHC programme by adding necessary elements which are provided by high energy deep inelastic scattering. As has been shown in this paper, the external DIS input transforms the LHC to a much more powerful facility, with a new level of resolving matter substructure, a more precise Higgs programme, challenging and complementing that of a next e^+e^- collider, and with a hugely extended potential to discover physics beyond the Standard Model.

The very high luminosity and the substantial extension of the kinematic range in deep inelastic scattering, compared to HERA, make the LHeC on its own a uniquely powerful TeV energy collider. Realising the *Electrons for LHC* programme developed with the previous and the present "white" papers, will create the cleanest, high resolution microscope accessible to the world, which one may term the "CERN Hubble Telescope for the Micro-Universe". It is directed to unravel the substructure of matter encoded in the complex dynamics of the strong interaction, and to provide the necessary input for precision and discovery physics at the HL-LHC and for future hadron colliders.

This programme, as has been described in this paper, comprises the complete resolution of the partonic densities in an unexplored range of kinematics, the foundations for new, generalised views on proton structure and the long awaited clarification of the QCD dynamics at high densities, as are observed at small Bjorken x. New high precision measurements on diffraction and vector mesons will shed new light on the puzzle of confinement. As a complement to the LHC and a possible future e^+e^- machine, the LHeC would scrutinise the Standard Model deeper than

ever before, and possibly discover new physics in the electroweak and chromodynamic sectors as is outlined in the paper.

Through the extension of the kinematic range by about three orders of magnitude in lepton-nucleus (eA) scattering, the LHeC is the most powerful electron-ion research facility one can build in the next decades, for clarifying the partonic substructure and dynamics inside nuclei for the first time and elucidating the chromodynamic origin of the Quark-Gluon-Plasma.

The Higgs programme at the LHeC is astonishing in its precision. It relies on CC and NC precision measurements for which an inverse atobarn of luminosity is desirable to achieve. The prospective results on the Higgs couplings from the HL-LHC, when combined with those here presented from the LHeC, will determine the couplings in the most frequent six Higgs decay channels to one per cent level accuracy. This is as precise as one expects measurements from linear e^+e^- colliders but obtained dominantly from gg and WW fusion respectively, as compared to Higgs-strahlung in electron-positron scattering which has the advantage of providing a Higgs width determination too. The combined $pp+ep$ LHC facility at CERN may then be expected to remain the centre of Higgs physics for two more decades.

Searches for BSM physics at the LHeC offer great complementarity to similar searches at the HL-LHC. The core advantage of the LHeC is the clean, QCD-background and pileup-free environment of an electron-proton collider with a cms energy exceeding a TeV. This enables discoveries of signatures that could be lost in the hadronic noise at pp or possibly unaccessible due to the limited com energy at ee. Prominent examples for discovery enabled with ep are heavy neutral leptons (or sterile neutrinos) that mix with the electron flavour, dark photons below the di-muon threshold, which are notoriously difficult to detect in other experiments, long-lived new particles in general or new physics scenarios with a compressed mass spectrum, such as SUSY electrowikinos and heavy scalar resonances with masses around and below $500\,\text{GeV}$, which may exist but literally be buried in di-top backgrounds at the LHC.

The LHeC physics programme reaches far beyond any specialised goal which underlines the unique opportunity for particle physics to build a novel laboratory for accelerator based energy frontier research at CERN. The project is fundable within the CERN budget, and not preventing much more massive investments into the further future. It offers the possibility for the current generation of accelerator physicists to build a new collider using and developing novel technology while preparations proceed for the next grand step in particle physics for generations ahead.

The main technical innovation through the LHeC is the first ever high energy application of energy recovery technology, based on high quality superconducting RF developments, a major contribution to the development of *green* collider technology which is an appropriate response to demands of our time. The ERL technique is more and more seen to have major further applications, beyond ep at HE-LHC and FCC-eh, such as for FCC-ee, as a $\gamma\gamma$ Higgs facility or, beyond particle physics, as the highest energy XFEL of hugely increased brightness.

The paper describes the plans and configuration of PERLE, the first $10\,\text{MW}$ power ERL facility, which is being prepared in international collaboration for built at Irène Joliot-Curie Laboratory at Orsay. PERLE has adopted the 3-pass configuration, cavity and cryomodule technology, source and injector layout, frequency and electron current parameters from the LHeC. This qualifies it to be the ideal machine to accompany the development of the LHeC. However, through its technology innovation and its challenging parameters, such as an intensity exceeding that of ELI by orders of magnitude, PERLE has an independent, far reaching low energy nuclear and particle physics programme with new and particularly precise measurements. It also has a possible program on industrial applications, which has not been discussed in the present paper.

The LHeC provides an opportunity for building a novel collider detector which is sought for as the design of the HL-LHC detector upgrades is approaching completion. A novel *ep* experiment enables modern detection technology, such as HV CMOS Silicon tracking, to be further developed and exploited in a new generation, 4π acceptance, no pile-up, high precision collider detector in the decade(s) hence. This paper presented an update of the 2012 detector design, in response to developments of physics, especially Higgs and BSM, and of technology in detectors and analysis. The LHeC requires to be installed at IP2 at the LHC for there is no other interaction region available while the heavy ion programme at the LHC is presently limited to the time until LS4. In the coming years it will have to be decided whether this or alternative proposals for using IP2 during the final years of LHC operation are considered attractive enough and realistic to be realised.

The next steps in this development are rather clear: the emphasis on ERL, beyond LHeC, requires the PERLE development to rapidly proceed. Limited funds are to be found for essential components with the challenging IR quadrupole as the main example. ECFA is about to establish a detector and physics series of workshops, including possible future Higgs facilities, and *ep*, which is a stimulus for further developing the organisational base of the LHeC towards a detector proto-Collaboration. These developments shall include preparations for FCC-he and provide a necessary basis when in a few years time, as recommended by the IAC, a decision on building the LHeC at CERN may be taken.

The recent history teaches a lesson about the complementarity required for energy frontier particle physics. In the seventies and eighties, CERN hosted the $p\bar{p}$ energy frontier, with UA1 and UA2, and the most powerful DIS experiments with muons (EMC, BCDMS, NMC) and neutrinos (CDHSW, CHARM), while e^+e^- physics was pursued at PEP, PETRA and also TRISTAN. Following this, the Fermi scale could be explored with the Tevatron, HERA and LEP. The here advertised next logical step is to complement the HL-LHC by a most powerful DIS facility, the LHeC, while preparations will take shape for a next e^+e^- collider, currently at CERN and in Asia. Hardly a decision on LHeC may be taken independently of how the grand future unfolds. Still, this scenario would give a realistic and yet exciting base for completing the exploration of TeV scale physics which may not be achieved with solely the LHC.

The ERL concept and technology here presented has the potential to accompany the FCC for realising the FCC-eh machine when the time comes for the next, higher energy hadron collider, and the search for new physics at the $\mathcal{O}(10)\,$TeV scale.

Acknowledgement

we have been working closely but who meanwhile left this development, perhaps temporarily, or work at non-particle physics institutions while wishing LHeC success. The current situation of particle physics reminds us on the potential we have when resources and prospects are combined, for which this study is considered to be a contribution.

Appendix A

Statement of the International Advisory Committee

End of 2014, the CERN Directorate appointed an International Advisory Committee (IAC) for advice on the direction of energy frontier electron-hadron scattering at CERN, for their mandate see below. The committee and its chair, em. DG of CERN Herwig Schopper, was reconfirmed when a new DG had been appointed. The IAC held regular sessions at the annual LHeC workshops in which reports were heard by the co-coordinators of the project, Oliver Brüning and Max Klein. Its work and opinion shaped the project development considerably and it was pivotal for the foundation of the PERLE project. The committee was in close contact and advised especially on the documents, on the LHeC [8, 10] and PERLE [11], submitted end of 2018 to the update of the European strategy on particle physics. In line with the present updated LHeC design report and the strategy process, the IAC formulated a brief report to the CERN DG, in which its observations and recommendations have been summarised. This report was also sent to the members of the European particle physics strategy group. It is reproduced here.

Report by the IAC on the LHeC to the DG of CERN

The development of the LHeC project was initiated by CERN and ECFA, in cooperation with NuPECC. It culminated in the publication of the Conceptual Design Report (CDR), arXiv:1206.2913 in 2012, which received by now about 500 citations. In 2014, the CERN Directorate invited our committee to advise the CERN Directorate, and the Coordination Group, on the directions of future energy frontier electron-hadron scattering as are enabled with the LHC and the future FCC (for the mandate see below). In 2016, Council endorsed the HL-LHC, which offers a higher LHC performance and strengthened the interest in exploring the Higgs phenomenon. In view of the imminent final discussions for the European Road Map for particle physics, a short summary report is here presented.

Main Developments 2014–2019

A series of annual workshops on the LHeC and FCC-eh was held, and this report is given following the latest workshop https://indico.cern.ch/event/835947 , October 24/25, 2019.

Based on recent developments concerning the development of the LHC accelerator and physics, and the progress in technology, a new default configuration of the LHeC and FCC-eh has been worked out with a tenfold increased peak luminosity goal, of $10^{34}\,\mathrm{cm}^{-2}\mathrm{s}^{-1}$, as compared to the CDR. A comprehensive paper, "The LHeC at the HL-LHC", is being finalised for publication this year.

Within this work, it has been shown that the LHeC represents the cleanest, high resolution microscope the world can currently build, a seminal opportunity to develop and explore QCD, to study high precision Higgs and electroweak physics and to substantially extend the range and prospects for accessing BSM physics, on its own and in combination of pp with ep. The LHeC, in eA scattering mode, has a unique discovery potential on nuclear structure, dynamics and QGP physics.

Intense eh collisions with LHeC and FCC-eh are enabled through a special electron-beam race-track arrangement with energy recovery linac (ERL) technology. If LHeC were to be considered either on its own merits, or as a bridge project to FCC-eh, it seemed important to find a configuration, which could be realised within the existing CERN budget. Several options were studied and found.

Before a decision on such a project can be taken, the ERL technology has to be further developed. Considerable progress has been made in the USA, and a major effort is now necessary to develop it further in Europe. An international collaboration (ASTeC, BINP, CERN, Jefferson Lab, Liverpool, Orsay) has been formed to realise the first multi-turn 10 MW ERL facility, PERLE at Orsay, with its main parameters set by the LHeC and producing the first encouraging results on 802 MHz cavity technology, for the CDR see arXiv:1705.08783.

This radically new accelerator technology, ERL, has an outstanding technical (SRF), physics (nuclear physics) and industrial (lithography, transmutations, ..) impact, and offers possible applications beyond ep (such as a racetrack injector or ERL layout for FCC-ee, a high energy FEL or $\gamma\gamma$ collider).

In conclusion it may be stated

- The installation and operation of the LHeC has been demonstrated to be commensurate with the currently projected HL-LHC program, while the FCC-eh has been integrated into the FCC vision;
- The feasibility of the project as far as accelerator issues and detectors are concerned has been shown. It can only be realised at CERN and would fully exploit the massive LHC and HL-LHC investments;
- The sensitivity for discoveries of new physics is comparable, and in some cases superior, to the other projects envisaged;
- The addition of an ep/A experiment to the LHC substantially reinforces the physics program of the facility, especially in the areas of QCD, precision Higgs and electroweak as well as heavy ion physics;
- The operation of LHeC and FCC-eh is compatible with simultaneous pp operation; for LHeC the interaction point 2 would be the appropriate choice, which is currently used by ALICE;
- The development of the ERL technology needs to be intensified in Europe, in national laboratories but with the collaboration of CERN;
- A preparatory phase is still necessary to work out some time-sensitive key elements, especially the high power ERL technology (PERLE) and the prototyping of Intersection

Region magnets.

Recommendations

i) It is recommended to further develop the ERL based ep/A scattering plans, both at LHC and FCC, as attractive options for the mid and long term programme of CERN, resp. Before a decision on such a project can be taken, further development work is necessary, and should be supported, possibly within existing CERN frameworks (e.g. development of SC cavities and high field IR magnets).

ii) The development of the promising high-power beam-recovery technology ERL should be intensified in Europe. This could be done mainly in national laboratories, in particular with the PERLE project at Orsay. To facilitate such a collaboration, CERN should express its interest and continue to take part.

iii) It is recommended to keep the LHeC option open until further decisions have been taken. An investigation should be started on the compatibility between the LHeC and a new heavy ion experiment in Interaction Point 2, which is currently under discussion.

After the final results of the European Strategy Process will be made known, the IAC considers its task to be completed. A new decision will then have to be taken for how to continue these activities.

Herwig Schopper, Chair of the Committee,   Geneva, November 4, 2019

Mandate of the International Advisory Committee

Advice to the LHeC Coordination Group and the CERN directorate by following the development of options of an ep/eA collider at the LHC and at FCC, especially with: Provision of scientific and technical direction for the physics potential of the ep/eA collider, both at LHC and at FCC, as a function of the machine parameters and of a realistic detector design, as well as for the design and possible approval of an ERL test facility at CERN. Assistance in building the international case for the accelerator and detector developments as well as guidance to the resource, infrastructure and science policy aspects of the ep/eA collider. (December 2014)

Members of the Committee

Sergio Bertolucci (U Bologna)
Nichola Bianchi (INFN, now Singapore)
Frederick Bordy (CERN)
Stan Brodsky (SLAC)
Oliver Brüning (CERN, coordinator)
Hesheng Chen (IHEP Beijing)
Eckhard Elsen (CERN)
Stefano Forte (U Milano)
Andrew Hutton (Jefferson Lab)
Young-Kee Kim (U Chicago)

Max Klein (U Liverpool, coordinator)
Shin-Ichi Kurokawa (KEK)
Victor Matveev (JINR Dubna)
Aleandro Nisati (Rome I)
Leonid Rivkin (PSI Villigen)
Herwig Schopper (CERN, em.DG, Chair)
Jürgen Schukraft (CERN)
Achille Stocchi (IJCLab Orsay)
John Womersley (ESS Lund)

Appendix B

Membership of Coordination

Coordinating Group

Gianluigi Arduini (CERN)
Néstor Armesto (University of Santiago de Compostela)
Oliver Brüning (CERN) – Co-Chair
Andrea Gaddi (CERN)
Erk Jensen (CERN)
Walid Kaabi (IJCLab Orsay)
Max Klein (University of Liverpool) – Co-Chair
Peter Kostka (University of Liverpool)
Bruce Mellado (University of Witwatersrand)
Paul R. Newman (University of Birmingham)
Daniel Schulte (CERN)
Frank Zimmermann (CERN)

Physics Convenors

Parton Distributions and QCD
Claire Gwenlan (University of Oxford)
Fred Olness (Texas University, Dallas)
Physics at Small x
Paul R. Newman (University of Birmingham)
Anna M. Stasto (Pennsylvania State University)
Top and Electroweak Physics
Olaf Behnke (DESY Hamburg)
Daniel Britzger (MPI Munich)
Christian Schwanenberger (DESY Hamburg)
Electron – Ion Physics
Néstor Armesto (University of Santiago de Compostela)
Higgs Physics
Uta Klein (University of Liverpool)
Masahiro Kuze (Institute of Technology Tokyo)
BSM Physics
Georges Azuelos (University of Montreal)
Monica D'Onofrio (University of Liverpool)
Oliver Fischer (MPIK Heidelberg)
Detector Design
Peter Kostka (University of Liverpool)
Alessandro Polini (INFN Bologna)

Bibliography

[1] LHeC Study Group, J. L. Abelleira *et al.*, *J. Phys.* G39 (2012) 075001, `arXiv:1206.2913`.

[2] H. Burkhardt, *ICFA Beam Dyn. Newslett.* 58 (2012) 76.

[3] G. Apollinari, I. Béjar Alonso, O. Brüning, P. Fessia, M. Lamont, L. Rossi and L. Tavian (eds.), *High-Luminosity Large Hadron Collider (HL-LHC)*, vol. 4. CERN Yellow Rep. Monogr., CERN-2017-007-M, 2017.

[4] L. Rossi and O. Brüning, "Progress with the High Luminosity LHC project at CERN," in *Proceedings, 10th International Particle Accelerator Conference (IPAC2019): Melbourne, Australia, May 19-24, 2019*, Jun 2019.

[5] G. Hoffstaetter *et al.*, `arXiv:1706.04245`.

[6] A. Bartnik *et al.*, *Phys. Rev. Lett.* 125 (2020) 044803.

[7] D. Angal-Kalinin *et al.*, *J. Phys.* G45 (2018) 065003, `arXiv:1705.08783`.

[8] LHeC Study Group, O. Brüning, M. Klein *et al.*, "Exploring the Energy Frontier with Deep Inelastic Scattering at the LHC," A Contribution to the Update of the European Strategy on Particle Physics, CERN-ACC-NOTE-2018-0084, Dec 2018. `http://cds.cern.ch/record/2652313`.

[9] LHeC and PERLE Collaborations, O. Brüning, M. Klein *et al.*, *J. Phys.* G46 (2019) 123001.

[10] LHeC Study Group, O. Brüning, M. Klein *et al.*, "Addendum. Exploring the Energy Frontier with Deep Inelastic Scattering at the LHC," A Contribution to the Update of the European Strategy on Particle Physics, CERN-ACC-NOTE-2018-0085, Dec 2018.

[11] PERLE Collaboration, M. Klein, A. Stocchi *et al.*, "PERLE: A High Power Energy Recovery Facility for Europe," A Contribution to the Update of the European Strategy on Particle Physics, CERN-ACC-NOTE-2018-0086, Dec 2018. `https://cds.cern.ch/record/2652336`.

[12] G. Altarelli, *Frascati Phys. Ser.* 58 (2014) 102, `arXiv:1407.2122`.

[13] J. De Hondt, "Talk on the Future of Particle Physics and on ECFA Matters," Plenary Session, ECFA, CERN, November, 2019.

[14] FCC Collaboration, A. Abada *et al.*, *Eur. Phys. J.* C79 (2019) 474.

[15] FCC Collaboration, A. Abada *et al.*, *Eur. Phys. J. ST* 228 (2019) 261.

[16] FCC Collaboration, A. Abada *et al.*, *Eur. Phys. J. ST* 228 (2019) 755.

[17] CEPC-SPPC Study Group, M. Ahmad *et al.*, "CEPC-SPPC Preliminary Conceptual Design Report. 2. Accelerator," IHEP-CEPC-DR-2015-01, IHEP-AC-2015-01, 2015.

[18] CEPC Study Group, M. Dong *et al.*, "CEPC Conceptual Design Report: Volume 2 - Physics & Detector," 2018. `arXiv:1811.10545`.

[19] R. P. Feynman, *Photon-hadron interactions*. Westview Press, Reading, MA, 1972.

[20] E. D. Bloom *et al.*, *Phys. Rev. Lett.* 23 (1969) 930.

[21] M. Breidenbach *et al.*, *Phys. Rev. Lett.* 23 (1969) 935.

[22] R. P. Feynman, *Phys. Rev. Lett.* 23 (1969) 1415.

[23] J. D. Bjorken and E. A. Paschos, *Phys. Rev.* 185 (1969) 1975.

[24] C. Y. Prescott *et al.*, *Phys. Lett.* 77B (1978) 347.

[25] S. Weinberg, *Phys. Rev. Lett.* 19 (1967) 1264.

[26] B. H. Wiik, *Acta Phys. Polon.* B16 (1985) 127.

[27] M. Klein and R. Yoshida, *Prog. Part. Nucl. Phys.* 61 (2008) 343, `arXiv:0805.3334`.

[28] A. De Rujula, S. L. Glashow, H. D. Politzer *et al.*, *Phys. Rev.* D10 (1974) 1649.

[29] J. Dainton, M. Klein, P. Newman, E. Perez and F. Willeke, *JINST* 1 (2006) P10001, `arXiv:hep-ex/0603016`.

[30] FCC Collaboration, A. Abada *et al.*, *Eur. Phys. J. ST* 228 (2019) 1109.

[31] F. Marhauser *et al.*, "802 MHz ERL Cavity Design and Development," in *Proceedings, 9th International Particle Accelerator Conference (IPAC 2018): Vancouver, BC Canada, April 29-May 4, 2018*, 2018.

[32] V. N. Litvinenko, T. Roser and M. Chamizo-Llatas, *Phys. Lett. B* 804 (2020) 135394, `arXiv:1909.04437`.

[33] O. Brüning, "FCC-eh Cost Estimate," CERN-ACC-NOTE-2018-0061, 2018.

[34] A. Bogacz, "The LHeC ERL - Optics and Performance Optimisation," Talk given at ERL Workshop, Berlin, 2019.

[35] O. Brüning, J. Jowett, M. Klein, D. Pellegrini, D. Schulte and F. Zimmermann, "Future Circular Collider Study FCC-eh Baseline Parameters," 2017. CERN FCC-ACC-RPT-012.

[36] F. Bordry *et al.*, "Machine Parameters and Projected Luminosity Performance of Proposed Future Colliders at CERN," 2018. `arXiv:1810.13022`.

[37] C. Quigg, *PoS* DIS2013 (2013) 034, `arXiv:1308.6637`.

[38] J. C. Collins, D. E. Soper and G. F. Sterman, *Factorization of Hard Processes in QCD*, vol. 5, pp. 1–91. 1989. `arXiv:hep-ph/0409313`.

[39] LHeC Study Group, J. L. Abelleira *et al.*, "On the Relation of the LHeC and the LHC," 2012. `arXiv:1211.5102`.

[40] G. R. Boroun, *Phys. Lett.* B744 (2015) 142, `arXiv:1503.01590`.

[41] T. J. Hobbs, J. T. Londergan, D. P. Murdock and A. W. Thomas, *Phys. Lett.* B698 (2011) 123, `arXiv:1101.3923`.

[42] M. Klein, "The structure of the proton and HERA," in *International Conference on the Structure and Interactions of the Photon and 18th International Workshop on Photon-Photon Collisions and International Workshop on High Energy Photon Linear Colliders*, Jan 2010.

[43] H1 and ZEUS Collaborations, F. Aaron *et al.*, *JHEP* 1001 (2010) 109, `arXiv:0911.0884`.

[44] H1 and ZEUS Collaborations, H. Abramowicz *et al.*, *Eur. Phys. J.* C75 (2015) 580, `arXiv:1506.06042`.

[45] HERAFitter Group, S. Alekhin *et al.*, *Eur. Phys. J.* C75 (2015) 304, `arXiv:1410.4412`.

[46] H1 Collaboration, F. Aaron *et al.*, *Eur. Phys. J.* C64 (2009) 561, `arXiv:0904.3513`.

[47] M. Botje, *Comput. Phys. Commun.* 182 (2011) 490, `arXiv:1005.1481`.

[48] M. Botje, "Erratum for the time-like evolution in QCDNUM," 2016. `arXiv:1602.08383`.

[49] R. Thorne, *Phys. Rev. D* 73 (2006) 054019, `arXiv:0601245`.

[50] R. Thorne, *Phys. Rev. D* 86 (2012) 074017, `arXiv:1201.6180`.

[51] S. Alekhin, J. Blümlein and S. Moch, *Phys. Rev.* D86 (2012) 054009, `arXiv:1202.2281`.

[52] S. Alekhin, J. Blümlein, S.-O. Moch and R. Placakyte, *Phys. Rev. D* 96 (2017) 014011, `arXiv:1701.05838`.

[53] M. Klein, "Future Deep Inelastic Scattering with the LHeC," in *From My Vast Repertoire ...: Guido Altarelli's Legacy*, A. Levy, S. Forte and G. Ridolfi (eds.), p. 303. 2019. `arXiv:1802.04317`.

[54] M. Klein and V. Radescu, "Partons from the LHeC," CERN-LHeC-Note-2013-002, Jul 2013. `https://cds.cern.ch/record/1564929`.

[55] S. Bentvelsen, J. Engelen and P. Kooijman, "Reconstruction of (x, Q**2) and extraction of structure functions in neutral current scattering at HERA," in *Workshop on Physics at HERA Hamburg, Germany, October 29-30, 1991*, 1992.

[56] U. Bassler and G. Bernardi, *Nucl. Instrum. Meth.* A361 (1995) 197, `arXiv:hep-ex/9412004`.

[57] U. Bassler and G. Bernardi, *Nucl. Instrum. Meth.* 426 (1999) A583, `arXiv:hep-ex/9801017`.

[58] J. Blümlein and M. Klein, "Kinematics and resolution at future e p colliders," in *1990 DPF Summer Study on High-energy Physics: Research Directions for the Decade (Snowmass 90) Snowmass, Colorado, June 25-July 13, 1990*, 1990.

[59] R. Abdul Khalek, S. Bailey, J. Gao, L. Harland-Lang and J. Rojo, *SciPost Phys.* 7 (2019) 051, `arXiv:1906.10127`.

[60] S. J. Brodsky and G. R. Farrar, *Phys. Rev. Lett.* 31 (1973) 1153.

[61] S. J. Brodsky and G. R. Farrar, *Phys. Rev.* D11 (1975) 1309.

[62] V. A. Matveev, R. M. Muradian and A. N. Tavkhelidze, *Lett. Nuovo Cim.* 7 (1973) 719.

[63] ATLAS Collaboration, G. Aad *et al.*, *Eur. Phys. J. C* 79 (2019) 970, `arXiv:1907.05120`.

[64] H1 and ZEUS Collaborations, H. Abramowicz *et al.*, *Eur. Phys. J.* C78 (2018) 473, `arXiv:1804.01019`.

[65] J. Kuti and V. F. Weisskopf, *Phys. Rev. D* 4 (1971) 3418.

[66] T.-J. Hou *et al.*, `arXiv:1912.10053`.

[67] W. G. Seligman *et al.*, *Phys. Rev. Lett.* 79 (1997) 1213, `arXiv:hep-ex/9701017`.

[68] NuTeV Collaboration, M. Tzanov *et al.*, *Phys. Rev.* D74 (2006) 012008, `arXiv:hep-ex/0509010`.

[69] CHORUS Collaboration, G. Onengut *et al.*, *Phys. Lett.* B632 (2006) 65.

[70] J. P. Berge *et al.*, *Z. Phys.* C49 (1991) 187.

[71] NOMAD Collaboration, O. Samoylov *et al.*, *Nucl. Phys.* B876 (2013) 339, `arXiv:1308.4750`.

[72] ATLAS Collaboration, G. Aad *et al.*, *Phys. Rev. Lett.* 109 (2012) 012001, `arXiv:1203.4051`.

[73] CMS Collaboration, S. Chatrchyan *et al.*, *JHEP* 02 (2014) 013, `arXiv:1310.1138`.

[74] ATLAS Collaboration, G. Aad *et al.*, *JHEP* 05 (2014) 068, `arXiv:1402.6263`.

[75] ATLAS Collaboration, M. Aaboud *et al.*, *Eur. Phys. J.* C77 (2017) 367, `arXiv:1612.03016`.

[76] S. Alekhin, J. Blümlein and S.-O. Moch, *Phys. Lett.* B777 (2018) 134, `arXiv:1708.01067`.

[77] A. M. Cooper-Sarkar and K. Wichmann, *Phys. Rev.* D98 (2018) 014027, `arXiv:1803.00968`.

[78] S. Alekhin, J. Blumlein, S. Kulagin, S.-O. Moch and R. Petti, *PoS* DIS2018 (2018) 008, `arXiv:1808.06871`.

[79] H. Abdolmaleki *et al.*, `arXiv:1907.01014`.

[80] O. Behnke, A. Geiser and M. Lisovyi, *Prog. Part. Nucl. Phys.* 84 (2015) 1, `arXiv:1506.07519`.

[81] O. Zenaiev, *Eur. Phys. J.* C77 (2017) 151, `arXiv:1612.02371`.

[82] M. A. G. Aivazis, F. I. Olness and W.-K. Tung, *Phys. Rev. Lett.* 65 (1990) 2339.

[83] M. A. G. Aivazis, F. I. Olness and W.-K. Tung, *Phys. Rev.* D50 (1994) 3085, `arXiv:hep-ph/9312318`.

[84] M. A. G. Aivazis, J. C. Collins, F. I. Olness and W.-K. Tung, *Phys. Rev.* D50 (1994) 3102, `arXiv:hep-ph/9312319`.

[85] R. S. Thorne and R. G. Roberts, *Eur. Phys. J.* C19 (2001) 339, `arXiv:hep-ph/0010344`.

[86] S. Alekhin, J. Blümlein and S. Moch, *Phys. Rev.* D89 (2014) 054028, `arXiv:1310.3059`.

[87] S. Alekhin, J. Blümlein, S. Klein and S. Moch, *Phys. Rev.* D81 (2010) 014032, `arXiv:0908.2766`.

[88] S. Forte, E. Laenen, P. Nason and J. Rojo, *Nucl. Phys.* B834 (2010) 116, `arXiv:1001.2312`.

[89] A. D. Martin, W. J. Stirling, R. S. Thorne and G. Watt, *Eur. Phys. J.* C70 (2010) 51, `arXiv:1007.2624`.

[90] R. D. Ball, V. Bertone, F. Cerutti, L. Del Debbio, S. Forte, A. Guffanti, J. I. Latorre, J. Rojo and M. Ubiali, *Nucl. Phys.* B849 (2011) 296, `arXiv:1101.1300`.

[91] R. D. Ball, M. Bonvini and L. Rottoli, *JHEP* 11 (2015) 122, `arXiv:1510.02491`.

[92] S. Moch, B. Ruijl, T. Ueda, J. A. M. Vermaseren and A. Vogt, *JHEP* 10 (2017) 041, `arXiv:1707.08315`.

[93] F. Herzog, S.-O. Moch, B. Ruijl, T. Ueda, J. A. M. Vermaseren and A. Vogt, *Phys. Lett.* B790 (2019) 436, `arXiv:1812.11818`.

[94] G. Das, S.-O. Moch and A. Vogt, `arXiv:1912.12920`.

[95] R. D. Ball, *AIP Conf. Proc.* 1819 (2017) 030002, `arXiv:1612.03790`.

[96] M. Klein and T. Riemann, *Z. Phys.* C24 (1984) 151.

[97] A. Argento *et al.*, *Phys. Lett.* 140 (1984) B142.

[98] S. Drell and T.-M. Yan, *Phys. Rev. Lett.* 25 (1970) 316. [Erratum: *Phys. Rev. Lett.* 25 (1970) 902].

[99] J. Kubar, M. Le Bellac, J. Meunier and G. Plaut, *Nucl. Phys. B* 175 (1980) 251.

[100] A. Accardi *et al.*, *Eur. Phys. J.* A52 (2016) 268, `arXiv:1212.1701`.

[101] M. Lomnitz and S. Klein, *Phys. Rev. C* 99 (2019) 015203, `arXiv:1803.06420`.

[102] A. V. Belitsky, X.-d. Ji and F. Yuan, *Phys. Rev.* D69 (2004) 074014, `arXiv:hep-ph/0307383`.

[103] N. N. Nikolaev and B. G. Zakharov, *Z. Phys.* C49 (1991) 607.

[104] N. Nikolaev and B. G. Zakharov, *Z. Phys.* C53 (1992) 331.

[105] N. N. Nikolaev and B. G. Zakharov, *J. Exp. Theor. Phys.* 78 (1994) 598. [*Zh. Eksp. Teor. Fiz.* 105 (1994) 1117].

[106] N. N. Nikolaev, B. G. Zakharov and V. R. Zoller, *Z. Phys.* A351 (1995) 435.

[107] A. H. Müller, *Nucl. Phys.* B415 (1994) 373.

[108] A. H. Müller and B. Patel, *Nucl. Phys.* B425 (1994) 471, `arXiv:hep-ph/9403256`.

[109] U. Amaldi and K. R. Schubert, *Nucl. Phys.* B166 (1980) 301.

[110] S. Munier, A. M. Stasto and A. H. Müller, *Nucl. Phys.* B603 (2001) 427, `arXiv:hep-ph/0102291`.

[111] N. Armesto and A. H. Rezaeian, *Phys. Rev.* D90 (2014) 054003, `arXiv:1402.4831`.

[112] H. Kowalski and D. Teaney, *Phys. Rev.* D68 (2003) 114005, `arXiv:hep-ph/0304189`.

[113] H. Kowalski, L. Motyka and G. Watt, *Phys. Rev.* D74 (2006) 074016, `arXiv:hep-ph/0606272`.

[114] G. Watt and H. Kowalski, *Phys. Rev.* D78 (2008) 014016, `arXiv:0712.2670`.

[115] L. N. Lipatov, *Sov. Phys. JETP* 63 (1986) 904. [*Zh. Eksp. Teor. Fiz.* 90 (1986) 1536].

[116] Y. Hatta, B.-W. Xiao and F. Yuan, *Phys. Rev. Lett.* 116 (2016) 202301, `arXiv:1601.01585`.

[117] T. Altinoluk, N. Armesto, G. Beuf and A. H. Rezaeian, *Phys. Lett.* B758 (2016) 373, `arXiv:1511.07452`.

[118] H. Mäntysaari, N. Muller and B. Schenke, *Phys. Rev.* D99 (2019) 074004, `arXiv:1902.05087`.

[119] F. Salazar and B. Schenke, *Phys. Rev.* D100 (2019) 034007, `arXiv:1905.03763`.

[120] H. Mäntysaari and B. Schenke, *Phys. Rev. Lett.* 117 (2016) 052301, `arXiv:1603.04349`.

[121] H. Mäntysaari and B. Schenke, *Phys. Rev.* D94 (2016) 034042, `arXiv:1607.01711`.

[122] H. Mäntysaari and B. Schenke, *Phys. Lett.* B772 (2017) 832, `arXiv:1703.09256`.

[123] H. Mäntysaari and B. Schenke, *Phys. Rev.* D98 (2018) 034013, `arXiv:1806.06783`.

[124] J. Cepila, J. G. Contreras and J. D. Tapia Takaki, *Phys. Lett.* B766 (2017) 186, `arXiv:1608.07559`.

[125] D. Bendova, J. Cepila and J. G. Contreras, *Phys. Rev.* D99 (2019) 034025, `arXiv:1811.06479`.

[126] M. Krelina, V. P. Goncalves and J. Cepila, *Nucl. Phys.* A989 (2019) 187, `arXiv:1905.06759`.

[127] A. J. Baltz, *Phys. Rept.* 458 (2008) 1, `arXiv:0706.3356`.

[128] S. R. Klein, *Nucl. Phys. A* 967 (2017) 249, `arXiv:1704.04715`.

[129] G. Zweig, "An SU(3) model for strong interaction symmetry and its breaking. Version 1," 1964. CERN-TH-401.

[130] H. Fritzsch, M. Gell-Mann and H. Leutwyler, *Phys. Lett.* 47B (1973) 365.

[131] D. J. Gross and F. Wilczek, *Phys. Rev. Lett.* 30 (1973) 1343.

[132] H. D. Politzer, *Phys. Rev. Lett.* 30 (1973) 1346.

[133] G. Dissertori, *Adv. Ser. Direct. High Energy Phys.* 26 (2016) 113, `arXiv:1506.05407`.

[134] Particle Data Group, M. Tanabashi *et al.*, *Phys. Rev.* D98 (2018) 030001.

[135] D. d'Enterria *et al.*, *PoS* ALPHAS2019 (2019) 001, `arXiv:1907.01435`.

[136] K. H. Streng, T. F. Walsh and P. M. Zerwas, *Z. Phys.* C2 (1979) 237.

[137] H1 Collaboration, F. D. Aaron *et al.*, *Eur. Phys. J.* C67 (2010) 1, `arXiv:0911.5678`.

[138] S. D. Ellis and D. E. Soper, *Phys. Rev.* D48 (1993) 3160, `arXiv:hep-ph/9305266`.

[139] H1 Collaboration, C. Adloff *et al.*, *Eur. Phys. J.* C13 (2000) 397, `arXiv:hep-ex/9812024`.

[140] H1 Collaboration, C. Adloff *et al.*, *Eur. Phys. J.* C19 (2001) 289, `arXiv:hep-ex/0010054`.

[141] H1 Collaboration, C. Adloff *et al.*, *Phys. Lett.* B542 (2002) 193, `arXiv:hep-ex/0206029`.

[142] H1 Collaboration, A. Aktas *et al.*, *Eur. Phys. J.* C33 (2004) 477, `arXiv:hep-ex/0310019`.

[143] H1 Collaboration, A. Aktas *et al.*, *Eur. Phys. J.* C37 (2004) 141, `arXiv:hep-ex/0401010`.

[144] H1 Collaboration, A. Aktas *et al.*, *Phys. Lett.* B653 (2007) 134, `arXiv:0706.3722`.

[145] H1 Collaboration, F. D. Aaron *et al.*, *Eur. Phys. J.* C65 (2010) 363, `arXiv:0904.3870`.

[146] H1 Collaboration, V. Andreev *et al.*, *Eur. Phys. J.* C75 (2015) 65, `arXiv:1406.4709`.

[147] H1 Collaboration, V. Andreev *et al.*, *Eur. Phys. J.* C77 (2017) 215, `arXiv:1611.03421`.

[148] ZEUS Collaboration, J. Breitweg *et al.*, *Phys. Lett.* B479 (2000) 37, `arXiv:hep-ex/0002010`.

[149] ZEUS Collaboration, S. Chekanov *et al.*, *Eur. Phys. J.* C23 (2002) 13, `arXiv:hep-ex/0109029`.

[150] ZEUS Collaboration, S. Chekanov *et al.*, *Phys. Lett.* B547 (2002) 164, `arXiv:hep-ex/0208037`.

[151] ZEUS Collaboration, S. Chekanov *et al.*, *Eur. Phys. J.* C35 (2004) 487, `arXiv:hep-ex/0404033`.

[152] ZEUS Collaboration, S. Chekanov *et al.*, *Nucl. Phys.* B765 (2007) 1, `arXiv:hep-ex/0608048`.

[153] ZEUS Collaboration, S. Chekanov *et al.*, *Phys. Lett.* B649 (2007) 12, `arXiv:hep-ex/0701039`.

[154] ZEUS Collaboration, H. Abramowicz *et al.*, *Eur. Phys. J.* C70 (2010) 965, `arXiv:1010.6167`.

[155] ZEUS Collaboration, H. Abramowicz *et al.*, *Phys. Lett.* B691 (2010) 127, `arXiv:1003.2923`.

[156] CMS Collaboration, V. Khachatryan *et al.*, *JHEP* 03 (2017) 156, `arXiv:1609.05331`.

[157] K. Rabbertz, *Springer Tracts Mod. Phys.* 268 (2017) 1.

[158] ATLAS Collaboration, M. Aaboud *et al.*, *JHEP* 09 (2017) 020, `arXiv:1706.03192`.

[159] ATLAS Collaboration, M. Aaboud *et al.*, *JHEP* 05 (2018) 195, `arXiv:1711.02692`.

[160] J. Currie, T. Gehrmann and J. Niehues, *Phys. Rev. Lett.* 117 (2016) 042001, `arXiv:1606.03991`.

[161] J. Currie, T. Gehrmann, A. Huss and J. Niehues, *JHEP* 07 (2017) 018, `arXiv:1703.05977`.

[162] T. Gehrmann *et al.*, *PoS* RADCOR2017 (2018) 074, `arXiv:1801.06415`.

[163] J. R. Andersen *et al.*, "Les Houches 2017: Physics at TeV Colliders Standard Model Working Group Report," 2018. `arXiv:1803.07977`.

[164] S. Amoroso *et al.*, "Les Houches 2019: Physics at TeV Colliders: Standard Model Working Group Report," in *11th Les Houches Workshop on Physics at TeV Colliders: PhysTeV Les Houches*, Mar 2020. `arXiv:2003.01700`.

[165] D. Britzger *et al.*, *Eur. Phys. J.* C79 (2019) 845, `arXiv:1906.05303`.

[166] T. Carli, G. P. Salam and F. Siegert, "A Posteriori inclusion of PDFs in NLO QCD final-state calculations," in *HERA and the LHC: A Workshop on the Implications of HERA for LHC Physics, CERN, Geneva, Switzerland, October 11-13, 2004*, 2005. `arXiv:hep-ph/0510324`.

[167] T. Carli *et al.*, *Eur. Phys. J. C* 66 (2010) 503, `arXiv:0911.2985`.

[168] T. Kluge, K. Rabbertz and M. Wobisch, "FastNLO: Fast pQCD calculations for PDF fits," in *Proceedings, 14th International Workshop of deep inelastic scattering (DIS 2006), Tsukuba, Japan, April 20-24, 2006*, 2006. `arXiv:hep-ph/0609285`.

[169] D. Britzger, K. Rabbertz, F. Stober and M. Wobisch, "New features in version 2 of the fastNLO project," in *Proceedings, 20th International Workshop on Deep-Inelastic Scattering and Related Subjects (DIS 2012): Bonn, Germany, March 26-30, 2012*, 2012. `arXiv:1208.3641`.

[170] H1 Collaboration, V. Andreev *et al.*, *Eur. Phys. J.* C77 (2017) 791, `arXiv:1709.07251`.

[171] CMS Collaboration, V. Khachatryan *et al.*, *JINST* 12 (2017) P02014, `arXiv:1607.03663`.

[172] ATLAS Collaboration, M. Aaboud *et al.*, "Determination of jet calibration and energy resolution in proton-proton collisions at $\sqrt{s} = 8$ TeV using the ATLAS detector," 2019. `arXiv:1910.04482`.

[173] R. Kogler, *Measurement of jet production in deep-inelastic e p scattering at HERA*. PhD thesis, Hamburg U., 2011.

[174] J. R. Ellis, E. Gardi, M. Karliner and M. A. Samuel, *Phys. Lett.* B366 (1996) 268, `arXiv:hep-ph/9509312`.

[175] S. J. Brodsky and X.-G. Wu, *Phys. Rev.* D85 (2012) 034038, `arXiv:1111.6175`. [Erratum: *Phys. Rev.* D86 (2012) 079903].

[176] S. J. Brodsky and X.-G. Wu, *Phys. Rev. Lett.* 109 (2012) 042002, `arXiv:1203.5312`.

[177] S. J. Brodsky and L. Di Giustino, *Phys. Rev.* D86 (2012) 085026, `arXiv:1107.0338`.

[178] M. Mojaza, S. J. Brodsky and X.-G. Wu, *Phys. Rev. Lett.* 110 (2013) 192001, `arXiv:1212.0049`.

[179] S. J. Brodsky, M. Mojaza and X.-G. Wu, *Phys. Rev.* D89 (2014) 014027, `arXiv:1304.4631`.

[180] S.-Q. Wang, S. J. Brodsky, X.-G. Wu, J.-M. Shen and L. Di Giustino, *Phys. Rev.* D100 (2019) 094010, `arXiv:1908.00060`.

[181] Particle Data Group, M. Tanabashi *et al.*, "2019 Update of the Review of Particle Physics,". `http://pdg.lbl.gov/2019/`. To be published in *Prog. Theor. Exp. Phys.* 083C01 (2020).

[182] Flavour Lattice Averaging Group, S. Aoki *et al.*, arXiv:1902.08191.

[183] D. Boito, M. Golterman, K. Maltman, J. Osborne and S. Peris, *Phys. Rev.* D91 (2015) 034003, arXiv:1410.3528.

[184] Gfitter Group, M. Baak *et al.*, *Eur. Phys. J.* C74 (2014) 3046, arXiv:1407.3792.

[185] P. Azzi *et al.*, *CERN Yellow Rep. Monogr.* 7 (2019) 1, arXiv:1902.04070.

[186] I. Abt, A. M. Cooper-Sarkar, B. Foster, V. Myronenko, K. Wichmann and M. Wing, *Phys. Rev.* D96 (2017) 014001, arXiv:1704.03187. [Phys. Rev.D96,014001(2017)].

[187] J. Ablinger, J. Blümlein, S. Klein, C. Schneider and F. Wissbrock, *Nucl. Phys.* B844 (2011) 26, arXiv:1008.3347.

[188] J. Ablinger, J. Blümlein, A. De Freitas, A. Hasselhuhn, A. von Manteuffel, M. Round, C. Schneider and F. Wissbrock, *Nucl. Phys.* B882 (2014) 263, arXiv:1402.0359.

[189] J. Ablinger, A. Behring, J. Blümlein, A. De Freitas, A. von Manteuffel and C. Schneider, *Nucl. Phys.* B890 (2014) 48, arXiv:1409.1135.

[190] A. Behring, I. Bierenbaum, J. Blümlein, A. De Freitas, S. Klein and F. Wißbrock, *Eur. Phys. J.* C74 (2014) 3033, arXiv:1403.6356.

[191] J. Ablinger, J. Blümlein, A. De Freitas, C. Schneider and K. Schönwald, *Nucl. Phys.* B927 (2018) 339, arXiv:1711.06717.

[192] J. Ablinger, J. Blümlein, A. De Freitas, A. Goedicke, C. Schneider and K. Schönwald, *Nucl. Phys.* B932 (2018) 129, arXiv:1804.02226.

[193] M. Dasgupta and G. P. Salam, *J. Phys.* G30 (2004) R143, arXiv:hep-ph/0312283.

[194] H1 Collaboration, A. Aktas *et al.*, *Eur. Phys. J.* C46 (2006) 343, arXiv:hep-ex/0512014.

[195] ZEUS Collaboration, S. Chekanov *et al.*, *Nucl. Phys.* B767 (2007) 1, arXiv:hep-ex/0604032.

[196] D. Kang, C. Lee and I. W. Stewart, *Phys. Rev.* D88 (2013) 054004, arXiv:1303.6952.

[197] Z.-B. Kang, X. Liu and S. Mantry, *Phys. Rev.* D90 (2014) 014041, arXiv:1312.0301.

[198] D. Kang, C. Lee and I. W. Stewart, *PoS* DIS2015 (2015) 142.

[199] G. Abelof, R. Boughezal, X. Liu and F. Petriello, *Phys. Lett.* B763 (2016) 52, arXiv:1607.04921.

[200] S. Höche, S. Kuttimalai and Y. Li, *Phys. Rev.* D98 (2018) 114013, arXiv:1809.04192.

[201] J. Currie, T. Gehrmann, E. W. N. Glover, A. Huss, J. Niehues and A. Vogt, *JHEP* 05 (2018) 209, arXiv:1803.09973.

[202] T. Gehrmann, A. Huss, J. Mo and J. Niehues, *Eur. Phys. J. C* 79 (2019) 1022, arXiv:1909.02760.

[203] H1 Collaboration, C. Adloff *et al.*, *Eur. Phys. J.* C29 (2003) 497, arXiv:hep-ex/0302034.

[204] H1 Collaboration, A. Aktas *et al.*, *Phys. Lett.* B639 (2006) 21, arXiv:hep-ex/0603014.

[205] ZEUS Collaboration, S. Chekanov *et al.*, *Phys. Rev.* D76 (2007) 072011, arXiv:0706.3809.

[206] ZEUS Collaboration, H. Abramowicz *et al.*, *Nucl. Phys.* B864 (2012) 1, arXiv:1205.6153.

[207] M. Klasen, *Rev. Mod. Phys.* 74 (2002) 1221, arXiv:hep-ph/0206169.

[208] M. Glück, E. Reya and A. Vogt, *Phys. Rev.* D46 (1992) 1973.

[209] K. Sasaki, T. Ueda and T. Uematsu, *CERN Proc.* 1 (2018) 7.

[210] H1 and ZEUS Collaborations, H. Abramowicz *et al.*, *JHEP* 09 (2015) 149, arXiv:1503.06042.

[211] A. J. Larkoski, I. Moult and B. Nachman, arXiv:1709.04464.

[212] F. Ringer, *PoS* ALPHAS2019 (2019) 010.

[213] I. I. Balitsky and L. N. Lipatov, *Sov. J. Nucl. Phys.* 28 (1978) 822. [*Yad. Fiz.* 28 (1978) 1597].

[214] E. A. Kuraev, L. N. Lipatov and V. S. Fadin, *Sov. Phys. JETP* 45 (1977) 199. [*Zh. Eksp. Teor. Fiz.* 72 (1977) 377].

[215] V. S. Fadin and L. N. Lipatov, *Phys. Lett.* B429 (1998) 127, arXiv:hep-ph/9802290.

[216] M. Ciafaloni and G. Camici, *Phys. Lett.* B430 (1998) 349, arXiv:hep-ph/9803389.

[217] D. A. Ross, *Phys. Lett.* B431 (1998) 161, arXiv:hep-ph/9804332.

[218] Y. V. Kovchegov and A. H. Müller, *Phys. Lett.* B439 (1998) 428, arXiv:hep-ph/9805208.

[219] E. Levin, *Nucl. Phys.* B545 (1999) 481, arXiv:hep-ph/9806228.

[220] N. Armesto, J. Bartels and M. A. Braun, *Phys. Lett.* B442 (1998) 459, `arXiv:hep-ph/9808340`.

[221] J. Blümlein and A. Vogt, *Phys. Lett.* B370 (1996) 149, `arXiv:hep-ph/9510410`.

[222] J. Blümlein and A. Vogt, *Phys. Rev.* D58 (1998) 014020, `arXiv:hep-ph/9712546`.

[223] M. Ciafaloni, *Nucl. Phys.* B296 (1988) 49.

[224] B. Andersson, G. Gustafson and J. Samuelsson, *Nucl. Phys.* B467 (1996) 443.

[225] J. Kwiecinski, A. D. Martin and P. J. Sutton, *Z. Phys.* C71 (1996) 585, `arXiv:hep-ph/9602320`.

[226] R. Ellis, Z. Kunszt and E. Levin, *Nucl. Phys. B* 420 (1994) 517. [Erratum: *Nucl. Phys.* B433 (1995) 498].

[227] R. Ellis, F. Hautmann and B. Webber, *Phys. Lett.* B348 (1995) 582, `arXiv:hep-ph/9501307`.

[228] J. Kwiecinski, A. D. Martin and A. M. Stasto, *Phys. Rev.* D56 (1997) 3991, `arXiv:hep-ph/9703445`.

[229] S. Catani, M. Ciafaloni and F. Hautmann, *Phys. Lett.* B307 (1993) 147.

[230] S. Catani and F. Hautmann, *Phys. Lett.* B315 (1993) 157.

[231] S. Catani and F. Hautmann, *Nucl. Phys. B* 427 (1994) 475, `arXiv:hep-ph/9405388`.

[232] G. P. Salam, *JHEP* 07 (1998) 019, `arXiv:hep-ph/9806482`.

[233] M. Ciafaloni, D. Colferai and G. P. Salam, *JHEP* 10 (1999) 017, `arXiv:hep-ph/9907409`.

[234] M. Ciafaloni, D. Colferai and G. P. Salam, *Phys. Rev.* D60 (1999) 114036, `arXiv:hep-ph/9905566`.

[235] M. Ciafaloni, D. Colferai, G. P. Salam and A. M. Stasto, *Phys. Lett.* B576 (2003) 143, `arXiv:hep-ph/0305254`.

[236] M. Ciafaloni, D. Colferai, G. P. Salam and A. M. Stasto, *Phys. Lett.* B587 (2004) 87, `arXiv:hep-ph/0311325`.

[237] M. Ciafaloni, D. Colferai, G. P. Salam and A. M. Stasto, *Phys. Rev.* D68 (2003) 114003, `arXiv:hep-ph/0307188`.

[238] M. Ciafaloni, D. Colferai, G. P. Salam and A. M. Stasto, *JHEP* 08 (2007) 046, `arXiv:0707.1453`.

[239] G. Altarelli, R. D. Ball and S. Forte, *Nucl. Phys.* B575 (2000) 313, `arXiv:hep-ph/9911273`.

[240] G. Altarelli, R. D. Ball and S. Forte, *Nucl. Phys.* B599 (2001) 383, `arXiv:hep-ph/0011270`.

[241] G. Altarelli, R. D. Ball and S. Forte, *Nucl. Phys.* B621 (2002) 359, `arXiv:hep-ph/0109178`.

[242] G. Altarelli, R. D. Ball and S. Forte, *Nucl. Phys.* B674 (2003) 459, `arXiv:hep-ph/0306156`.

[243] G. Altarelli, R. D. Ball and S. Forte, *Nucl. Phys.* B799 (2008) 199, `arXiv:0802.0032`.

[244] R. S. Thorne, *Phys. Rev.* D64 (2001) 074005, `arXiv:hep-ph/0103210`.

[245] A. Sabio Vera, *Nucl. Phys.* B722 (2005) 65, `arXiv:hep-ph/0505128`.

[246] M. Bonvini, S. Marzani and T. Peraro, *Eur. Phys. J.* C76 (2016) 597, `arXiv:1607.02153`.

[247] V. Bertone, S. Carrazza and J. Rojo, *Comput. Phys. Commun.* 185 (2014) 1647, `arXiv:1310.1394`.

[248] M. Bonvini, S. Marzani and C. Muselli, *JHEP* 12 (2017) 117, `arXiv:1708.07510`.

[249] A. H. Müller, *Nucl. Phys.* B335 (1990) 115.

[250] R. D. Ball, V. Bertone, M. Bonvini, S. Marzani, J. Rojo and L. Rottoli, *Eur. Phys. J.* C78 (2018) 321, `arXiv:1710.05935`.

[251] H. Abdolmaleki *et al.*, *Eur. Phys. J.* C78 (2018) 621, `arXiv:1802.00064`.

[252] J. Butterworth *et al.*, *J. Phys.* G43 (2016) 023001, `arXiv:1510.03865`.

[253] S. Carrazza, S. Forte, Z. Kassabov, J. I. Latorre and J. Rojo, *Eur. Phys. J.* C75 (2015) 369, `arXiv:1505.06736`.

[254] H. Paukkunen and P. Zurita, *JHEP* 12 (2014) 100, `arXiv:1402.6623`.

[255] J. Rojo and F. Caola, "Parton distributions and small-x QCD at the Large Hadron Electron Collider," in *17th International Workshop on Deep-Inelastic Scattering and Related Subjects (DIS 2009): Madrid, Spain, April 26-30, 2009*, Berlin, Germany, 2009. `arXiv:0906.2079`.

[256] R. Abdul Khalek, S. Bailey, J. Gao, L. Harland-Lang and J. Rojo, *Eur. Phys. J.* C78 (2018) 962, `arXiv:1810.03639`.

[257] J. Bartels, K. J. Golec-Biernat and H. Kowalski, *Phys. Rev.* D66 (2002) 014001, `arXiv:hep-ph/0203258`.

[258] K. J. Golec-Biernat and S. Sapeta, *Phys. Rev.* D74 (2006) 054032, `arXiv:hep-ph/0607276`.

[259] K. J. Golec-Biernat and S. Sapeta, *JHEP* 03 (2018) 102, `arXiv:1711.11360`.

[260] J. Gao, L. Harland-Lang and J. Rojo, *Phys. Rept.* 742 (2018) 1, `arXiv:1709.04922`.

[261] V. Bertone, R. Gauld and J. Rojo, *JHEP* 01 (2019) 217, `arXiv:1808.02034`.

[262] L. N. Hand, D. G. Miller and R. Wilson, *Rev. Mod. Phys.* 35 (1963) 335.

[263] G. Miller *et al.*, *Phys. Rev.* D5 (1972) 528.

[264] E. M. Riordan *et al.*, *Phys. Rev. Lett.* 33 (1974) 561.

[265] H1 Collaboration, F. D. Aaron *et al.*, *Eur. Phys. J.* C71 (2011) 1579, `arXiv:1012.4355`.

[266] G. Altarelli and G. Martinelli, *Phys. Lett.* 76B (1978) 89.

[267] M. Glück, E. Hoffmann and E. Reya, *Z. Phys.* C13 (1982) 119.

[268] C. Ewerz and O. Nachtmann, *Annals Phys.* 322 (2007) 1670, `arXiv:hep-ph/0604087`.

[269] F. Hautmann, *Phys. Lett.* B535 (2002) 159, `arXiv:hep-ph/0203140`.

[270] S. Marzani, R. D. Ball, V. Del Duca, S. Forte and A. Vicini, *Nucl. Phys. B* 800 (2008) 127, `arXiv:0801.2544`.

[271] M. Bonvini and S. Marzani, *Phys. Rev. Lett.* 120 (2018) 202003, `arXiv:1802.07758`.

[272] H1 Collaboration, V. Andreev *et al.*, *Eur. Phys. J.* C74 (2014) 2814, `arXiv:1312.4821`.

[273] ATLAS Collaboration, G. Aad *et al.*, *Phys. Rev.* D85 (2012) 072004, `arXiv:1109.5141`.

[274] G. Altarelli, *Nuovo Cim.* C035N1 (2012) 1, `arXiv:1106.3189`.

[275] J. Blümlein and M. Klein, *Nucl. Instrum. Meth.* A329 (1993) 112.

[276] T. Gehrmann, A. Huss, J. Niehues, A. Vogt and D. Walker, *Phys. Lett.* B792 (2019) 182, `arXiv:1812.06104`.

[277] S. Catani, F. Fiorani and G. Marchesini, *Nucl. Phys.* B336 (1990) 18.

[278] G. Marchesini and B. Webber, *Nucl. Phys. B* 386 (1992) 215.

[279] F. Hautmann and H. Jung, *JHEP* 10 (2008) 113, `arXiv:0805.1049`.

[280] A. H. Mueller, *J. Phys. G* 17 (1991) 1443.

[281] J. R. Forshaw, A. Sabio Vera and B. Webber, *J. Phys. G* 25 (1999) 1511, `arXiv:hep-ph/9812318`.

[282] F. Hautmann, *Acta Phys. Polon. B* 40 (2009) 2139.

[283] J. Bartels, V. Del Duca, A. De Roeck, D. Graudenz and M. Wusthoff, *Phys. Lett. B* 384 (1996) 300, `arXiv:hep-ph/9604272`.

[284] J. Kwiecinski, A. D. Martin and A. Stasto, *Phys. Lett. B* 459 (1999) 644, `arXiv:hep-ph/9904402`.

[285] B. Andersson, G. Gustafson, H. Kharraziha and J. Samuelsson, *Z. Phys. C* 71 (1996) 613.

[286] H. Jung *et al.*, *Eur. Phys. J. C* 70 (2010) 1237, `arXiv:1008.0152`.

[287] F. Hautmann, H. Jung and S. T. Monfared, *Eur. Phys. J. C* 74 (2014) 3082, `arXiv:1407.5935`.

[288] A. van Hameren, *Comput. Phys. Commun.* 224 (2018) 371, `arXiv:1611.00680`.

[289] A. van Hameren, *PoS* DIS2019 (2019) 139.

[290] G. Chachamis and A. Sabio Vera, *Phys. Rev. D* 93 (2016) 074004, `arXiv:1511.03548`.

[291] S. Hoeche, F. Krauss and T. Teubner, *Eur. Phys. J. C* 58 (2008) 17, `arXiv:0705.4577`.

[292] J. R. Andersen, H. M. Brooks and L. Lönnblad, *JHEP* 09 (2018) 074, `arXiv:1712.00178`.

[293] ZEUS Collaboration, S. Chekanov *et al.*, *Nucl. Phys. B* 786 (2007) 152, `arXiv:0705.1931`.

[294] F. Hautmann and H. Jung, *Nucl. Phys. B* 883 (2014) 1, `arXiv:1312.7875`.

[295] F. Hautmann, H. Jung, A. Lelek, V. Radescu and R. Zlebcik, *Phys. Lett. B* 772 (2017) 446, `arXiv:1704.01757`.

[296] F. Hautmann, H. Jung, A. Lelek, V. Radescu and R. Zlebcik, *JHEP* 01 (2018) 070, `arXiv:1708.03279`.

[297] A. Bermudez Martinez, P. Connor, H. Jung, A. Lelek, R. ˘ Zleb˘ cík, F. Hautmann and V. Radescu, *Phys. Rev. D* 99 (2019) 074008, `arXiv:1804.11152`.

[298] S. Höche, F. Krauss and S. Prestel, *JHEP* 10 (2017) 093, `arXiv:1705.00982`.

[299] S. Höche and S. Prestel, *Phys. Rev. D* 96 (2017) 074017, `arXiv:1705.00742`.

[300] A. Bermudez Martinez *et al.*, *Eur. Phys. J. C* 80 (2020) 598, `arXiv:2001.06488`.

[301] NuSea Collaboration, J. Webb *et al.*, `arXiv:hep-ex/0302019`.

[302] PHENIX Collaboration, C. Aidala *et al.*, *Phys. Rev. D* 99 (2019) 072003, `arXiv:1805.02448`.

[303] R. Gandhi, C. Quigg, M. H. Reno and I. Sarcevic, *Phys. Rev.* D58 (1998) 093009, `arXiv:hep-ph/9807264`.

[304] IceCube Collaboration, M. G. Aartsen *et al.*, *JINST* 12 (2017) P03012, `arXiv:1612.05093`.

[305] J. Kwiecinski, A. D. Martin and A. M. Stasto, *Phys. Rev.* D59 (1999) 093002, `arXiv:astro-ph/9812262`.

[306] IceCube Collaboration, M. G. Aartsen *et al.*, *Nature* 551 (2017) 596, `arXiv:1711.08119`.

[307] T. K. Gaisser, *Cosmic rays and particle physics*. 1990.
`http://www.cambridge.org/uk/catalogue/catalogue.asp?isbn=0521326672`.

[308] IceCube Collaboration, M. G. Aartsen *et al.*, *Phys. Rev. Lett.* 113 (2014) 101101, `arXiv:1405.5303`.

[309] G. Gelmini, P. Gondolo and G. Varieschi, *Phys. Rev.* D61 (2000) 056011, `arXiv:hep-ph/9905377`.

[310] A. Bhattacharya, R. Enberg, Y. S. Jeong, C. S. Kim, M. H. Reno, I. Sarcevic and A. Stasto, *JHEP* 11 (2016) 167, `arXiv:1607.00193`.

[311] Pierre Auger Collaboration, A. Aab *et al.*, *Phys. Rev. D* 90 (2014) 122006, `arXiv:1409.5083`.

[312] Pierre Auger Collaboration, A. Aab *et al.*, *Phys. Rev. D* 90 (2014) 122005, `arXiv:1409.4809`.

[313] H. Drescher, A. Dumitru and M. Strikman, *Phys. Rev. Lett.* 94 (2005) 231801, `arXiv:hep-ph/0408073`.

[314] S. R. Klein and H. Mäntysaari, *Nature Rev. Phys.* 1 (2019) 662, `arXiv:1910.10858`.

[315] H1 Collaboration, C. Adloff *et al.*, *Z. Phys.* C76 (1997) 613, `arXiv:hep-ex/9708016`.

[316] ZEUS Collaboration, J. Breitweg *et al.*, *Eur. Phys. J.* C1 (1998) 81, `arXiv:hep-ex/9709021`.

[317] P. Newman and M. Wing, *Rev. Mod. Phys.* 86 (2014) 1037, `arXiv:1308.3368`.

[318] G. Ingelman and P. Schlein, *Phys. Lett.* B152 (1985) 256.

[319] W. Buchmüller, T. Gehrmann and A. Hebecker, *Nucl. Phys. B* 537 (1999) 477, `arXiv:hep-ph/9808454`.

[320] F. Hautmann, Z. Kunszt and D. Soper, *Phys. Rev. Lett.* 81 (1998) 3333, `arXiv:hep-ph/9806298`.

[321] F. Hautmann, Z. Kunszt and D. Soper, *Nucl. Phys. B* 563 (1999) 153, `arXiv:hep-ph/9906284`.

[322] S. J. Brodsky, R. Enberg, P. Hoyer and G. Ingelman, *Phys. Rev. D* 71 (2005) 074020, `arXiv:hep-ph/0409119`.

[323] G. Ingelman, R. Pasechnik and D. Werder, *Phys. Rev. D* 93 (2016) 094016, `arXiv:1511.06317`.

[324] C. O. Rasmussen and T. Sjöstrand, *JHEP* 02 (2016) 142, `arXiv:1512.05525`.

[325] J. Bjorken, *Phys. Rev. D* 47 (1993) 101.

[326] J. Bartels, J. R. Ellis, H. Kowalski and M. Wusthoff, *Eur. Phys. J. C* 7 (1999) 443, `arXiv:hep-ph/9803497`.

[327] F. Hautmann and D. Soper, *Phys. Rev. D* 63 (2001) 011501, `arXiv:hep-ph/0008224`.

[328] F. Hautmann and D. E. Soper, *Phys. Rev. D* 75 (2007) 074020, `arXiv:hep-ph/0702077`.

[329] V. N. Gribov, *Sov. Phys. JETP* 29 (1969) 483. [*Zh. Eksp. Teor. Fiz.* 56 (1969) 892].

[330] J. C. Collins, *Phys. Rev.* D57 (1998) 3051, `arXiv:hep-ph/9709499`. [Erratum: *Phys. Rev.* D61 (2000) 019902].

[331] A. Berera and D. E. Soper, *Phys. Rev.* D53 (1996) 6162, `arXiv:hep-ph/9509239`.

[332] L. Trentadue and G. Veneziano, *Phys. Lett.* B323 (1994) 201.

[333] N. Armesto, P. R. Newman, W. Slominski and A. M. Stasto, *Phys. Rev.* D100 (2019) 074022, `arXiv:1901.09076`.

[334] H. Khanpour, *Phys. Rev.* D99 (2019) 054007, `arXiv:1902.10734`.

[335] H1 Collaboration, A. Aktas *et al.*, *Eur.Phys.J.* C48 (2006) 715, `arXiv:hep-ex/0606004`.

[336] ZEUS Collaboration, S. Chekanov *et al.*, *Nucl.Phys.* B816 (2009) 1, `arXiv:0812.2003`.

[337] H1 Collaboration, F. Aaron *et al.*, *Eur.Phys.J.* C72 (2012) 2074, `arXiv:1203.4495`.

[338] H1 and ZEUS Collaborations, F. D. Aaron *et al.*, *Eur. Phys. J.* C72 (2012) 2175, `arXiv:1207.4864`.

[339] ZEUS Collaboration, S. Chekanov *et al.*, *Nucl. Phys.* B713 (2005) 3, `arXiv:hep-ex/0501060`.

[340] H1 Collaboration, A. Aktas *et al.*, *Eur. Phys. J.* C48 (2006) 749, `arXiv:hep-ex/0606003`.

[341] ZEUS Collaboration, S. Chekanov *et al.*, *Nucl.Phys.* B831 (2010) 1, `arXiv:0911.4119`.

[342] H1 Collaboration, F. Aaron *et al.*, *Eur.Phys.J.* C71 (2011) 1578, `arXiv:1010.1476`.

[343] V. N. Gribov and L. N. Lipatov, *Sov. J. Nucl. Phys.* 15 (1972) 675. [*Yad. Fiz.* 15 (1972) 1218].

[344] V. N. Gribov and L. N. Lipatov, *Sov. J. Nucl. Phys.* 15 (1972) 438. [*Yad. Fiz.* 15 (1972) 781].

[345] G. Altarelli and G. Parisi, *Nucl. Phys.* B126 (1977) 298.

[346] Y. L. Dokshitzer, *Sov. Phys. JETP* 46 (1977) 641. [*Zh. Eksp. Teor. Fiz.* 73 (1977) 1216].

[347] J. C. Collins and W.-K. Tung, *Nucl. Phys.* B278 (1986) 934.

[348] R. S. Thorne and W. K. Tung, arXiv:0809.0714.

[349] J. F. Owens, *Phys. Rev.* D30 (1984) 943.

[350] M. Glück, E. Reya and A. Vogt, *Z. Phys.* C53 (1992) 651.

[351] R. S. Thorne and R. G. Roberts, *Phys. Rev.* D57 (1998) 6871, arXiv:hep-ph/9709442.

[352] ATLAS Collaboration, G. Aad *et al.*, *Phys. Lett.* B754 (2016) 214, arXiv:1511.00502.

[353] D. Britzger, J. Currie, T. Gehrmann, A. Huss, J. Niehues and R. Žlebčík, *Eur. Phys. J.* C78 (2018) 538, arXiv:1804.05663.

[354] Z. Nagy, *Phys. Rev.* D68 (2003) 094002, arXiv:hep-ph/0307268.

[355] S. Moch, J. Vermaseren and A. Vogt, *Nucl. Phys. B* 688 (2004) 101, arXiv:hep-ph/0403192.

[356] A. Vogt, S. Moch and J. Vermaseren, *Nucl. Phys. B* 691 (2004) 129, arXiv:hep-ph/0404111.

[357] D. de Florian, G. F. Sborlini and G. Rodrigo, *JHEP* 10 (2016) 056, arXiv:1606.02887.

[358] J. Vermaseren, A. Vogt and S. Moch, *Nucl. Phys. B* 724 (2005) 3, arXiv:hep-ph/0504242.

[359] J. Ablinger, A. Behring, J. Blümlein, A. De Freitas, A. Hasselhuhn, A. von Manteuffel, M. Round, C. Schneider and F. Wißbrock, *Nucl. Phys. B* 886 (2014) 733, arXiv:1406.4654.

[360] J. Ablinger, J. Blümlein, A. De Freitas, A. Hasselhuhn, C. Schneider and F. Wißbrock, *Nucl. Phys. B* 921 (2017) 585, arXiv:1705.07030.

[361] J. Niehues and D. Walker, *Phys. Lett.* B788 (2019) 243, arXiv:1807.02529.

[362] V. Hirschi, R. Frederix, S. Frixione, M. V. Garzelli, F. Maltoni and R. Pittau, *JHEP* 05 (2011) 044, arXiv:1103.0621.

[363] F. Cascioli, P. Maierhofer and S. Pozzorini, *Phys. Rev. Lett.* 108 (2012) 111601, arXiv:1111.5206.

[364] G. Cullen *et al.*, *Eur. Phys. J. C* 74 (2014) 3001, arXiv:1404.7096.

[365] R. Frederix, S. Frixione, V. Hirschi, D. Pagani, H.-S. Shao and M. Zaro, *JHEP* 07 (2018) 185, arXiv:1804.10017.

[366] F. Buccioni, J.-N. Lang, J. M. Lindert, P. Maierhöfer, S. Pozzorini, H. Zhang and M. F. Zoller, *Eur. Phys. J. C* 79 (2019) 866, arXiv:1907.13071.

[367] J. Alwall, R. Frederix, S. Frixione, V. Hirschi, F. Maltoni, O. Mattelaer, H. S. Shao, T. Stelzer, P. Torrielli and M. Zaro, *JHEP* 07 (2014) 079, arXiv:1405.0301.

[368] J. Bellm *et al.*, *Eur. Phys. J.* C76 (2016) 196, arXiv:1512.01178.

[369] Sherpa Collaboration, E. Bothmann *et al.*, *SciPost Phys.* 7 (2019) 034, arXiv:1905.09127.

[370] M. Dasgupta and G. P. Salam, *JHEP* 08 (2002) 032, arXiv:hep-ph/0208073.

[371] S. J. Brodsky, P. Hoyer, C. Peterson and N. Sakai, *Phys. Lett.* 93B (1980) 451.

[372] S. J. Brodsky, A. Kusina, F. Lyonnet, I. Schienbein, H. Spiesberger and R. Vogt, *Adv. High Energy Phys.* 2015 (2015) 231547, arXiv:1504.06287.

[373] S. J. Brodsky and S. Gardner, *Phys. Rev. Lett.* 116 (2016) 019101, arXiv:1504.00969.

[374] G. F. de Teramond and S. J. Brodsky, *Phys. Rev. Lett.* 102 (2009) 081601, arXiv:0809.4899.

[375] SELEX Collaboration, A. Ocherashvili *et al.*, *Phys. Lett.* B628 (2005) 18, arXiv:hep-ex/0406033.

[376] ANDY Collaboration, L. C. Bland *et al.*, arXiv:1909.03124.

[377] S. J. Brodsky, G. F. de Teramond, H. G. Dosch and J. Erlich, *Phys. Rept.* 584 (2015) 1, arXiv:1407.8131.

[378] G. F. de Teramond, H. G. Dosch and S. J. Brodsky, *Phys. Rev.* D87 (2013) 075005, arXiv:1301.1651.

[379] V. de Alfaro, S. Fubini and G. Furlan, *Nuovo Cim.* A34 (1976) 569.

[380] G. Veneziano, *Nuovo Cim.* A57 (1968) 190.

[381] A. Deur, S. J. Brodsky and G. F. de Teramond, *Prog. Part. Nucl. Phys.* 90 (2016) 1, arXiv:1604.08082.

[382] G. Grunberg, *Phys. Lett.* 95B (1980) 70. [Erratum: *Phys. Lett.* B110 (1982) 501].

[383] J. D. Bjorken, *Phys. Rev.* 148 (1966) 1467.

[384] A. Deur *et al.*, *Phys. Rev. Lett.* 93 (2004) 212001, `arXiv:hep-ex/0407007`.

[385] A. Deur, Y. Prok, V. Burkert, D. Crabb, F. X. Girod, K. A. Griffioen, N. Guler, S. E. Kuhn and N. Kvaltine, *Phys. Rev.* D90 (2014) 012009, `arXiv:1405.7854`.

[386] A. Deur *et al.*, *Phys. Rev.* D78 (2008) 032001, `arXiv:0802.3198`.

[387] S. J. Brodsky and H. J. Lu, *Phys. Rev.* D51 (1995) 3652, `arXiv:hep-ph/9405218`.

[388] S. J. Brodsky, G. F. de Teramond and A. Deur, *Phys. Rev.* D81 (2010) 096010, `arXiv:1002.3948`.

[389] A. Deur, S. J. Brodsky and G. F. de Teramond, *Phys. Lett.* B750 (2015) 528, `arXiv:1409.5488`.

[390] S. J. Brodsky, G. F. de Téramond, A. Deur and H. G. Dosch, *Few Body Syst.* 56 (2015) 621, `arXiv:1410.0425`.

[391] A. Deur, V. Burkert, J.-P. Chen and W. Korsch, *Phys. Lett.* B650 (2007) 244, `arXiv:hep-ph/0509113`.

[392] A. Deur, V. Burkert, J. P. Chen and W. Korsch, *Phys. Lett.* B665 (2008) 349, `arXiv:0803.4119`.

[393] S. J. Brodsky, *J. Phys. Conf. Ser.* 1137 (2019) 012027.

[394] G. P. Lepage and S. J. Brodsky, *Phys. Lett.* 87B (1979) 359.

[395] A. V. Efremov and A. V. Radyushkin, *Phys. Lett.* 94B (1980) 245.

[396] S. J. Brodsky, G. F. De Téramond and H. G. Dosch, *Phys. Lett.* B729 (2014) 3, `arXiv:1302.4105`.

[397] S. J. Brodsky, *Few Body Syst.* 57 (2016) 703, `arXiv:1601.06328`.

[398] R. S. Sufian, G. F. de Téramond, S. J. Brodsky, A. Deur and H. G. Dosch, *Phys. Rev.* D95 (2017) 014011, `arXiv:1609.06688`.

[399] HLFHS Collaboration, G. F. de Teramond, T. Liu, R. S. Sufian, H. G. Dosch, S. J. Brodsky and A. Deur, *Phys. Rev. Lett.* 120 (2018) 182001, `arXiv:1801.09154`.

[400] T. Gutsche, V. E. Lyubovitskij, I. Schmidt and A. Vega, *Phys. Rev.* D91 (2015) 114001, `arXiv:1501.02738`.

[401] T. Gutsche, V. E. Lyubovitskij and I. Schmidt, *Phys. Rev.* D94 (2016) 116006, `arXiv:1607.04124`.

[402] H. G. Dosch, G. F. de Teramond and S. J. Brodsky, *Phys. Rev.* D91 (2015) 085016, `arXiv:1501.00959`.

[403] S. J. Brodsky, G. F. de Téramond, H. G. Dosch and C. Lorcé, *Int. J. Mod. Phys.* A31 (2016) 1630029, `arXiv:1606.04638`.

[404] M. Nielsen, S. J. Brodsky, G. F. de Téramond, H. G. Dosch, F. S. Navarra and L. Zou, *Phys. Rev.* D98 (2018) 034002, `arXiv:1805.11567`.

[405] G. F. de Teramond, H. G. Dosch and S. J. Brodsky, *Phys. Rev.* D91 (2015) 045040, `arXiv:1411.5243`.

[406] S. L. Glashow, *Nucl. Phys.* 22 (1961) 579.

[407] S. Weinberg, *Phys. Rev. Lett.* 27 (1971) 1688.

[408] S. Weinberg, *Phys. Rev.* D5 (1972) 1412.

[409] A. Salam and J. C. Ward, *Phys. Lett.* 13 (1964) 168.

[410] P. W. Higgs, *Phys. Lett.* 12 (1964) 132.

[411] P. W. Higgs, *Phys. Rev. Lett.* 13 (1964) 508.

[412] F. Englert and R. Brout, *Phys. Rev. Lett.* 13 (1964) 321.

[413] H1 Collaboration, A. Aktas *et al.*, *Phys. Lett.* B632 (2006) 35, `arXiv:hep-ex/0507080`.

[414] ZEUS Collaboration, H. Abramowicz *et al.*, *Phys. Rev.* D93 (2016) 092002, `arXiv:1603.09628`.

[415] H1 Collaboration, V. Andreev *et al.*, *Eur. Phys. J.* C78 (2018) 777, `arXiv:1806.01176`.

[416] D. Britzger, M. Klein and H. Spiesberger, `arXiv:2007.11799`.

[417] M. Böhm and H. Spiesberger, *Nucl. Phys.* B294 (1987) 1081.

[418] D. Yu. Bardin, C. Burdik, P. C. Khristova and T. Riemann, *Z. Phys.* C42 (1989) 679.

[419] Hollik, W. and Bardin, D. Yu. and Blümlein, J. and Kniehl, B. A. and Riemann, T. and Spiesberger, H., "Electroweak parameters at HERA: Theoretical aspects," in *Workshop on physics at HERA Hamburg, Germany, October 29-30, 1991*, 1992.

[420] M. Böhm and H. Spiesberger, *Nucl. Phys.* B304 (1988) 749.

[421] D. Yu. Bardin, K. C. Burdik, P. K. Khristova and T. Riemann, *Z. Phys.* C44 (1989) 149.

[422] A. Sirlin, *Phys. Rev.* D22 (1980) 971.

[423] M. Böhm, H. Spiesberger and W. Hollik, *Fortsch. Phys.* 34 (1986) 687.

[424] W. F. L. Hollik, *Fortsch. Phys.* 38 (1990) 165.

[425] H1 Collaboration, F. D. Aaron *et al.*, *JHEP* 09 (2012) 061, `arXiv:1206.7007`.

[426] D. Britzger and M. Klein, *PoS* DIS2017 (2018) 105.

[427] H. Spiesberger, "EPRC: A program package for electroweak physics at HERA," in *Future physics at HERA. Proceedings, Workshop, Hamburg, Germany, September 25, 1995-May 31, 1996. Vol. 1, 2*, 1995.

[428] G. Cowan, K. Cranmer, E. Gross and O. Vitells, *Eur. Phys. J.* C71 (2011) 1554, `arXiv:1007.1727`. [Erratum: *Eur. Phys. J.* C73 (2013) 2501].

[429] CDF and D0 Collaborations, "2012 Update of the Combination of CDF and D0 Results for the Mass of the W Boson," 2012. `arXiv:1204.0042`.

[430] ALEPH, DELPHI, L3, OPAL, LEP Electroweak Collaboration, S. Schael *et al.*, *Phys. Rept.* 532 (2013) 119, `arXiv:1302.3415`.

[431] ATLAS Collaboration, M. Aaboud *et al.*, *Eur. Phys. J.* C78 (2018) 110, `arXiv:1701.07240`. [Erratum: *Eur. Phys. J.* C78 (2018) 898].

[432] J. de Blas, M. Ciuchini, E. Franco, S. Mishima, M. Pierini, L. Reina and L. Silvestrini, *JHEP* 12 (2016) 135, `arXiv:1608.01509`.

[433] J. Haller, A. Höcker, R. Kogler, K. Mönig, T. Peiffer and J. Stelzer, *Eur. Phys. J.* C78 (2018) 675, `arXiv:1803.01853`.

[434] MuLan Collaboration, V. Tishchenko *et al.*, *Phys. Rev.* D87 (2013) 052003, `arXiv:1211.0960`.

[435] M. Schott, "Global EW fits: experimental and theoretical issues," Talk presented at the Ultimate Precision at Hadron Colliders, Sarclay, France, 2019.

[436] ALEPH, DELPHI, L3, OPAL, SLD Collaborations, LEP Electroweak Working Group, SLD Electroweak Heavy Flavour Groups, S. Schael *et al.*, *Phys. Rept.* 427 (2006) 257, `arXiv:hep-ex/0509008`.

[437] D0 Collaboration, V. M. Abazov *et al.*, *Phys. Rev.* D84 (2011) 012007, `arXiv:1104.4590`.

[438] CDF and D0 Collaborations, T. A. Aaltonen *et al.*, *Phys. Rev.* D97 (2018) 112007, `arXiv:1801.06283`.

[439] LHCb Collaboration, R. Aaij *et al.*, *JHEP* 11 (2015) 190, `arXiv:1509.07645`.

[440] ATLAS Collaboration, "Measurement of the effective leptonic weak mixing angle using electron and muon pairs from Z-boson decay in the ATLAS experiment at $\sqrt{s} = 8$ TeV," 2018. ATLAS-CONF-2018-037.

[441] CMS Collaboration, A. M. Sirunyan *et al.*, *Eur. Phys. J.* C78 (2018) 701, `arXiv:1806.00863`.

[442] J. Erler, "Global fits of the SM parameters," in *7th Large Hadron Collider Physics Conference (LHCP 2019) Puebla, Puebla, Mexico, May 20-25, 2019*, 2019. `arXiv:1908.07327`.

[443] J. Erler and M. Schott, *Prog. Part. Nucl. Phys.* 106 (2019) 68, `arXiv:1902.05142`.

[444] E. Accomando *et al.*, *JHEP* 10 (2019) 176, `arXiv:1907.07727`.

[445] E. Accomando, J. Fiaschi, F. Hautmann and S. Moretti, *Eur. Phys. J. C* 78 (2018) 663, `arXiv:1805.09239`. [Erratum: *Eur.Phys.J.* C79 (2019) 453].

[446] E. Accomando, J. Fiaschi, F. Hautmann and S. Moretti, *Phys. Rev. D* 98 (2018) 013003, `arXiv:1712.06318`. [Erratum: *Phys. Rev.* D99 (2019) 079902].

[447] ZEUS Collaboration, S. Chekanov *et al.*, *Phys. Lett.* B672 (2009) 106, `arXiv:0807.0589`.

[448] H1 Collaboration, F. D. Aaron *et al.*, *Eur. Phys. J.* C64 (2009) 251, `arXiv:0901.0488`.

[449] H1 and ZEUS Collaborations, F. D. Aaron *et al.*, *JHEP* 03 (2010) 035, `arXiv:0911.0858`.

[450] U. Baur and D. Zeppenfeld, *Nucl. Phys.* B325 (1989) 253.

[451] U. Baur, B. A. Kniehl, J. A. M. Vermaseren and D. Zeppenfeld, "Single W and Z production at LEP / LHC," in *ECFA Large Hadron Collider Workshop, Aachen, Germany, 4-9 Oct 1990: Proceedings.2.*, 1990.

[452] U. Baur, J. A. M. Vermaseren and D. Zeppenfeld, *Nucl. Phys.* B375 (1992) 3.

[453] NNPDF Collaboration, R. D. Ball *et al.*, *Nucl. Phys.* B877 (2013) 290, `arXiv:1308.0598`.

[454] K. Hagiwara, S. Ishihara, R. Szalapski and D. Zeppenfeld, *Phys. Rev.* D48 (1993) 2182.

[455] K. Hagiwara, S. Ishihara, R. Szalapski and D. Zeppenfeld, *Phys. Lett.* B283 (1992) 353.

[456] A. De Rujula, M. B. Gavela, P. Hernandez and E. Masso, *Nucl. Phys.* B384 (1992) 3.

[457] S. S. Biswal, M. Patra and S. Raychaudhuri, `arXiv:1405.6056`.

[458] I. T. Cakir, O. Cakir, A. Senol and A. T. Tasci, *Acta Phys. Polon.* B45 (2014) 1947, `arXiv:1406.7696`.

[459] R. Li, X.-M. Shen, K. Wang, T. Xu, L. Zhang and G. Zhu, *Phys. Rev.* D97 (2018) 075043, `arXiv:1711.05607`.

[460] M. Köksal, A. A. Billur, A. Gutiérrez-Rodríguez and M. A. Hernández-Ruíz, `arXiv:1910.06747`.

[461] A. Gutiérrez-Rodríguez, M. Köksal, A. A. Billur and M. A. Hernández-Ruíz, `arXiv:1910.02307`.

[462] CMS Collaboration, A. M. Sirunyan *et al.*, *Phys. Lett.* B772 (2017) 21, `arXiv:1703.06095`.

[463] CMS Collaboration, A. M. Sirunyan *et al.*, `arXiv:1907.08354`.

[464] S. Villa, *Nucl. Phys. Proc. Suppl.* 142 (2005) 391, `arXiv:hep-ph/0410208`.

[465] S. Dutta, A. Goyal, M. Kumar and B. Mellado, *Eur. Phys. J.* C75 (2015) 577, `arXiv:1307.1688`.

[466] A. O. Bouzas and F. Larios, *Phys. Rev.* D88 (2013) 094007, `arXiv:1308.5634`.

[467] S. Ovyn, X. Rouby and V. Lemaitre, "DELPHES, a framework for fast simulation of a generic collider experiment," 2009. `arXiv:0903.2225`.

[468] CMS Collaboration, V. Khachatryan *et al.*, *JHEP* 06 (2014) 090, `arXiv:1403.7366`.

[469] I. A. Sarmiento-Alvarado, A. O. Bouzas and F. Larios, *J. Phys.* G42 (2015) 085001, `arXiv:1412.6679`.

[470] H. Sun, *PoS* DIS2018 (2018) 167.

[471] CMS Collaboration, V. Khachatryan *et al.*, *Phys. Lett.* B736 (2014) 33, `arXiv:1404.2292`.

[472] J. A. Aguilar-Saavedra, *Acta Phys. Polon.* B35 (2004) 2695, `arXiv:hep-ph/0409342`.

[473] J. Charles *et al.*, *Phys. Rev.* D91 (2015) 073007, `arXiv:1501.05013`.

[474] S. Atag and B. Sahin, *Phys. Rev.* D73 (2006) 074001.

[475] A. O. Bouzas and F. Larios, *Phys. Rev. D* 87 (2013) 074015, `arXiv:1212.6575`.

[476] B. Coleppa, M. Kumar, S. Kumar and B. Mellado, *Phys. Lett.* B770 (2017) 335, `arXiv:1702.03426`.

[477] NNPDF Collaboration, R. D. Ball *et al.*, *Eur. Phys. J. C* 77 (2017) 663, `arXiv:1706.00428`.

[478] F. Demartin, S. Forte, E. Mariani, J. Rojo and A. Vicini, *Phys. Rev. D* 82 (2010) 014002, `arXiv:1004.0962`.

[479] I. Turk Cakir, A. Yilmaz, H. Denizli, A. Senol, H. Karadeniz and O. Cakir, *Adv. High Energy Phys.* 2017 (2017) 1572053, `arXiv:1705.05419`.

[480] O. Cakir, A. Yilmaz, I. Turk Cakir, A. Senol and H. Denizli, *Nucl. Phys.* B944 (2019) 114640, `arXiv:1809.01923`.

[481] J. A. Aguilar-Saavedra and T. Riemann, "Probing top flavor changing neutral couplings at TESLA," in *5th Workshop of the 2nd ECFA, Obernai, France, October 16-19, 1999*, 2001. `arXiv:hep-ph/0102197`.

[482] Top Quark Working Group, K. Agashe *et al.*, "Working Group Report: Top Quark," in *Community Summer Study on the Future of U.S. Particle Physics: Minneapolis, MN, USA, July 29-August 6, 2013*, 2013. `arXiv:1311.2028`.

[483] S. Behera, R. Islam, M. Kumar, P. Poulose and R. Rahaman, *Phys. Rev. D* 100 (2019) 015006, `arXiv:1811.04681`.

[484] H. Sun and X. Wang, *Eur. Phys. J.* C78 (2018) 281, `arXiv:1602.04670`.

[485] European Muon Collaboration, J. J. Aubert *et al.*, *Phys. Lett.* 123B (1983) 275.

[486] J. Gomez *et al.*, *Phys. Rev.* D49 (1994) 4348.

[487] New Muon Collaboration, P. Amaudruz *et al.*, *Nucl. Phys.* B441 (1995) 3, `arXiv:hep-ph/9503291`.

[488] New Muon Collaboration, M. Arneodo *et al.*, *Nucl. Phys.* B441 (1995) 12, `arXiv:hep-ex/9504002`.

[489] New Muon Collaboration, M. Arneodo *et al.*, *Nucl. Phys.* B481 (1996) 3.

[490] European Muon Collaboration, J. Ashman *et al.*, *Z. Phys.* C57 (1993) 211.

[491] New Muon Collaboration, M. Arneodo *et al.*, *Nucl. Phys.* B481 (1996) 23.

[492] New Muon Collaboration, P. Amaudruz *et al.*, *Nucl. Phys.* B371 (1992) 3.

[493] M. Arneodo, *Phys. Rept.* 240 (1994) 301.

[494] D. F. Geesaman, K. Saito and A. W. Thomas, *Ann. Rev. Nucl. Part. Sci.* 45 (1995) 337.

[495] K. J. Eskola, P. Paakkinen, H. Paukkunen and C. A. Salgado, *Eur. Phys. J.* C77 (2017) 163, `arXiv:1612.05741`.

[496] C. A. Salgado *et al.*, *J. Phys.* G39 (2012) 015010, `arXiv:1105.3919`.

[497] K. J. Golec-Biernat and M. Wusthoff, *Phys. Rev.* D59 (1998) 014017, `arXiv:hep-ph/9807513`.

[498] L. Frankfurt, V. Guzey and M. Strikman, *Phys. Rept.* 512 (2012) 255, `arXiv:1106.2091`.

[499] F. Gelis, E. Iancu, J. Jalilian-Marian and R. Venugopalan, *Ann. Rev. Nucl. Part. Sci.* 60 (2010) 463, `arXiv:1002.0333`.

[500] Y. V. Kovchegov and E. Levin, *Camb. Monogr. Part. Phys. Nucl. Phys. Cosmol.* 33 (2012) 1.

[501] Z. Citron *et al.*, "Future physics opportunities for high-density QCD at the LHC with heavy-ion and proton beams," in *HL/HE-LHC Workshop: Workshop on the Physics of HL-LHC, and Perspectives at HE-LHC Geneva, Switzerland, June 18-20, 2018*, 2018. `arXiv:1812.06772`.

[502] B. L. Ioffe, V. S. Fadin and L. N. Lipatov, *Quantum chromodynamics: Perturbative and nonperturbative aspects*, vol. 30. Cambridge Univ. Press, 2010.

[503] J. Collins, *Foundations of perturbative QCD*, vol. 32. Cambridge University Press, Nov 2013.

[504] H. Paukkunen, *Nucl. Phys.* A967 (2017) 241, `arXiv:1704.04036`.

[505] H. Paukkunen, *PoS* HardProbes2018 (2018) 014, `arXiv:1811.01976`.

[506] K. J. Eskola, H. Paukkunen and C. A. Salgado, *JHEP* 04 (2009) 065, `arXiv:0902.4154`.

[507] D. de Florian, R. Sassot, P. Zurita and M. Stratmann, *Phys. Rev.* D85 (2012) 074028, `arXiv:1112.6324`.

[508] K. Kovarik *et al.*, *Phys. Rev.* D93 (2016) 085037, `arXiv:1509.00792`.

[509] H. Khanpour and S. Atashbar Tehrani, *Phys. Rev.* D93 (2016) 014026, `arXiv:1601.00939`.

[510] NNPDF Collaboration, R. Abdul Khalek, J. J. Ethier and J. Rojo, *Eur. Phys. J.* C79 (2019) 471, `arXiv:1904.00018`.

[511] H. Paukkunen and C. A. Salgado, *JHEP* 07 (2010) 032, `arXiv:1004.3140`.

[512] K. Kovarik, I. Schienbein, F. I. Olness *et al.*, *Phys. Rev. Lett.* 106 (2011) 122301, `arXiv:1012.0286`.

[513] H. Paukkunen and C. A. Salgado, *Phys. Rev. Lett.* 110 (2013) 212301, `arXiv:1302.2001`.

[514] N. Armesto, *J. Phys.* G32 (2006) R367, `arXiv:hep-ph/0604108`.

[515] K. J. Eskola, P. Paakkinen and H. Paukkunen, *Eur. Phys. J.* C79 (2019) 511, `arXiv:1903.09832`.

[516] N. Armesto, H. Paukkunen, J. M. Penín, C. A. Salgado and P. Zurita, *Eur. Phys. J.* C76 (2016) 218, `arXiv:1512.01528`.

[517] A. Kusina, F. Lyonnet, D. B. Clark, E. Godat *et al.*, *Eur. Phys. J.* C77 (2017) 488, `arXiv:1610.02925`.

[518] N. Armesto, A. Capella, A. B. Kaidalov, J. Lopez-Albacete and C. A. Salgado, *Eur. Phys. J.* C29 (2003) 531, `arXiv:hep-ph/0304119`.

[519] N. Armesto, A. B. Kaidalov, C. A. Salgado and K. Tywoniuk, *Eur. Phys. J.* C68 (2010) 447, `arXiv:1003.2947`.

[520] M. Krelina and J. Nemchik, `arXiv:2003.04156`.

[521] S. J. Brodsky, I. Schmidt and J.-J. Yang, *Phys. Rev.* D70 (2004) 116003, `arXiv:hep-ph/0409279`.

[522] M. Klein, *EPJ Web Conf.* 112 (2016) 03002.

[523] LHeC Study Group, H. Paukkunen, *PoS* DIS2017 (2018) 109, `arXiv:1709.08342`.

[524] E. C. Aschenauer, S. Fazio, M. A. C. Lamont, H. Paukkunen and P. Zurita, *Phys. Rev.* D96 (2017) 114005, `arXiv:1708.05654`.

[525] LHCb Collaboration, R. Aaij *et al.*, *JHEP* 10 (2017) 090, `arXiv:1707.02750`.

[526] LHCb Collaboration, R. Aaij *et al.*, *Phys. Rev.* D99 (2019) 052011, `arXiv:1902.05599`.

[527] K. J. Eskola, I. Helenius, P. Paakkinen and H. Paukkunen, *JHEP* 05 (2020) 037, `arXiv:1906.02512`.

[528] I. Helenius, K. J. Eskola and H. Paukkunen, *JHEP* 09 (2014) 138, `arXiv:1406.1689`.

[529] J. Pumplin, D. Stump, R. Brock *et al.*, *Phys. Rev.* D65 (2001) 014013, `arXiv:hep-ph/0101032`.

[530] N. Armesto, "Nuclear pdfs." 2nd FCC Physics Workshop (CERN, January 15th-19th 2018), 2018.

[531] N. Armesto, *PoS* HardProbes2018 (2019) 123.

[532] HERAFitter Group, S. Alekhin *et al.*, *Eur. Phys. J.* C75 (2015) 304, `arXiv:1410.4412`.

361

[533] T. Lappi and H. Mäntysaari, *Phys. Rev.* C87 (2013) 032201, `arXiv:1301.4095`.

[534] STAR Collaboration, L. Adamczyk *et al.*, *Phys. Rev. C* 96 (2017) 054904, `arXiv:1702.07705`.

[535] T. Toll and T. Ullrich, *Phys. Rev. C* 87 (2013) 024913, `arXiv:1211.3048`.

[536] H. Mäntysaari, `arXiv:2001.10705`.

[537] V. N. Gribov and A. A. Migdal, *Sov. J. Nucl. Phys.* 8 (1969) 583. [*Yad. Fiz.* 8 (1968) 1002].

[538] L. L. Frankfurt, G. A. Miller and M. Strikman, *Ann. Rev. Nucl. Part. Sci.* 44 (1994) 501, `arXiv:hep-ph/9407274`.

[539] C. Marquet, M. R. Moldes and P. Zurita, *Phys. Lett.* B772 (2017) 607, `arXiv:1702.00839`.

[540] L. L. Frankfurt and M. I. Strikman, *Phys. Lett.* B382 (1996) 6.

[541] H. Kowalski, T. Lappi, C. Marquet and R. Venugopalan, *Phys. Rev.* C78 (2008) 045201, `arXiv:0805.4071`.

[542] A. H. Müller and H. Navelet, *Nucl. Phys.* B282 (1987) 727.

[543] M. Deak, F. Hautmann, H. Jung and K. Kutak, *Eur. Phys. J.* C72 (2012) 1982, `arXiv:1112.6354`.

[544] J. L. Albacete and C. Marquet, *Phys. Rev. Lett.* 105 (2010) 162301, `arXiv:1005.4065`.

[545] T. Lappi and H. Mäntysaari, *Nucl. Phys.* A908 (2013) 51, `arXiv:1209.2853`.

[546] A. Stasto, S.-Y. Wei, B.-W. Xiao and F. Yuan, *Phys. Lett.* B784 (2018) 301, `arXiv:1805.05712`.

[547] A. van Hameren, P. Kotko, K. Kutak, C. Marquet, E. Petreska and S. Sapeta, *JHEP* 12 (2016) 034, `arXiv:1607.03121`. [Erratum: *JHEP* 02 (2019) 158].

[548] CMS Collaboration, V. Khachatryan *et al.*, *JHEP* 09 (2010) 091, `arXiv:1009.4122`.

[549] S. Schlichting and P. Tribedy, *Adv. High Energy Phys.* 2016 (2016) 8460349, `arXiv:1611.00329`.

[550] C. Loizides, *Nucl. Phys.* A956 (2016) 200, `arXiv:1602.09138`.

[551] B. Schenke, *Nucl. Phys.* A967 (2017) 105, `arXiv:1704.03914`.

[552] P. Romatschke, *Eur. Phys. J.* C77 (2017) 21, `arXiv:1609.02820`.

[553] ATLAS Collaboration, "Two-particle azimuthal correlations in photo-nuclear ultra-peripheral Pb+Pb collisions at 5.02 TeV with ATLAS," ATLAS-CONF-2019-022, 2019.

[554] A. Badea, A. Baty, P. Chang, G. M. Innocenti, M. Maggi, C. Mcginn, M. Peters, T.-A. Sheng, J. Thaler and Y.-J. Lee, *Phys. Rev. Lett.* 123 (2019) 212002, `arXiv:1906.00489`.

[555] ZEUS Collaboration, "Two-particle azimuthal correlations as a probe of collective behaviour in deep inelastic *ep* scattering at HERA," 2019. `arXiv:1912.07431`.

[556] CMS Collaboration, S. Chatrchyan *et al.*, *Phys. Lett.* B724 (2013) 213, `arXiv:1305.0609`.

[557] CMS Collaboration, V. Khachatryan *et al.*, *Phys. Lett.* B765 (2017) 193, `arXiv:1606.06198`.

[558] S. D. Glazek, S. J. Brodsky, A. S. Goldhaber and R. W. Brown, *Phys. Rev.* D97 (2018) 114021, `arXiv:1805.08847`.

[559] J. D. Bjorken, S. J. Brodsky and A. Scharff Goldhaber, *Phys. Lett.* B726 (2013) 344, `arXiv:1308.1435`.

[560] S. J. Brodsky, H.-C. Pauli and S. S. Pinsky, *Phys. Rept.* 301 (1998) 299, `arXiv:hep-ph/9705477`.

[561] P. A. M. Dirac, *Rev. Mod. Phys.* 21 (1949) 392.

[562] D. Ashery, *Nucl. Phys. Proc. Suppl.* 161 (2006) 8, `arXiv:hep-ex/0511052`.

[563] G. Bertsch, S. J. Brodsky, A. S. Goldhaber and J. F. Gunion, *Phys. Rev. Lett.* 47 (1981) 297.

[564] L. Frankfurt, G. A. Miller and M. Strikman, *Phys. Rev.* D65 (2002) 094015, `arXiv:hep-ph/0010297`.

[565] S. J. Brodsky, C.-R. Ji and G. P. Lepage, *Phys. Rev. Lett.* 51 (1983) 83.

[566] S. J. Brodsky and A. H. Müller, *Phys. Lett.* B206 (1988) 685.

[567] S. J. Brodsky, I. A. Schmidt and G. F. de Teramond, *Phys. Rev. Lett.* 64 (1990) 1011.

[568] S. J. Brodsky and H. J. Lu, *Phys. Rev. Lett.* 64 (1990) 1342.

[569] S. J. Brodsky, I. Schmidt and S. Liuti, `arXiv:1908.06317`.

[570] ATLAS Collaboration, G. Aad *et al.*, *Phys. Lett.* B716 (2012) 1, `arXiv:1207.7214`.

[571] CMS Collaboration, S. Chatrchyan *et al.*, *Phys. Lett.* B716 (2012) 30, `arXiv:1207.7235`.

[572] G. S. Guralnik, C. R. Hagen and T. W. B. Kibble, *Phys. Rev. Lett.* 13 (1964) 585. [,162(1964)].

[573] A. A. Migdal and A. M. Polyakov, *Sov. Phys. JETP* 24 (1967) 91. [*Zh. Eksp. Teor. Fiz.* 51 (1966) 135].

[574] S. Gori, C. Grojean, A. Juste and A. Paul, *JHEP* 01 (2018) 108, `arXiv:1710.03752`.

[575] T. Cohen, N. Craig, G. F. Giudice and M. McCullough, *JHEP* 05 (2018) 091, `arXiv:1803.03647`.

[576] J. Blümlein, G. J. van Oldenborgh and R. Rückl, *Nucl. Phys.* B395 (1993) 35, `arXiv:hep-ph/9209219`.

[577] J. Pumplin, D. R. Stump, J. Huston, H. L. Lai, P. M. Nadolsky and W. K. Tung, *JHEP* 07 (2002) 012, `arXiv:hep-ph/0201195`.

[578] M. Kumar, X. Ruan, R. Islam, A. S. Cornell, M. Klein, U. Klein and B. Mellado, *Phys. Lett.* B764 (2017) 247, `arXiv:1509.04016`.

[579] E. by M. Benedikt et al., .

[580] LHC Higgs Cross Section Working Group, D. de Florian *et al.*, `arXiv:1610.07922`.

[581] D. M. Asner *et al.*, "ILC Higgs White Paper," in *Proceedings, 2013 Community Summer Study on the Future of U.S. Particle Physics: Snowmass on the Mississippi (CSS2013): Minneapolis, MN, USA, July 29-August 6, 2013*, 2013. `arXiv:1310.0763`.
`http://www.slac.stanford.edu/econf/C1307292/docs/submittedArxivFiles/1310.0763.pdf`.

[582] H. Abramowicz *et al.*, *Eur. Phys. J.* C77 (2017) 475, `arXiv:1608.07538`.

[583] Higgs Cross Section Working Group, *https://twiki.cern.ch/twiki/bin/view/ LHCPhysics/CERNYellowReportPageBR* .

[584] T. Han and B. Mellado, *Phys. Rev.* D82 (2010) 016009, `arXiv:0909.2460`.

[585] M. Tanaka, "Study of the higgs measurements at the lhec," in *Bachelor of Science Thesis, Tokyo Institute of Technology, and Talk at DIS Workshop 2017*, 2014.
`https://indico.cern.ch/event/568360/contributions/2523555/`.

[586] E. Kay, "Higgs Studies at a High Luminosity LHeC," in *Master Thesis, University of Liverpool*, 2014.

[587] U. Klein, *Poster at 37th International Conference on High Energy Physics (ICHEP), Valencia* (2014) .
`https://indico.ific.uv.es/event/2025/contributions/937/`.

[588] U. Klein, *Talk at LHeC Workshop, CERN and Chavannes-de-Bogis* (2015) .
`https://indico.cern.ch/event/356714/contributions/844946/`.

[589] D. Hampson, "Precision Higgs coupling measurements at a high luminosity LHeC," in *Master Thesis, University of Liverpool*, 2016.

[590] I. Harris, "Finding higgs to charm decays in electron-proton collisions," in *Bachelor of Science Theses, University of Liverpool*, 2017.

[591] ATLAS Collaboration, M. Aaboud *et al.*, *Phys. Lett.* B786 (2018) 59, `arXiv:1808.08238`.

[592] CMS Collaboration, A. M. Sirunyan *et al.*, *Phys. Rev. Lett.* 121 (2018) 121801, `arXiv:1808.08242`.

[593] ATLAS and CMS Collaborations, *CERN Yellow Rep. Monogr.* 7 (2019) Addendum, `arXiv:1902.10229`.

[594] T. Sjöstrand, S. Mrenna and P. Skands, *JHEP* 05 (2006) .

[595] U. Klein, *Talk at Workshop on the LHeC, Chavannes-de-Bogis* (2014) .
`https://indico.cern.ch/event/278903/contributions/631181`.

[596] J. de Favereau, C. Delaere, P. Demin, A. Giammanco, V. Lematre, A. Mertens and M. Selvaggi, *Journal of High Energy Physics* 02 (2014) .

[597] A. Höcker *et al.*, "TMVA - Toolkit for Multivariate Data Analysis," CERN-OPEN-2007-007, 2007.
`arXiv:physics/0703039`.

[598] S. Greder, *b quark tagging and cross-section measurement in quark pair production at D0*. PhD thesis, Louis Pasteur U., Strasbourg I, 2004.

[599] Y. Banda, T. Lastovicka and A. Nomerotski, "Measurement of the Higgs boson decay branching ratio to charm quarks at the ILC," 2009. `arXiv:0909.1052`.

[600] ATLAS Collaboration, G. Aad *et al.*, *Phys. Rev.* D100 (2019) 032007, `arXiv:1905.07714`.

[601] ATLAS Collaboration, M. Aaboud *et al.*, *Eur. Phys. J.* C77 (2017) 361, `arXiv:1702.05725`.

[602] C. Englert, R. Kogler, H. Schulz and M. Spannowsky, *Eur. Phys. J.* C76 (2016) 393, `arXiv:1511.05170`.

[603] LHC Higgs Cross Section Working Group Collaboration, S. Dittmaier *et al.*, `arXiv:1101.0593`.

[604] T. Barklow, K. Fujii, S. Jung, R. Karl, J. List, T. Ogawa, M. E. Peskin and J. Tian, *Phys. Rev.* D97 (2018) 053003, `arXiv:1708.08912`.

[605] M. Trott, *Invited Talk at the LHeC Workshop, Chavannes* (2014) .
`https://indico.cern.ch/event/278903/contributions/631177/`.

[606] S. D. Rindani, P. Sharma and A. Shivaji, *Phys. Lett.* B761 (2016) 25, `arXiv:1605.03806`.

[607] S. S. Biswal, R. M. Godbole, B. Mellado and S. Raychaudhuri, *Phys. Rev. Lett.* 109 (2012) 261801, `arXiv:1203.6285`.

[608] A. Alloul, N. D. Christensen, C. Degrande, C. Duhr and B. Fuks, *Comput. Phys. Commun.* 185 (2014) 2250, `arXiv:1310.1921`.

[609] R. D. Ball *et al.*, *Nucl. Phys.* B867 (2013) 244, `arXiv:1207.1303`.

[610] Y.-L. Tang, C. Zhang and S.-h. Zhu, *Phys. Rev.* D94 (2016) 011702, `arXiv:1508.01095`.

[611] C. Bernaciak, T. Plehn, P. Schichtel and J. Tattersall, *Phys. Rev.* D91 (2015) 035024, `arXiv:1411.7699`.

[612] R. J. Cashmore *et al.*, *Phys. Rept.* 122 (1985) 275.

[613] S. Buddenbrock, A. S. Cornell, Y. Fang, A. Fadol Mohammed, M. Kumar, B. Mellado and K. G. Tomiwa, *JHEP* 10 (2019) 157, `arXiv:1901.05300`.

[614] W. Liu, H. Sun, X. Wang and X. Luo, *Phys. Rev.* D92 (2015) 074015, `arXiv:1507.03264`.

[615] X. Wang, H. Sun and X. Luo, *Adv. High Energy Phys.* 2017 (2017) 4693213, `arXiv:1703.02691`.

[616] ATLAS Collaboration, M. Aaboud *et al.*, *Phys. Rev.* D98 (2018) 032002, `arXiv:1805.03483`.

[617] CMS Collaboration, V. Khachatryan *et al.*, *JHEP* 02 (2017) 079, `arXiv:1610.04857`.

[618] J. Hernandez-Sanchez, O. Flores-Sanchez, C. G. Honorato, S. Moretti and S. Rosado, *PoS* CHARGED2016 (2017) 032, `arXiv:1612.06316`.

[619] CMS Collaboration, A. M. Sirunyan *et al.*, *JHEP* 11 (2018) 115, `arXiv:1808.06575`.

[620] CMS Collaboration, V. Khachatryan *et al.*, *JHEP* 12 (2015) 178, `arXiv:1510.04252`.

[621] S. P. Das, J. Hernandez-Sanchez, S. Moretti and A. Rosado, `arXiv:1806.08361`.

[622] H. Sun, X. Luo, W. Wei and T. Liu, *Phys. Rev.* D96 (2017) 095003, `arXiv:1710.06284`.

[623] G. Azuelos, H. Sun and K. Wang, *Phys. Rev.* D97 (2018) 116005, `arXiv:1712.07505`.

[624] CMS Collaboration, A. M. Sirunyan *et al.*, *Phys. Rev. Lett.* 119 (2017) 141802, `arXiv:1705.02942`.

[625] CMS Collaboration, A. M. Sirunyan *et al.*, *Phys. Rev. Lett.* 120 (2018) 081801, `arXiv:1709.05822`.

[626] C. Mosomane, M. Kumar, A. S. Cornell and B. Mellado, *J. Phys. Conf. Ser.* 889 (2017) 012004, `arXiv:1707.05997`.

[627] L. Delle Rose, O. Fischer and A. Hammad, *Int. J. Mod. Phys.* A34 (2019) 1950127, `arXiv:1809.04321`.

[628] CMS Collaboration, A. M. Sirunyan *et al.*, *JHEP* 06 (2018) 127, `arXiv:1804.01939`. [Erratum: *JHEP* 03 (2019) 128].

[629] CMS Collaboration, "Search for a new scalar resonance decaying to a pair of Z bosons at the High-Luminosity LHC," CMS-PAS-FTR-18-040, 2019.

[630] S. P. Das, J. Hernández-Sánchez, S. Moretti, A. Rosado and R. Xoxocotzi, *Phys. Rev.* D94 (2016) 055003, `arXiv:1503.01464`.

[631] S. P. Das and M. Nowakowski, *Phys. Rev.* D96 (2017) 055014, `arXiv:1612.07241`.

[632] A. Senol, *Nucl. Phys.* B873 (2013) 293, `arXiv:1212.6869`.

[633] I. T. Cakir, O. Cakir, A. Senol and A. T. Tasci, *Mod. Phys. Lett.* A28 (2013) 1350142, `arXiv:1304.3616`.

[634] H. Hesari, H. Khanpour and M. Mohammadi Najafabadi, *Phys. Rev.* D97 (2018) 095041, `arXiv:1805.04697`.

[635] S. Liu, Y.-L. Tang, C. Zhang and S.-h. Zhu, *Eur. Phys. J.* C77 (2017) 457, `arXiv:1608.08458`.

[636] D. Curtin, K. Deshpande, O. Fischer and J. Zurita, *JHEP* 07 (2018) 024, `arXiv:1712.07135`.

[637] G. Azuelos, M. D'Onofrio, S. Iwamoto and K. Wang, `arXiv:1912.03823`.

[638] C. Han, R. Li, R.-Q. Pan and K. Wang, *Phys. Rev.* D98 (2018) 115003, `arXiv:1802.03679`.

[639] S. Kuday, *J. Korean Phys. Soc.* 64 (2014) 1783, `arXiv:1304.2124`.

[640] R.-Y. Zhang, H. Wei, L. Han and W.-G. Ma, *Mod. Phys. Lett.* A29 (2014) 1450029, `arXiv:1401.4266`.

[641] X.-P. Li, L. Guo, W.-G. Ma, R.-Y. Zhang, L. Han and M. Song, *Phys. Rev.* D88 (2013) 014023, `arXiv:1307.2308`.

[642] J. A. Evans and D. Mckeen, "The Light Gluino Gap," 2018. `arXiv:1803.01880`.

[643] D. Curtin, K. Deshpande, O. Fischer and J. Zurita, *Phys. Rev.* D99 (2019) 055011, `arXiv:1812.01568`.

[644] S. Antusch and O. Fischer, *JHEP* 05 (2015) 053, `arXiv:1502.05915`.

[645] S. Antusch, E. Cazzato and O. Fischer, *Int. J. Mod. Phys.* A32 (2017) 1750078, `arXiv:1612.02728`.

[646] S. Antusch, O. Fischer and A. Hammad, `arXiv:1908.02852`.

[647] A. Das, S. Jana, S. Mandal and S. Nandi, *Phys. Rev.* D99 (2019) 055030, `arXiv:1811.04291`.

[648] ATLAS Collaboration, G. Aad *et al.*, `arXiv:1905.09787`.

[649] S. Antusch, E. Cazzato and O. Fischer, *Phys. Lett.* B774 (2017) 114, `arXiv:1706.05990`.

[650] DELPHI Collaboration, P. Abreu *et al.*, *Z. Phys.* C74 (1997) 57. [Erratum: *Z. Phys.* C75 (1997) 580].

[651] MEG Collaboration, J. Adam *et al.*, *Phys. Rev. Lett.* 110 (2013) 201801, `arXiv:1303.0754`.

[652] L. Duarte, G. A. González-Sprinberg and O. A. Sampayo, *Phys. Rev.* D91 (2015) 053007, `arXiv:1412.1433`.

[653] L. Duarte, G. Zapata and O. A. Sampayo, *Eur. Phys. J.* C78 (2018) 352, `arXiv:1802.07620`.

[654] S. Mondal and S. K. Rai, *Phys. Rev.* D93 (2016) 011702, `arXiv:1510.08632`.

[655] M. Lindner, F. S. Queiroz, W. Rodejohann and C. E. Yaguna, *JHEP* 06 (2016) 140, `arXiv:1604.08596`.

[656] S. Mondal and S. K. Rai, *Phys. Rev.* D94 (2016) 033008, `arXiv:1605.04508`.

[657] A. Das and S. Mandal, `arXiv:2006.04123`.

[658] Planck Collaboration, N. Aghanim *et al.*, `arXiv:1807.06209`.

[659] S. Jana, N. Okada and D. Raut, `arXiv:1911.09037`.

[660] A. Das, S. Mandal and T. Modak, `arXiv:2005.02267`.

[661] B. Holdom, *Phys. Lett.* 166B (1986) 196.

[662] M. D'Onofrio, O. Fischer and Z. S. Wang, "Searching for Dark Photons at the LHeC and FCC-he," 2019. `arXiv:1909.02312`.

[663] LHCb Collaboration, R. Aaij *et al.*, *Phys. Rev. Lett.* 120 (2018) 061801, `arXiv:1710.02867`.

[664] S. Heeba and F. Kahlhoefer, "Probing the freeze-in mechanism in dark matter models with $U(1)'$ gauge extensions," 2019. `arXiv:1908.09834`.

[665] C.-X. Yue, M.-Z. Liu and Y.-C. Guo, *Phys. Rev.* D100 (2019) 015020, `arXiv:1904.10657`.

[666] K. O. Mikaelian, M. A. Samuel and D. Sahdev, *Phys. Rev. Lett.* 43 (1979) 746.

[667] S. J. Brodsky and R. W. Brown, *Phys. Rev. Lett.* 49 (1982) 966.

[668] R. W. Brown, K. L. Kowalski and S. J. Brodsky, *Phys. Rev.* D28 (1983) 624. [Addendum: Phys. Rev.D29,2100(1984)].

[669] M. A. Samuel and J. H. Reid, *Prog. Theor. Phys.* 76 (1986) 184.

[670] HFLAV Collaboration, Y. S. Amhis *et al.*, `arXiv:1909.12524`.

[671] J. C. Pati and A. Salam, *Phys. Rev.* D10 (1974) 275. [Erratum: *Phys. Rev.* D11 (1975) 703].

[672] W. Buchmüller, R. Rückl and D. Wyler, *Phys. Lett.* B191 (1987) 442. [Erratum: *Phys. Lett.* B448 (1999) 320].

[673] I. Doršner, S. Fajfer, A. Greljo, J. F. Kamenik and N. Košnik, *Phys. Rept.* 641 (2016) 1, `arXiv:1603.04993`.

[674] ATLAS Collaboration, "ATLAS Exotics Searches,". `https://atlas.web.cern.ch/Atlas/GROUPS/PHYSICS/CombinedSummaryPlots/EXOTICS/ATLAS_Exotics_Summary/ATLAS_Exotics_Summary.pdf`.

[675] CMS Collaboration, "Overview of CMS Exo Results,". `http://cms-results.web.cern.ch/cms-results/public-results/publications/EXO/index.html`.

[676] J. Zhang, C.-X. Yue and Z.-C. Liu, *Mod. Phys. Lett.* A33 (2018) 1850039.

[677] I. Doršner and A. Greljo, *JHEP* 05 (2018) 126, `arXiv:1801.07641`.

[678] M. Bahr *et al.*, *Eur. Phys. J.* C58 (2008) 639, `arXiv:0803.0883`.

[679] S. Mandal, M. Mitra and N. Sinha, *Phys. Rev.* D98 (2018) 095004, `arXiv:1807.06455`.

[680] R. Padhan, S. Mandal, M. Mitra and N. Sinha, `arXiv:1912.07236`.

[681] S. Antusch, A. Hammad and A. Rashed, `arXiv:2003.11091`.

[682] ATLAS Collaboration, M. Aaboud *et al.*, *Phys. Rev.* D98 (2018) 092008, `arXiv:1807.06573`.

[683] ATLAS Collaboration, G. Aad *et al.*, *Phys. Lett.* B796 (2019) 68, `arXiv:1903.06248`.

[684] BaBar Collaboration, B. Aubert *et al.*, *Phys. Rev. Lett.* 104 (2010) 021802, `arXiv:0908.2381`.

[685] K. Hayasaka *et al.*, *Phys. Lett.* B687 (2010) 139, `arXiv:1001.3221`.

[686] Y.-J. Zhang, L. Han and Y.-B. Liu, *Phys. Lett.* B768 (2017) 241.

[687] Y.-B. Liu, *Nucl. Phys.* B923 (2017) 312, `arXiv:1704.02059`.

[688] L. Han, Y.-J. Zhang and Y.-B. Liu, *Phys. Lett.* B771 (2017) 106.

[689] A. Ozansoy, V. Arı and V. Çetinkaya, *Adv. High Energy Phys.* 2016 (2016) 1739027, `arXiv:1607.04437`.

[690] A. Caliskan, *Adv. High Energy Phys.* 2017 (2017) 4726050, `arXiv:1706.09797`.

[691] A. Caliskan and S. O. Kara, *Int. J. Mod. Phys.* A33 (2018) 1850141, `arXiv:1806.02037`.

[692] Y. O. Günaydın, M. Sahin and S. Sultansoy, *Acta Phys. Polon.* B49 (2018) 1763, `arXiv:1707.00056`.

[693] M. Sahin, *Acta Phys. Polon.* B45 (2014) 1811, `arXiv:1302.5747`.

[694] Y. C. Acar, U. Kaya, B. B. Oner and S. Sultansoy, *J. Phys.* G44 (2017) 045005, `arXiv:1605.08028`.

[695] ZEUS Collaboration, H. Abramowicz *et al.*, *Phys. Lett.* B757 (2016) 468, `arXiv:1604.01280`.

[696] A. F. Zarnecki, "Leptoquarks and Contact Interactions at LeHC," in *Proceedings, 16th International Workshop on Deep Inelastic Scattering and Related Subjects (DIS 2008): London, UK, April 7-11, 2008*, 2008. `arXiv:0809.2917`.

[697] P. C. M. Yock, *Int. J. Theor. Phys.* 2 (1969) 247.

[698] J. S. Schwinger, *Science* 165 (1969) 757.

[699] ATLAS Collaboration, G. Aad *et al.*, *Phys. Rev. Lett.* 124 (2020) 031802, `arXiv:1905.10130`.

[700] R. Hofstadter, *Rev. Mod. Phys.* 28 (1956) 214.

[701] A. F. Zarnecki, *Eur. Phys. J.* C11 (1999) 539, `arXiv:hep-ph/9904334`.

[702] ATLAS Collaboration, M. Aaboud *et al.*, *JHEP* 10 (2017) 182, `arXiv:1707.02424`.

[703] CMS Collaboration, A. M. Sirunyan *et al.*, *JHEP* 04 (2019) 114, `arXiv:1812.10443`.

[704] A. Michel and M. Sher, *Phys. Rev.* D100 (2019) 095011, `arXiv:1909.10627`.

[705] G. R. Boroun, *Chin. Phys.* C41 (2017) 013104, `arXiv:1510.02914`.

[706] G. R. Boroun, B. Rezaei and S. Heidari, *Int. J. Mod. Phys.* A32 (2017) 1750197, `arXiv:1606.02864`.

[707] H.-Y. Bi, R.-Y. Zhang, H.-Y. Han, Y. Jiang and X.-G. Wu, *Phys. Rev.* D95 (2017) 034019, `arXiv:1612.07990`.

[708] K. He, H.-Y. Bi, R.-Y. Zhang, X.-Z. Li and W.-G. Ma, *J. Phys.* G45 (2018) 055005, `arXiv:1710.11508`.

[709] H.-Y. Bi, R.-Y. Zhang, X.-G. Wu, W.-G. Ma, X.-Z. Li and S. Owusu, *Phys. Rev.* D95 (2017) 074020, `arXiv:1702.07181`.

[710] ATLAS Collaboration, "Prospect for a measurement of the Weak Mixing Angle in $pp \to Z/\gamma^* \to e^+ e^-$ events with the ATLAS detector at the High Luminosity Large Hadron Collider," ATL-PHYS-PUB-2018-037, CERN, Geneva, Nov 2018. `https://cds.cern.ch/record/2649330`.

[711] CMS Collaboration, "A proposal for the measurement of the weak mixing angle at the HL-LHC," CMS-PAS-FTR-17-001, CERN, Geneva, 2017. `https://cds.cern.ch/record/2294888`.

[712] W. J. Barter, "Prospects for measurement of the weak mixing angle at LHCb," LHCb-PUB-2018-013. CERN-LHCb-PUB-2018-013, CERN, Geneva, Nov 2018. `https://cds.cern.ch/record/2647836`.

[713] L. A. Harland-Lang, A. D. Martin, P. Motylinski and R. S. Thorne, *Eur. Phys. J.* C75 (2015) 204, `arXiv:1412.3989`.

[714] S. Dulat *et al.*, *Phys. Rev.* D93 (2016) 033006, `arXiv:1506.07443`.

[715] ATLAS Collaboration, G. Aad *et al.*, *JHEP* 09 (2015) 049, `arXiv:1503.03709`.

[716] ATLAS Collaboration, "Prospects for the measurement of the W-boson mass at the HL- and HE-LHC," ATL-PHYS-PUB-2018-026, CERN, Geneva, Oct 2018. `http://cds.cern.ch/record/2645431`.

[717] F. Zimmermann, *ICFA Beam Dynamics Newsletter* 72 (2017) 138.

[718] M. E. Peskin and T. Takeuchi, *Phys. Rev.* D46 (1992) 381.

[719] J. De Blas *et al.*, *Eur. Phys. J.* C80 (2020) 456, `arXiv:1910.14012`.

[720] M. Cepeda *et al.*, *CERN Yellow Rep. Monogr.* 7 (2019) 221, `arXiv:1902.00134`.

[721] J. Campbell and T. Neumann, *JHEP* 12 (2019) 034, `arXiv:1909.09117`.

[722] B. Mistlberger, *JHEP* 05 (2018) 028, `arXiv:1802.00833`.

[723] F. Dulat, A. Lazopoulos and B. Mistlberger, *Comput. Phys. Commun.* 233 (2018) 243, `arXiv:1802.00827`.

[724] LHC Higgs Cross Section Working Group Collaboration, A. David *et al.*, "LHC HXSWG interim recommendations to explore the coupling structure of a Higgs-like particle," 2012. `arXiv:1209.0040`.

[725] ATLAS Collaboration, G. Aad *et al.*, *Phys. Rev.* D101 (2020) 012002, `arXiv:1909.02845`.

[726] J. de Blas *et al.*, *JHEP* 01 (2020) 139, `arXiv:1905.03764`.

[727] ATLAS Collaboration, "Study of correlation of PDF uncertainty in single top and top pair production at the LHC," ATL-PHYS-PUB-2015-010, Geneva, May 2015.

[728] CMS Collaboration, V. Khachatryan *et al.*, *Phys. Rev.* D94 (2016) 072002, `arXiv:1605.00116`.

[729] Tevatron Electroweak Working Group, T. Aaltonen *et al.*, "Combination of CDF and D0 results on the mass of the top quark using up 9.7 fb^{-1} at the Tevatron," 2016. `arXiv:1608.01881`.

[730] CMS Collaboration, V. Khachatryan *et al.*, *Phys. Rev.* D93 (2016) 072004, `arXiv:1509.04044`.

[731] ATLAS Collaboration, M. Aaboud *et al.*, *Phys. Lett.* B761 (2016) 350, `arXiv:1606.02179`.

[732] CMS Collaboration, A. M. Sirunyan *et al.*, *Eur. Phys. J.* C77 (2017) 354, `arXiv:1703.02530`.

[733] CMS Collaboration, A. M. Sirunyan *et al.*, *Eur. Phys. J.* C78 (2018) 891, `arXiv:1805.01428`.

[734] ATLAS Collaboration, "Prospects for measurement of the top quark mass using $t\bar{t}$ events with $J/\psi \to \mu^+\mu^-$ decays with the upgraded ATLAS detector at the High Luminosity LHC," ATL-PHYS-PUB-2018-042, Geneva, Dec 2018. `http://cds.cern.ch/record/2649882`.

[735] D. Britzger, K. Rabbertz, D. Savoiu, G. Sieber and M. Wobisch, *Eur. Phys. J.* C79 (2019) 68, `arXiv:1712.00480`.

[736] ATLAS Collaboration, M. Aaboud *et al.*, *Phys. Rev.* D98 (2018) 092004, `arXiv:1805.04691`.

[737] ATLAS Collaboration, M. Aaboud *et al.*, *Eur. Phys. J.* C77 (2017) 872, `arXiv:1707.02562`.

[738] M. Johnson and D. Maître, *Phys. Rev.* D97 (2018) 054013, `arXiv:1711.01408`.

[739] T. Klijnsma, S. Bethke, G. Dissertori and G. P. Salam, *Eur. Phys. J.* C77 (2017) 778, `arXiv:1708.07495`.

[740] CMS Collaboration, A. M. Sirunyan *et al.*, *Submitted to: Eur. Phys. J.* (2019) , `arXiv:1904.05237`.

[741] CMS Collaboration, A. M. Sirunyan *et al.*, "Determination of the strong coupling constant $\alpha_S(m_Z)$ from measurements of inclusive W$^\pm$ and Z boson production cross sections in proton-proton collisions at $\sqrt{s} = 7$ and 8 TeV," 2019. `arXiv:1912.04387`.

[742] D. d'Enterria and A. Poldaru, *JHEP* 06 (2020) 016, `arXiv:1912.11733`.

[743] B. Bouzid, F. Iddir and L. Semlala, `arXiv:1703.03959`.

[744] M. Grazzini, S. Kallweit, D. Rathlev and M. Wiesemann, *Phys. Lett.* B761 (2016) 179, `arXiv:1604.08576`.

[745] M. Grazzini, S. Kallweit and M. Wiesemann, *Eur. Phys. J.* C78 (2018) 537, `arXiv:1711.06631`.

[746] ATLAS Collaboration, M. Aaboud *et al.*, *Eur. Phys. J.* C79 (2019) 535, `arXiv:1902.05759`. Auxiliary figure.

[747] CMS Collaboration, A. M. Sirunyan *et al.*, *JHEP* 04 (2019) 122, `arXiv:1901.03428`.

[748] X. Cid Vidal *et al.*, *CERN Yellow Rep. Monogr.* 7 (2019) 585, `arXiv:1812.07831`.

[749] ATLAS Collaboration, M. Aaboud *et al.*, *Phys. Rev.* D97 (2018) 112001, `arXiv:1712.02332`.

[750] CMS Collaboration, A. M. Sirunyan *et al.*, *JHEP* 05 (2018) 025, `arXiv:1802.02110`.

[751] NNPDF Collaboration, R. D. Ball *et al.*, *JHEP* 04 (2015) 040, `arXiv:1410.8849`.

[752] C. Schmidt, J. Pumplin, C. P. Yuan and P. Yuan, *Phys. Rev.* D98 (2018) 094005, `arXiv:1806.07950`.

[753] B.-T. Wang, T. J. Hobbs, S. Doyle, J. Gao, T.-J. Hou, P. M. Nadolsky and F. I. Olness, *Phys. Rev.* D98 (2018) 094030, `arXiv:1803.02777`.

[754] T. J. Hobbs, B.-T. Wang, P. M. Nadolsky and F. I. Olness, *PoS* DIS2019 (2019) 247, `arXiv:1907.00988`.

[755] C. Brenner Mariotto and M. Machado, *Phys. Rev. D* 86 (2012) 033009, `arXiv:1208.5685`.

[756] R. Coelho and V. Goncalves, `arXiv:2002.10713`.

[757] R. Coelho and V. Goncalves, *Nucl. Phys. B* 956 (2020) 115013.

[758] M. Bonvini, *Eur. Phys. J. C* 78 (2018) 834, `arXiv:1805.08785`.

[759] M. Bonvini, R. Gauld, T. Giani and S. Marzani in preparation.

367

[760] M. Bonvini and F. Silvetti in preparation.

[761] J. C. Collins, D. E. Soper and G. F. Sterman, *Nucl. Phys. B* 250 (1985) 199.

[762] R. Angeles-Martinez *et al.*, *Acta Phys. Polon. B* 46 (2015) 2501, arXiv:1507.05267.

[763] M. Diehl, *Eur. Phys. J. A* 52 (2016) 149, arXiv:1512.01328.

[764] T. C. Rogers, *Eur. Phys. J. A* 52 (2016) 153, arXiv:1509.04766.

[765] I. Balitsky and A. Tarasov, *JHEP* 06 (2016) 164, arXiv:1603.06548.

[766] S. Catani, M. Ciafaloni and F. Hautmann, *Phys. Lett.* B242 (1990) 97.

[767] S. Catani, M. Ciafaloni and F. Hautmann, *Nucl. Phys. B* 366 (1991) 135.

[768] J. C. Collins and R. Ellis, *Nucl. Phys. B* 360 (1991) 3.

[769] E. Levin, M. Ryskin, Y. Shabelski and A. Shuvaev, *Sov. J. Nucl. Phys.* 53 (1991) 657.

[770] T. Altinoluk and R. Boussarie, *JHEP* 10 (2019) 208, arXiv:1902.07930.

[771] N. Armesto and E. Scomparin, *Eur. Phys. J. Plus* 131 (2016) 52, arXiv:1511.02151.

[772] W. Busza, K. Rajagopal and W. van der Schee, *Ann. Rev. Nucl. Part. Sci.* 68 (2018) 339, arXiv:1802.04801.

[773] P. Romatschke and U. Romatschke, *Relativistic Fluid Dynamics In and Out of Equilibrium*. Cambridge Monographs on Mathematical Physics. Cambridge University Press, 2019. arXiv:1712.05815.

[774] Y. Mehtar-Tani, J. G. Milhano and K. Tywoniuk, *Int. J. Mod. Phys.* A28 (2013) 1340013, arXiv:1302.2579.

[775] A. Andronic *et al.*, *Eur. Phys. J.* C76 (2016) 107, arXiv:1506.03981.

[776] "Proceedings, 9th International Conference on Hard and Electromagnetic Probes of High-Energy Nuclear Collisions: Hard Probes 2018 (HP2018)," SISSA, 2018. https://pos.sissa.it/345.

[777] H. A. Andrews *et al.*, arXiv:1808.03689.

[778] ALICE Collaboration, B. B. Abelev *et al.*, *Phys. Lett.* B734 (2014) 314, arXiv:1311.0214.

[779] H. Song, S. A. Bass, U. Heinz, T. Hirano and C. Shen, *Phys. Rev. Lett.* 106 (2011) 192301, arXiv:1011.2783. [Erratum: *Phys. Rev. Lett.* 109 (2012) 139904].

[780] H. Niemi, K. J. Eskola and R. Paatelainen, *Phys. Rev.* C93 (2016) 024907, arXiv:1505.02677.

[781] J. Liu, C. Shen and U. Heinz, *Phys. Rev.* C91 (2015) 064906, arXiv:1504.02160. [Erratum: *Phys. Rev.* C92 (2015) 049904].

[782] B. Schenke, P. Tribedy and R. Venugopalan, *Phys. Rev. Lett.* 108 (2012) 252301, arXiv:1202.6646.

[783] J.-Y. Ollitrault, A. M. Poskanzer and S. A. Voloshin, *Phys. Rev.* C80 (2009) 014904, arXiv:0904.2315.

[784] STAR Collaboration, J. Adams *et al.*, *Phys. Rev.* C72 (2005) 014904, arXiv:nucl-ex/0409033.

[785] STAR Collaboration, B. I. Abelev *et al.*, *Phys. Rev.* C79 (2009) 034909, arXiv:0808.2041.

[786] CMS Collaboration, A. M. Sirunyan *et al.*, arXiv:1905.01486.

[787] V. Guzey and M. Zhalov, *JHEP* 10 (2013) 207, arXiv:1307.4526.

[788] J. G. Contreras, *Phys. Rev.* C96 (2017) 015203, arXiv:1610.03350.

[789] V. Guzey and M. Klasen, *Eur. Phys. J.* C79 (2019) 396, arXiv:1902.05126.

[790] ATLAS Collaboration, M. Aaboud *et al.*, *Phys. Rev. Lett.* 121 (2018) 212301, arXiv:1806.08708.

[791] ATLAS Collaboration, M. Aaboud *et al.*, *Phys. Rev.* C100 (2019) 034903, arXiv:1901.10440.

[792] R. Aaij *et al.*, "Expression of Interest for a Phase-II LHCb Upgrade: Opportunities in flavour physics, and beyond, in the HL-LHC era," CERN-LHCC-2017-003, CERN, Geneva, Feb 2017.

[793] O. Brüning, "Accelerator design." Presented at the lhec workshop, June 2015. https://indico.cern.ch/event/356714/contributions/844912/.

[794] D. Brandt, H. Burkhardt, M. Lamont, S. Myers and J. Wenninger, *Rept. Prog. Phys.* 63 (2000) 939.

[795] D. Pellegrini, A. Latina, D. Schulte and S. A. Bogacz, *Phys. Rev. ST Accel. Beams* 18 (2015) 121004.

[796] S. A. Bogacz *et al.*, *ICFA Beam Dynamics Newsletter* 71 (2017) 135.

[797] P. Williams, "A Staged, Multi-User X-Ray Free Electron Laser and Nuclear Physics Facility based on a Multi-Pass Recirculating Superconducting CW Linac," in *Proceedings, Future Light Sources 2018, Shanghai*, 2018.

[798] 12 GeV CEBAF Upgrade, Reference Design: www.jlab.org/physics/GeV/accelerator (2012).

[799] G. H. Hoffstaetter and I. V. Bazarov, *Phys. Rev. ST Accel. Beams* 7 (2004) 054401, arXiv:physics/0405106.

[800] J. S. Schwinger, *Phys. Rev.* 70 (1946) 798.

[801] D. Pellegrini, *Ph.D. Thesis, EPFL, Switzerland* (2016) .

[802] A. Milanese, *Talk presented at the LHeC workshop at CERN* (2014) .

[803] J. Jowett *et al.*, "The 2018 heavy-ion run of the LHC," in *Proceedings, 10th International Particle Accelerator Conference (IPAC2019): Melbourne, Australia, May 19-24, 2019*, 2019.

[804] T. Argyropoulos, T. Bohl, A. Lasheen, G. Papotti, D. Quartullo and E. Shaposhnikova, "Momentum slip-stacking in CERN SPS for the ion beams," in *Proceedings, 10th International Particle Accelerator Conference (IPAC2019): Melbourne, Australia, May 19-24, 2019*, 2019.

[805] M. Schaumann, *Phys. Rev. ST Accel. Beams* 18 (2015) 091002, arXiv:1503.09107.

[806] O. Brüning *et al.*, *ICFA Beam Dynamics Newsletter* 68 (2015) 46.

[807] R. Calaga and E. Jensen, "A Proposal for an ERL Test Facility at CERN," in *Proceedings, 4th International Particle Accelerator Conference (IPAC 2013): Shanghai, China, May 12-17, 2013*, 2013. http://JACoW.org/IPAC2013/papers/wepwo049.pdf.

[808] F. Marhauser, "Cost Rationales for an SRF Proton Linac," in *Proceedings, 5th International Particle Accelerator Conference (IPAC 2014): Dresden, Germany, June 15-20, 2014*, 2014.

[809] F. Marhauser, "Recent results on a multi-cell 802 mhz bulk nb cavity." Presented at fcc week 2018, https://indico.cern.ch/event/656491/contributions/2932251/attachments/1629681/2597650/5_cell_Cavity_Marhauser.pdf, 2018.

[810] W. Schneider, I. Campisi, E. Daly *et al.*, "Design of the sns cryomodule," in *Proceedings, the 2001 Particle Accelerator Conference (PACS2001)*, 2001.

[811] V. Parma *et al.*, "Conceptual design of the superconducting proton linac short cryo-module," in *Proceedings of the SRF2011, Chicago, July*, 2011.

[812] G. Olivier, J. Thermeau and P. Bosland, "Ess cryomodules for elliptical cavities," in *Proceedings of the 2013 Superconducting Radio Frequency Conference*, 2013.

[813] H. Bluem, D. Dowell, A. Todd and L. Young, "High Brightness Thermionic Electron Gun Performance," in *Procings, 50th Advanced ICFA Beam Dynamics Workshop on Energy Recovery Linacs (ERL'11), Tsukuba, Japan, Oct. 2011*, 2011.

[814] F. Sannibale *et al.*, "The VHF-Gun, the LBNL High-Brightness Electron Photo-Injector for MHz-Class Repetition-Rate Applications," in *High-Brightness Sources and Light-Driven Interactions*, Optical Society of America, 2016.

[815] Z. Wang, Q. Gu, G. Wang and M. Zhao, "Injector Physics Design at SHINE," in *Proceedings, 10th International Particle Accelerator Conference (IPAC'19), Melbourne, Australia, 19-24 May 2019*, JACoW Publishing, Geneva, Switzerland, Jun. 2019.

[816] G. Shu, Y. Chen, S. Lal, H. Qian, H. Shaker and F. Stephan, "FIRST DESIGN STUDIES OF A NC CW RF GUN FOR EUROPEAN XFEL," in *Proceedings, 10th International Particle Accelerator Conference (IPAC'19), Melbourne, Australia, 19-24 May 2019*, JACoW Publishing, Geneva, Switzerland, Jun. 2019.

[817] J. Teichert *et al.*, *Nuclear Instruments and Methods in Physics Research Section A: Accelerators, Spectrometers, Detectors and Associated Equipment* 743 (2014) 114.

[818] J. Bisognano *et al.*, "Wisconsin srf electron gun commisioning," in *Proceedings, North American Particle Accelerator Conf. (NAPAC'13), Pasadena, CA, USA, Sep.-Oct. 2013*, 09 2013. http://accelconf.web.cern.ch/AccelConf/PAC2013/papers/tupma19.pdf.

[819] E. Vogel *et al.*, "SRF Gun Development at DESY," JACoW, Geneva, Sep 2018.

[820] A. Neumann, and others, "Status of SRF Gun for bERLinPro," in *Proceedings, ERL'19, Berlin, Germany, Sept. 2019*, 2019.

[821] Belomestnykh, S.A. and others, "Commissioning of the 112 MHz SRF Gun," in *Proceedings, 17th Int. Conf. RF Superconductivity, Whistler, Canada, Sep. 2015*, 2015.

[822] Hernandez-Garcia, C. and others, "JLab FEL DC Gun," in *Proceedings, 45th ICFA Advanced Beam Dynamics Workshop on Energy Recovery LINAC Workshop (ERL'09), Ithaca, NY, USA, June 2009* , 2009.

369

[823] L. B. Jones, J. W. McKenzie, K. J. Middleman, B. L. Militsyn, Y. M. Saveliev and S. L. Smith, *Journal of Physics: Conference Series* 298 (2011) 012007.

[824] R. Kato, Y. Honda, H. Kawata, T. Miyajima, N. Nakamura, H. Sakai, M. Shimada, Y. Tanimoto, K. Tsuchiya, "Ir-fel project at the cerl and future euv-fel lithography," in *Presented at the 39th Int. Free Electron Laser Conf. (FEL'19), Hamburg, Germany, Aug. 2019*, 2019.

[825] Hoffstaetter, G.H. and others, "CBETA: The Cornell/BNL 4-turn ERL with FFAG Return Arcs for eRHIC Prototyping," in *Proceedings, 28th Linear Accelerator Conf. (LINAC'16)*, East Lansing, MI, USA, 2016.

[826] B. Hounsell, W. Kaabi, M. Klein, B. Militsyn and C. Welsch, "Optimisation of the PERLE injector," in *Proceedings, ERL'19, Berlin, Germany, Sept. 2019*, 2019.

[827] R. Suleiman, P. Adderley, J. Grames, J. Hansknecht, M. Poelker and M. Stutzman, *AIP Conference Proceedings* 1970 (2018) 050007, https://aip.scitation.org/doi/pdf/10.1063/1.504022.

[828] C. K. Sinclair *et al.*, "Performance of a very high voltage photoemission electron gun for a high brightness, high average current ERL injector," in *Proceedings, 22nd Particle Accelerator Conf. (PAC'07), Albuquerque, NM, USA*, 2007. https://accelconf.web.cern.ch/AccelConf/p07/PAPERS/TUPMS021.PDF.

[829] N. Nishimori, R. Nagai, S. Matsuba, R. Hajima, M. Yamamoto, T. Miyajima, Y. Honda, H. Iijima, M. Kuriki and M. Kuwahara, *Applied Physics Letters* 102 (2013) 234103.

[830] N. Nishimori, R. Nagai, R. Hajima, M. Yamamoto, Y. Honda, T. Miyajima and T. Uchiyama, *Phys. Rev. Accel. Beams* 22 (2019) 053402.

[831] W. Liu, Y. Chen, W. Lu, A. Moy, M. Poelker, M. Stutzman and S. Zhang, *Applied Physics Letters* 109 (2016) 252104, https://doi.org/10.1063/1.4972180.

[832] E. Wang, *AIP Conference Proceedings* 1970 (2018) 050008, https://aip.scitation.org/doi/pdf/10.1063/1.5040227.

[833] A. Sokolov and I. Ternov, *Sov. Phys. Dokl.* 8 (1964) 1203.

[834] F. Zimmermann, O. Brüning and M. Klein, "The LHeC as a Higgs Boson Factory," in *4th International Particle Accelerator Conference*, 2013.

[835] M. Antonelli, M. Boscolo, R. Di Nardo and P. Raimondi, *Nucl. Instrum. Meth. A* 807 (2016) 101, arXiv:1509.04454.

[836] M. Boscolo, M. Antonelli, O. Blanco-Garcia, S. Guiducci, S. Liuzzo, P. Raimondi and F. Collamati, *Phys. Rev. Accel. Beams* 21 (2018) 061005, arXiv:1803.06696.

[837] M. Aicheler, P. Burrows, M. Draper, T. Garvey, P. Lebrun, K. Peach, N. Phinney, H. Schmickler, D. Schulte and N. Toge, "A Multi-TeV Linear Collider Based on CLIC Technology: CLIC Conceptual Design Report," CERN-2012-007, Oct 2012.

[838] C. Adolphsen *et al.*, "The International Linear Collider Technical Design Report - Volume 3.II: Accelerator Baseline Design," Jun 2013. arXiv:1306.6328.

[839] P. Bambade *et al.*, "The International Linear Collider: A Global Project," Mar 2019. arXiv:1903.01629.

[840] M. W. Krasny, "The Gamma Factory proposal for CERN," An Executive Summary of the Gamma Factory proposal addressed to the CERN management, Nov 2015. arXiv:1511.07794.

[841] F. Zimmermann, *J. Phys. Conf. Ser.* 1067 (2018) 022017.

[842] F. Zimmermann, H. Aksakal, A. Aksoy and Z. Nergiz, "Free electron laser driven by a high-energy high-current energy-recovery linac," in *10th International Particle Accelerator Conference*, 2019.

[843] A. Zaltsman and R. Lambiase, *Proceedings of the 24-th Particle Accelerator Conference, PAC-2011, TUP125* (2011) .

[844] B. Parker, "Latest Developments and Progress on the IR magnet design." presented at the LHeC and FCC-eh Workshop, Sept 2017.

[845] B. Parker, "Superconducting Magnet Concepts for Electron Hadron Collider IRs." Presented at the electrons for the lhc - lhec/fcceh and perle workshop, Sept 2018.

[846] E. Cruz-Alaniz, D. Newton, R. Tomás and M. Korostelev, *Phys. Rev. ST Accel. Beams* 18 (2015) 111001.

[847] R. Martin and R. Tomás Garcia, "Length optimization of the detector region dipoles in LHeC and FCC-eh," CERN-ACC-2018-0042, CERN, Geneva, Oct 2018. http://cds.cern.ch/record/2644892.

[848] S. Fartoukh, *Phys. Rev. ST Accel. Beams* 16 (2013) 111002.

[849] "Lattice repository." https://gitlab.cern.ch/lhec-optics/lhec-lattice, 2019.

[850] A. Gaddi, "Installation Issues of eh Detectors (LHC and FCC)," Talk presented at the LHeC and FCC-eh Workshop, CERN, Sept 2017.

[851] A. Gaddi. Private communication, Jan 2019.

[852] R. Bruce, C. Bracco, R. De Maria, M. Giovannozzi, S. Redaelli, R. Tomás Garcia, F. M. Velotti and J. Wenninger, "Updated parameters for HL-LHC aperture calculations for proton beams," CERN-ACC-2017-0051, CERN, Geneva, Jul 2017. https://cds.cern.ch/record/2274330.

[853] R. De Maria et al., "HLLHCV1.3 Optics repository." http://lhc-optics.web.cern.ch/lhc-optics/HLLHCV1.3/.

[854] E. Cruz-Alaniz, R. Martin and R. Tomás, "LHeC optics with $\beta^* = 10$ cm and $L^* = 15$ m," CERN-ACC-NOTE-2019-0049, CERN, Geneva, 2019. https://cds.cern.ch/record/2701426.

[855] Sixtrack web site: http://sixtrack.web.cern.ch/SixTrack/.

[856] E. Cruz-Alaniz, J. L. Abelleira, L. van Riesen-Haupt, A. Seryi, R. Martin and R. Tomás, "Methods to increase the dynamic aperture of the fcc-hh lattice," in *Proceedings. International Particle Accelerator Conference (IPAC'18), Vancouver, Canada, 2018*, JACoW, Geneva, Switzerland, May 2018. https://accelconf.web.cern.ch/AccelConf/ipac2018/papers/thpak145.pdf.

[857] F. Zimmermann et al., "Interaction-Region Design Options for a Linac-Ring LHeC," in *Proceedings, International Particle Accelerator Conference (IPAC'10), Kyoto, Japan, May 23-28, 2010*, JACoW, Geneva, Switzerland, May 2010.

[858] J. L. Abelleira, H. Garcia, R. Tomás and F. Zimmermann, "Final-Focus Optics for the LHeC Electron Beam Line," in *Proceedings, International Particle Accelerator Conference (IPAC'12), New Orleans, Louisiana, USA, May 20-25, 2012*, JACoW, Geneva, Switzerland, May 2012.

[859] LHeC Study Group, FCC-eh Study Group, PERLE Collaboration, G. Arduini, O. Brüning and M. Klein, *PoS* DIS2018 (2018) 183.

[860] R. Tomás, "LHeC interaction region," Talk presented at DIS 2012 Workshop, Bonn, 2012.

[861] J. A. Parrell, M. B. Field, Y. Zhang and S. Hong, *AIP Conf. Proc.* 711 (2004) 369–375.

[862] S. Russenschuck, *Field computation for accelerator magnets: analytical and numerical methods for electromagnetic design and optimization*. Wiley, Weinheim, 2010.

[863] E. Fern, V. Di Murro, K. Soga, Z. Li, J. Osborne and L. Scibile, *Tunnelling and Underground Space Technology* 77 (2018) 249.

[864] C. Laughton, *Int. J. of Mining and Geological Engineering* 6 (1988) 353.

[865] M. Tigner, *Nuovo Cim.* 37 (1965) 1228.

[866] V. Litvinenko et al., "Coherent Electron Cooling Experiment at RHIC: Status and Plans," in *12th International Workshop on Beam Cooling and Related Topics*, 2019.

[867] C. Tennant, "Energy Recovery Linacs," in *Challenges and Goals for Accelerators in the XXI Century*, O. Brüning and S. Myers (eds.), World Scientific, 2016.

[868] C. Tennant, "Progress at the Jefferson Laboratory FEL," in *Particle accelerator. Proceedings, 23rd Conference, PAC'09, Vancouver, Canada, May 4-8, 2009*, 2010. http://www1.jlab.org/Ul/publications/view_pub.cfm?pub_id=8641.

[869] G. H. Hoffstaetter and I. V. Bazarov, *Phys. Rev. ST Accel. Beams* 7 (2004) 054401.

[870] D. R. Douglas et al., *Phys. Rev. ST Accel. Beams* 9 (2006) 064403.

[871] S. Di Mitri, M. Cornacchia and S. Spampinati, *Phys. Rev. Lett.* 110 (2013) 014801.

[872] M. G. Fedurin, D. Kayran, V. Yakimenko, A. V. Fedotov, V. Litvinenko and P. Muggli, *Conf. Proc.* C110328 (2011) 1677.

[873] S. Heifets, G. Stupakov and S. Krinsky, *Phys. Rev. ST Accel. Beams* 5 (2002) 064401.

[874] Z. Huang and K.-J. Kim, *Phys. Rev. ST Accel. Beams* 5 (2002) 074401.

[875] S. Di Mitri and M. Cornacchia, *EPL (Europhysics Letters)* 109 (2015) 62002.

[876] C.-Y. Tsai, D. Douglas, R. Li and C. Tennant, *Phys. Rev. Accel. Beams* 19 (2016) 114401.

[877] C.-Y. Tsai, S. Di Mitri, D. Douglas, R. Li and C. Tennant, *Phys. Rev. Accel. Beams* 20 (2017) 024401.

[878] D. Douglas et al. Jefferson Laboratory Technical Note 12-017, 2012.

[879] R. Alarcon et al., *Phys. Rev. Lett.* 111 (2013) 164801.

[880] T. Powers and C. Tennant, "Implications of incomplete energy recovery in srf-based energy recovery linacs," in *Proceedings of the 2007 ICFA Workshop on Energy Recovery Linacs, Daresbury, UK*, 2007.

[881] S. Setiniyaz, R. Apsimon and P. Williams, *Phys. Rev. Accel. Beams* 23 (2020) 072002, arXiv:2001.04156.

[882] T. Powers, "Control of Microphonics for Narrow Control Bandwidth Cavities," Talk presented at the 2017 International Conference on RF Superconductivity, Lanzhou, China, 2017.

[883] S. Benson *et al.*, *Conf. Proc.* C070625 (2007) 79.

[884] T. Powers, "Optimization of SRF Linacs," in *Proceedings of the 2013 International Conference on RF Superconductivity, Paris, France*, 2013.

[885] S. Benson *et al.*, "Development of a Bunched-Beam Electron Cooler for the Jefferson Lab Electron-Ion Collider," in *Proceedings, 9th International Particle Accelerator Conference (IPAC 2018), Vancouver, BC Canada*, 2018.

[886] C. Tennant. https://userweb.jlab.org/~tennant/.

[887] C. Tennant, "Analysis of the Baseline PERLE Lattice," Jefferson Laboratory Technical Note 18-031, 2018.

[888] D. Douglas *et al.*, ""Why PERLE?" Historical Context and Technological Motivation," Jefferson Laboratory Technical Note 18-014, 2018.

[889] T. Satogata *et al.*, "ER@CEBAF: A test of 5-pass energy recovery at CEBAF," Program Advisory Committee Proposal, Jun 2016.

[890] A. Donnachie and P. Landshoff, *Phys. Lett.* B296 (1992) 227, arXiv:hep-ph/9209205.

[891] M. Frank, F. Gaede, M. Petric and A. Sailer, "Aidasoft/dd4hep," Oct. 2018.

[892] GEANT4 Collaboration, S. Agostinelli *et al.*, *Nucl. Instrum. Meth.* A506 (2003) 250.

[893] CMS Collaboration, G. Bianchi, *JINST* 9 (2014) C03054.

[894] I. Peric, *Nucl. Instrum. Meth.* A582 (2007) 876.

[895] A. Blondel *et al.*, "Research Proposal for an Experiment to Search for the Decay $\mu \to eee$," Jan 2013. arXiv:1301.6113.

[896] A. Schöning *et al.*, "MuPix and ATLASPix - Architectures and Results," in *28th International Workshop on Vertex Detectors*, Feb 2020. arXiv:2002.07253.

[897] M. Prathapan *et al.*, *PoS* TWEPP2019 (2020) 010.

[898] M. Dyndal *et al.*, *JINST* 15 (2020) P02005, arXiv:1909.11987.

[899] M. Oreglia, *A Study of the Reactions $\psi' \to \gamma\gamma\psi$*. PhD thesis. https://search.proquest.com/docview/303269954.

[900] J. E. Gaiser, *Charmonium Spectroscopy From Radiative Decays of the J/ψ and ψ'*. PhD thesis. https://search.proquest.com/docview/303269954.

[901] T. Skwarnicki, *A study of the radiative CASCADE transitions between the Upsilon-Prime and Upsilon resonances*. PhD thesis, Cracow, INP, 1986. http://www-library.desy.de/cgi-bin/showprep.pl?DESY-F31-86-02.

[902] ATLAS Collaborartion Collaboration, "Technical Design Report for the Phase-II Upgrade of the ATLAS Muon Spectrometer," 2017.

[903] CMS Collaboration, "The Phase-2 Upgrade of the CMS Muon Detectors," 2017.

[904] FP420 R&D Collaboration, M. G. Albrow *et al.*, *JINST* 4 (2009) T10001, arXiv:0806.0302.

[905] LHCf Collaboration, O. Adriani *et al.*, *Phys. Lett.* B780 (2018) 233, arXiv:1703.07678.